Antenna Shape Synthesis Using Characteristic Mode Concepts

Jonathan Ethier

A thesis submitted to the
Faculty of Graduate and Postdoctoral Studies
In partial fulfillment of the requirements
For the PhD degree in Electrical Engineering

Ottawa-Carleton Institute for Electrical and Computing Engineering
School of Electrical Engineering and Computer Science
Faculty of Engineering
University of Ottawa

Abstract

Characteristic modes (CMs) provide deep insight into the electromagnetic behaviour of any arbitrarily shaped conducting structure because the CMs are unique to the geometry of the object. We exploit this very fact by predicting a perhaps surprising number of important antenna metrics such as resonance frequency, radiation efficiency and antenna Q (bandwidth) without needing to specify a feeding location. In doing so, it is possible to define a collection of objective functions that can be used in an optimizer to shape-synthesize antennas without needing to define a feed location a priori. We denote this novel form of optimization “feedless” or “excitation-free” antenna shape synthesis. Fundamentally, we are allowing the electromagnetics to dictate how the antenna synthesis should proceed and are in no way imposing the physical constraints enforced by fixed feeding structures. This optimization technique is broadly applied to three major areas of antenna research: electrically small antennas, multi-band antennas and reflectarrays. Thus, the scope of applicability ranges from small antennas, to intermediate sizes and concludes with electrically large antenna designs, which is a testament to the broad applicability of characteristic mode theory. Another advantage of feedless electromagnetic shape synthesis is the ability to synthesize antennas whose desirable properties approach the fundamental limits imposed by electromagnetics. As an additional benefit, the feedless optimization technique is shown to have greater computational efficiency than traditional antenna optimization techniques.

Publications Related to PhD Work

[1] **J. Ethier** and D. A. McNamara, “A New Objective Function for the Synthesis of Electrically Small Antennas”, *URSI Radio Science Meeting Digest*, Charleston, North Carolina, USA, June 1 – 5, 2009

[2] **J. Ethier** and D. A. McNamara, “Through the Looking Glass: A Characteristic Mode View of Electromagnetic Modeling & Design”, *Proceedings of the 14th Int. Symposium on Antenna Technology & Applied Electromagnetics (ANTEM’2010)*, Ottawa, July 2010. [1]

[3] **J. Ethier** and D. A. McNamara, “The Use of the Generalized Port Mode Concept in MIMO Antenna Design”, *URSI Radio Science Meeting Digest*, Toronto, Canada, July 11 – 17, 2010.

[4] **J. Ethier** and D. A. McNamara, “An Examination of the Characteristic Modes of Lossy Structures”, *URSI Radio Science Meeting Digest*, Toronto, Canada, July 11 – 17, 2010.

[5] **J. Ethier** and D. A. McNamara, “Observations on the Characteristic Modes of Periodic Structures”, *URSI Radio Science Meeting Digest*, Toronto, Canada, July 11 – 17, 2010.

[6] **J. Ethier** and D. A. McNamara, “Multiband Antenna Synthesis using Characteristic Mode Indicators as an Objective Function for Optimization”, *2010 IEEE International Conference on Wireless Information Technology and Systems*, Hawaii, USA, August 27th – September 3rd, 2010. [Invited Paper]

[7] **J. Ethier** and D. A. McNamara, “Computational Estimates of Electrically Small Antenna High-Contrast Polarizabilities,” *IEEE Antennas and Wireless Propagation Letters*, Vol. 10, Nov. 2011, pp. 1309 – 1312.

[8] **J. Ethier** and D. McNamara, “A Sub-Structure Characteristic Mode Concept for Antenna Shape Synthesis,” *Electronics Letters*, Vol. 48, No. 9, April 2012, pp. 471 – 472.

[1] This paper received a “Best Student Paper Award”.

[9] J. Ethier and D. McNamara, “Further Applications of a Characteristic Mode Based Antenna Shape Synthesis Method”, *2012 IEEE International Conference on Wireless Information Technology and Systems*, Hawaii, USA, July 29 – August 3, 2012. [Invited Paper]

[10] **J. Ethier** and D. McNamara, “Predicting Infinite Periodic Structure Properties from Finite Structure Models,” *Accepted for Future Publication in Microwave and Optical Technology Letters*

[11] **J. Ethier** and D. McNamara, “Feedless Antenna Shape Synthesis,” *Manuscript in Preparation for Submission to Transactions on Antennas and Propagation*

[12] **J. Ethier** and D. McNamara, “Reflectarray Synthesis Using Fragmented Sub-Wavelength Elements,” *Manuscript in Preparation for Submission to Transactions on Antennas and Propagation.*

Other Publications

[1] **J. Ethier** and D. A. McNamara, “The Use of Generalized Modes in the Design of MIMO Antennas”, *IEEE Trans. on Magnetics*, Vol. 45, Number 3, March 2009, pp. 1124 – 1127.

[2] **J. Ethier** and D. A. McNamara, “An Interpretation of Mode-Decoupled MIMO Antennas in Terms of Characteristic Port Modes”, *IEEE Trans. on Magnetics*, Vol. 45, Number 3, March 2009, pp. 1128 – 1131.

[3] **J. Ethier** and D. A. McNamara, “A Modal Significance Measure in the Characteristic Mode Analysis of Radiating Structures”, *Electronics Letters*, Vol. 46, No. 2, January 21, 2010.

[4] P. Pelland, **J. Ethier**, D. J. Janse van Rensburg, D. A. McNamara, L. (Leili) Shafai and S. Mishra, “Towards routine automated error assessment in antenna spherical near-field measurements”, *Proc. of the 4th European Conf. on Antennas and Propagation (EuCAP 2010),* Barcelona, Spain, April 2010.

[5] P. Pelland, **J. Ethier**, D. J. Janse van Rensburg, D. A. McNamara, L. (Leili) Shafai and S. Mishra “Automated Error Assessment in the Spherical Near-Field Measurement of Antennas”, *URSI Radio Science Meeting Digest*, Toronto, Canada, July 2010.

[6] **J. Ethier**, M.R. Chaharmir, J. Shaker, “Novel Approach for Low-Loss Reflectarray Designs”, *IEEE Intl Symposium on Antennas and Propagation (URSI/APS)*, Spokane, Washington, USA, July 3 – 8, 2011.

[7] M.R. Chaharmir**, J. Ethier**, J. Shaker, D. Lee, " Novel Low-cost Reflectarray Designs for Commercial Applications," *33rd ESA Antenna Workshop*, Noordwijk, Netherlands, Oct. 18 – 21, 2011.

[8] **J. Ethier**, M. R. Chaharmir, J. Shaker, “Reflectarray design comprised of sub-wavelength coupled-resonant square loop elements,” *Electronics Letters*, Vol. 47, No. 22, October 27, 2011.

[9] **J. Ethier**, M. R. Chaharmir, J. Shaker, “Reflectarray Thinning using Sub-wavelength Coupled-Resonant Elements,” *Electronics Letters*, Vol. 48, No. 8, March 2012, pp. 359 – 360.

Acknowledgements

First and foremost I would like to thank my supervisor, Dr. Derek McNamara, for his contributions, discussions and constant support throughout the development of this thesis. His willingness to devote time and effort to his graduate students goes well beyond the call of duty for a thesis supervisor.

I would also like to acknowledge:

- NSERC and the University of Ottawa for the substantial financial support over the years.

- Dr. Aldo Petosa, Mr. Michel Cuhaci and Mr. David Lee at the Communications Research Centre Canada (CRC) for the gracious use of CRC's fabrication and measurement facilities.

- Research colleagues Dr. Reza Chaharmir, Dr. Jafar Shaker, Mr. Igor Acimovic and Mr. Eqab Almajali for their support in all things theoretical, measurement and otherwise.

Finally, I would like to thank my parents Donald and Anne Ethier for their guidance that began long before graduate studies. To my wife Dawn and daughters Charlotte, Elizabeth and Isadora – thank you for being supportive of this thorn among roses.

List of Symbols

a	radius of circumscribing sphere
$\underline{A}$	vector potential
c	velocity of light
D	antenna directivity
e_{rad}	radiation efficiency
$e_{rad,n}$	modal radiation efficiency
$\underline{E}_n$	characteristic electric fields
$\underline{E}^{inc}$	incident electric field
$\underline{E}^{inc}_{\tan}$	incident tangential electric field
f	frequency
$\underline{F}_n$	characteristic far-field pattern
G	antenna gain
$\underline{H}_n$	characteristic magnetic fields
I_{edge}	edge current coefficient (RWG)
I_{in}	input port current
j	imaginary unit, $\sqrt{-1}$
$\underline{J}$	arbitrary current density vector
J	arbitrary current density coefficients
$\underline{J}_n$	characteristic mode current density vector
J_n	characteristic mode current density coefficients
k	wave number
k_o	wave number at resonance
L	electric field integral equation operator
$L_{\tan}$	tangential electric field integral equation operator

ℓ_{edge}	length of common triangle edge, moment method
$\underline{n}$	normal unit vector
$O\left(N^m\right)$	order N^m operation
P	perturbation operator, continuous
$[P]$	perturbation operator, discrete
$P_{rad,n}$	modal radiated power
$P_{reac,n}$	modal reactive power
Q	antenna Q
Q_n	modal Q
Q_{chu}	Chu limit
Q_{lb}	lower bound on Q, geometry dependent
Q_{ratio}	ratio of antenna Q to lower bound
Q_{res}	antenna Q at resonance
r	radial distance
$\underline{r}$	radial vector, observation location
$\underline{r}'$	radial vector, source location
R	resistance operator, continuous form
$[R]$	resistance operator, discrete form
$[R]_{sub}$	sub-structure resistance operator, discrete form
S	scattering operator, continuous
$[S]$	scattering operator, discrete
S_∞	sphere at infinity
V_n^i	modal excitation coefficient
V_{in}	input port voltage
$W_{net,n}$	modal net stored energy

X	reactance operator, continuous form
$[X]$	reactance operator, discrete form
$[X]_{sub}$	sub-structure reactance operator, discrete form
Y_{in}	input admittance
Y_n	modal admittance
Z_{in}	input impedance
Z_n	modal resistance
Z	impedance operator, continuous form
$[Z]$	impedance operator, discrete form
Z_L	impedance loading operator, continuous form
$[Z_L]$	impedance loading operator, discrete form
$\left[Z^M\right]_{ps}$	IFF impedance matrix
$\left[Z^M\right]_{ps}^{avg}$	IFF impedance matrix, averaged
∇	gradient operator
$\nabla\cdot$	divergence operator
$\nabla\times$	curl operator
δ_{mn}	Kronecker delta
$\delta(\underline{r})$	delta function
ε	permittivity
μ	permeability
η	intrinsic impedance
$\tilde{\eta}$	absorption efficiency
η_i	illumination efficiency
η_s	spillover efficiency
η_p	phase efficiency
γ	static polarizability

γ_{norm}	normalized static polarizability
Φ	scalar potential
ψ	freespace Green's function
σ_a	absorption cross-section
σ_{ext}	extinction cross-section
α_n	modal expansion coefficient
λ_n	characteristic mode eigenvalue, perfect conductors
τ_n	characteristic mode eigenvalue, lossy conductors
Ψ	characteristic mode matrix trace
Ψ_{sub}	characteristic mode sub-structure matrix trace
ω	radial frequency
ω_o	resonant radial frequency
Γ	reflection coefficient
Γ_n	modal reflection coefficient
T	transmission coefficient
T_n	modal transmission coefficient

List of Acronyms

CM	Characteristic Mode
CP	Circular Polarization
CPM	Characteristic Port Mode
CRC	Communications Research Centre
DMM	Direct Matrix Manipulation
ESA	Electrically Small Antenna
FDTD	Finite Difference Time Domain
FEM	Finite Element Method
FR4	Flame Resistant 4
FSS	Frequency Selective Surface
LP	Linear Polarization
LPDA	Log Periodic Dipole Array
GA	Genetic Algorithm
GCM	Generalized Characteristic Mode
GCPM	Generalized Characteristic Port Mode
IFF	Infinite-from-Finite
MIMO	Multiple-input Multiple-output
MOM	Method of Moments
NVIS	Near Vertical Incidence Skywave
PEC	Perfect Electrical Conductor
PMC	Perfect Magnetic Conductor
RA	Reflectarray
RFID	Radio Frequency Identification
RWG	Rao-Wilton-Glisson expansion functions
SATCOM	Satellite Communications
SLL	Side Lobe Level
UAV	Unmanned Aerial Vehicle
UWB	Ultrawideband
VNA	Vector Network Analyzer

Table of Contents

Chapter 1

Introduction

1.1 – Introductory Remarks

It is indeed true that the ideal antenna synthesis procedure would allow one to “start with a set of electrical, mechanical, and system specifications that would lead to a particular antenna together with its specific geometry and material specification”, but that “this ideal general antenna synthesis method does not exist in the antenna field” [1]. Those synthesis methods already in use in antenna design can be categorized as excitation optimization, size optimization, shape optimization and material optimization.

Excitation optimization includes the determination of the complex excitations of an array of known radiating elements required to provide some desired radiation pattern performance [2, 3], usually called array pattern synthesis. *Size optimization* is the adjustment of the values of a pre-determined set of feature dimensions; the majority of antenna design procedures fall into this category. As its designation suggests, in *shape optimization* the shape of the final antenna structure is an outcome of the synthesis process, although there is usually some starting structure that is perturbed by the synthesis procedure and results in the final antenna shape. This category includes the shaping of reflector antenna surfaces to maximize gain [4] or to have radiation patterns other than pencil beams [5], with similar approaches for dielectric lenses [6]. The shape optimization of low gain microstrip [7, 8, 9] and wire antennas [10], with only the conductor geometry undergoing shaping through the removal or retention of conducting pixels/segments into which the starting shape is divided, has allowed miniaturization and bandwidth increases; the structural planarity is preserved, and so this can be described as two-dimensional shaping. The shaping of an antenna with its conductors confined to a spherical surface is described in [11]. Fully three-dimensional shaping of thin-wire antennas is performed in [12, 13, 14], with some restrictions placed on the allowed occupied volume to maintain a sense of practicality. The shaping of planar elements for frequency selective surfaces and reflectarrays is discussed in [15] and [16], respectively. Finally, the only antenna *material optimization* technique we are aware of used [17] a rectangular parallelepiped starting shape that is divided into voxels, which can individually be conducting or consist of dielectric/magnetic material.

The above classification is not a crisp one. For instance, we can define so many features whose dimensions may be adjusted, or represent the geometry in parameterized form and then adjust the parameters, that such adjustments for all practical purposes alter the antenna shape [18, 19, 20], and what might be thought of as size optimization then takes on the appearance of shape optimization. The categorization allows us to place the work of the thesis into context, namely shape optimization of antennas. However, there is one difference between this work and all previous methods: the feedpoint location and type is not specified prior to shaping. Once the optimum shape has been found we let the electromagnetics tell us where to locate the feed(s). This is made possible through the use of characteristic mode concepts in the definition of the objective functions to be extremized during antenna shape optimization.

Nature is inherently modal. Many phenomena, spanning engineering, physics, mathematics and the biological sciences, can be described in terms of modes. Modes have different definitions and properties. Natural modes, for example, are commonly encountered in science and engineering – these modes can exist without excitation and obey the boundary conditions imposed by the system they are described within. Hence, they are physical solutions. On the other hand, characteristic modes (the type of mode used throughout this thesis) exist without excitation but do not satisfy the necessary boundary conditions to allow them to be physical in their own right. However, all of the work contained in this thesis is concerned with antenna design. Antennas must have an incident field to be useful (i.e. the excitation of the antenna port or an impinging incident field destined to be scattered). The combination of the incident field and a single characteristic mode can be sufficient to yield a physical solution. A characteristic mode is non-physical (a mere basis function) unless an incident field is applied, at which point it becomes physical. This condition is always the case for an antenna problem and hence we shall judiciously apply characteristic mode theory in the feedless shape synthesis of antenna structures.

1.2 – Overview of Thesis

In Chapter 2, we will begin our discussion on the theory of characteristic modes (CMs), providing a thorough but succinct summary of their theoretical foundations. The generalized eigenvalue problem will be stated, with the resulting orthogonality properties of the eigenvectors, and the interpretation of the eigenvalues, subsequently discussed. This foray into CM theory will form the foundation upon which the remainder of the thesis is built. This theoretical discussion will be followed by a literature review of papers, theses and reports on the topic of CM theory. We will begin with a discussion on the foundational papers by Garbacz and Harrington, as well as additional CM formulations derived principally by researchers at Syracuse University in the 1970s and 1980s. Following these papers, a few publications investigated the application of CM theory on topics such as pattern synthesis and antenna placement. In recent years (2000s) there has been a resurgence of interest in CM theory, furthering the research on past topics but also delving into new topics such as multiple-input, multiple-output (MIMO) antenna design, mobile phone design, ultrawideband (UWB) antenna design, near vertical incidence skywave (NVIS) pattern synthesis, as well as interesting methods and formulations where the CMs are obtained analytically for canonical conducting structures. The resurgence of interest can be largely attributed to the increase in computational power and to the availability of commercial (and often free) moment method codes where one can obtain the discretized impedance operator and thus solve for the characteristic modes. We will show through the course of the literature review that the recent surge of interest has led to a plethora of qualitative results using CM theory, but only a few quantitative approaches where the researchers actively use the characteristic modes in the design and optimization process of antennas and electromagnetic structures.

In Chapter 3 we begin with the thorough analysis of the single-mode antenna[2]. We show that it is possible for a single-mode antenna (along with a single-mode scatterer) to have its electrical behaviour completely described by the properties of the antenna's (or scatterer's) single dominant characteristic mode. This special class of antennas and scatterers is therefore unique in that the entire characteristic mode spectrum is not required to describe its behaviour and thus the single dominant characteristic mode is electromagnetically complete if excited. We are most interested in exploiting the fact that this single-mode antenna behaviour is entirely described using the results of eigenanalysis, which is an

[2] The definition of "single-mode antenna" will be discussed in Chapter 3

inherently feedless form of analysis. This provides us with a truly unique method of synthesizing an antenna since one is no longer required (restricted) to defining a feed location at the start of a synthesis process. Eigenanalysis, however, is a computationally costly approach to use in the synthesis of antennas. To solve this problem, we exploit the matrix trace operator in lieu of the characteristic mode eigenvalue problem and develop a new technique to extract electromagnetic behaviour of an object without having to excite the structure or perform costly eigenanalysis. This computationally efficient approach leads us to define a new set of objective functions for the shape synthesis of single-mode antennas. These objective functions are specifically used in the optimization of electrically small antennas. Feedless optimization is shown to be computationally efficient and capable of synthesizing antennas with electrical performance that reaches fundamental electromagnetic limits of bandwidth. Abundant experimental results confirm these claims of optimality.

Extending the concepts of Chapter 3, we apply the feedless shape-synthesis approach to multi-band antennas in Chapter 4. Rectangular PEC plates are shape synthesized into having a dominant characteristic mode at a defined set of frequencies, with the single-mode condition being obtained at each of the desired bands. The lower frequency bands are shown to be in the electrically-small regime while the higher frequency bands placed the shape synthesized plates in intermediate electrically-sized regimes, thereby showing the applicability of the single mode concept beyond that of electrically small antennas. A limitation in the optimization process is found when inaccessible[3] dominant modes are present, which act to muddle the difference between directly excitable dominant modes and dominant modes that are inaccessible. A solution is found by defining a new modal formulation that we will call sub-structure characteristic modes. By numerically incorporating the presence of problematic regions where we know a priori that direct excitation will not be possible (or would be undesirable) the sub-structure characteristic modes allow for the feedless shape-synthesis of single-mode, multi-band antennas that would otherwise be multi-mode.

In Chapter 5, we explore the concept of characteristic mode analysis of periodic structures. Particular emphasis is placed on the single-mode periodic structure, weaving the thesis with a common thematic thread. Both free-standing periodic structures, and periodic structures with supporting infinite ground planes, are considered. Staying true to the theme of the thesis, we show that the various critical

[3] The term “inaccessible” will be defined in Chapter 4.

performance metrics of periodic structures can be obtained without having to directly excite the structure, thereby giving us access to quantities such as transmission and reflection coefficients in an excitation-free formulation. Additionally, computationally simple shortcuts are derived using the matrix trace, similar to what was done in Chapters 3 and 4, which allows for simpler and unambiguous retrieval of transmission and reflection coefficients for both free-standing and ground plane backed periodic structures. Objective functions are proposed to allow for the excitation-free shape-synthesis of a wide variety of periodic structures provided they are single-mode. One such ground-plane backed periodic structure example is the reflectarray. A shape-synthesis technique we denote “similarity-optimization” is proposed where we show conclusively a novel method of synthesizing very high aperture efficiency reflectarrays with excellent bandwidth and side-lobe performance. The work is further applied to synthesize a unique and perhaps surprising invention: the mosaic reflectarray. A mosaic reflectarray is a high gain antenna that simultaneously exhibits a recognizable visual (optical) image.

Lastly, in Chapter 6, we conclude with a list of the major contributions of the thesis. We will also comment on the future potential research using characteristic mode analysis in the synthesis of antennas and electromagnetic systems in general.

Chapter 1 References

[1] W.Stutzman and S.Licul, “Synthesis Methods for Antennas” in C.A.Balanis (Edit.), *Modern Antenna Handbook* (Wiley, 2008) pp.631.

[2] O.M.Bucci, G.Franceschetti, G.Mazzarella and G.Panriello, "The intersection approach to array synthesis", Proc. Inst. Elec. Eng., Pt.H, Vol.137, pp.349-357, 1990.

[3] E.Botha, J.Joubert & D.A.McNamara, “Alternative formulation & applications aspects of the generalised projection method for array antenna synthesis”, *International Journal of RF and Microwave Computer-Aided Engineering*, Vol.19, No.6, pp.657-668, Nov.2009.

[4] A.Cha, "An offset dual shaped reflector with 84.5 percent efficiency", *IEEE Trans. Antennas Propagat.*, Vol. 31, No. 6, pp.896-902, Nov.1983.

[5] A.R.Charette, S.W.Lee and R.J.Acosta, "A method for producing a shaped contour radiation pattern using a single shaped reflector and a single feed", *IEEE Trans. Antennas Propagat.*, Vol.37, No. 6, pp.698-706, June 1989.

[6] B.Chantraine-Barès, R.Sauleau, L. Le Coq and K.Mahdjoubi, “A new accurate design method for millimeter-wave homogeneous dielectric substrate lens antennas of arbitrary shape”, *IEEE Trans. Antennas Propagat.*, Vol. 53, No. 3, pp. 1069-1082, March 2005.

[7] J.M.Johnson and Y.Rahmat-Samii, "Genetic algorithms and method of moments (GA/MOM) for the design of integrated antennas", *IEEE Trans. Antennas Propagat.*, Vol.47, No.10, pp.1606-1614, Oct.1999.

[8] J.M.Johnson and Y.Rahmat-Samii, "Evolutionary Designs of Integrated Antennas Using Genetic Algorithms and Methods of Moments (GA/MoM)", Chapter 9 in : Y. Rahmat-Samii and E. Michielssen (Edits.), *Electromagnetic Optimization by Genetic Algorithms* (Wiley, 1999).

[9] B.Thors, H.Steyskal and H.Holter, "Broad-band fragmented aperture phased array element design using genetic algorithms", *IEEE Trans. Antennas Propagat*., Vol.53, No.10, pp.3280-3287, Oct.2005.

[10]T.Yamamoto, K.Fujimori, M.Sanagi, S.Nogi and T.Tsukagoshi, "Efficient antenna miniaturization technique by cut off of chromosome-length in genetic algorithm", *Proc. Asia-Pacific Microwave Conference* (*APMC*), pp.1837-1840, Singapore, Dec.2009.

[11]A.Erentok and O.Sigmund, “Topology optimization of sub-wavelength antennas”, *IEEE Trans. Antennas Propagat*., Vol.59, No.1, pp.55-68, January 2011.

[12]D.Linden and E.Altshuler, "Design of Wire Antennas Using Genetic Algorithms", Chapter 8 in : Y. Rahmat-Samii and E. Michielssen (Edits.), *Electromagnetic Optimization by Genetic Algorithms* (Wiley, 1999).

[13]E.E.Altshuler, “Electrically small self-resonant wire antennas optimized using a genetic algorithm,” *IEEE Trans. Antennas Propagat*., vol. 50, pp. 297-300, March 2002.

[14]H.Choo, R.L.Rogers and H.Ling, “Design of electrically small wire antennas using a Pareto genetic algorithm”, *IEEE Trans. Antennas Propagat*., Vol.53, No.3, pp.1038-1046, March 2005.

[15]M. Ohira, H. Deguchi, M. Tsuji and H. Shigesawa, “Multiband single-layer frequency selective surface design by combination of genetic algorithm and geometry-refinement technique,” *IEEE Transactions on Antennas Prop.*, Vol. 52, No. 11, Nov. 2004, pp. 2925 – 2931.

[16]Y. Aoki, H. Deguchi and M. Tsuji, “Reflectarray with arbitrarily-shaped conductive elements optimized by genetic algorithm”, *IEEE Int. Antennas Propagat. Symp. Digest*, USA, July 2011.

[17]S.Koulouridis, D.Psychoudakis and J.Volakis, “Multiobjective optimal antenna design based on volumetric material optimization”, *IEEE Trans. Antennas Propagat.*, Vol.55, No.3, pp.594-603, March 2007.

[18]L.A.Griffiths, C.Furse and C. You Chung, "Broadband and Multiband Antenna Design Using the Genetic Algorithm to Create Amorphous Shapes Using Ellipses", *IEEE Trans. Antennas and Propagat.*, Vol.54, No.10, pp.2776 – 2782, Oct.2006

[19]M.John and M.J.Ammann, “Antenna optimization with a computationally efficient multiobjective evolutionary algorithm”, *IEEE Trans. Antennas Propagat*., Vol.57, No.1, pp.260-263, January 2009.

[20]J.I.Toivanen, R.A.E.Makinen, J.Rahola, S.Jarvenpaa and P.Yla-Oijala, “Gradient-based shape optimisation of ultra-wideband antennas parameterized using splines", *IET Microw. Antennas Propaga*., Vol.4, No.9, pp.1406-1414, 2010.

Chapter 2

Literature Review and Theoretical Background

2.1 – Introductory Remarks

The development of this thesis relies on CM theory and thus we lay the foundation of this work in Section 2.2 by discussing the theoretical underpinnings of characteristic modes. Included is a literature review of the foundational papers as well as a description of more recent works where CM theory is used in various antenna applications. Chapter 3 applies CM theory to electrically small antenna shape synthesis in the form of a complete description of single mode antennas. Chapter 4 uses similar single-mode concepts albeit in a multi-band fashion. We therefore discuss the fundamental concepts of electrically small antennas in Section 2.3 which allows for the development of Chapters 3 and 4. In Chapter 5 we will show the development of a reflectarray element synthesis technique whereby the elements in the reflectarray are shape-synthesized to have maximum physical similarity between adjacent elements. In Section 2.4 we will thus discuss the concept of reflectarrays and the design difficulties we will attempt to overcome in Chapter 5. Oftentimes, the analysis of periodic structures is used in the design of reflectarrays and so a discussion of their properties is included. Lastly, in Section 2.5 we will discuss the computational methods required to obtain the characteristic modes – namely the method of moments (MoM).

2.2 – Review of Characteristic Mode Theory and its Antenna Applications

2.2.1 – Introductory Remarks on CM Theory

The theory of characteristic modes finds its foundations in the efforts of R. J. Garbacz at Ohio State University in the late 1960s and early 1970s [1] – [3]. The goal of his research was to obtain a set of currents and patterns to act as basis functions to describe both the currents on an arbitrary perfectly conducting scatterer and the scattered field due to any arbitrary impressed electric field. However, the approach used to obtain the CMs was not straightforward and was difficult to code. Enter the work by Harrington and Mautz in the early 1970s [4] – [5]. Building off the then recent success of Harrington's introduction of the moment method in electromagnetics [6], the authors proposed that the characteristic modes could be obtained by solving an appropriate generalized eigenvalue problem [4]. This gave the characteristic modes a broader audience since one no longer required a specialized piece of software to obtain the CMs – they could be computed using any moment method based computational electromagnetics formulation [5]. Harrington and Mautz extended the characteristic mode (CM) formulations to include dielectric and magnetic materials [7] using volumetric currents and additionally in a surface equivalence formulation [8]. Included within the work in [7] and [8] was the allowance of lossy materials (including finite conductivity conductors). In every formulation, the orthogonality of far-field patterns of the modes is maintained – a cornerstone of CM theory. It should also be stated that the original formulation of [4] can be considered to be a special case of the volumetric formulation of [7] under the conditions of strictly PEC metal structures.

An alternative formulation followed the initial work on characteristic modes where rather than solving for the modes on the surface or within the volume of a scatterer, the modes are determined at a fixed number of ports (or terminals). These modes were given the name "characteristic port modes" or CPMs [9]. Lastly, different formulations were developed by Inagaki and Garbacz [10] (Inagaki modes), and later by Pozar, Garbacz and Liu [11] and called the Generalized Characteristic Modes (GCMs). These alternative theories allowed for orthogonality of modal far-field patterns relative to an arbitrarily chosen weight rather than orthogonality over the entire sphere (which is effectively a unity weighting function). We begin by introducing the CMs.

2.2.2 – The Impedance Operator

Consider an arbitrary conducting surface S, situated within an impressed field $\underline{E}^i$ as shown in Figure 2.1. From Maxwell's Equations and the boundary conditions derived therein, the total tangential electric field must be zero on the surface of the conductor. As such, surface currents must appear on the conductor that produce a scattered field that enforces this boundary condition. We define the surface currents generated in this way using the operator relationship

$$\left[L(\underline{J}) - \underline{E}^i\right]_{\tan} = 0 \tag{1.1}$$

The operator L acts on the surface current density $\underline{J}$ and produces a tangential electric field on the surface S that precisely cancels the contribution of the tangential impressed field. The operator L is defined in the following manner for a time-harmonic electromagnetic system [6]:

$$L\left(\underline{J}\right) = j\omega\underline{A}\left(\underline{J}\right) + \nabla\Phi\left(\underline{J}\right) \tag{1.2}$$

The symbol ω refers to radial frequency and the symbol ∇ represents the gradient operator. The functions $\underline{A}\left(\underline{J}\right)$ and $\Phi\left(\underline{J}\right)$ are the magnetic vector and electric scalar potentials respectively, defined

$$\underline{A}\left(\underline{J}\right) = \mu\oiint_S \underline{J}\left(\underline{r}'\right)\psi\left(\underline{r},\underline{r}'\right)ds' \tag{1.3}$$

$$\Phi\left(\underline{J}\right) = \frac{j}{\omega\varepsilon}\oiint_S \nabla'\cdot\underline{J}\left(\underline{r}'\right)\psi\left(\underline{r},\underline{r}'\right)ds' \tag{1.4}$$

We consider the variables $\underline{r}$ and $\underline{r}'$ to be observation and source coordinates, and ε, μ, and k as the permittivity, permeability and wave number of the supporting medium. Furthermore, $\psi\left(\underline{r},\underline{r}'\right)$, the kernel of the integrals (2.3) and (2.4), is known as the Green's function of the medium, defined as

$$\psi\left(\underline{r},\underline{r}'\right) = \frac{e^{-jk\left|\underline{r}-\underline{r}'\right|}}{4\pi\left|\underline{r}-\underline{r}'\right|} \tag{1.5}$$

The operator L in equation (1.1) transforms a current density $\underline{J}$ into an electric field quantity, and hence has units of impedance. We introduce notation for the tangential operator L

$$Z\left(\underline{J}\right) = \left[L\left(\underline{J}\right)\right]_{\tan} \tag{1.6}$$

which allows us to write equation (1.1) in the following manner

$$\left[Z\left(\underline{J}\right) - \underline{E}_{\tan}^{i} \right] = 0 \tag{1.7}$$

Note that we can express the operator Z (formally known as $L_{\tan}$, hereafter known simply as Z) in terms of its real and imaginary parts as follows

$$Z = R + jX \tag{1.8}$$

The operators R and X are both real and by virtue of the fact that Z is symmetric, are symmetric themselves. A real, symmetric operator is also known as a Hermitian operator. Satisfying physical interpretations can be made for these operators if we consider the complex power associated with an arbitrary complex current density $\underline{J}$, namely

$$P_{complex} = \left\langle \underline{J}^{*}, Z\left(\underline{J}\right) \right\rangle = \left\langle \underline{J}^{*}, R\left(\underline{J}\right) \right\rangle + j\left\langle \underline{J}^{*}, X\left(\underline{J}\right) \right\rangle \tag{1.9}$$

where we define $\langle *,* \rangle$ as the inner product for all square integrable functions in the Hilbert space on the surface S, and hence $\left\langle \underline{a}^{*}, \underline{b} \right\rangle = \oiint_{S} \underline{a}^{*} \cdot \underline{b} dS$. We can interpret R and X as being responsible for the *real power* and *net stored energy* (*reactive power*) of the current $\underline{J}$ respectively since the relationships $P_{rad} = \left\langle \underline{J}^{*}, R\left(\underline{J}\right) \right\rangle$ and $P_{reac} = \left\langle \underline{J}^{*}, X\left(\underline{J}\right) \right\rangle$ hold true. Since real power must be greater than or equal to zero, it implies that the operator R must be positive definite in addition to being Hermitian.

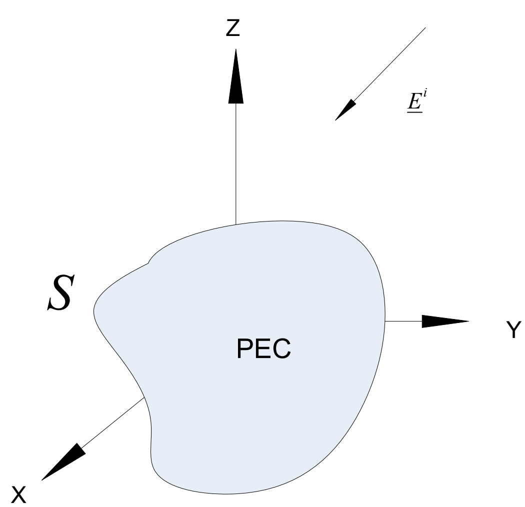

Figure 2.1 – Arbitrary PEC Object in an Impressed Field

2.2.3 – The Generalized Eigenvalue Problem

We now consider eigenvalue problems formed from the impedance operator. Consider the most general form of an eigenvalue problem involving the operator Z

$$Z\left(\underline{J}_n\right)=\nu_n M\left(\underline{J}_n\right) \tag{1.10}$$

with the operator M yet to be specified. We are free to explore the various operators that can take the place of M including the identity I operator, as well as the real and imaginary parts of the impedance operator itself. If the identity operator is selected, one obtains a set of eigenvectors (in this case, and most proceeding cases, they are eigencurrents) with uninteresting orthogonality properties. Only by selecting the operator M to be equal to the real part of the impedance operator (i.e. R) does the eigenvalue problem yield interesting orthogonality properties. In selecting $M=R$, we obtain the characteristic mode eigenvalue equation [4]

$$Z\left(\underline{J}_n\right)=\nu_n R\left(\underline{J}_n\right) \tag{1.11}$$

By making a change of variables $\nu_n=1+j\lambda_n$ we can re-write the eigenvalue problem in the alternative form $Z\left(\underline{J}_n\right)=\left(1+j\lambda_n\right)R\left(\underline{J}_n\right)$ which can be further simplified, leading to the final generalized eigenvalue problem

$$X\left(\underline{J}_n\right)=\lambda_n R\left(\underline{J}_n\right) \tag{1.12}$$

The operators R and X are both real symmetric operators, making the eigenvalues λ_n real with the eigenvectors $\underline{J}_n$ real or equiphase (complex vectors with all vectors entries sharing the same phase).

2.2.4 – Orthogonality Properties of Characteristic Modes

Since the operators R and X are real symmetric operators as well as Hermitian operators, we recognize the orthogonality properties of the eigencurrents

$$\left\langle \underline{J}_m, R\left(\underline{J}_n\right)\right\rangle = \left\langle \underline{J}_m^*, R\left(\underline{J}_n\right)\right\rangle = 0 \tag{1.13}$$

$$\left\langle \underline{J}_m, X\left(\underline{J}_n\right)\right\rangle = \left\langle \underline{J}_m^*, X\left(\underline{J}_n\right)\right\rangle = 0 \tag{1.14}$$

and

$$\left\langle \underline{J}_m, Z\left(\underline{J}_n\right)\right\rangle = \left\langle \underline{J}_m^*, Z\left(\underline{J}_n\right)\right\rangle = 0 \tag{1.15}$$

which hold for $m \neq n$. Since eigenanalysis yields eigencurrents of indeterminate magnitude we wish to normalize the eigencurrents to some intuitive value. Traditionally, normalization occurs such that each eigencurrent radiates 1 Watt. In order to accomplish this, we compute the scaling factor

$$scale_n = \sqrt{\left\langle \underline{J}_n, R\left(\underline{J}_n\right)\right\rangle} \tag{1.16}$$

which normalizes the modal currents such that

$$\mathrm{P}_{rad,n} = \left\langle \underline{J}_n^{norm}, R\left(\underline{J}_n^{norm}\right)\right\rangle = \left\langle \underline{J}_n^{un-norm} \big/ scale_n\,, R\left(\underline{J}_n^{un-norm}\right)\big/ scale_n\right\rangle = 1 \tag{1.17}$$

If the characteristic mode currents are normalized in the manner specified, we can generalize the orthogonality relationships for all index values m and n in the following manner

$$\left\langle \underline{J}_m, R\left(\underline{J}_n\right)\right\rangle = \left\langle \underline{J}_m^*, R\left(\underline{J}_n\right)\right\rangle = \delta_{mn} \tag{1.18}$$

$$\left\langle \underline{J}_m, X\left(\underline{J}_n\right)\right\rangle = \left\langle \underline{J}_m^*, X\left(\underline{J}_n\right)\right\rangle = \lambda_n \delta_{mn} \tag{1.19}$$

and

$$\left\langle \underline{J}_m, Z\left(\underline{J}_n\right)\right\rangle = \left\langle \underline{J}_m^*, Z\left(\underline{J}_n\right)\right\rangle = \left(1 + j\lambda_n\right)\delta_{mn} \tag{1.20}$$

where δ_{mn} is the Kronecker delta (0 if $m \neq n$, 1 if $m = n$). All subsequent derivations within this thesis assume normalized currents unless otherwise noted.

Additionally, we can derive the orthogonality properties of the modal fields using the complex Poynting theorem. The complex power associated with an arbitrary current can be written in terms of the impedance operator and its corresponding inner products as

$$P_{complex} = \left\langle \underline{J}^*, Z\left(\underline{J}\right)\right\rangle = \left\langle \underline{J}^*, R\left(\underline{J}\right)\right\rangle + j\left\langle \underline{J}^*, X\left(\underline{J}\right)\right\rangle \tag{1.21}$$

If we consider the sphere at infinity (also known as the far field) surrounding the conducting surface, the complex power for any modal surface current $\underline{J}$ on S is expressed as

$$P_{complex} = \iint_{S_\infty} \underline{E} \times \underline{H}^* \cdot d\underline{S} + j\omega \iiint_{V_\infty} \left(\mu \underline{H} \cdot \underline{H}^* - \varepsilon \underline{E} \cdot \underline{E}^* \right) dV \tag{1.22}$$

where S_∞ is the sphere at infinity enclosing S and V_∞ is the volume enclosed by S_∞.

When considering the modal currents, we derive a similar expression for the complex power associated with the m[th] and n[th] characteristic mode as

$$P_{complex,n} = \left\langle \underline{J}_m^*, R(\underline{J}_n) \right\rangle + j \left\langle \underline{J}_m^*, X(\underline{J}_n) \right\rangle = (1 + j\lambda_{\text{n}}) \delta_{mn} \tag{1.23}$$

which further implies that

$$\iint_{S_\infty} \underline{E}_m \times \underline{H}_n^* \cdot d\underline{S} = \delta_{mn} \tag{1.24}$$

and

$$\omega \iiint_{V_\infty} \left(\mu \underline{H}_m \cdot \underline{H}_n^* - \varepsilon \underline{E}_m \cdot \underline{E}_n^* \right) dV = \lambda_{\text{n}} \delta_{mn} \tag{1.25}$$

which can be interpreted as the orthogonality of radiated power and orthogonality of net stored energy between characteristic modes. If the observation points are in the far field, the fields there take the form of purely outward traveling waves, with the form

$$\underline{E}_n = \eta_o \underline{H}_n \times \hat{n} = \frac{-j\omega\mu}{4\pi} \frac{e^{-jkr}}{r} \underline{F}_n(\theta, \phi) \tag{1.26}$$

where the variable η_o is the intrinsic impedance of freespace, r is the radial distance from the origin, $\hat{n}$ is the unit normal to the sphere at infinity, and $\underline{F}_n(\theta, \phi)$ is the characteristic pattern or eigenpattern associated with the eigencurrents $\underline{J}_n$.

Adding equation (1.23) to its conjugate, with m and n interchanged, gives us the orthogonality properties of the characteristic fields $\underline{E}_n$ and $\underline{H}_n$

$$\frac{1}{\eta_o} \oiint_{S_\infty} \underline{E}_m \cdot \underline{E}_n^* dS = \delta_{mn} \tag{1.27}$$

and

$$\eta_o \iint_{S_\infty} \underline{H}_m \cdot \underline{H}_n^* dS = \delta_{mn} \tag{1.28}$$

Equations (1.27) and (1.28) show that the far fields associated with the characteristic modes are mutually orthogonal. The orthogonality properties of the CMs run quite deep from the currents to the fields. Next we will show how these orthogonality properties allow arbitrary currents and fields to be written as characteristic mode expansions.

2.2.5 – Modal Expansions using Characteristic Modes

The scattered field from an arbitrary PEC scatterer can be expressed in terms of the characteristic modes of that structure. In other words, the surface currents can be written as a linear sum of the eigencurrents, and consequently the scattered field can be written as a linear sum of the eigenfields. Given some arbitrary excitation, it is possible to determine to what extent each of the characteristic modes is excited. The excitation can come in the form of a feeding mechanism (voltage gap, coaxial feed, aperture coupling) or arbitrary incident electromagnetic waves. Any excitation will produce a surface current over the conducting surface S. Since the modal currents are weighted orthogonal over the surface S, we can expand any arbitrary current as follows

$$\underline{J} = \sum_{n=1}^{\infty} \alpha_n \underline{J}_n \tag{1.29}$$

Substituting equation (1.29) into equation (2.7) and taking the inner product of (2.7) with respect to $\underline{J}_m$, we obtain the expression

$$\sum_{n=1}^{\infty} \alpha_n \left\langle \underline{J}_m^*, Z\left(\underline{J}_n\right)\right\rangle - \left\langle \underline{J}_m^*, E_{\tan}^i \right\rangle = 0 \tag{1.30}$$

By the orthogonality properties of the modal currents, we end up with

$$\alpha_n \left(1 + j\lambda_n\right) = \left\langle \underline{J}_n, \underline{E}_{\tan}^i \right\rangle \tag{1.31}$$

where we define the *modal excitation* and *modal expansion coefficients,* respectively, as

$$V_n^i = \oiint_S \underline{J}_n \cdot \underline{E}_{\tan}^i dS = \left\langle \underline{J}_n, \underline{E}_{\tan}^i \right\rangle \tag{1.32}$$

and

$$\alpha_n = \frac{\left\langle \underline{J}_n, \underline{E}_{\tan}^i \right\rangle}{1 + j\lambda_n} = \frac{V_n^i}{1 + j\lambda_n} \tag{1.33}$$

The orthogonality properties allows us to express any arbitrary surface current, and its respective fields, as

$$\underline{J} = \sum_{n=1}^{\infty} \alpha_n \underline{J}_n = \sum_{n=1}^{\infty} \frac{V_n^i \underline{J}_n}{1 + j\lambda_n} \tag{1.34}$$

$$\underline{E} = \sum_{n=1}^{\infty} \alpha_n \underline{E}_n = \sum_{n=1}^{\infty} \frac{V_n^i \underline{E}_n}{1 + j\lambda_n} \tag{1.35}$$

and

$$\underline{H} = \sum_{n=1}^{\infty} \alpha_n \underline{H}_n = \sum_{n=1}^{\infty} \frac{V_n^i \underline{H}_n}{1 + j\lambda_n} \tag{1.36}$$

2.2.6 – Interpretation of Relevant Modal Quantities

It is important to understand the properties of the modes and what makes their existence meaningful for electromagnetic analysis and design. The eigenvalue for the generalized eigenvalue problem can be expressed as the ratio of inner products

$$\lambda_n = \frac{\left\langle \underline{J}_n^*, X\left(\underline{J}_n\right) \right\rangle}{\left\langle \underline{J}_n^*, R\left(\underline{J}_n\right) \right\rangle} = \frac{\mathrm{P}_{reac,n}}{\mathrm{P}_{rad,n}} = \frac{\omega W_{net,n}}{\mathrm{P}_{rad,n}} \tag{1.37}$$

where $W_{n,net}$ is the net stored energy of the specified mode 'n'. This allows interpretation of the eigenvalue λ_n explicitly as follows:

- If λ_n > 0, the mode is considered an *inductive mode* since it predominantly stores magnetic energy.
- If λ_n < 0, the mode is considered a *capacitive mode* since it predominantly stores electrical energy.

- If $\lambda_{\mathrm{n}} = 0$, the mode has *no net stored energy* and is called *externally resonant*
- If $\lambda_{\mathrm{n}} \to \infty$, the mode has *no radiated power* and is called *internally resonant*

If we are specifically trying to excite individual modes for some antenna design, we would like to excite modes with $\lambda_{\mathrm{n}} \approx 0$ since these modes will have the lowest possible contribution to net stored energy and to input reactance. Alternatively, if we wish to minimize scattering, we would want to excite only modes with large magnitude eigenvalues, namely those with magnitudes approaching infinity. The arbitrary excitation of a conducting surface S will result in the excitation of a myriad of modes, with each mode contributing to the radiated power and reactive energies associated with the excitation. The contribution to the overall net stored energy of the arbitrary PEC surface can be expressed in terms of the CMs in the following manner:

$$\begin{aligned} \omega W_{net} &= \left\langle \underline{J}^{*}, X\left(\underline{J}\right)\right\rangle \\ &= \left\langle \sum_{n=1}^{\infty} \alpha_n^{*} \underline{J}_n^{*}, X\left(\sum_{n=1}^{\infty} \alpha_n \underline{J}_n\right)\right\rangle \\ &= \sum_{n=1}^{\infty} \alpha_n^{*} \alpha_n \left\langle \underline{J}_n^{*}, X\left(\underline{J}_n\right)\right\rangle \\ &= \sum_{n=1}^{\infty} \left|\alpha_n\right|^2 \lambda_n \end{aligned} \tag{1.38}$$

Thus we can express the individual contribution of each mode to the net stored energy as

$$P_{reac,n} = \omega W_{net,n} = \lambda_n \left|\alpha_n\right|^2 \tag{1.39}$$

In a similar manner we can also expand the radiated power as

$$\begin{aligned} P_{rad} &= \left\langle \underline{J}^{*}, R\left(\underline{J}\right)\right\rangle \\ &= \left\langle \sum_{n=1}^{\infty} \alpha_n^{*} \underline{J}_n^{*}, R\left(\sum_{n=1}^{\infty} \alpha_n \underline{J}_n\right)\right\rangle \\ &= \sum_{n=1}^{\infty} \alpha_n^{*} \alpha_n \underbrace{\left\langle \underline{J}_n^{*}, R\left(\underline{J}_n\right)\right\rangle}_{=1} \\ &= \sum_{n=1}^{\infty} \left|\alpha_n\right|^2 \end{aligned} \tag{1.40}$$

with the individual contribution of each mode expressed as

$$P_{rad,n} = \left|\alpha_n\right|^2 \tag{1.41}$$

The aforementioned expression allows us to determine the amount of power radiated by mode ‘n’. Using these expressions one can determine to what extent a mode is being excited as well as how detrimental the excitation is as far as large stored energy is concerned, and hence potentially high input reactance assuming an antenna application.

2.2.7 – Foundational Papers and First Applications of Characteristic Modes

The exhaustive list of papers, theses, reports and other publications related to the theory of characteristic modes (CMs) contains less than two-hundred references, making it a relatively small area of research in the applied electromagnetics community. No textbooks are dedicated to communicate the theory in a pedagogic manner, though some text chapters have brief mention to emphasize particular aspects of the theory. We will include an extensive and thorough list of references pertaining to CM theory for two main reasons:

(1) To ensure future authors recognize previous publications in the literature. From a review of the literature pertaining to CM theory, it was made obvious that a significant amount of previously published work is repeated as new research groups begin investigating CM theory.

(2) Many papers have been written on interesting aspects of CM theory such as the implications of physical symmetry and alternative integral equations, with no further investigations being performed. By collecting these references in a comprehensive list, we hope to garner more interest in these oft-overlooked works.

Our discussion begins with the initial work on CM theory by R. J. Garbacz. His work consisted of two impactful journal papers [1], [3] culminating in his PhD thesis at Ohio State University [2]. Garbacz’ intention was to develop a method of obtaining a set of modes unique to any arbitrary perfectly conducting (PEC) electromagnetic scatterer. The modes consisted of currents (which could be used to expand any arbitrary current on the scatterer) and the currents' far-field patterns (which could be used to expand the scattered field of the arbitrary set of currents). His initial work in [1] showed that these modes diagonalized the scattering matrix of an arbitrary scatterer and thus represented a natural means of expanding the scattered field. Garbacz was able to show that when the scatterer coincided with a coordinate system with separable variables (spherical, cylindrical and the like) the characteristic modes were one and the same as the eigenmodes of the coordinate system (spherical waves, cylindrical waves and so on). This motivated him to speculate as to how these modes could be obtained for scatterers of arbitrary shape. The technique initially proposed in [1] and further developed in [2] and [3] involved assuming a set of propagating spherical waves of both the incoming and outgoing types external to the scatterer and standing waves internal to the scatterer. The tangential field components of the spherical propagating waves external to the scatterer and the standing waves internal to it are matched such that continuity is maintained. This matching of internal to external fields is done at N points and thus provides N modes when the scattering matrix is diagonalized. The only assumption Garbacz makes in his formulation is that the incoming spherical waves are related to the outgoing spherical waves for a particular mode via a phase factor. This phase factor ultimately becomes the key quantity in CM theory in that it indicates whether a mode is inductive, capacitive, or resonant. The formulation used to compute the characteristic modes using Garbacz' original technique is a laborious one, requiring substantial computational overhead. Nevertheless, it is the first successful attempt at computing the characteristic modes of arbitrary scatterers.

In 1971, R.F. Harrington and J. Mautz introduced their approach to the theory of characteristic modes in their seminal paper [4], immediately followed by a description of how to obtain the characteristic modes numerically using a moment method formulation [5]. Rather than diagonalizing the scattering matrix directly, Harrington and Mautz instead diagonalized the impedance operator. In doing so, they obtained a set of currents, and their respective far-field patterns, that were orthogonal and could be used in general as expansion functions for the currents and scattered field. What sets this formulation apart from the previous attempt by Garbacz is that it allowed a universal technique (the method of moments) to obtain the characteristic modes, and with the detailed knowledge of the impedance operator allowed a slew of properties to be derived that would otherwise be difficult to obtain using Garbacz' original formulation. Moreover, Harrington and Mautz were able to show that the characteristic modes obtained using their formulation (including the eigencurrents, eigenfields and eigenvalues) were identical to that of Garbacz' formulation. To obtain the characteristic modes of a PEC scatterer, one must solve the generalized eigenvalue problem

$$Z\left(\underline{J}_n\right)=\left(1+j\lambda_n\right)R\left(\underline{J}_n\right) \tag{1.42}$$

The operators Z and R can be discretized into matrix form (which is the basis of the method of moments) which can be represented in a similar form as

$$\left[Z\right]\left[J_n\right]=\left(1+j\lambda_n\right)\left[R\right]\left[J_n\right] \tag{1.43}$$

with the square brackets indicating that we are no longer dealing with continuous operators and vector fields but rather discrete operators and discrete vectors.

The formulation in [4] was valid only for scattering objects consisting of perfect electrical conductors (PEC). Harrington et al. further elaborated on the characteristic mode theory in 1972 [7] by including dielectric and magnetic materials in the formulation and additionally included the ability to account for lossy materials. The modal currents are no longer strictly surface currents and can now be volumetric when penetrable materials are considered. In order to handle magnetic materials, the modal currents now consist of both electric (J) and magnetic (M) currents. This of course complicates the formulation, with the eigenvalue problem to be solved now taking the form

$$\begin{bmatrix} Z & N \\ N & Y \end{bmatrix}\begin{bmatrix} J_n \\ jM_n \end{bmatrix}=\left(1+j\lambda_n\right)\mathrm{Re}\left\{\begin{bmatrix} Z & N \\ N & Y \end{bmatrix}\right\}\begin{bmatrix} J_n \\ jM_n \end{bmatrix} \tag{1.44}$$

where Z and Y are the impedance and admittance operators, and N is a coupling matrix that accounts for the electromagnetic coupling between electric and magnetic currents. If we assume the magnetic currents are zero and thus the operator N is null, we obtain the classical characteristic mode eigenvalue problem [4], thus making the volumetric formulation in [7] the most general eigenvalue problem one can solve to obtain the CMs, with the CM formulation in [4] being a special case of the formulation in [7].

The first application of CM theory can be found in [12], where CM theory is used as a means of controlling radar scattering. Firstly, they show that any of the modal currents on a scatterer can be brought to resonance (i.e. its currents can have zero net stored energy) via reactive loading. Furthermore, and of significant importance to this thesis, they define a quality factor Q_n that represents a measure of the frequency sensitivity of a particular mode via the frequency derivative of its eigenvalue

$$Q_n = \frac{\omega}{2}\frac{d\lambda_n}{d\omega} \tag{1.45}$$

This Q_n can be obtained exactly from the CM eigenvalue, but the authors propose an approximate means of obtaining this derivative, namely using the eigenvalue problem

$$\left[\frac{\omega}{2}\frac{dX}{d\omega}\right][J_n] = Q_n[R][J_n] \tag{1.46}$$

where Q_n is the Q of the n^th mode and $[dX/d\omega]$ is the frequency derivative of the imaginary part of the impedance matrix (which is still a matrix itself). The assumption that is made in order to obtain this eigenvalue problem is that the frequency derivative of the matrix $[R]$ and of the eigencurrent $[J_n]$ are negligible compared to the frequency derivative of the eigenvalue and of the imaginary part of the impedance matrix. By solving for the modal currents with the smallest Q, and then reactively loading the structure appropriately, the authors of [12] show that one can obtain a broadband scatterer.

An interesting paper by Yee and Garbacz [13] explores the possibility of expanding the input admittance of wire antennas in terms of the characteristic modes of the antenna. This is a consequence of the modal expansion of arbitrary current in terms of the modal currents. In doing so, it is possible to identify which modes are the principal contributors to the input conductance and susceptance. It is relevant to note that this is the first CM paper where an antenna, and not simply a scatterer, is considered from a CM perspective.

Chang and Harrington devised a method in [8] where the characteristic modes of penetrable objects can be determined via an equivalent surface current formulation. This approach reduces the discretization requirements from a volume to a surface, which is beneficial for computing scattering from larger objects. On the other hand, the surface equivalence currents are not physical currents. A key advantage of the PEC and volumetric characteristic modes is the physical currents, potentially making the surface equivalence characteristic modes less appealing as an investigative tool.

In [14], Newman looks at small antenna placement on larger conducting bodies such as an aircraft. He notes that the modes of the large conducting body are critical in locating the ideal placement of the small antenna. In particular, exciting inductive or capacitive modes (i.e. modes with large magnitude eigenvalues) leads to low radiation resistance and large input reactance. Newman points out that the location where the modal current magnitude peaks for a near-resonant mode of the aircraft (modeled using a wire cross) is the ideal location for the antenna since this will cause the loop to couple to a mode that is a good radiator. This is the first paper that suggests that the CMs of a chassis or armature are relevant to the radiating properties of an antenna, and in the case of Newman's example, becomes the principal radiator. In [15], Newman and Garbacz further investigate the wire cross and show the consistency of the CMs in predicting symmetric and asymmetric modes with what is found using other numerical techniques in electromagnetics.

In 1982, Garbacz and Pozar published a paper [16] on the shape synthesis of body-of-revolution (BOR) antennas. The authors use the CMs to shape the antenna such that one of the modes has a specified far-field pattern (in a minimum error approximation). The shapes were synthesized and the far-field of one of the modes (often the dominant mode) agreed well with the desired pattern. The authors considered schemes that would lead to exciting just the desired mode but did not consider how to feed the antenna or the modes' frequency dependence. Unfortunately, no further papers were published by the authors on this topic, and further research certainly remains on this particular topic.

In their last major contribution to the theory of characteristic modes, Harrington and Mautz consider the CMs of apertures in [17]. The theory is similar to the CMs of freespace PEC scatterers, only now an admittance operator is used and magnetic currents are solved for, which form the equivalent aperture currents. The authors show that the theory is particularly useful in determining the power coupling through apertures, and that the real aperture currents (and orthogonality) make for a quickly converging series when performing CM modal expansions. The work on aperture modes was further explored by Kabalan in [18] and [19] where the authors considered the modes of an infinitely long slot aperture for the excitations of TE and TM cases respectively. Kabalan continued to explore the CMs of apertures in [20], considering the case where the slot in [18] and [19] is straddled by different media, and in [21] where the slot now appears on a conducting cylinder rather than a plane.

A new perspective on CM theory is used in [22] where Hilbert, Tilston and Balmain consider the characteristic mode analysis of a log-periodic dipole array (LPDA). The dominant modes of each dipole in the array are used to determine the overall performance of the LPDA. The authors note that the modes of each dipole are the modes of a relatively small scatterer, and yet the combination of these modes leads to accurate prediction of the performance of a relatively large aggregate of scatterers.

Solid conducting surfaces are sometimes modeled by wire grids in electromagnetics simulations. In [23], Mayhan considers the characteristic modes of solid plates and cylinders and compares their eigenvalues with those of the equivalent mesh grid plate and cylinder. Mayhan develops mesh grid density rules for proper modeling based on the eigenvalue convergence information. It is interesting to note that showing convergence for many eigenvalues shows convergence for arbitrary excitation, which is a more efficient approach than trying a plethora of feeding locations and excitation by numerous plane waves to measure impedance and scattering convergence.

Murray and Austin from the University of Liverpool published numerous conference papers on antenna synthesis using characteristic modes in the mid 1990s with the fruit of their labour discussed in [24] and [25]. Using the characteristic modes of the chassis of a vehicle (a military jeep), these authors attempted to synthesize ideal far-field patterns for NVIS communications. The CMs of the vehicle chassis were computed and an attempt to synthesize the pattern was performed using the far-fields of the CMs as the basis functions. It is interesting to point out that both Garbacz [2] and Harrington [4] noted that the CMs of any scatterer form a complete basis set for the far-field. That is to say, given unrestricted access to excitation of the modes of a scatterer, any square-integrable far-field pattern can be synthesized from the modes of any scatterer. Practicality obviously places this fact into remission, especially for smaller antennas where there is typically only a single mode with a small eigenvalue, making excitation of higher order modes extremely difficult. Nevertheless, the goal of radiating the majority of power into the upper hemisphere, ideal for NVIS communications, was accomplished in [24, 25].

Garbacz promoted in his work [1] – [3] that the CMs of canonical scatterers conforming to the coordinate systems such as cylindrical or spherical coordinates are one and the same as the eigenfunctions that satisfy the source-free Helmholtz equation. Explicit expressions for the eigencurrents and eigenvalues of the cylinder were not shown in any work to confirm this fact until the paper by Amendola et al. [26]. Reference [26] gives closed form expressions for the eigencurrents and eigenvalues of perfectly conducting infinite elliptic cylinders, using familiar special functions such as Bessel functions of the 1st and 2nd kind.

2.2.8 – Resurgence of Interest in CM Theory: Recent Developments

Aside from the research efforts by Garbacz at Ohio State University and Harrington at Syracuse University, prior to 2000, the publications and research work on characteristic modes were not numerous given the time span of more than 30 years. However, from 2002 onward there have been numerous publications utilizing the theory of characteristic modes. In fact, in the last 10 years (2002 – 2012) there have been a greater number of publications than in the first 30 years of CM history.

Starting in 2002, a research group at the University of Valencia focused their research on utilizing characteristic mode theory. Their work concentrated mainly on the development of analysis and design techniques for mobile phone antennas, MIMO antennas and ultra-wideband antennas, using CM theory to those ends. The summary of their work can be found in references [27–39]. In particular, reference [34] considers the modes of the chassis of mobile phones, with the authors showing that there exist multiple modes that can be used as effective radiators. This fact suggested that the mobile phone antenna is not necessarily the principal radiator, but rather one of these “chassis modes”. This work is reminiscent of the work by Newman [14] in 1977. By placing the antenna close to the peak in modal current for one of the radiating modes, the bandwidth, efficiency and impedance matching can be maximized. The other work accomplished by the Valencia group includes CM-based explanations as to why planar monopole antennas have wideband performance [28–30, 33, 35] the development of alternative feeding mechanisms for mobile phones to excite particular chassis modes [32, 34, 36–38], and the derivation of closed-form exact expressions for the eigencurrents and eigenvalues for numerous canonical scatterers including spheres, cylinders, prolate spheroids and circular plates [27].

An interesting pair of papers appeared in 2004 by Surittikul et al. [40, 41], where an FDTD-based numerical method was used to extract the characteristic modes of various antenna structures. The advantage of such a technique is the ability to simulate structures with arbitrary material properties, which is a difficult task with a Moment Method code (e.g. dielectrics, anisotropic materials). These papers are to date the only examples of obtaining the characteristic modes from a numerical method other than the method of moments.

Continuing in a similar vein as the University of Valencia work, Famdie, Solbach and Schroeder [42] – [44] considered the beneficial use of the chassis modes of mobile phones for improving impedance bandwidth and obtaining desirable radiation characteristics. Rather than directly exciting the chassis with a voltage gap or coaxial feed, the authors use capacitively coupled plates as the feeding mechanism. CMs with desirable properties are identified and their excitation enforced.

A relatively new research field where characteristic modes have found a suitable partner is the design of MIMO antennas. The author of this dissertation wrote his masters thesis [49] on the application of CM theory to MIMO antenna design. During 2007, both Chaudhury et. al [45] and Ethier et al. [50] published papers outlining the fact that the orthogonality of the CMs naturally lends itself to the design of MIMO antennas. An ideal set of MIMO antennas have patterns that are orthogonal in the far-field, which is a natural property of the characteristic modes. If one were to excite the modes individually (or properly phased) this orthogonality condition would be met. The work by Chaudhury was elaborated upon in [46] – [48], using four ports to excite a mobile chassis, effectively providing four MIMO antennas. While the work produced excellent MIMO antennas from the orthogonality perspective, the impedance matching was rather poor for at least one of the antennas (or modes from the CM perspective). The work by Ethier [50] employed three MIMO antennas in a similarly shaped and sized region, and found both excellent impedance matching and orthogonality over the desired frequency band. The work in [49] showed that for the 2.5 GHz band, a typically sized handheld is only capable of supporting at most three efficient radiating modes, which is why [49] was able to have good impedance matching and orthogonality while Chaudhury [45] – [48] was able to obtain only the orthogonality. The work by Ethier was further elaborated on in [51] by developing CM-based figures of merit for the specific case of analyzing structures that will solely be used as an antenna and have some form of direct excitation via voltage gap or coaxial feed. This is shown to be useful in distinguishing ‘antenna’ modes from purely ‘scattering’ modes, both of which are indistinguishable if only the eigenvalue is used to evaluate their behaviour.

There has also been a renewed effort in using CM theory for antenna modeling and design at Ohio State University (which is the “birthplace” of CM theory). Obeidat, Raines and Rojas [52] focused their attention on the proper modeling of multi-mode antennas (such as wideband or helical antennas) using CM theory. In a later paper [53], they went on to suggest a loading scheme to create broadband antennas. The “catch” was that the loads were necessarily non-Foster, almost certainly requiring active elements to achieve the bandwidth improvements. Similar techniques were later extended to the design of multi-band antennas [54]. Chalas et al. [55] have investigated the use of CM theory for pattern synthesis of antennas on UAVs. This work is very similar to the work by Austin and Murray [24,25]. Chalas at al. [56] have focused their efforts on the analysis of electrically small antennas, in particular, the computation of the currents of an arbitrary antenna that exhibit the lowest possible Q (widest bandwidth response), which he obtains using the characteristic modes of said antenna.

More recently, a research group at the University of Illinois has investigated the use of CM theory for the design of electrically small multi-mode antennas. In particular, Adams and Bernhard [57] considered the fact that electrically small antennas typically have a single good radiating mode and numerous poorly radiating modes. They showed that these poorly radiating modes could be used to extend the bandwidth of the antenna beyond that of the restrictions of a single resonant mode.

2.2.9 – Alternative Modal Theories Related to Characteristic Modes

A. Characteristic Port Modes (Network Characteristic Modes)

Alternative modal theories have been developed that are similar to the characteristic modes, the first of which was developed by Harrington and Mautz where they developed the theory of characteristic port modes (CPMs) [58]. These modes are very similar to the original characteristic modes [4], only now the currents exist at a discrete number of ports rather than as continuous currents that subsist on the entire surface of the scatterer. The CPMs involve diagonalizing the matrix containing the Z-parameters, while the original CMs diagonalize the discretized Z-operator. In truth, the CPMs and CMs are strongly tied together in the sense that when the number of ports is great enough, the Z-parameters become proportional to the entries of the discretized Z-operator, linking the CPMs to the CMs. Harrington and Mautz used the CPMs to control the scattering of N-port antennas in [59] and [60]. By properly terminating the ports, a particular mode can be brought to resonance to scatter in a desirable manner (for example to reduce radar cross section) or the ports can be terminated such that a particular aggregate of modes are excited to synthesize a desired scattered field.

Chaloupka [61] and Eber [62] both use the characteristic port mode theory to design MIMO antennas. Analyzing an N-port radiator leads to N modes that are orthogonal which is ideal for MIMO antenna design. The authors suggested that N streams of MIMO data could be superimposed (properly weighted) onto the N ports, where each stream would remain isolated (orthogonal) in the far-field since they would each individually be radiated by a characteristic port mode. Ethier [63, 64] investigated some of the unexplored properties of the CPMs in the context of Chaloupka's and Eber's work in [61] and [62]. One interesting fact fleshed out in [63] and [64] is that the nature of the antennas being analyzed in [61] and [62] leads to Toeplitz impedance matrices. These types of matrices arise when the ports in the N-port system all see the same system (i.e. there is deep symmetry in the port layout). The consequence of this is that the eigencurrents of any N-port system diagonalize any other N-port system sharing the same symmetry, regardless of the nature of the antennas, materials or frequencies involved.

B. Characteristic Modes with Different Weighted Orthogonality

The characteristic modes of the perfectly conducting variety [4] and of the penetrable material and lossy material variety [7] yield eigencurrents with eigenfields that are orthogonal in the far-field. Inagaki [65] proposed an alternative operator, $G^H G$, which is complex symmetric like the Z-operator and is defined such that the modes determined from the Inagaki eigenvalue problem are orthogonal not over the far-field, but orthogonal relative to an arbitrarily defined weight applied in the far-field. The eigenvalue problem is defined

$$\left(G^H G\right)\left(\underline{J}_n\right) = \gamma_n \left(\underline{J}_n\right) \tag{1.47}$$

Explicit expressions for this operator was not given in the paper, but was followed up by a paper by Pozar [66]. In this paper, they define the operator $H = G^H G$ and solve the eigenvalue problem

$$\left(Z^H Z\right)\left(\underline{J}_n\right) = \gamma_n \left(G^H G\right)\left(\underline{J}_n\right) \tag{1.48}$$

The operator H is discretized in matrix form with the entries of the matrix given as follows

$$H_{ij} = \left\langle W \underline{F}_{ei}, W \underline{F}_{ej} \right\rangle_{S_\infty} \tag{1.49}$$

where W is an arbitrary weight that can be a function of spherical angles, i.e. $W = W\left(\theta, \phi\right)$, $\underline{F}_{ei}$ is the far-field of the ith moment method expansion function and S_∞ refers to the sphere at infinity (far field) where the inner product (integration) occurs.

The eigencurrents and their far-fields have the desired weighted orthogonality as follows

$$\left\langle W\underline{E}_m, W\underline{E}_n \right\rangle = \eta_o K_n \delta_{mn} \tag{1.50}$$

where $\underline{E}_n$ is the far-field of the m^th^ mode and K_n is the power radiated into the weighted region defined by the arbitrary weighting function $W = W(\theta, \phi)$.

In a follow-up paper, Liu, Pozar and Garbacz [67] introduced another eigenvalue problem that neatly tied the original characteristic modes to this newly defined operator H. In particular, they defined what they called the generalized characteristic modes (GCMs), which are obtained from the eigenvalue problem

$$X(\underline{J}_n) = \lambda_n H(\underline{J}_n) \tag{1.51}$$

The originally intended orthogonality properties of the Inagaki modes [65] are preserved in this case, only now there is a physically meaningful eigenvalue (that is, the ratio of net stored energy to weighted radiated power). A satisfying result of this new formulation is that when the weighting function W is set equal to unity for all angles, i.e. $W(\theta, \phi) = 1$, the GCMs become the same as the CMs, hence the "generalized" moniker.

Ethier [68], [69] used the generalized characteristic modes for the purpose of designing MIMO antennas not only for idealized scattering environments, as in [50], but for any arbitrary scattering environment, the details of which is defined within the weighting function $W = W(\theta, \phi)$. The formulation was also extended to allow for a vector weighting function. MIMO antennas were designed and measured to handle a scattering environment with parameters based on the measurements of a typical urban environment.

2.3 – Review of Electrically Small Antenna Theory

It is likely the case that the reader is familiar with antenna concepts such as input impedance, bandwidth, VSWR and other fundamental concepts. On the other hand, concepts such as quality factor Q might not be so clear when applied to antennas. In particular, the Q that is well known for circuits and resonators is not the same as the Q defined for antennas. In this section we will discuss the various antenna Q concepts relevant to this thesis. In particular, we will discuss the definition of antenna Q and its relation to impedance bandwidth and perhaps of greatest importance, what the fundamental bounds are on antenna Q given the restriction of antenna electrical size. The most popular research topics among antenna engineers concerned with the design of electrically small antennas are (1) the determination of the fundamentally widest bandwidth (lowest Q) for a given antenna electrical size and (2) design methods to actually achieve this lower bound. As such, research in the design of electrically small antennas is intricately tied to the development of the definitions and bounds on antenna Q. The body of work concerned with the definition and computation of the limitations on antenna Q is contained within references [70] – [98].

We begin this discussion by defining what is meant by an electrically small antenna. As originally defined by H. Wheeler [70], an electrically small antenna (often known as an ESA) is any antenna that fits within a spherical volume with radius a less than $\lambda/2\pi$ or as Wheeler termed it, any antenna that can fit within the radiansphere. This can be stated in two ways as:

$$a < \frac{\lambda}{2\pi} \tag{1.52}$$

$$ka < 1 \tag{1.53}$$

though in recent times, the electrical limit of $ka < 0.5$ is far more common and has been widely adopted. For example, the self-resonant half-wavelength long dipole and self-resonant loop with one wavelength circumference do not qualify as electrically small antennas (though the loop operates on the boundary of this limit). Electrically small antennas are infamous for their limitations: narrow bandwidth, low radiation efficiency, high reactive energies, and small radiation resistance, to name a few. What bounds exist for electrically small antennas in terms of the gain and bandwidth? Chu asked this very question in his widely referenced paper in 1948 [71].

In this seminal work, Chu [71] analyzed the case of arbitrary sources contained within a fixed sized sphere and expanded these fields in terms of the vector spherical waves. By observing the wave impedances of these spherical waves as equivalent circuits, he noted that the lowest Q circuit is obtained when the lowest order spherical wave is solely radiated. Adding additional circuits (i.e. additional spherical waves) lead to an increase in the Q of the circuit. It should be noted that Chu also limited the polarization of the far-field to linear. Chu additionally did not account for the energy that would be contained within this fictitious sphere since the sources are treated as unknowns. Hence, the energies used in computing this bound on Q assume zero energy in the sphere, and so form somewhat ambitious bounds. The Chu-limits on Q are defined

$$Q_{chu} = \left(\frac{1}{ka} + \frac{1}{(ka)^3} \right) \tag{1.54}$$

where k is the wave number ($k = 2\pi/\lambda$) and a is the radius of the fictitious sphere surrounding the arbitrary antenna. In [72] and [74], Harrington investigated the connection between maximum gain of an antenna and its bandwidth (Q). He showed, using similar arguments to Chu [71], that the concept of gain and bandwidth are tied to each other. As the gain increases, the bandwidth necessarily decreases (or equivalently, Q increases). The work was carried out for antennas of arbitrary electrical size, with the results readily applied to the electrically small antenna regime.

In the mid to late 1960s, Collin & Rothschild [75] and Fante [76] reopened the topic of the lower bounds of antenna Q. Rather than using the equivalent circuits in Chu's work, [75] used the exact spherical wave fields and their respective radiating fields and energy storage (reactive) fields to obtain the same values for Q that Chu discovered. Fante [76] further investigated the work of [75] and showed that equal excitation of the two lowest order modes (TE and TM) together lead to an even lower Q than the Q obtained from the excitation of one alone. What is of greatest importance in their work is their demonstration of the ability to separate the energies associated with energy storage (which is relevant to Q) and the energies associated with propagating fields (which is infinite and thus irrelevant for antenna Q).

Rhodes [77], [78] investigated the problem of energy when defining Q for an antenna. This work was done independently of the antenna Q problem and was more of a physics-related investigation rather than an engineering investigation. It is worth noting that his conclusions were similar to those made in [75] and [76] in their separation of the energies associated with storage and the energies associated with propagating fields.

Fante re-explored the antenna Q problem in [81] by computing the minimum Q one must incur in order to obtain a particular gain. Naturally, if the gain is selected to be 1.5, the Q is the minimum Q defined by all previous authors since this is the gain of the lowest order TE or TM mode. If two modes are allowed in the problem and the gain is selected to be 3.0, the Q is once again the minimum Q which occurs when both TE and TM are excited with equal strength. As the gain goes above these minimum values (1.5 and 3.0) the minimum Q begins to increase, approaching what is called the supergain condition. An additional interesting fact is that if the gain drops below 1.5 (or 3.0 for two modes) there is loss in the system being analyzed and the Q begins to decrease. This reaffirms the fact that the inclusion of losses can in fact increase bandwidth, but clearly at the expense of lower gain.

In [84], Geyi attempts to utilize Foster's Reactance Theorem in the determination of minimum Q for arbitrary antennas, but as Best [86] points out, Foster's Reactance Theorem is only valid for lossless circuits. Even an antenna made from lossless materials is still a lossy circuit from the viewpoint of its terminals since the radiation into space is "lost" though certainly not dissipated. Hence, the results in Geyi's paper are erroneous as he states that the Q for an antenna at any frequency can be written

$$Q(\omega) \approx \frac{\omega\left(X_{in}^{'}(\omega) \pm X_{in}(\omega)/\omega\right)}{2R_{in}(\omega)} \tag{1.55}$$

which is true only when an antenna is in the vicinity of a resonance.

In a significant contribution, Yaghjian and Best derived expressions for antenna Q based on the antenna input impedance [90]. The work is important in the sense that the formulas are valid for antennas in both their resonant and anti-resonant regimes and thus are valid for all frequencies. As a result they show how the bandwidth of an antenna can be estimated strictly from the frequency derivative of the input impedance at the desired frequency. The expression for Q they obtained was

$$Q(\omega) \approx \frac{\omega \left| Z_o^{'}(\omega) \right|}{2R_{in}(\omega)} = \frac{\omega \sqrt{\left(R_{in}^{'}(\omega) \right)^2 + \left(X_{in}^{'}(\omega) + \left| X_{in}(\omega) \right| / \omega \right)^2}}{2R_{in}(\omega)} \tag{1.56}$$

Provided an antenna has a single resonance over any given range of frequencies, expression (2.56) can accurately predict the impedance bandwidth of the antenna. Interestingly, the fundamental bounds on antenna Q [70] – [93] all implicitly require this precise restriction of single resonance. A great deal of effort was also placed in connecting bandwidth (as defined in terms of VSWR), the definition of Q, and the new formula for antenna Q they derived in terms of input impedance.

Pozar [89] pointed out that the use of electric and magnetic dipole sources can shed light on the connections that exist between polarization, gain, pattern shape and bandwidth. The gains and bandwidths of sets of electric and magnetic dipoles producing linear and circular polarization were considered. Pozar showed that obtaining the minimum Q is independent of polarization – the same minimum Q can be achieved with either linear or circular polarization. Moreover, Pozar showed the same is true for omni-directional, bi-directional and directional patterns – the same minimum Q can be obtained in all cases. However, he did show that the minimum Q can only be obtained when both electric and magnetic sources are present (or equivalently when both TE and TM spherical waves are produced).

Thal [90] investigated wire antennas that conform to the surface of a sphere. It was shown that these antennas can be physically laid out in a manner that mimics the equivalent surface currents on a fictitious sphere that radiate the fundamental TM spherical wave. Thal further investigated, quite ingeniously for the first time, the energies stored within the sphere. This is contrary to all previous work before [90] that assume the energies within the Chu sphere are zero. Thal noted in [90] that no antenna has ever achieved the bounds imposed by the Chu limit (nor the updated limits by newer authors). The justification for the inability to achieve the bound was that all antennas considered thus far had significant energy stored within the volume occupied by said antennas. Since the Chu limit (and other Q limits) assumes no stored energy within the sphere occupied by the antenna, we find the justification for the inability to reach the limit. By accounting for the energies within the sphere, Thal was able to show that particular forms of these wire antennas were achieving the lowest possible Q for an antenna consisting solely of metal conforming to a sphere. It will later be shown that including magnetic materials can push the Q towards the Chu limit, thereby preventing energy storage within the Chu sphere. In [91], Thal continues his investigation by looking at the practicalities in simultaneously exciting a TE and TM spherical wave from a single antenna. He shows that this excitation is necessarily coupled and prevents the idealized antenna radiating a purely superimposed TE and TM spherical wave. As a result, the Q-bounds derived recently by Pozar [92] and numerous previous authors where the TE and TM modes are excited together are lower than what is actually achievable. This is not necessarily a problem as they still remain bounds – only now more recent results show that higher bounds exist. It should be noted that the most pertinent of criticisms pointed out by Thal is the assumption that one can achieve the lower bound on Q and simultaneously obtain a gain of 3. Thal shows quite convincingly that due to coupling between the TE and TM modes this simultaneous condition cannot hold.

In previous works, the focus has been determining the bounds on antenna Q for antennas that conform to a sphere and in some rare cases, prolate spheroids. Other geometries had not been considered until the work by Sohl, Gustafsson & Kristensson [92], [93] at Lund University. They developed a method to compute the lower bounds on antenna Q for any arbitrary geometry determined solely from the static polarizability of said geometry. These bounds are achieved via the inequality formed between the gain-bandwidth product and the static electric and magnetic polarizabilities. For the case of antennas made of purely PEC material, the bounds can be described via

$$\frac{D}{Q} \leq \tilde{\eta} \frac{k^3}{2\pi} \gamma \tag{1.57}$$

where k is the operating wave number, D is directivity, Q is the antenna Q, $\tilde{\eta}$ is the absorption efficiency and γ is the static polarizability. They point out that the absorption efficiency of the majority of antennas they have encountered is 0.5. Only in extreme cases does the absorption efficiency deviate from this value (it being bounded between 0 and 1). As for the static polarizability – it is an electric field orientation sensitive quantity. The field orientation is often defined along the scatterer axes of symmetry, or along whatever axis is of interest to the investigator. What is most relevant is selection of the electric-field orientation that leads to the largest static polarizability and hence the lowest possible Q of the scatterer being analyzed. Interestingly, selecting a PEC sphere and computing its static polarizability and selecting absorption efficiency to be 0.5 and the directivity to 1.5, the bound one obtains is

$$Q = \frac{1.5}{(ka)^3} \tag{1.58}$$

which is precisely the same bound that Thal derived in his work, showing the consistency between methods – the Thal bound was derived for a specific case, the Lund bound derived from the general case. One of the major investigations in this thesis is the synthesis of small antennas that achieve the lowest Q possible for their geometric shape. Antennas conforming to spheres, prolate spheroids and cylinders have been shown to achieve these bounds (see [91], [93]). However, other geometries such as circular, square and rectangular plates – collectively known as planar antennas – have not been thoroughly investigated. Additionally, and of greatest interest to this thesis, is the ability to synthesize antennas out of entirely arbitrary geometries, i.e. those that do not conform to the canonical geometric shapes.

In the work by Stuart et. al [94] – [96], the authors investigate the applicability of Q-theory in predicting the bandwidth of multi-resonant circuits. In general, the literature spanning from reference [70] – [93] discuss the definition of Q for antennas with a single resonance. Nearly every antenna has multiple resonances, but they are often sufficiently separated in frequency to allow for the traditional definition of antenna Q to be valid. When multiple resonances are closely spaced, the bandwidth of the antenna is wider than that which is predicted from the traditional antenna Q, a fact thoroughly discussed in [92]. The fundamentally widest bandwidth of an antenna as a function of the electrical volume it occupies is in fact wider than even the lowest bound predicted for Q since the bounds only exist for single-resonance structures. This presents a new and exciting research topic because (a) it remains unclear how to define antenna Q for multi-resonant antennas, (b) the bounds on gain and bandwidth of multi-resonant antennas have not been fully explored and lastly (c) it offers the opportunity to extend the bandwidth of small antennas beyond the limits imposed by Chu and successive authors.

Lastly, there exists the short text by Hansen [97] that contains a concise chapter on these topics. A more detailed and lengthy discussion can be found in the text by Volakis [98]. In particular, the text provides an excellent discussion on the history of small antennas and antenna Q and gives a fairly comprehensive list of references on the topic.

2.4 – Review of Reflectarray Antennas

2.4.1 – The Reflectarray Antenna

The operation and general design guidelines for reflectarrays is discussed in the text by Encinar and Huang [99]. A succinct definition of a reflectarray is simply that it is a space-fed antenna array. Rather than being excited via a corporate, parallel or otherwise constrained feeding network, it is excited using space waves (plane, cylindrical, spherical or any arbitrary wave). The resulting scattered field is controlled by the elements with the phase of the scattered field being of paramount importance. In particular, we will be discussing the design of etched microstrip technology based reflectarrays, a topic for which Pozar [100] has an excellent exposition. Reflectarrays do not require periodic structure analysis, but it has been shown to be invaluable in describing the element properties. By analyzing an infinite periodic structure of identical elements, one obtains a fairly good approximation to the element's behaviour when used in an actual reflectarray. While it is possible in theory to analyze a single element in the presence of all other elements in a reflectarray, this is computationally costly and un-solvable in many cases. It is much simpler to simulate an infinite periodic structure (as paradoxical as that may seem).

Reflectarrays can be categorized based on the type of element used in their array. One type involves the use of fairly simple elements (e.g. patches), each with an additional variable passive or active delay structure that yields the desired reflection phase. Another type involves using variable elements, where the element's geometry dictates the value of reflection phase. Each type of reflectarray has its advantages and disadvantages, but we shall strictly focus on variable element reflectarrays for the purpose of minimizing fabrication complexity. The layout of a typical reflectarray is shown in Figure 2.2(a) and a photograph shown in Figure 2.2(b). Note that the reflectarray is represented by a ground plane and substrate with elements etched on the surface of the substrate. Hence, the reflectarray is represented as a flat, planar surface. This need not be the case, but is the most common configuration as it dramatically reduces the profile of a high gain antenna design relative to, for example, a high gain parabolic dish of equivalent aperture size. The typical application of a reflectarray is to replace (mimic) conic shaped antennas such as parabolic, hyperbolic and elliptically shaped dishes [99]. Of the three, the synthesis of parabolic dishes is the most common design technique. However, there is nothing inherently "conic" about a reflectarray – it is fundamentally an array that is space-fed rather than the traditional constrained fed.

Overviews of the state of modern reflectarray design can be found in the works by Shaker and Chaharmir in [101] where they provide a thorough look at recent advancements. In particular, they identify four major topics that have yet to be addressed, or are currently being addressed in earnest by the research community:

(1) Increasing the aperture efficiency (gain) of reflectarrays

(2) Improving the bandwidth performance of reflectarrays

(3) Decreasing the fabrication costs of reflectarrays

(4) Understanding the fundamental operation of reflectarrays in order to broaden the applications

In this thesis we will focus on increasing the aperture efficiency of reflectarrays. In doing so, we will uncover some design principles regarding reflectarrays that do indeed improve the general understanding of their ideal operation.

Some references of particular interest to this thesis include [103] – [106] since, as in Chapter 5 of this thesis, they use sub-wavelength elements in the design of reflectarrays. Traditional reflectarray designs, keeping with the most common traditional array design, spaces the elements half-wavelength apart. This is a sensible (and often necessary) design practice for traditional arrays since each element is individually excited, making mutual coupling a detrimental phenomenon for spacing below half-wavelength. For reflectarrays, however, it can be shown that this mutual coupling is beneficial, if not key in improving reflectarray performance. The justifications proposed for this improvement are varied, but certainly the lack of a constrained feed in a space-fed array (reflectarray) means all of the incident field intercepted by the aperture is reflected (save for material losses) whereas a constrained fed system can scatter power back into the feeding network, decreasing gain and bandwidth in the process. The first author to explicitly propose the use of sub-wavelength elements was by Pozar [104]. Two papers that followed their work [105], [106] showed that the use of sub-wavelength elements can improve bandwidth performance as well as dramatically reduce the material losses thereby allowing for the use of lossy, low-cost substrate materials. These two points clearly address the bandwidth and cost issues with reflectarrays. In this thesis, we wish to maintain these levels of improved bandwidth performance while further improving other areas of necessity. There is sufficient justification to consider the reflectarray designed using sub-wavelength elements as an impedance surface, the discussion of which can be found in [107,108]. Lastly, Aoki et. al [109] discuss the concept of fragmented reflectarray elements for the purpose of reducing mutual coupling between elements. No explicit technique was described to reduce mutual coupling beyond preventing adjacent elements from being connected electrically (though strong coupling can occur regardless of physical connection). The inter-element spacing used in [109] was resonant spacing ($\lambda/2$) which sets their work quite apart from our own sub-wavelength spacing ($<< \lambda/2$). Explicit mention of aperture efficiency and bandwidth were not mentioned in the paper, though we suspect given the dramatically varied element shapes over the reflectarray surface that aperture efficiency will noticeably suffer in the reflectarray design of [109]. This assertion is confirmed in Chapter 5, Section 3.

In principle, a properly designed reflectarray will achieve the highest aperture efficiency allowable for its designed illumination and spillover. In practice, however, this is rarely (if ever) the case [99]. Lower-than-expected aperture efficiency can be partly attributed to a gain drop due to material losses. If high quality materials are used in the construction of the reflectarray, the remaining source of gain drop is due to errors in the reflection phase of scattered fields in the aperture. This phase error stems from the fact that the reflectarray elements are designed using an infinite periodic structure approach and then placed in a periodic structure with non-identical adjacent elements, i.e. a quasi-periodic structure. This quasi-periodicity is what gives rise to phase error. In this thesis we will provide a design technique to help mitigate this phase error. Combined with characteristic mode theory, the resulting reflectarray synthesis technique will provide a computationally efficient technique to synthesize high-gain, high aperture efficiency reflectarrays.

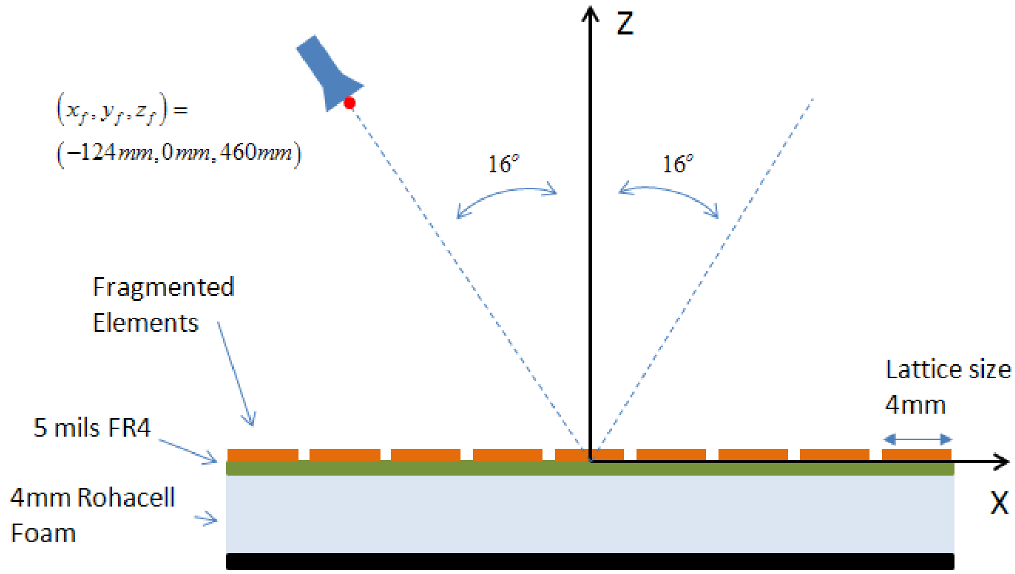

(a)

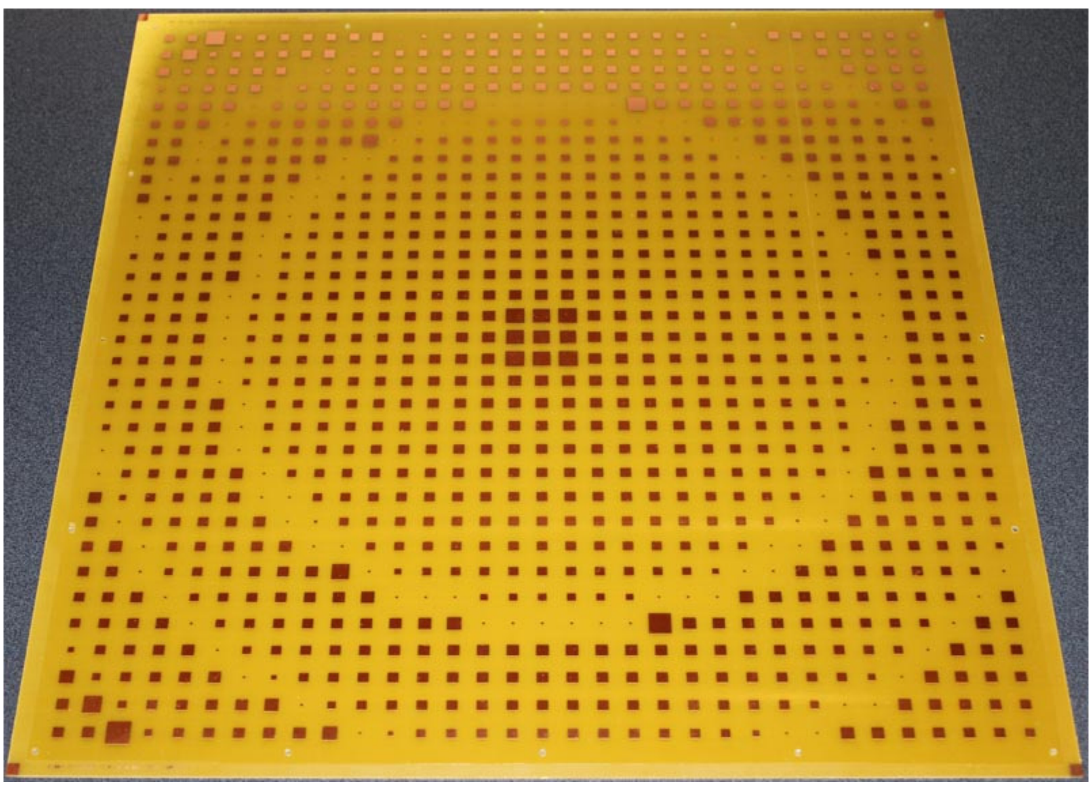

(b)

Figure 2.2 – Reflectarray (a) layout with example horn feed and (b) photograph (feed not shown)

2.4.2 – Periodic Structures

An electromagnetic periodic structure is an aggregate of finite material objects with their locations determined in a periodic fashion. Oftentimes, periodic structures are considered to be of infinite extent which (perhaps counter intuitively) dramatically simplifies the numerical analysis. In any case, periodic structures are most often used for their infinite periodic structure behaviour, with their finite equivalent structure having very similar performance to the infinite case. Further details of periodic structures can be found in [110,111]. Examples of 1D, 2D and 3D periodic structures are shown in Figures 2.3a – c. The purpose of introducing periodic structures in this thesis is to exploit the characteristic modes of these structures. At the time of writing this thesis, there are no publications (save for the authors' works) involving the analysis of periodic structure using characteristic mode theory. As such, we will delegate this exploration to Chapter 5, where we compute the characteristic modes of periodic structures for the first time and interpret many important metrics concerning periodic structures from a characteristic mode perspective.

The most important metrics of periodic structures are its transmission and reflection coefficients. We will restrict our discussion to planar periodic structures with two-dimensional periodicity existing in three-dimensional space making the most relevant form of excitation being an incident plane wave. The reflection and transmission coefficients of periodic structures can be defined in terms of the plane wave spectrum generated by an arbitrary incident plane wave [110,111]. Periodic structures of this variety are most commonly excited with a normally incident plane wave where the normal is defined as the perpendicular direction to the plane of periodicity (e.g. if the periodic structure is periodic in the x-y plane, a normally incident plane wave would propagate in the +/- z-direction). We will principally consider periodic structures excited with normally incident plane waves.

Historically, periodic structure analysis finds its foundations in the analysis of crystal structures by Ewald [112]. Nevertheless, periodic structures have found many applications in the mm-wave and microwave regime, perhaps beginning with the work by Kock [113]. Another important aspect of periodic structure analysis is how to simulate their behaviour using a numerical technique as opposed to a purely analytical one. Of greatest interest to our work are numerical methods using the method of moments in order to procure the impedance operator of the periodic structure being analyzed, allowing us to obtain its characteristic modes. One such example is the method of moments employing Ewald's method [114].

In order to perform characteristic mode analysis of the periodic structure, we require access to the impedance matrix. Furthermore, we require knowledge of the expansion functions used in the moment formulation since the eigencurrents determined through the eigenanalysis are current coefficients and not the actual physical currents. In other words, to properly perform CM analysis of a periodic structure (or of any structure for that matter) one requires complete access to the moment method formulation details. This is of course wishful thinking when considering a commercial piece of software since commercial interests, being what they are, prevent one from having complete access to all of the internal details of the software. Alternatively, developing one's own code may be considered, which is certainly a worthwhile endeavor but can create enormous overhead and reduces the ability to fully investigate the characteristic modes within the confines of a single piece of research. A compromise is made in Chapter 5 where we develop a moment method formulation that can obtain the impedance matrix of a periodic structure utilizing a freespace Green's function formulation. This will allow us to leverage off of previously developed moment method code that was designed for the analysis of finite scatterers and apply it to infinite scatterers (albeit using a newly developed technique).

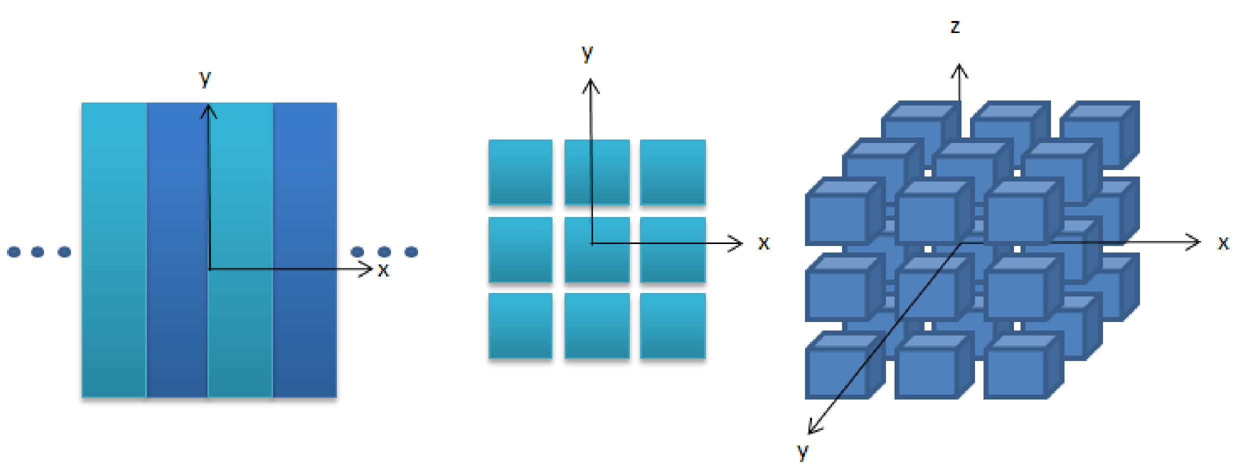

(a) (b) (c)

Figure 2.3 – Examples of (a) 1D, (b) 2D and (c) 3D Periodic Structures

2.5 – Brief Remarks on the Computational Methods Required

The method of moments is an invaluable tool in radiating and scattering problems in electromagnetics. It is a source method rather than a field method in that the unknowns to be solved for are the source currents that exist on and within physical scatterers. This is contrary to the finite element (FEM) and finite-difference time-domain (FDTD) methods which are field methods – at least in their most popular forms. The source method offers significant flexibility in that one must discretize only in regions where these currents exist. These advantages are balanced by the fact that the linear system of equations to be solved (hereafter known as the impedance matrix) is a fully filled matrix, unlike the FEM and FDTD methods which tend to have sparse matrices. The original intention of Garbacz [1] for the development of the theory of characteristic modes was to diagonalize the scattering matrix. Harrington et al. [5] showed a connection with the impedance operator thereby connecting the method of moments with the theory of characteristic modes. It might very well be possible for other numerical methods to obtain the characteristic modes (e.g. [40]), but the source approach used in the method of moments will serve us quite well for the purposes of this thesis – a claim that will be supported in Chapters 3 through 5.

The birth of the method of moments in electromagnetics is attributed to Harrington with the summary of his work found in the influential textbook [115]. Commercial numerical codes exist that utilize the method of moments, but obviously lack the flexibility an open-source code offers. One such open-source moment method code is included with the text by Makarov [116]. This code was used extensively in this authors' master's thesis [49], where it was adapted to accommodate the analysis of more complicated electromagnetics problems. The same code, now further adapted, shall be used in the work of this thesis.

Makarov's code, which is the moment method code used in this thesis, is based on the RWG element [117], an example of which is shown in Figure 2.4. This element forms the basis functions used in describing the unknown surface currents. A general description as to how the basis (and testing) functions are utilized in the method of moments, as well as a general introduction to the topic, can be found in Appendix A of this thesis. A major advantage of the RWG expansion function is the triangular shape, which allows one to describe fairly complicated structures with minimal approximations to the shape of the scatterer. These expansion functions are also vector-functions, allowing for a complete polarization-sensitive description of time-harmonic scattering of PEC objects. It should be noted that the RWG expansion functions can be adapted to include the effects of finite conductivity (lossy metals) so one is not necessarily restricted to PEC objects. This adaptation is described by the author in [49, Sect. 3.5].

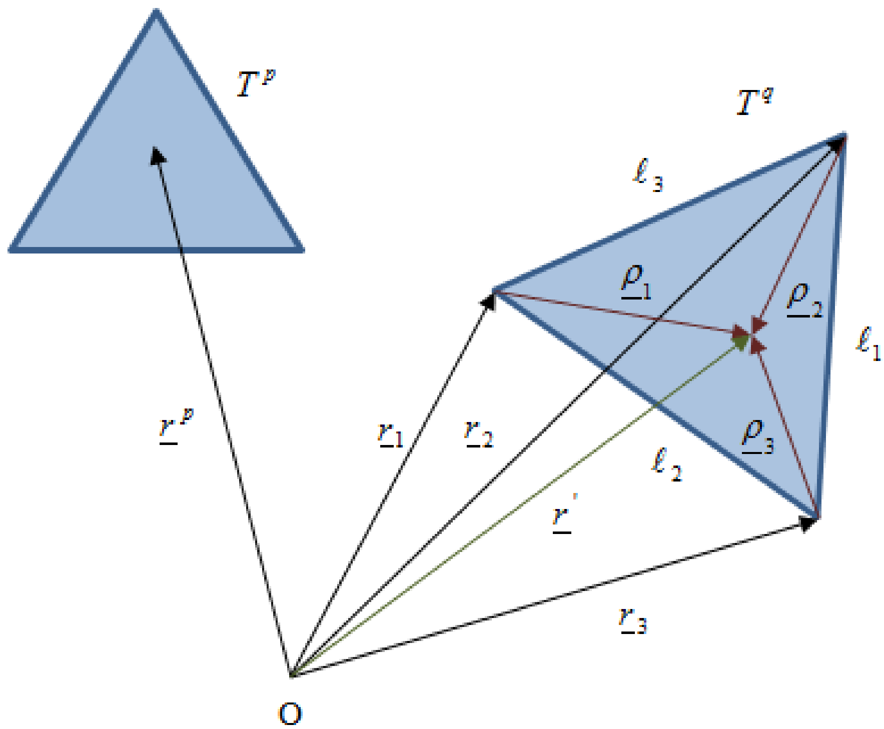

Figure 2.4 – RWG expansion function, adapted from [72]

2.6 – Concluding Remarks

In the preceding Chapter, we discussed the historical and theoretical background necessary for the development of this thesis. In Section 2.2 we outlined the theoretical development of characteristic mode theory which forms the cornerstone of this dissertation. The orthogonality properties of the characteristic modes and the interpretation of the eigenvalues were specifically emphasized as they are integral to understanding many of the theoretical developments in this thesis. We further summarized the literature pertaining to the theoretical development and application of characteristic mode theory. This began with the description of the intentions and success of foundational papers on characteristic mode theory. A fairly quiet period of research followed the initial derivations, mainly due to the computational difficulties in obtaining the characteristic modes. With the advent of the personal computer coupled with the accessibility of computational electromagnetic codes, a resurgence of interest was shown spanning approximately the past 20 years. The applicability of CM theory was shown to be far-reaching, traversing diverse disciplines within applied electromagnetics from antenna pattern synthesis, antenna placement optimization, MIMO antenna design, wideband antenna design and electrically small antennas. In Section 2.3 we discussed the theory of electrically small antennas and the notion of antenna Q. In Section 2.4 we considered the operation of reflectarray antennas and the use of periodic structures in their analysis and design. Lastly, in Section 2.5 we considered the computational techniques required in this thesis, namely the method of moments, which is used to obtain the characteristic modes and to perform full-wave electromagnetic simulations of antenna structures.

Chapter 2 References

[1] R. J. Garbacz, "Modal Expansions for Resonance Scattering Phenomena," *Proceedings of the IEEE*, pp. 856 – 864, August 1965.

[2] R. J. Garbacz, "A Generalized Expansion for Radiation and Scattered Fields," Ph.D. dissertation, Ohio State University, Columbus, 1968.

[3] R. J. Garbacz, R. Turpin, "A Generalized Expansion for Radiated and Scattered Fields," *IEEE Transactions on Antennas and Propagation*, Vol. AP-19, No. 3, pp. 856 – 864, May 1971.

[4] R.F. Harrington, J. Mautz, "Theory of Characteristic Modes for Conducting Bodies,*" IEEE Transactions on Antennas and Propagation*, Vol. AP-19, No. 5, pp. 622 – 628, September 1971.

[5] R. F. Harrington, J. Mautz, *"*Computation of Characteristic Modes for Conducting Bodies," *IEEE Transactions on Antennas and Propagation*, Vol. AP-19, No. 5, pp. 629 – 639, September 1971.

[6] R. F. Harrington, *Field Computation by Moment Methods,* Wiley-IEEE Press, 1st Edition, 1993.

[7] R. F. Harrington, J. Mautz, Y. Chang, "Characteristic Modes for Dielectric and Magnetic Bodies," *IEEE Transactions on Antennas and Propagation*, Vol. AP-20, No. 2, pp. 194 – 198, March 1972.

[8] Y. Chang, R.F. Harrington, "A Surface Formulation for Characteristic Modes of Material Bodies," *IEEE Transactions on Antennas and Propagation*, Vol. 25, No. 6, pp 789 – 795, November 1977.

[9] J. Mautz, R.F. Harrington, "Modal Analysis of Loaded N-Port Scatterers", *IEEE Transactions on Antennas and Propagation*, Vol. AP-21, No. 2, March 1973.

[10] N. Inagaki, R. Garbacz, "Eigenfunctions of Composite Hermitian Operators with Application to Discrete and Continuous Radiating Systems", *IEEE Transactions on Antennas and Propagation*, Vol. AP-30, No. 4, pp 571 – 575, July 1982.

[11] D. Liu, R. Garbacz, D. Pozar, “Antenna Synthesis and Optimization Using Generalized Characteristic Modes”, *IEEE Transactions on Antennas and Propagation*, Vol. 38, No. 6, pp 862 – 868, June 1990.

[12] R. F. Harrington, J. Mautz, “Control of Radar Scattering by Reactive Loading,” *IEEE Transactions on Antennas and Propagation*, Vol. AP-20, No. 4, pp 446 – 454, July 1972.

[13] A. Yee, R. Garbacz “Self- and Mutual-Admittances of Wire Antennas in Terms of Characteristic Modes,” *IEEE Transactions on Antennas and Propagation*, Vol. 21, No. 6, pp 868 – 871, November 1973.

[14] E.H. Newman, “Small Antenna Location Synthesis using Characteristic Modes,” *IEEE Transactions on Antennas and Propagation*, Vol. AP-25, No. 4, pp 530 – 795, November 1977.

[15] R. Garbacz, E.H. Newman, “Characteristic Modes of a Symmetric Wire Cross,” *IEEE Transactions on Antennas and Propagation*, Vol. AP-28, No. 5, pp 712 – 715, September 1980.

[16] R. Garbacz, D. Pozar, “Antenna Shape Synthesis using Characteristic Modes,” *IEEE Transactions on Antennas and Propagation*, Vol. 30, No. 3, pp 340 – 350, May 1982.

[17] R.F. Harrington, J.R. Mautz, “Characteristic Modes for Aperture Problems,” *IEEE Transactions on Microwave Theory and Techniques*, Vol. 33, No. 6, pp. 500 – 505, 1985.

[18] K. Kabalan, R.F. Harrington, H. Auda, J.R. Mautz, “Characteristic Modes for Slots in a Conducting Plane, TE Case,” *IEEE Transactions on Antennas and Propagation*, Vol. 35, No. 2, pp. 162 – 168, February 1987.

[19] K. Kabalan, R.F. Harrington, H. Auda, J.R. Mautz, “Characteristic Modes for Slots in a Conducting Plane, TM Case,” *IEEE Transactions on Antennas and Prop.*, Vol. 35, No. 3, pp. 331 – 335, March 1987.

[20] K. Kabalan, A. El-Hajj, R.F. Harrington, “Characteristic Mode Analysis of a Slot in a Conducting Plane Separating Different Media,” *IEEE Transactions on Antennas and Propagation*, Vol. 38, No. 4, pp. 476 – 481, April 1990.

[21] A. El-Hajj, K. Kabalan, R.F. Harrington, “Characteristic Modes of a Slot in a Conducting Cylinder and their use for Penetration and Scattering, TE Case,” *IEEE Transactions on Antennas and Propagation*, vol. 40, no. 2, pp. 156 – 161, February 1992.

[22] M. Hilbert, M.A. Tilston, K.G. Balmain, “Resonance Phenomena of Log-Periodic Antennas: Characteristic-Mode Analysis,” *IEEE Transactions on Antennas and Propagation*, Vol. 37, No. 10, pp. 1224 – 1234, October 1989.

[23] J.T. Mayhan, “Characteristic Modes and Wire Grid Modeling,” *IEEE Transactions on Antennas and Propagation*, Vol. 38, No. 4, pp. 457 – 469, April 1990.

[24] K.P. Murray, B.A. Austin, “Synthesis of Vehicular Antenna NVIS Radiation Patterns using the Method of Characteristic Modes,” *IEE Proceedings of Microwaves, Antennas and Propagation,* Vol. 141, No. 3, pp. 151 – 154, June 1994.

[25] B.A. Austin, K.P. Murray, “The Application of Characteristic-Mode Techniques to Vehicle-Mounted NVIS Antennas,” *IEEE Antennas and Propagation Magazine*, Vol. 40, Issue 1, pp. 7 – 21 & 30, February 1998.

[26] G. Amendola, G. Angiulli, G. Di Massa, “Numerical and Analytical Characteristic Modes for Conducting Elliptic Cylinders,” *Microwave and Optical Technology Letters*, Vol. 16, No.4, pp. 243 – 249, November 1997.

[27] M. Cabedo-Fabres, A. Valero-Nogueira, M. Ferrando-Bataller, “Systematic Study of Elliptical Loop Antennas using Characteristic Modes,” *IEEE Antennas and Propagation Society International Symposium*, Vol.1, pp. 156 – 159, 2002.

[28] M. Cabedo-Fabres, E. Antonino-Daviu, M. Ferrando-Bataller, A. Valero-Nogueira, “On the Use of Characteristic Modes to Describe Patch Antennas Performance,” *IEEE Antennas and Propagation Society International Symposium*, Vol. 2, pp. 712 – 715, 2003.

[29] M. Cabedo-Fabres, E. Antonino-Daviu, A. Valero-Nogueira, M. Ferrando-Bataller, “Analysis of Wide Band Planar Monopole Antennas using Characteristic Modes,” *IEEE Antennas and Propagation Society International Symposium*, Vol. 3, pp. 733 – 736, 2003.

[30] E. Antonino-Daviu, M. Cabedo-Fabres, M. Ferrando-Bataller, A. Valero-Nogueira, “Wideband Double-fed Planar Monopole Antennas,” *Electronics Letters,* Vol. 39, No. 23, September 2003.

[31] M. Cabedo-Fabres, E. Antonino-Daviu, A. Valero-Nogueira, M. Ferrando-Bataller, “Optimization of the Polarization of Reflectarrays using Characteristic Modes,” *IEEE Antennas and Propagation Society International Symposium*, Vol. 1, pp. 13 – 16, 2004.

[32] M. Cabedo-Fabres, A. Valero-Nogueira, J.I. Herranz-Herruzo, M. Ferrando-Bataller, “A Discussion on the Characteristic Mode Theory Limitations and its Improvement for the Effective Modeling of Antennas and Arrays,” *IEEE Antennas and Propagation Society International Symposium*, vol. 1, pp. 121 – 124, 2004.

[33] E. Antonino-Daviu, M. Cabedo-Fabres, M. Ferrando-Bataller, A. Valero-Nogueira, “A Discussion on the Feed Configuration of Planar Monopole Antennas to Obtain Ultra Wide Band Performance,” *IEEE Antennas and Propagation Society International Symposium*, vol. 2, pp. 1867 – 1870, 2004.

[34] E. Antonino-Daviu, M. Cabedo-Fabres, M. Ferrando-Bataller, J.I. Herranz-Herruzo, “Analysis of the Coupled Chassis-Antenna Modes in Mobile Handsets,” *IEEE Antennas and Propagation Society International Symposium*, vol. 3, pp. 2751 – 2754, 2004.

[35] M. Cabedo-Fabres, E. Antonino-Daviu, A. Valero-Nogueira, M. Ferrando-Bataller, “Wideband Radiating Ground Plane with Notches,” *IEEE Antennas and Propagation Society International Symposium*, vol. 2B, pp. 560 – 563, 2005.

[36] E. Antonino-Daviu, M. Cabedo-Fabres, M. Ferrando-Bataller, A. Valero-Nogueira, M. Martinez-Vazquez, “Novel Antenna for Mobile Terminals based on the Chassis-Antenna Coupling,” *IEEE Antennas and Propagation Society International Symposium*, vol. 1A, pp. 503 – 506, 2005.

[37] M. Cabedo-Fabres, A. Valero-Nogueira, E. Antonino-Daviu, M. Ferrando-Bataller, "Modal Analysis of a Radiating Slotted PCB for Mobile Handsets," *1st European Conference on Antennas and Propagation (EuCAP 2006),* pp. 1 – 6, 2006.

[38] E. Antonino-Daviu, M. Cabedo-Fabres, M. Ferrando-Bataller, A. Valero-Nogueira, "Resonant modes in antenna handsets," *Joint COST 273/284 Workshop*, Sweden, June 2004.

[39] E. Antonino-Daviu, C.A. Suarez-Fajardo, M. Cabedo-Fabres, M. Ferrando-Bataller, "Wideband Antenna for Mobile Terminals Based on the Handset PCB Resonance," *Microwave and Optical Technology Letters,* Vol. 48, No. 7, pp. 1408 – 1411, July 2006.

[40] N. Surittikul, R.G. Rojas, "Analysis of Reconfigurable Printed Antenna using Characteristic Modes: FDTD Approach," *IEEE Antennas and Propagation Society Intl Symposium*, vol. 2, pp. 1808 – 1811, 2004.

[41] N. Surittikul, R.G. Rojas, "Time Domain Method of Characteristic Modes for the Analysis / Design of Reconfigurable Antennas," *IEEE Antennas and Propagation Society International Symposium*, vol. 2B, pp. 585 – 588, 2005.

[42] W.L. Schroeder, C.T. Famdie, K. Solbach, "Utilisation and Tuning of the Chassis Modes of a Handheld Terminal for the Design of Multiband Radiation Characteristics," *IEE Wideband and Multi-band Ant. and Arrays*, pp. 117 – 121, 2005.

[43] C.T. Famdie, W.L. Schroeder, K. Solbach, "Numerical Analysis of Characteristic Modes on the Chassis of Mobile Phones," *1st European Conf. on Antennas and Propagation (EuCAP 2006),* pp. 1 – 6, 2006.

[44] W.L. Schroeder, A.A. Vila, C. Thome, "Extremely Small, Wide-band Mobile Phone Antennas by Inductive Chassis Mode Coupling," *Proceedings of the 9th European Conference on Wireless Technology*, pp. 407 – 410, 2006.

[45] S. K. Chaudhury, W. L. Schroeder, H. J. Chaloupka, "Multiple Antenna Concept Based on Characteristic Modes of Mobile Phone Chassis," 2nd *European Conference on Antennas and Propagation (EuCAP 2006),* pp. 1 – 6, 2007.

[46] S. K. Chaudhury, W. L. Schroeder, H. J. Chaloupka, "MIMO antenna system based on orthogonality of the characteristic modes of a mobile device," *2nd International ITG Conference on Antennas*, pp. 58 – 62, 2007.

[47] S. K. Chaudhury, H. J. Chaloupka, A. Ziroff, "Novel MIMO Antennas for Mobile Terminals," *38th European Microwave Conference (EuMC),* pp. 1751 – 1754, 2008.

[48] S. K. Chaudhury, H. J. Chaloupka, A. Ziroff, "Multiport Antenna systems for MIMO and diversity," 4th *European Conference on Antennas and Propagation (EuCAP 2010),* pp. 1 – 5, 2010.

[49] J. Ethier, *MIMO Antenna Design using Characteristic Mode Concepts*, Master's Thesis, University of Ottawa, Canada, 2008.

[50] J. Ethier, E. Lanoue, D. McNamara, "MIMO Handheld Antenna Design Approach Using Characteristic Mode Concepts", *Microwave and Optical Technology Letters*, Volume 50, No. 7, July 2008, pp.1724 – 1727.

[51] J. Ethier, D. McNamara, "A Modal Significance Measure in the Characteristic Mode Analysis of Radiating Structures", *Electronics Letters*, Vol. 46, No. 2, January 21, 2010.

[52] K. Obeidat, B. Raines, R.G. Rojas, "Design and Analysis of a helical spherical antenna using the theory of characteristic modes," *Antennas and Propagation Society International Symposium (APS*), pp. 1 – 4, 2008.

[53] K. Obeidat, B. Raines, R.G. Rojas, "Application of Characteristic Modes and Non-Foster Multiport Loading to the Design of Broadband Antennas," *IEEE Transactions on Antennas and Propagation,* vol. 58, Issue 1, pp 203 – 207, 2010.

[54] B. Raines, R.G. Rojas, "Design of multiband reconfigurable antennas," 4th *European Conference on Antennas and Propagation (EuCAP 2010),* pp. 1 – 5, 2010.

[55] J. Chalas, K. Sertel, J. L. Volakis, "Antenna Optimization for UAV Platforms using Characteristic Modes," *Antennas and Propagation Society International Symposium (APS*), 2010.

[56] J. Chalas, K. Sertel, J. L. Volakis, "Computation of the Q Limits for Arbitrary-Shaped Antennas using Characteristic Modes," *Antennas and Propagation Society International Symposium (APS*), 2011.

[57] J. Adams, J. Bernhard, "A Modal Approach to Tuning and Bandwidth Enhancement of an Electrically Small Antenna," *IEEE Transactions on Antennas and Propagation,* vol. 59, No. 4, pp 1085 – 1092, April 2011.

[58] J. Mautz, R.F. Harrington, "Modal Analysis of Loaded N-Port Scatterers", *IEEE Transactions on Antennas and Propagation*, Vol. AP-21, No. 2, March 1973.

[59] R.F. Harrington, J. Mautz, "Pattern Synthesis for Loaded N-Port Scatterers", *IEEE Transactions on Antennas and Propagation*, Vol. AP-22, No. 2, March 1974.

[60] R.F. Harrington, J. Mautz, "Optimization of Radar Cross Section of N-Port Loaded Scatterers", *IEEE Transactions on Antennas and Propagation*, Vol. AP-22, No. 5, September 1974.

[61] H. Chaloupka, X. Wang, "Novel Approach for Diversity and MIMO antennas at small Mobile Platforms," *IEEE PIMRC-Symposium Digest*, Vol. 1, pp. 1229 – 1232, 2004.

[62] D. Eber, H. Chaloupka, "Design Approach for a Class of Compact Multiport Antennas," *Microwave, Antennas, Propagation and EMC Technologies for Wireless Comm.*, Vol. 1, pp 144 – 147, Aug 2005.

[63] J. Ethier, D. McNamara, "An Interpretation of Mode-Decoupled MIMO Antennas in Terms of Characteristic Port Modes", *13th Biennial IEEE Conference on Electromagnetic Field Computation Digest*, Athens, Greece, May 11 – 15, 2008.

[64] J. Ethier, D. McNamara, "An Interpretation of Mode-Decoupled MIMO Antennas in Terms of Characteristic Port Modes", *IEEE Transactions on Magnetics*, Volume 45, Number 3, March 2009, pp. 1128 – 1131.

[65] N. Inagaki, R. Garbacz, “Eigenfunctions of Composite Hermitian Operators with Application to Discrete and Continuous Radiating Systems”, *IEEE Transactions on Antennas and Propagation*, Vol. AP-30, No. 4, pp 571 – 575, July 1982.

[66] D. Pozar, “Antenna Synthesis and Optimization Using Weighted Inagaki Modes”, *IEEE Transactions on Antennas and Propagation*, Vol. AP-32, No. 2, pp 159 – 165, February 1984.

[67] D. Liu, R. Garbacz, D. Pozar, “Antenna Synthesis and Optimization Using Generalized Characteristic Modes”, *IEEE Transactions on Antennas and Propagation*, Vol. 38, No. 6, pp 862 – 868, June 1990.

[68] J. Ethier, D. McNamara, “The Use of Generalized Modes in the Design of MIMO Antennas”, *13th Biennial IEEE Conference on Electromagnetic Field Computation Digest*, Athens, Greece, May 11 – 15, 2008.

[69] J. Ethier, D. McNamara “The Use of Generalized Modes in the Design of MIMO Antennas”, *IEEE Transactions on Magnetics*, Volume 45, Number 3, March 2009, pp. 1124 – 1127.

[70] H. A. Wheeler, “Fundamental Limitations of Small Antennas”, *Proceedings of the IRE*, Vol. 35, Issue 12, pp. 1479 – 1484, December 1947.

[71] L. J. Chu, “Physical Limitations of Omni-directional Antennas,” *Journal of Applied Physics*, Vol. 10, pp. 1163 – 1175, 1948.

[72] R. F. Harrington, “On the Gain and Beamwidth of Directional Antennas,” *IRE Transactions on Antennas and Propagation*, Vol. 6, pp. 219 – 225, July 1958.

[73] H. A. Wheeler, “The Radiansphere around a Small Antenna”, *Proceedings of the IRE*, Vol. 47, Issue 8, pp. 1325 – 1331, August 1959.

[74] R. F. Harrington, “Effect of Antenna Size on Gain, Bandwidth and Efficiency”, *Journal of Research of the National Bureau of Standards*, Vol. 64-D, pp. 1 – 12, January – February 1960.

[75] R. E. Collin, S. Rothschild, “Evaluation of Antenna Q”, *IEEE Transactions on Antennas and Propagation*, Vol. 12, Issue 1, pp. 23 – 27, January 1964.

[76] R. L. Fante, “Quality Factor of General Ideal Antennas”, *IEEE Transactions on Antennas and Propagation*, Vol. AP-17, No. 2, pp. 151 – 155, March 1969.

[77] D. R. Rhodes, “Observable Stored Energies of Electromagnetic Systems,” *Journal of the Franklin Institute*, Vol. 302, No. 3, pp. 225 – 237, 1976.

[78] D. R. Rhodes, “A Reactance Theorem,” *Proceedings of the Royal Society of London*, Vol. 353, pp. 1 – 10, February 1977.

[79] H. L. Thal, “Exact Circuit Analysis of Spherical Waves,” *IEEE Transactions on Antennas and Propagation*, Vol. AP-26, No. 2, pp. 282 – 287, March 1978.

[80] R. C. Hansen, “Fundamental Limitations in Antennas”, *Proceedings of the IEEE*, Vol. 69, No. 2, pp. 170 – 182, February 1981.

[81] R.L. Fante, “Maximum Possible Gain for an Arbitrary Ideal Antenna with Specified Quality Factor”, *IEEE Transactions on Antennas and Propagation*, Vol. 40, No. 12, pp. 1586 – 1588, December 1992.

[82] J. S. McLean, “A Re-Examination of the Fundamental Limits on the Radiation Q of Electrically Small Antennas,” *IEEE Transactions on Antennas and Propagation*, Vol. 44, No. 5, pp 672 – 676, May 1996.

[83] R. E. Collin, “Minimum Q of Small Antennas”, *Journal of Electromagnetic Waves and Applications*, Vol. 12, pp. 1369 – 1393, 1998.

[84] W. Geyi, “The Foster Reactance Theorem for Antennas and Radiation Q,” *IEEE Transactions on Antennas and Propagation*, Vol. 48, No. 3, pp. 401 – 408, March 2000.

[85] G. A. Thiele, P. L. Detweiler, R. P. Penno, “On the Lower Bound of the Radiation Q for Electrically Small Antennas,” *IEEE Transactions on Antennas and Prop.*, Vol. 51, No. 6, pp. 1263 – 1268, June 2003.

[86] S. R. Best, “The Foster Reactance Theorem and Quality Factor for Antennas,” *IEEE Antennas and Wireless Propagation Letters*, Vol. 3, pp. 306 – 309, 2004.

[87] A. D. Yaghjian, S. R. Best, “Impedance, Bandwidth, and Q of Antennas,” *IEEE Transactions on Antennas and Propagation*, Vol. 53, No. 4, pp. 1298 – 1324, April 2005.

[88] S. R. Best, “A Discussion on the Quality Factor of Impedance Matched Electrically Small Wire Antennas”, *IEEE Transactions on Antennas and Propagation*, Vol. 53, No. 1, pp. 502 – 508, January 2005.

[89] D.M. Pozar, “Polarization of Maximum Gain Antennas”, *IEEE Transactions on Antennas and Propagation*, Vol. 55, No. 7, pp 2113 – 2115, July 2007.

[90] H. L. Thal, “New Radiation Q Limits for Spherical Wire Antennas,” *IEEE Transactions on Antennas and Propagation*, Vol. 54, No. 10, pp. 2757 – 2763, October 2006.

[91] H. L. Thal, “Gain and Q Bounds for Coupled TM-TE Modes,” *IEEE Transactions on Antennas and Propagation*, Vol. 57, No. 7, pp. 1879 – 1885, July 2009.

[92] C. Sohl, M. Gustafsson, G. Kristensson, “Physical limitations on broadband scattering by heterogeneous obstacles,” *Journal of Physics A: Mathematical & Theoretical*, September 2007.

[93] M. Gustafsson, “Polarizability and physical bounds on antennas in cylindrical and rectangular geometries,” Technical Report LUTEDX / TEAT-7195 / 1-11, Lund University, Department of Electrical and Information Technology, Lund, Sweden, 2010.

[94] H.R. Stuart, S.R. Best, A.D. Yaghjian “Limitations in Relating Quality Factor to Bandwidth in a Double Resonance Small Antenna,” *IEEE Antennas and Wireless Propagation Letters*, Vol. 6, pp. 460 – 463, 2007.

[95] H. R. Stuart, “Eigenmode Analysis of Small Multielement Spherical Antennas”, *IEEE Transactions on Antennas and Propagation*, Vol. 56, No. 9, pp. 2841 – 2851, September 2008.

[96] H.R. Stuart, S.R. Best, "A Small Wideband Multimode Antenna," *IEEE International Symposium on Antennas and Propagation*, pp. 1 – 4, 5-11 July 2008.

[97] R.C. Hansen, *Electrically Small, Superdirective, and Superconducting Antennas*, New Jersey: John Wiley & Sons, 2006.

[98] J. Volakis, C. Chen, K. Fujimoto, *Small Antennas: Miniaturization Techniques & Applications, McGraw-Hill Professional*, 1st Edition, 2010.

[99] J. Huang, A. Encinar, *Reflectarray Antennas*, IEEE, John Wiley & Sons, 2008.

[100] D.M. Pozar, S.D. Targonski and H.D. Syrigos, "Design of Millimeter Wave Microstrip Reflectarray," *IEEE Transactions on Antennas Propagation*, Vol. 45, No. 2, Feb. 1997. pp. 286 – 295.

[101] J. Shaker, M.R. Chaharmir, M. Cuhaci, A. Ittipiboon, "Reflectarray Research at the Communications Research Centre Canada," *IEEE Antennas and Propagation Magazine*, Vol. 50, No. 4, Aug. 2008, pp. 31 – 52.

[102] J. Shaker, M. R. Chaharmir, "Microstrip Reflectarray Antennas", Chapter 5 in D. Guha, Y.M.M. Antar, *Microstrip and Printed Antennas: New Trends, Techniques and Applications*, (Wiley, 2010).

[103] L. Moustafa, R. Gillard, F. Peris, R. Loison, H. Legay, E. Girard, "The Phoenix Cell: A New Reflectarray Cell with Large Bandwidth and Rebirth Capabilities", *IEEE Antennas and Wireless Propagation Letters*, Vol. 10, 2011, pp. 71 – 74.

[104] D.M. Pozar, "Wideband Reflectarrays using Artificial Impedance Surfaces", *Electronics Lett.*, Vol. 43, No. 3, February 1, 2007, pp. 148 – 149.

[105] P. Nayeri, F. Yang, A.Z. Elsherbeni, "Broadband Reflectarray Antennas using Double-Layer Sub-wavelength Patch Elements," *IEEE Ant. and Wireless Prop. Letters*, Vol. 9, 2010, pp. 1139 – 1142.

[106] J. Ethier, M.R. Chaharmir, J. Shaker, “Novel Approach for Low-Loss Reflectarray Designs”, *IEEE Intl. Symp. on Antennas and Propagation (URSI/APS)*, Spokane, Washington, USA, July 3 – 8, 2011.

[107] D. Sievenpiper, Lijun Zhang, R.F.J Broas, N.G. Alexopolous, E. Yablonovitch, “High-impedance electromagnetic surfaces with a forbidden frequency band”, *IEEE Transactions on Microwave Theory and Techniques*, vol 46, Issue 11, November 1999, pp. 2059 – 2074.

[108] B. H. Fong, J. S. Colburn, J.J. Ottusch, J.L. Visher, D.F. Sievenpiper, “Scalar and Tensor Holographic Artificial Impedance Surfaces,” *IEEE Transactions on Antennas and Propagation*, vol. 58, Issue 10, October 2010, pp. 3212 – 3221.

[109] Y. Aoki, H. Deguchi and M. Tsuji, “Reflectarray with arbitrarily-shaped conductive elements optimized by genetic algorithm”, *IEEE Int. Antennas Propagat. Symp. Digest*, USA, July 2011.

[110] B. A. Munk, *Frequency Selective Surfaces: Theory and Design*, Wiley, New York, 2000.

[111] B. A. Munk, *Finite Antenna Arrays and FSS*, Wiley, Hoboken, New Jersey, 2003.

[112] P. P. Ewald, “The Analysis of Crystal Optics,” *Annals of Physics*, Vol. 45, pp. 1 – 28, 1916.

[113] W. E. Kock, “Metallic delay lenses,” *Bell System Technical Journal*, Vol. 27, 1948.

[114] I. Stevanovic, P. Crespo-Valero, K. Blagovic, F. Bongard, J.R. Mosig, “Integral-Equation Analysis of 3-D Metallic Objects Arranged in 2-D Lattices using the Ewald Transformation,” *IEEE Transactions on Microwave Theory and Techniques*, vol. 54, Issue 10, October 2006, pp. 3688 – 3697.

[115] R.F. Harrington, *Field Computation by Moment Methods*, IEEE Press, Piscataway, NJ, 1993.

[116] Sergey N. Makarov, *Antenna and EM Modeling with MATLAB®*. New York: John Wiley & Sons, 2002.

[117] S. Rao, D. Wilton, A. Glisson, “Electromagnetic Scattering by Surfaces of Arbitrary Shape”, *IEEE Transactions on Antennas and Propagation*, Vol. AP-30, No. 3, May 1982.

Chapter 3

Single-Mode, Single-Band Antenna Shape Synthesis using Characteristic Modes

3.1 – Introduction

In this chapter we will discuss the concept of single-mode antennas and develop a new shape synthesis technique for their design. Single-mode antenna operation, as we shall define it, is the frequency regime over which an antenna's electrical performance can be completely described using a single characteristic mode. The antenna is then a single-mode antenna over that frequency range, the word "mode" referring to a characteristic mode.

In Section 3.2 we describe the critical electrical performance metrics such as resonance frequency, input impedance, radiation efficiency and antenna Q (bandwidth) of single-mode antennas solely in terms of characteristic mode quantities (namely the eigenvalues and eigencurrents). There are numerous reasons to consider single-mode antennas, the first of which is the fact that the majority of small and intermediately sized antennas are in fact single mode, giving us a plethora of antenna examples to work with. Intermediately sized antennas include resonant dipole and loop antennas, patch antennas, and other radiating structures with largest electrical dimension on the order of a half-wavelength or less. The author's masters thesis [1] examined many such single-mode antennas, although shape synthesis was not attempted there. Another frequency regime where antennas tend to be single mode is the electrically small regime. As discussed in Chapter 2, this regime is often defined as the range of frequencies for which an antenna's largest electrical dimension is less than $\lambda/2\pi$. This frequency regime will form the focus of this chapter. The important antenna metrics mentioned thus far (resonance frequency, input impedance, radiation efficiency, antenna Q) are typically associated with the necessary excitation of the antenna in question, either through a feeding mechanism or by an incident field. Eigenanalysis requires no such excitation and as such the ability to predict a single-mode antenna's performance using eigenvalues and eigenvectors is indeed a feedless or excitation-free approach.

In Section 3.3, we propose an alternative technique to obtain these single mode antenna parameters through the novel use of the matrix trace of the impedance matrix. Not only does this approach give rise to a feedless antenna analysis technique, but it also provides a computationally simpler approach to perform what is effectively eigenanalysis.

This is followed by Section 3.4, where we discuss the development of a new antenna shape-synthesis technique that utilizes the analysis of Section 3.3 to form objective functions for the feedless synthesis of single-mode antennas. The optimization framework is further developed to incorporate the feedless objective functions with a genetic algorithm (GA) optimization scheme employing what is known as the direct matrix manipulation (DMM) method. We show that the newly defined objective functions work well with a GA-DMM optimization scheme. The optimization approach is applied to circularly shaped planar structures with the resultant synthesized antennas shown to exhibit antenna bandwidths that approach the fundamental limitations imposed by electromagnetics. From these optimized antenna structures, a new planar antenna is described (as an example) that achieves the fundamentally widest possible bandwidth for its chosen geometry with experimental results confirming these claims.

In Section 3.5, it is shown that the feedless optimization can be applied to a myriad of canonical geometries such as planar rectangles and triangles, with success found in minimizing the antenna Q, approaching the lowest possible Q for the given geometry. The feedless optimization approach is pushed to its limit via the synthesis of antennas from arbitrarily shaped starting geometries, showing success in dozens of applications of the technique. The advantages of the feedless shape-synthesis is shown conclusively in its ability to shape-synthesize any starting shape into a resonant antenna with high radiation efficiency with an antenna Q approaching the fundamental bounds on Q imposed by the starting shape's geometry.

3.2 – Antenna Input Impedance and Q in terms of Characteristic Modes

3.2.1 – Antenna Input Impedance in Terms of Characteristic Modes

The first paper that expressed the input admittance of an antenna in terms of its characteristic modes was by Yee and Garbacz [2]. In their paper they showed that the input admittance (which can be easily expressed as input impedance through its reciprocal) can be written as a summation of the modal currents that exist at the selected port, appropriately weighted by the eigenvalue of each modal current. We will derive a similar expansion, only for the specific case of a moment method formulation using RWG expansion functions. The new results of the derivations in Section 3.2 and 3.3 was summarized [3, 4] by the author, with the later publication garnering a *best student paper award*.

Firstly, we define the input admittance of the antenna structure in the usual manner as

$$Y_{in} = \frac{I_{in}}{V_{in}} \tag{2.1}$$

where I_{in} is the input current and V_{in} is the input voltage at the defined port. In [2] the authors analyzed simple wire structures that had a one-to-one correspondence between modal surface current and modal port current due to the nature of the expansion functions they used. In our work, we utilize RWG expansion functions, which have relatively simple expressions to convert from surface currents and fields to port currents and voltages.

In order to excite an antenna in a moment method formulation, a feed model must be devised. A simple but very effective model known as delta-gap excitation [5, Ch. 4] will be used in this thesis. The model consists of placing a voltage generator in the gap between two separated regions of metal

$$\underline{E} = -\nabla\varphi = \frac{V}{\Delta}\hat{n} \tag{2.2}$$

where $\underline{E}$ is the uniform electric field in the gap, φ is the electric potential, Δ is the gap separation, V is the applied voltage and $\hat{n}$ is the normal vector relative to the metal edges (tangent to the surface). This model is shown in Figure 3.1(a). As the gap separation vanishes, the electric field in the gap is represented by a delta function $\underline{E} = V\delta(\underline{r})\hat{n}$. Integration across this gap simply suggests that the integral of the electric field is simply equal to the applied voltage V. The delta-gap excitation is implemented using RWG expansion functions by assuming an incident electric field is applied between the common edges of the triangles in a single RWG expansion function. This scenario is depicted in Figure 3.1(b). We refer the reader to reference [5, Ch. 4] for further details on this subject matter. Using the delta-gap source model as the working model of our antenna port, the input current and input voltage can be written respectively as

$$I_{in} = \ell_{edge} I_{edge} \tag{2.3}$$

$$V_{in} = E_{inc} / \ell_{edge} \tag{2.4}$$

where ℓ_{edge} refers to the length of the RWG expansion function edge where the port is defined, I_{edge} is the current coefficient associated with the RWG expansion function acting as the antenna port, and E_{inc} is the applied electric field at the port.

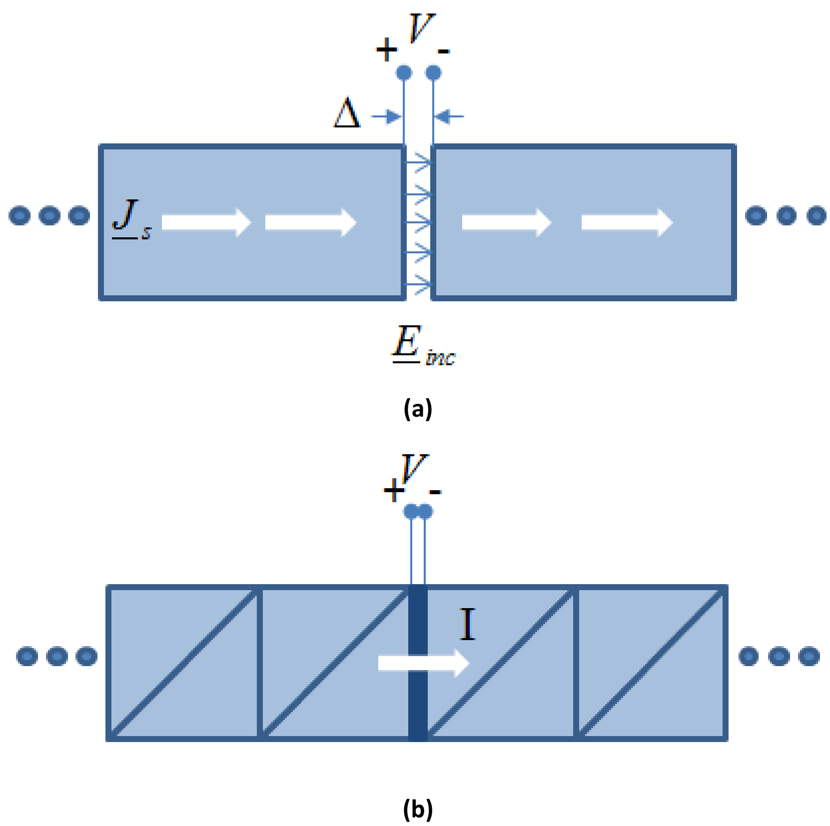

Figure 3.1 – Delta-gap excitation model shown on (a) an arbitrary PEC strip and (b) on an equivalent RWG meshed structure

Since the characteristic modes are defined by their modal current density it is natural to expand the input current rather than the input voltages in terms of the CMs. We begin by expanding the modal surface currents (which are distinct from the input current). Due to the orthogonality (Equation 2.34) properties of the characteristic modes, one can expand the surface current density at any location on the scatterer in terms of the characteristic modes as follows

$$\underline{J}\left(\underline{r}_o\right) = \sum_{n=1}^{\infty} \frac{V_n^i \underline{J}_n\left(\underline{r}_o\right)}{1 + j\lambda_n} \tag{2.5}$$

where $\underline{r}_o$ refers to an arbitrary physical location on the scatterer where the surface current density will be expanded in terms of the CMs. Once again, the current in this example refers to the surface currents and not the port currents and therefore cannot be directly used in the admittance expansion. In a similar manner, one can expand the moment method current coefficients in terms of the characteristic mode current coefficients.

Consider expression (3.5) and now assume that we expand the RWG expansion function current coefficient I_{edge} from expression (3.3) associated with the selected port in terms of the characteristic mode current coefficients

$$I_{edge} = \sum_{n=1}^{\infty} \frac{V_n^i J_n}{1 + j\lambda_n} \tag{2.6}$$

where J_n is a single real scalar and not a magnitude or vector quantity. In other words, J_n is the characteristic mode current density coefficient for the selected RWG function acting as our port. We now multiply both sides of (3.7) by ℓ_{edge} – this gives us an expression for the input current I_{in}

$$I_{in} = \sum_{n=1}^{\infty} \frac{V_n^i \ell_{edge} J_n}{1 + j\lambda_n} \tag{2.7}$$

We continue by considering the modal excitation coefficient which can be computed as (Equation 2.32)

$$V_n^i = \left\langle \underline{E}_{inc}, \underline{J}_n \right\rangle = \ell_{edge} V_{in} J_n \tag{2.8}$$

where the inner product is reduced to a product of three scalars by virtue of the fact that we are considering a single antenna port and J_n is the characteristic mode current coefficient at the selected port. If we substitute (3.6) into (3.8) we have the expression for input current written solely in terms of characteristic mode eigenvalues and eigencurrents

$$I_{in} = \left(\ell_{edge}\right)^2 V_{in} \sum_{n=1}^{\infty} \frac{J_n^2}{1 + j\lambda_n} \tag{2.9}$$

Recall (Section 2.2) that the modal current density $\underline{J}_n$ is real and thus the RWG modal current coefficients J_n are real scalars as well making the squaring of J_n in (3.9) mathematically sound. Finally, dividing (3.9) by V_{in}, one can obtain the input admittance and impedance of the antenna solely in terms of the characteristic modes of said structure

$$Y_{in} = \frac{I_{in}}{V_{in}} = \ell_{edge}^2 \sum_{n=1}^{\infty} \frac{J_n^2}{1 + j\lambda_n} \tag{2.10}$$

$$Z_{in} = \frac{V_{in}}{I_{in}} = \ell_{edge}^{-2} \left[\sum_{n=1}^{\infty} \frac{J_n^2}{1 + j\lambda_n} \right]^{-1} \tag{2.11}$$

Note that our expressions differ from [2] by the factor ℓ_{edge}^2 since our moment method formulation uses RWG expansion function and not pulse expansion functions. The concept of modal admittance (and modal impedance) as the contribution of the nth mode to the overall admittance and impedance of the antenna is defined as follows

$$Y_n = \ell_{edge}^2 \frac{J_n^2}{1 + j\lambda_n} \tag{2.12}$$

$$Z_n = \frac{1}{\ell_{edge}^2} \left(\frac{1 + j\lambda_n}{J_n^2} \right) \tag{2.13}$$

It is interesting to note that the modal admittances are summed to yield the input admittance, while the modal impedance is clearly placed in a parallel-sense (it is not a linear sum) showing unambiguously that the modal admittance and impedances are placed in parallel to describe the behavior of the antenna being analyzed. This can be shown via the two expressions

$$Y_{in} = \sum_{n=1}^{\infty} Y_n \tag{2.14}$$

$$Z_{in} = \left(\sum_{n=1}^{\infty} \frac{1}{Z_n} \right)^{-1} \tag{2.15}$$

both of which are represented by connecting admittances (3.14) and impedances (3.15) in parallel. As a last step, we express the modal admittance (3.12) and impedance (3.13) in terms of their real and imaginary parts, thereby obtaining the modal conductance and susceptance

$$Y_n = G_n + jB_n = \frac{\ell_{edge}^2 J_n^2}{1+\lambda_n^2}\left(1 - j\lambda_n\right) = \frac{\ell_{edge}^2 J_n^2}{1+\lambda_n^2} + j\frac{-\ell_{edge}^2 \lambda_n J_n^2}{1+\lambda_n^2} \tag{2.16}$$

as well as the modal resistance and reactance

$$Z_n = R_n + jX_n = \frac{1}{\ell_{edge}^2 J_n^2}\left(1 + j\lambda_n\right) = \frac{1}{\ell_{edge}^2 J_n^2} + j\frac{\lambda_n}{\ell_{edge}^2 J_n^2} \tag{2.17}$$

These expressions will prove to be useful in coming derivations.

3.2.2 – Antenna Q in Terms of Characteristic Modes

The work by Yaghjian and Best [6] showed that the antenna Q can be written rather succinctly using the expression (2.56) from Chapter 2. Their expression is dependent solely on the frequency behavior of the antenna's input impedance. We proceed with our investigation by combining the results of the previous section where admittances and impedance were written in terms of CM eigenvalues and currents, with expression (2.56) to yield an expression for antenna Q in terms of the CMs.

The expansion of an antenna input resistance and reactance can be written in terms of the antenna ports' modal conductance and susceptance

$$Z_{in} = \frac{1}{Y_{in}} = \frac{1}{G_{in} + jB_{in}} = \frac{G_{in} - jB_{in}}{G_{in}^2 + B_{in}^2} \tag{2.18}$$

thus allowing us to write the input resistance and reactance

$$R_{in} = \frac{G_{in}}{G_{in}^2 + B_{in}^2} \tag{2.19}$$

$$X_{in} = \frac{-B_{in}}{G_{in}^2 + B_{in}^2} \tag{2.20}$$

where $G_{in} = \sum_{n=1}^{\infty} G_n$ and $B_{in} = \sum_{n=1}^{\infty} B_n$.

The frequency derivatives of these quantities become relevant, namely

$$\frac{dR_{in}}{d\omega} = \frac{d}{d\omega}\frac{G_{in}}{G_{in}^2 + B_{in}^2} \tag{2.21}$$

$$\frac{dX_{in}}{d\omega} = \frac{d}{d\omega}\frac{-B_{in}}{G_{in}^2 + B_{in}^2} \tag{2.22}$$

The magnitude of the input reactance

$$\left|X_{in}\right| = \frac{\left|B_{in}\right|}{G_{in}^2 + B_{in}^2} \tag{2.23}$$

Combining expressions (3.19) through (3.23) with expression (2.56) for antenna Q we obtain

$$\begin{aligned} Q(\omega_o) &= \frac{\omega_o \sqrt{\left(R_{in}^{'}(\omega_o)\right)^2 + \left(X_{in}^{'}(\omega_o) + \left|X_{in}(\omega_o)\right|/\omega_o\right)^2}}{2R_{in}(\omega_o)} \\ &= \frac{\omega_o}{2}\left(\frac{G_{in}^2 + B_{in}^2}{G_{in}}\right)\sqrt{\left(\frac{d}{d\omega}\frac{G_{in}}{G_{in}^2 + B_{in}^2}\right)^2 + \left(\frac{d}{d\omega}\frac{-B_{in}}{G_{in}^2 + B_{in}^2} + \frac{1}{\omega_o}\frac{\left|B_{in}\right|}{G_{in}^2 + B_{in}^2}\right)^2} \end{aligned} \tag{2.24}$$

If we further substitute the expressions for input conductance and susceptance (see 3.16) in terms of CM quantities, we obtain

$$Q(\omega_o) = \frac{\omega_o}{2}\left(\frac{\left(\sum_{n=1}^{\infty} G_n\right)^2 + \left(\sum_{n=1}^{\infty} B_n\right)^2}{\left(\sum_{n=1}^{\infty} G_n\right)^2}\right)\sqrt{\left(\frac{d}{d\omega}\frac{\left(\sum_{n=1}^{\infty} G_n\right)^2}{\left(\sum_{n=1}^{\infty} G_n\right)^2 + \left(\sum_{n=1}^{\infty} B_n\right)^2}\right)^2 + \left(\frac{d}{d\omega}\frac{-\left(\sum_{n=1}^{\infty} B_n\right)^2}{\left(\sum_{n=1}^{\infty} G_n\right)^2 + \left(\sum_{n=1}^{\infty} B_n\right)^2} + \frac{1}{\omega_o}\frac{\left|\left(\sum_{n=1}^{\infty} B_n\right)^2\right|}{\left(\sum_{n=1}^{\infty} G_n\right)^2 + \left(\sum_{n=1}^{\infty} B_n\right)^2}\right)^2} \tag{2.25}$$

At this juncture, expression (3.25) is indeed an expression for antenna Q that is written solely in terms of the characteristic mode quantities of the antenna structure since G_n and B_n are written in terms of the modal current density J_n and eigenvalue λ_n in expression (3.16). However, this expression is too unruly to be used effectively in analysis and little information can be obtained from the expression in its present form. Nevertheless, valid assumptions can be made about the nature of the antenna being analyzed, namely the number of significant modes needed in the expansions and the nature of the net stored energy associated with the port being excited, that greatly simplifies expression (3.25) to a useful form. These assumptions will be explored in the remaining sub-sections of Section 3.2.

3.2.3 – Input Impedance of a Single Mode Antenna

In this section we will delve into the implications of having a single mode antenna. Such an antenna can be viewed as having negligible higher order characteristic modes, with a single dominant CM. This can be numerically described as the existence of a single CM having a low-magnitude eigenvalue while all remaining modes have very large magnitude eigenvalues. Such a scenario leads to the performance of the antenna being solely described by the dominant CM.

Firstly, we consider the modal admittance Y_n, given in expression (3.12). If the eigenvalue of mode n is very large, the modal admittance becomes negligible. In other words,

Statement #1: For $|\lambda_n|$ large, $Y_n \approx 0$

Secondly, if the eigenvalue is small in magnitude, the admittance becomes significant

Statement #2: For $|\lambda_n|$ small, Y_n is significant

Therefore, in the expression (3.10) the modes with small eigenvalues become significant in describing the input admittance of the antenna, while modes with large eigenvalues are insignificant. If we assume that a single dominant characteristic mode exists (hereafter denoted mode 1), the expression for input admittance simplifies to

$$Y_{in} \approx Y_1 = \frac{\ell_{edge}^2 J_1^2}{1+\lambda_1^2} + j\frac{-\ell_{edge}^2 \lambda_1 J_1^2}{1+\lambda_1^2} \qquad (2.26)$$

If the input admittance can be expressed succinctly in this manner under the single mode assumption, so too can the input impedance. Taking the inverse of (3.26), we obtain the expression for input impedance under the single mode assumption

$$Z_{in} = \frac{1}{Y_{in}} = \frac{1}{Y_1} = Z_1 = \frac{1 + j\lambda_1}{\ell^2_{edge} J_1^2} \tag{2.27}$$

showing that the input impedance of a single mode antenna is also equal to the dominant modal impedance. In summary, the input admittance and impedance of a single mode antenna can be written

$$Y_{in} = \frac{\ell^2_{edge} J_1^2}{1 + \lambda_1^2} + j\frac{-\ell^2_{edge} \lambda_1 J_1^2}{1 + \lambda_1^2} \tag{2.28}$$

$$Z_{in} = \frac{1}{\ell^2_{edge} J_1^2} + j\frac{\lambda_1}{\ell^2_{edge} J_1^2} \tag{2.29}$$

where J_1 and λ_1 are assumed to have frequency dependence. We have obtained expressions for the input impedance and admittance of a single-mode antenna in terms of quantities related to the dominant CM. These will be used in Section 3.2.4 to find a useful set of expressions for the Q of a single-mode antenna.

3.2.4 – Antenna Q of a Single Mode Antenna

We now have succinct and workable expressions for input resistance and reactance and have the ability to clearly define their frequency derivatives. Consideration of expression (3.27) with its real and imaginary parts separated and its frequency derivative computed, we obtain

$$R_{in} = \frac{1}{\ell^2_{edge} J_1^2} \tag{2.30}$$

$$X_{in} = \frac{\lambda_1}{\ell^2_{edge} J_1^2} \tag{2.31}$$

$$\left| X_{in} \right| = \frac{\left| \lambda_1 \right|}{\ell^2_{edge} J_1^2} \tag{2.32}$$

$$\frac{dR_{in}}{d\omega} = \frac{1}{\ell_{edge}^2} \frac{d}{d\omega} \frac{1}{J_1^2} \tag{2.33}$$

$$\frac{dX_{in}}{d\omega} = \frac{1}{\ell_{edge}^2} \frac{d}{d\omega} \frac{\lambda_1}{J_1^2} \tag{2.34}$$

Expressions (3.33) and (3.34) can be further simplified to

$$\frac{dR_{in}}{d\omega} = \frac{1}{\ell_{edge}^2} \left[\frac{-2}{J_1^3} \frac{dJ_1}{d\omega} \right] \tag{2.35}$$

$$\frac{dX_{in}}{d\omega} = \frac{1}{\ell_{edge}^2 J_1^2} \left[\frac{d\lambda_1}{d\omega} - 2\frac{\lambda_1}{J_1} \frac{dJ_1}{d\omega} \right] \tag{2.36}$$

where expressions (3.30) – (3.32) as well as (3.35) and (3.36) are all valid for single-mode antennas. If we substitute expressions (3.30) through (3.32) as well as (3.35) and (3.36) into (2.56), we obtain a more succinct expression for antenna Q as follows

$$Q(\omega) = \frac{\ell_{edge}^2 J_1^2 \omega}{2} \sqrt{\left(\frac{1}{\ell_{edge}^2} \frac{-2}{J_1^3} \frac{dJ_1}{d\omega} \right)^2 + \left(\frac{1}{\ell_{edge}^2 J_1^2} \left[\frac{d\lambda_1}{d\omega} - 2\lambda_1 \frac{1}{J_1} \frac{dJ_1}{d\omega} \right] + \frac{1}{\omega} \frac{|\lambda_1|}{\ell_{edge}^2 J_1^2} \right)^2} \tag{2.37}$$

Further simplifications can be made, namely the removal of the dependence on ℓ_{edge}^2 as well as removing a J_1^2 dependence giving us

$$Q(\omega) = \frac{\omega}{2} \sqrt{\left(\frac{2}{J_1} \frac{dJ_1}{d\omega} \right)^2 + \left(\frac{d\lambda_1}{d\omega} - 2\frac{\lambda_1}{J_1} \frac{dJ_1}{d\omega} + \frac{|\lambda_1|}{\omega} \right)^2} \tag{2.38}$$

Expression (3.38) can be used to compute the antenna Q for a single mode antenna strictly in terms of modal quantities (the eigenvalues and eigencurrent and their respective frequency derivatives). It is relevant to point out that the antenna Q obtained in this manner is independent of the edge length, implying that the antenna Q derived from modal quantities is independent of the moment method formulation used to obtain the characteristic modes.

Antennas show their greatest utility around their resonance, as this provides the ability to forgo the need for a matching network (at least for tuning out the input reactance). Antenna resonance occurs when $X_{in} \approx 0$ which further implies that $\lambda_1 \approx 0$ at resonance (from expression 3.31). This implies expression (3.38) can be simplified for a resonant antenna to the form

$$Q(\omega_o) = \frac{\omega_o}{2} \sqrt{\left(\frac{1}{J_1^2} \frac{dJ_1}{d\omega} \right)^2 + \left(\frac{d\lambda_1}{d\omega} \right)^2} \tag{2.39}$$

where ω_o is used rather than ω to signify that one is considering a resonance frequency where $\lambda_1 \approx 0$.

The type of resonance is also an important property to identify. As Yaghjian and Best [6] remind us, there exist resonances and anti-resonances. A resonance occurs when $X_{in} \approx 0$ with $dX_{in}/d\omega > 0$ while an anti-resonance has $X_{in} \approx 0$ with $dX_{in}/d\omega < 0$. Consideration of expression (3.36) shows that if $\lambda_1 \approx 0$, a resonance occurs only if $d\lambda_1/d\omega > 0$ while an anti-resonance would occur only if $d\lambda_1/d\omega < 0$. Furthermore, as discussed in [6], the frequency derivative of the input resistance is negligible compared to the frequency derivative of input reactance for frequencies around resonance. On the other hand, both frequency derivatives become relevant in describing antenna behavior around anti-resonance. The properties of a resonance allows us to further simplify (3.39) for the case of an antenna around a resonance (as opposed to anti-resonance). Namely, since $\frac{dR_{in}}{d\omega} \alpha \frac{dJ_1}{d\omega}$ (from 3.35) and $\frac{dX_{in}}{d\omega} \alpha \frac{d\lambda_1}{d\omega}$ (from 3.36, if $\lambda_1 \approx 0$), expression (3.39) simplifies to the following in the vicinity of a resonance

$$Q(\omega_o) \approx \frac{\omega_o}{2} \left| \frac{d\lambda_1}{d\omega} \right| \tag{2.40}$$

since $\frac{dX_{in}}{d\omega} \gg \frac{dR_{in}}{d\omega}$ and thus $\left| \frac{d\lambda_1}{d\omega} \right| \gg \left| \frac{dJ_1}{d\omega} \right|$. Expression (3.40) represents the Q of a single-mode antenna at resonance. Note that this is the same as the modal Q (save for the absolute value) defined in (2.45). In other words, the Q of a single mode antenna is equal to its modal Q at resonance. Furthermore, [6] also mentions that $dR_{in}/d\omega \approx 0$ precisely at an anti-resonant frequency, making expression (3.40) valid for both resonance and anti-resonance.

As a final comment on these derivations, note that the expression (3.38) and (3.39) for antenna Q requires knowledge of the modal currents and requires a port to be selected (an obvious result). In contrast, note that expression (3.40) is only a function of the eigenvalue, which is entirely independent of excitation and port selection. This will have major implications in later derivations and forms the foundation of the contributions of the present chapter of this dissertation.

3.2.5 – Radiation Efficiency and its Effect on Antenna Q of a Single Mode Antenna

In [7], Harrington and Mautz discuss the CMs of penetrable objects (objects consisting of any materials be they metals, dielectrics or magnetic materials). The derivations for the CMs of lossy structures were also included in [7], but only very briefly discussed. The present author offered another look at these modes in [1, 8]. We use the latter embellishments in finding expression for the Q of lossy structures in terms of CM parameters.

The eigenvalue problem to be solved in the presence of losses is as follows

$$\left[Z+Z_L\right]\left[J_n\right]=\tau_n\left[R\right]\left[J_n\right] \tag{2.41}$$

where $\left[Z_L\right]=\left[R_L\right]+j\left[X_L\right]$ is the operator strictly associated with losses, $\left[Z\right]$ and $\left[R\right]$ are the impedance and resistance operators for the lossless case and τ_n is the eigenvalue associated with the eigenvalue problem. The form of this eigenvalue problem ensures orthogonality of the characteristic modes, even in the presence of loss. Other formulations are possible, but it is this form that leads to the orthogonality of the far-field patterns of the modal currents. The interpretation of the eigenvalue is of relevance and was first considered in the authors' work [8]. Taking the inner product of the eigenvalue problem with respect to $\left[J_n\right]$ and isolating for the eigenvalue itself, we obtain the following expression

$$\tau_n=\frac{\left[J_n^*\right]\left[Z\right]\left[J_n\right]+\left[J_n^*\right]\left[Z_L\right]\left[J_n\right]}{\left[J_n^*\right]\left[R\right]\left[J_n\right]} \tag{2.42}$$

We can further expand the expressions into real and imaginary parts as follows

$$\tau_n = \frac{\left[J_n^*\right]\left[R\right]\left[J_n\right] + \left[J_n^*\right]\left[R_L\right]\left[J_n\right] + j\left\{\left[J_n^*\right]\left[X\right]\left[J_n\right] + \left[J_n^*\right]\left[X_L\right]\left[J_n\right]\right\}}{\left[J_n^*\right]\left[R\right]\left[J_n\right]} \tag{2.43}$$

We can define the quantities in (3.43) as $P_{rad,n} = \left[J_n^*\right]\left[R\right]\left[J_n\right]$, $P_{reac,n} = \left[J_n^*\right]\left[X + X_L\right]\left[J_n\right]$ and $P_{loss,n} = \left[J_n^*\right]\left[R_L\right]\left[J_n\right]$ where $P_{rad,n}$, $P_{reac,n}$ and $P_{loss,n}$ are radiated, reactive and dissipated power quantities respectively. Using this interpretation, we can express the eigenvalue τ_n in the form $\tau_n = 1 + \frac{P_{loss,n}}{P_{rad,n}} + j\lambda_n$. Furthermore, using the relationship $1 + \frac{P_{loss,n}}{P_{rad,n}} = \frac{1}{e_{rad,n}}$ gives us the more useful interpretation of the eigenvalue in terms of radiation efficiency as follows

$$\tau_n = \frac{1}{e_{rad,n}} + j\lambda_n \tag{2.44}$$

where $e_{rad,n}$ is defined as the modal radiation efficiency. We can also write this modal radiation efficiency as a function of the eigenvalue simply as

$$e_{rad,n} = \left(\mathrm{Re}\left\{\tau_n\right\}\right)^{-1} \tag{2.45}$$

The imaginary part of the eigenvalue has the same interpretation as the PEC characteristic modes, while the real part is equal to the reciprocal of the radiation efficiency of the mode in question. When losses are present, the expression for the input impedance in terms of the CMs remains largely unchanged, but care must be taken to include the effects of loss appropriately. The modal resistance is the only factor that changes, giving us the expression

$$R_n = \frac{1}{e_{rad,n}} \frac{1}{\ell_{edge}^2 J_n^2} \tag{2.46}$$

If the analyzed structure were lossless ($e_{rad,n} = 1$), (3.46) simply becomes $R_n = \frac{1}{\ell_{edge}^2 J_n^2}$ which is the same expression for the lossless case (real part of expression 3.17). Further consider that we can write the modal resistance as a sum of modal radiation and loss resistances as follows

$$R_{n,rad} + R_{n,loss} = \frac{1}{e_{rad,n}} \frac{1}{\ell_{edge}^2 J_n^2} \tag{2.47}$$

which allows us to solve for the modal radiation and loss resistances respectively as follows

$$R_{n,rad} = \frac{1}{\ell_{edge}^2 J_n^2} \tag{2.48}$$

$$R_{n,loss} = \left(\frac{1 - e_{rad,n}}{e_{rad,n}} \right) \frac{1}{\ell_{edge}^2 J_n^2} \tag{2.49}$$

The frequency derivative of the modal resistance becomes

$$\frac{dR_n}{d\omega} = \frac{-1}{e_{rad,n} \ell_{edge}^2 J_n^2} \left\{ \frac{1}{e_{rad,n}} \frac{de_{rad,n}}{d\omega} + \frac{2}{J_n} \frac{dJ_n}{d\omega} \right\} \tag{2.50}$$

Through similar arguments and simplifications as discussed previously for the lossless case, the antenna Q of the lossy single mode antenna can be written as follows

$$Q(\omega) = \frac{\omega}{2} \sqrt{ \left(\frac{1}{e_{rad,1}} \frac{de_{rad,1}}{d\omega} + \frac{2}{J_1} \frac{dJ_1}{d\omega} \right)^2 + e_{rad,1}{}^2 \left(\left[\frac{d\lambda_1}{d\omega} - 2\lambda_1 \frac{1}{J_1} \frac{dJ_1}{d\omega} \right] + \frac{|\lambda_1|}{\omega} \right)^2 } \tag{2.51}$$

If ω is selected to be ω_o (a resonant mode, or $\lambda_1 \approx 0$), (3.51) becomes

$$Q(\omega_o) = \frac{\omega_o}{2} \sqrt{ \left(\frac{1}{e_{rad,1}} \frac{de_{rad,1}}{d\omega} + \frac{2}{J_1} \frac{dJ_1}{d\omega} \right)^2 + \left(e_{rad,1} \frac{d\lambda_1}{d\omega} \right)^2 } \tag{2.52}$$

We once again use the property $\frac{d\lambda_1}{d\omega} \gg \frac{dJ_1}{d\omega}$ and further conclude that $\frac{d\lambda_1}{d\omega} \gg \frac{de_{rad,1}}{d\omega}$ since the radiation efficiency will be proportional to the current J_1 and so will the frequency derivative of $e_{rad,1}$, making the entire term within the first square of (3.52) negligible compared to the second squared element. This leaves us with the final approximate expression for the Q of a lossy single mode antenna

$$Q(\omega_o) \approx e_{rad,1} \frac{\omega_o}{2} \left| \frac{d\lambda_1}{d\omega} \right| \tag{2.53}$$

As expected, a larger Q (narrower bandwidth) is obtained when the antenna is lossless ($e_{rad,1} = 1$) for identical frequency behavior of its dominant eigenvalue. This is not surprising since loss will increase the bandwidth of antennas and electromagnetic devices in general [6].

3.2.6 – A Further Point of Interest

An interesting property of the single-mode antenna is the interrelationship between the real and imaginary parts of the input impedance, namely

$$X_{in} = \lambda_1 R_{in} \tag{2.54}$$

This is easily seen from (3.30) and (3.31), with (3.33) and (3.34) in turn implying

$$\frac{dX_{in}}{d\omega} = R_{in}\frac{d\lambda_1}{d\omega} + \lambda_1\frac{dR_{in}}{d\omega} \tag{2.55}$$

If the antenna is resonant ($\lambda_1 \approx 0$), this further simplifies to

$$\frac{dX_{in}}{d\omega} = R_{in}\frac{d\lambda_1}{d\omega} \tag{2.56}$$

which is a surprisingly simple relationship between the real and imaginary parts of the frequency derivative of input impedance. It also implies that if one is confident experimentally that a single mode antenna is being measured, the frequency derivative of the dominant eigenvalue can be estimated from experimentally measured input impedance data.

Two different forms of (3.39) can be derived by substituting (3.54) and (3.56) into (3.39) at resonant single-mode structure, giving us

$$Q(\omega_o) = \frac{\omega_o}{2}\left|\frac{d\lambda_1}{d\omega}\right|\sqrt{1+\left(\frac{R_{in}^{'}(\omega_o)}{X_{in}^{'}(\omega_o)}\right)^2} \tag{2.57}$$

$$Q(\omega_o) = \frac{\omega_o}{2}\sqrt{\left(\frac{d\lambda_1}{d\omega}\right)^2+\left(\frac{R_{in}^{'}}{R_{in}}\right)^2} \tag{2.58}$$

If both the inequalities $R_{in}^{'}(\omega_o) \ll X_{in}^{'}(\omega_o)$ and $R_{in}^{'}(\omega_o) \ll R_{in}(\omega_o)$ are true, then (3.57) and (3.58) give us the same result as expression (3.40) for the case of a single-mode, resonant antenna. Note that [6] explicitly states both of the inequalities are true for an antenna around resonance.

3.3 – Single-Mode Antenna Performance Prediction without Excitation

3.3.1 – Preliminaries

In Section 3.2 we showed that for a single-mode antenna, the dominant mode of the structure describes numerous relevant electromagnetic quantities. We also showed that, quite surprisingly, the resonance frequency (3.31), bandwidth (3.53) and radiation efficiency (3.45) were all predicted strictly from the frequency behavior of the eigenvalue of the dominant mode. The eigencurrents were not required in these expressions – without having to define an antenna port or excitation, the above antenna properties can be determined. All of these properties can be obtained by solving a characteristic mode eigenvalue problem. However, it is well known that eigenanalysis is computationally costly and may prove difficult to efficiently incorporate in, for example, an optimization routine. Our intention is to develop a computationally efficient manner by which eigenvalue information can be used to optimize the performance of antenna structures in a feedless manner.

As a preliminary step, we wish to re-define the two characteristic mode eigenvalue problems for the lossless and lossy cases such that all operators appear on one side of the equation and therefore represent a simple eigenvalue problem as opposed to a generalized eigenvalue problem. This is accomplished by re-organizing the matrices in (2.11) and (3.41). First we consider the lossless case

$$[Z]^{-1}[R][J_n] = (1 + j\lambda_n)^{-1}[J_n] \tag{2.59}$$

and then the lossy case

$$[Z + Z_L]^{-1}[R][J_n] = \left(e_{rad,n}^{-1} + j\lambda_n\right)^{-1}[J_n] \tag{2.60}$$

We will define two matrices, hereafter referred to as the CM matrices, with the following definitions:

$$[CM]_{PEC} = [Z]^{-1}[R] \tag{2.61}$$

$$[CM]_{LOSSY} = [Z + Z_L]^{-1}[R] \tag{2.62}$$

The justification for re-defining the eigenvalue problems as shown in (3.59) and (3.60) as well as the definition of the CM matrices in (3.61) and (3.62) will be discussed in Section 3.3.2 through 3.3.4.

3.3.2 – Feedless Resonance Prediction

We wish to find a computationally simple method of predicting whether an antenna is resonant. The proposed approach involves the operator known as the trace of a matrix. The matrix trace is a rather simple operator, being equal to the sum of diagonal terms of the matrix. Quite surprisingly, this operator is also equal to the sum of the eigenvalues of said matrix. These properties can be expressed in the following manner for an arbitrary matrix $\left[A\right]$

$$Trace\left[A\right]=\sum_{n=1}^{N}a_{nn}=\sum_{n=1}^{N}\nu_{n} \tag{2.63}$$

where a_{nn} are the diagonal entries of the matrix $\left[A\right]$ and the ν_n are the eigenvalues of the matrix $\left[A\right]$, obtained by solving the eigenvalue problem $\left[A\right]\left[x_n\right]=\nu_n\left[x_n\right]$ where $\left[x_n\right]$ are the eigenvectors of $\left[A\right]$. Consider now the matrix trace of the CM matrices for the lossless (3.61) and lossy (3.62) cases

$$Trace\left(\left[Z\right]^{-1}\left[R\right]\right)=\sum_{n=1}^{N}\frac{1}{1+j\lambda_n} \tag{2.64}$$

$$Trace\left(\left[Z+Z_L\right]^{-1}\left[R\right]\right)=\sum_{n=1}^{N}\frac{1}{e_{rad,n}^{-1}+j\lambda_n} \tag{2.65}$$

If a single dominant characteristic mode is present, with all other modes having large magnitude eigenvalues (i.e. the single mode antenna case), the expressions for the matrix trace become

$$Trace\left(\left[Z\right]^{-1}\left[R\right]\right)=\frac{1}{1+j\lambda_1}+\underbrace{\frac{1}{1+j\lambda_2}+\cdots\frac{1}{1+j\lambda_N}}_{\approx 0}\approx\frac{1}{1+j\lambda_1} \tag{2.66}$$

$$Trace\left(\left[Z+Z_L\right]^{-1}\left[R\right]\right)=\frac{1}{e_{rad,1}^{-1}+j\lambda_1}+\underbrace{\frac{1}{e_{rad,2}^{-1}+j\lambda_2}+\cdots\frac{1}{e_{rad,N}^{-1}+j\lambda_N}}_{\approx 0}\approx\frac{1}{e_{rad,1}^{-1}+j\lambda_1} \tag{2.67}$$

Moreover, if the dominant mode is resonant ($\lambda_1\approx 0$), the matrix traces become purely real. Another perspective is to view the matrix trace as a general complex number – if at the specified frequency its argument becomes zero (its phase is zero) the analyzed structure defined by $\left[Z\right]$ or $\left[Z+Z_L\right]$ is resonant at that frequency. Notice that this prediction of resonance remains free of excitation, true to its origins in eigenanalysis.

3.3.3 – Feedless Radiation Efficiency Prediction

A corollary of the prediction of resonance is the prediction of radiation efficiency. If an antenna is resonant, its radiation efficiency can be directly inferred from the matrix trace. In particular, for the lossless case the CM matrix trace is equal to one when the antenna structure is resonant

$$Trace\left(\left[Z\right]^{-1}\left[R\right]\right)\Big|_{\lambda_1\approx 0} \approx \frac{1}{1+j\underbrace{\lambda_1}_{\approx 0}} \approx 1 \tag{2.68}$$

while for the lossy case the matrix trace is equal to the radiation efficiency (again, when the antenna is resonant)

$$Trace\left(\left[Z+Z_L\right]^{-1}\left[R\right]\right)\Big|_{\lambda_1\approx 0} \approx \frac{1}{e_{rad,1}^{-1}+j\underbrace{\lambda_1}_{\approx 0}} \approx e_{rad,1} \tag{2.69}$$

We can therefore interpret the unity magnitude of (3.68) as being representative of the radiation efficiency of a PEC antenna which is necessarily 100%.

3.3.4 – Feedless Antenna Q (Bandwidth) Prediction

Consider the frequency derivative of the trace of the CM matrix (3.61) describing a PEC scatterer with a single dominant mode,

$$\begin{aligned}\frac{d}{d\omega}Trace\left(\left[Z\right]^{-1}\left[R\right]\right) &= \frac{d}{d\omega}\frac{1}{1+j\lambda_1}\\ &= \frac{d}{d\omega}\frac{1}{1+\lambda_1^2} - j\frac{d}{d\omega}\frac{\lambda_1}{1+\lambda_1^2}\\ &= \frac{-2\lambda_1}{\left(1+\lambda_1^2\right)^2}\frac{d\lambda_1}{d\omega} - j\frac{\left(1-\lambda_1^2\right)}{\left(1+\lambda_1^2\right)^2}\frac{d\lambda_1}{d\omega}\end{aligned} \tag{2.70}$$

If the dominant mode is resonant ($\lambda_1 \approx 0$) then we have the simplification

$$\frac{d}{d\omega}Trace\left(\left[Z\right]^{-1}\left[R\right]\right)\Big|_{\lambda_1\approx 0} = -j\frac{d\lambda_1}{d\omega} \tag{2.71}$$

This implies that at resonance the antenna Q of the structure being analyzed can be predicted solely in terms of frequency derivative of the matrix via the expression

$$Q = \frac{\omega_o}{2}\left|\frac{d\lambda_1}{d\omega}\right| \approx \frac{\omega_o}{2}\left|\frac{d}{d\omega}Trace\left(\left[Z\right]^{-1}\left[R\right]\right)\right|_{\lambda_1\approx 0} \tag{2.72}$$

If losses are present, the problem takes the alternative form

$$\begin{aligned}\frac{d}{d\omega}Trace\left(\left[Z+Z_L\right]^{-1}\left[R\right]\right) &= \frac{d}{d\omega}\frac{1}{e_{rad,1}^{-1}+j\lambda_1} \\ &= \frac{d}{d\omega}\frac{e_{rad,1}^{-1}}{e_{rad,1}^{-2}+\lambda_1^2} - j\frac{d}{d\omega}\frac{\lambda_1}{e_{rad,1}^{-2}+\lambda_1^2}\end{aligned} \tag{2.73}$$

At resonance the two derivatives in (3.73) become

$$\left.\frac{d}{d\omega}\frac{e_{rad,1}^{-1}}{e_{rad,1}^{-2}+\lambda_1^2}\right|_{\lambda_1\approx 0} = \left.\frac{-\left(e_{rad,1}^{-2}+\lambda_1^2\right)e_{rad,1}^{-2}\dfrac{de_{rad,1}}{d\omega} - e_{rad,1}^{-1}\left\{2\lambda_1\dfrac{d\lambda_1}{d\omega} - 2e_{rad,1}^{-3}\dfrac{de_{rad,1}}{d\omega}\right\}}{\left(e_{rad,1}^{-2}+\lambda_1^2\right)^2}\right|_{\lambda_1\approx 0} = \frac{de_{rad,1}}{d\omega} \tag{2.74}$$

$$\left.\frac{d}{d\omega}\frac{\lambda_1}{e_{rad,1}^{-2}+\lambda_1^2}\right|_{\lambda_1\approx 0} = \left.\frac{\left(e_{rad,1}^{-2}+\lambda_1^2\right)\dfrac{d\lambda_1}{d\omega} - \lambda_1\left\{\dfrac{-2}{e_{rad,1}^{3}}\dfrac{de_{rad,1}}{d\omega} + 2\lambda_1\dfrac{d\lambda_1}{d\omega}\right\}}{\left(e_{rad,1}^{-2}+\lambda_1^2\right)^2}\right|_{\lambda_1\approx 0} = e_{rad,1}^{2}\frac{d\lambda_1}{d\omega} \tag{2.75}$$

Thus the frequency derivative of the trace of the CM matrix for a lossy single-mode structure at resonance becomes

$$\frac{d}{d\omega}Trace\left(\left[Z+Z_L\right]^{-1}\left[R\right]\right) = \frac{de_{rad,1}}{d\omega} - je_{rad,1}^{2}\frac{d\lambda_1}{d\omega} \tag{2.76}$$

This allows us to write an expression for the antenna Q (3.53) of a resonant lossy structure in terms of the matrix trace. First, we note that $\left|\mathrm{Im}\left\{\frac{d}{d\omega}Trace\left(\left[Z+Z_L\right]^{-1}\left[R\right]\right)\right\}\right| = e_{rad,1}^{2}\left|\frac{d\lambda_1}{d\omega}\right|$ and that $\left|Trace\left(\left[Z+Z_L\right]^{-1}\left[R\right]\right)\right| = e_{rad,1}$ and hence we can write

$$Q = e_{rad,1}\frac{\omega_o}{2}\left|\frac{d\lambda_1}{d\omega}\right| \approx \frac{\omega_o}{2}\frac{\left|\mathrm{Im}\frac{d}{d\omega}\left\{Trace\left(\left[Z+Z_L\right]^{-1}\left[R\right]\right)\right\}\right|}{\left|Trace\left(\left[Z+Z_L\right]^{-1}\left[R\right]\right)\right|} \tag{2.77}$$

Although (3.77) appears as a lengthy expression, it is in fact a numerically simple computation. It should be noted that (3.77) becomes (3.72) if a lossless structure is assumed.

3.3.5 – Summary of Computationally Efficient Performance Predictors

It is worthwhile to summarize the results of Section 3.3 as it forms the foundation of Chapters 3 and 4, and greatly influences Chapter 5. Let us first define a new variable in the hope of simplifying derivations in Section 3.4 and beyond. We define a variable that represents the trace of the CM matrix as

$$\Psi\left(\omega\right) = Trace\left(\left[Z+Z_L\right]^{-1}\left[R\right]\right) \tag{2.78}$$

In the case of a PEC structure, $\Psi\left(\omega\right)$ in (3.78) simply has the loading matrix, representing losses, set equal to zero. We showed that resonance occurs whenever the matrix trace has an argument of zero (3.66). This is true for both lossless and lossy cases and is summarized succinctly via the expression

$$\angle\Psi\left(\omega_o\right) = 0^o \text{ at resonance} \tag{2.79}$$

This was followed by showing the ability to predict the radiation efficiency at resonance (3.46), which can now be summarized as follows, valid for both lossless and lossy structures:

$$e_{rad} = \left|\Psi\left(\omega_o\right)\right| \text{ at resonance} \tag{2.80}$$

We use e_{rad} rather than $e_{rad,1}$ since the modal radiation efficiency becomes the radiation efficiency of the antenna. Finally, our derivations concluded with the determination of antenna Q via the frequency derivative of the matrix trace leading us to an expression valid for lossless and lossy structures

$$Q \approx \frac{\omega_o}{2}\left|\frac{1}{\Psi\left(\omega_o\right)}\mathrm{Im}\left\{\frac{d\Psi\left(\omega_o\right)}{d\omega}\right\}\right| \text{ at resonance} \tag{2.81}$$

A thorough analysis of a single-mode antenna is shown in Appendix B to help elucidate the concepts discussed thus far in this chapter.

3.4 – A New Antenna Shape Synthesis Technique: Feedless Optimization

3.4.1 – Objective Functions for Feedless Optimization

From Section 3.3, and in particular the summary contained in Section 3.3.5, we have the makings of a new antenna shape synthesis technique. In particular, note that expressions (3.79) through (3.81) can be used without the need to define excitation, neither through a port nor through an incident field – yet the resonance frequency, bandwidth and radiation efficiency can be predicted. In an antenna optimization scheme one would typically specify a port and compute input impedance and radiated fields and then optimize parameters such resonance frequency, bandwidth and radiation efficiency. We can instead rely on expressions (3.79) – (3.81) to develop a feedless optimization approach. This approach is unique in the sense that the shape of the antenna can be synthesized (that is, the optimization process carried out) without having to specify the feed location(s) beforehand.

Our primary objective function is expression (3.79), namely $\angle\Psi(\omega)$. If we minimize the magnitude of this function we obtain an angle of zero degrees, signifying resonance

$$\text{Objective Function \#1: } \min\left|\angle\Psi(\omega)\right| \tag{2.82}$$

If this objective function is indeed minimized for an antenna being shape synthesized, we will obtain a resonant antenna. The feed location need not be specified a priori, but can be determined after the shape synthesis is complete. However, we will show that there is an ideal feed location that can be unambiguously determined once the shape synthesis is complete. That is to say, the resulting optimized antenna structure can be fed in a manner that leads to zero net stored energy (i.e. $X_{in} \approx 0$).

The secondary objective function, should we wish to use it, involves expression (3.80), namely $\left|\Psi(\omega)\right|$. We can optimize antenna radiation efficiency, again without having to define a feed. If we maximize the objective function, provided the first objection function criterion is met (that of resonance) we maximize radiation efficiency and hence use the objection function

$$\textit{Objection Function \#2:}\ \max\left|\Psi(\omega)\right| \text{ provided } \angle\Psi(\omega)=0^o \tag{2.83}$$

Lastly, we can optimize the bandwidth of an antenna using expression (3.81), forming our third objective function.

$$\textit{Objection Function \#3:}\ \min\left|\frac{\omega}{2}\frac{1}{\Psi(\omega)}\operatorname{Im}\left\{\frac{d\Psi(\omega)}{d\omega}\right\}\right| \text{ provided } \angle\Psi(\omega)=0^o \tag{2.84}$$

By minimizing expression (3.84), we minimize the antenna Q and consequently maximize bandwidth as long as objective function #1 (3.82) is simultaneously minimized. The flowchart employing these three objective functions is shown in Figure 3.2.

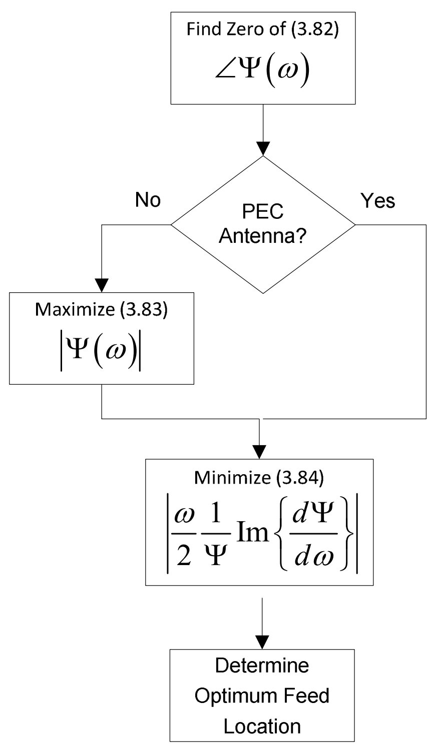

Figure 3.2 – Flowchart of the antenna shape synthesis procedure using the CM-derived objective functions

3.4.2 – A Natural Selection: Feedless Optimization, Genetic Algorithms and the DMM Method

The objective functions defined in Section 3.4.1 can be used with any optimization algorithm. Such algorithms range from purely deterministic methods such as conjugate gradient [9], mixed deterministic / stochastic genetic algorithms [10], to purely stochastic random walk approaches [10]. Optimization algorithms like the conjugate gradient method work well for many applications but tend to have difficulties with problems that have many local min/max. Random walk algorithms are not susceptible to prematurely converging on local min/max, but are computationally wasteful. Genetic algorithms offer a trade-off; the stochastic portion of the genetic algorithm helps to prevent premature convergence at local min/max while the deterministic portion of the algorithm leads to fairly good computational efficiency. Genetic algorithms also tend to be both robust and straightforward to implement, making them an ideal optimization technique to use in conjunction with the three proposed objective functions from Section 3.4.1.

A genetic algorithm is based on the principles of natural selection. An initial large population of random members (in our case, antennas) is generated, with their fitness (e.g. impedance, bandwidth, or other electromagnetic metrics) computed, thereby ranking them among the population. The population members are then mated (known as crossover), generating new members (offspring) that share properties with their parents. These offspring are subsequently integrated within the population and are ranked as well. The members within the population with the lowest fitness are removed or simply not selected for mating. The end result is a population whose members gradually improve in fitness until convergence is reached. Many details regarding genetic algorithms can be found in [10] – [12], including concepts such as mutation, mating schemes, how to control the population numbers and so on. An interesting fact of genetic algorithms is their ability to function well with a very wide range of optimization parameters, leading to their inherent robustness. An example genetic algorithm flow diagram is shown in Figure 3.3.

A technique described in [13], known as the direct-matrix-manipulation (DMM) method, will be used extensively in this thesis to manipulate the moment method model as the shape synthesis proceeds. The method works by recognizing the fact that the meshed geometry of an antenna is typically represented by geometrically described expansion functions. In particular, the RWG basis functions described in

Chapter 2 exist over triangular regions of metal. If one were to remove a triangle from a mesh (and its associated expansion functions), the geometry of the problem will change. Fortunately, the removal of portions of a moment method mesh can be accounted for in a very computationally efficient manner. An example simple mesh is shown in Figure 3.4(a), with the corresponding impedance matrix shown in a general form. The mesh contains 18 triangles, but the nature of the triangles, their edges and how RWG functions are defined leads to 21 expansion functions. Thus, the Z-matrix is 21 X 21 in size.

Assume we remove triangle #1, which has a single expansion function (for the sake of argument, assume it is expansion function #1). The resulting mesh is shown in Figure 3.4(b) with the newly updated Z-matrix reflecting the fact that the rows and columns associated with expansion function #1 are simply removed. The new matrix is now 20 X 20 in size rather than 21 x 21. The new matrix describes the updated geometry. Note that the impedance matrix was not re-computed for the new geometry but rather was retrieved as a “sub-matrix” of the initial matrix. The initial matrix is called the “mother matrix” as it contains the necessary information to describe all sub-matrices. In that sense, we also introduce the terminology “mother geometry” and sub-geometry for the sake of completeness. To conclude the description of the DMM method, we point out the fact that the technique allows one to generate a mother matrix that can, with great computational simplicity, describe a myriad of possible geometries without having to re-generate the matrix for each new geometry. This forms the foundations for the DMM method.

Our proposed algorithm will work as follows:

- The objective functions will be maximized or minimized using a standard genetic algorithm.
- Each member of the population will have a genome that is N bits long, with each bit representing the inclusion (bit = 1) or removal (bit = 0) of the triangle associated with the bit number. This is how each member is described within the genetic algorithm. There are initially N triangles.
- The fitness of each member of the population is determined by computing the objective functions 1 through 3 described in Section 3.4.1. This is accomplished by computing the magnitude, phase and frequency derivative of the trace of the characteristic mode matrix $[Z]^{-1}[R]$ or $[Z+Z_L]^{-1}[R]$ for each member of the population.
- The generation of the matrix $[Z]$ and thus of $[Z]^{-1}$ and $[R]$, is performed in an efficient manner using the mother matrix of the full geometry (all bits = 1).

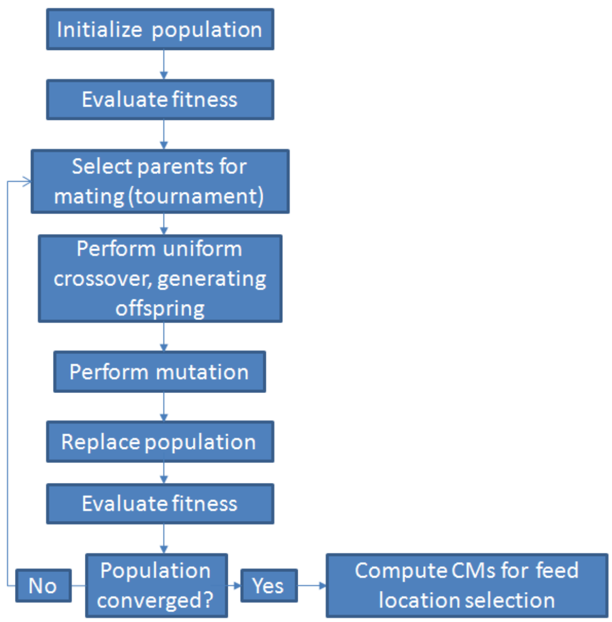

Figure 3.3 – Flow diagram for GA-based optimization algorithms

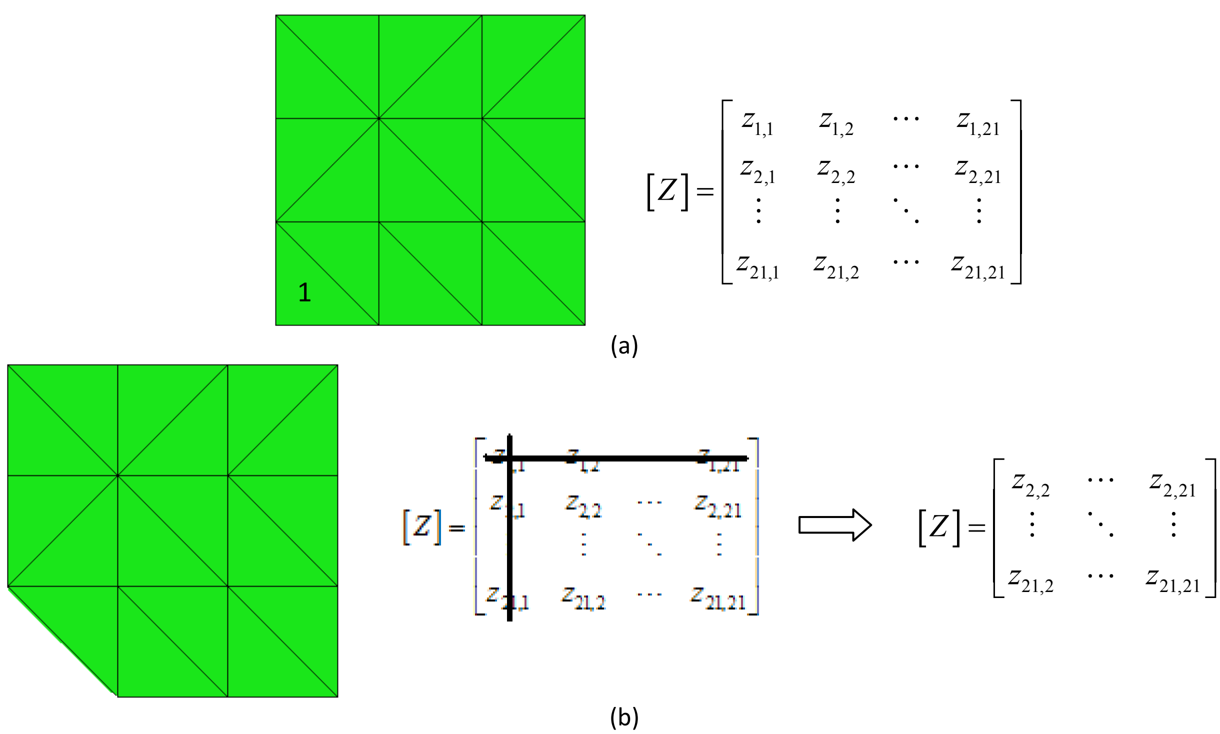

Figure 3.4 – Example meshed structure (a) containing 21 expansion functions with its impedance matrix shown. A triangle associated with expansion function 1 is denoted numerically and (b) Illustrative example showing the removal of triangle 1 and its effect on the content of the impedance matrix – this forms for the basis for the DMM method

3.4.3 – An Optimization Example: Problem Definition to Final Simulated Result

We proceed with a complete optimization process from problem definition to final simulated antenna design. We shall utilize the feedless shape synthesis scheme discussed in 3.4.1 combined with a genetic algorithm optimizer using the DMM method described in 3.4.2.

The mother structure or starting shape we begin with is a densely meshed circular plate, as shown in Figure 3.6(a). Each triangle in the mesh is given an index (in this case there are N = 258 triangles, hence indices 1 through 258). A large population of random structures derived from the mother structure is generated. Each member has a genome that is 258 bits long, with each bit naturally being a 1 or 0, with 1 representing the inclusion of the triangle and 0 representing the removal of the triangle. Since we are using triangles (geometry) in the genome, there are multiple expansion functions associated with each triangle (at most three expansion functions). This approach is, by definition, the DMM method.

As discussed in [10] through [12], the minimum recommended population size should be at least six times the number of genes in each population member. This ensures that a large enough variety of genes exist in the initial population, thereby not relying on mutation to generate genetic diversity. The larger the population, the better the chances are the optimization scheme obtains the global min/max. A larger population will obviously increase computation time, so six times the number of genes acts as a trade-off between convergence to global min/max and computation time. Depending on the computational resources and time constraints, as large a population as is reasonable should be used. A very low mutation rate is also used (< 0.5%), as per the generally accepted approach to using genetic algorithms. The mating scheme employed is uniform crossover, a common approach for strictly-binary genomes. The selection scheme used to determine the parents that produce offspring is tournament selection, again one of the more popular and successful approaches to genetic algorithms. The population size is always held constant, with a large fraction of the population replaced each generation with the offspring from the previous generation. The population members with the lowest fitness are the ones replaced with each generation crossover, ensuring a gradual improvement of the members of the population. Convergence is obtained when the most fit member of the population does not improve over a specified number of generations, or the genetic diversity of the population stagnates.

The objective functions used in this optimization example are slightly altered versions of the three objective functions defined in Section 3.4. In particular, we do not force a strictly zero value objective function #1 (3.82) since this would potentially prevent the optimization scheme from moving towards the secondary objective function. We use a tolerance of $\pi/36$ radians (5 degrees) and assume that any angle with magnitude less than $\pi/36$ radians meets the criteria of objective function #1. We would prefer to maximize all objective functions, so we redefine the primary objective function as

$$\textit{New Objective Function \#1:} \quad \begin{cases} 1-\left|\angle\Psi\right|/\pi & if\ \left|\angle\Psi\right| > \left|\angle\Psi\right|_{threshold} \\ 1 & if\ \left|\angle\Psi\right| \leq \left|\angle\Psi\right|_{threshold} \end{cases} \tag{2.85}$$

When the magnitude of the angle $\angle\Psi$ is less than the threshold $\left|\angle\Psi\right|_{threshold}$, the objective function takes a value of 1. All other angles lead to an objective function with magnitude less than 1. This gives us an objective function with bounds between 0 and 1 – an ideal situation for an optimization scheme. We simply set the objective function #1 equal to unity if the angle we observe is indeed less than $\pi/36$ radians (5 degrees).

This is followed by the maximization of objective function #2 (3.83) for the purpose of maximizing radiation efficiency. Fortunately, this objective function is always set to be maximized and furthermore is bound between 0 and 1. Hence we leave the objective function #2 in its current form of $\left|\Psi\right|$. Again, we must contend with the fact that radiation efficiency can reach 100%, but this is likely an unrealistic requirement. We therefore specify some threshold $\left|\Psi\right|_{threshold}$ for which the efficiency meets some requirement and further improvement is not required (e.g. 90% efficiency). Efficiencies greater than or equal to the threshold are artificially set to be equal to 1 as to not give higher fitness for designs with radiation efficiency larger than the threshold. This objective function is only computed for population members that have already met the criteria of objective function #1:

$$\textit{New Objective Function \#2:} \quad \begin{cases} \left|\Psi\right| & if\ \left|\Psi\right| < \left|\Psi\right|_{threshold} \\ 1 & if\ \left|\Psi\right| \geq \left|\Psi\right|_{threshold} \end{cases} \tag{2.86}$$

Lastly, we can minimize the antenna Q, and thus maximize the antenna bandwidth as defined in objective function #3 (3.84). Since we want to minimize antenna Q and we would prefer to keep objective functions that we strictly maximize, our implemented objective function becomes the inverse of (3.84).

$$\textit{New Objective Function \#3:}\quad \left| \frac{\omega}{2} \frac{1}{\Psi} \mathrm{Im}\left\{ \frac{d\Psi}{d\omega} \right\} \right|^{-1} \tag{2.87}$$

The fitness of each population member is therefore computed by simply summing the contributions of each objective function. Note that the objective function #2 (3.86) is only computed if the threshold of objective function #1 (3.85) is met and likewise, objective function #3 (3.87) is only computed if the threshold of objective function #2 (3.86) is met.

Antennas that are not resonant have fitness less than magnitude 1. When an antenna becomes resonant, its fitness becomes at least one, with the radiation efficiency adding to its fitness. For example, a resonant antenna with efficiency 50% would have a fitness function value of 1.50. When an antenna has radiation efficiency greater than the threshold (while still remaining resonant) the fitness acquires a magnitude of 2, with the inverse of Q added to the fitness to further improve the bandwidth performance. We do not specify a bound on the bandwidth and it is allowed to be improved until convergence occurs. This gives us an appealing range of fitness values in that:

- members with fitness less than 1 are non-resonant,
- members with fitness greater than 1 but less than 2 are resonant, and
- members with fitness greater than 2 are resonant members with the minimum required radiation efficiency and can thus be ranked solely on their bandwidth performance.

Typically, a population begins with all members having fitness less than 1 until the population gradually improves to include resonant members. The fitness further improves until members begin to be both resonant and have sufficiently high radiation efficiency. The fitness of the population is then allowed to increase through the maximization of bandwidth until convergence (defined in 3.4.3) occurs. The end result is a population of resonant antennas with high radiation efficiency and maximized bandwidth, with the fittest individual having the widest bandwidth for the specified minimum radiation efficiency. The progression of an example population from the most fit member perspective is shown in Figure 3.5 with the composite objective function (3.85) – (3.87) plotted as a function of generation number. The GA parameters used are typical, with the population size of 2,400 members for a circular plate (ka = 0.5 at the desired resonance frequency of 300 MHz) meshed with 258 triangles thereby having an equivalent 258 binary genes. The population size is nine times the number of genes, indicating a large enough population to properly search through the possible configurations. The mutation rate is set very low at 0.5%. Mating is accomplished via tournament selection by drawing on a sub-population of 20 random population members during the selection process. The offspring are generated using a standard uniform mask [11, pp. 43]. Three "eras" are noted in Figure 3.5. The first of which involves a population consisting solely of non-resonant antennas. By the 10th generation, the most fit member of the population becomes resonant thereby marking the second era. By the 16th generation, the most fit member of the population meets the criterion of radiation efficiency (in this case set to be 95% or greater, or $\left|\Psi\right|_{threshold} = 0.95$). The population continues to improve by minimizing Q (maximizing its inverse) until the most fit member of the population remains unchanged for a sufficient number of generations. The resulting most fit member is shown in Figure 3.6(b), with the original "mother structure" or starting shape shown in Figure 3.6(a).

We have shape synthesized an antenna without the limitation that would have been imposed if we had been required to specify the feed location at the start. Selection of the best feed location on the shaped antenna is now accomplished by computing the characteristic mode currents of the shaped antenna in consideration. The dominant mode's eigencurrents are shown in Figure 3.7. Referring back to expression (2.32), if we consider modal currents at the structure's resonance frequency (which is the case in this and future examples) the greatest power is coupled to a given mode if the feed is placed where the modal current magnitude is largest. In Figure 3.7, this location is denoted with a green circle. The excitation is accomplished using a voltage gap feed placed at the common edge of two triangles, which forms an RWG basis function. This feeding mechanism is described in Section 3.2.1 and experimentally validated extensively in [1].

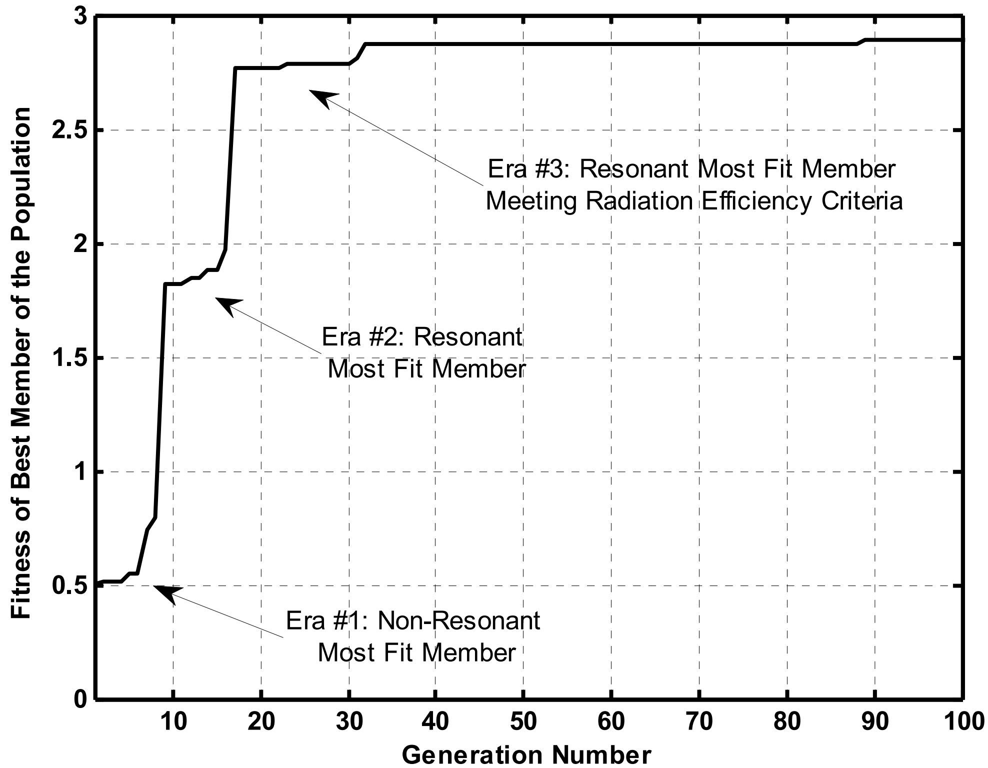

Figure 3.5 – Cost function of the most fit member as a function of generation number for an example genetic algorithm driven optimization run

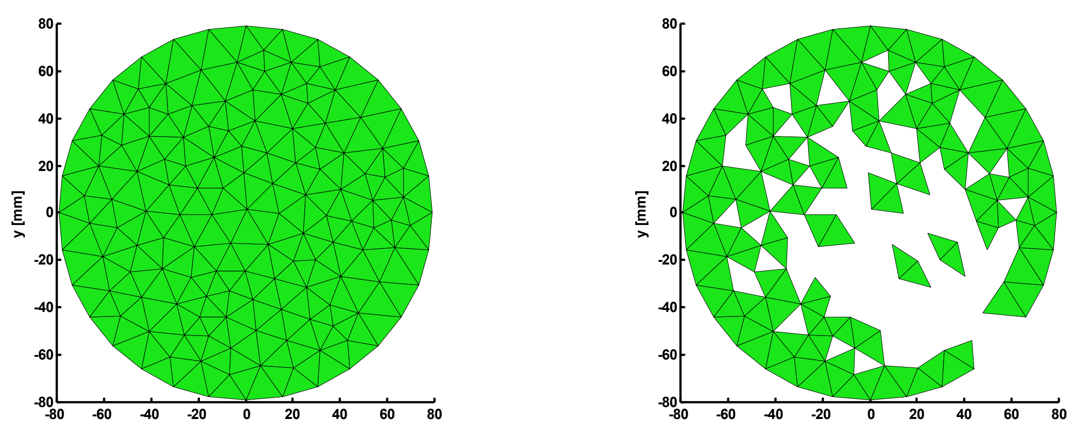

(a)

(b)

Figure 3.6 – Layout of planar antenna (a) mother structure and (b) optimized antenna from genetic algorithm results shown in Figure 3.5.

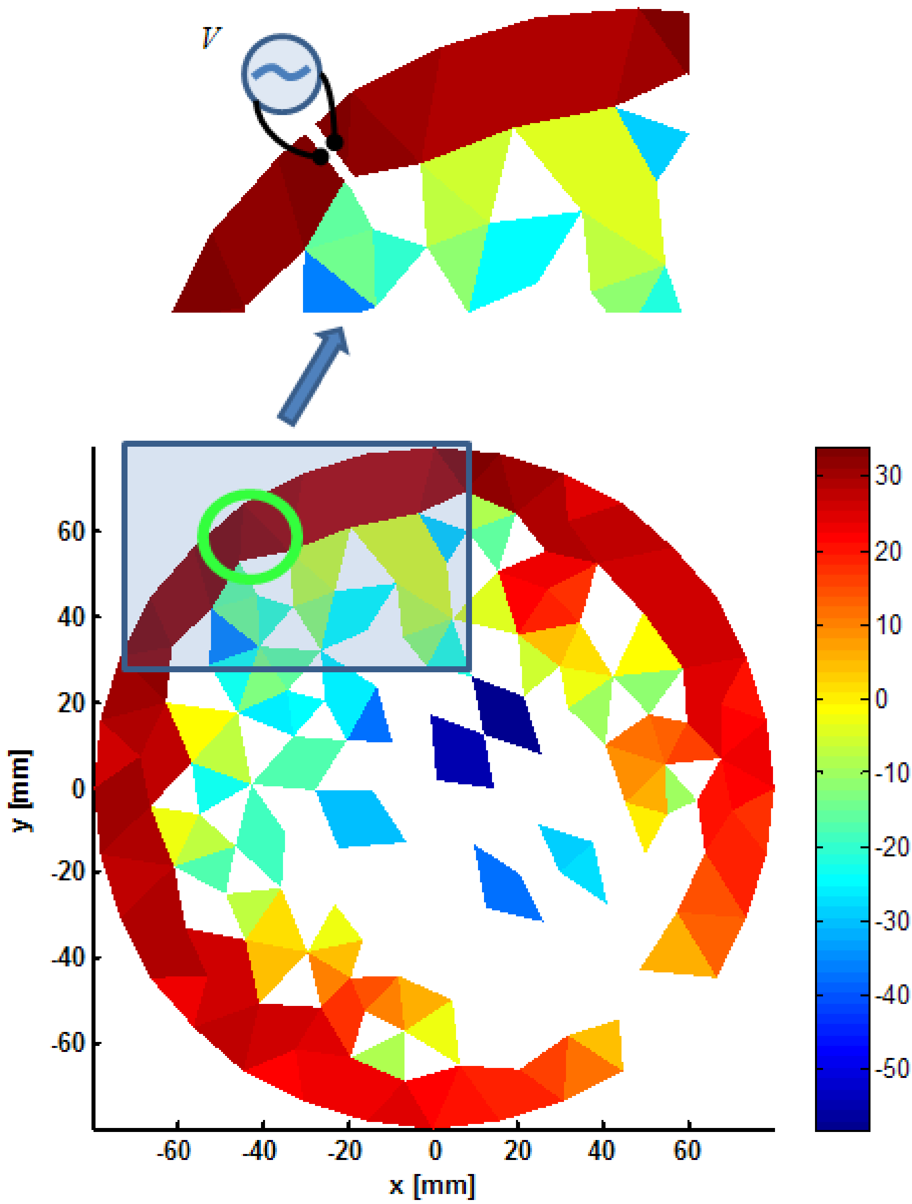

Figure 3.7 – Eigencurrent of dominant mode of optimized antenna with surface current density shown in dB

With the feeding location selected, we can proceed to simulate the fed structure to obtain the input impedance, input reflection coefficient, radiation efficiency and antenna Q at all frequencies of interest and determine how successful we were in the shape synthesis. First consider Figure 3.8, where we plot the magnitude and phase of the trace of the CM matrix given in expression (3.78). We see that the phase of the function Ψ is indeed zero at 300 MHz. Furthermore, the magnitude of Ψ peaks at 300 MHz as well. We follow this analysis with the computation of input impedance of the antenna for the feed location shown in Figure 3.7. The computed input resistance and reactance is shown in Figure 3.9. We clearly have a resonance at 300 MHz with $X_{in} \approx 0$, while the input resistance is approximately 10Ω at this frequency. The low input resistance is typical of electrically small antennas and is reduced further due to the planarity of the antenna. This confirms that the first portion of the optimization has performed properly – we have obtained a resonant antenna at the desired frequency of 300 MHz. Lastly, by selecting a reference impedance of 10Ω, we compute the input reflection coefficient as shown in Figure 3.10. For the input reflection coefficient magnitude thresholds of -6dB and -10dB, we find percentage bandwidths of 4% and 2.33% respectively.

Next we turn to the simulated radiation efficiency. We have considered that the antenna is constructed from copper, with the resulting radiation efficiency shown by the solid line in Figure 3.11. On the same plot, the magnitude of the CM matrix trace given by (3.80) is shown, which from (3.69) is equal to the radiation efficiency at the resonance frequency. We see that this is indeed the case, with the predicted radiation efficiency at resonance being equal to 96.6% via the above analysis done with the selected feed location and 96.9% via the feedless matrix trace approach using expression (3.80).

The Q of the antenna will be discussed in Section 3.4.4. Note that the far-field radiation pattern of the antenna is not discussed. As expected for an electrically small antenna, the far-field patterns of this particular antenna and all forthcoming antennas in Chapter 3 exhibit the typical omni-directional, torus shaped, electrically small dipole-like behavior.

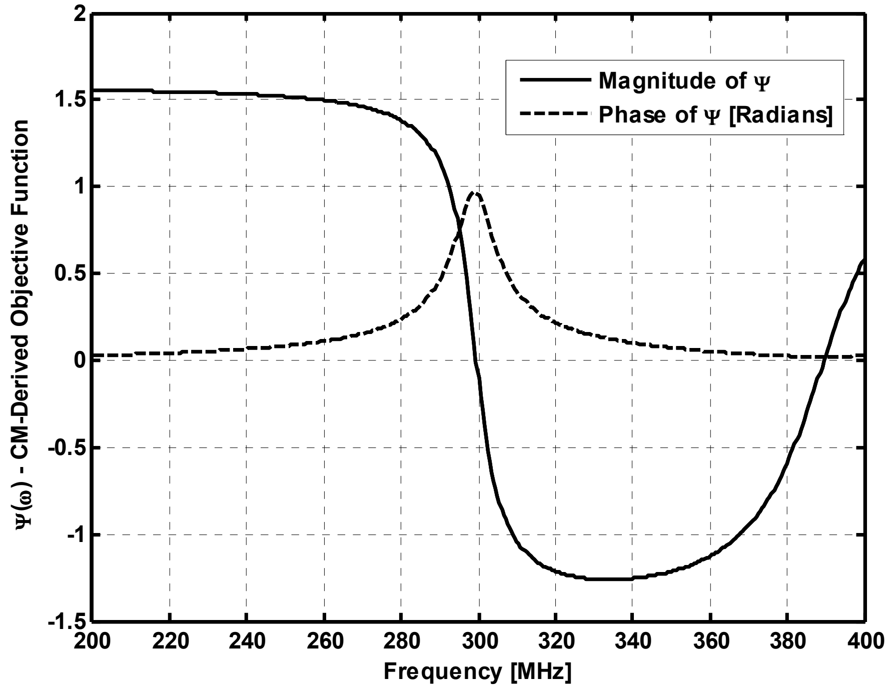

Figure 3.8 – Magnitude and phase of the CM matrix trace

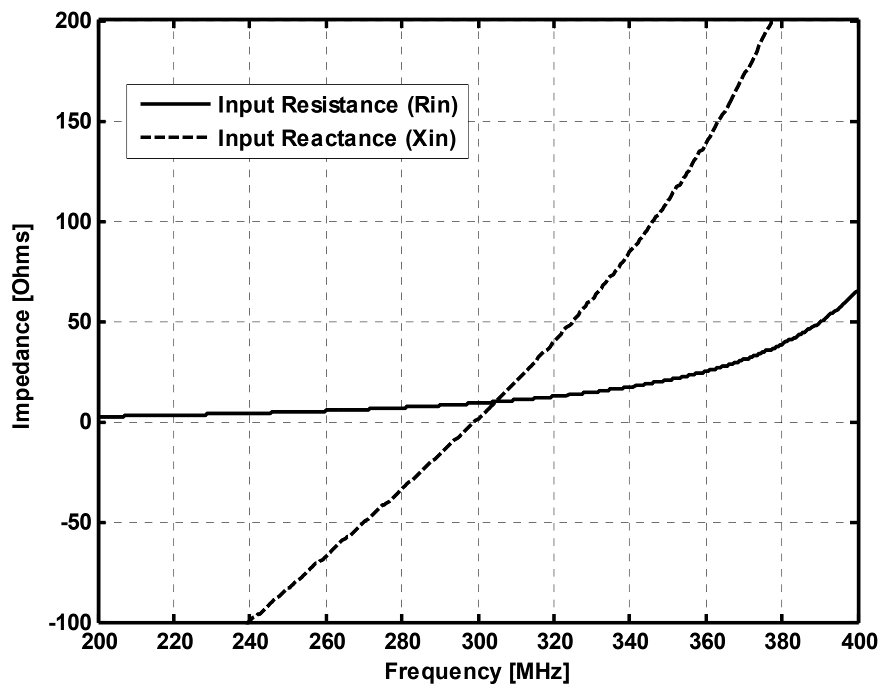

Figure 3.9 – Input impedance of optimized antenna, clearly exhibiting resonance around 300 MHz and low input resistance

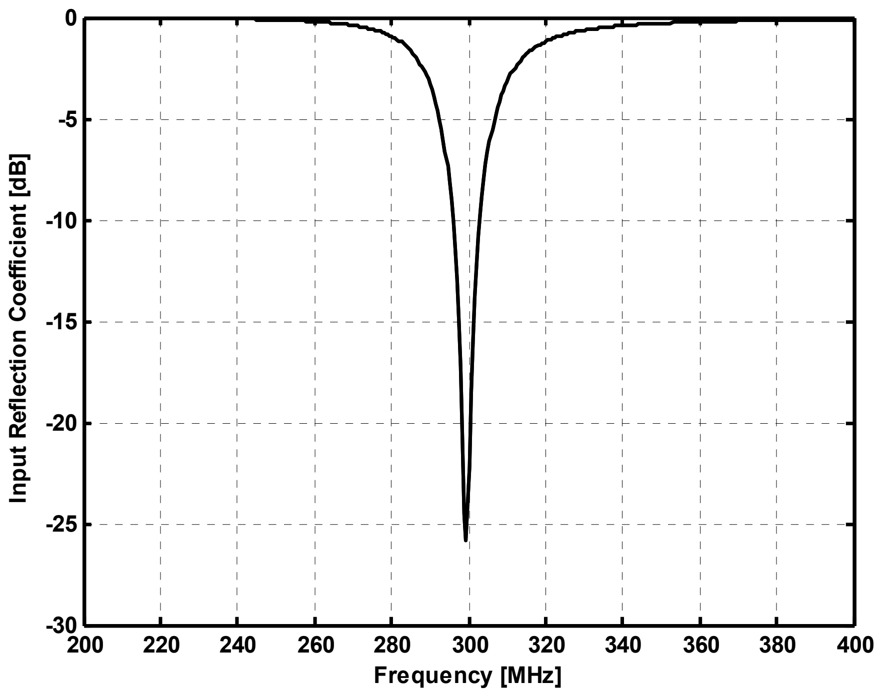

Figure 3.10 – Input reflection coefficient of optimized antenna for reference impedance of Zo = 10 Ohms

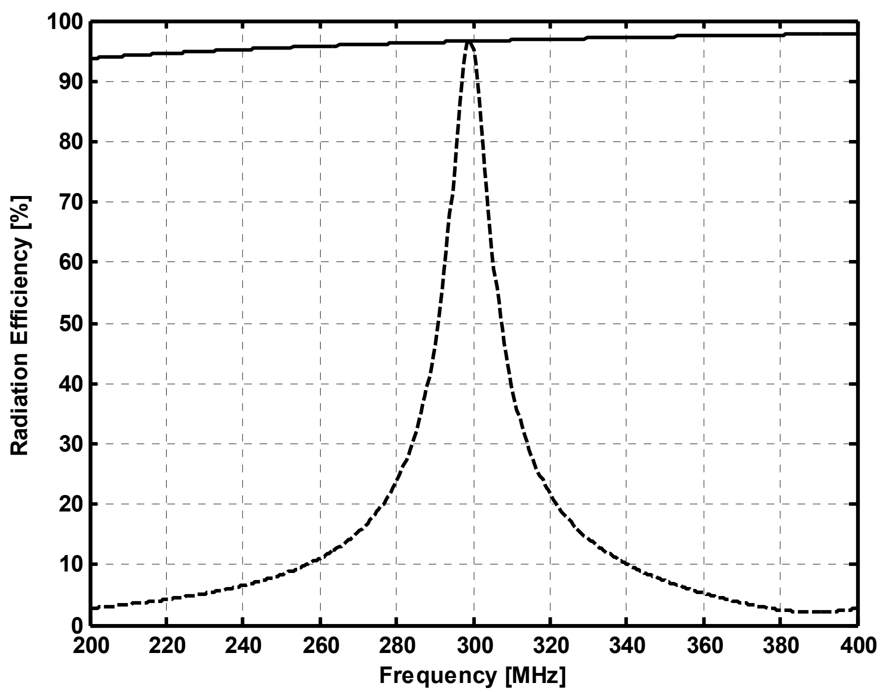

Figure 3.11 – Radiation efficiency obtained (——) via simulation with selected feed location and (- - - -) via the feedless approach using the matrix trace magnitude (expression 3.80)

3.4.4 – Fundamental Bounds on Antenna Q for Planar Antennas

Once we obtain a resonance at the desired frequency, we have completed that objective since achieving a resonance is a binary type qualifier – one either has resonance or does not. Radiation efficiency is also a strictly bound quantity between 0% and 100%. If we know how efficient we wish our antenna to be, we can set the threshold accordingly and know unambiguously that this particular portion of the shape optimization scheme is complete.

It is not as straightforward to determine how well a shape optimization scheme is performing as far as bandwidth is concerned. We can allow the optimizer to increase bandwidth until convergence occurs, but the question remains regarding whether the converged result is indeed the global maximum or at least close to the global maximum. If our goal is to maximize bandwidth, it is of little use to make claims about the antenna without knowing how well we are performing relative to fundamental physical limitations. The first problem encountered is determining what value this global maximum value is. Given that we are dealing with an electromagnetic system, the global maximum will necessarily be a function of the operating frequency, electrical size and shape of the starting antenna. We have the ability to compare our antenna Q against the bounds imposed by the Chu limit [4], but the Chu limit makes two restrictive assumptions: (1) the antenna is confined to a spherical volume and (2) no energy is stored within the fictitious bounding spherical region. If a starting antenna shape were, for example, a circular plate (as in the previous example) we could never achieve the Chu limit since we are not taking advantage of the assumed volume. The ideal approach would be to have knowledge of the Q-limits, similar to the Chu-limits, but specifically for the arbitrary shape used as the starting point in our shape optimization scheme. Fortunately, we can do this thanks to the work by Gustafsson et. al at Lund University [14, 15]. Using arguments derived from the static behaviour of electric and magnetic objects, the Lund University research group has derived fundamental bounds on antenna Q for arbitrarily shaped structures. Closed-form expressions exist for canonical shapes such as spheres, cylinders, and circular plates. The Q-limits of other shapes can be obtained by computing the static polarizability of their shape using an electrostatic formulation. This author has shown as part of the work of the present thesis (see Appendix C and [16] for the theoretical development and validation) that the same time-harmonic moment method code used to determine the antenna input impedance, radiation efficiency, far-field pattern and the like, can be used to find this polarizability.

The lower bound on antenna Q for an antenna that occupies an arbitrary shape

$$Q_{lb} = e_{rad} \frac{2\pi D}{\tilde{\eta} k^3 \gamma} \tag{2.88}$$

where D is the directivity, e_{rad} is the radiation efficiency, $\tilde{\eta}$ is the absorption efficiency (the 'tilde' is used to coincide with the notation in [13]), $k = \omega\sqrt{\mu\varepsilon}$ is the wave number and γ is the static polarizability.

The directivity is typically assumed to be 1.5, which is invariably the case for an electrically small antenna except under rare circumstances involving superdirectivity. The absorption efficiency $\tilde{\eta}$ is dependent on the antenna type, but is typically equal to 0.5 and only in extreme cases does it stray from this value (see [15]). The validity of this assumption of $\tilde{\eta} \approx 0.5$ is discussed in Appendix D. Lastly, and of greatest importance, is the static polarizability γ. This quantity is of course a function of the orientation of the applied electric field, so the assumed polarizability is equal to the largest polarizability among all field orientations (see Appendix C), thereby giving us the lowest possible Q among all field orientations. Substituting our assumed values ($D \approx 1.5$ and $\tilde{\eta} \approx 0.5$) into expression (3.88) gives us

$$Q_{lb} = e_{rad} \frac{6\pi}{k^3 \gamma} \tag{2.89}$$

Since we are specifically considering circular disks for the moment, we can use the known [15] closed-form normalized polarizability of a circular PEC disk, namely $\frac{\gamma}{a^3} = \frac{16}{3}$ where a is the radius of the smallest circumscribing sphere. Substitution into (3.89) gives us the lower bound for a circular disk

$$Q_{lb,circle} = e_{rad} \frac{9\pi}{8} \frac{1}{(ka)^3} \approx e_{rad} \frac{3.5353}{(ka)^3} \approx 2.356 Q_{lb,sphere} \tag{2.90}$$

This gives us the ability to determine how well our shape optimization process has performed in regards to the antenna Q upon convergence.

We consider the Q of the shape optimized antenna (in our example) over frequency to compare with the lower bounds of Q for a circular planar antenna and additionally for a volumetric antenna occupying the same circumscribing sphere. The antenna Q is shown in Figure 3.12, computed using

(2.56) via the excitation of the antenna port and estimated via the matrix trace (expression 3.81). Also shown are the fundamental lower bounds on antenna Q for a circular plate and sphere. The actual antenna Q was computed to be 29.51 at 300 MHz, and estimated to be 30.35 using the matrix trace, representing an estimation error of 2.8% (with the matrix trace overestimating the antenna Q). The lower bound on antenna Q for the circular plate is found to be 28.76 at 300 MHz, implying that our optimized antenna is within 2.5% of the minimum possible Q for its geometric shape. A Q within 2.5% of the lowest possible Q is an excellent result, especially considering that antennas that operate within 20% of their lower bound are considered to be performing well [6]. It should also be noted that the antenna's Q approaches the lower bound as the electrical size decreases. One would not want to operate the antenna in this regime as the antenna is no longer self-resonant – a reactive tuning element would be required. Nevertheless, it is interesting to note that the lower bound is essentially maintained for frequencies ka $\leq$ 0.5.

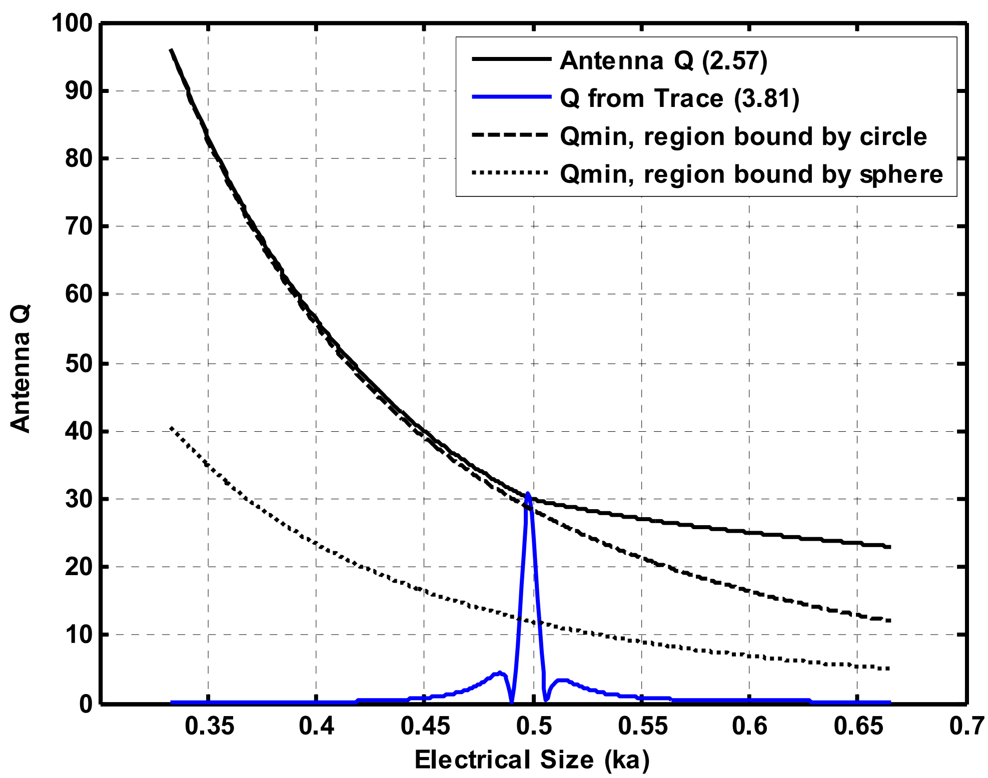

Figure 3.12 – Antenna Q of example antenna with the lower bounds shown for comparison

3.4.5 – Addressing the Issue of Modeling Accuracy of the Moment Method Mesh

Three potential issues of practicality arise with the antenna discussed in the previous example, all of which are related to the nature of the mesh used:

(1) The potentially low mesh density improperly modeling the geometry
(2) The issue of single triangle vertex connections
(3) The necessity (and possible inaccuracy) of isolated "floating islands" of metal

The first issue is the matter of sufficient mesh density. The starting "mother structure" consisting of a fully meshed plate is certainly sufficiently meshed. With 258 triangles modeling a plate with electrical size ka = 0.5, there is an average expansion function edge length (triangle size) well below $\lambda/50$. However, as pieces of the original mesh are removed and the antenna is shaped, there is the possibility of poorly representing the geometry. For an electrically larger geometry this will most certainly be a reality, but we suspect that given the antenna's small electrical size the seemingly coarse mesh is sufficiently accurate. Nevertheless, we shall investigate the accuracy of the mesh by increasing the mesh density and recomputing the quantities such as input impedance and antenna Q.

By introducing a new vertex at the midpoint of every edge in the triangle mesh, the triangle density is quadrupled. This places the average length of the triangle edges at $\lambda/100$. The resulting quadrupled mesh antenna is shown in Figure 13.13. The feed location remains unchanged – the only difference in this example is the inclusion of two edges in the modeling of the voltage gap feed rather than a single edge. The applied voltage is selected to be the same for both RWG expansion functions making the port voltage equal to the applied voltage over the RWG elements. The resulting input current is simply the sum of the total current flowing across each RWG element. The input reflection coefficient of the quadrupled mesh structure is shown in Figure 13.14. The performance of the original unaltered mesh is included for comparison purposes. It is noted that the predicted resonance frequency shifts upwards in frequency by approximately 0.8%. The design with the quadrupled mesh density has identical percentage bandwidth as the antenna modeled using the original mesh. It should be noted that if the shift in frequency were large enough to warrant a re-design, it is a simple matter to scale the design (larger in this case) such that the desired resonance frequency is obtained. This has very little impact on the performance of the resulting antenna, though its footprint is increased slightly.

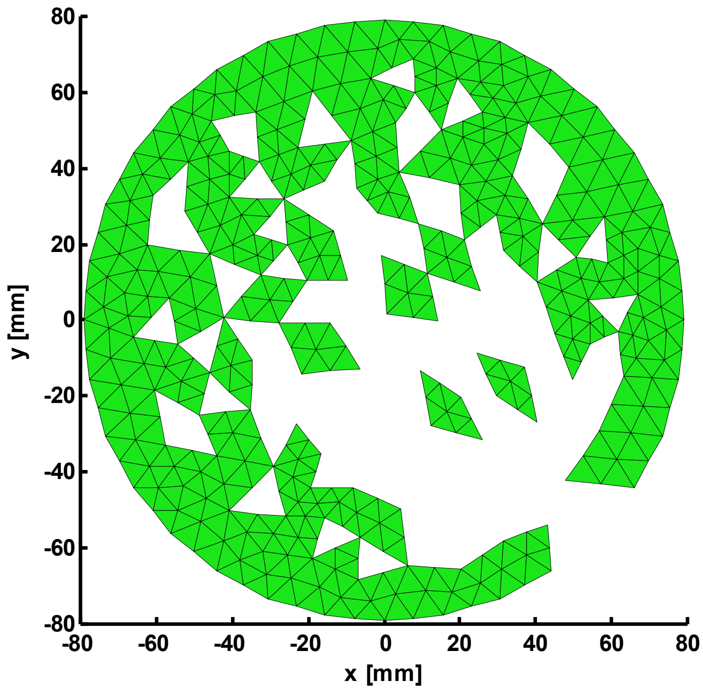

Figure 3.13 – Example circularly shaped electrically small antenna with increased mesh density

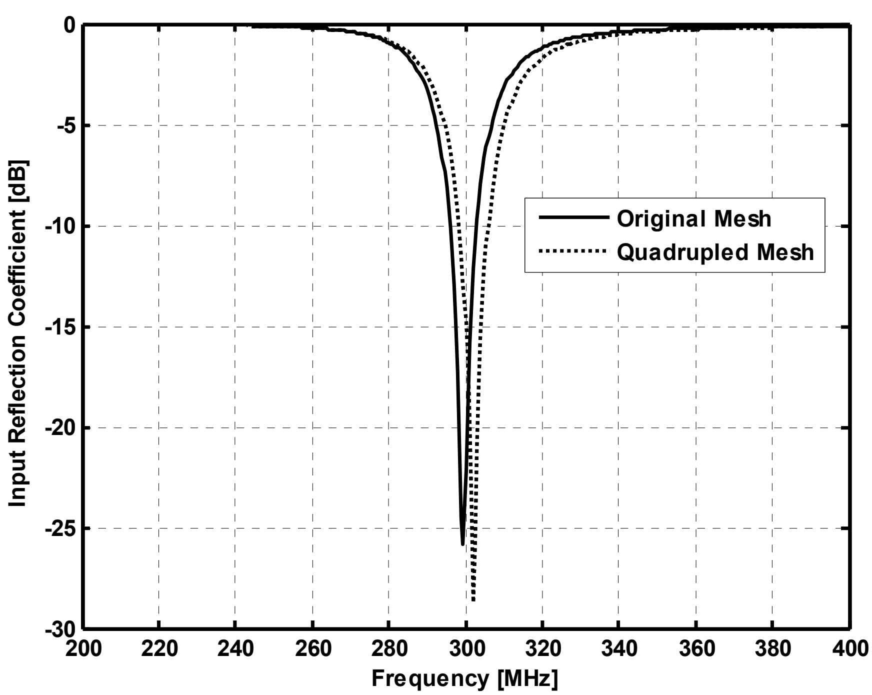

Figure 3.14 – Comparison of the reflection coefficient for the original triangular mesh and the quadrupled mesh for the circularly shaped electrically small antenna example

The second issue is a matter of practicality when fabricating the antenna under consideration. Note that the antenna design shown in Figures 3.6(b) and 3.13 have regions where the triangles from the mesh share a single vertex (and not an edge); these are highlighted in Figure 3.15[4]. These “single vertex connections” are not physically connected – no current can flow across them in the simulated antenna but can do so in the fabricated antenna – depending on the etching tolerance of the fabrication procedure. For the sake of fabrication issues, we would rather “split” these vertices into two unconnected vertices, preventing any possible current flow from occurring there. Such a split changes both the mesh and the antenna geometry (albeit to an expected minor degree), thus requiring an investigation into the effects on input impedance and antenna Q. A coding script was written to automatically identify these single vertices and split them into two (or more) distinct vertices. The layout of the antenna with the single vertex connections split is shown in Figure 3.16. A plot of the input reflection coefficient is shown in Figure 3.17 for both the original antenna and the antenna with the vertices “fixed” – by fixed we refer to single vertex connections that have been split into two more separate vertices. There is minor difference between the performance of both designs, but not a large enough shift (a mere 0.2% shift up in frequency) to preclude the fabrication of the design with the vertices fixed.

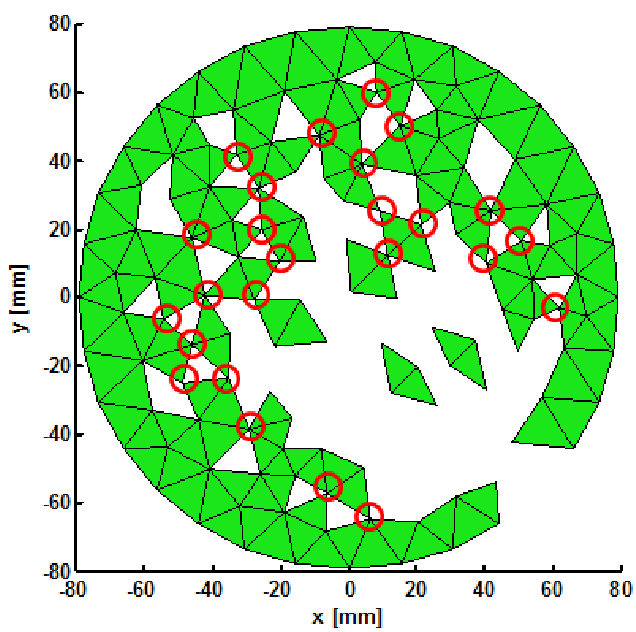

Figure 3.15 – Circular shaped small antenna with potentially problematic single vertex connections emphasized

[4] Further discussion on the “single vertex connections” issue is provided in Section 5.4.7

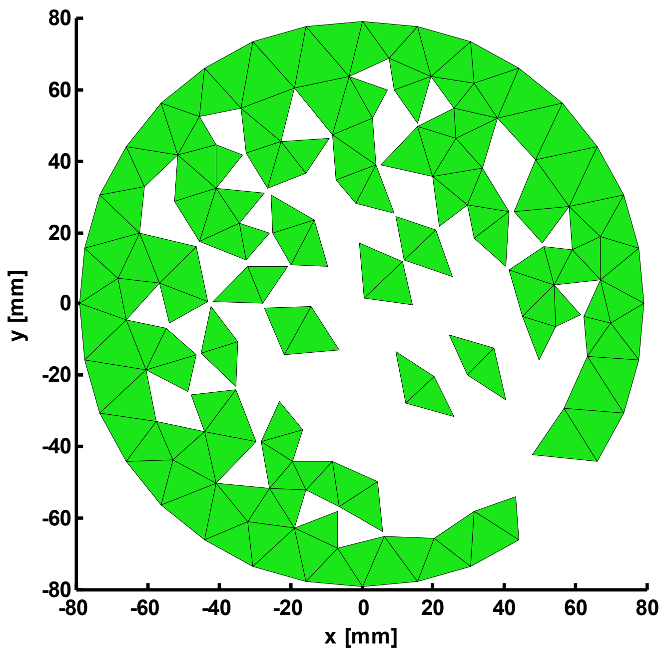

Figure 3.16 – Circular shaped small antenna with single vertex connections broken

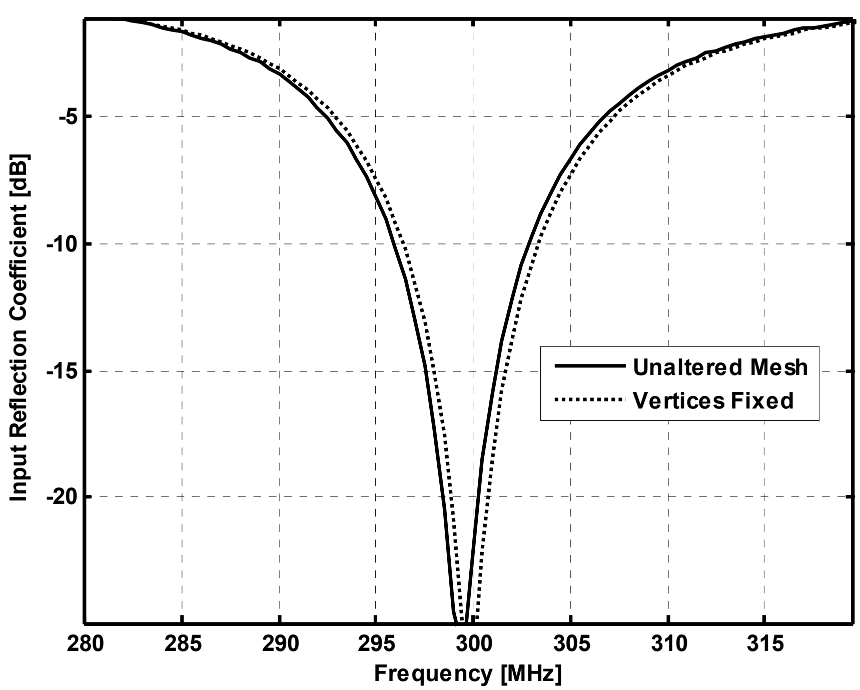

Figure 3.17 – Comparison of the reflection coefficient of the original mesh compared to the altered mesh with the vertices fixed mesh of the electrically small circularly shaped antenna

A last possible point of contention involves the presence of "floating islands" of metal. These floating islands are physically separate from the major metal portion of the antenna, which in our example consists of what is effectively a broken loop antenna. These floating islands act as parasitic objects and will possibly affect the electromagnetic behavior of the antenna. The degree to which these "islands" are necessary is a worthwhile discussion, as removal of these islands will result in a single contiguous radiating structure which can be fabricated from a single piece of copper or other metal. This forgoes the need for a supporting substrate. It should be noted that we are not suggesting that the use of substrates is detrimental – we simply wish to investigate alternative means of fabricating these example antennas. The example mesh with the islands identified and then removed is shown in Figure 3.18(a) and 3.18(b), respectively. The resulting input reflection coefficient is shown in Figure 3.19 for both the unaltered mesh and the mesh with the metal islands removed. It is abundantly clear that the additional islands of metal have negligible effect on the performance of the antenna – the bandwidth remains unchanged (because antenna Q is unchanged), with the resonance frequency shifting by 0.06%, and so the islands need not be fabricated.

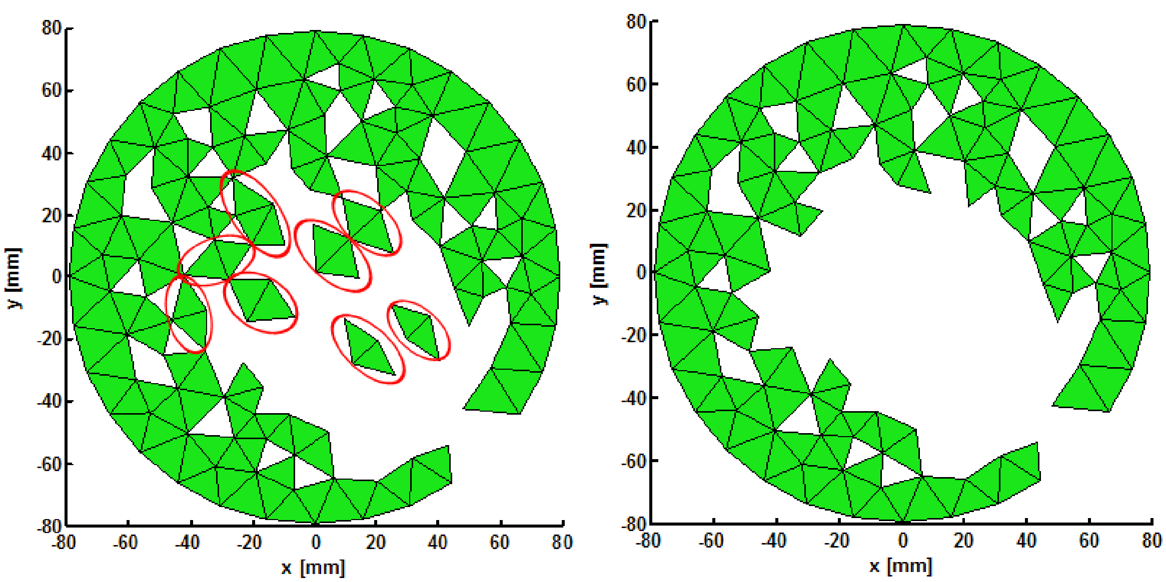

(a) (b)

Figure 3.18 – Potentially problematic or unwanted isolated islands of metallization identified in (a) with the islands removed as shown in (b)

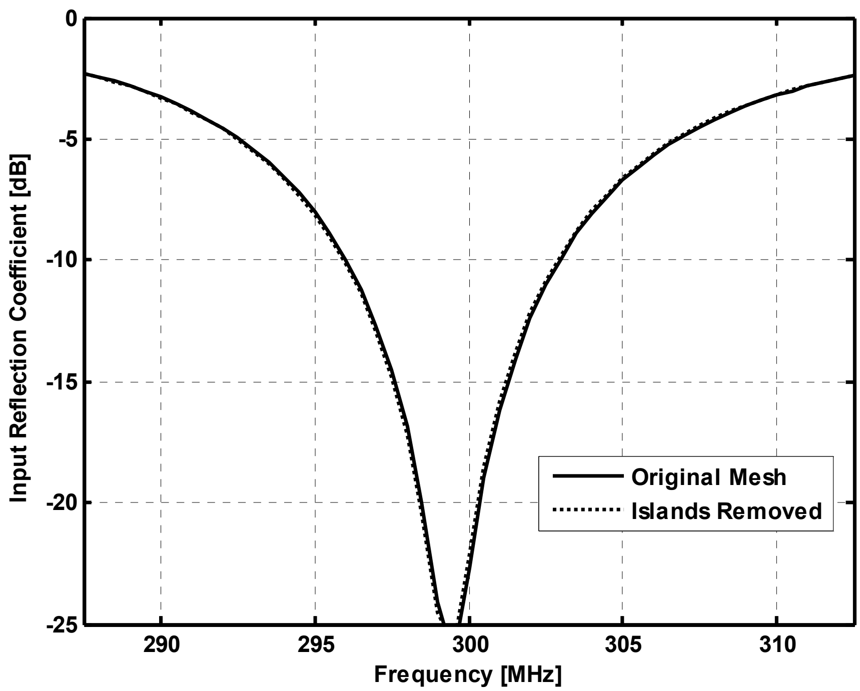

Figure 3.19 – Comparison of reflection coefficient between the normal mesh and the mesh with the isolated islands of metal removed

3.4.6 – Optimization Convergence Study for Small Circularly Shaped Planar Antennas

A convergence study involving the optimization of circular plates (with ka = 0.5 at the desired frequency) was performed, optimizing 200 unique resonant antennas. The structural and genetic algorithm parameters are identical to that of the previously discussed example in Section 3.4.3. The antennas were shape-synthesized to have their resonance at 300 MHz, a radiation efficiency greater than 95% and antenna Q minimized until convergence is achieved. A histogram of these antennas' Q-ratios is shown in Figure 3.20. Note that Q-ratio is simply defined as the ratio of the antenna Q to its lower bound. As far as optimizer success is concerned, nearly 70% of converged designs achieved an antenna Q within 5% of the lowest possible Q for a circular plate. Additionally, close to 90% of the converged designs achieved antenna Q's within 10% of the lowest possible Q. The fact that many electrically small antenna designs are deemed successful if their obtained Q is within 20% of the lower bound of Q [6], suggests that the shape optimization developed in this chapter performs quite well. Moreover, if we begin with a much larger population and take special care to run the optimizer for additional generations, the resulting antenna Q of the optimum antenna is within 2% of the lower bound, as evident from the results of Section 3.4.3. It should be noted that the number of necessary generations before convergence for all 200 example antennas was less than 500 generations, indicating the GA optimizer was performing well too.

We next consider the convergence of the shape optimization process as a function of the number of triangles used (mesh density). This will confirm that the electromagnetics remain consistent as the mesh density varies during the synthesis process. We deduced this fact from the results of Section 3.4.3, but also from the fact that the antennas being considered are electrically small and are therefore well modeled by fewer expansion functions compared to electrically larger antennas. For a circular plate with ka = 0.5, we consider mesh densities of 100 triangles, 200 triangles and 400 triangles with ten antennas shape synthesized for each noted mesh density (30 antennas were obtained in total). The average Q-ratios (simply the sum of Q's divided by the number of antennas considered) of the ten antennas for each of the three mesh densities were 1.062, 1.022 and 1.013 (or within 6.2%, 2.2% and 1.3% of the minimum Q). This implies that when we use a denser mesh we can obtain a structure with a lower average Q. This is not surprising considering that a denser mesh can be synthesized into a more complex structure and hence can achieve a wider bandwidth. It does however indicate that diminishing returns occur for denser meshes, since the more reasonable mesh of 200 triangles achieved an average Q within 2.2% of the minimum. In actual fact, some of these designs were in the 0.5% - 1% range indicating that with tuning of the GA (e.g. larger population, allowing for more generations, optimizing mutation and mating parameters) would lead to consistently low-Q designs. Most importantly is the fact that at least some of the optimized antennas have antenna Q nearly reaching the minimum Q.

Simulations were performed for circular plate sizes ka = 0.475 and ka = 0.450 with similar results, only with slightly higher Q-ratios for the same mesh density as their ka = 0.500 counterparts. This indicates that smaller plates require denser meshes to achieve similar Q-ratios. This is reasonable since the electrically smaller plates require more complex structures due to their lower resonance frequencies.

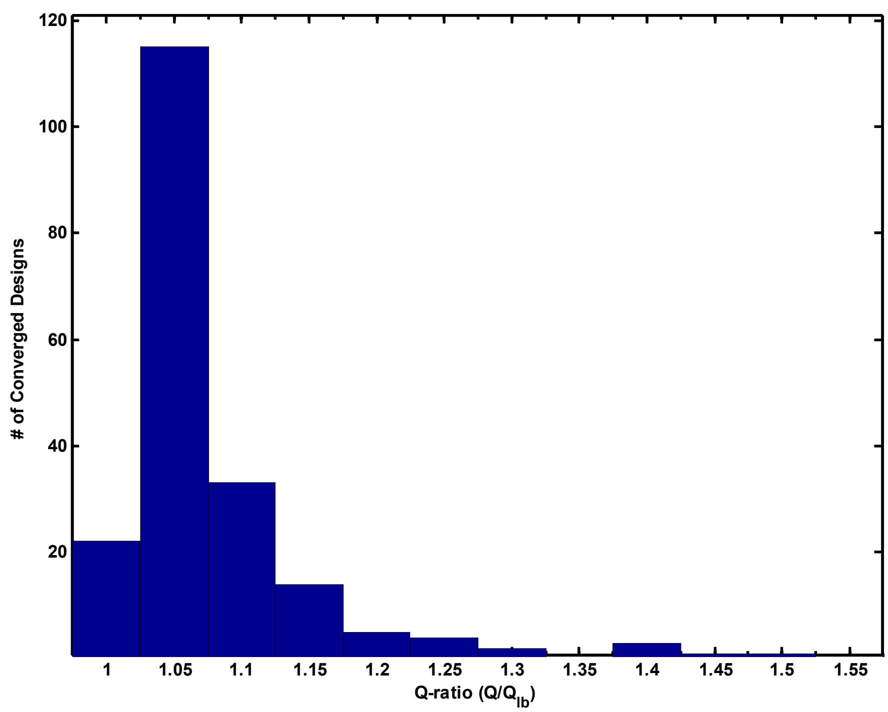

Figure 3.20 – Histogram of Q-ratios for 200 optimized circularly-shaped antennas

3.4.7 – Knowing Where to Look: Establishing Design "Rules" Using the Shape-Synthesis Procedure

In order to obtain more than the output of an optimization routine, we illustrate how one can establish design principles from the shape optimization results. In particular, we consider the optimization of 500 small antennas with maximum electrical size ka = 0.5 with a circular plate as the starting shape. All 500 antennas were superimposed in an image[5], with the superposition shown in Figure 3.21(a). If we set the densest regions to have density of 100% and all other remaining regions to have 0% density, we obtain the image shown in Figure 3.21(b). Through this superposition of antenna shapes, we observe a very clear principle, namely that of taking full advantage of the circumscribing area; this is similar to the principle of taking full advantage of the circumscribing volume for volumetric antennas. If we additionally consider the optimization of 500 circularly shaped antennas but for electrical size ka = 0.4, the resulting superimposed collection of antenna shapes is shown in Figure 3.22. We find the same principle applies where the bounding area must be taken advantage of, but we see the requirement of having additional metallization within the bounding area and not just along the boundaries. As the electrical size decreases further, we find this trend continues. Note that in both examples (ka = 0.5 and ka = 0.4) the average Q-ratio (the ratio of antenna Q to the lower bound of Q for a circular plate) is less than 1.05, implying the superimposed shapes are indeed representative of antenna shapes capable of obtaining the lower bound on antenna Q.

Three principles can be deduced (from the above numerical shape synthesis experiment) for the design of planar antennas with the widest possible bandwidth:

(1) Maintain the overall shape of a circular plate as it has the lowest possible Q of all possible planar geometric shapes (this is easily shown from the expressions in [13,14]). In other words, the circular shape has the largest possible polarizability of all planar geometric shapes.
(2) Maintain the presence of the metal boundary of this circular shape to best take advantage of the circumscribing circle.
(3) Utilize the inner portions of the circumscribing circle with connective pieces of metallization to lower the resonance frequency of the antenna while still maintaining a low Q.

[5] Note that the antennas are oriented such that their approximate line of symmetry occurs vertically.

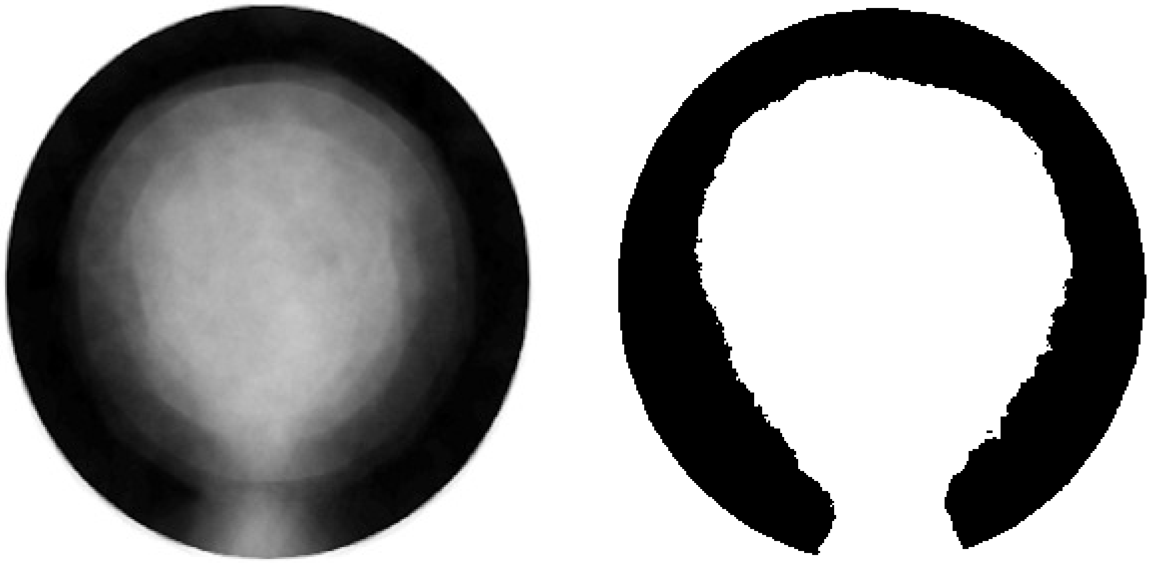

(a) (b)

Figure 3.21 – Antenna layout of 500 superimposed optimized antenna shapes with electrical dimensions ka = 0.5 and starting circular plate shown in (a) while (b) shows the same superimposed collection of antennas only with densities less than 50% filtered from the image, leaving a solid contiguous structure.

Figure 3.22 – Additional example of superimposed and filtered collection of 500 antenna shapes, similar to the previous figure only with the electrical size of the antennas equal to ka = 0.40 (circular antenna shapes are used)

With these three design principles in mind, we consider the starting structure shown in Figure 3.23(a). It consists of a circular plate residing in the x-y plane with multiple elliptical holes removed from the circular structure. These holes are described by the minor/major axis of the ellipses as well as the (x, y) coordinates of their centres relative to the centre of the main plate. By controlling the number of elliptical holes and their size and position, the antenna can be shape synthesized into a resonant, highly efficient and Q-minimized antenna. Using the exact same objective functions as used previously, and a similarly structured genetic algorithm, a feedless optimization can proceed. The only difference is that rather than dealing with binary genes (0's and 1's) we are now considering real valued genes. Each gene corresponds to, for example, an ellipse's major axis or its x- and y-coordinate of its centre. Rather than using the uniform crossover technique to generate offspring, the genes from the two selected parents are averaged [10, pp. 82], producing a real-valued gene with a parameter between both parents' genes. An example optimized antenna shape is shown in Figure 3.23(b).

Notice that symmetry is enforced in the optimization procedure. This is enforced for two reasons:

(1) the antennas optimized in section 3.4.5, 3.4.6 and in this section are approximately symmetric
(2) a symmetric antenna is simpler to measure through the use of a ground plane.

It is difficult to feed and measure electrically small antennas using differential feeds as typical measurement apparatus, such as vector network analyzers, use unbalanced excitation (e.g. coaxial connectors). Such a measurement scenario requires a balun to transform the unbalanced signal of the VNA to a balanced signal as required by the electrically small antenna. In order to forgo the need for a balun, we consider electrically small antennas with a single plane of symmetry. Antennas with a single symmetry plane can, according to image theory, be physically cut along their symmetry plane and then placed over a ground plane for measurement. This allows for the use of an unbalanced feed (e.g. coaxial probe) fed through the ground plane. The resulting performance of the antenna over the ground plane should exhibit twice the directivity and half the input impedance (both resistance and reactance). The presence of a ground plane is very typical for electrically small antenna measurements as evidenced by references [73] – [101] from Chapter 2 – all experimental measurements of electrically small antennas from these references utilize a ground plane. Examples of differentially fed electrically small antennas include RFID antennas [17, 18]. Though experimental measurement of such antennas will not be the focus of this work, the antennas presented in this chapter can be readily adapted to RFID antenna design.

Three example antennas were considered, all of which began with a circular plate, each having a different number of elliptical holes removed. We denote these three antennas as Design A through C having 4, 6 and 8 elliptical holes removed from the main circular plate respectively. All three antennas were optimized to be resonant at 600 MHz, with radiation efficiency maximized and their Q minimized. The distinguishing factor between antennas is their electrical size, which is reduced as the number of specified holes increases. Since all antennas share the same resonance frequency, the reduction in electrical size is synonymous with the reduction in physical size. The electrical size at resonance for the three antennas are ka = 0.449, 0.403 and 0.390 for Designs A through C, respectively. This corresponds to physical sizes of a = 35.73, 32.07 and 31.03 mm for Designs A through C respectively (note that 'a' represents the radius of the smallest circumscribing sphere that can surround the antenna).

The three antennas are shown in Figure 3.24(a)-(c), with their fabricated counterparts shown connected to a large ground plane for comparison purposes. In fabrication, a very thin (5 mils or 0.127mm) supporting FR4 substrate (ε_r= 4.4) is used for chemical etching purposes. The presence of the FR4 substrate will change the antenna performance since it is unaccounted for in simulation. The simulated radiation efficiency of the antennas was optimized to be above 90%. The resulting simulated and measured[6] input reflection coefficients of the three antennas are shown in Figure 3.25(a)-(c) for a reference impedance of 10Ω. The antenna Q of the three antennas is shown in Figure 3.26 with the lower bounding curve for circular shaped planar antennas including as well. Further details of the three simulated and measured designs can be found in Table 3.1. All three fabricated and measured antennas showed a similar shift in resonance frequency from 600 MHz down to approximately 575 MHz. This is mainly due to the presence of the unaccounted for supporting dielectric substrate. All three antennas achieved antenna Q's that approached the fundamentally lowest Q possible for an antenna conforming to a circular planar geometry.

[6] The measure Zin is multiplied by a factor of 2 n order to compare against the simulated impedance

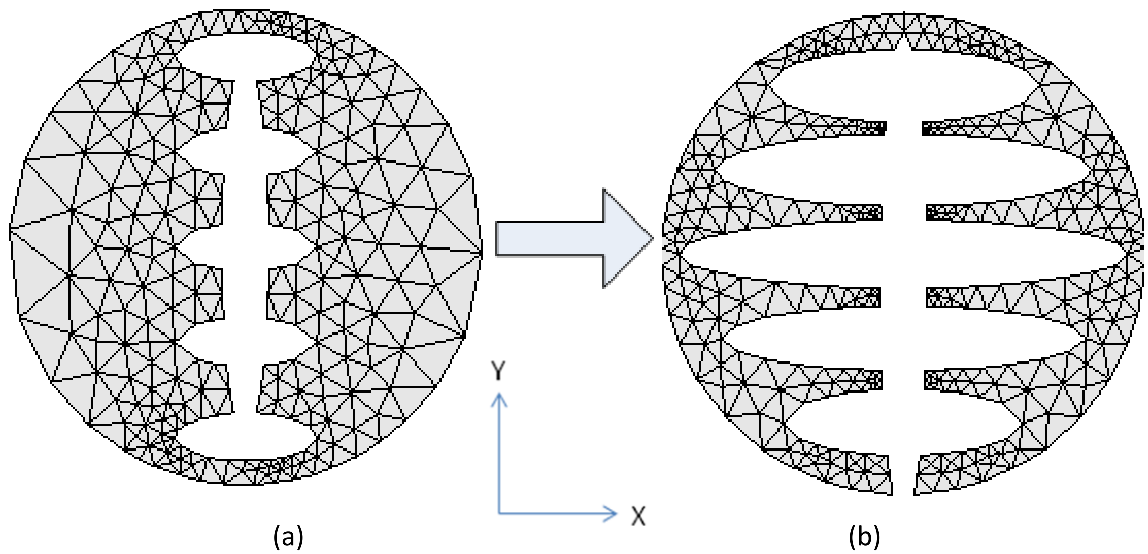

Figure 3.23 – Example starting shape (a) with the location and size of the ellipses in (a) optimized to yield a resonant, high radiation efficiency, low-Q antenna shown in (b)

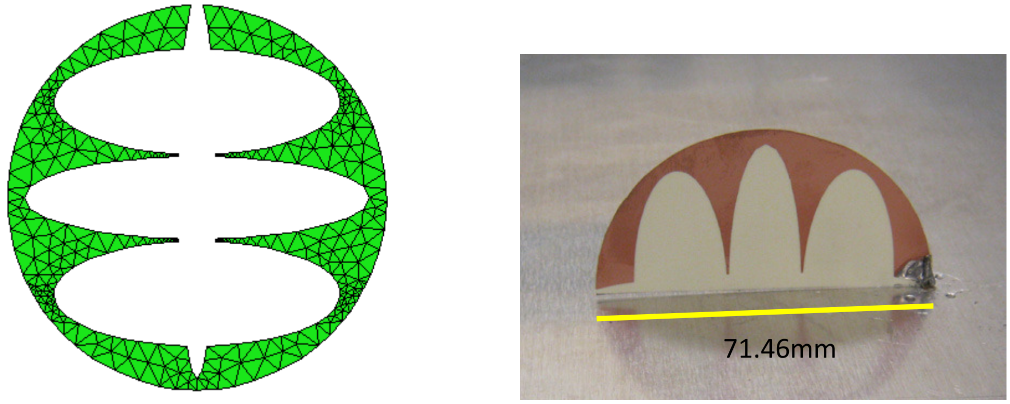

(a)

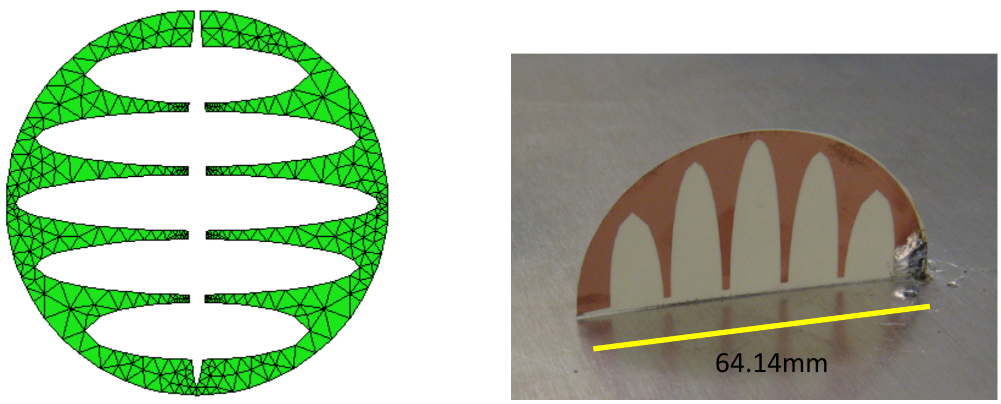

(b)

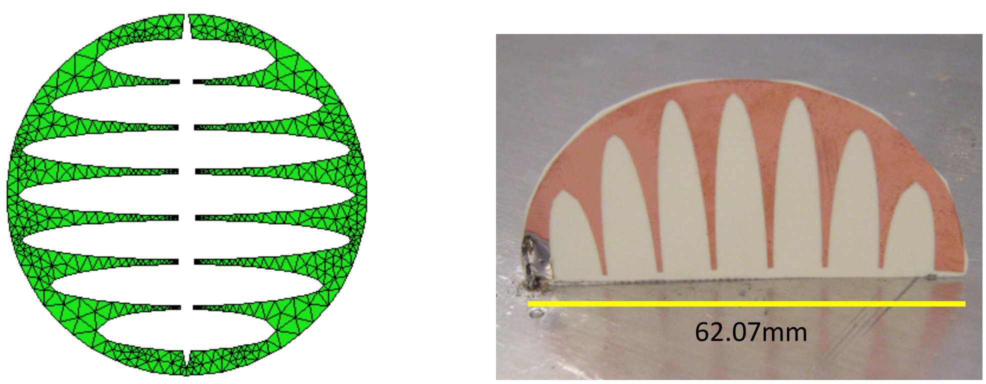

(c)

Figure 3.24 – Plots of three example antennas with photographs of the fabricated models, designs A through C shown and are labeled as such – all antenna designed to have a resonance frequency of 600 MHz.

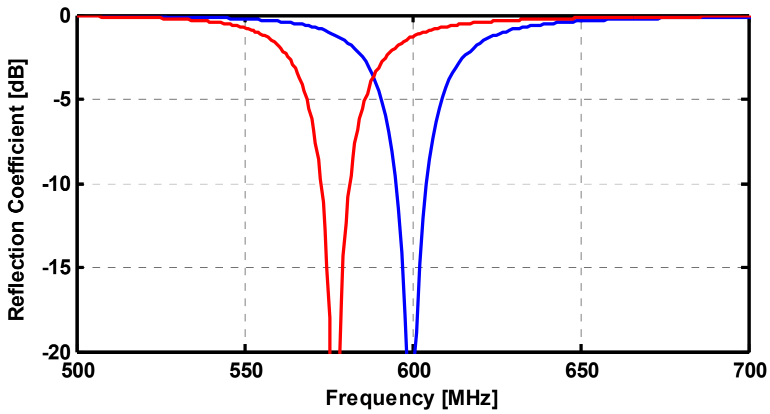

(a)

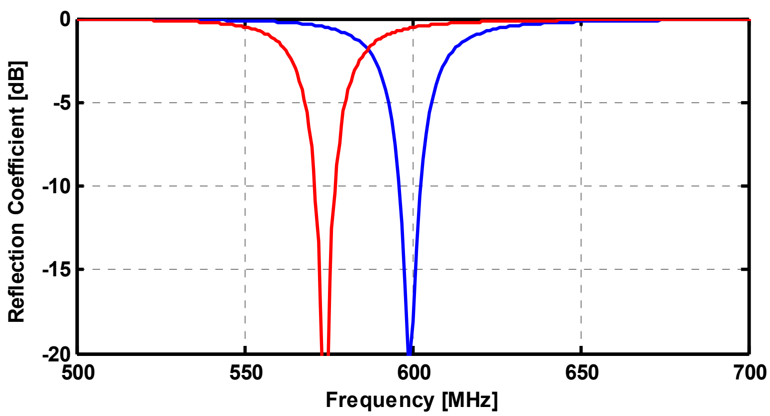

(b)

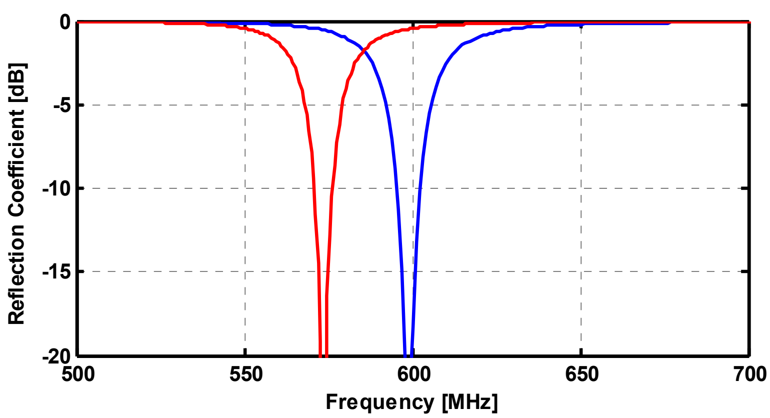

(c)

Figure 3.25 – Plot of reflection coefficient of electrically small antenna (a) through (c), numbered as such. Red curves (——) are experimental measurements while blue curves (——) are simulated results. Note the expected shift down in frequency for the experimental results due to the inclusion of the supporting FR4 substrate.

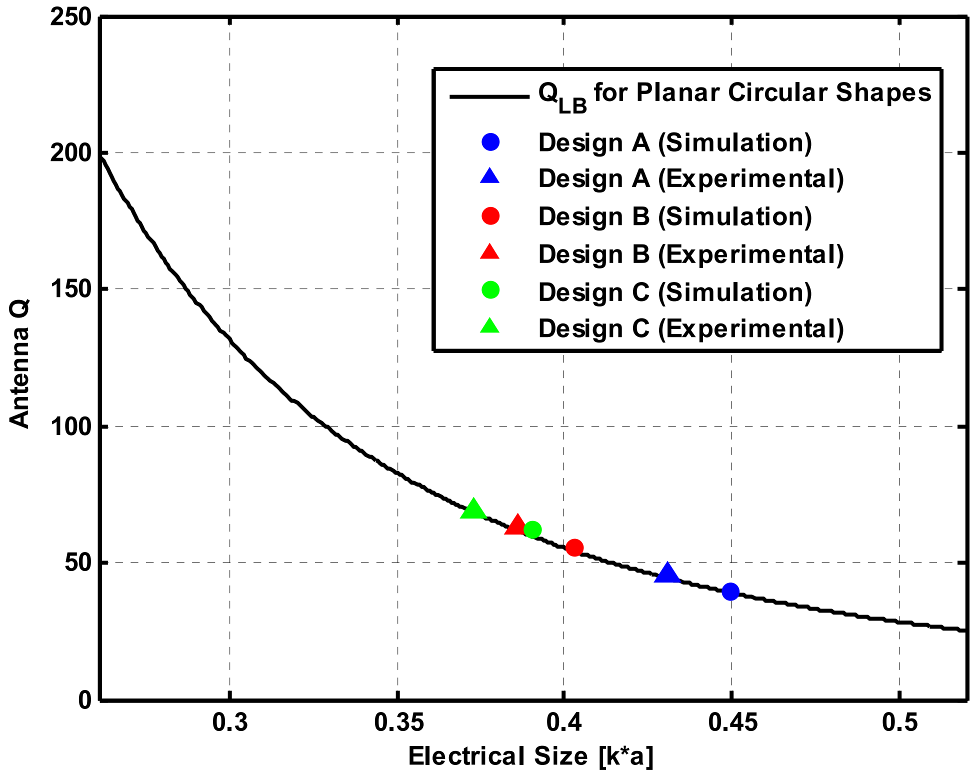

Figure 3.26 – The lower bound of Q for electrically small antennas conforming to a planar circular shape, with the simulated and experimentally determined antenna Q's of Designs A through C with simulated resonant frequencies at 600 MHz and experimental resonant frequencies at approximately 575 MHz.

		ka		Q_{LB}		Q_{res}		Q_{ratio}		% BW [7]		e_{rad}
Design	Holes	*Sim*	*Exp*	*Sim*	*Exp*	*Sim*	*Exp*	*Sim*	*Exp*	*Sim*	*Exp*	*Sim*
A	4	0.449	0.431	39.5	44.5	40.2	45.5	1.018	1.023	1.66%	1.47%	98%
B	6	0.403	0.386	54.3	61.8	55.7	63.5	1.026	1.028	1.20%	1.05%	95%
C	8	0.390	0.373	60.5	68.5	62.5	68.9	1.033	1.005	1.07%	0.97%	94%

Table 3.1 – Summary of Simulated and Experimental Properties of Designs A through C

[7] The % BW is defined as the percentage bandwidth over which reflection coefficient is less than -10 dB with 10-Ohm reference impedance.

3.4.8 – Minimization of Resonance Frequency for Electrically Small Antennas

In this section we attempt to lower the resonance of a planar antenna to as low a resonance frequency as possible, thereby minimizing the value of ka for a self-resonant antenna. In theory, there is likely no lower bound on resonance frequency (a literature search reveals no mention of such a limit). We investigate the lowest possible resonance frequency that can be shaped synthesized from a particular mesh density.

Four antennas were optimized with mesh densities of 100, 200, 400 and 800 triangles, with the dominant CM currents shown at their respective resonance frequency in Figure 3.27. The physical size is identical in all cases considered with a largest physical dimension of 31.81 mm. The magnitude of the CM matrix trace for the PEC and copper varieties is shown in Figure 3.28 and 3.29 respectively for the four antennas considered. The four resonant electrical sizes obtained were ka = 0.2932, 0.2389, 0.1813 and 0.1621 for the four listed mesh densities respectively. These electrical sizes correspond to resonant frequencies of 880.2, 717.2, 544.3 and 486.6 MHz respectively. As the resonance frequency decreases, the radiation efficiency of the structure decreases as well since we are not explicitly optimizing for this quantity (this is only true for the copper structure, see Figure 3.29). It is clear that a denser mesh allows for a lower resonance frequency – as expected from the results of Section 3.4.6.

It should be noted that the electrical size at resonance for all four antennas considered in this section is well below the electrical sizes experimentally considered in this chapter. We believe this indicates that any moment method mesh used in a shape synthesis optimization procedure will not be synthesizing antennas with resonant frequencies approaching the lower bounds on resonance frequency imposed by the number of moment method expansion functions used. This further supports our claim that the synthesis procedures are guided predominantly by the electromagnetics and not by the density of the moment method mesh.

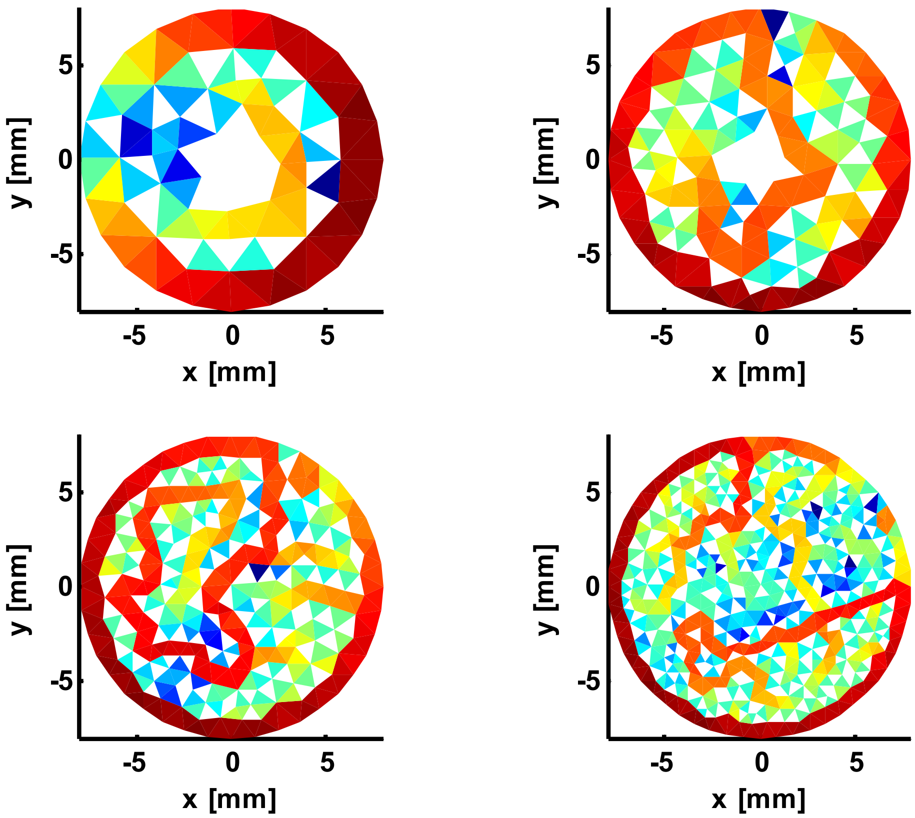

Figure 3.27 – Resonant characteristic mode currents for the four synthesized electrically small antennas with the lowest possible resonance frequency for the given triangle mesh density

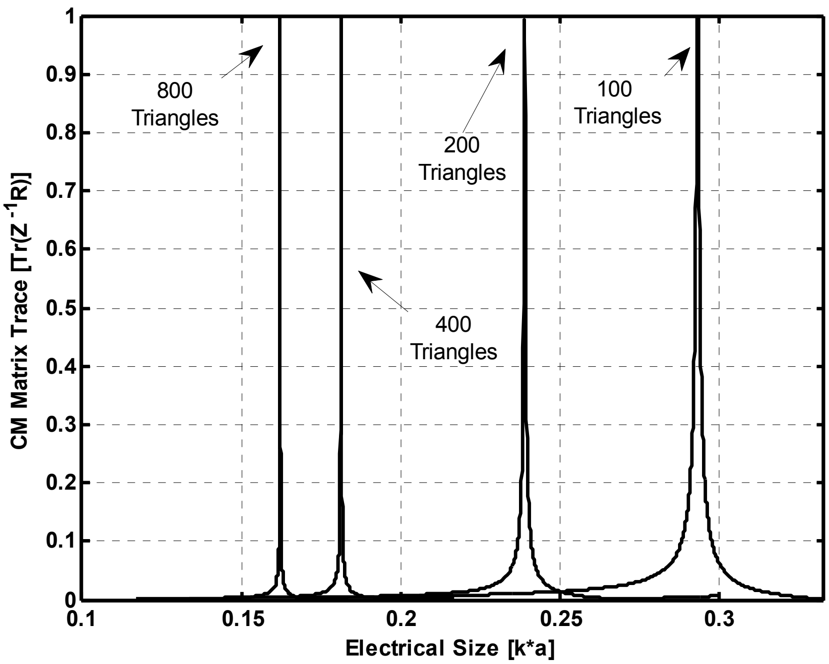

Figure 3.28 – Magnitude of the CM matrix trace (PEC) for the four optimized mesh densities with each mesh density showing a unique resonance frequency (resonance occurring at the peak magnitude of the trace)

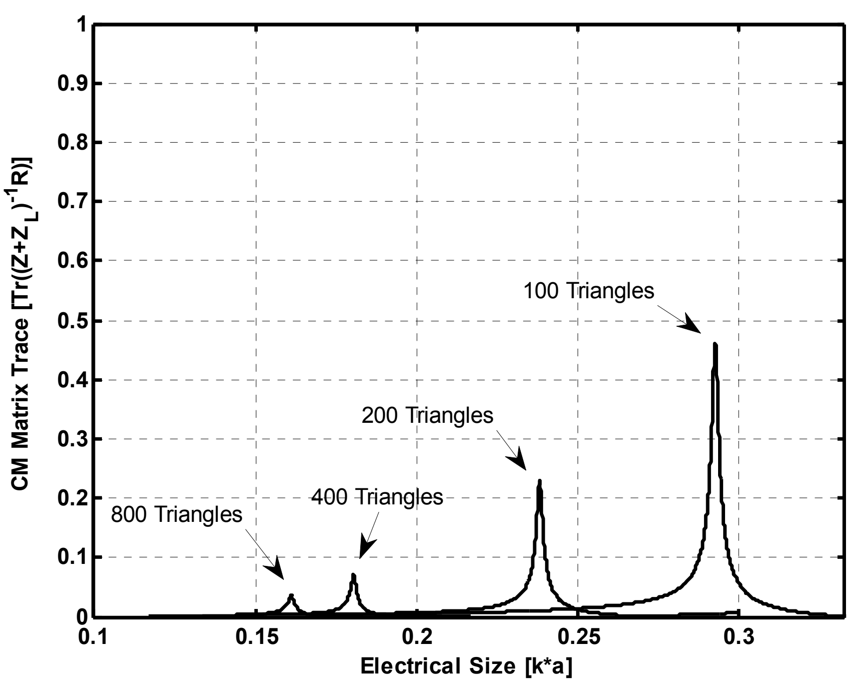

Figure 3.29 – Magnitude of the CM matrix trace (Copper) for the four optimized mesh densities with each mesh density showing a unique resonance frequency (peak magnitude of the trace) along with fairly low radiation efficiency since this performance metric was not explicitly maximized in the optimization

3.4.9 – The Computational Advantages of Feedless Optimization

In the previous sections, the starting shape in the GA-DMM method was a circular metal plate which conforms to the geometry with the lowest possible Q among all planar structures. In order to fully test our new shape synthesis technique, we must consider alternative geometries that have lower static polarizabilities and therefore have larger lower bounds on Q, making it inherently more challenging to obtain a resonant, low-Q antenna that conforms to said alternative geometry. This is where the feedless optimization finds its greatest utility. Following our introductory remarks in Section 3.4.1 and 3.4.2, our contention is that by forcing a feed location, one immediately restricts the possible antenna shapes that can result from an optimizer. In a feedless optimization approach, such a restriction does not exist.

If we wish to turn an irregularly shaped conductor into an antenna, we would traditionally need to specify a feed location. It can be argued that for a highly irregular shape, the ideal starting feed location is not known a priori. The potential lack of symmetries in the arbitrary shape and no prior knowledge of the arbitrary shape's properties can lead one to perform guesswork in where to place the feed location. In the extreme, one would need to attempt placing a feed at every conceivable location on the structure, which in this case would necessitate a gap feed at every expansion function. This is of course a computationally inefficient approach, but a necessary one in feed-restricted optimization. In order to obtain the surface currents (and thus obtain input impedance) one would need to "invert" the $N \times N$ impedance matrix, which is an $O\left(N^3\right)$ operation. This would need to be performed N times for each feed location with the same order of complexity, leading to an overall complexity of $O\left(N^4\right)$ to optimize an antenna by testing every port (expansion function). In our proposed synthesis technique, every port is tested simultaneously, since no particular excitation is being specified. The short-cuts involving the matrix trace are of $O\left(N^3\right)$ since they involve a matrix inverse, but this does not need to be repeated for multiple ports since the ports are all inherently tested in tandem due to the nature of modal analysis. This leads us to argue that our synthesis technique is at least an order of magnitude lower in complexity than a traditional antenna optimization technique.

In order to demonstrate the computational efficiency of the newly proposed technique, consider Figure 3.30. Here, we show the computation time to perform a particular optimization computation versus the number of expansion functions present in the optimization procedure. The solid black line is called the “traditional” technique and involves computing the surface currents due to a different excitation N times, i.e. $[J]=[Z]^{-1}[V]$. We must compute the currents N times because a feed must be selected in $[V]$ and N potential feeds exist. In order to consider all feeds in the optimization, N optimization runs must be performed with the total simulation time shown with a solid black line.

On the other hand, if one uses characteristic modes by directly performing eigenanalysis (Figure 3.30, dashed line) there is no need to compute the modes for different feeds, since the modes are independent of excitation. While eigenanalysis is computationally costly, computing the modes but once is approximately 10 dB second lower in computational time than computing the currents N times. Note that this approximate 10 dB second advantage exists for all numbers of expansion functions (matrix sizes) considered.

Lastly, we consider our new synthesis technique involving the matrix trace shown with a dotted line in Figure 3.30. It has the lowest computation time of all techniques since the operations involved including a single matrix inverse and trace, which is computationally simpler than eigenanalysis or computing the currents N times. It is approximately 15 dB second faster than direct eigenanalysis and approximately 25 dB second faster than the traditional multiple-matrix inversion approach. It is clear that our newly proposed synthesis technique is computationally superior to traditional techniques as well as the direct approach using eigenanalysis. It should be stressed that if the feed location is fixed as per a design requirement, there is no immediately apparent computational advantage in using eigenanalysis or the matrix trace technique, but this is not the problem we wish to address.

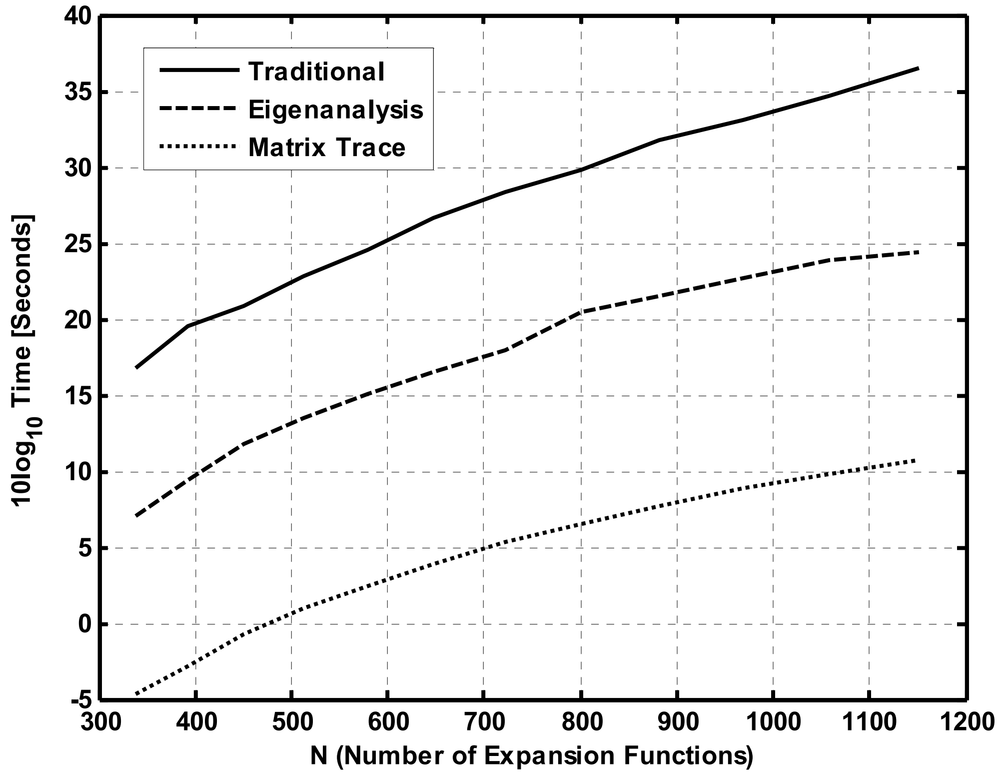

Figure 3.30 – Computation time (dB seconds) to perform an objective function measurement as a function of the number of expansion functions N for the three cases of a traditional optimizer involving multiple matrix inverses, the alternative use of CM eigenanalysis and our proposed use of the trace of the CM matrix

3.5 – Boundary Constrained Optimization using CM Objective Functions

3.5.1 – Optimization of Constrained Conducting Regions

Among all planar geometries, the circular shape yields the lowest possible Q [14], [15]. If an antenna requirement forces us to use a different starting geometry we must suffer an increase in Q (narrowing of bandwidth). Despite this restriction, using our optimization technique it should be possible to shape-synthesize geometries other than a circular shape and still obtain an antenna whose Q approaches that of the lower bound for its geometry. We consider two alternative antenna geometries – the square and equilateral triangle – shown in Figure 3.31. The square and triangular shapes have maximum normalized polarizabilities (γ/a^3) of 2.806 and 2.931 respectively, computed using the numerical technique described in [16]. These results imply the square and equilateral triangle geometries have roughly the same limit in terms of achievable minimum Q.

The two geometric shapes are synthesized into Q-minimized antennas. The minimum radiation efficiency is set to 90% in the optimization procedure. The resulting shape-optimized antennas are shown in Figure 3.32 (with the arrow signifying the feed location selected after optimization occurs – feed selection is described in Section 3.4.3). In Figure 3.33 and 3.34, we consider the antenna Q of each geometry compared to the lower bound of antenna Q for that particular geometry. The Q of the square antenna design is within 5% of the lower bound on square shaped antennas (a Q-ratio of 1.05) while the Q of the triangular antenna design is within 6% of the lower bound of Q (a Q-ratio of 1.06).

We next consider the outcome of the optimization of 200 antennas for each of the square and triangular shapes and plot histograms of the Q ratios obtained in each case in Figures 3.35 and 3.36. A total of 83% of the square shaped antennas achieved a Q ratio less than 1.10 while 85% of the triangular antennas managed a Q-ratio of 1.10 or lower. Similar to the results for the optimization of circular plates in Section 3.4.6, we see excellent results in terms of the consistency of the output of the optimizer and the effectiveness in minimizing the antenna Q.

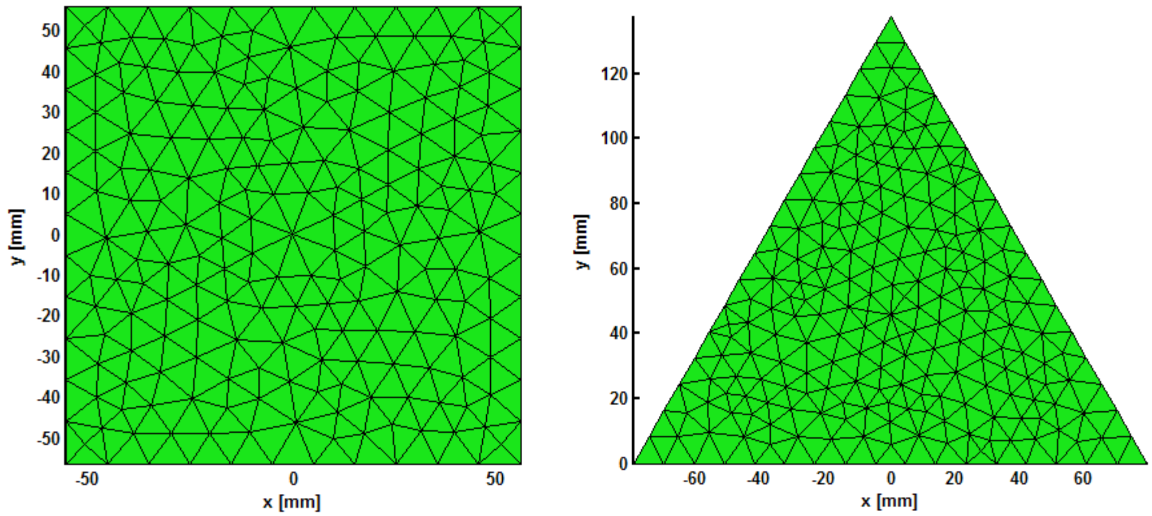

(a) (b)

Figure 3.31 – Example geometries of (a) square shape and (b) equilateral triangle shape

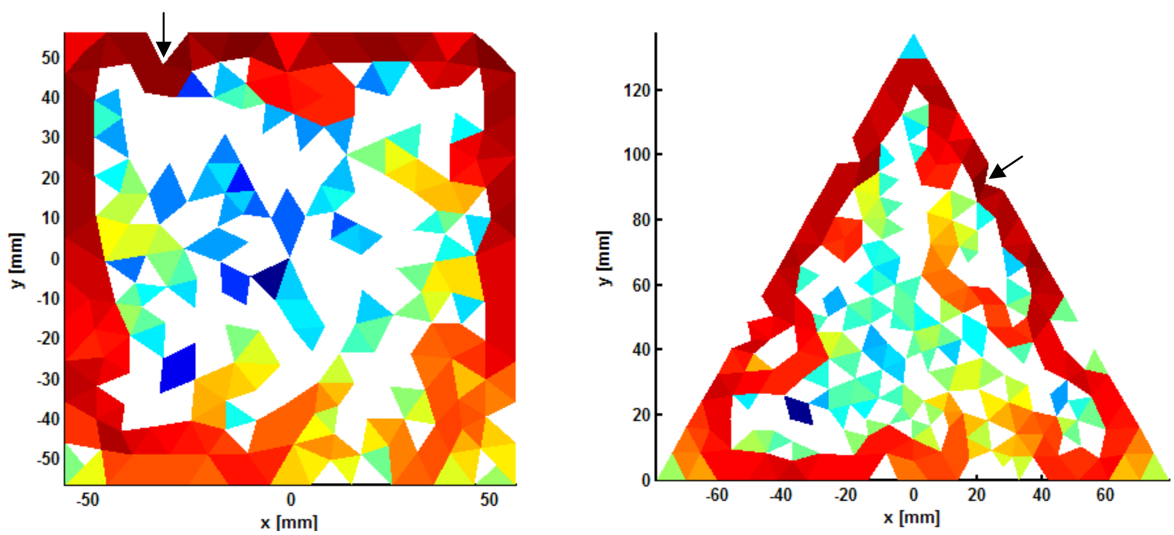

(a) (b)

Figure 3.32 – Optimized antennas synthesized from example geometries of (a) square shape and (b) equilateral triangle shape, with the ideal feed locations shown with an arrow

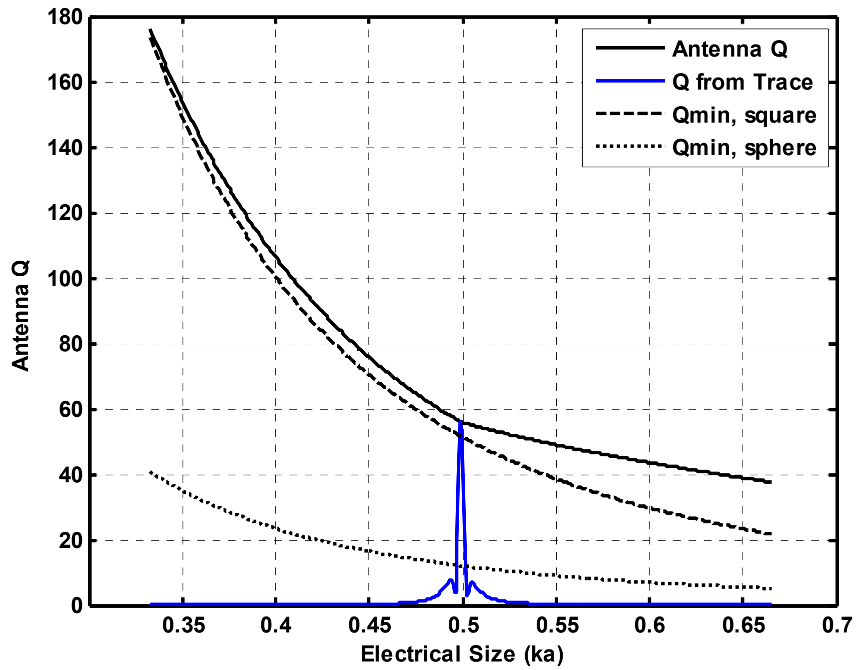

Figure 3.33 – Antenna Q of the square shaped electrically small antenna obtained via the input impedance and alternatively using the matrix trace. The Q-bound for the square and sphere geometries is shown for reference.

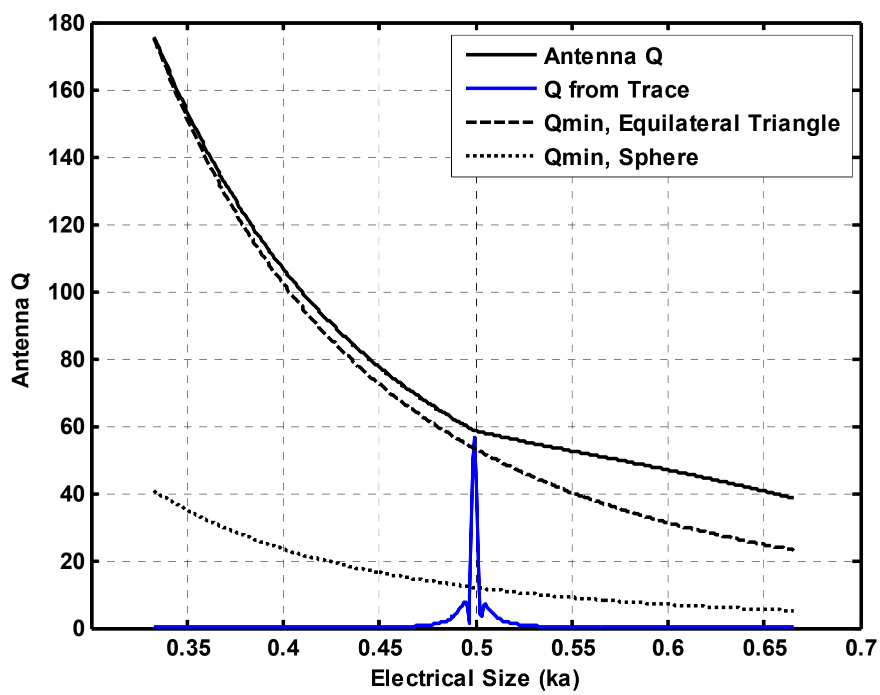

Figure 3.34 – Antenna Q of the triangular electrically small antenna obtained via the input impedance and alternatively using the matrix trace. The Q-bound for triangle and spherical geometries is shown for reference.

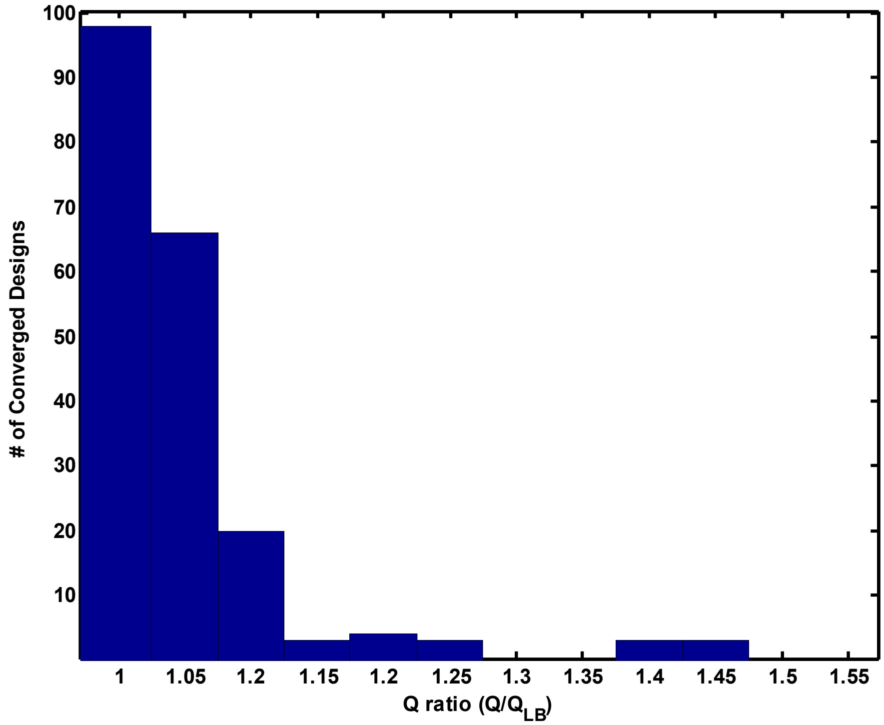

Figure 3.35 – Histogram Q-Ratios for Square Shaped Antennas

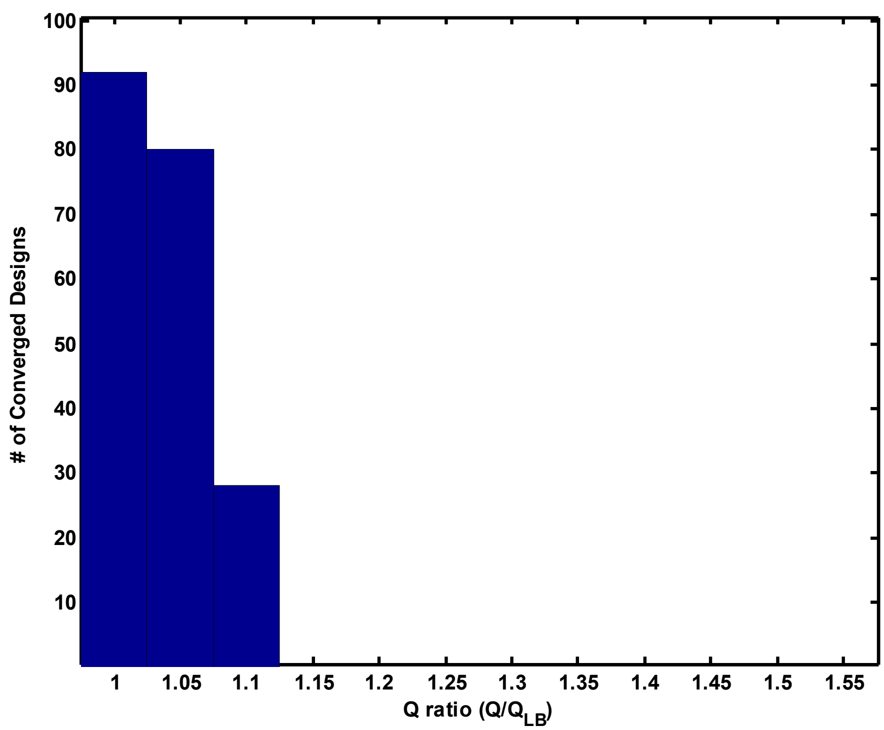

Figure 3.36 – Histogram Q-Ratios for Triangular Shaped Antennas

3.5.2 – Shape Synthesis of Highly Irregular Shapes

In order to complete our investigation of the optimization scheme's ability to shape synthesize, we now turn to the synthesis of antennas starting from somewhat arbitrary shapes. By considering randomly shaped four-vertex polygons, we test what is perhaps the most extreme and confining synthesis problem considered thus far. Most importantly, these example geometries could not be efficiently synthesized using a traditional optimization technique due to their arbitrary layout – any pre-selected feed location would necessarily be a guess and hence there would be no guarantee that an antenna with minimized Q would be obtained by the optimizer. Recall that in our shape optimization scheme no feed is selected, so the optimization process can proceed uninhibited by this restriction. In this sense, we allow the electromagnetics to tell us how to shape the antenna and thus where to feed the structure. An example synthesized antenna that is shaped from an arbitrarily shape starting piece of conductor is shown in Figure 3.37 (for illustrative purposes only).

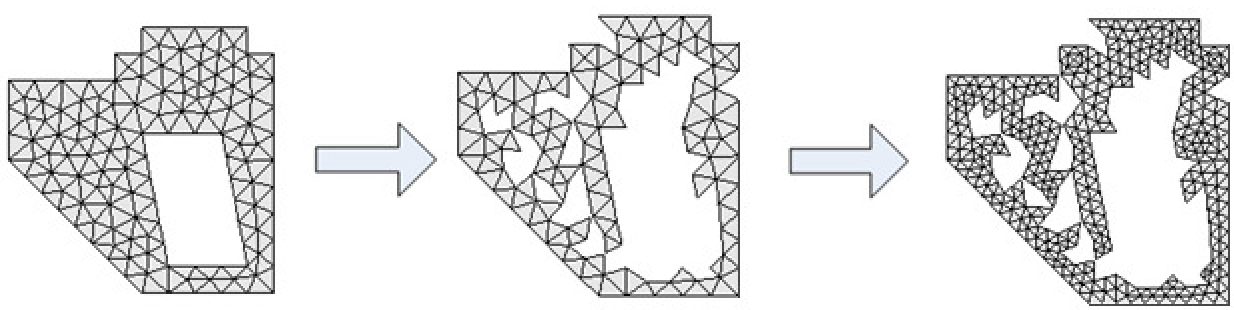

Figure 3.37 – Illustrative example of a truly arbitrary starting mesh being shape synthesized into a resonant, high radiation efficiency, low-Q antenna structure

In order to garner additional confidence in the optimization method, a total of 32 arbitrarily shaped polygonal starting geometries were considered, with their meshed geometries shown in Figure 3.38. The first step in the optimization process was to compute their maximum polarizabilities, as discussed in Section 3.4.4. This is of course an angle-dependent quantity – a sweep through the possible orientation of the electric field excitation is necessary. Obtaining the maximum polarizability (see Appendix C) allows us to determine how well we are performing in terms of the optimized antenna Q. Prior to optimization, all geometries are sized such that the electrical radius of the smallest circumscribing sphere corresponds to ka = 0.5. We expect that the optimization would return an antenna with a Q that approaches the maximum polarizability since we do not specify a feed location and thus will not restrict the antenna orientation. We enforce radiation efficiency greater than 85%. The resulting shape synthesized antennas are shown in Figure 3.39. A summary of the properties of the 32 optimized antennas is shown in Table 3.2. The majority of Q ratios of the 32 optimized designs were less than 10%, indicating a Q-minimized collection of antennas. However, geometries 22, 28 and 29 did not return an antenna Q as low as we would prefer, with ratios 17.7%, 30.0% and 19.9%, respectively. Increasing the mesh density of these structures and then re-running the optimizer showed improved Q ratios below 10%. It is suspected that larger lower bounds on antenna Q for these designs implies greater difficulty in synthesizing an antenna, let alone an antenna with a Q approaching the lower bound. The input resistances of the 32 antennas range between 13.73Ω and 1.51Ω. This obviously presents a difficulty in matching to standard reference impedances. However, low input resistances are typical of small antennas and additionally one finds that the radiation efficiency is quite good, despite the low input resistances. The range of impedances present in the 32 shaped antennas is ideally suited for RFID integrated circuits, as discussed in [17, 18].

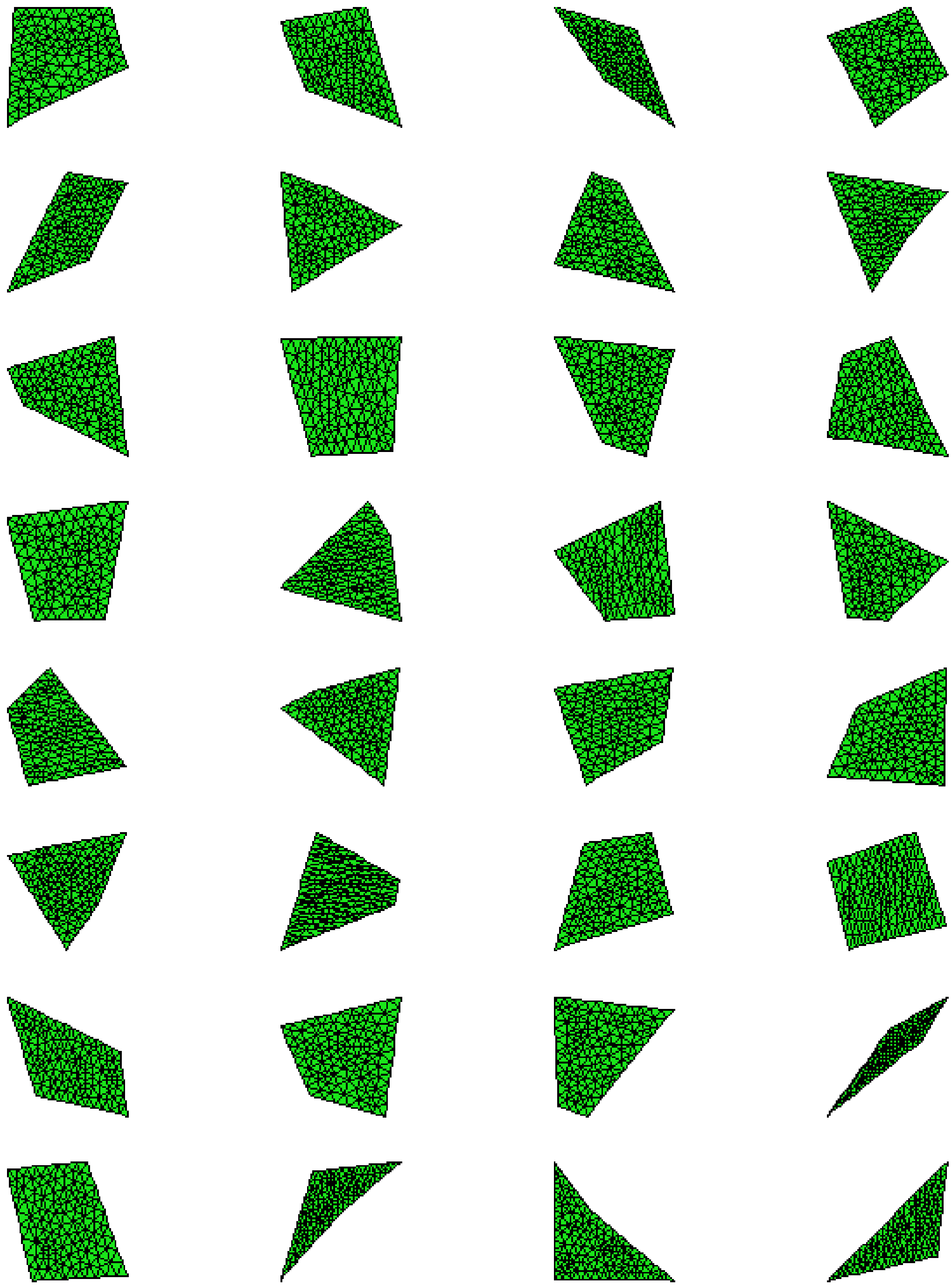

Figure 3.38 – Example collection of 32 arbitrarily shaped polygonal starting shapes destined to be shape synthesized into resonant, efficient, low-Q antennas. The geometries are numbered from 1 to 32, starting with the top left corner moving to the right, row by row.

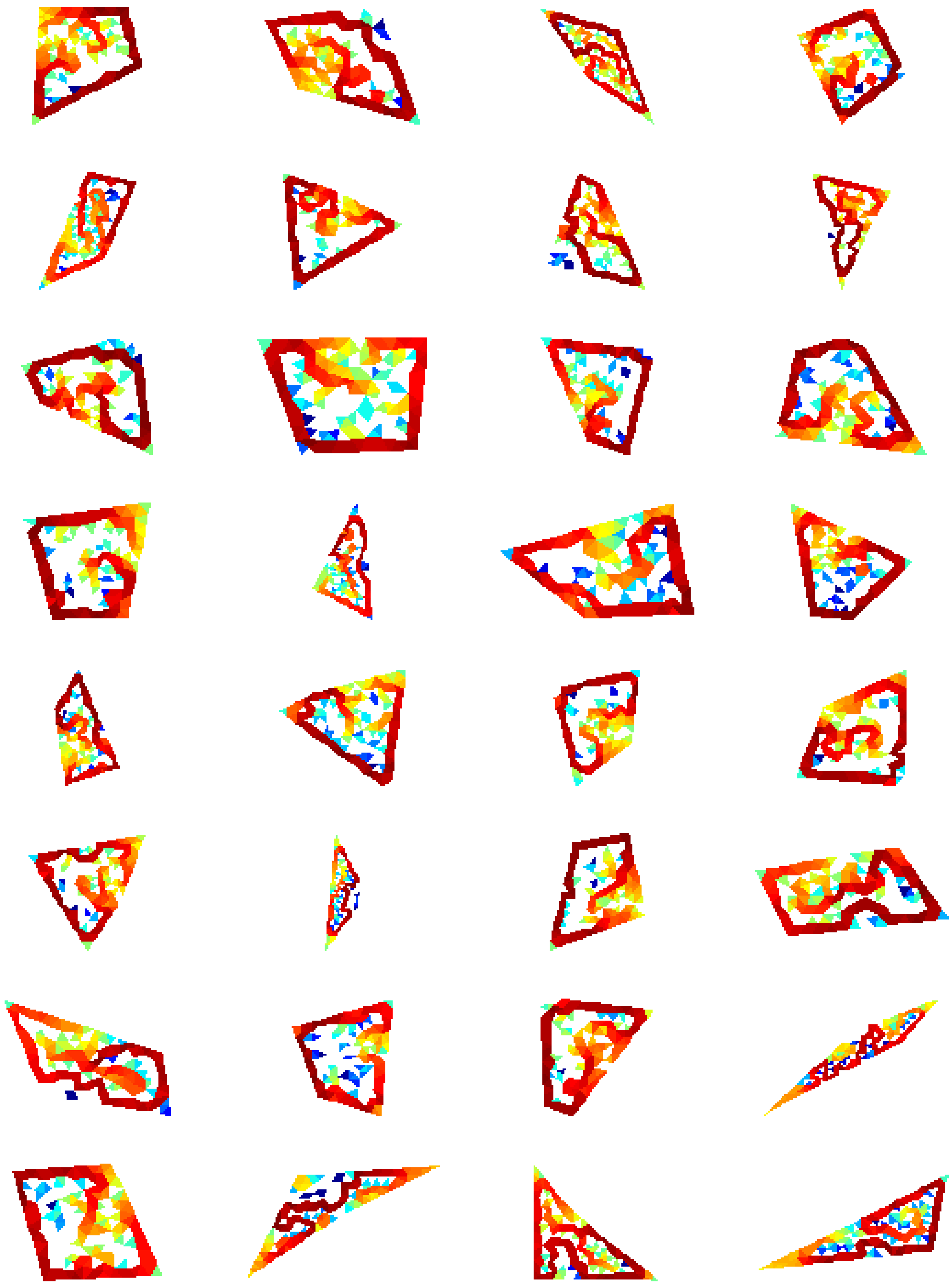

Figure 3.39 – Example collection of 32 shape synthesized antennas all starting from an arbitrarily shaped polygon geometry shown in the Figure 3.38. The dominant characteristic mode currents are shown.

Geometry	Minimum Normalized Polarizability	Maximum Normalized Polarizability	Minimum Antenna Q	Minimum Antenna Q with Losses	Antenna Q	Q Ratio	Rin [Ω]	e_{rad} [%]
1	1.624	2.607	57.84	54.75	58.43	1.067	9.54	94.66
2	0.924	2.173	69.42	62.90	69.41	1.103	3.78	90.61
3	0.275	1.666	90.54	82.56	87.50	1.060	1.51	91.18
4	2.467	2.920	51.65	45.12	49.34	1.094	12.53	87.34
5	0.540	2.218	67.98	59.18	62.41	1.055	2.67	87.05
6	2.227	2.682	56.22	52.36	55.04	1.051	10.83	93.13
7	1.183	2.351	64.16	57.81	60.42	1.045	4.20	90.10
8	0.994	2.307	65.37	59.19	63.62	1.075	2.47	90.54
9	1.496	2.479	60.84	53.87	59.88	1.112	7.09	88.54
10	1.893	2.928	51.51	45.28	49.68	1.097	11.36	87.91
11	1.563	2.512	60.03	52.50	54.00	1.029	8.31	87.45
12	1.650	2.767	54.50	50.27	55.53	1.105	11.38	92.24
13	2.522	2.845	53.00	46.75	48.50	1.037	13.73	88.20
14	0.726	2.157	69.92	61.84	65.94	1.066	2.35	88.45
15	1.118	2.518	59.90	55.94	57.08	1.020	6.27	93.37
16	1.918	2.908	51.86	48.65	54.10	1.112	10.98	93.81
17	0.839	2.566	58.78	52.91	56.92	1.076	6.07	90.02
18	2.334	2.893	52.13	44.52	49.39	1.109	11.58	85.40
19	1.381	2.380	63.37	58.04	59.42	1.024	7.70	91.60
20	1.454	2.392	63.04	56.20	62.92	1.120	7.30	89.15
21	2.006	2.606	57.87	53.68	55.96	1.043	9.46	92.76
22	0.219	1.612	93.53	81.83	96.35	**1.177**	1.85	87.49
23	1.313	2.426	62.15	57.46	59.36	1.033	7.33	92.45
24	0.708	2.377	63.44	57.06	63.43	1.112	2.44	89.94
25	0.557	2.145	70.32	61.89	66.84	1.080	2.36	88.01
26	2.670	3.218	46.86	40.35	44.14	1.094	15.99	86.09
27	1.659	2.749	54.86	46.85	48.73	1.040	10.09	85.41
28	0.057	1.315	114.72	102.71	133.55	**1.300**	9.75	89.53
29	1.413	2.406	62.67	58.67	70.35	**1.199**	8.01	93.61
30	0.185	1.502	100.43	93.90	103.47	1.102	12.97	93.51
31	0.653	1.927	78.25	72.33	79.10	1.094	2.62	92.42
32	0.204	1.693	89.06	77.12	85.25	1.105	6.12	86.59

Table 3.2 – Performance of shape-optimized antenna with 32 different arbitrary starting shapes

3.5.3 – Antenna Synthesis in the Presence of "Do not Touch" Regions

An additional application of the feedless optimization technique is the inclusion of "do not touch" regions of metallization. By "do not touch" regions, we refer to regions of metal where the optimizer is not permitted to shape synthesize – they must remain untouched. Three example geometries with "do not touch" regions are shown in Figure 3.40(a), 3.41(a) and 3.42(a) with the "do not touch" regions shown in red, and the shape-synthesizable regions shown in green.

By forcing certain metal regions to remain untouched, we are inherently limiting the possible shapes the optimizer can synthesize. Therefore, it is difficult to determine what the true bounds on antenna Q are for such restricted geometries since the polarizability approach discussed in Section 3.4.4 and Appendix C used to obtain the bounds do not give allowance for these restrictions. We suspect that the bound lies somewhere between the bound for the full geometric shape (including the "do not touch" regions) and an alternative shape with the "do not touch" regions removed.

The three example antennas with "do not touch" regions were shape synthesized with the resulting antennas and their dominant and resonant characteristic mode currents are shown in Figure 3.40(b), 3.41(b) and 3.42(b). This shape synthesis was accomplished in precisely the same manner as before, only the genome of every antenna is restricted to describe only the "green" regions that are shape synthesizable, while the red regions remain untouched though certainly electromagnetically present. The antenna Q obtained in the three scenarios was 69.35, 81.54 and 132.3, with the lower bound on Q for all three antennas (for the square geometry) being 51.67. The Q ratios obtained are 1.342, 1.578 and 2.560, which signifies that we are not achieving the lowest possible Q for the geometry, unlike previous attempts. We surmise that this is due to the restriction imposed by the "do not touch" regions. Notice that the Q ratio increases as more of the structure is prevented from being shaped synthesized, indicating that the entire structure must be shape synthesized to truly minimize the antenna Q. Nevertheless, these regions pose a difficult task for a traditional optimization technique in that one does not necessarily know where to begin with a feed location, a restriction our optimization scheme is not subject to.

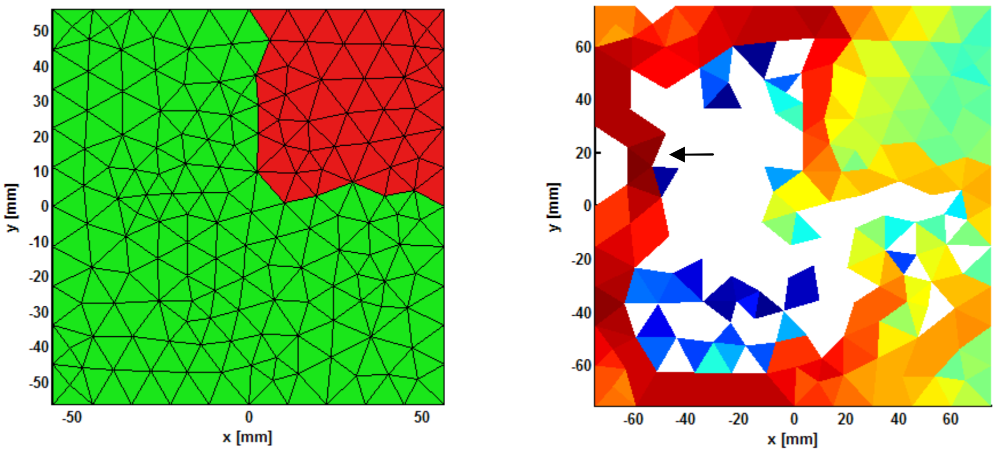

(a) (b)

Figure 3.40 – Plot of the one-quarter "do not touch" square plate and its optimized counterparts' modal current

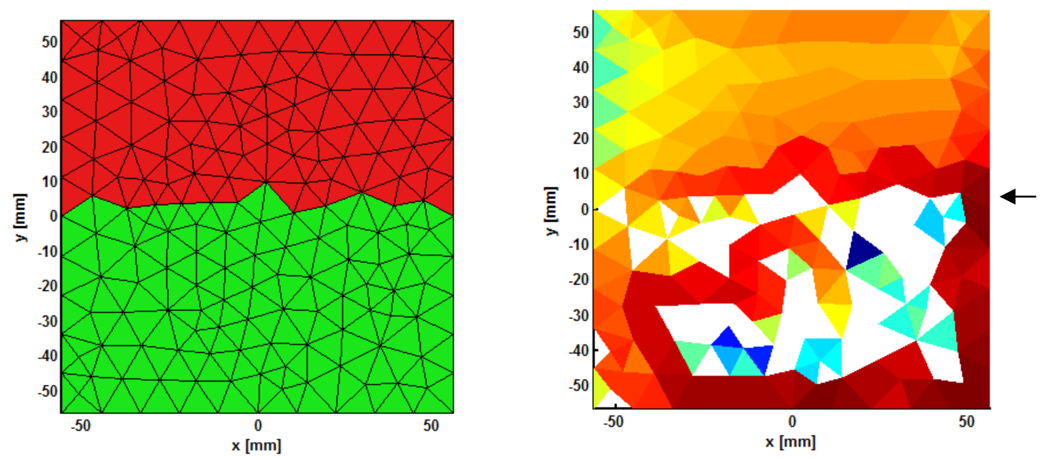

(a) (b)

Figure 3.41 – Plot of the one-half "do not touch" square plate and its optimized counterparts' modal current

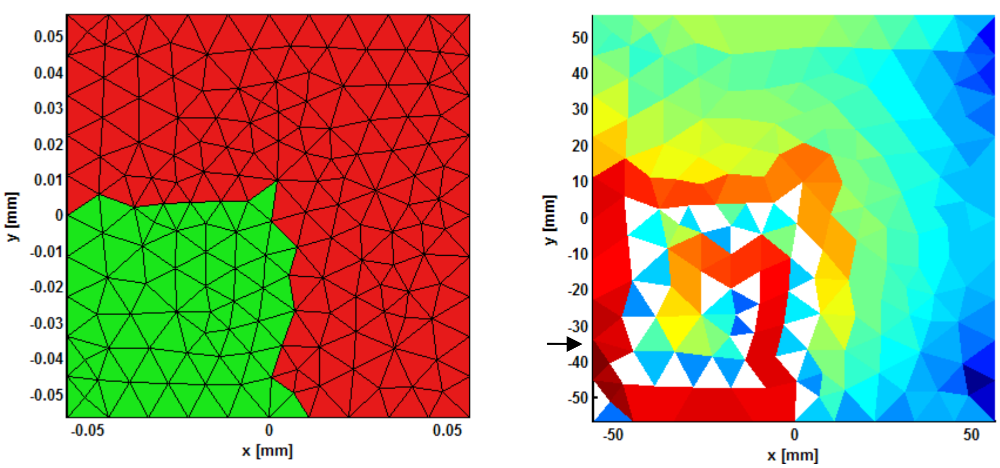

(a) (b)

Figure 3.42 – Plot of the three-quarter "do not touch" plate and its optimized counterparts' modal current

3.5.4 – Experimental Measurements of Synthesized Constrained Shaped Antennas

We now turn to experimentally confirming the optimization schemes' ability to synthesize low-Q antennas with arbitrary starting shapes. As in Section 3.4.7, we consider symmetrical antennas fed through a ground plane. This has the added bonus of simultaneously testing an unbalanced design (half of the antenna over the ground plane) and a balanced design (the full antenna) since the full antenna will have twice the input impedance and half of the gain of the unbalanced ground plane based design. Three constrained geometries, a square shape, a plus shape and a rectangular shape are considered as shown in Figure 3.43. Their respective normalized polarizabilities are shown for reference. The parameters have the relationships t = 2d and L = 2W. The orientation of the electrical field in determining the polarizability of the rectangle is along the dimension W.

Meshed starting shapes of the three geometric shapes were optimized to be resonant at 300 MHz, have high radiation efficiency and low-Q antennas, each with an electrical size of approximately ka = 0.5 using the same optimization techniques described thus far. The meshed antennas are shown in Figure 3.44 with the fabricated antennas cut in half and placed over a large ground plane shown on the right in the same figure. Similar to the previous example involving circular shaped antennas in Section 3.4.3 and 3.4.7, we require the optimized antenna to have a radiation efficiency of 90% or greater to ensure radiation efficiency does not play a large role in the behaviour of the antenna being measured. The resulting measured and simulated input reflection coefficients are shown in Figure 3.45. The reference impedance used in these examples is Z_o = 5 Ohms, half of that of the circularly shaped antennas from Section 3.4.3 and 3.4.7. The simulated and measured antenna Q of the three antennas is shown in Figure 3.46 with their associated lower bounds shown overlaid. The results are summarized in Table 3.3. We note that all antennas considered achieved fairly low antenna Q to within 4% or better of their respective lower bounds. Note that the frequency shift introduced by the unaccounted for FR4 substrate is significantly less than for the circular shaped antennas in Section 3.4.7 since the electrical thickness in this example is less in this example since we are operating at 300 MHz as opposed to 600 MHz.

The low input resistance is to be expected from electrically small antennas, though many relevant applications would be far better served with lower input resistances rather than the 50Ω standard, especially scenarios involving miniaturized amplifiers in mobile phones or even high power radio transceivers, all of which typically operate with impedances in the range of 5Ω [19]. If one did have the requirement of a specific input resistance in order to better match to an external reference impedance, one could first optimize to have a resonant structure in the usual feedless manner described thus far. This would be followed by determining the null space of $\left[X\right]^{-1}\left[R\right]$. If $\left[Z\right]=\left[R\right]+j\left[X\right]$ describes a structure with a single resonant and dominant characteristic mode, the aforementioned null space would in fact be the eigenvector of this dominant mode. Furthermore, with the eigenvector known, one could proceed to optimize the input resistance using expression (3.30). The current coefficient to use in this case would be the maximum coefficient within the vector. Again, this is a feedless approach in the sense that the location of this maximum modal current coefficient is not forced and hence it is strictly guided by the feedless optimization process.

A literature search reveals only one reference where a constrained-shaped planar antenna has been shown to achieve the lower bounds of Q [20]. A planar rectangular shaped antenna is considered in [20], with antenna Q's approaching the bounds imposed by the Gustaffson-limit. That being said, the antennas in [20] showed simulated radiation efficiency in the 60% - 80% range, lower than the efficiency simulated in this section. It should also be noted that the antennas considered in [20] are specifically designed to conform to planar rectangular shapes. It is expected that irregular antenna shapes such as the plus shaped geometry (Figure 3.43 and 3.44) and the irregular shaped planar geometries in Figure 3.38 could not be easily designed (if at all) using the techniques described in [20]. This is the advantage of the feedless antenna shape-synthesis approach: the ability to shape any arbitrarily shaped structure into a high radiation efficiency, resonant and low-Q antenna.

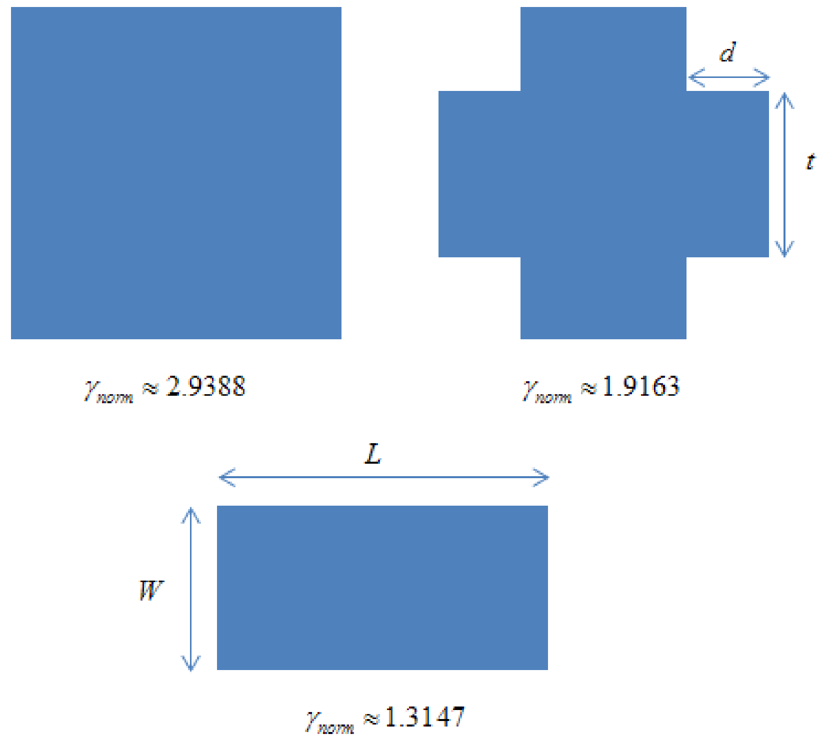

Figure 3.43 – Various Geometries and their Associated Normalized Polarizabilities

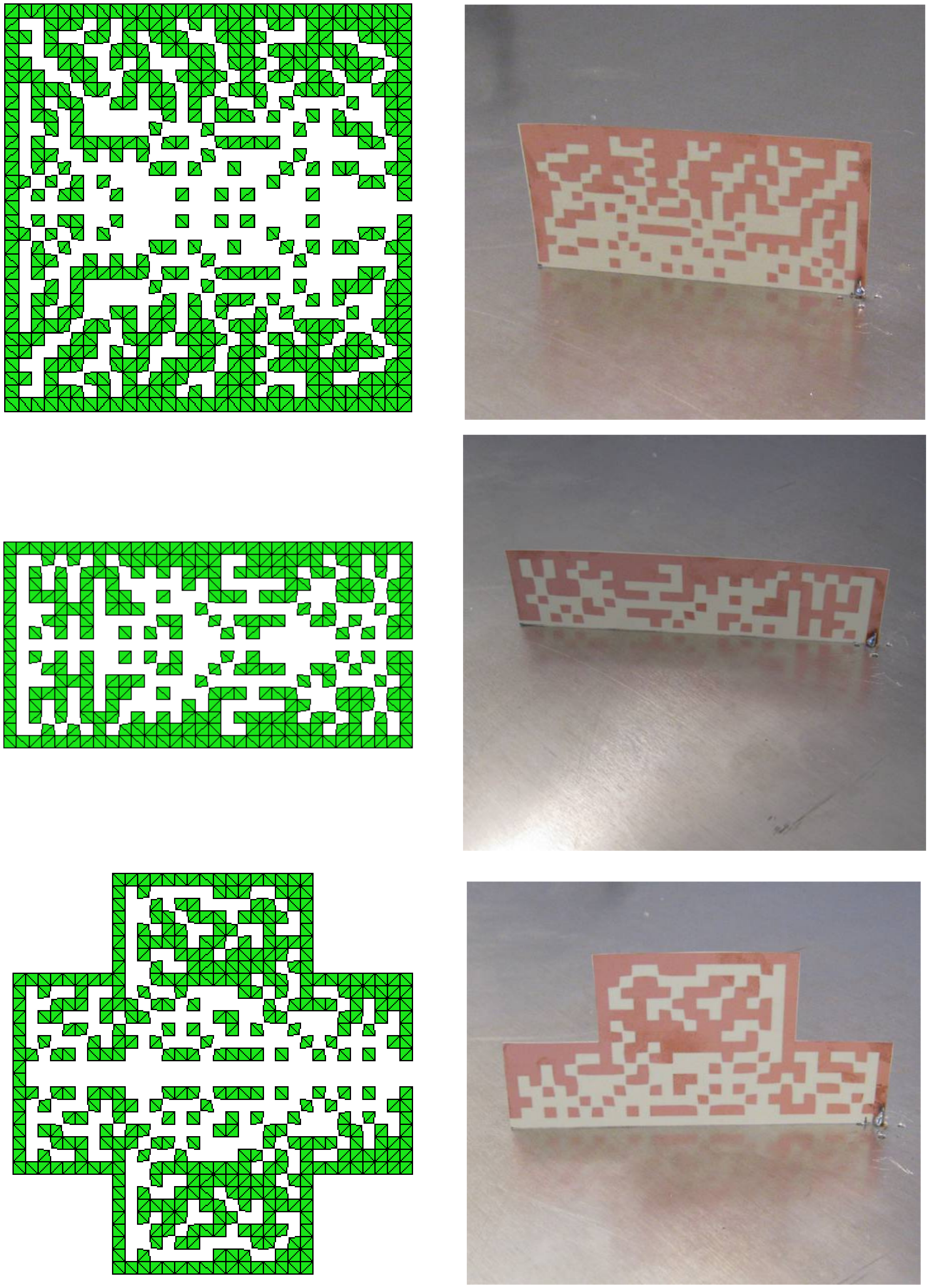

Figure 3.44 – Example low-Q shape synthesized antennas conforming to constrained geometric shapes of square, rectangle (2:1) and plus shape geometries

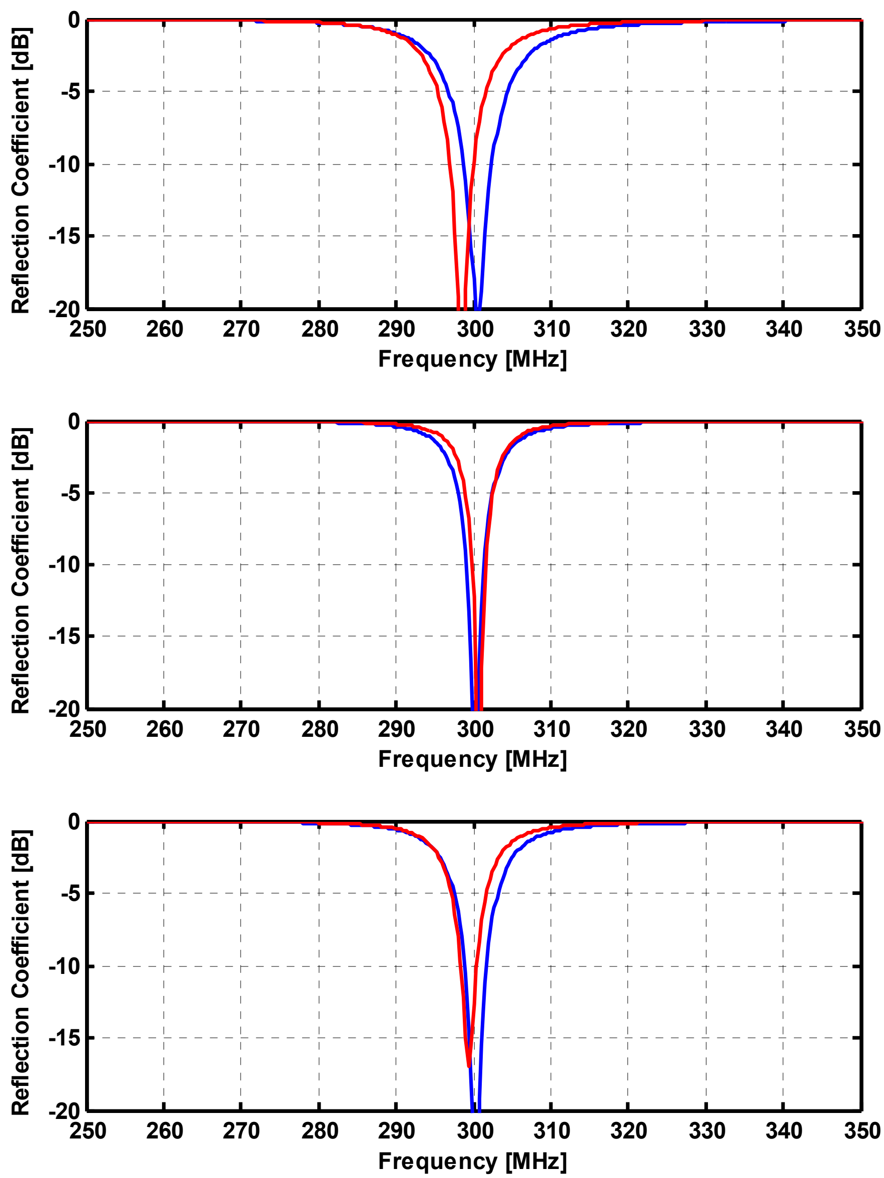

Figure 3.45 – Plot of reflection coefficients of electrically small antenna (a) square shape (b) rectangle shape, (c) plus shape. Red curves (——) are experimental measurements while blue curves (——) are simulated results.

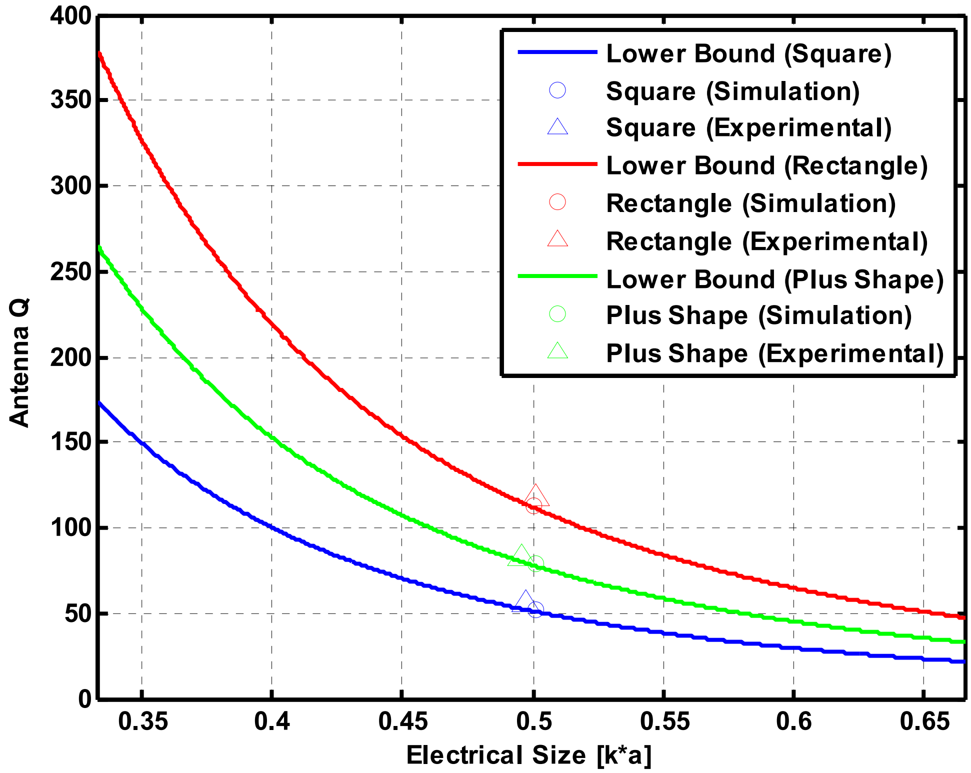

Figure 3.46 – A plot of the lower bound of Q for electrically small antennas conforming to a various constrained geometric shapes with the simulated and experimentally determined antenna Q's of the square, rectangle and plus shaped antennas shown at their respective resonance frequencies

	ka		Q_{LB}		Q_{res}		Q_{ratio}		*% BW RL 10dB*		e_{rad}
Design	*Sim*	*Exp*	*Sim*	*Exp*	*Sim*	*Exp*	*Sim*	*Exp*	*Sim*	*Exp*	*Sim*
Square	0.501	0.497	51.1	53.4	52.3	55.2	1.023	1.034	1.27%	1.21%	97%
Rectangle	0.500	0.501	112.0	113.0	113.4	117.8	1.013	1.042	0.586%	0.565%	93%
Plus Shape	0.501	0.496	78.2	80.1	79.5	82.1	1.017	1.025	0.840%	0.804%	95%

Table 3.3 – Summary of predicted and measured properties of square, rectangular and plus shaped electrically small shape synthesized antennas in Figure 3.44.

3.6 – Concluding Remarks

In this chapter we have developed the analysis framework to describe the properties of single-mode antennas. These properties were described entirely using characteristic mode quantities, namely the eigenvalues and eigencurrents obtained via eigenanalysis, as described in Section 3.2. Quantities such as resonance frequency, impedance bandwidth and radiation efficiency were shown to be obtainable without having to excite the structure or define a feeding mechanism – such is the nature of eigenanalysis. Furthermore, in Section 3.3 we showed computationally simpler techniques involving the CM matrix trace that allowed us to effectively retrieve the same information as eigenanalysis for far less computational effort. In Section 3.4 we recognized the fact that these computationally simple techniques for analysis could be used as objective functions for the purpose of antenna shape synthesis. These feed-independent objective functions were incorporated in a genetic algorithm optimization scheme combined with the moment method and an additional computational refinement technique using the direct matrix manipulation method. It was shown that the combination of these techniques lead to a computationally efficient optimization approach which gave rise to the synthesis of antennas with antenna Q approaching that of the fundamental lowest bounds. The feedless optimization technique was further applied in Section 3.5 where the synthesis of irregularly shaped start geometries was considered. Similar success was found with these irregular shapes being synthesized into Q-minimized antennas. Experimental measurements confirmed much of the theories and conclusions put forth in Chapter 3.

Chapter 3 References

[1] **J. Ethier**, "MIMO Antenna Design using Characteristic Mode Concepts," *Master's Thesis, University of Ottawa*, 2008.

[2] A. Yee, R. Garbacz "Self- and Mutual-Admittances of Wire Antennas in Terms of Characteristic Modes," *IEEE Transactions on Antennas and Propagation*, Vol. 21, No. 6, pp 868 – 871, November 1973.

[3] **J. Ethier** and D. McNamara, "A New Objective Function for the Synthesis of Electrically Small Antennas", *IEEE URSI Radio Science Meeting Digest*, Charleston, North Carolina, USA, June 1 – 5, 2009.

[4] **J. Ethier** and D. A. McNamara, "Through the Looking Glass: A Characteristic Mode View of Electromagnetic Modeling & Design", *Proc. 14th Int. Symposium on Antenna Technology & Applied Electromagnetics (ANTEM'2010)*, Ottawa, July 2010.[8]

[5] S. N. Makarov, *Antenna and EM Modeling with MATLAB®*. New York: John Wiley & Sons, 2002.

[6] A. D. Yaghjian, S. R. Best, "Impedance, Bandwidth, and Q of Antennas," *IEEE Transactions on Antennas and Propagation*, Vol. 53, No. 4, pp. 1298 – 1324, April 2005.

[7] R. F. Harrington, J. Mautz, Y. Chang, "Characteristic Modes for Dielectric and Magnetic Bodies," *IEEE Transactions on Antennas and Propagation*, Vol. AP-20, No. 2, pp. 194 – 198, March 1972.

[8] **J. Ethier** and D. A. McNamara, "An Examination of the Characteristic Modes of Lossy Structures", *URSI Radio Science Meeting Digest*, Toronto, Canada, July 11 – 17, 2010.

[9] O. Guler, *Foundations of Optimization*, Springer, 1st Edition, August 2010.

[8] This paper was awarded "Best Student Paper" during the ANTEM 2010 conference

[10] D.E. Goldberg, *Genetic Algorithms in Search, Optimization and Machine Learning*. Addison-Wesley, Reading, MA, 1989.

[11] R.L. Haupt, D.H. Werner, Genetic Algorithms in Electromagnetics, Wiley-IEEE Press, John Wiley & Sons, New York, 2007.

[12] Y. Rahmat-Samii, E. Michielssen (*Edits.*), *Electromagnetic Optimization by Genetic Algorithms*, John Wiley & Sons, New York, 1999.

[13] *Ibid*., Chapter 9, pp. 249 – 278.

[14] C. Sohl, M. Gustafsson, G. Kristensson, "Physical limitations on broadband scattering by heterogeneous obstacles," *Journal of Physics A: Mathematical & Theoretical*, September 2007.

[15] M. Gustafsson, "Polarizability and physical bounds on antennas in cylindrical and rectangular geometries," *Technical Report LUTEDX / TEAT-7195 / 1-11*, Lund University, Department of Electrical and Information Technology, Lund, Sweden, 2010.

[16] **J. Ethier** and D. A. McNamara, "Computational Estimates of Electrically Antenna High-Contrast Polarizabilities," *IEEE Antennas and Wireless Propagation Letters*, Vol. 10, Nov. 2011, pp. 1309 – 1312.

[17] Alien Technologies, Morgan Hill, California, USA, *Alien-Higgs RFID Tag IC Product Overview*, URL: http://www.alientechnology.com/docs/products/DS_H2.pdf

[18] M.M. Tentzeris, "Novel paper-based inkjet-printed antennas and wireless sensor modules," *Proc. Int. Conf. on Microwaves, Comm., Ant.& Elec. Sys.* (COMCAS 2008), Tel-Aviv, Israel, 13 – 14 May, 2008.

[19] Private Communication, I. Acimovic, *Alcatel-Lucent Research and Innovation Centre*, Ottawa, Canada, October 2011.

[20] S. Best, "Optimization of the bandwidth of electrically small planar antennas," *2009 Antenna Applications Symposium*, Monticello, IL, September 2009.

Chapter 4

Multi-Band, Single-Mode Antenna Shape Synthesis

4.1 – Introduction

In Chapter 3 we investigated the application of CM theory in the shape-synthesis of single-mode antennas, and in particular focused on the synthesis of electrically small antennas. The emphasis was on obtaining a single-mode antenna with a wideband response centered around a single frequency: a single-band antenna. In Section 4.2 we will extend the theoretical developments of Chapter 3 to single-mode, multi-band antennas. At a fundamental level, the extension of Chapter 3's work in this manner is to apply the optimization scheme at multiple frequencies rather than for a single frequency. However, as we will show, the devil is in the details and difficulties creep in for structures that are electrically larger or antenna structures with large regions where direct excitation is not possible (or not permitted). In Section 4.3 we overcome these difficulties by introducing a new modal formulation, which we will call sub-structure characteristic modes, that allows us to restrict our window on the characteristic modes to those that we can directly excite. Section 4.4 concludes the chapter.

4.2 – Multi-Band Antenna Synthesis using Characteristic Modes

4.2.1 – Proposed Multi-Band Synthesis Technique

A multi-band antenna is one that has two or more distinct operating bandwidths. Ideally, the antenna would be self-resonant in each of these bands, forgoing the need for tuning circuitry. Multi-band antenna design is not a simple process [1] – [3], as the frequencies required are usually application dependent and thus a general design technique applicable to any scenario does not exist. Techniques exist whereby a feed port is selected and the antenna is shape-synthesized. Given the very large number of possible feeding locations, such approaches naturally restrict the optimizers' ability to actually obtain a multi-band structure. Trial and error might be required until a suitable feeding location is obtained. As shown in Chapter 3, the feedless optimization scheme developed forgoes the need for a feed location to be specified before or during the optimization procedure, with the preferred feeding location becoming apparent after the optimization process concludes. A similar optimization scheme can be developed for multi-band antennas.

The multi-band synthesis technique we propose closely follows that of Chapter 3. The algorithm discussed in Section 3.4 and the objective functions shown in expressions (3.85), (3.86) and (3.87) are also used in the synthesis of multi-band antennas, except that multiple frequencies are considered, as indicated in the flow diagram of Figure 4.1. Rather than finding the zeros of $\angle\Psi(\omega)$ at one frequency to obtain a resonant antenna, the condition is enforced at multiple frequencies. The same is true for the maximization of $\left|\Psi(\omega)\right|$ for radiation efficiency, and additionally the minimization of antenna Q via the minimization of the frequency derivative of the matrix trace. Once the antenna is resonant and has sufficient radiation efficiency at each of the desired frequencies, the antenna Q is minimized in a balanced manner, placing the emphasis on reducing antenna Q for the frequency where the antenna Q is the largest. Notice also that the algorithm shown in Figure 4.1 allows for eventual selection of a plurality of feed locations since we are no longer dealing with a single mode at a single frequency. There may be multiple locations at which to feed the optimized antenna structure, with each feed location exciting a different (albeit single) mode in a different band.

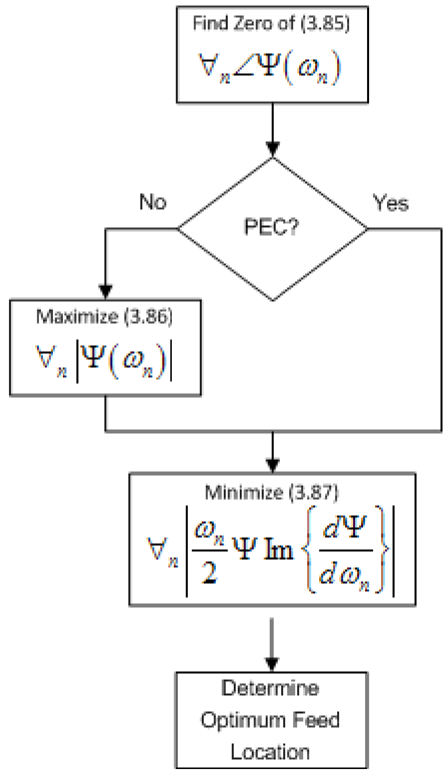

Figure 4.1 – Flow diagram of the proposed optimization scheme for multi-band antenna synthesis

4.2.2 – Example Simple Single- and Dual-Band Antennas

A rectangular PEC plate (50mm by 100mm) is used as the starting shape, with the DMM/GA method coupled to the CM-derived objective functions used to optimize the plate for operation centered at 700 MHz. The selected plate size and subsequent frequencies that will be considered fall in line with typical mobile phone communication devices sizes and frequencies. The shape-optimized resonant antenna is shown in Figure 4.2(a). We additionally show the magnitude of the matrix trace in Figure 4.2(b). Note that we are assuming a PEC structure and thus radiation efficiency is not considered. The electrical size of this particular structure corresponds to ka = 0.8, well above the electrically small antenna limit. Ergo, we are not as concerned with low radiation efficiency and additionally recognize the fact that the bounds on antenna Q are not necessarily limiting for larger electrical sizes (due to the presence of multi-modes), with ka = 0.8 approaching such inapplicable frequency regimes.

The selected feed location is shown in Figure 4.3(a) with the dominant CM current (the eigencurrent of mode 1) shown in Figure 4.3(b). The CM current shows a plethora of possible feed locations due to the abundance of high current magnitude regions, with the selected feed chosen for the most desirable input impedance value. This can be accomplished using an impedance map, as discussed in Appendix B. The resulting input impedance is plotted in Figure 54(a) and the input reflection coefficient for a reference impedance of 63Ω shown in Figure 54(b). A respectable bandwidth of 4.3% was found with a -10dB reflection coefficient. While acting as a preliminary investigation of a single-band design, this example also shows the applicability of the novel feedless optimization approach to non-electrically small antennas, and hence its applicability to more than the electrically small cases discussed in Chapter 3.

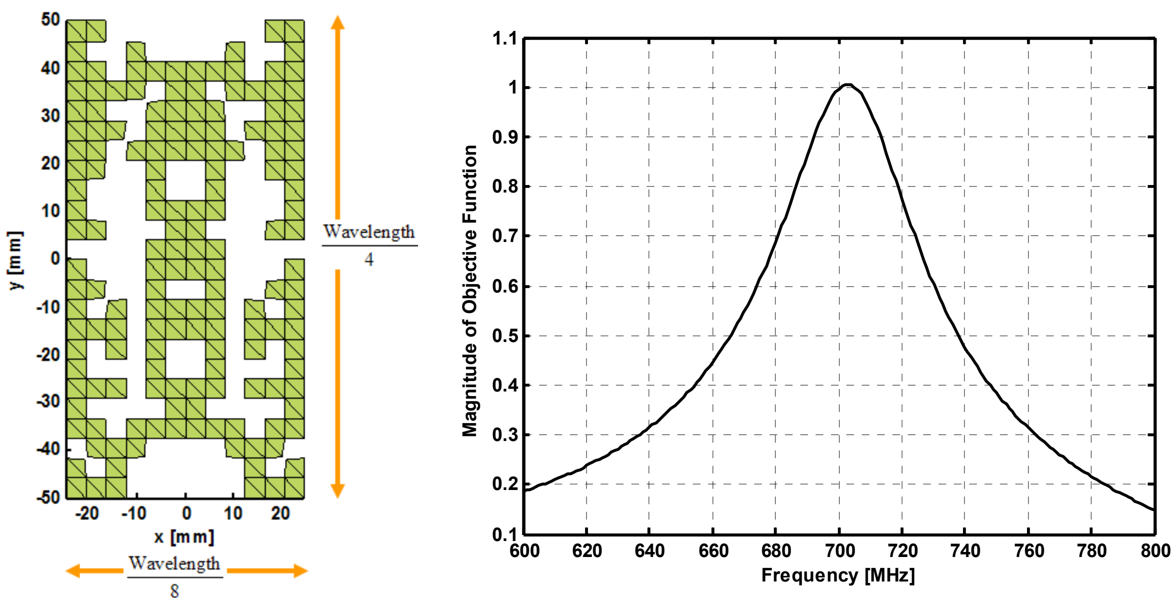

(a) (b)

Figure 4.2 – Example single-band meshed structure (a) and the magnitude of the CM matrix trace in (b). Note that this structure is not within the electrically small antenna regime and yet can be treated like a single mode antenna as evidenced from the plot shown in (b)

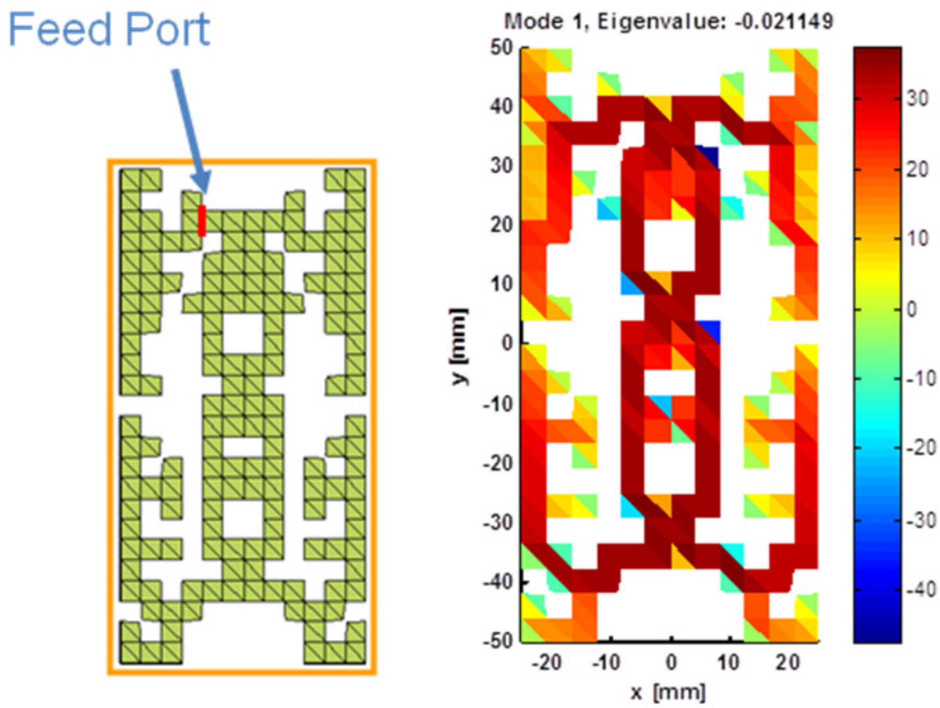

(a) (b)

Figure 4.3 – Example single-band structure with feed port shown in (a) and modal currents shown in (b). The ideal feed location is any location where the modal current peaks in magnitude, thereby maximizing the power that is coupled to the particular mode.

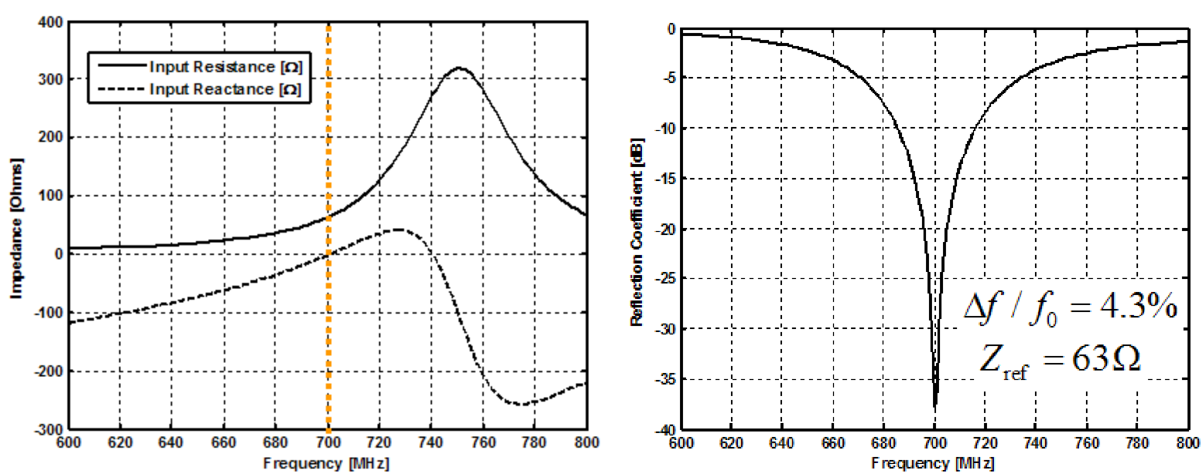

(a) (b)

Figure 4.4 – (a) resistance and reactance and (b) input reflection coefficient for the single-band antenna

We then apply the same algorithm, only now including an additional frequency at 900 MHz in which to enforce resonance and Q-minimization. The resulting antenna shape is shown in Figure 4.5(a) with the matrix trace shown in Figure 4.5(b). Two distinct peaks in the trace magnitude are shown, each representing a separate antenna resonance, one at 700 MHz, the other at 900 MHz.

The feeding location selection is, as always, dependent on the characteristic mode currents with the selected feed location shown in Figure 4.6(a) and the dominant modal currents at 700 and 900 MHz shown in Figure 4.6(b) and 4.6(c) respectively. As chance would have it, the feeding location that is selected is strongly associated with both resonances and thus a multi-band antenna is obtained from single excitation port. New to our discussion is the notion that the single feed location excites entirely different modes at each frequency of interest. Consequently, we have a multi-mode antenna structure. The resulting antenna input impedance is shown in Figure 4.7. Note the clearly shown resonances at 700 and 900 MHz. The input reflection coefficients for both bands are shown in Figure 4.8. Both curves are generated from the same port with different reference impedances used in both cases (as shown). However, the ideal reference impedance is different for both resonances: 40Ω for 700 MHz and 10Ω for 900 MHz. This makes simultaneous operation of both bands a potentially difficult task since one would need to switch reference impedances depending on which band is in use. Given that the reference impedances are, at the very least, close to 50Ω, it is conceivable that a matching network could be constructed out of lumped components (e.g. surface mount capacitors and inductors) that would match both 10Ω and 40Ω at different frequencies to a 50Ω reference impedance. More discussion on this concept of impedance matching can be found in Section 4.3.2.

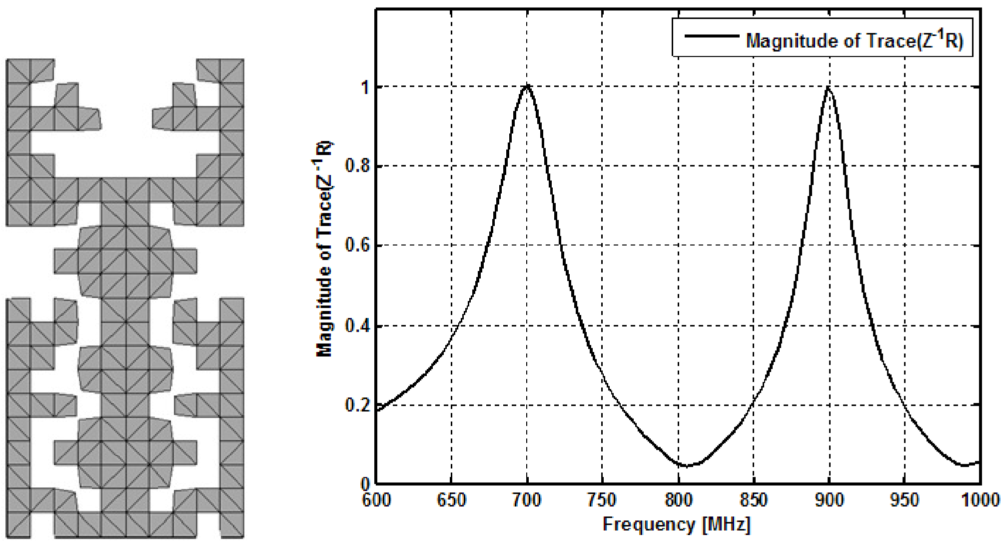

(a) (b)

Figure 4.5 – Example dual-band meshed structure shown in (a) and the magnitude of the CM matrix trace shown in (b). Note that this structure is not within the electrically small antenna regime at either of its resonant frequencies and yet can be treated as a single-mode antenna in each band as shown in (b)

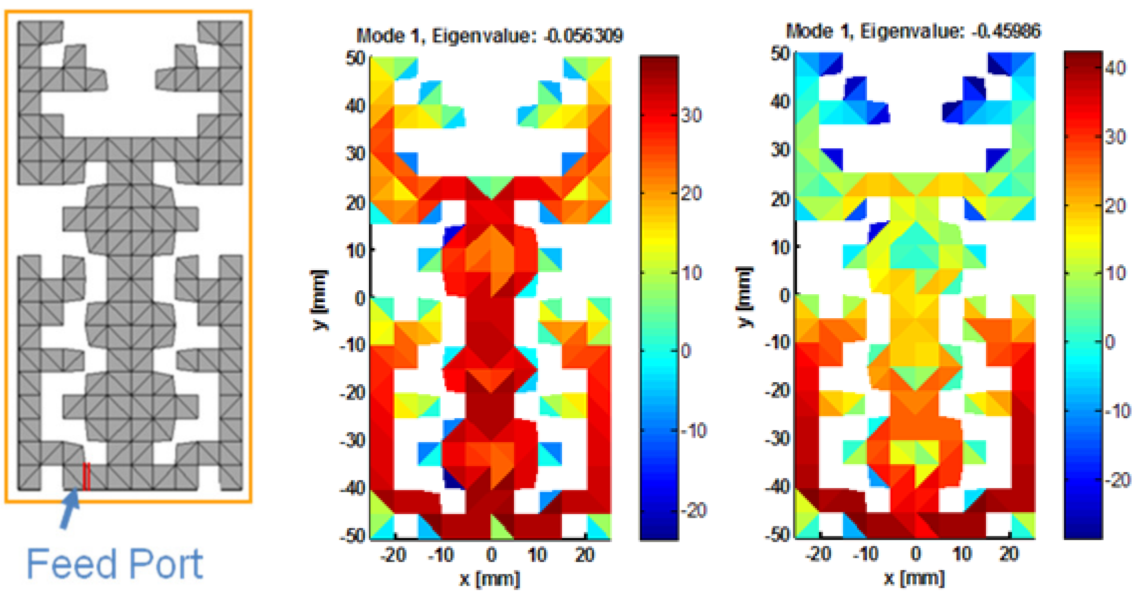

(a) (b) (c)

Figure 4.6 – Example single-band structure with feed port shown in (a) and modal currents shown in (b) at 700 MHz and (c) at 900 MHz. The ideal feed location is any location where the modal current peaks in magnitude but peaking for both modes which resonate at different frequencies

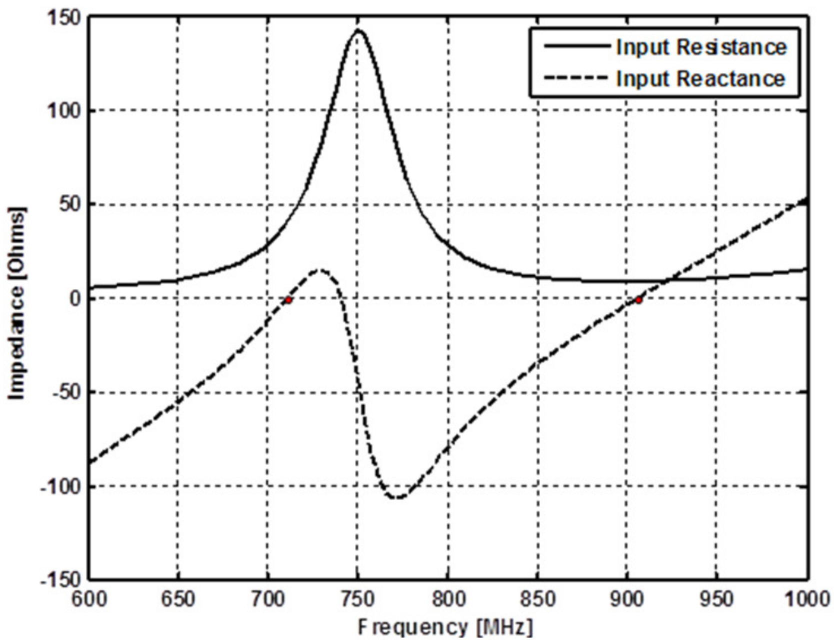

Figure 4.7 – Simulated input resistance and reactance of the dual-band structure clearly showing the dual-band behaviour at 700 and 900 MHz

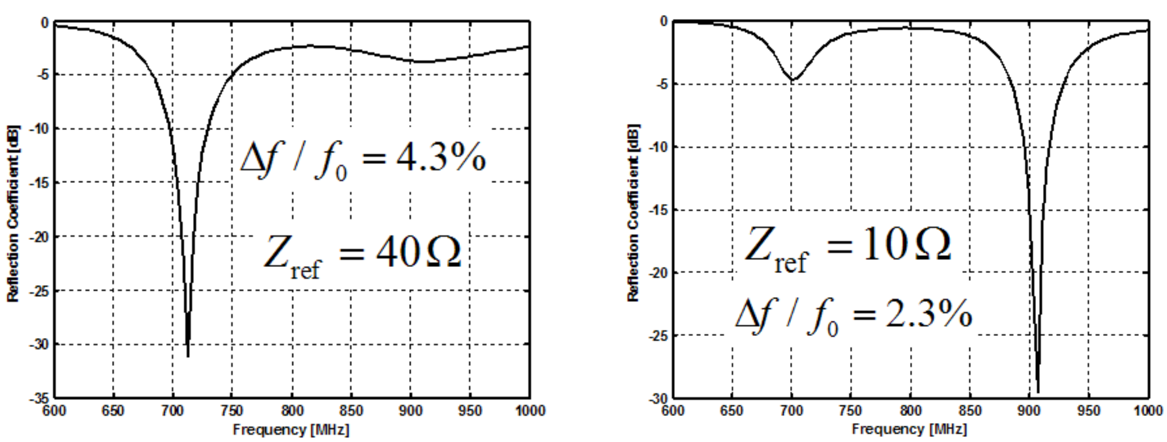

(a) (b)

Figure 4.8 – Input reflection coefficient for (a) the 700 MHz band (with Z_o = 40Ω) and for (b) the 900 MHz band (with Z_o = 10Ω). Note that since the input resistance is not explicitly constrained during shape-optimization, the resulting multi-band structure may have different ideal reference impedances at each of the antenna's operating bands

4.2.3 – Extending the Multi-band Synthesis Concept to Antennas with Many Operating Bands

The veracity of the feedless optimization scheme is in the ability to arbitrarily specify the number of required bands. Let us now consider a tri-band design (700, 900 and 1100 MHz), with the shape-synthesized antenna shown in Figure 4.9. The feed locations were determined for each band in the same manner as in the previous examples. It should be noted that a much denser mesh was required to successfully obtain a tri-band design. This is to be expected given that the more stringent the design requirements, the more complex the physical layout would necessarily be. The resulting input reflection coefficients are shown in Figure 4.10a-c for the selected set of references impedances $Z_o = \left[10\Omega \quad 15\Omega \quad 10\Omega\right]$ for the three ports. Figure 4.11 shows the coupling S-parameters, with less than -15dB of coupling between ports at all frequencies. The mutual coupling is fairly low, but is especially notable considering that the structure is contiguous. The ability to have port isolation from a contiguous structure is the fact that each port excites a single mode rather than a multitude of modes – the consequence of the latter is increased mutual coupling.

As a last example, as quad-band shape-synthesized design is shown in Figure 4.12(a) with the magnitude of the CM matrix trace in Figure 4.12(b) showing four distinct resonances at 700, 900, 1100 and 1300 MHz. It is conceivable that any reasonable number of bands can be synthesized in this manner, provided the structure is electrically small enough to preclude the presence of multiple simultaneous dominant modes. Such a multi-mode scenario will be discussed in Section 4.2.4.

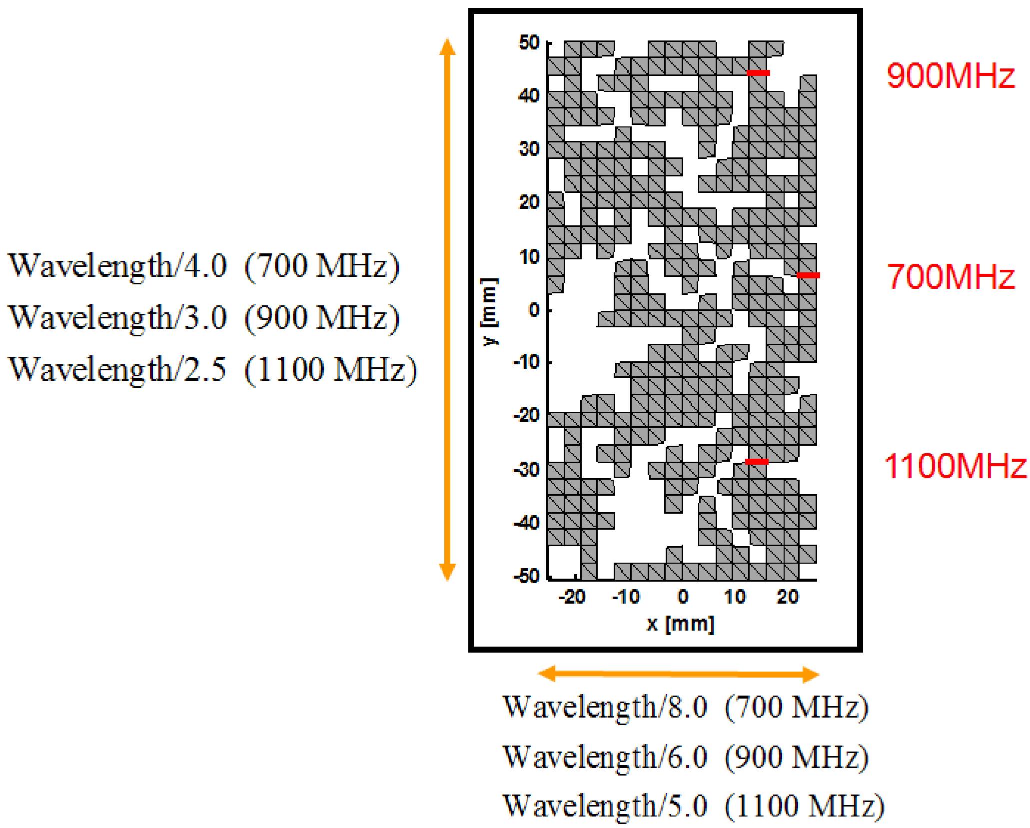

Figure 4.9 – Example tri-band structure with three distinct feed locations identified for each of the bands

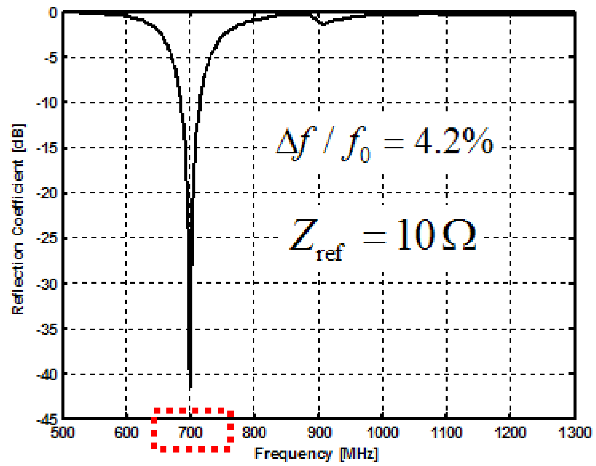

(a)

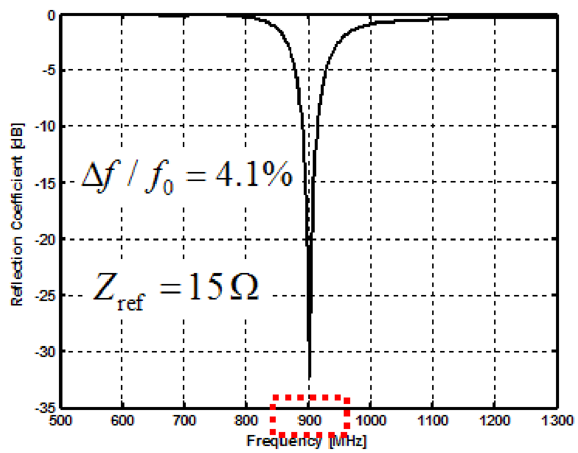

(b)

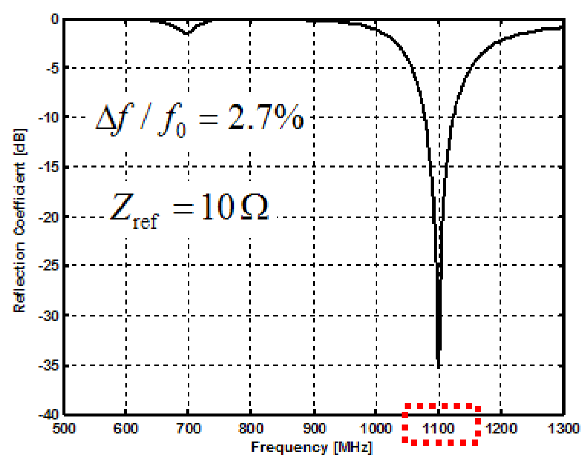

(c)

Figure 4.10 – Simulated reflection coefficient for tri-band structure at (a) 700 MHz, (b) 900 MHz and (c) 1.1 GHz

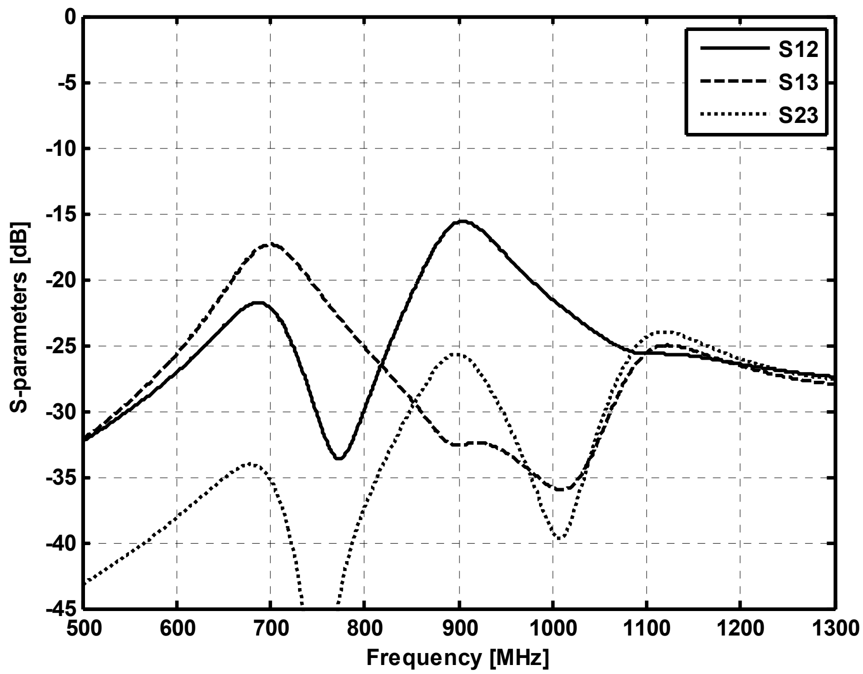

Figure 4.11 – Simulated S-parameters, coupling terms for three-port, tri-band antenna design example

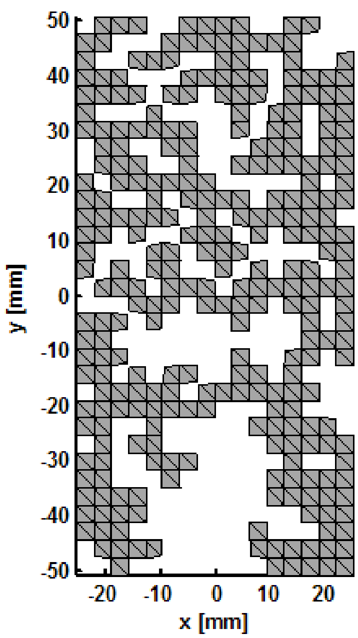

(a)

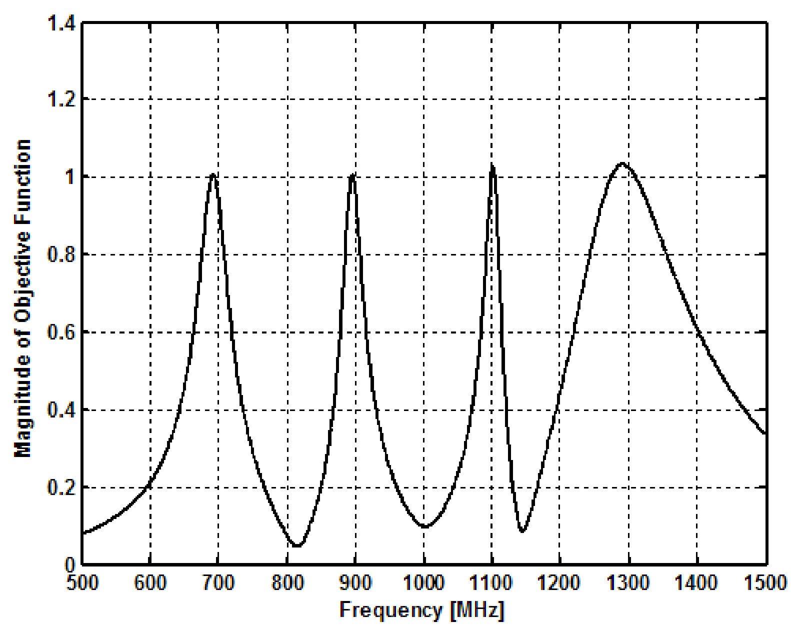

(b)

Figure 4.12 – Example optimized antenna structure shown in (a) exhibiting closely spaced quad-band behaviour as shown in (b) through the magnitude of the CM matrix trace

4.2.4 – A Multi-Mode Problem

Because our intention is to utilize the entire physical structure (rectangular plates) in our previous multi-band synthesis examples, we find no presence of multiple modes for any given band or the presence of inaccessible modes at our bands of interest. In situations where electrically significant regions are inaccessible via excitation[9], undesirable to excite or simply regions we wish to remain unchanged (not shape synthesized), the current form of the synthesis objective functions leads to undesirable consequences. To emphasize this point, consider Figure 4.13, where we show two views of a mock-up of a mobile phone with dimensions $\left(L_x, L_y, L_z\right) = \left(60mm, 120mm, 15mm\right)$ and $W = 30mm$. We consider the red regions as a partial ground plane, which we will denote a "do not touch" region both from the synthesis and excitation perspectives. The green meshed region is denoted the antenna portion of the structure and is the region we wish to shape synthesize. This is reminiscent of the work performed in Section 3.5.4 involving electrically small antennas. The issue, however, in this problem is the fact that this structure is no longer electrically small in the desirable operating bands of mobiles phones. Consider Figure 4.14 where we plot the CM matrix trace magnitude and phase for this particular structure. A resonance (see Section 3.3.2) is predicted at 685 MHz while a second resonance appears to be predicted around 2.5 GHz – both cases predicted by the fact that the trace has zero phase at these frequencies. Note that the second modal resonance does not show a distinct peak in the CM matrix trace magnitude, which is contrary to the results shown in Chapter 3. The matrix trace no longer represents an accurate assessment of the potential properties of this radiating system because the structure is no longer single-mode for the frequencies of interest.

Figure 4.15 shows the dominant modal currents of this structure at 685 MHz, the CM eigenvalue being $\lambda_1 \approx -2.25$. The next two closest modes have eigenvalues $\lambda_2 \approx -14.25$ and $\lambda_3 \approx +29.49$. These additional modes have eigenvalues who magnitudes are sufficiently large that the CM matrix trace being close to zero at 685 MHz in 4.14 is no longer an indication that any individual CM is at resonance. The first actual characteristic mode resonance, identified by observing the individual eigenvalues rather than CM matrix trace, occurs around 900 MHz, which is quite distant in frequency from 685 MHz. The

[9] Note that by 'inaccessible by excitation' we mean regions where the placement of a port, for example, would not be allowed due to difficulty in accessing the area, or the presence of sensitive components.

dominant modal current at 900 MHz is shown in Figure 4.16, with a spatial distribution and magnitude nearly identical to that of the mode at 685 MHz, except that at 685 MHz the current has greater net stored energy associated with it because λ_1 is not zero. There is also the additional issue of excitation of the dominant mode. The modal current distributions in Figures 4.15 and 4.16 clearly show that this mode is best accessible through direct excitation of the ground plane, which could either be difficult or undesirable for other reasons. Another resonant characteristic mode around 2150 MHz is observed for the same structure, with the dominant modal current shown in Figure 4.17; note the high current density present on what we called the “antenna” portion of the structure in the first paragraph of this section. Yet the matrix trace again in Figure 4.14 gives no indication of this second resonant mode being present on the structure. This is because the first mode’s eigenvalue is small enough in magnitude to hide the presence of a new, distinct low-magnitude eigenvalue mode in the matrix trace. There are also numerous additional modes with small eigenvalues that further muddle the presence of a new resonant mode. In this case, the predicted resonance is not shifted (as was the case for 685 MHz rather than 900 MHz) but rather not predicted at all. Clearly, an alternative approach must be taken if a feedless synthesis approach is to be used involving the matrix trace. In the next section we propose such a solution. Before proceeding to Section 4.2.5, it will be worthwhile to remind the reader why we shall not, given the problem discussed immediately above, use some combination of the eigenvalues of several modes. One reason is computational efficiency, as already noted in Section 3.4.9. More importantly is the fact that the analyses of Section 3.2 and 3.3 assuming a single-mode antenna would no longer apply, and so the CM eigenvalues would not be providing information on a (as yet feedless) potential antenna.

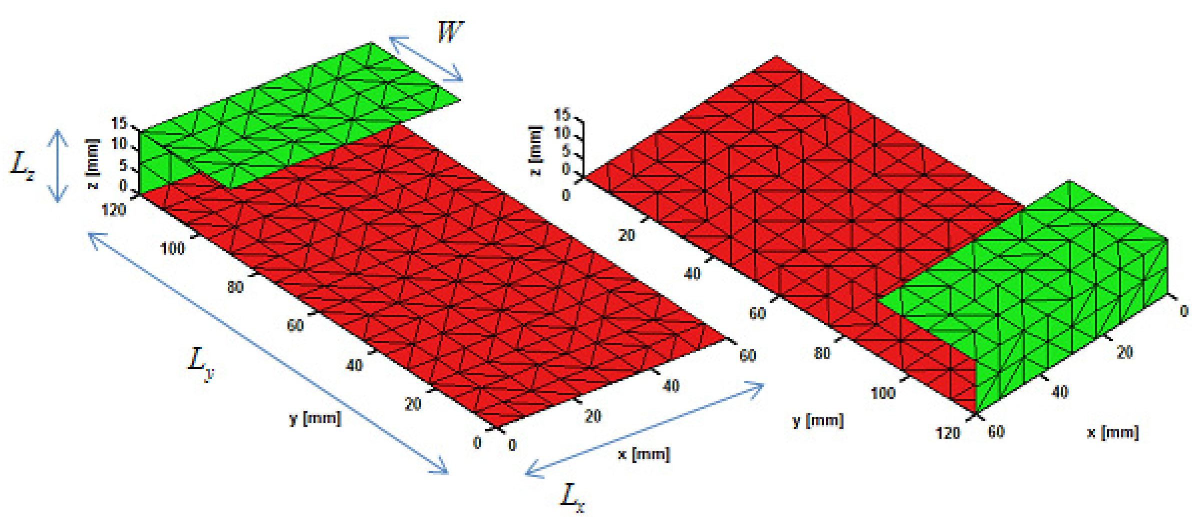

Figure 4.13 – Example mobile phone mock-up viewed from two different angles

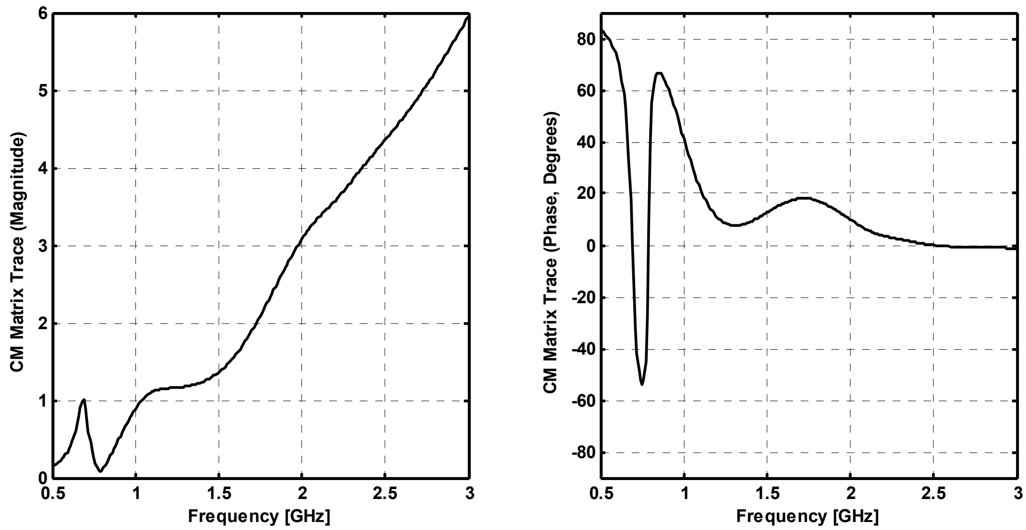

Figure 4.14 – The magnitude and phase of the trace of the CM matrix for the mobile phone mock-up

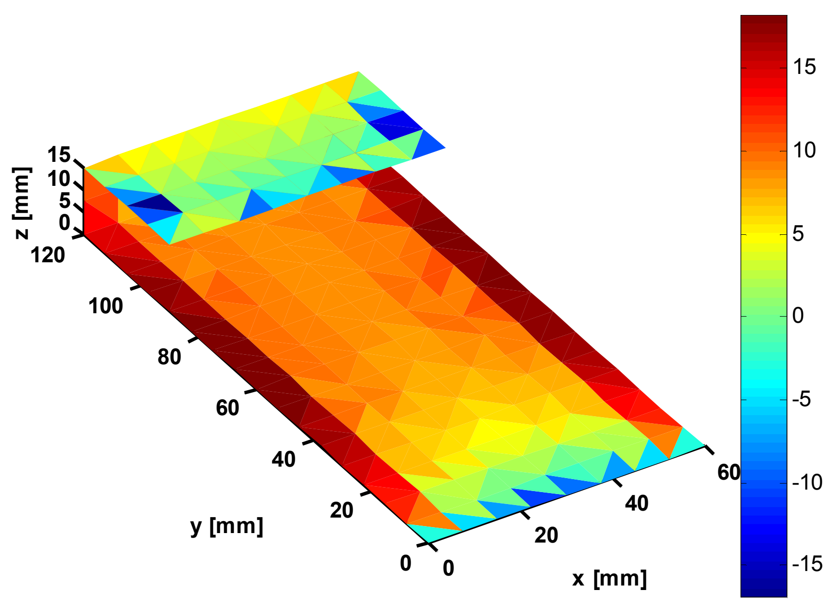

Figure 4.15 – Dominant modal currents of the mobile phone example at 685 MHz, $\lambda_1 \approx -2.25$

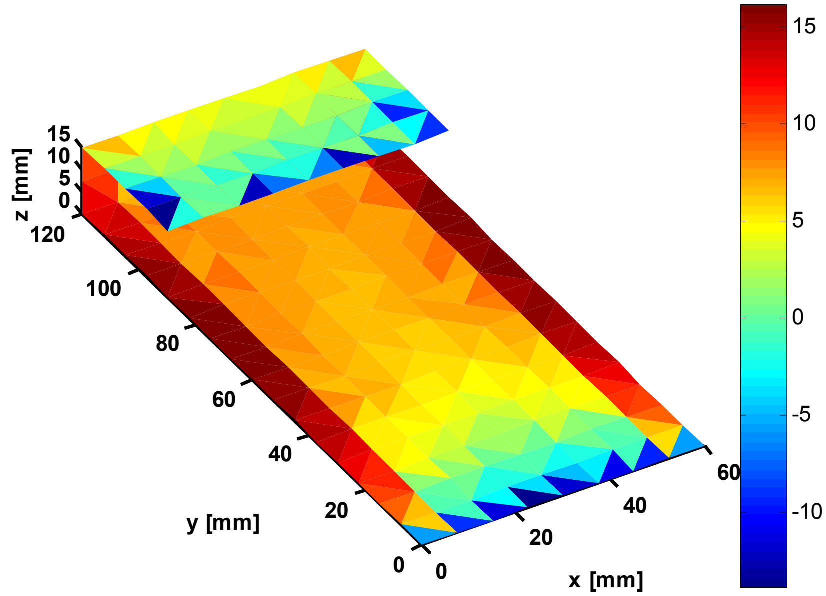

Figure 4.16 – Dominant (and resonant) modal currents of the mobile phone example at 900 MHz, $\lambda_1 \approx 0$

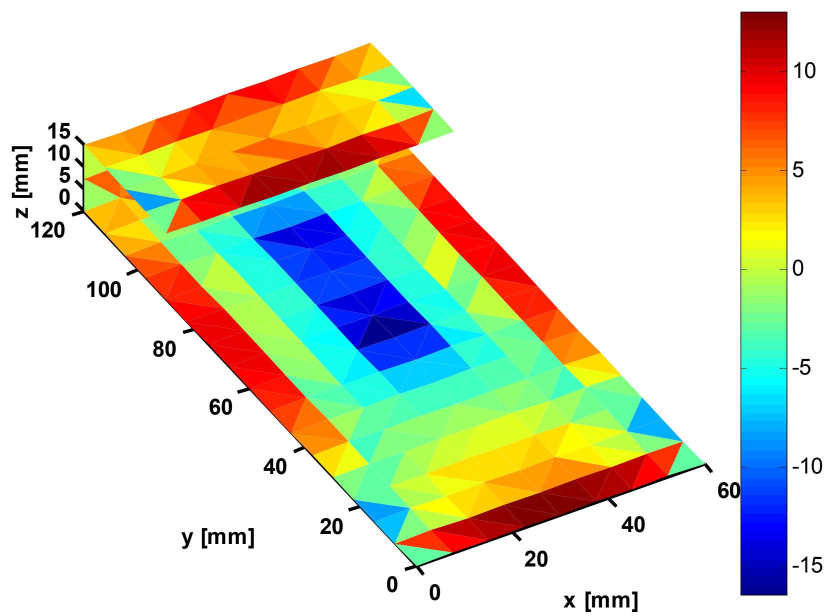

Figure 4.17 – Dominant (and resonant) modal currents of the mobile phone example at 2150 MHz, $\lambda_2 \approx 0$

4.3 – Sub-Structure Characteristic Modes

4.3.1 – Introducing Sub-Structure Characteristic Modes

The structures in Sections 4.2.2 and 4.2.3 were illustrative examples used to emphasize the details of the optimization scheme. In order to bring some specific applications into the mix, let us now consider some antenna design examples that are realistic in their implementation and performance for, say, mobile phone antennas. Mobile phones consist of RF circuitry, batteries, displays and the like. These portions of the cell phone are usually fixed objects that cannot be changed. In any mobile phone antenna design process, these components remain unchanged while the antenna is synthesized. Most importantly, these regions do not have any excitation directly applied to them – they only experience excitation in a secondary fashion (in other words, they act to scatter any fields from the antenna proper). The perspective one can use for such a scenario builds off of the work in [4].

Reference [4], albeit not for the purposes of antenna shape synthesis or characteristic mode computation, viewed physical scatterers that are not directly excited as being part of the environment. As such, they can be "worked" into the Green's function numerically – hence the name used in [4] – numerical Green's functions. The Green's function we typically use to describe a scatterer and thus obtain the impedance matrix is that of freespace. An impedance matrix obtained in this fashion allows one to excite the structure described by the impedance matrix in any arbitrary manner and obtain the resulting currents and scattered field. Alternatively, one can restrict the excitation (the incident field) to isolated scatterers or specified regions and numerically incorporate the effects of all other scatterers into the Z-matrix, thereby using what is effectively a new Green's function.

Let us begin our investigation by considering the generic example of two arbitrary scatterers A and B as shown in Figure 4.18. The impedance matrix for such a structure can be partitioned into a block matrix with four identifiable parts, as shown in expression (4.1).

$$\begin{bmatrix} [E_A] \\ [E_B] \end{bmatrix} = \begin{bmatrix} [Z_{AA}] & [Z_{AB}] \\ [Z_{BA}] & [Z_{BB}] \end{bmatrix} \begin{bmatrix} [J_A] \\ [J_B] \end{bmatrix} \qquad (3.1)$$

where subscript A refers to fields, currents and impedance terms associated with scatterer A, with similar arguments for subscript B. The terms with *AB* and *BA* are impedance matrices associated with the coupling between scatterers A and B. It should be noted that $[Z_{AA}]$ and $[Z_{BB}]$ are the impedance matrices of scatterers A and B in isolation, respectively.

Using the ideas provided in [4] as a starting point, rather assume that the incident field is restricted to scatterer A alone with no incident field applied to scatterer B, as in done in [5], albeit once again without any characteristic mode intentions. This scenario prevents the incident field from being caused by external excitation from sources separate from the scatterers. Rather, it restricts the excitation to a feed concentrated on scatterer A, although distributed excitations (i.e. over the entire surface of A) are also permitted. Mathematically, this implies that $[E_B]=0$ in expression (4.1).

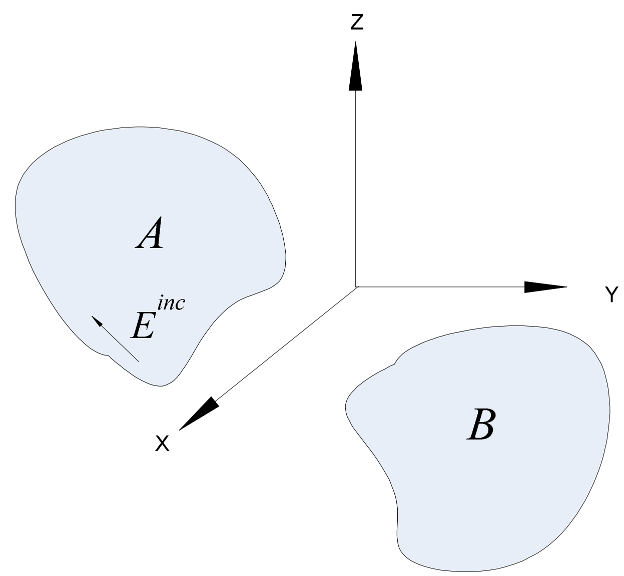

Figure 4.18 – Example scattering system where two scatterers are identified as scatterer A and scatterer B. Only scatterer A is assumed to have an incident field where scatterer B is destined to be numerically included in the Green's function of the overall electromagnetic system

Under the condition of $\left[E_B\right]=0$, the matrix equation relating the incident field to the surface currents is written simplified into the two matrix equations

$$\begin{aligned} \left[E_A\right] &= \left[Z_{AA}\right]\left[J_A\right]+\left[Z_{AB}\right]\left[J_B\right] \\ 0 &= \left[Z_{BA}\right]\left[J_A\right]+\left[Z_{BB}\right]\left[J_B\right] \end{aligned} \tag{3.2}$$

The latter equation can be re-written as $\left[J_B\right]=-\left[Z_{BB}\right]^{-1}\left[Z_{BA}\right]\left[J_A\right]$, which when substituted into the first expression of (4.7) gives us

$$\left[E_A\right]=\left\{\left[Z_{AA}\right]-\left[Z_{AB}\right]\left[Z_{BB}\right]^{-1}\left[Z_{BA}\right]\right\}\left[J_A\right] \tag{3.3}$$

Expression (4.3) relates the current on scatterer A to the incident fields on scatterer A, in the presence of scatterer B, assuming scatterer B has no incident field. Thus the matrix

$$\left[Z\right]_{sub}=\left[Z_{AA}\right]-\left[Z_{AB}\right]\left[Z_{BB}\right]^{-1}\left[Z_{BA}\right] \tag{3.4}$$

can be viewed as the impedance matrix of sub-structure A, in the presence of B. We shall denote $\left[Z\right]_{sub}$ the sub-structure impedance matrix.

Assume now that we wish to shape-synthesize scatterer A in the presence of scatterer B, with scatterer B remaining unchanged throughout the shape-synthesis process. Scatterer B is treated similar to the “do not touch” regions from Section 3.5.3, with the additional condition of no incident field on the “do not touch” region. If a DMM / GA optimization approach were applied to the sub-structure impedance matrix shown in (4.4), a great deal of computational advantage can be had by allowing the scatterer B to remain unshaped by the optimization process. In particular, if scatterer B does indeed remain as a “do not touch” region and a region where the incident field is zero, the matrix inverse $\left[Z_{BB}\right]^{-1}$ in (4.4) need only be computed once before the optimization begins and can be reused through the optimization process. We certainly have computational savings, but can this technique be effectively applied to our CM-based objective functions for antenna shape synthesis?

To answer this question, let us consider the matrix $[Z]_{sub}$ from expression (4.4) in the conventional CM eigenvalue problem, which now becomes

$$[Z]_{sub}[J_n]=(1+j\lambda_n)[R]_{sub}[J_n] \tag{3.5}$$

If we denote $[C]=[Z_{AB}][Z_{BB}]^{-1}[Z_{BA}]$, this can be re-written as

$$\{[Z_{AA}]-[C]\}[J_n]=(1+j\lambda_n)\{[R_{AA}]-\mathrm{Re}[C]\}[J_n] \tag{3.6}$$

The modal currents $[J_n]$ and the eigenvalue λ_n are not the conventional CMs of either scatterer A, B or their combination. They are the eigenmodes for the special case of arbitrary excitation of A in the presence of B. Expression (4.6) can be alternatively written as

$$\{[X_{AA}]-\mathrm{Im}[C]\}[J_n]=\lambda_n\{[R_{AA}]-\mathrm{Re}[C]\}[J_n] \tag{3.7}$$

As the contribution of scatterer B diminishes either through large separation distances between A and B (making coupling terms small) or diminishing size of scatterer B (thereby making the entries of $[C]$ vanishingly small) the traditional CM eigenvalue problem for an isolated scatterer A results. Taking the inner product of expression (4.7) with respect to $[J_n]^*$, we obtain a meaningful ratio representing the eigenvalue

$$\lambda_n=\frac{[J_n]^*[X_{AA}][J_n]-[J_n]^*\mathrm{Im}[C][J_n]}{[J_n]^*[R_{AA}][J_n]-[J_n]^*\mathrm{Re}[C][J_n]} \tag{3.8}$$

We see that by expression (4.8) these new modes are very similar to the traditional CMs, only with an augmenting term (due to $\mathrm{Im}[C]$ and $\mathrm{Re}[C]$, or $[C]$ in general) that increases or decreases the radiated and reactive powers depending on the nature of the secondary scatterer B and the coupling between A and B. Ultimately, the modes represent the possible orthogonal radiating modes associated with the scatterer A in the presence of scatterer B if only scatterer A were excited. If one were to excite a resonant characteristic mode of the matrix $[Z]_{sub}$, this would still represent an overall resonant structure (no net stored energy in the system) despite only needing to excite scatterer A and not B. We will denote these modes as sub-structure characteristic modes.

If we have a shape-synthesis problem whereby a large portion of the meshed structure remains unchanged (which could be treated like a “do not touch” region from Section 3.5.3), the sub-structure characteristic modes and the numerical Green’s function described in this section will prove very useful as a computationally efficient optimization approach. However, while having a scatterer B inaccessible as far as *shaping* is concerned can easily be incorporated into the usual shape synthesis procedure (as done in Section 3.5.3), having a scatterer B inaccessible for *feed point location* requires use of the new sub-structure CMs just introduced.

The modal currents associated with these sub-structure characteristic modes are restricted to the scatterer A in our examples. That is to say, the currents that exist on scatterer B are already accounted for in the numerical Green’s function. However, the currents on scatterer B can still be determined by using the second of the expressions in (4.2) to obtain

$$[J_B] = -[Z_{BB}]^{-1}[Z_{BA}][J_A] \tag{3.9}$$

For the sake of clarity, let us denote the modal currents determined from expression (4.5) as $\left[J_{A,n}\right]$ to emphasize that the currents exist on scatterer A and the mode in question is mode ‘n’. The currents on scatterer B take the naming convention $\left[J_{B,n}\right]$, again to emphasize the currents exist on scatterer B and are associated with mode ‘n’. The aggregate of these currents forms the currents on the complete structure, which we shall name

$$[J_n]_{total,sub} = \begin{bmatrix} J_{A,n} \\ J_{B,n} \end{bmatrix} \tag{3.10}$$

If we repeat what we did to obtain Figure 4.14, only including the trace magnitude and phase of the sub-structure CM matrix, we obtain the plot shown in Figure 4.19. A resonant characteristic mode is predicted at 695 MHz since the phase of the CM matrix trace is zero at that frequency. Recall that these results assume that excitation is restricted to the antenna portion (or scatterer A in our general derivations thus far in this section). The aggregate of the sub-structure modal currents (expression 4.10) at 695 MHz is shown in Figure 4.20. Note the distinct difference between these sub-structure currents (Figure 4.20) and the classical characteristic mode currents of Figure 4.15 at nearly the same frequency. They are necessarily different due to the different impedance operator being used in the eigenanalysis problem. However, there is a reassuring sight in that the peak modal current appears at the junction between the antenna portion (green, synthesizable region) and the ground plane portion (red, "do not touch" region). In other words, the peak in modal current is no longer concentrated on the ground plane, but rather at the junction between the "radiator" and "ground plane" portions. This strongly suggests the ability to discern both the resonance and the ideal feed location using the sub-structure characteristic modes – an impossible feat using the classical characteristic modes. It should be noted that the next mode (mode 2) in the CM sub-structure spectrum has a magnitude of approximately 100, which supports our assertion of being able to filter the presence in inaccessible modes. Interestingly, the CM sub-structure model is a superposition of but a few modes of the full structure.

We additionally consider the modes at 2150 MHz and note another resonant sub-structure characteristic mode as shown in Figure 4.21. Again, the resonance is accurately predicted via the matrix trace (zero phase in Figure 4.19) and we find intense modal currents peaking along the antenna region of the structure, precisely as we would desire from our separation of the overall scatterer into sub-structures.

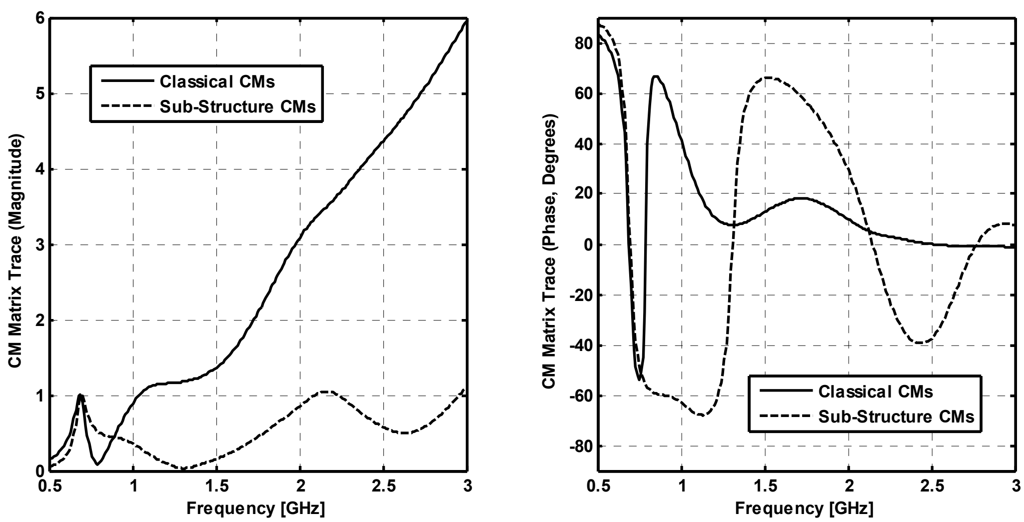

Figure 4.19 – The magnitude and phase of the trace of the CM matrix for the mobile phone mock-up showing the results for both the traditional characteristic modes and the sub-structure characteristic modes

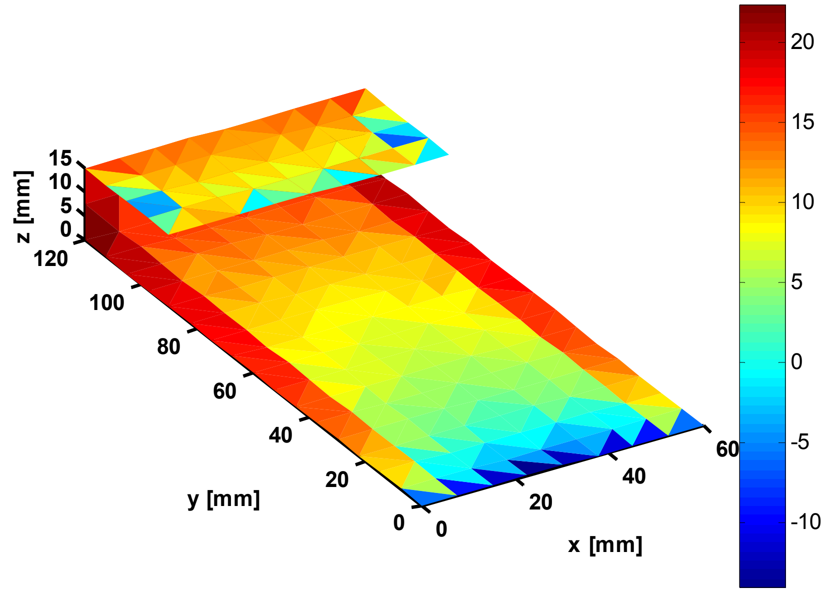

Figure 4.20 – Dominant modal currents of the mobile phone example at 695 MHz, $\lambda_{1,sub} \approx 0$

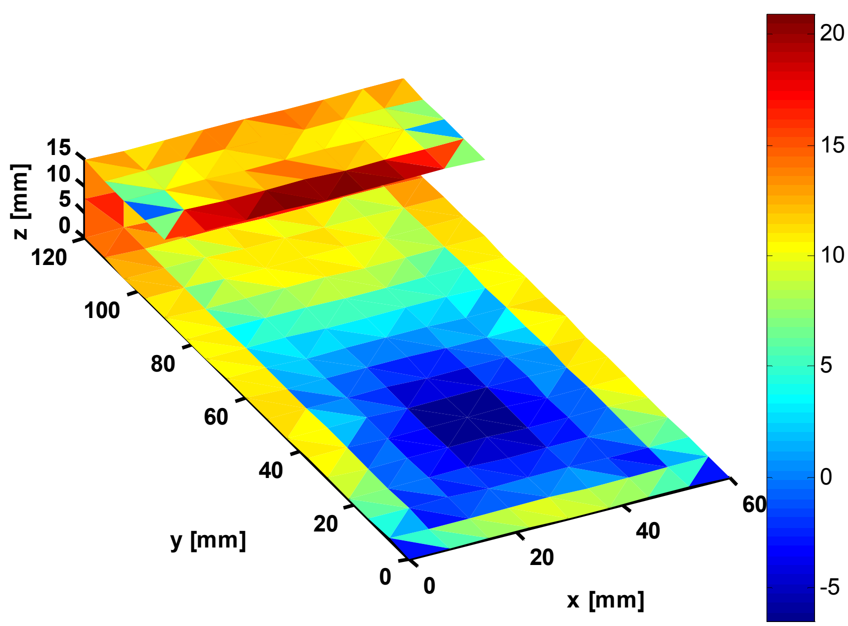

Figure 4.21 – Dominant modal currents of the mobile phone example at 2150 MHz, $\lambda_{2,sub} \approx 0$

4.3.2 – Mobile Handset Multi-band Antennas: Design and Experiment

Mobile phone antennas are a canonical example of multi-band antenna designs [6] – [8]. In order to maintain coverage in a multitude of regions as well as having the ability to communicate with a whole host of carriers, mobile phone antennas must necessarily be multi-band structures. An example mock-up of a mobile phone was shown previously in Figure 4.13. The overall dimensions we will continue to use in this section are $(L_x, L_y, L_z) = (60mm, 120mm, 15mm)$ and $W = 30mm$, representing the typical dimensions of a mobile phone. The thickness (15mm) is somewhat larger than typical phones (though not by much) in order to compensate for the lack of dielectric materials in our moment method formulation that would otherwise reduce the antenna profile. We specify the green region as the synthesizable portions of the structure (the antenna) while the red region (effectively the partial ground plane of the handheld device) as the "do not touch" region. Note that the ground plane is substantially larger than the antenna region from both the surface area and the number of expansion functions perspective. In particular, the ground plane region has 256 triangles to describe its behaviour while the antenna portion has 96. Since we do not shape synthesize nor directly excite the ground plane, a great deal of computational savings are to be had for this particular optimization problem. Anytime the number of expansion functions in the region that is incorporated numerically into the Green's function is greater than the number of expansion functions that remain, the problem is handled in a computationally faster manner using the sub-structure approach. In order to get a sense of the wide range of frequencies and electrical sizes of the analyzed mobile phone mock-up being considered in this section, a summary table is given in Table 4.1.

Frequency [MHz]	λ wavelength, [mm]	L_x [wavelengths]	L_y [wavelengths]	L_z [wavelengths]	W [wavelengths]
700	428.6	0.1400	0.2800	0.0350	0.0700
900	333.3	0.1800	0.3600	0.0450	0.0900
1525	196.7	0.3050	0.6100	0.0763	0.1525
1900	157.9	0.3800	0.7600	0.0950	0.1900
2500	120.0	0.5000	1.0000	0.1250	0.2500

Table 4.1 – Summary of electrical sizes of mobile phone mock-up at the frequencies of interest

Three antenna designs were considered labeled designs A through C:

- Design A: A single-band design with a resonance at 700 MHz
- Design B: A dual-band design with a resonance at 700 and 1900 MHz
- Design C: A tri-band design with a resonance at 700, 1525 and 2500 MHz

The synthesis technique was followed in precisely the same manner as in Section 4.2, whereby the CM matrix trace is optimized to have zero phase as the desired resonant frequencies and the Q at each frequency minimized in a balanced manner, identical to the approach in Section 4.2. The only difference in this problem is the trace function is computed for the sub-structure impedance matrix (expression 4.4) rather than the entire structure's impedance matrix.

The three designs were fabricated (see Figure 4.22) and measured. In all three cases, a single obvious feed location was discovered after simulating (see Section 3.4.3). A set of close-up views of the feeding mechanism in Design C is shown in Figure 4.23. It is important to remember that this feed location is not selected a priori. Combining the computationally efficient feedless approach with the sub-structure technique yields further computational benefits beyond any traditional approach.

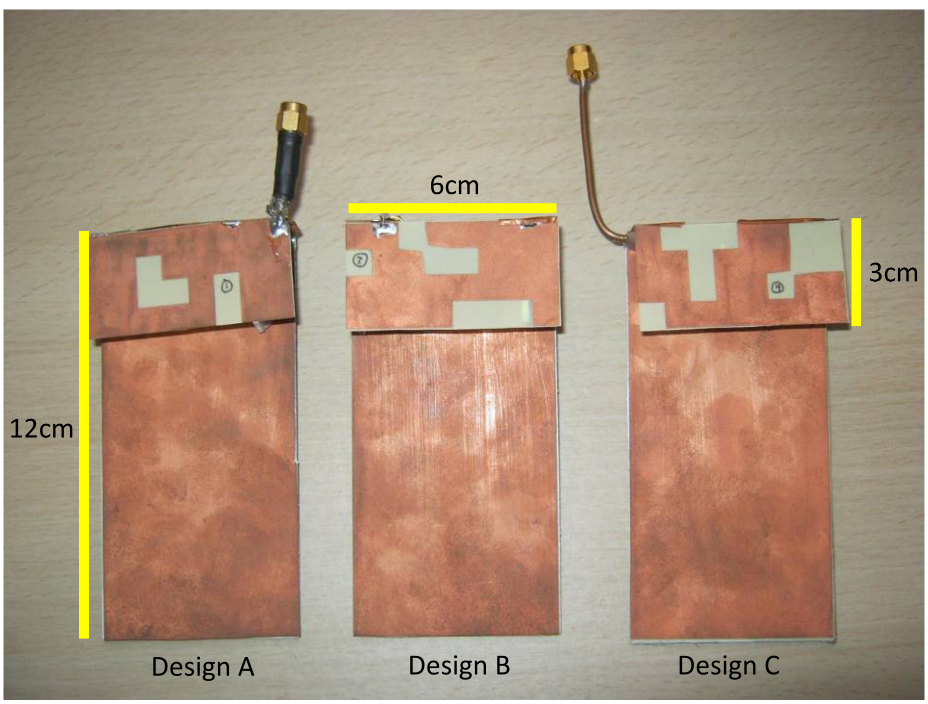

Figure 4.22 – Example multi-band designs A through C (listed left-right and top-bottom)

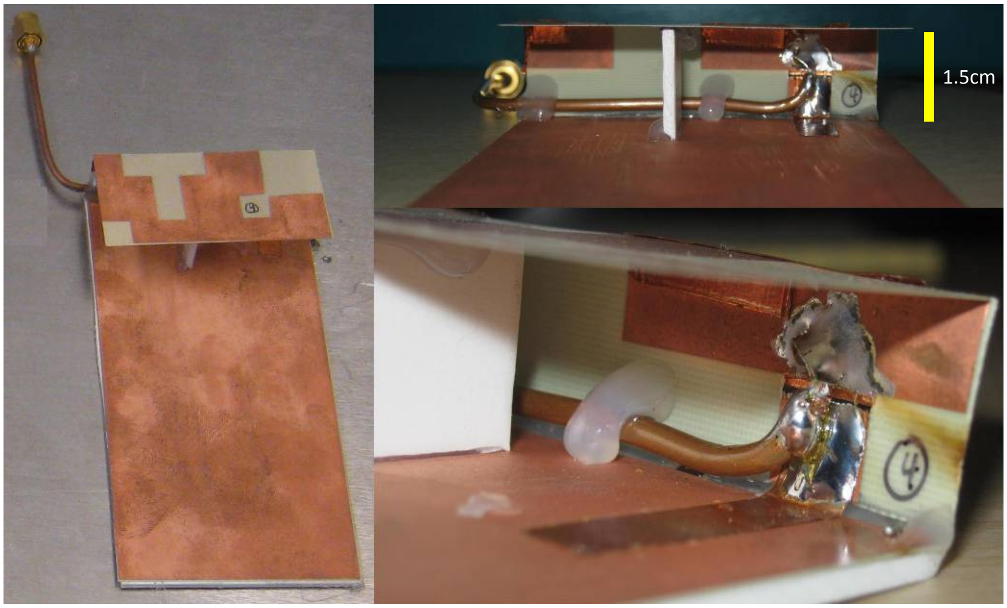

Figure 4.23 – A close-up collection of views of the feeding mechanism of Design C

The modes associated with the partial ground plane, which cannot be efficiently excited directly from a gap feed, are not present for the sub-structure modes. The presence of the ground plane is of course accounted for in the numerical Green's function. This advantage is further shown by plotting the magnitude of CM matrix trace (the function $\Psi(\omega)$ from Section 3.3.5) for the two cases

$$\Psi(\omega) = Trace\left\{[Z]^{-1}[R]\right\} \tag{3.11}$$

which is the CM matrix trace for the entire structure including the ground plane and additionally

$$\Psi_{sub}(\omega) = Trace\left\{[Z]_{sub}^{-1}[R]_{sub}\right\} \tag{3.12}$$

which is the CM matrix trace for the sub-structure. The latter expression has far greater utility as the modes associated with the ground plane are effectively filtered out, preventing the "ground plane modes" of the electrically sizable structure from muddling the presence of what we shall denote "antenna modes" of the complete structure. Figures 4.24 – 4.26 shows the plots of the magnitude and phase of expression (4.11) and (4.12) for the three optimized designs A through C respectively. The magnitude of the matrix trace of the sub-structure impedance matrix (expression 4.12) clearly peaks at each resonance frequency that was explicitly optimized for while the angle of the same function is zero as required. On the other hand, the resonance is not clearly shown through the matrix trace of the entire structure neither through the magnitude or phase of (4.11). This expression does not peak or exhibit zero phase at each resonance in a consistent fashion since the “ground plane modes” are also included in the trace, thereby making it impossible to distinguish the antenna modes from the ground plane modes. By restricting our view of the CMs from the entire structure to the antenna portion-only, we have effectively transformed multi-mode analysis to single-mode analysis. Ergo, the developments of single-mode antenna shape synthesis from Chapter 3 and Section 4.2 are applicable to the structure, with success found in the three shape synthesized design examples.

Note that Design A was optimized for single band operation, but an unintentional additional band appears at 2150 MHz. This would not be predictable from the matrix trace of the full structure as shown in Figure 4.24(a) and 4.24(b) but is very clearly shown through the zero phase of the matrix trace and the magnitude peak of the sub-structure matrix trace.

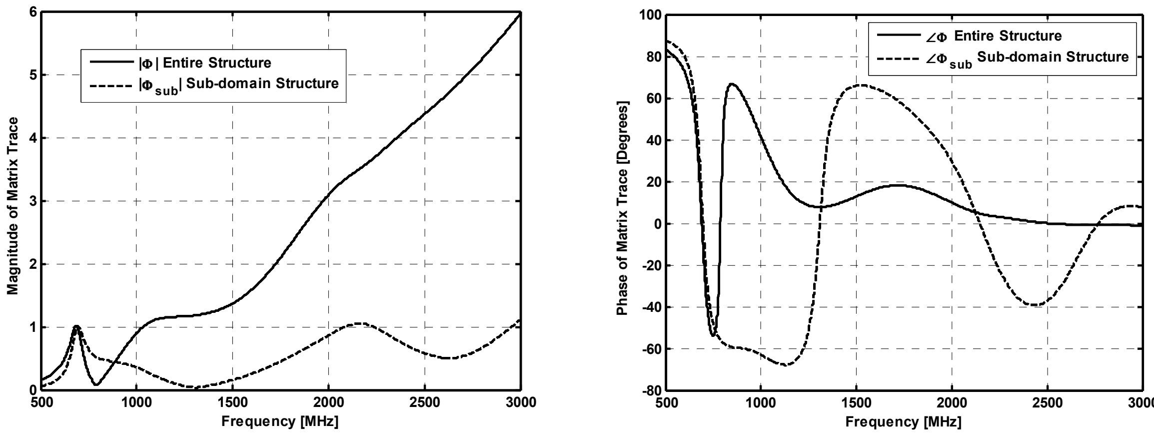

(a) (b)

Figure 4.24 – Sub-structure CM matrix trace (a) magnitude, (b) phase for Design A (single band, 700 MHz)

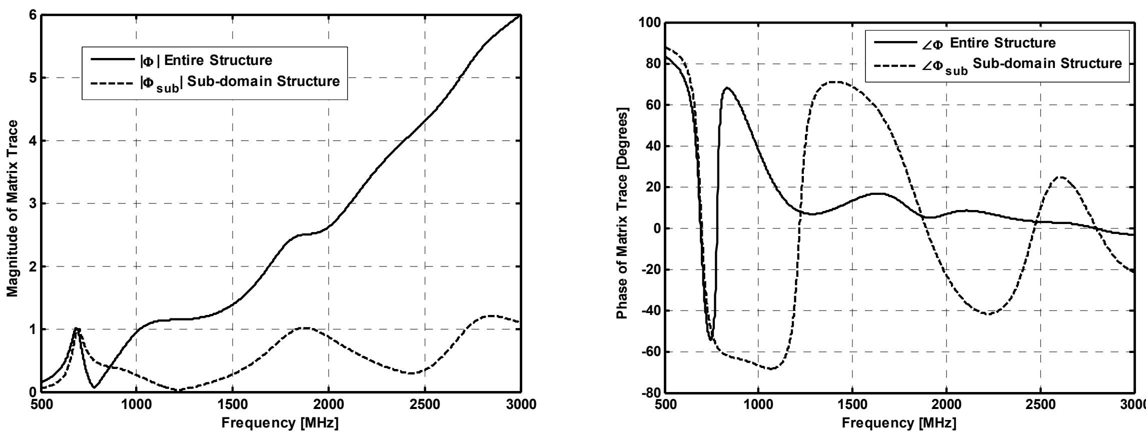

(a) (b)

Figure 4.25 – Sub-structure CM matrix trace (a) magnitude, (b) phase for Design B (dual band, 700 & 1900 MHz)

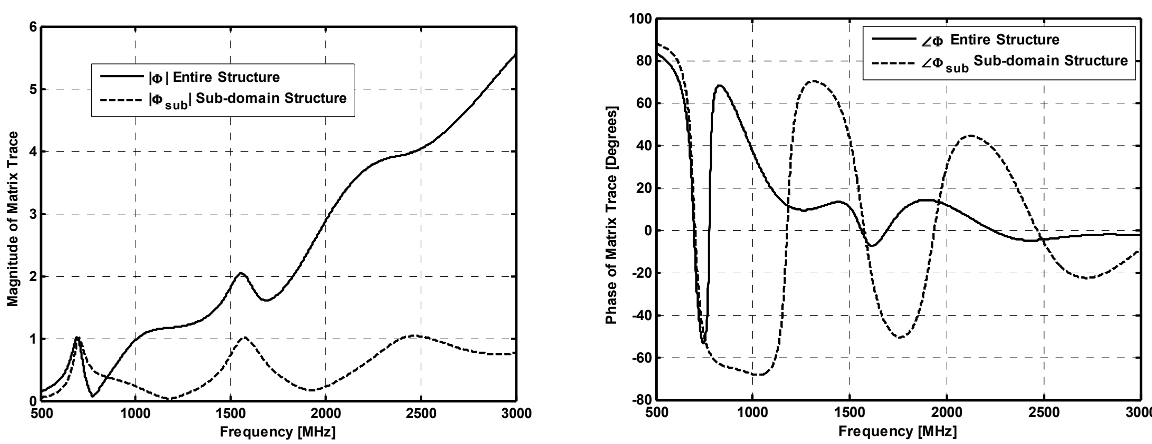

(a) (b)

Figure 4.26 – Sub-structure CM matrix trace (a) magnitude, (b) phase for Design C (700, 1525 & 2500 MHz)

Comparisons between the simulated and experimentally measured results of Designs A through C are shown in Figures 4.27 – 4.29. Reasonable agreement between simulation and experiment is found for all designs, though Design B shows the greatest discrepancies. A discussion on these discrepancies can be found in Appendix L.

An interesting set of results are found for the simulation and measurements of Design B in that the ideal reference impedance is unique for each band of interest (10Ω for 700 MHz, 50Ω for 1900 MHz). It should be stressed that both bands do indeed resonate simultaneously when excited by the port, but that the input current obviously differs in both bands since the ideal reference impedance is different for both bands. A filter/PA/transceiver combination that can match 10/50-Ohm reference impedance for the 700/1900 MHz bands would provide the solution for such a scenario and is, in theory[10], possible to implement [9] (especially using lumped surface mount components).

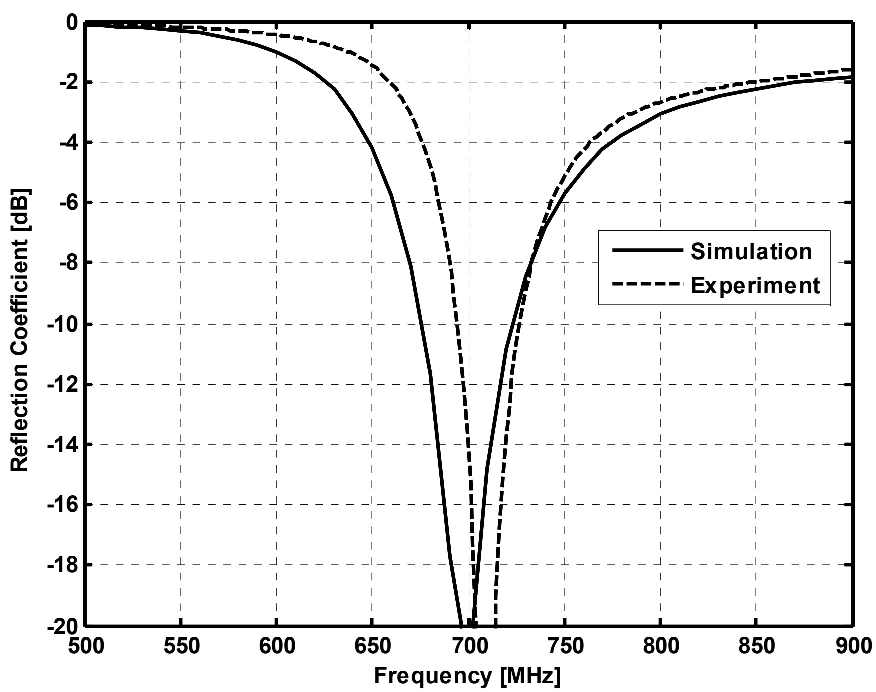

Figure 4.27 – Single-band design using 50Ω reference impedance (Design A)

[10] A simple transmission line with Z_o = 82Ω and length d = 86mm provides a better than 10dB RL match for 10Ω and 50Ω to a 50Ω transceiver at the frequencies 700 and 1900 MHz respectively. This is by no means optimized and is only a crude approach to matching the antenna to a 50-Ohm transceiver. Lumped elements or multi-stage transmission line matching networks would provide a more reasonable approach with a much smaller footprint.

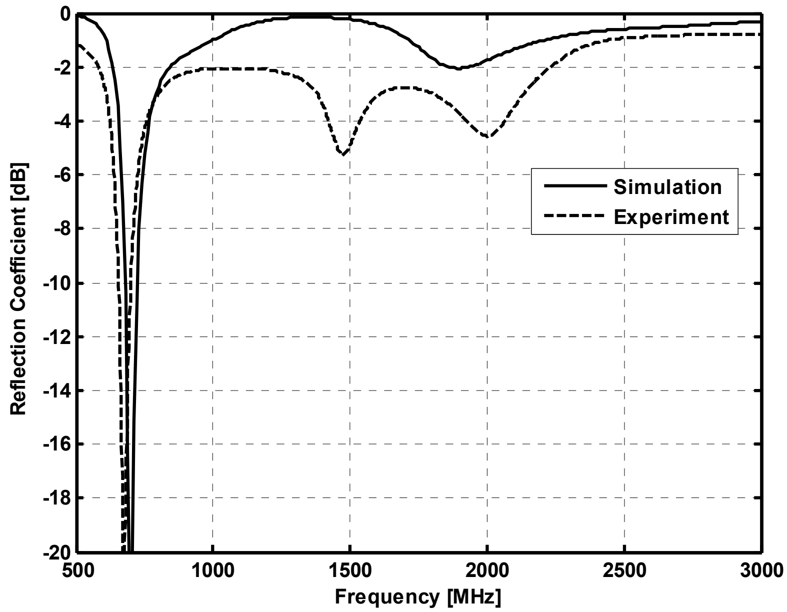

(a)

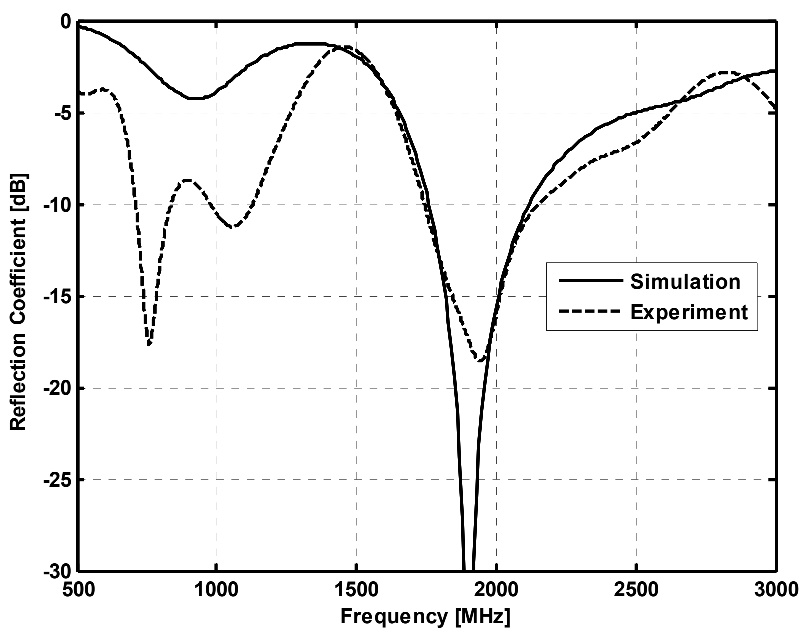

(b)

Figure 4.28 – Dual-band design using (a) 10Ω reference impedance showing a good match at 700 MHz and (b) 50Ω reference impedance showing a good match at 1900 MHz (Design B)

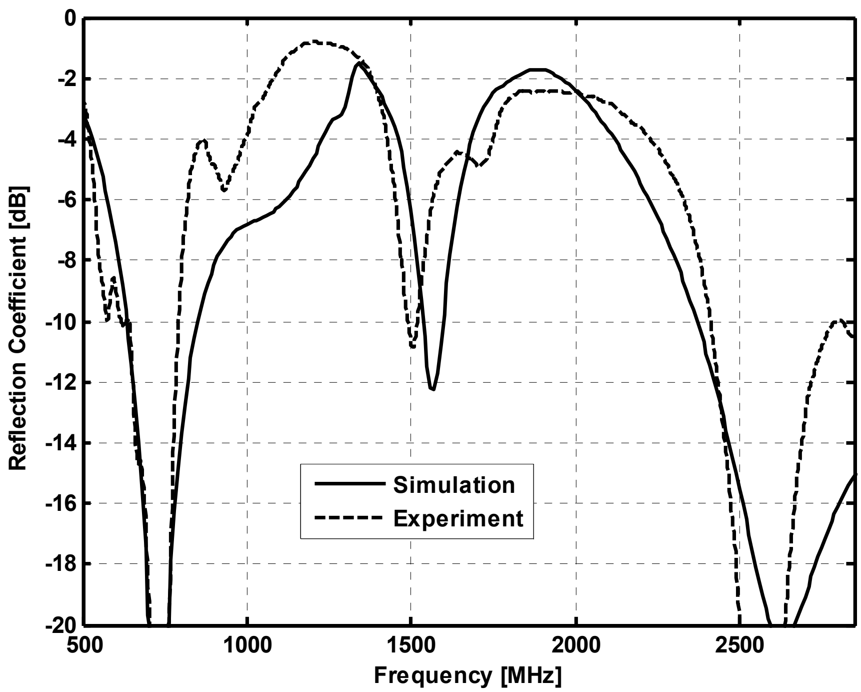

Figure 4.29 – Tri-band Design C using a single 50Ω reference impedance, well matched for the 700 and 2500 MHz bands with a reasonable match for the 1525 MHz band.

4.4 – Concluding Remarks

In this chapter we extended the concepts of Chapter 3 to be able to perform the single-mode antenna feedless shape-synthesis at multiple frequencies, thereby obtaining multi-band antenna structures. In Section 4.2, a collection of multi-band antennas were shape-synthesized in this manner, with single-, dual-, tri- and quad-band designs having been shown successfully synthesized from the same starting shape. In the concluding remarks of Section 4.2, we emphasized scenarios where the traditional characteristic modes and their corresponding CM matrix trace are incapable of providing the necessary information in situations where large regions of the object to be optimized either cannot be excited directly (via a port), or mustn't be shaped as part of the optimization, or perhaps both. The particular example was shown where the "antenna" portion of a mobile handheld phone is much smaller than the adjoining ground plane, making the ground plane very significant in terms of its characteristic mode dominance.

A new modal formulation was presented in Section 4.3, denoted the sub-structure characteristic modes, which determines a new set of characteristic modes of the radiating structure with the ability to enforce zero incident field on certain regions of the scattering system. This lead to a set of modes that could only be excited within scatterer regions where the incident field is non-zero, allowing us to work with a restricted but desirable set of sub-structure characteristic modes. Computational advantages are also present using this technique, not only because of the feedless nature of the optimization, but also through a reduction in computational redundancy that is obtained via the impedance operators associated with regions that are not shaped during the shape-synthesis procedure. Experimentally verified single-, dual- and tri-band designs were shown, with good agreement shown between simulation and measurement.

Chapter 4 References

[1] C. Puente, J. Romeu, R. Pous, X. Garcia, F. Benitez, "Fractal multiband antenna based on the Sierpinski gasket," *Electronics Letters*, Vol. 32, Issue 1, January 1996, pp. 1 – 2.

[2] P. Ciais, R. Staraj, G. Kossiavas, C. Luxey, "Compact internal multiband antenna for mobile phone and WLAN standards," *Electronics Letters*, Vol. 40, Issue 15, July 2004, pp. 920 – 921.

[3] W.-S. Lee, W.-G. Lim, J.-W. Yu, "Multiple band-notched planar monopole antenna for multiband wireless systems," *IEEE Microwave and Wireless Components Letters*, Vol. 16, Issue 9, September 2005, pp. 576 – 578.

[4] P. Parhami, Y. Rahmat-Samii, R. Mittra, "Technique for calculating the radiation and scattering characteristics of antennas mounted on a finite ground plane," *Proceedings of the IEE*, Vol. 124, Issue 11, November 1977, pp. 1009 – 1016.

[5] J.M. Johnson, Y. Rahmat-Samii, "Genetic algorithms and method of moments (GA/MOM) for the design of integrated antennas," *IEEE Transactions on Antennas and Propagation*, Vol. 47, Issue 10, October 1999, pp 1606 – 1614.

[6] K. Fujimoto, *Mobile Antenna Systems Handbook*, 3rd Edition, Artech House, Norwood, MA, 2008.

[7] S.-Y. Lin, "Multiband folder planar monopole antenna for mobile handset," *IEEE Transactions on Antennas and Propagation*, Vol. 52, Issue 7, July 2004, pp 1790 – 1794.

[8] A.K. Skrivervik, J.-F. Zurcher, O. Staub, J.R. Mosig, "PCS antenna design: the challenge of miniaturization," *IEEE Antennas and Propagation Magazine*, Vol. 43, Issue 4, August 2001, pp 12 – 27.

[9] Private Communication, I. Acimovic, Alcatel-Lucent Research and Innovation Centre, Ottawa, Canada, October 2011.

Chapter 5

Characteristic Modes and Periodic Structures

5.1 – Introduction

5.1.1 – Introductory Remarks

In this chapter we consider, for the first time in the literature, the characteristic mode analysis of infinite periodic structures.

The first problem one must contend with in such an endeavour is the interpretation of the CMs of a periodic structure, as one cannot obtain a single, finite impedance operator that describes the scattering of an arbitrary incident field from an infinite structure. This problem arises due to that troublesome word: infinite. Since the structure is infinite, one must restrict the nature of the excitation, and in the case of periodic structures this restriction takes the form of specifying plane wave excitation with a specific angle of incidence. We will show that this does not impact the usefulness of the characteristic modes, but it should be emphasized that these modes are not identical in form to the classical characteristic modes, though their function is mostly the same.

The second problem one encounters when analyzing a periodic structure from the characteristic mode perspective is the difficulty in obtaining the actual impedance matrix describing the infinite array.

Commercial codes are reluctant to provide such details, and when they do, provide a restrictive environment within which to work. In particular, the desire to apply genetic algorithms in conjunction with a proprietary commercial moment method code drove us to develop our own periodic structure moment method formulation. This method is described in Section 5.2, where we develop the so-called Infinite-from-Finite (IFF) method. Necessity is the mother of invention!

With this computational capability, we proceed in Section 5.3 to investigate the characteristic modes of periodic structures. We place particular emphasis on the properties and limitations of single-mode periodic structures to maintain the overall theme of the thesis, but a brief investigation of multi-mode periodic structures has been included as Appendix H. Much the same as in Chapters 3 and 4, we find a plethora of information that can be gleaned from eigenanalysis, all without the need to directly compute excitation currents. Additionally, computational simplicity is found through the use of the CM matrix trace in a similar vein as in the previous chapters. From these results, it is possible to define objective functions for the synthesis of periodic structures by optimizing their transmission and reflection coefficients to take specific, desired values.

In Section 5.4, we apply these objective functions in the shape-synthesis of reflectarray elements. A new synthesis technique is developed that uses the CM objective functions to design high aperture efficiency reflectarray structures of shaped elements. By maximizing the physical similarity between adjacent elements in the reflectarray the errors due to the quasi-periodic implementation of elements whose properties are determined in an infinite periodic environment is reduced. The synthesis technique is novel in its own right and can be viewed from a non-CM perspective. Additionally, the use of CM-derived objective functions reduces the computational complexity and reduces ambiguity in simulating the scattered near fields of periodic structures and attempting to reference reflection and transmission phases onto the surface of the periodic structure. Ample experimental results confirm the claims of the synthesis technique, with significant efforts made to address issues of practicality in fabrication as part of the element shape-synthesis technique.

Lastly, in Section 5.5 we introduce an entirely new reflectarray design concept whereby a reflectarray can be designed to maximize gain while simultaneously having its metal surface patterned in a manner visually representative of an optical image – the mosaic reflectarray. Experimental examples emphasize the practical and successful use of this new reflectarray design technique.

5.1.2 – An Interpretation of the CMs of Periodic Structures

The characteristic mode analyses of finite sized structures with both electrically small and intermediately sized dimensions were considered in Chapters 3 and 4, respectively. We now turn to the analysis of infinitely sized structures known as periodic structures. One immediately challenging aspect of such an endeavour is the need for an infinite number of expansion functions and thus an infinitely sized impedance matrix since the structure is of infinite extent. Two mutually exclusive approaches to analyze such structures present themselves: (1) restrict the nature of the excitation described by the impedance matrix and (2) analyze a very large but finite version of the periodic structure as an approximation. The majority of successful moment method based analysis tools that obtain the impedance matrix of a periodic structure restrict excitation to that of plane waves with a specified angle of incidence relative to the lattice of the periodic structure. This presents a very interesting conundrum for the characteristic modes: what significance do the CMs have when the nature of excitation is restricted and no longer arbitrary? The answer connects Chapter 5 with the work from Section 4.3 where we first defined the sub-structure characteristic modes. By restricting the nature of excitation, we limit our view of the characteristic modes to those only relevant to the partial range of excitation.

The classical characteristic mode formulation makes no assumption on the nature excitation – it remains arbitrary and can take any form. This signifies that in the matrix equation [Z][J] = [V], the excitation vector [V] can be any conceivable vector, provided the incident field producing [V] satisfies Maxwell's equations. If one were to restrict the values that [V] can possibly take, it does not change the matrix [Z]. Working from the opposite direction, however, one can define the Green's function used to construct the matrix [Z] to inherently restrict the nature of the excitation. In this approach, the matrix [Z] will only be capable of describing scattering due to this restricted range of excitation. Consequently, the characteristic modes of an excitation-restricted structure will form a set of eigencurrents and eigenvalues that exhibit orthogonality properties (forming a basis set) for the possible scattered fields due to the restricted excitation. If the [Z] matrix of any structure was formed assuming only one form of excitation (e.g. a plane wave incident from a single direction) the characteristic modes associated with the [Z] matrix determines a set of orthogonal modes that fully describe the scattered field to the single plane wave. Removing the restriction obviously gives one access to modes capable of describing the scattered field due to any excitation.

In many situations it is undesirable to analyze periodic structures using the approach (2) described earlier whereby a finite (but very large) version of the infinite structure is analyzed. Two major obstacles must be dealt with in this case: (1) the Z-matrix becomes very large, making the numerical analysis computationally costly (and possibly intractable) and (2) the number of dominant characteristic modes becomes too numerous to become useful as an analysis tool. We will focus exclusively on the former approach where the nature of the excitation is restricted, mostly due to its widespread adoption but also for the sake computational simplicity.

5.2 – An Accessible Moment Method Formulation for the Analysis of Infinite Periodic Structures

5.2.1 – Preliminaries

Many techniques have been proposed that determine the properties of an infinitely sized structure, quite often for the purpose of analyzing frequency selective surfaces (FSS) or array antennas [1] – [4]. Naturally, one never uses an infinite structure in practice, but rather uses its properties to accurately approximate the behaviour of a finite version. The mathematics and physics are such that the analysis of the infinite structure is computationally simple enough to warrant its use. However, such an analysis requires very specific numerical codes and techniques [1] – [4] that also presents issues involving Green's functions singularities, as well slow series convergence [5]. These issues can certainly be overcome, but not without a substantial amount of algorithm and software development overhead. Hence the reason commercial software codes are often used in the analysis of periodic structures. However, this presents another roadblock for our purposes. We must have access to the moment method impedance matrix [Z] in order to compute the eigencurrents and eigenvalues. Additionally, we require the visualization of the currents, and therefore need access to expansion function details. Lastly, we wish to incorporate our customized GA/MoM/DMM optimization technique with the numerical method and thus we require fairly intimate control over the inner workings of the numerical code. Unfortunately, no commercial code is known to the author that gives access to all these details. Open-source numerical codes exist, but none of the codes obtained allows for the analysis of full 3-D periodic structures with elements of arbitrary shape. In this section we will discuss a newly developed numerical technique by which to analyze infinite periodic structures using only a finite scatterer formulation. We currently have an entirely open-source finite scatterer formulation from the work of Makarov [6] developed within MATLAB, which has been adapted and expanded upon by the author.

5.2.2 – The Infinite-from-Finite (IFF) Formulation

The derivation of the newly defined periodic structure moment method formulation, the so-called "IFF" or infinite-from-finite method, begins with the impedance operator equation for a finite periodic structure of M elements:

$$\begin{bmatrix} [Z_{11}] & [Z_{12}] & \cdots & [Z_{1M}] \\ [Z_{21}] & [Z_{22}] & \cdots & [Z_{2M}] \\ \vdots & \vdots & \ddots & \vdots \\ [Z_{M1}] & [Z_{M2}] & \cdots & [Z_{MM}] \end{bmatrix} \begin{bmatrix} [I_1] \\ [I_2] \\ \vdots \\ [I_M] \end{bmatrix} = \begin{bmatrix} [V_1] \\ [V_2] \\ \vdots \\ [V_M] \end{bmatrix} \tag{4.1}$$

The sub-matrices $[Z_{nn}]$ refer to the impedance matrix of the n[th] element while $[Z_{mn}]$ refers to the coupling matrix between elements m and n. If we allow M to be infinite, we obtain the impedance matrix of the infinite periodic structure. We immediately see one possible technique that can be used in the development of a periodic structure code that uses only finite scatterer information: simply build the $[Z]$ matrix large enough such that sufficient accuracy is obtained. This is of course a brute-force approach and can in fact be impossible to solve since the size of the matrix $[Z]$ may approach intractable proportions. Additionally, consider the fact that this matrix will likely be inverted or be involved with eigenanalysis numerous times, compounding the numerical and computational difficulties in handling such a scenario. Let us begin the process of simplification by making a first reasonable assumption: all of the scatterers in the periodic structure will have identical excitation. This will also lead to all elements having identical currents due to excitation. This is a reasonable assumption as one does quite often assume a single plane wave incident on a periodic structure. In order to make this excitation assumption true, we must excite with a *normally* incident plane wave. Again, this is reasonable as it is often the assumption used when designing FSS and reflectarray structures that are not angle-of-incidence sensitive designs[11]. Such a scenario requires the two conditions

$$[V_m] = [V] \forall m = 1 \ldots M \tag{4.2}$$

$$[I_m] = [I] \forall m = 1 \ldots M \tag{4.3}$$

[11] Consideration is given to arbitrary angle of incidence in Appendix J

This leads to the altered operator equation

$$\begin{bmatrix} [Z_{11}] & [Z_{12}] & \cdots & [Z_{1M}] \\ [Z_{21}] & [Z_{22}] & \cdots & [Z_{2M}] \\ \vdots & \vdots & \ddots & \vdots \\ [Z_{M1}] & [Z_{M2}] & \cdots & [Z_{MM}] \end{bmatrix} \begin{bmatrix} [I] \\ [I] \\ \vdots \\ [I] \end{bmatrix} = \begin{bmatrix} [V] \\ [V] \\ \vdots \\ [V] \end{bmatrix} \tag{4.4}$$

Since the current is identical on every element, as is the excitation, we can observe the current on any element and know we are solving it for all elements. Let us now assume that element 1 is a central element among all other M–1 scatterers. Assume also that the scatterers surrounding element 1 are placed in a symmetric fashion surrounding scatterer 1, as shown in Figure 5.1. Consider the first row of block matrices $[Z_{11}]\ [Z_{12}]\ \cdots\ [Z_{1M}]$ and their interaction with the excitation and current column vectors:

$$[Z_{11}][I]+[Z_{12}][I]+\cdots+[Z_{1M}][I]=[V] \tag{4.5}$$

Factoring the current vector $[I]$ leads us to an expression related current to voltage vectors

$$\{[Z_{11}]+[Z_{12}]+\cdots+[Z_{1M}]\}[I]=[V] \tag{4.6}$$

Let us denote the matrix

$$\begin{aligned} \left[Z^{(M)}\right]_{ps} &= [Z_{11}]+[Z_{12}]+\cdots+[Z_{1M}] \\ &= [Z_{11}]+\sum_{n=2}^{M}[Z_{1n}] \\ &= [Z_{11}]+\left[Q^{(M)}\right] \end{aligned} \tag{4.7}$$

It is interesting to note that the matrix $[Z]_{ps}$ has two distinct contributions: (1) $[Z_{11}]$ which is the impedance matrix of the central element in isolation and (2) $\left[Q^{(M)}\right]$ which is the sum of all coupling matrices of the adjacent elements. If the properties of the single element in isolation is insufficient to predict the behaviour of the periodic structure, the emergent properties of the periodic array must come from the matrix $\left[Q^{(M)}\right]$. Because of (5.2) and (5.3) we can relate the current on element 1 to the excitation on element 1 simply as

$$\left[Z^{(M)}\right]_{ps}[I]_{ps}=[V]_{ps} \tag{4.8}$$

where $\left[Z^{(M)}\right]_{ps}$ is the same as expression (5.7).

In order to obtain accurate results and have convergence occur at a faster rate we employ an averaging technique on the impedance matrices obtained. This is similar in theme to an ARMA/PRONY type technique. Whenever a complete ring of elements is added to the overall periodic structure matrix, this matrix is stored in memory. The matrix obtained for each completed loop is averaged with all matrices obtained in previous loops. A ring of elements is completed when the total number of elements in the summation in expression (5.7) is 8, 24, 48, and so on. We denote this averaged matrix as $\left[Z^{(M)}\right]_{ps}^{avg}$. For example, consider the case where we have three complete rings of elements. The impedance matrix that describes this scenario is given by

$$\left[Z^{(49)}\right]_{ps}^{avg} = \frac{1}{3}\left\{\left[Z^{(9)}\right]_{ps} + \left[Z^{(25)}\right]_{ps} + \left[Z^{(49)}\right]_{ps}\right\} \tag{4.9}$$

In practice, more than 3 complete rings would be added to obtain what would be considered the converged “final” impedance matrix.

The assumption of identical excitation and identical currents only occurs under the condition of an infinite periodic structure. In solving this problem for finite M, we are necessarily incurring errors. Nevertheless, this is our approximation. Only when M is infinite is expression (5.4) exact. Such is the nature of computational electromagnetics. The fact of the matter is, for example, that expression (5.1) is only exact (in the sense of solving a continuous problem rather a discretized one) when the sub-matrices themselves are infinite. Moreover, any moment method mesh is an approximation and only becomes exact when the number of expansion functions becomes infinite. The only question that remains is how many elements “M” are required before the assumption of identical current and excitation is such that a minimum amount of error is incurred and the current density on the central element is practically what it would be in an infinite ($M \to \infty$) periodic environment.

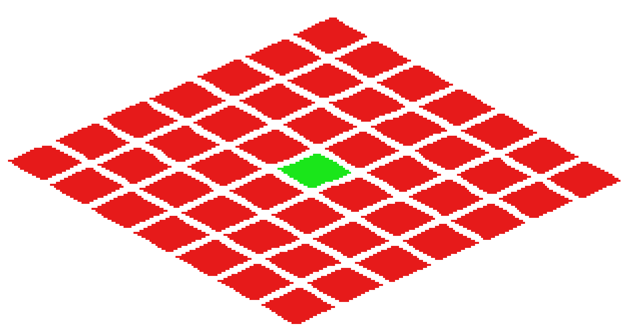

Figure 5.1 – Example periodic structure with central element surrounded by M–1 elements where M = 36

5.2.3 – Convergence and Validation Results for the IFF Method

In order to test for convergence, we consider the transmission and reflection coefficients as metrics. A normally incident plane is used to excite the periodic structure with the periodic structure impedance matrix of (5.7) being used to describe the resulting scattering. A point 'P' above the periodic structure (above the central element) is selected at which to measure the scattered field. This point is set to be approximately 2λ from the scatterer. As one moves farther away from the surface of the central element one begins to observe the finiteness of the periodic structure by way of observing more than a single scattered plane wave, even for the case of lattice sizes less than $\lambda/2$. More details regarding this phenomenon can be found in Appendix F.

Our first example showing convergence and validation is a dogbone-shaped element, shown in Figure 5.2. The incident plane wave is y-polarized, normal to the periodic structure plane of periodicity and is therefore -z directed. The dimensions are $d_x = d_y =$ 7.5mm, A = 4 mm, B = 7.4 mm and t = 0.5 mm. The resulting reflection coefficient magnitude of the periodic structure is shown in Figure 5.3 for the case of 1, 2, 5 and 10 rings and is compared to the commercially available code FEKO [7]. One can see that by the time the number of rings reaches 10, there is good agreement between our numerical technique and the commercial code. There is some semblance of the technique converging as well, as the accuracy of the technique clearly increases as the number of rings increase. Consider additionally Figure 5.4, which shows the convergence of the reflection phase as a function of the number of rings, strictly for the frequency 9.9 GHz. This represents the most sensitive frequency of the periodic structure since the reflection phase is approximately -180 degrees – a resonance. Again, we see very good agreement between the IFF method and the commercial code FEKO. For all intents and purposes, the numerical technique is converged by 10 rings, though 1 degree in reflection phase error would be incurred if only 4 rings were used. This shows the possibility of trading accuracy for speed of computation.

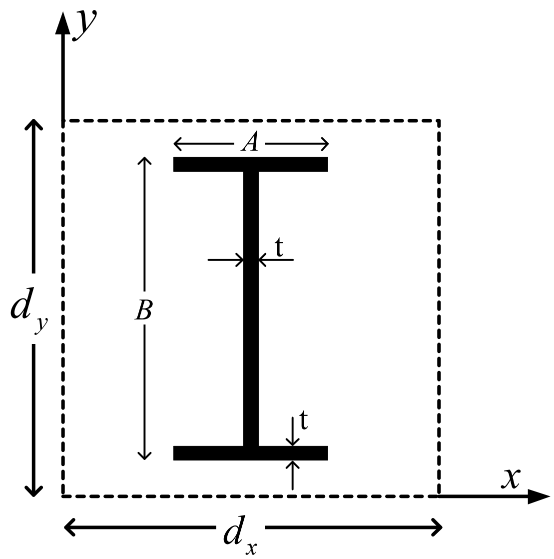

Figure 5.2 – Example periodic structure consisting of a dogbone-shaped element

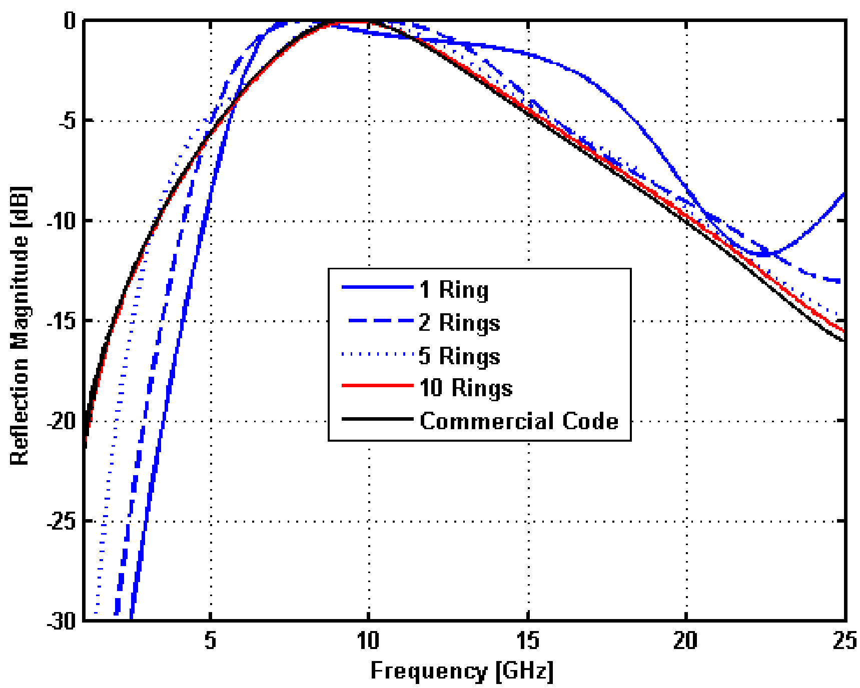

Figure 5.3 – Reflection magnitude convergence as a function of the number of element rings over frequency

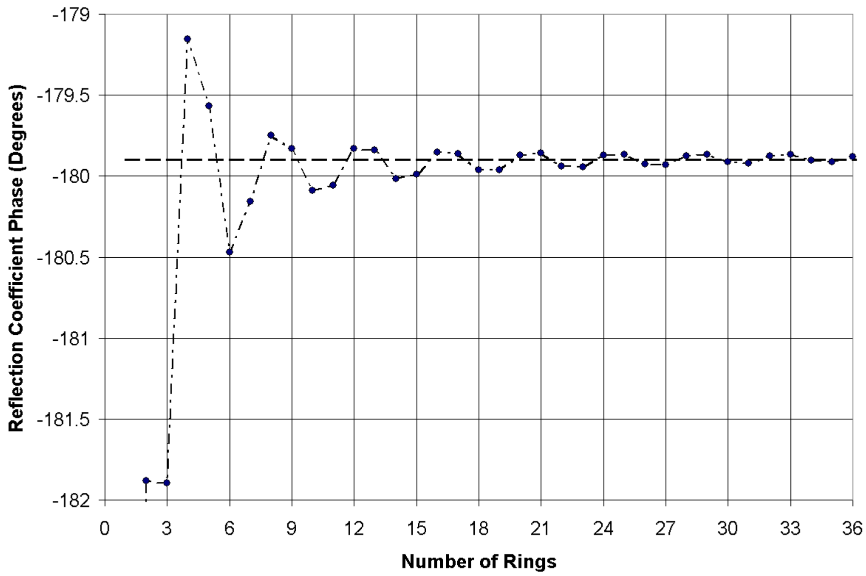

Figure 5.4 – Phase of the reflection coefficient of a periodic array of dogbone elements at 9.9 GHz as a function of the number of rings used in the IFF method (-•-•-•-). The horizontal dashed line (----) is the value predicted using code FEKO using its infinite periodic structure capability for the dogbone elements.

We also wish to consider periodic structures in the presence of an infinite ground plane. In order to do so, the Green's function must account for the presence of such an infinite structure. We propose an efficient technique to include the effects of an infinite ground plane for the case of purely planar structures. The details of this technique are in Appendix G. The example periodic structure we will consider in the presence of an infinite ground plane is a square patch element shown in Figure 5.5. The dimensions are $d_x = d_y = 4.0\ \mathrm{mm}$, W = L = 3.8 mm at a distance of 10mm from the ground plane. We excite the structure with a y-polarized normally incident plane wave. The resulting reflection phase is shown in Figure 5.6 over a very wide range of frequencies. In particular, note that the structure has three resonances (5, 16, and 32 GHz) from 0 to 40 GHz with the IFF method properly predicting their behaviour in each instance. This example uses 20 rings for the converged and accurate results, though fewer rings could have been used to very little noticeable difference. Additional convergence results as well as more details on the accuracy of the IFF method can be found in Appendix F.

Note that we will not use finite conductivity scatterers and oblique plane wave incidence in this thesis. Nevertheless, the IFF can deal with these cases as described in Appendix J.

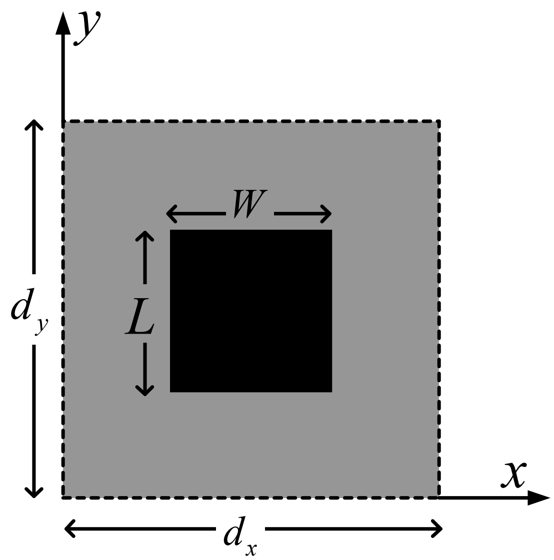

Figure 5.5 – Example patch-based periodic structure with an adjacent ground plane

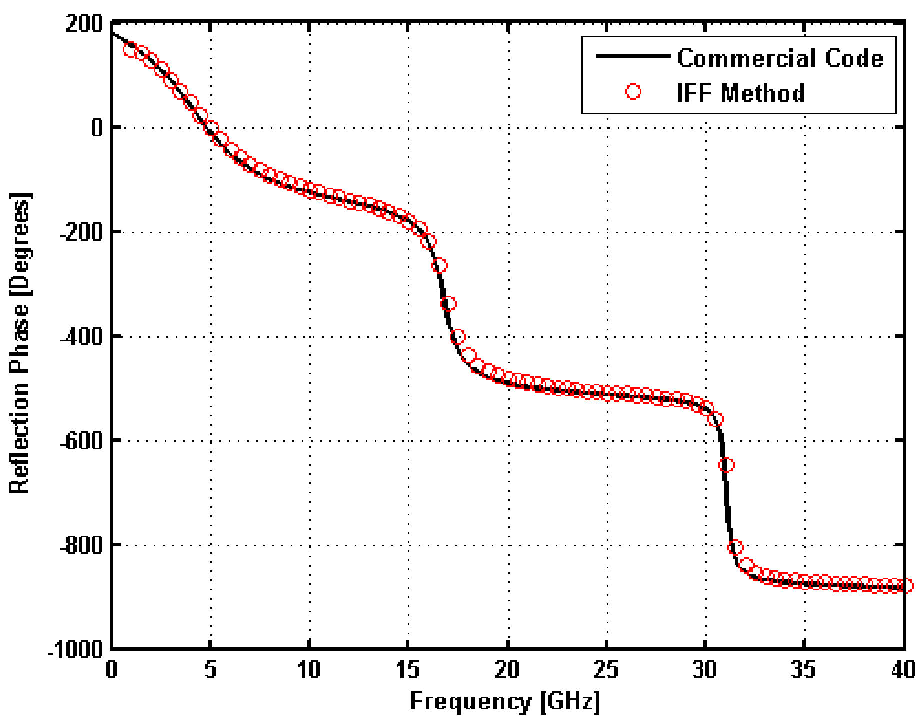

Figure 5.6 – Simulated reflection phase obtained from the commercial code FEKO (solid black curve) and alternatively obtained from our moment method IFF formulation (red circles). Very good agreement is found at all frequencies including the transition through multiple resonances

5.3 – Characteristic Mode Analysis of Periodic Structures

5.3.1 – Characteristic Modes and Periodic Structures

As discussed in [8], one can use the characteristic mode eigenfields as expansions of incoming and outgoing waves. The summation of all incoming and outgoing waves gives us an expression for the total field

$$\underline{E}_{total} = \underline{E}_{in} + \underline{E}_{out} \tag{4.10}$$

where $\underline{E}_{in}$ and $\underline{E}_{out}$ are the incoming and outgoing fields respectively. The total field can also be written in terms of the incident and scattered fields

$$\underline{E}_{total} = \underline{E}_{inc} + \underline{E}_{scat} \tag{4.11}$$

where $\underline{E}_{inc}$ differs from $\underline{E}_{in}$ in that $\underline{E}_{inc}$ can consist of both incoming and outgoing waves (e.g. a plane wave, a spherical wave and its conjugate and so on). The scattered and outgoing fields can be written solely in terms of the incoming fields

$$\underline{E}_{scat} = 2P\left(\underline{E}_{in}\right) \tag{4.12}$$

$$\underline{E}_{out} = S\left(\underline{E}_{in}\right) \tag{4.13}$$

where P and S are called the perturbation and scattering operators. The perturbation operation P transforms incoming waves into the scattered fields, while S transforms incoming waves into outgoing waves. The scattered field is a purely outgoing wave, though it is not necessarily identical to the outgoing field.

In [8], they consider the expansion of general incoming and outgoing fields in terms of the characteristic modes. They express the outgoing waves in terms of the characteristic mode fields (eigenfields) and the incoming waves in terms of the complex conjugates of the same fields.

$$\underline{E}_{out} = \sum_n b_n \underline{E}_n \tag{4.14}$$

$$\underline{E}_{in} = \sum_n a_n \underline{E}_n^* \tag{4.15}$$

Additionally, the scattered field is also written in terms of the characteristic mode fields

$$\underline{E}_{scat} = \sum_n c_n \underline{E}_n \tag{4.16}$$

Since the characteristic modes produce scattered fields, they produce only outgoing fields. Hence, they are naturally used as expansion functions for both the outgoing fields and scattered fields. If one were to take the complex conjugate of a characteristic mode field, it would turn the outgoing field into an entirely incoming field and hence, the complex conjugate of the characteristic mode fields makes excellent expansion functions for the incoming field, as in (5.15).

Under these conditions (5.14 – 5.16) of field expansion, the perturbation and scattering operators are diagonalized (see [8, sec VIII] for proof) and are given in matrix form as

$$[P] = \begin{bmatrix} \dfrac{-1}{1+j\lambda_1} & 0 & \cdots & 0 \\ 0 & \dfrac{-1}{1+j\lambda_2} & & \vdots \\ \vdots & & \ddots & 0 \\ 0 & \cdots & 0 & \dfrac{-1}{1+j\lambda_N} \end{bmatrix} \tag{4.17}$$

and

$$[S] = \begin{bmatrix} -\dfrac{1-j\lambda_1}{1+j\lambda_1} & 0 & \cdots & 0 \\ 0 & -\dfrac{1-j\lambda_2}{1+j\lambda_2} & & \vdots \\ \vdots & & \ddots & 0 \\ 0 & \cdots & 0 & -\dfrac{1-j\lambda_N}{1+j\lambda_N} \end{bmatrix} \tag{4.18}$$

Therefore, $[P]$and$[S]$ act to transform the characteristic modes into the scattered and outgoing fields respectively. These matrices now relate the coefficients in (5.14) – (5.16) via

$$[b] = [S][a] \tag{4.19}$$

$$[c] = 2[P][a] \tag{4.20}$$

where $[a],[b],[c]$ are column vectors containing the coefficients a_n, b_n, c_n.

Transmission and reflection coefficients of a scattering system are typically defined as the ratio of total field to incident field, and scattered field to incident field, respectively. Since we already have an expression for the scattered field (5.12), we require an expression for either the total or incident field to obtain the transmission and reflection coefficients. By combining (5.10) and (5.13), we obtain an expression for the total field in terms of the incoming field

$$\underline{E}_{total} = \underline{E}_{in} + S\left(\underline{E}_{in}\right) \tag{4.21}$$

We can then substitute (5.12) and (5.21) into (5.11) to obtain an expression for the incident field in terms of the incoming field

$$\underline{E}_{inc} = \underline{E}_{in} + S\left(\underline{E}_{in}\right) - 2P\left(\underline{E}_{in}\right) \tag{4.22}$$

As discussed in [8], the incoming wave is written as an expansion of complex conjugates of the characteristic modes. We shall introduce the concept of modal reflection and transmission coefficients by observing the incident, scattered and total fields as strictly associated with a single mode. In other words, let us assume that the incident field excites a single mode ‘n’. Since the $\left[S\right]$ and $\left[P\right]$ matrices are diagonalized, if we assume only one mode is excited, the outgoing and scattered fields will consist only of the mode with index ‘n’. Under single-mode excitation the three key expressions (5.14) – (5.16) become

$$\underline{E}_{out} = b_n \underline{E}_n \tag{4.23}$$

$$\underline{E}_{in} = a_n \underline{E}_n^* \tag{4.24}$$

$$\underline{E}_{scat} = c_n \underline{E}_n \tag{4.25}$$

Under these single mode conditions, the incident, scattered and total fields can be written

$$\underline{E}_{inc} = a_n \left(1 + s_{nn} - 2p_{nn}\right) \underline{E}_n^* \tag{4.26}$$

$$\underline{E}_{scat} = 2p_{nn} a_n \underline{E}_n^* \tag{4.27}$$

$$\underline{E}_{total} = a_n \left(1 + s_{nn}\right) \underline{E}_n^* \tag{4.28}$$

where s_{nn} is the (n,n) indexed entry of matrix [S] from (5.18) and p_{nn} is the (n,n) indexed entry of matrix $\left[P\right]$ from (5.17). In can also be shown that $1 + s_{nn} - 2p_{nn} = 2$, allowing us to further simplify (5.26).

Therefore, we can write the modal transmission and reflection coefficients in terms of the expressions in (5.26) – (5.28) relative to any arbitrary polarization $\underline{p}$.

$$\mathrm{T}_{n,\underline{p}} = \frac{\underline{p}\cdot\underline{E}_{total}}{\underline{p}\cdot\underline{E}_{inc}} = \frac{a_n\left(1+s_{nn}\right)\left(\underline{p}\cdot\underline{E}_n^*\right)}{a_n 2\left(\underline{p}\cdot\underline{E}_n^*\right)} = \frac{1+s_{nn}}{2} = \frac{j\lambda_n}{1+j\lambda_n} \tag{4.29}$$

$$\Gamma_{n,\underline{p}} = \frac{\underline{p}\cdot\underline{E}_{scat}}{\underline{p}\cdot\underline{E}_{inc}} = \frac{2p_{nn}a_n\left(\underline{p}\cdot\underline{E}_n^*\right)}{a_n 2\left(\underline{p}\cdot\underline{E}_n^*\right)} = p_{nn} = \frac{-1}{1+j\lambda_n} \tag{4.30}$$

which shows that the modal transmission and reflection coefficients are independent of the polarization being measured. This allows us to simply express these modal coefficients strictly in terms of the mode's eigenvalue as follows

$$\boxed{\mathrm{T}_n = \frac{1+s_{nn}}{2} = \frac{j\lambda_n}{1+j\lambda_n}} \tag{4.31}$$

$$\boxed{\Gamma_n = p_{nn} = \frac{-1}{1+j\lambda_n}} \tag{4.32}$$

Expressions (5.31) and (5.32) are hereafter known as the modal transmission and reflection coefficients and are in fact a systems' transmission and reflection coefficients should the incident field solely excite the nth mode of the scatterer.

We have in fact made the effort not to mention periodic structures up to this point since all of the previous derivations are valid for any scatterer. However, we will now explicitly state that our interests lie in periodic structures since transmission and reflection coefficients are of paramount importance, with the latter term being the most important parameter for reflectarray design. A peculiarity of these results is that reflection and transmission coefficient often requires a measurement location in space, positioned somewhere above the periodic structure, which is not the case for the modal-based coefficients. This is a consequence of the characteristic mode theory and a phenomenon also observed from the results of Chapter 3 and 4.

5.3.2 – The Single Mode Periodic Structure in Freespace

In Chapters 3 and 4 we discussed the notion of single mode antennas at great length. We will now discuss the concept of a single mode periodic structure. As shown in the previous Section 5.3.1, a single-mode periodic structure's electromagnetic behaviour can be described solely in terms of the single mode's eigenvalue behaviour. The excitation of a single-mode periodic structure will only significantly excite its dominant mode. The transmission and reflection coefficients of such a structure will in fact be one and the same as the modal transmission and reflection coefficients (5.31) and (5.32). Let us denote these coefficients simply as (there reference plane locations are discussed in Section 5.3.5)

$$\mathrm{T} = \mathrm{T}_n = \frac{j\lambda_n}{1 + j\lambda_n} \tag{4.33}$$

$$\Gamma = \Gamma_n = \frac{-1}{1 + j\lambda_n} \tag{4.34}$$

If these modal coefficients truly are the reflection coefficients of the periodic structure, they must obey the law of power conservation, i.e. $|\mathrm{T}_n|^2 + |\Gamma_n|^2 = 1$. We can confirm this by evaluating

$$\left|\frac{j\lambda_n}{1 + j\lambda_n}\right|^2 + \left|\frac{-1}{1 + j\lambda_n}\right|^2 = \frac{|\lambda_n|^2}{1 + \lambda_n^2} + \frac{1}{1 + \lambda_n^2} = 1$$

and hence power is conserved.

Also, for a single interface the relationship $\mathrm{T} = 1 + \Gamma$ must hold. We can also confirm this by evaluating

$$\mathrm{T} - \Gamma = \frac{j\lambda_n}{1 + j\lambda_n} - \frac{-1}{1 + j\lambda_n} = \frac{1 + j\lambda_n}{1 + j\lambda_n} = 1$$

Thus, the expressions for transmission and reflection of a single-mode periodic structure are sound. We shall explore these claims through simulation examples in Section 5.3.7.

5.3.3 – The Circuit Model of Single Mode Periodic Structures in Freespace

Since the periodic structure being considered is single-mode and with normal plane wave incidence, we can approximate the electrical behaviour of the structure with a simple reactive element straddled by transmission lines, as shown in Figure 5.7. The transmission and reflection coefficients of such a structure can be written in terms of the equivalent impedance of the structure as follows

$$\Gamma = \frac{Z_{in} - Z_o}{Z_{in} + Z_o} \tag{4.35}$$

where Z_o is the intrinsic impedance of freespace $\eta_o = \sqrt{\mu/\varepsilon}$ and Z_{in} is the input impedance of the periodic structure with freespace on the opposite side and from (5.35) can be written

$$Z_{in} = \eta_o \frac{1+\Gamma}{1-\Gamma} \tag{4.36}$$

The impedance of the periodic structure is represented by Z_L and the infinite transmission line can be represented by the load impedance η_o. Hence, the expression for Z_{in} is Z_L in parallel with η_o

$$Z_{in} = \frac{\eta_o Z_L}{\eta_o + Z_L} \tag{4.37}$$

Equating (5.36) and (5.37) and solving for the shunt impedance Z_L gives us

$$Z_L = \eta_o \frac{1+\Gamma}{-2\Gamma} \tag{4.38}$$

Finally, substituting the expression for the reflection coefficient in (5.34) into (5.38) gives us

$$Z_L = j\frac{\eta_o}{2}\lambda_n \tag{4.39}$$

This is a reassuring result since it implies numerous necessary results:

(1) The equivalent impedance of the periodic structure is purely reactive and thus has no real part. This is necessary for a lossless periodic structure.

(2) If the dominant CM of the single mode periodic structure is capacitive or inductive, the equivalent reactive element is also capacitive or inductive by way of the sign of the eigenvalue.

(3) If the single mode is resonant, the eigenvalue is zero and hence the impedance is zero, representing a short circuit. A short circuit has a reflection coefficient of -1, precisely as the CM theory and standard periodic structure theory would predict.

(4) If the single mode has an infinite eigenvalue (positive or negative) the impedance becomes infinite as well and thus the circuit element is open circuit. The reflection coefficient is then zero, representing a transparent freespace periodic structure.

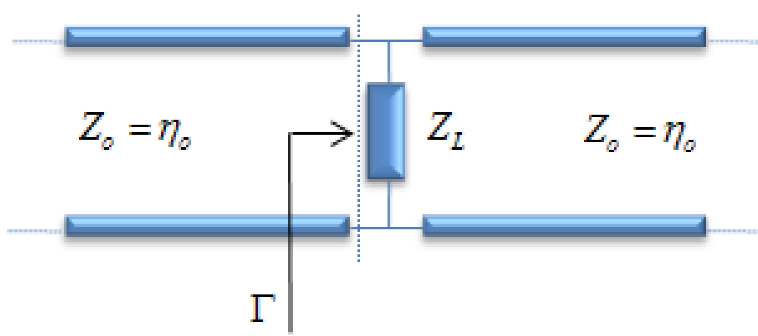

Figure 5.7 – Representation of a simple freespace periodic structure modeled as a reactive element straddled by transmission lines representing freespace. Note this model is valid for lossless periodic structures.

5.3.4 – Single Mode Periodic Structures in the Presence of an Infinite Ground Plane

We can also analyze the modal behaviour of periodic structures in the presence of an infinite ground plane. In particular, consider the arbitrary expansion of the scattered field as follows

$$\underline{E}_{scat} = \frac{V_n^i}{1+j\lambda_n}\underline{E}_n = \frac{\left\langle \underline{J}_n, \underline{E}^{inc} \right\rangle}{1+j\lambda_n}\underline{E}_n \tag{4.40}$$

where we have implicitly assumed the excitation of a single characteristic mode. Since the periodic structure exists over the infinite ground plane, and we excite it using an incident plane wave, we can simply express the incident field as the scaled complex conjugate of the characteristic field $\underline{E}^{inc} = a_n \underline{E}_n^*$ where a_n is an arbitrary complex scaling factor. This must be the case since the ground plane will act to ensure all incident fields are in fact incoming waves and outgoing fields are purely scattered fields. Under these conditions for excitation, we obtain the scattered field

$$\underline{E}_{scat} = \frac{\left\langle \underline{J}_n, \underline{E}^{inc} \right\rangle}{1+j\lambda_n}\underline{E}_n = \frac{\left\langle \underline{J}_n, a_n \underline{E}_n^* \right\rangle}{1+j\lambda_n}\underline{E}_n = a_n \frac{\left\langle \underline{J}_n, Z^*\left(\underline{J}_n\right) \right\rangle}{1+j\lambda_n}\underline{E}_n = a_n \frac{1-j\lambda_n}{1+j\lambda_n}\underline{E}_n \tag{4.41}$$

The scattered field will simply be a plane wave of identical amplitude but phase shifted by the complex quantity $\left(1-j\lambda_n\right)/\left(1+j\lambda_n\right)$. The reflection coefficient for a periodic structure over a ground plane then becomes

$$\Gamma = \Gamma_n = \frac{1-j\lambda_n}{1+j\lambda_n} \tag{4.42}$$

This is a sensible quantity as it suggests that a resonant mode ($\lambda_n = 0$) will yield a reflection coefficient of $\Gamma = +1$, while an infinite eigenvalue suggests a reflection coefficient of $\Gamma = -1$. The latter condition is particularly interesting since an infinite eigenvalue suggests infinite net stored energy and implies no scattered real power content. A single-mode periodic structure with an infinite CM eigenvalue does not scatter any incident fields. However, since the ground plane is present, the reflection coefficient becomes $\Gamma = -1$ and the only structure "observed" by the incoming field is the ground plane itself with the periodic structure becoming transparent.

5.3.5 – Reference Planes and Single Mode Periodic Structures

It should be noted, however, that the reflection coefficients obtained for both the freespace and infinite ground plane scattering scenarios have their fields referenced at the origin of the Green's function used to describe the scattering (e.g. using the IFF method). The most common location is selected to be the origin of the coordinate system, which is indeed the case in our example. Reflection and transmission coefficients, however, are typically referenced on the surface of the periodic structure rather than at the origin. For the case of a freespace periodic structure, we will continue to analyze periodic structures that are single layer that reside in the x-y plane and hence the phase reference is already located on the surface of the periodic structure.

However, this is not necessarily the case of the periodic structure with an adjacent ground plane. Oftentimes, the ground plane is placed in the x-y plane at z = 0, with the periodic structure placed at some distance z = d. For the purpose of practical analysis, we would rather have the phase reference on the surface of the periodic structure rather than the ground plane. We have two options presented to us:

(1) Perform a reference plane shift bringing the reflection coefficient from the ground plane reference to the surface of the periodic structure [11]. This amounts to the simple multiplication by the complex exponential $e^{-j2\beta d}$ which changes the phase of the reflection coefficient but leaves the magnitude unhindered (where $\beta = \omega\sqrt{\mu\varepsilon}$)

(2) Simulate the periodic structure with the ground plane located at z = -d and the periodic structure residing at the location z = 0.

We shall opt for the former solution because of its general adoption in the literature, as well as the simplicity in shifting the reference plane.

5.3.6 – Computational Short-Cuts Involving the Trace of the CM Matrix

In keeping with the tradition of Chapters 3 and 4, we consider what the trace of the characteristic mode matrix can tell us about a periodic structure. Recall that the trace of this matrix for a single mode structure (antenna, or periodic structure now) can be written

$$\Psi = Trace\left(\left[Z\right]^{-1}\left[R\right]\right) \approx \frac{1}{1+j\lambda_1} \tag{4.43}$$

This immediately allows us to write expressions for the transmission and reflection coefficients of freespace periodic structures as

$$\Gamma = \Gamma_n = -\Psi \tag{4.44}$$

$$\mathrm{T} = \mathrm{T}_n = 1-\Psi \tag{4.45}$$

Note that the CM matrix trace is valid at every frequency for the case of periodic structures as evidenced by (5.44) and (5.45). This is in contrast to the results of Chapters 3 and 4 where the trace was restricted to frequencies where a resonant characteristic mode exists. In the case of periodic structures with infinite ground planes, the matrix trace offers another short cut via the fact that

$$\Psi = Trace\left(\left[Z\right]^{-1}\left[R\right]\right) \approx \frac{1}{1+j\lambda_n} \tag{4.46}$$

and

$$\Psi^* = Trace\left(\left[Z\right]^{-1}\left[R\right]\right)^* \approx \frac{1}{1-j\lambda_n} \tag{4.47}$$

and through the combination of (5.46) and (5.47), we obtain

$$\Gamma = \Gamma_n = \frac{Trace\left(\left[Z\right]^{-1}\left[R\right]\right)}{Trace\left(\left[Z\right]^{-1}\left[R\right]\right)^*} = \frac{\Psi}{\Psi^*} = \frac{1-j\lambda_n}{1+j\lambda_n} \tag{4.48}$$

We have now obtained expressions to compute the transmission and reflection coefficients of single-mode periodic structures (both the freespace kind, and those with an adjacent infinite ground plane) without having to directly excite the structures and without having to measure any scattered fields.

5.3.7 – Simulations Confirming Single-Mode Periodic Structure Properties

In order to confirm that our derivations of single mode periodic structures are indeed correct, as well as introduce some examples of single mode periodic structures, we next explore various examples of transmission and reflection coefficients predicted using characteristic mode eigenvalues. Let us repeat the analysis of the dogbone-shaped element of Section 5.2.3 (see Figure 5.8a), only now consider both the transmission and reflection magnitudes over frequency range from low frequency to 25 GHz for a y-polarized normally incident plane wave. The transmission magnitude and phase for the dogbone is shown in Figures 5.9 and 5.10 respectively. The reflection magnitude and phase is also shown in Figure 5.11 and 5.12 respectively. The results show the simulated results using the commercial code FEKO in solid black lines, while the parameters are obtained using the IFF method using a traditional field based technique represented by a dashed line. Finally, the parameters are obtained using the matrix trace method (expressions 5.44 and 5.45) and are shown using triangle markers. Note that all three techniques show good agreement, with the latter technique being obtained simply through the matrix trace and without having to directly excite the periodic structure or sample scattered fields.

Consider now the square patch from section 5.2.3, shown in Figure 5.8b. An interesting property of the square patch is that it is not truly a single mode periodic structure. It is in fact a two-mode periodic structure by way of its symmetry. When excitation is polarized along y, a single mode is excited (denote this mode 1). If polarized along x, a single mode is excited as well (call this mode 2). Plots of the eigenvalues of these two modes are shown in Figure 5.13, showing that they are indistinguishable. This pair forms a set of degenerate modes (identical eigenvalues) with the eigencurrents being simple geometric rotations of each other. These eigencurrents are shown in Figure 5.14(a) and 5.14(b), the modes are associated with x- and y-polarized fields, respectively. The reflection phase obtained from a commercial code, from the IFF method and from the IFF trace method is shown in Figure 5.15. While not literally a single-mode periodic structure, the patch can still be treated as such given the association each of the two significant modes have with the incident field polarization. Note that with the degeneracy of two modes, both of which are significant modes (all other modes are deemed insignificant by way of their eigenvalue magnitudes), the matrix trace of such a structure can be written

$$\Psi = Trace\left(\left[Z\right]^{-1}\left[R\right]\right) \approx \frac{1}{1+j\lambda_1} + \frac{1}{1+j\lambda_2} \tag{4.49}$$

Since the eigenvalues are degenerate, i.e. $\lambda_1 \approx \lambda_2 \approx \lambda$, we can simply express the matrix trace as

$$\Psi = Trace\left(\left[Z\right]^{-1}\left[R\right]\right) \approx \frac{2}{1+j\lambda} \tag{4.50}$$

This change effects the expressions for the transmission and reflection coefficients in terms of the characteristic mode matrix trace as follows (for the freespace periodic structure)

$$\Gamma = \Gamma_n = -\frac{1}{2}\Psi \tag{4.51}$$

$$\mathrm{T} = \mathrm{T}_n = 1-\frac{1}{2}\Psi \tag{4.52}$$

For periodic structures with a supporting ground plane, the expression for the reflection coefficient does not change due to the cancelling effect of the ratio of traces

$$\Gamma = \Gamma_n = \frac{Trace\left(\left[Z\right]^{-1}\left[R\right]\right)}{Trace\left(\left[Z\right]^{-1}\left[R\right]\right)^*} = \frac{\Psi}{\Psi^*} = \frac{\dfrac{2}{1+j\lambda}}{\dfrac{2}{1-j\lambda}} = \frac{1-j\lambda_n}{1+j\lambda_n} \tag{4.53}$$

We will continue to denote these periodic structures as single-mode since in the majority of cases we encounter will excite these structures along either x or y – both cases view the periodic structure functionally as a single-mode periodic structure. A further look at the theoretical limitations and properties of single-mode periodic structures can be found in Appendix K.

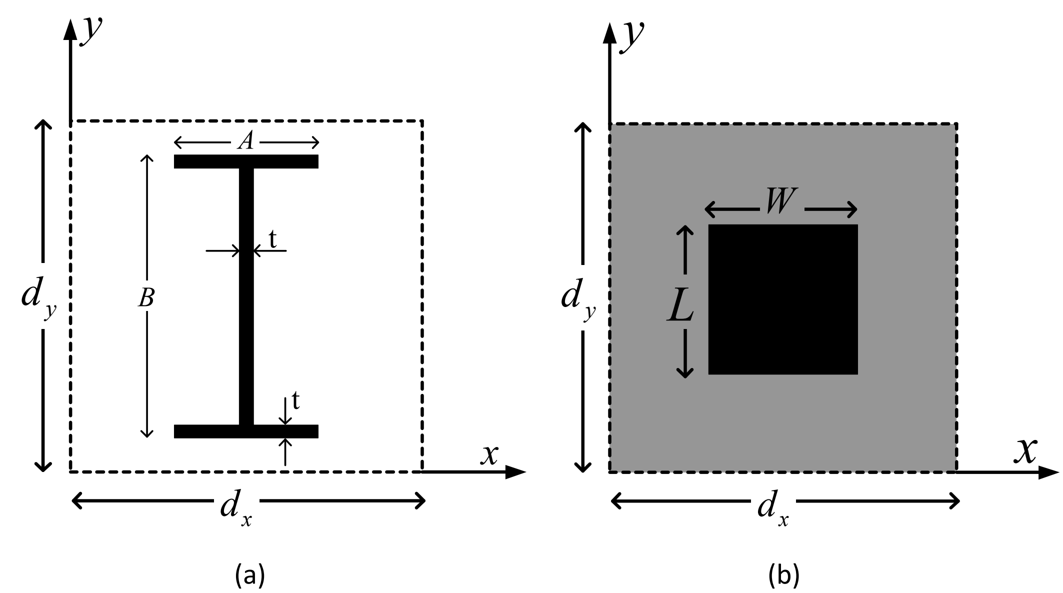

Figure 5.8 – Example periodic structures consisting of (a) freespace array of dogbone elements and (b) periodic structure of patch elements with an adjacent ground plane

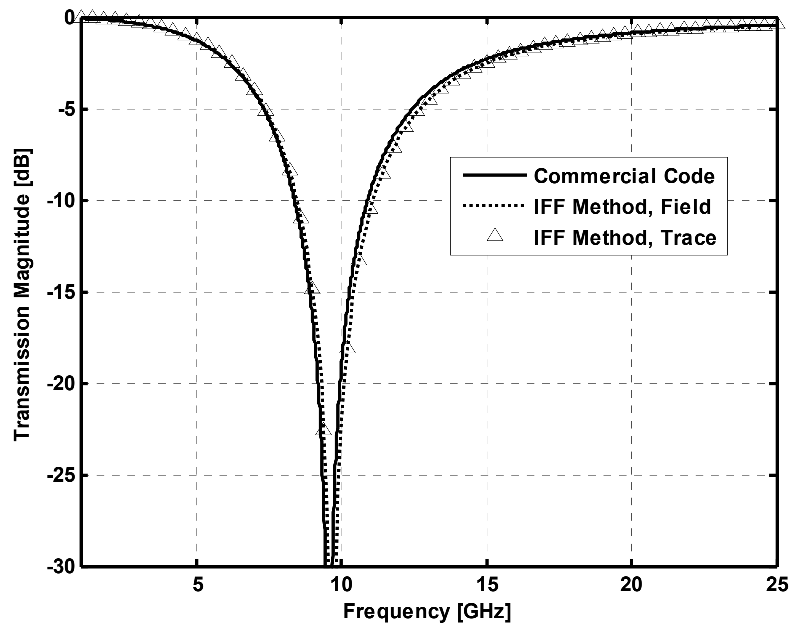

Figure 5.9 – Transmission magnitude of the freespace dogbone periodic structure comparing three methods: commercial code FEKO, the IFF method using field analysis and the IFF method using the CM matrix trace

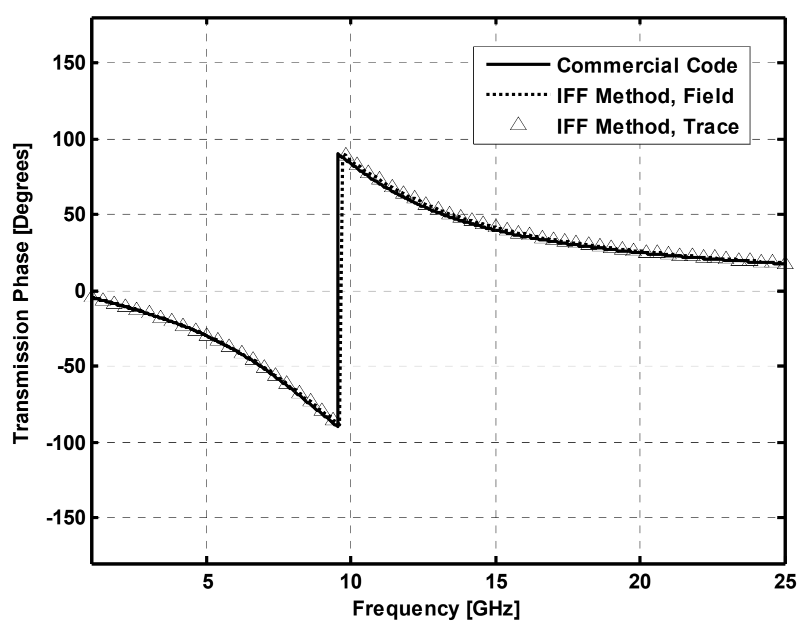

Figure 5.10 – Transmission phase of the freespace dogbone periodic structure comparing three methodologies: commercial code FEKO, the IFF method using field analysis and the IFF method using the CM matrix trace

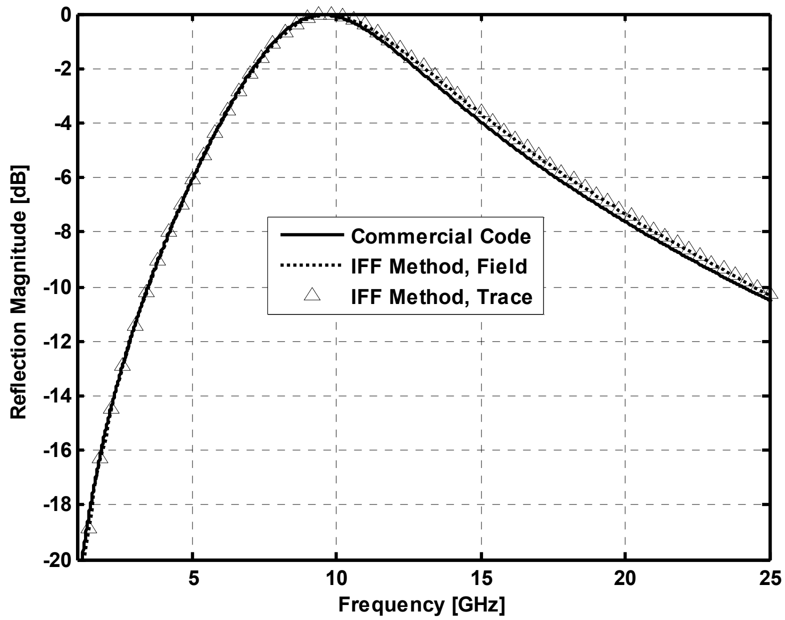

Figure 5.11 – Reflection magnitude of the freespace dogbone periodic structure comparing three methodologies: commercial code FEKO, the IFF method using field analysis and the IFF method using the CM matrix trace

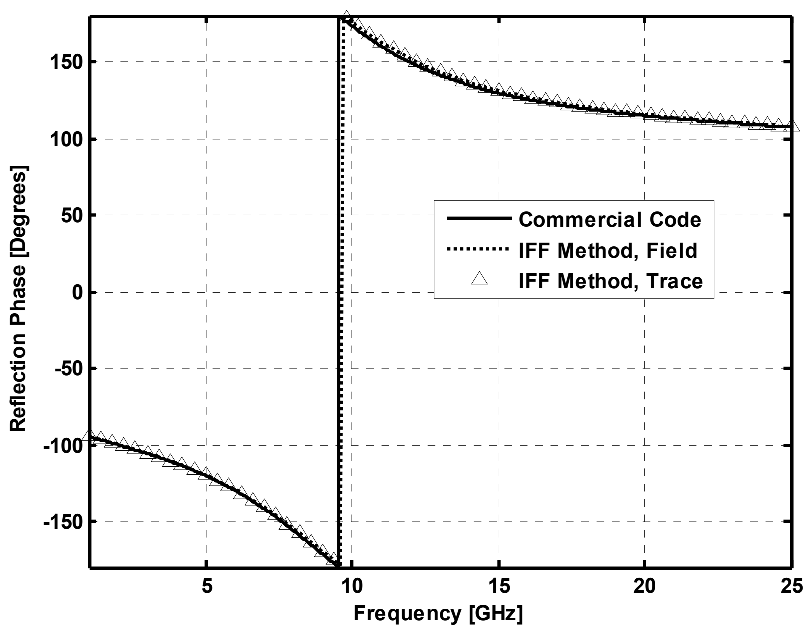

Figure 5.12 – Reflection phase of the freespace dogbone periodic structure comparing three methodologies: commercial code FEKO, the IFF method using field analysis and the IFF method using the CM matrix trace

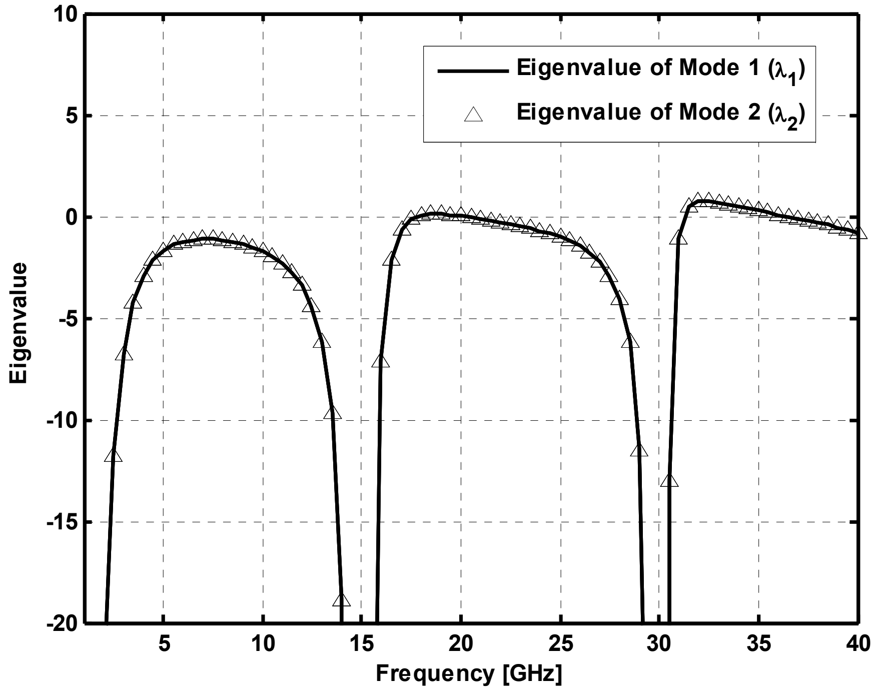

Figure 5.13 – Two degenerate modes with significant eigenvalues for the patch/ground plane periodic structure

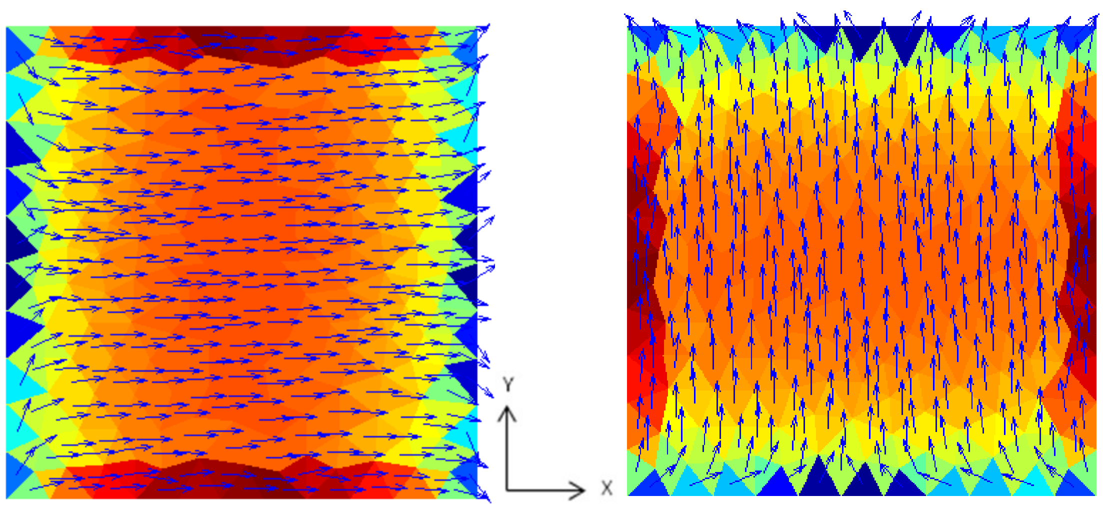

(a) (b)

Figure 5.14 – Degenerate mode eigencurrents for the patch/ground plane periodic structure

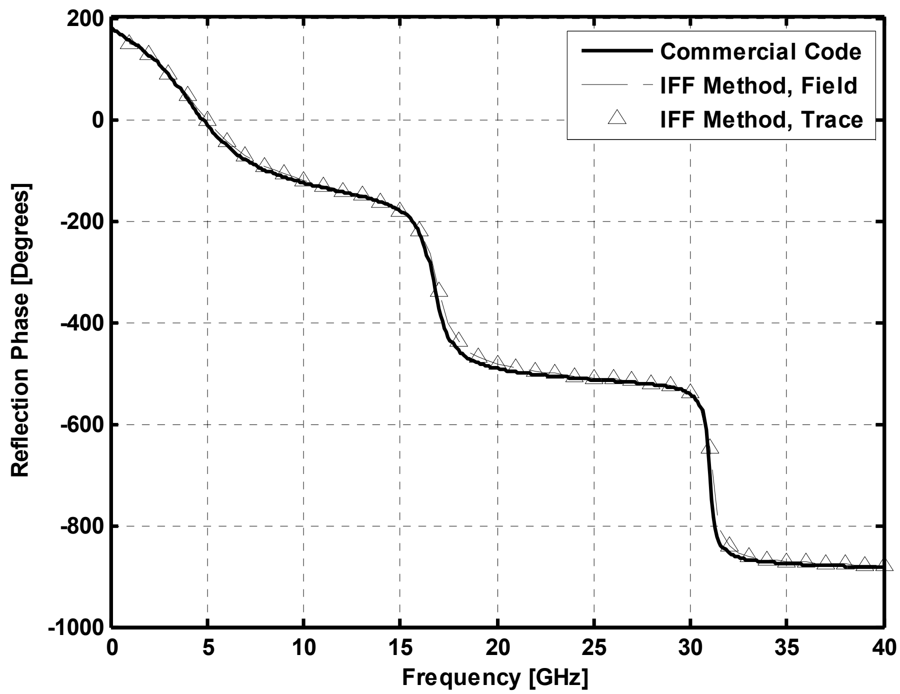

Figure 5.15 – Reflection phase of the patch/ground plane periodic structure comparing three methodologies: commercial code FEKO, the IFF method using field analysis and the IFF method using the CM matrix trace

5.4 – Reflectarray Design using CM Objective Functions

5.4.1 – Proposed Objective Function for Reflectarray Element Synthesis

Similar to what was done in Chapters 3 and 4, we propose a synthesis technique that is excitation-free and allows us to synthesize the shape of the reflectarray elements. Fundamentally, we will utilize expression (5.53) in our synthesis procedure. It should be noted that the derivations and techniques in this section are not necessarily unique to reflectarrays – they can be used to synthesize frequency selective surfaces, artificial magnetic conductors and metamaterials. One major motivation for concentrating on reflectarrays is the fact that they are fundamentally high gain antennas. The other examples of periodic structures are not typically used as antennas – at least not on their own. In this sense, reflectarrays provide us with immediately accessible experimental measurements using the same measurements facilities as in Chapters 3 and 4.

We therefore use expression (5.53) as our objective function in order to optimize our periodic structure element, only with the reference plane shifted to that of the surface of the periodic structure (as discussed in Section 5.3.5)

$$\textit{Objective function \#1:} \quad \angle\Gamma = Arg\left\{\frac{\Psi}{\Psi^*}\right\} - 2d\omega\sqrt{\mu\varepsilon} \tag{4.54}$$

where the function Ψ is the trace of the characteristic mode matrix, used throughout the thesis and first introduced in Section 3.3.5. The term $-2d\omega\sqrt{\mu\varepsilon}$ is included to shift the reference plane from that of the ground plane to the surface of the periodic structure.

The optimization technique used is identical to that of Chapters 3 and 4, whereby a GA/MoM optimizer is used as the search function, the DMM method is employed for computational simplicity and (5.54) is used to obtain the desired phase of the reflection coefficient.

5.4.2 –The Fragmented Reflectarray Element and the Indexing Approach to Element Shape Synthesis

The most commonly used technique of designing reflectarray elements is the variation of geometrical parameters. For example, consider the patch element (Figure 5.16) – the canonical test case for reflectarray designs. By varying either the patch length or width, one can control the reflection phase of the element in question. This variation of a geometrical parameter results in the reflection phase curve (known as an S-curve) shown in Figure 5.16. Multiple geometrical parameters can also be varied such as the variation of both the length and width. In this scenario, a reflection phase surface is generated rather than a reflection phase curve. More will be said about this approach in Section 5.4.4.

An alternative approach is proposed here whereby an element is described by an index rather than a particular geometrical parameter. In the development of our reflectarray synthesis technique, the index will correspond to a particular reflection phase. For example, index 1 might refer to a reflection phase of 180 degrees, index 19 to 0 degrees and index 36 to a reflection phase of -170 degrees. Under such conditions, the reflection phase becomes quantized with steps of 10 degrees with increasing the index number.

This indexing approach allows for an entirely new approach for reflectarray design whereby each required reflection phase can be synthesized uniquely in an element-by-element approach rather than the variation of a small number of geometric parameters. In our work we will consider elements that reside in lattices with electrical dimensions below $\lambda/2$ known as sub-wavelength elements. In particular we shall use $\lambda/6$ lattice sizes. Consider now the DMM method described and utilized throughout Chapters 3 and 4, applied to the synthesis of reflectarray elements. Assume the starting shape used in the DMM method begins with a square patch reflectarray element, meshed using 722 triangles. Such a starting shape is depicted in Figure 5.18(a), and an example of an element shape-synthesized from this starting shape shown in Figure 5.18(b). It is then feasible, using the objective function (5.54) from Section 5.4.1 to synthesize reflectarray elements with reflection phases that differ by steps of 10 degrees, with the resulting elements shown in Figure 5.18(c). Note that these elements are shown strictly for illustrative purposes and are not intended for practical use; but similar ones will be used successfully in Section 5.4.6. We shall denote these elements as sub-wavelength fragmented elements.

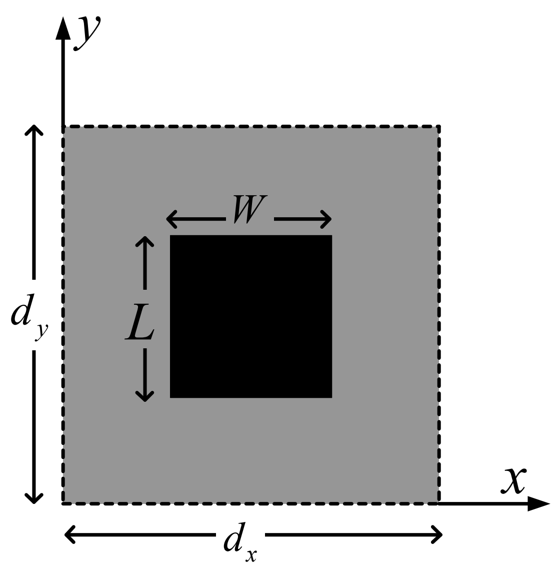

Figure 5.16 – Example canonical reflectarray element: the square resonant patch with an adjacent ground plane

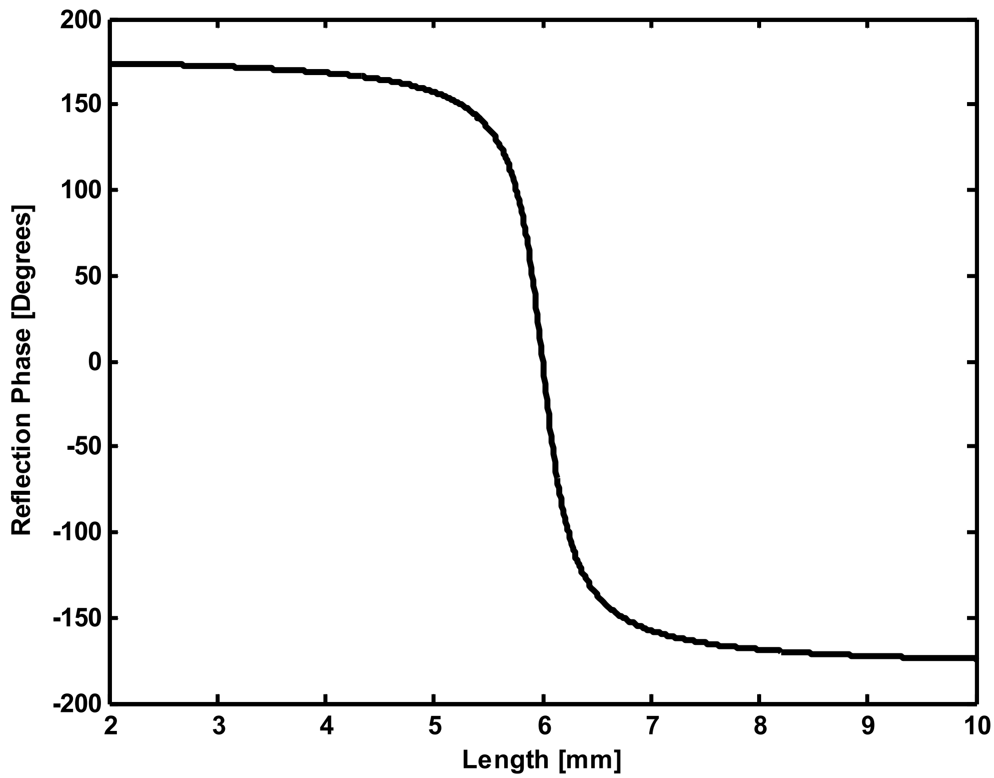

Figure 5.17 – Reflection phase of the canonical infinite periodic structure of patches over a ground plane

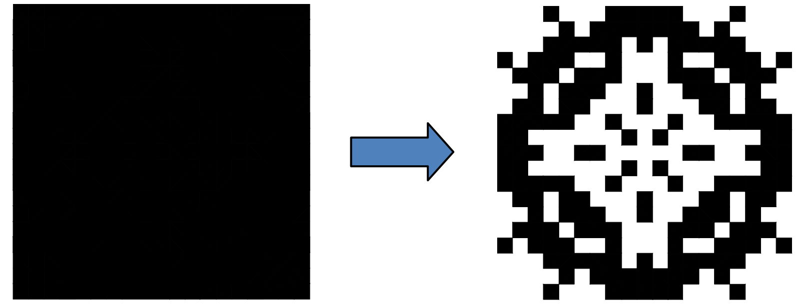

$Genome = \left[1111111\ldots111111111\right]$ $Genome = \left[1001111\ldots0110100101\right]$

(a) (b)

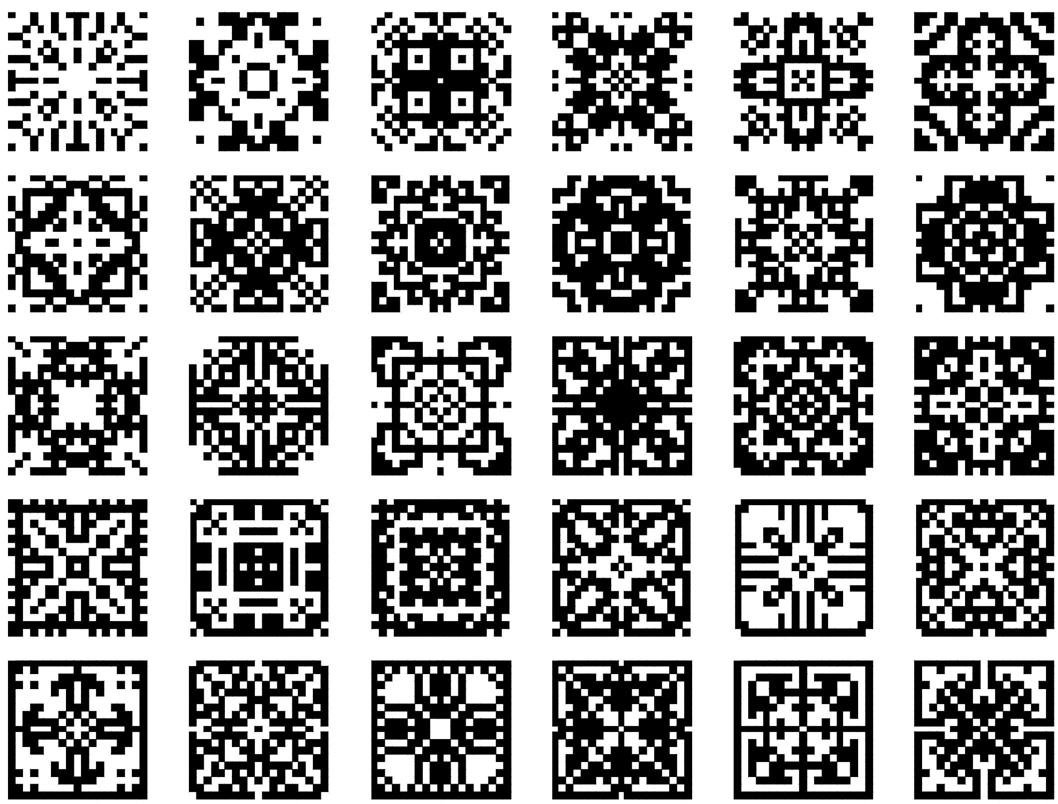

(c)

Figure 5.18 – Example fragmented elements including the starting shape shown in (a) consisting of a solid patch element which is then shape synthesized into (b) a particular element. A collection of fragmented elements is shown in (c) where each element has a unique reflection phase. Starting with the top-left element and working from left to right (in "matrix fashion") the elements' reflection phase begins at 180^{o} and decreases in 10 degree steps to -120^{o} for the bottom-rightmost element. Note these elements reside in a 4mm square lattice, the elements themselves being 3.8mm square and exist in vacuum over an infinite ground plane at a distance of 4mm. The resulting reflection phase is computed at 12 GHz.

5.4.3 –Symmetry and Optimization of the Fragmented Elements

Reflectarrays are often designed for satellite communications and are frequently required to properly handle circularly polarized (CP) signals [12]. Thus the elements in many reflectarrays must be designed such that the desired reflection phase is obtained for an incident CP plane wave as opposed to a linearly polarized (LP) wave. One can obviously excite an element with a CP wave and tune its geometrical (or otherwise physical) parameters until the desired reflection phase is obtained. On the other hand, one can alternatively ensure that the element has identical reflection phase response to any two arbitrary orthogonal linear polarizations. This is easily accomplished by maintaining symmetry of the new fragmented element such that the element appears unchanged after a 90 degree spatial rotation. Another means of describing such a scenario is the enforcement of identical symmetry along two orthogonal planes. An example of such an element is shown in Figure 5.19(c). This element has the additional benefit that is can be used interchangeably for both LP and CP reflectarrays, since the reflection phase is valid for both CP and LP incident plane waves. An example element with one plane of symmetry is shown in Figure 5.19(b) and an element without any symmetry in Figure 5.19(a). Any of these elements can be used in a linearly polarized reflectarray, but the benefits of the symmetry shown in Figure 5.19(c) are numerous as discussed.

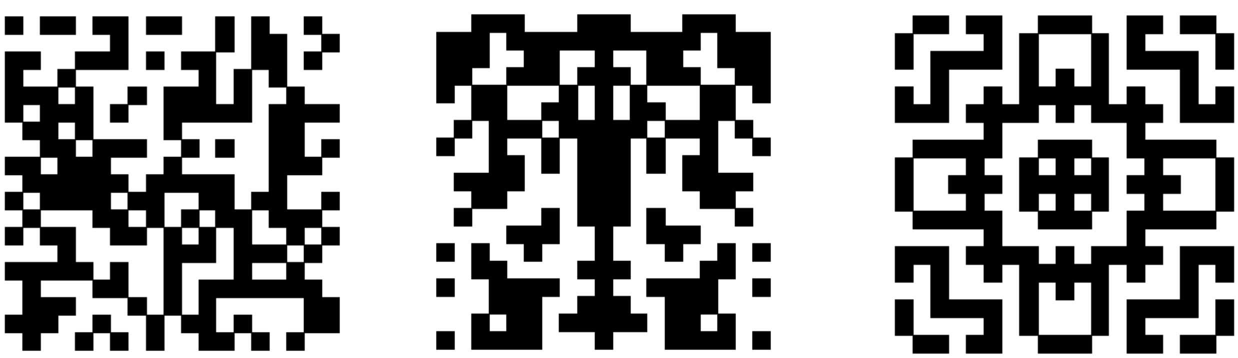

(a) No symmetry (b) Partial Symmetry (c) Full Symmetry

Figure 5.19 – Example fragmented elements exhibits varying degrees of symmetry from (a) no symmetry, (b) partial symmetry along a single plane and (c) symmetry along two planes with the additional property of identical symmetry along both planes which we will denote full symmetry

5.4.4 – Reflectarrays: The Periodic Structure Approximation

A reflectarray is fundamentally not a periodic structure and is better described as a finite array of reflecting elements. Nevertheless, periodic structure analysis is indispensable in describing reflectarray performance, in particular at the element level. Locally, a reflectarray can appear like a periodic structure with aggregates of elements sharing similar geometrical properties. This is characteristic of reflectarrays used to emulate parabolic reflectors since the required reflection phase can be defined as a monotonically increasing function from the center of the reflectarray outwards to its extremities.

The greater the geometrical variation of the elements in the reflectarray, the greater the potential for phase errors over the surface of the reflectarray. This phase error over the surface of the reflectarray results in a decrease in the reflectarray aperture efficiency. Various papers have attempted to quantify these errors [13] – [16]. In particular, using what is known as the "surrounded element technique", the authors of [13], [14] attempt to simulate the presence of non-identical adjacent elements and determine the reflection phase under these non-periodic or quasi-periodic conditions. The authors of [15] have pointed out that a source of error in reflection phase occurs in the vicinity of Fresnel zone boundaries, corresponding to the regions in the reflectarray where the phase rolls over from -180 to 180 degrees. Across this boundary the element size often varies quite dramatically which will act to introduce reflection phase errors due to the dramatic breaking of periodicity. The authors of [16] propose the first genuine attempt at mitigating these errors through the use of a novel element known as the "phoenix element". The novelty of this element is that the variation of the elements' geometric parameters maintains a relatively similar shape from 180 degrees reflection phase, through resonance and towards -180 degrees reflection phase. Most importantly, the geometrical parameters near -180 degrees are nearly identical to the geometrical parameters around 180 degrees, leading to a smooth transition around the Fresnel zone boundaries. However, the element is still subject to a small number of geometrical parameters and the variation is still noticeable over the surface of the reflectarray. We conjecture that should adjacent elements maintain a high degree of geometrical similarity, the reflection phase error will be reduced and the reflectarray gain will be maximized. The fragmented element idea introduced in Section 5.4.2 will be used to achieve this, as shown in the next two sections.

5.4.5 – New Reflectarray Design Technique: Similarity Optimization using Fragmented Elements

We are motivated to better approximate the infinite periodic structure in the implementation of the reflectarray. We propose that a new design technique whereby adjacent elements are optimized to have maximum physical (geometrical) similarity will aid us in this endeavour. We find a particularly good fit with the DMM / GA optimization technique since geometrical properties are coded in a binary genome with each geometrical feature (a pixel or triangle) being described by a 0 or 1. A 0 implies the removal of the pixel, while 1 indicates keeping the pixel (the pixel in this example consists of an RWG expansion function with two triangles). This offers us an unambiguous computational measure where the similarity between adjacent elements can be computed in a straightforward manner by performing a binary XNOR[12] operation between the element's genomes. The XNOR operation is normalized by the total number of bits in the genome, giving us an expression that is effectively a percentage measure of the similarity between elements. Consider elements A and B (shown in Figure 5.20) with genomes G_A and G_B. The percentage similarity between elements is fairly low at 30.19%. Further, consider elements C and D (shown in Figure 5.21) with genomes G_C and G_D. Their similarity is quite high at 78.67%. What is important to note is that each pair of elements (A&B and C&D) differs in reflection phase by 10 degrees. If used in a reflectarray context, there is a very high likelihood that these elements would appear in adjacent cells within the reflectarray. One cannot speak with certainty that the elements will be adjacent in any given reflectarray, only that elements with similar phase will, at the very least, have a higher chance of being adjacent.

Our proposal here is that a reflectarray consisting of adjacent fragmented elements with a high degree of similarity, with similarity measures as shown in Figure 5.21, will have lower phase error and thus higher aperture efficiency than a reflectarray with elements exhibiting reduced element similarity as shown in Figure 5.20. In truth, this is not the ideal approach to minimizing phase error as the fundamentally correct approach would be to directly observe the reflection phase in regions where the

[12] The XNOR operation is often written $\overline{A \oplus B}$ (the negation of NOR). XNOR's truth table is simply: $\overline{1 \oplus 1} = 1$, $\overline{1 \oplus 0} = 0$, $\overline{0 \oplus 1} = 0$ and $\overline{0 \oplus 0} = 1$. We can state this simply as if the two arguments are the same, you obtain true, if they are different, you obtain false.

elements vary shape over the surface. One would then shape-synthesize the elements to minimize the phase error in those particular regions. In order to do so, one would need to simulate aggregates of many elements numerous times to account for the many different regions on the surface of the reflectarray. Such an approach is very costly computationally in terms of both the time required and the memory requirements for the simulation. It can be shown that using the fragmented element approach requires substantial memory requirements (exceeding 96 GB of memory to simulate even 50 elements with symmetries exploited), bearing in mind that a moderately sized reflectarray, especially of the sub-wavelength variety, can contain over 10,000 elements. Entire reflectarrays can be simulated [17] but such simulations require elements with simple shapes such as patches and loops which have lower memory requirements than the more detailed fragmented elements.

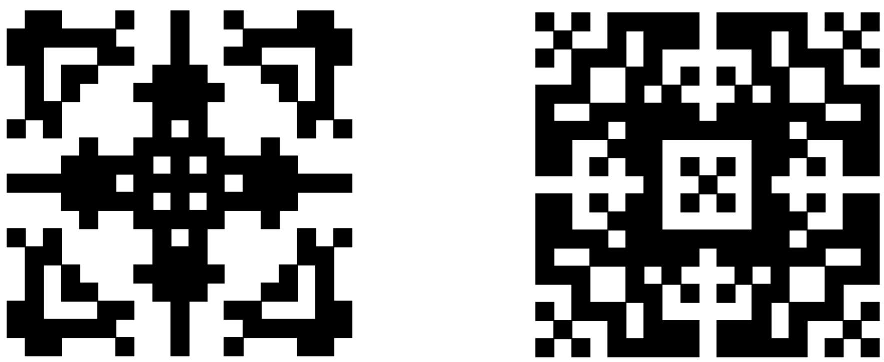

$G_A = [1001001\ldots100000111]$ (a) $G_B = [1011101\ldots110110111]$ (b)

Figure 5.20 – Two example fragmented elements with a fairly low degree of similarity. Using the described normalized XNOR operation we find a % similarity of 30.19% between the elements.

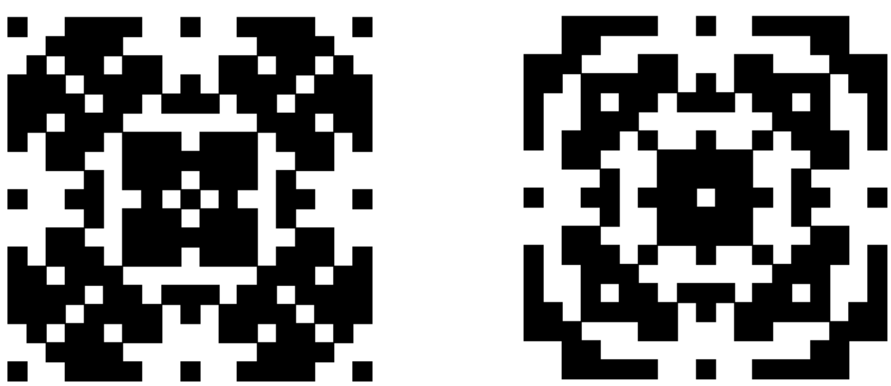

$G_C = [1111001\ldots100011111]$ (a) $G_D = [1111101\ldots110111111]$ (b)

Figure 5.21 – Two example fragmented elements with a fairly high degree of similarity. Using the described normalized XNOR operation we find a % similarity of 78.67% between the elements.

The proposed element shape-synthesis approach is shown in the flow diagram from Figure 5.22, and will be referred to as “similarity optimization” of reflectarrays. The synthesis begins by shaping an element with reflection phase 180^o (for example). Once this element is obtained, a new element is synthesized with reflection phase one step ahead that of the previous element (e.g. 170^o for a step of 10^o). Once the desired phase is achieved, the synthesis procedure does not proceed to the next element but rather computes the similarity the present element has with the previously synthesized element and begins to shape the elements for both its reflection phase and its similarity to the previous element. Specifying a particular allowable phase error (e.g. 170^o $\pm$ 2^o) allows for some flexibility in terms of which elements rank well in this multi-objective optimization scheme. The objective function used in the maximization of similarity between elements is given as

$$Similarity(m,n) = 100\% \times sum\left\{XNOR\left(G_m, G_n\right)\right\} / N_{bits} \tag{4.55}$$

where G_m and G_n are the genomes of the mth and nth population member, $XNOR\left(G_m, G_n\right)$ performs the XNOR logical operation in a bit-wise fashion on the genomes and N_{bits} is the total number of bits in the genome. Recall that N_{bits} is the number of triangles in the mother structure (here a square patch) which indicates that the similarity function is bound between 0% and 100% with 100% only be possible for identical elements.

Once the optimization converges (maximum similarity for a given maximum phase error) the optimizer proceeds with the next element, repeating the process. Once the last element is reached (e.g. –120^o, spanning 300^o of phase range) the optimization can conclude. However, it was determined that additional passes prove fruitful in terms of the similarity between elements and the optimization process can return to the original element (180^o) and optimize its similarity with the -120^o element. In this sense, the similarity is being enforced in a cyclical (circular) fashion rather than in a linear fashion (e.g. variation of a geometrical parameter) as is usually done when designing reflectarrays using conventional elements. This implies that our optimization scheme is somewhat similar to the scheme employed in the development of the “phoenix element” in [16]. What sets this work apart from [16] is the effective use of 722 geometrical parameters, with each triangle in the moment method mesh acting as a unique geometrical parameter. If we combine triangles as pixels, this number is reduced to 361 parameters. In any case, 361 binary geometrical parameters implies a search space of more than 10^{108}

unique elements! This is the advantage of the fragmented element approach. Since the number of elements that can be synthesized from the starting shape is over 10^{108} unique structures, we propose that all canonical reflectarray elements are in fact contained within the search space. In other words, one could synthesize patch, loop, dog-bone, Jerusalem crosses, slotted patches and even the phoenix element from the possible elements that can be synthesized from the fragmented starting shape. Only the mesh density restricts this proposition. With a pixel size of 0.2mm in a 4mm lattice, we propose that such a restriction is minimal in our shape synthesis approach. This phenomenon will become evident as we shall observe patches (both regular and slotted), loops and Jerusalem cross shaped elements born out of the GA-driven fragmented element shape-synthesis approach.

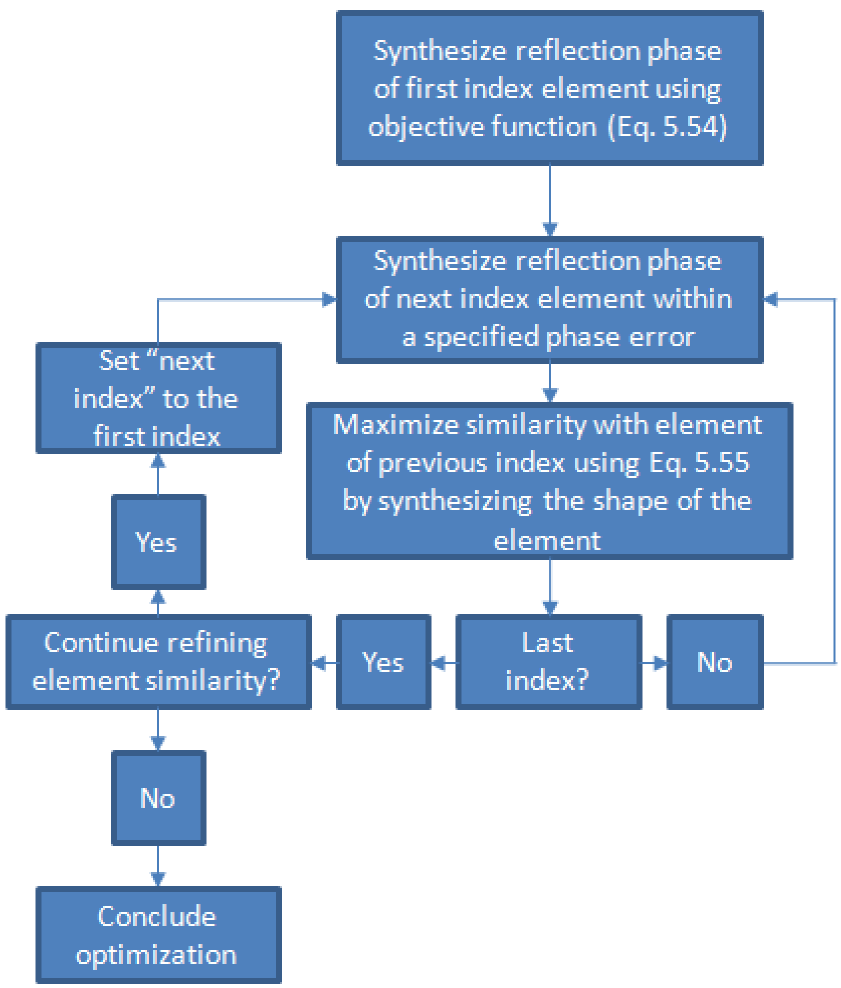

Figure 5.22 – Flow diagram of similarity shape synthesis optimization scheme for reflectarray Design

5.4.6 – Two Example Reflectarray Designs: Minimum and Maximum Similarity

An example set of reflectarray elements was optimized for maximum similarity with a reflection phase spanning from 180^o to -120^o in 10 degree steps, producing 31 distinct elements. The starting structure consisted of a 3.8mm square patch element at 12 GHz residing in a 4mm by 4mm square lattice meshed with a triangle density of 722 triangles implying an approximate “gene” density of 1 triangle per linear 0.2mm. This density was selected with conventional chemical etching limitations in mind. The distance of the element from the ground plane was set to be 4mm, though other heights could have been considered. The particular case of 4mm was selected due to the availability of high quality Rohacell™ material of this thickness. Rohacell™ is a foam-like substrate that has electrical properties similar to that of air ($\varepsilon_r \approx 1.08$ for microwave frequencies), and so our assumption of vacuum substrate (i.e. no dielectrics) is better approximated. It should be noted, however, that simulations did show reflectarray designs were possible using “vacuum substrate” thicknesses ranging from 1mm to 5mm. Additionally, a phase error of +/- 2 degrees was permitted, allowing some flexibility in terms of how the element’s similarity is optimized. The reflectarray metal pattern is to be etched on a very thin (5 mils) FR4 substrate which will be adhered to the Rohacell™ foam substrate.

The optimization process ran through five full runs, each step refining the similarity between adjacent elements, with the resulting similarity optimized elements shown in Figure 5.23. Recall that a single run optimizes all 31 elements, with each additional run acting to refine the similarity optimization in a cyclical fashion. Therefore, each element received a shape refinement a total of five times. Note that these elements are synthesized without a particular reflectarray in mind. However, due to the cyclical nature of the similarity optimization, these elements are ideally suited for pencil-beam reflectarrays as their design involves a reflection phase that is a monotonically increasing function as one observes the required phase from the centre of the reflectarray moving outwards to the edge of the surface. These elements will therefore begin with the 31st element at the center of the reflectarray and decrease in index moving outwards to the edge, thereby exhibiting a smooth transition from element to element over the reflectarray surface. Note that if one begins with element 31 and observes the change in the physical layout working backwards in index, the variation from element to element is very gradual which should yield low phase error if employed in a reflectarray design. An additional set of reflectarray elements was considered, with precisely the same physical and electrical properties, but "optimized" not for similarity but rather for dissimilarity. These elements are shown in Figure 5.24.

Some observations of the similarity optimized elements (Figure 5.23) include:

- In general, the elements are very dense in terms of the metal regions. This is likely due to the fact that any given reflection phase requires sufficient metal complexity to achieve said phase, with the similarity optimization forcing some elements that would otherwise not need to have such dense levels of metal to do so.
- The most dramatic transition in physical shape still occurs from the -120 degree reflection phase as it rolls over to 180 degrees. However, this transition is fairly smooth compared to that in other reflectarray designs [12] – [17]. Note that this implies that 60 degrees of reflection phase is missing from the collection of elements. However, it has been shown [12] that having as low as 300 degrees phase range in a reflectarray design results in a negligible loss in gain.

Some observations of the dissimilarity optimized elements (Figure 5.24) include:

- The transition from element to element is more abrupt than in the similarity optimized case.
- The overall metal density is fairly low for each element.
- An interesting phenomenon of the procedure is that every other element appears to have a high degree of similarity. In other words, element phase 121.751^{o} and 100.8877^{o} look similar, but are clearly dramatically different than element 111.0818^{o}. This may have implications on the overall performance of the dissimilarity optimized reflectarray since there seems to be reasonable degree of similarity despite the optimization's attempt to oppose such similarity.
- The most abrupt change occurs between the element with the most negative phase (index 31, -124.9806^{o}) and the element with the most positive phase (index 1, +179.8404^{o}).
- Another noticeably abrupt change occurs from -78.0638^{o} to -70.3734^{o}.

A comparison between the similarity-optimized and dissimilarity-optimized element sets:

- The elements with the most negative phase (-100^{o}, -110^{o} and -125^{o}) are very nearly identical between the similarity and dissimilarity optimized designs. This is because patch-like periodic structure elements that are sub-wavelength tend to only present capacitive surface impedance, with the structure relying on the fairly meager inductance introduced by the substrate and ground plane. This limits how negative a value reflection phase can obtain.

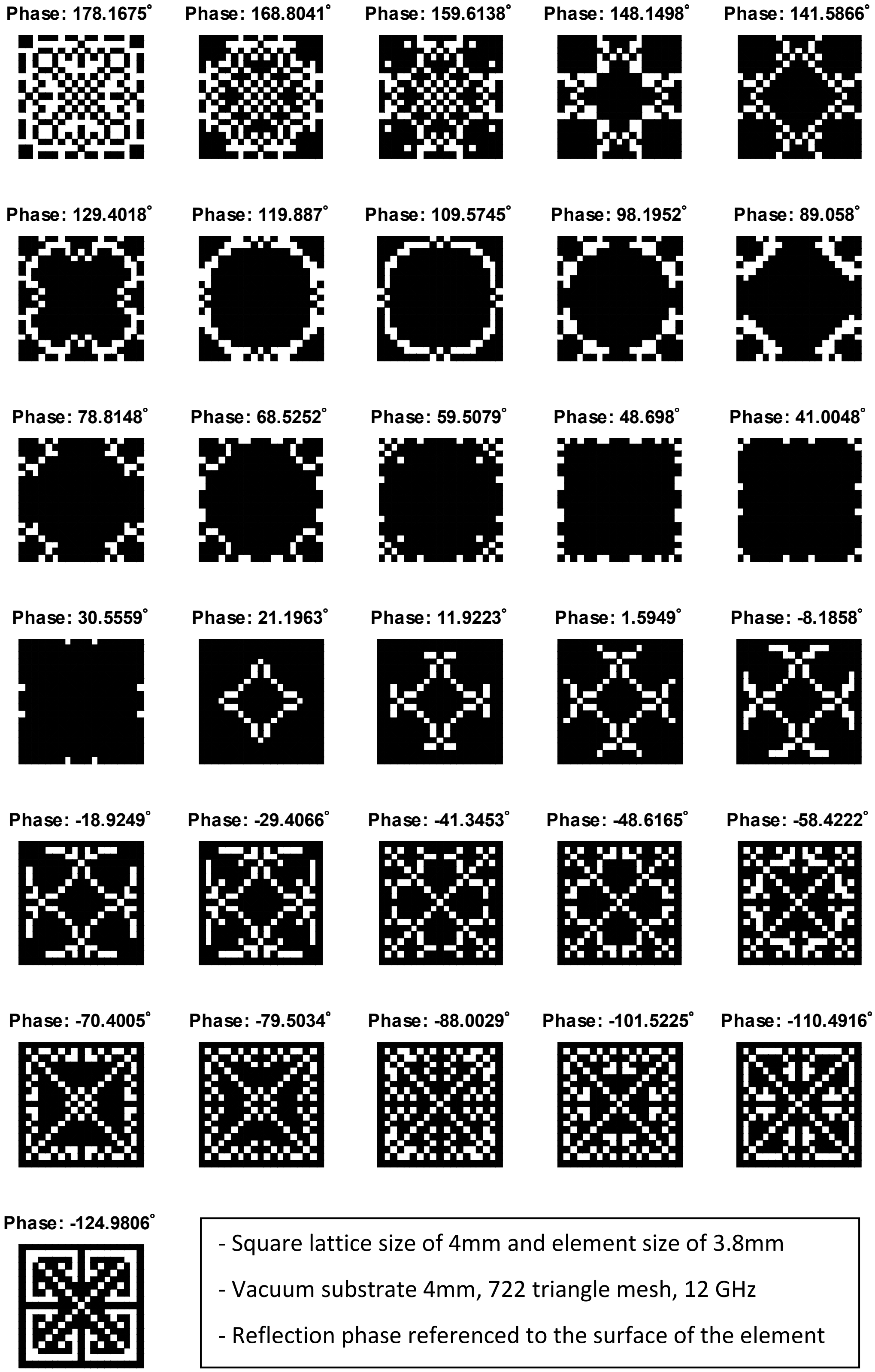

Figure 5.23 – Similarity optimized reflectarray elements

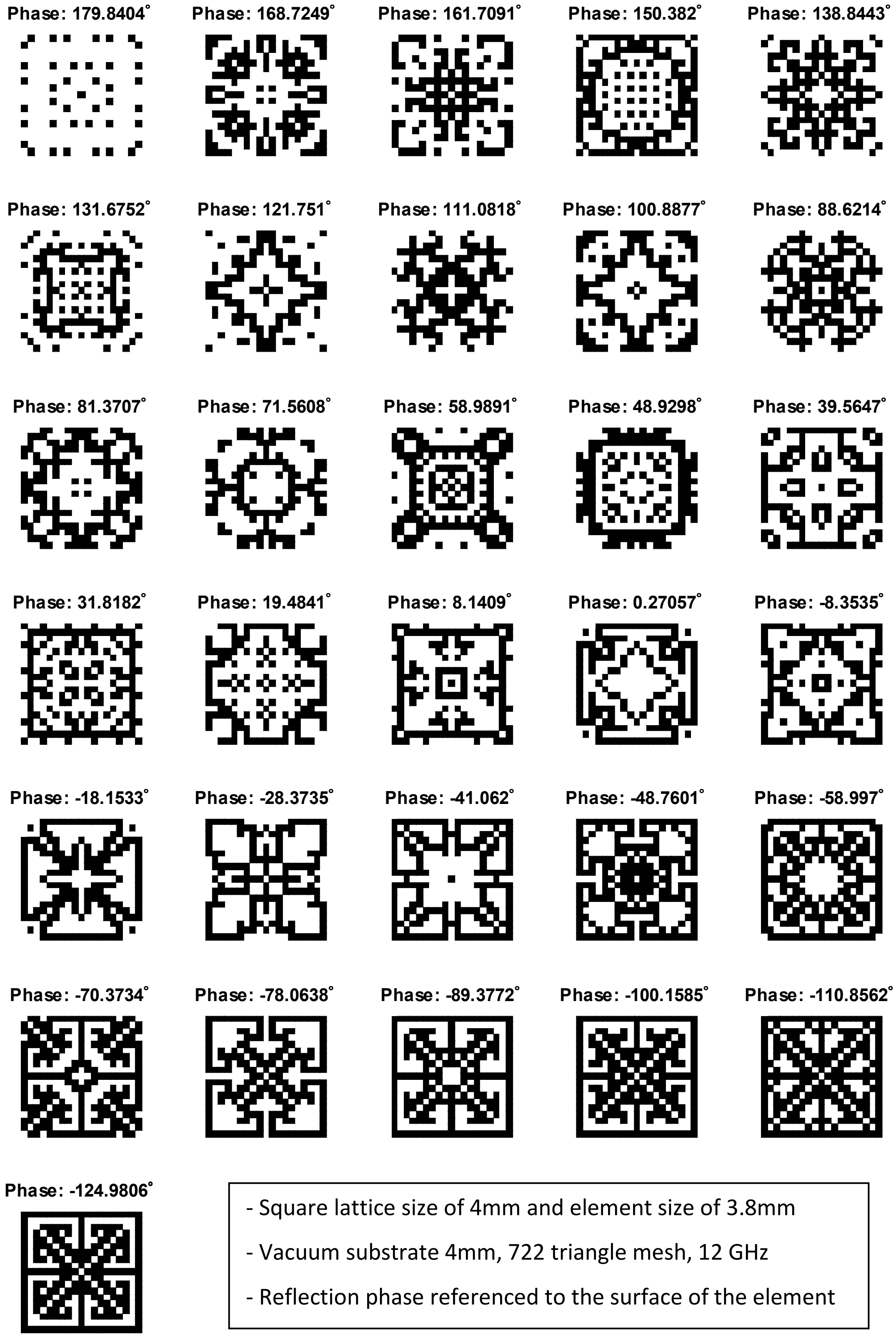

Figure 5.24 – Dissimilarity optimized reflectarray elements

Using these elements, it is possible to design a reflectarray with specified size, shape and feed location operating at 12 GHz. We choose to design an offset fed reflectarray, whereby the feed is offset to mitigate blockage of the reflectarray aperture. Such a reflectarray layout is shown in Figure 5.25. The diagram shows a 2D view of the reflectarray, but the reflectarray is a square aperture with the feed placed along the aperture's line of symmetry (y_{ref} = 0mm). The centre of the reflectarray is assumed to be located at the coordinate origin (x,y,z) = (0, 0, 0) while the feed horn is placed at (x,y,z) = (-124mm, 0, 432mm). The aperture size of the reflectarray was selected to be 396mm per side while the square lattice of the elements in the reflectarray is 4mm per side. Note that for these dimensions, the feed illuminates the reflectarray at an angle of 16^{o} relative to broadside with the resultant collimated beam directed 16^{o} off broadside to the opposite side of the normal to the reflectarray. In other words, the reflectarray is designed so that the main beam direction is in the so-called specular direction at the centre frequency. The F/D of the reflectarray (ratio of focal distance to aperture size) is $F/D = 448.44/396 \approx 1.1324$. The centre frequency is selected to be 12 GHz, a fairly common SATCOM frequency. At this frequency, the aperture of the reflectarray is just shy of 16 wavelengths along its side, indicating the reflectarray is of moderate size.

A pyramidal horn antenna is used as the feed for the reflectarray structure. Ideally, one would simulate (or retrieve from a datasheet) the location of the horn's phase centre and look to place this phase center coincident with the focal point of the reflectarray. Such a scenario best matches the spherical waves emanating from the horn onto the surface to allow the reflectarray to optimally transform the spherical wave into a plane wave. The horn antenna used was a Q-par (QSH17S15S) with mid-band gain of 15 dBi with best operation between 10 and 15 GHz. The waveguide connection was a standard WR75 (WG17). An example horn is shown in Figure 5.26. The Q-par horn has dimensions H = 50mm, W = 60mm, L = 90mm, a = 19.05mm and b = 9.525mm. For our chosen feed location and aperture size, the edge taper on the aperture of the reflectarray is approximately –10dB relative to that at the centre of the reflectarray. More details regarding the feed will be discussed in Section 5.4.10.

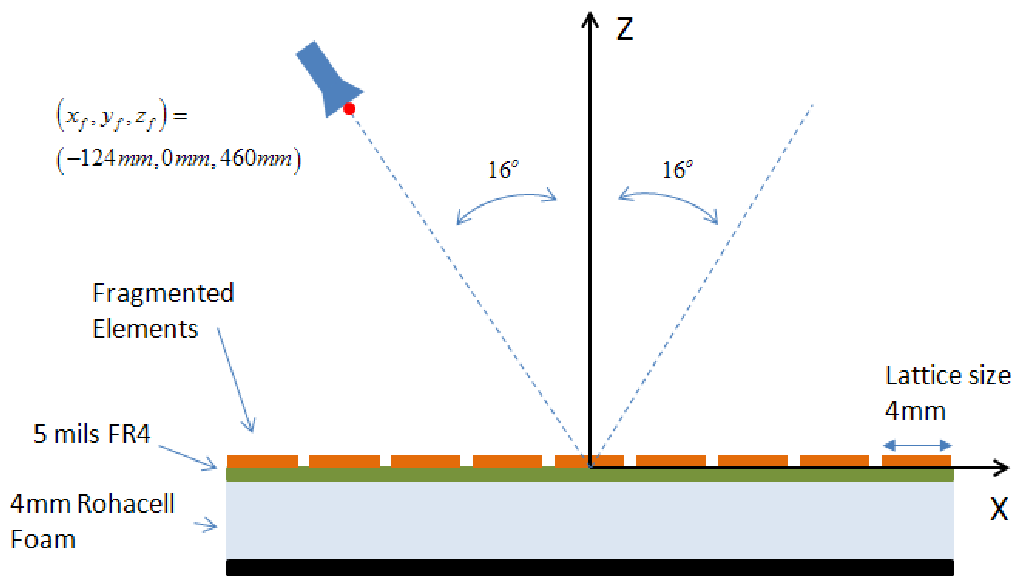

Figure 5.25 – Example Offset Fed Reflectarray Configuration

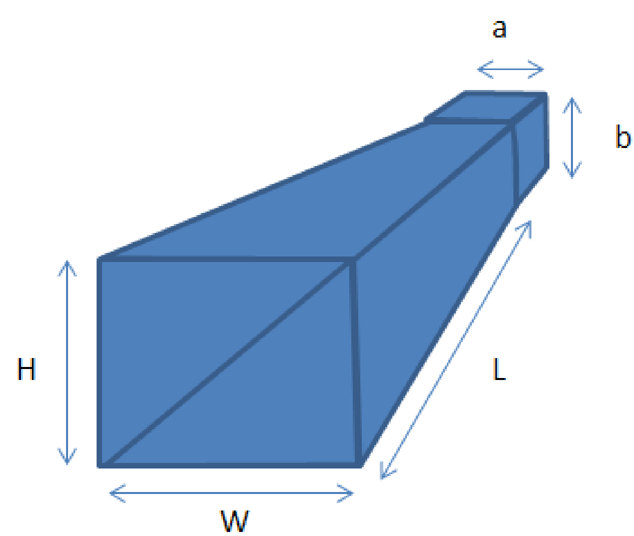

Figure 5.26 – Example feed horn with dimensions H = 50mm, W = 60mm, L = 90mm, a = 19.05mm and b = 9.525mm.

The process of implementing the reflectarray is straightforward and is accomplished by determining the necessary reflection phase that must be imposed by the elements on the reflectarray such that the incident spherical wave is corrected to produce a plane wave. Each physical location on the reflectarray has an ideal reflection phase and we find the element that minimizes the error between what is actually implemented and this desired phase. In a conventional reflectarray design, one would search for the ideal element dimension along the phase curve (colloquially called the S-curve) – in our approach we search among the indices for the element that minimizes phase error. The resulting aperture phase distribution of the reflectarray design is shown graphically in Figure 5.27 where we plot the desired reflection phase (the ideal reflectarray) and element indices (labeled "selected element indices", ranging from 1 to 31) that minimize the error with this desired reflection phase on the surface of the reflectarray. The resulting achieved reflection phase distribution is also plotted with the associated phase error over the aperture shown. As expected from the majority of reflectarray designs, the only significant phase error observed before fabrication occurs near the Fresnel zone boundaries where the element's limited phase range causes rings of phase error. However, as discussed previously, the phase error (due to limited phase range) in these regions does not greatly impact the overall performance of the reflectarray but rather the discontinuity at the Fresnel zone boundaries being the major source of phase error. Additionally, we plot the percentage similarity of each element in the reflectarray (the smallest of the percentage similarity value among the 8 possible adjacent elements) in Figure 5.28. We see that the percentage similarity is quite high, especially in the central regions of the reflectarray where the majority of power is incident from the feed. The average percentage similarity over the entire reflectarray is approximately 70.2%.

We next consider the design of the same reflectarray, only using the dissimilarity-optimized elements as our pool of elements with which to design the reflectarray. The resulting phase distributions for this reflectarray design is shown graphically in Figure 5.29 while the percentage similarity is shown in Figure 5.30. The average percentage similarity over the reflectarray is a mere 12.5%, substantially lower than the similarity-optimized reflectarray. However, it is relevant to observe that the centre of the reflectarray, which reflects the majority of the incident power, still remains with a fairly high degree of inter-element similarity. It is important to note that both reflectarrays should have identical measured gain as they have identical reflection phase and amplitude tapering as predicted by array theory. However, with electromagnetics not being a theory based solely on geometry, it is expected that the similarity-optimized reflectarray will outperform the dissimilarity-optimized reflectarray due to the reduction in phase error by better upholding the periodic structure approximation. We show in Section 5.4.8 that this is indeed the case.

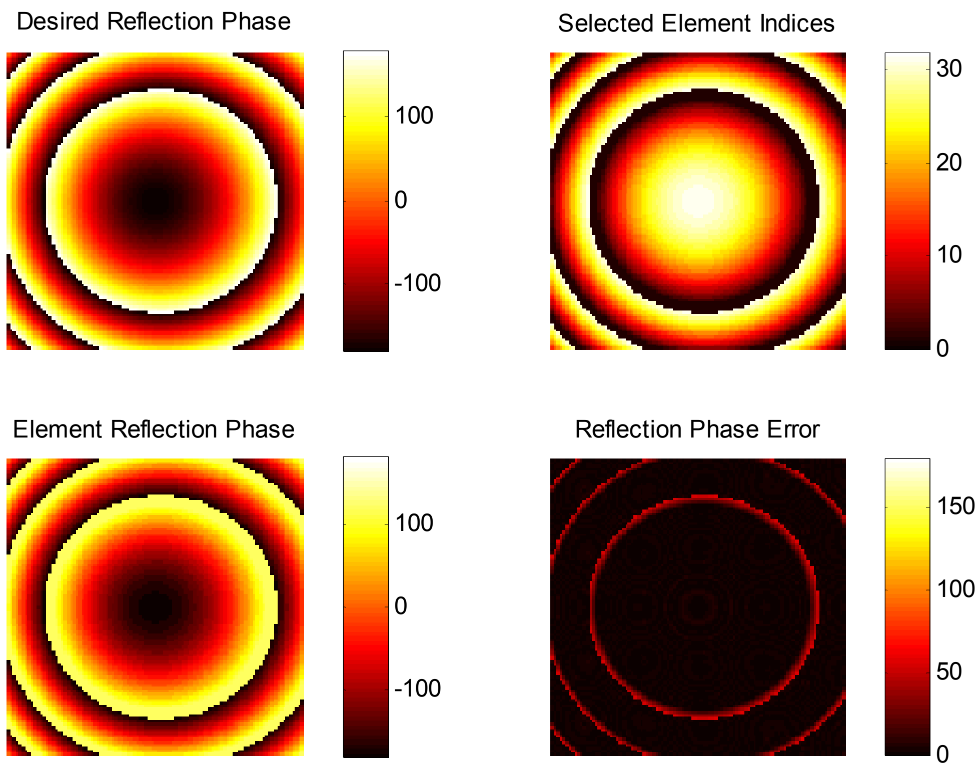

Figure 5.27 – Plots of the desired and achieved reflection phase for the similarity optimized reflectarray

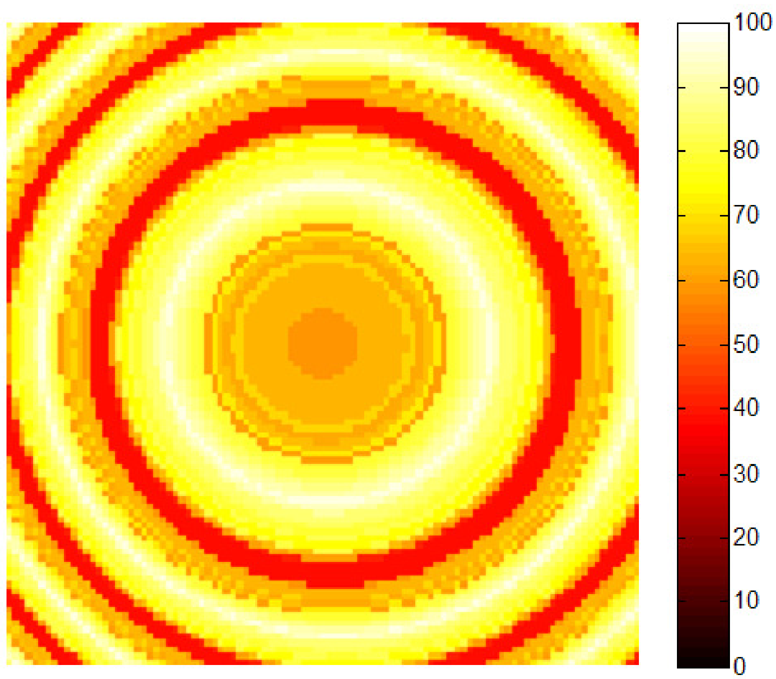

Figure 5.28 – Plot of the percentage similarity of the elements in the designed similarity-optimized reflectarray

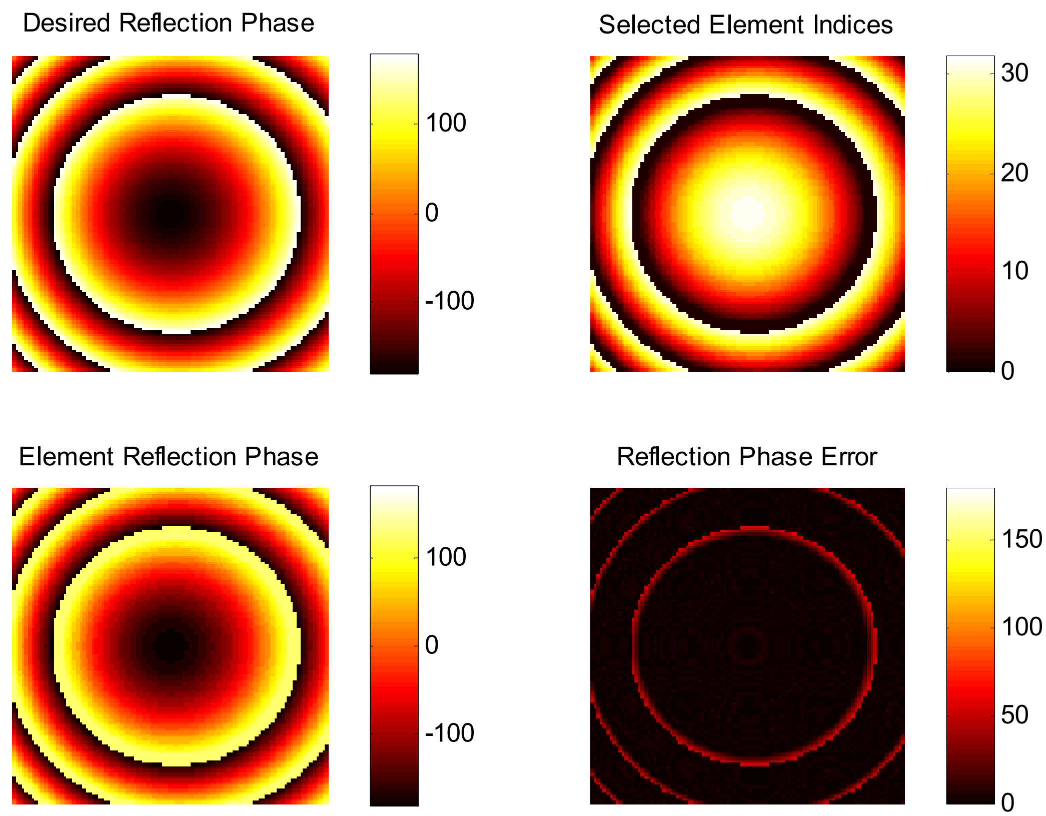

Figure 5.29 – Plots of the desired and achieved reflection phase for the dissimilarity optimized reflectarray

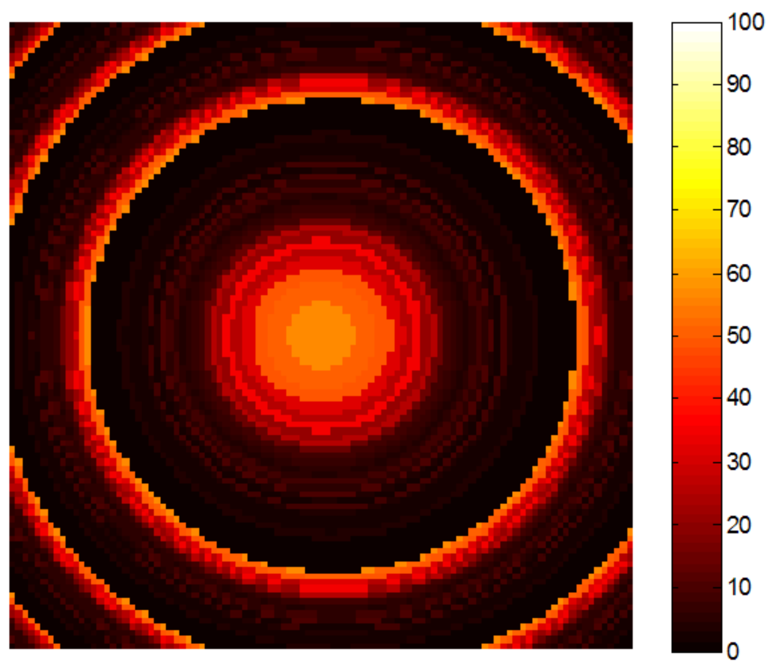

Figure 5.30 – Percentage similarity of the elements within the designed dissimilarity-optimized reflectarray

5.4.7 – Fabrication Issues with Fragmented Reflectarrays

One potential issue with fragmented reflectarray elements, and any fragmented electromagnetic design for that matter, is the issue of single vertex connections. This was discussed in Section 3.4.5 for the case of electrically small antennas. In that section we showed that the single vertices were not of major concern as far as simulation and fabrication were concerned. In this fragmented element work, the vertices are of little consequence as far as simulations are concerned, but fabrication becomes a great concern. In this reflectarray work, the smallest feature size (a pixel) is on the order of 0.2mm. Such a small feature size requires a fine etching tolerance that approaches the fundamental limitations of conventional chemical etching techniques. We expect that the single vertices, which are connections that are in theory non-physical, will present limitations in fabrication. The single vertices have a much higher likelihood of being physically connected in fabrication due to the tighter etching tolerances. The slightest amount of under-etching (copper regions not fully removed) occurring uniformly over the entire reflectarray will almost certainly impair the reflectarray's performance vis-à-vis reflection phase error. It is therefore desirable to "fix" these vertices; by "fix" we refer to the creation of two separate vertices in the moment method mesh and in the reflectarray layout. This generation of two physically separated vertices rather than a single shared vertex will hopefully mitigate any fabrication issues. An example of this single vertex issue is shown in Figure 5.31(a) while the vertices are fixed in Figure 5.31(b).

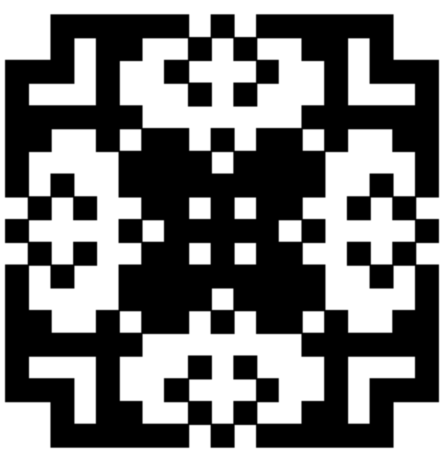

(a)

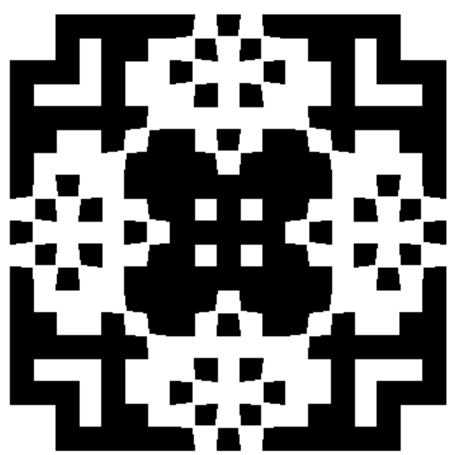

(b)

Figure 5.31 – Example reflectarray element (a) with the single vertex issue and (b) with the single vertices fixed

Another factor to consider is that the particular computational electromagnetics implementation of our element synthesis technique being used here cannot handle dielectrics (it utilizes a metal-only moment method formulation). Ergo, we need to utilize foam-like substrate with electrical properties as close as possible to vacuum. The Rohacell™ foam with relative permittivity 1.08 and very low loss tangent of 0.00035 which was used in our fragmented reflectarray fabricated designs between the elements and the ground plane. The elements themselves were etched onto a very thin (5 mils or 0.127mm) single-cladded FR4 substrate was used as the supporting structure. Two varieties of this thin FR4 substrate was used, one a higher quality variety by Isola known as GETEK RF300 while the other was a very low cost bulk FR4 substrate. The higher quality substrate was easier to etch (the copper was easier to remove from the substrate) despite both substrates having identical 0.5 oz copper. This resulted in a slight under-etching of the reflectarrays using the lower quality substrates. The two distinct substrates were used as a control to ensure that any unexpected performance discrepancies could be carefully explained. A total of four reflectarrays were fabricated as summarized in Table 5.1. Photos of the four fabricated reflectarrays are shown in Figure 5.32 for reference. All four designs used the maximum similarity design. A more detailed, high-quality professional photograph of Design D is shown in Figure 5.33. It should be noted that the element-free border around the edge of the reflectarray was required to ensure proper etching. If this boundary were included in the aperture size (as it should) the size of the reflectarray increases to 420mm per side.

Design	Vertices Fixed	Quality of FR4
A	No	Low
B	Yes	Low
C	No	High
D	Yes	High

Table 5.1 – Summary of fabricated reflectarray designs

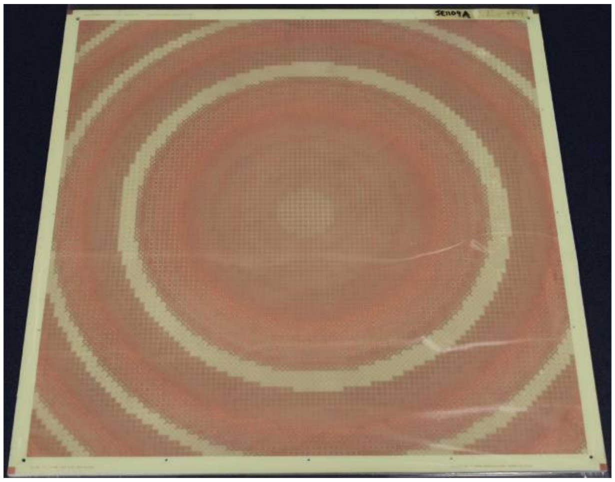

(a)

(b)

(c)

(d)

Figure 5.32 – Example four fabricated reflectarrays. Design (a) uses the lower quality FR4 without the vertices fixed, design (b) used lower quality FR4 with vertices fixed, design (c) used higher quality FR4 without the vertices fixed and lastly design (d) used higher quality FR4 with the vertices fixed. A protective plastic coating appears in the photographs which are in place to protect the copper from corrosion. This cover is removed when taking measurements.

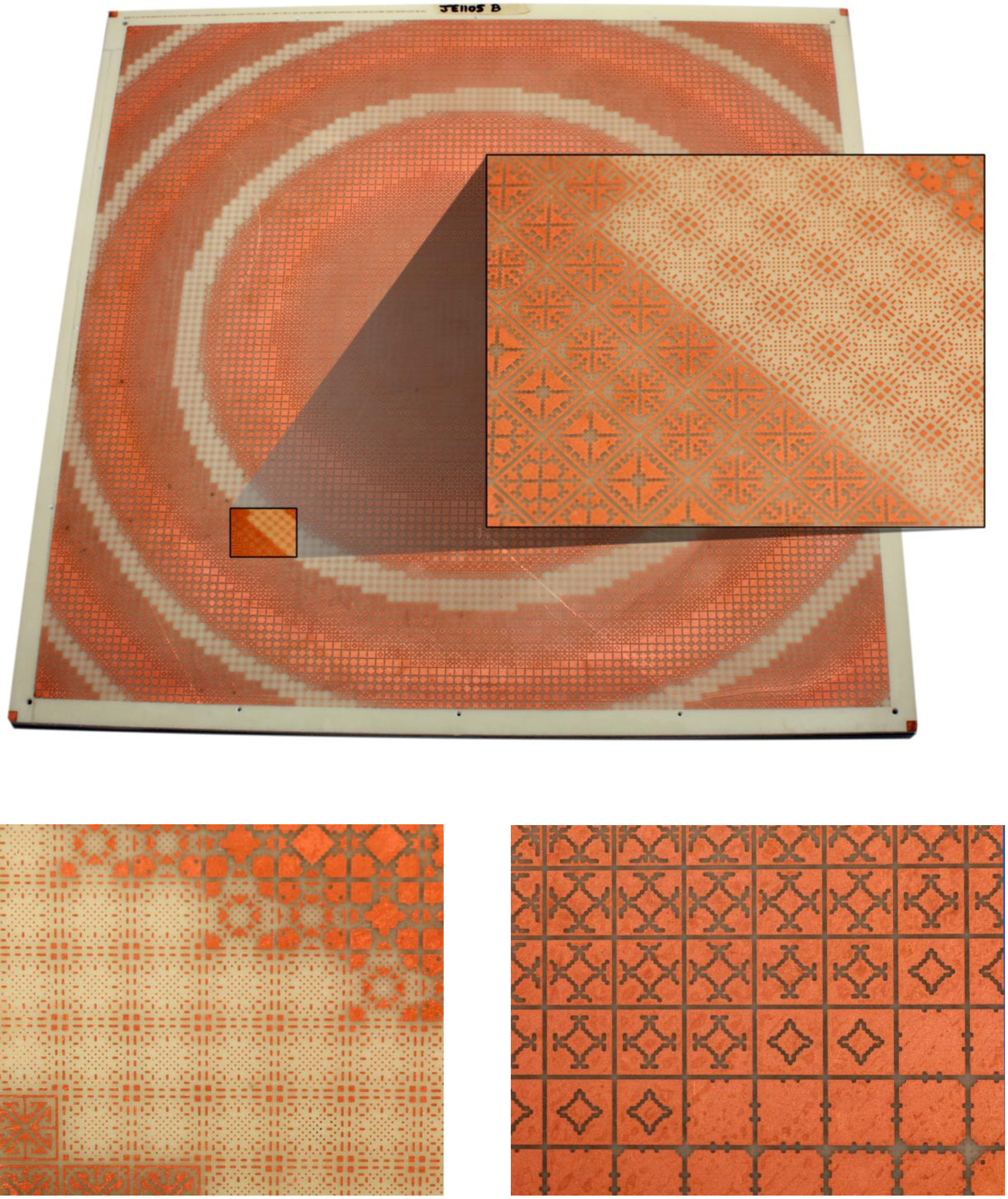

Figure 5.33 – High resolution and detailed photographs of similarity-optimized fragmented reflectarray with photo courtesy of Communications Research Centre Canada (CRC), Photographer: John Brebner.

An inspection of the fabricated designs was performed, with particular emphasis placed on the details of the elements where single vertices are (or were) present. A microscope photograph of one of the copper elements in Design A is shown in Figure 5.34(a) with a further magnified image of the single vertex connection showing a physical path for current to flow shown in Figure 5.34(b). Observations over the entirety of the reflectarray revealed that every single element investigated exhibited these physical single vertex connections. Recall that in simulation such physical connections are not present since a single vertex does not allow current to flow across it, while in the fabricated design, these single vertex connections would permit current flow and thus be problematic. By breaking the vertices, we mitigate these issues. Consider Figure 5.35, where we magnify the same element in Figure 5.34, only for Design D where we have broken the vertices before fabrication. We do not observe any unwanted physical connections which we suspect will aid in obtaining the expected performance.

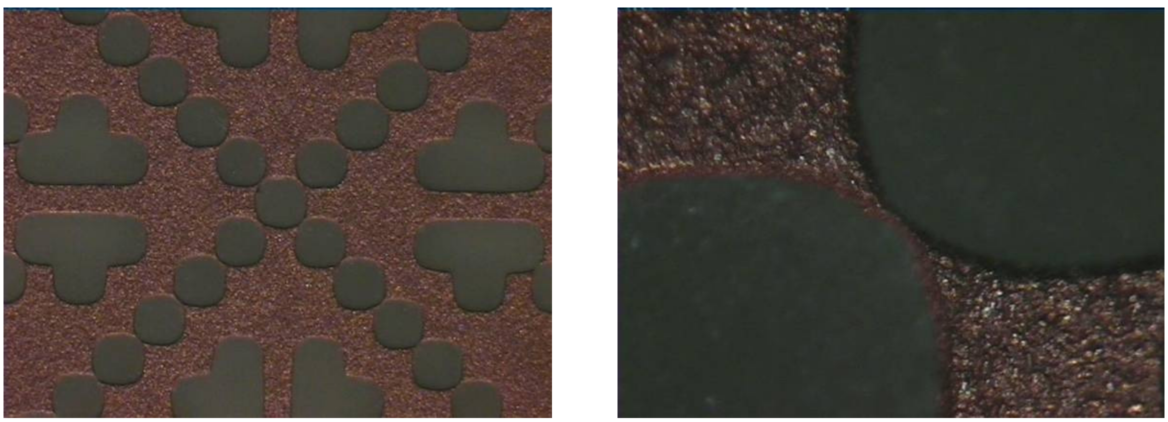

(a) (b)

Figure 5.34 – Microscope view of (a) fabricated reflectarray element showing multiple single-vertex connections and (b) closer view of a problematic single vertex connection

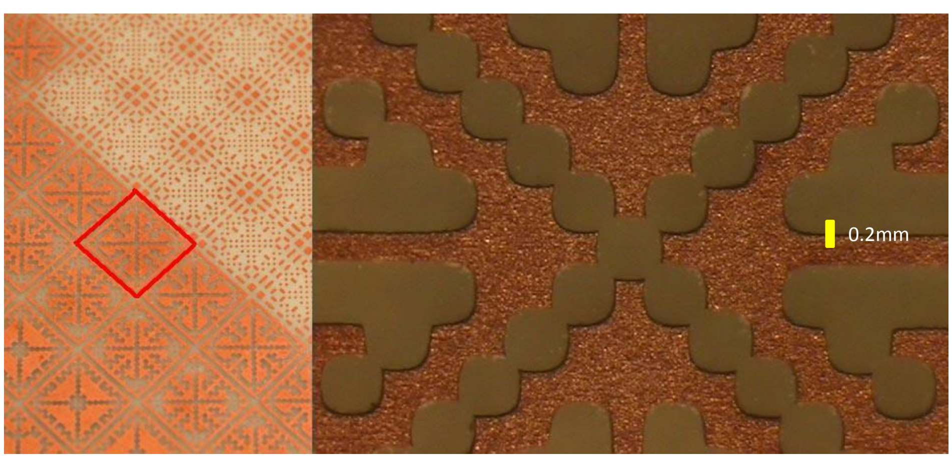

Figure 5.35 – Magnified view of a problem-free reflectarray element, achieved due to the vertex-fixing approach

Interestingly, the most laborious aspect of the fragmented reflectarray design process was not the theoretical developments, nor the element shape synthesis, nor the fabrication using conventional chemical etching techniques but rather the conversion from layout to photo mask. The full reflectarray design contains 9,801 elements, with each element being synthesized from a starting shape containing 722 triangles. Hence, the overall reflectarray can quite possibly be described using upwards of 7,076,322 triangles with the actual final result in the 6 million triangle range due to the reduced number of triangles in some of the elements. Furthermore, consider the fact that each triangle is described using three vertices, placing the total vertex count in the tens of millions. Needless to say, the complexity of representing the overall structure using triangles was out of the question for the purposes of transferring to a photo mask. The solution was to union the triangles together to create a distinct, though very complicated, polygon (or set of polygons) for each element. This acted to reduce the overall memory requirements and made it possible, although still difficult, to generate photo masks. Paradoxically (and perhaps ironically), the time requirements to simply generate the photo mask was greater than the time required to design the actual reflectarray, including the generation of the impedance matrix, through the element shape synthesis, to the selection of the elements. It is an interesting engineering observation to note the weakest links within the design chain, which in this case were the methodologies of transferring the design to photo mask.

5.4.8 – Comparison of Measured Results for the Four Fabricated "Similarity Optimized" Reflectarrays

The four fragmented reflectarray antennas were measured in a far-field anechoic chamber. All antennas were measured twice to check for consistency. The antennas were also re-measured after 4 weeks to check repeatability of the measurement. No notable discrepancies were observed between measurement sessions. Fragmented reflectarray Design A is shown mounted for measurement with its feed and test jig in Figure 5.36. The antenna gain in the specular direction vs. frequency of the four antennas is shown in Figure 5.37. The resulting far-field gain pattern of the four designs is shown in Figure 5.38 at 11.2 GHz (the frequency at which peak gain occurs in all four designs) and at 12 GHz in Figure 5.39 (which is the design frequency). Cross-pol measurements are shown in Figure 5.40. It is abundantly clear from Figures 5.37 – 5.40 that the best performance is found using the higher quality substrate and with the individual element single-vertices fixed in the antenna layout (Design D). There is a notable shift down in the centre frequency since the peak antenna gain occurs at 11.2 GHz. This is due to the presence of the non-vacuum substrate Rohacell™, the thin but nevertheless present FR4 layer, and the glue layers that held the thin FR4 layer attached to the Rohacell™ which was subsequently glued to the ground plane (a steel plate). These differences between the simulation models and the actual fabricated reflectarrays conspire to shift the centre frequency down as higher-than-expected permittivities tend to do. A summary of these results is shown in Table 5.2. It is interesting to note that all four antennas have their peak gain shifted to the same frequency. Since the only commonality between designs is the non-vacuum substrate and glue layers, it is proposed that this is the sole source of frequency shift. If the vertex-fixing of the elements caused a noticeable phase shift, we would see a different shift between Designs A & C and Designs B & D, which is not present.

There is no doubt that we have identified the best performing reflectarray from the quartet of cases that were designed, fabricated and measured. However, more should be said regarding the performance of Design D, considering its remarkably high gain for its electrical aperture size. We shall discuss this in Section 5.4.10. However, we proceeded to fabricate the dissimilarity optimized reflectarray using the same technique as Design D (i.e. vertices-fixed using a higher quality substrate), and its performance will first be compared to that of Design D in Section 5.4.9.

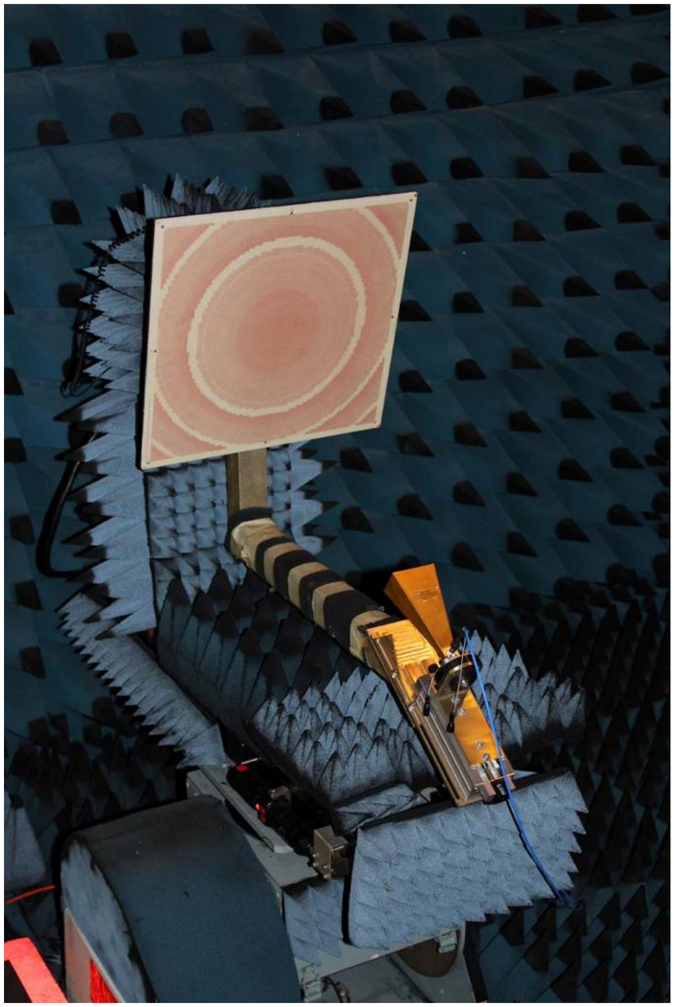

Figure 5.36 – Fragmented reflectarray 'Design A' shown in anechoic Chamber

Design	Maximum Gain (11.2 GHz)	1-dB Gain % bandwidth	1st Side-lobe Level	Cross-pol (11.2 GHz)	Maximum Gain (12.0 GHz)
A	24.30 dBi	7.4%	16.28 dBi (-8.02 dB)	-1.12 dBi (-25.42 dB)	21.82 dBi
B	29.54 dBi	10.3%	19.67 dBi (-9.87 dB)	4.69 dBi (-24.85 dB)	28.48 dBi
C	32.17 dBi	10.5%	17.16 dBi (-15.01 dB)	6.76 dBi (-25.41 dB)	31.26 dBi
D	33.06 dBi	12.3% [13]	12.44 dBi (-20.62 dB)	4.19 dBi (-28.87 dB)	32.56 dBi

Table 5.2 – Summary of electrical performance for the four fabricated fragmented reflectarrays

[13] It is worth noting that if a centre frequency of 11.6 GHz is considered, the 1-dB bandwidth increases to 18.1%.

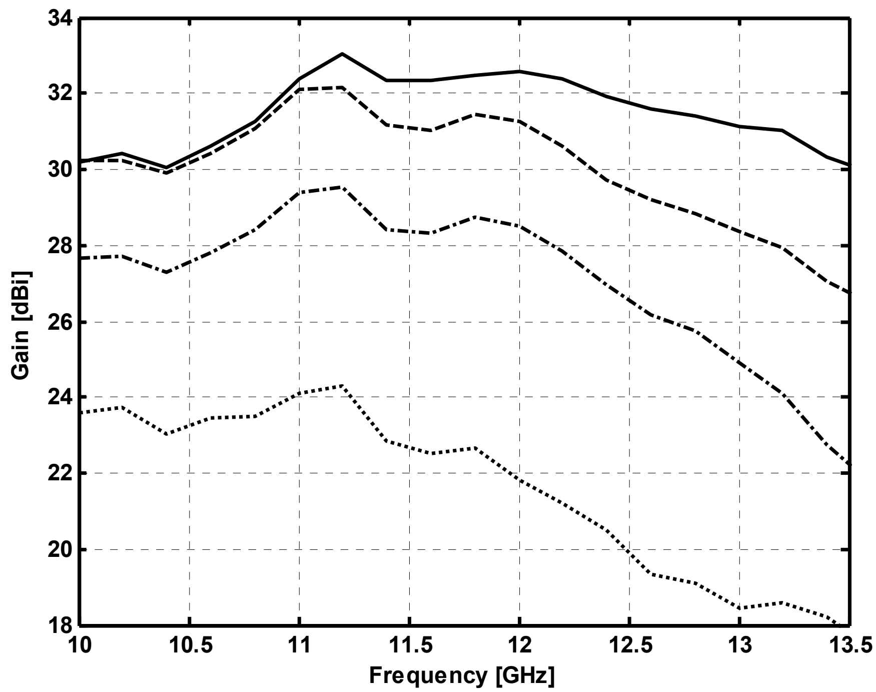

Figure 5.37 – Antenna gain in the specular direction (16° off broadside) of four fragmented reflectarrays over frequency (E-plane) with gain curves: (———) design D, (– – – –) design C, (• – • –) design B, (• • • •) design A

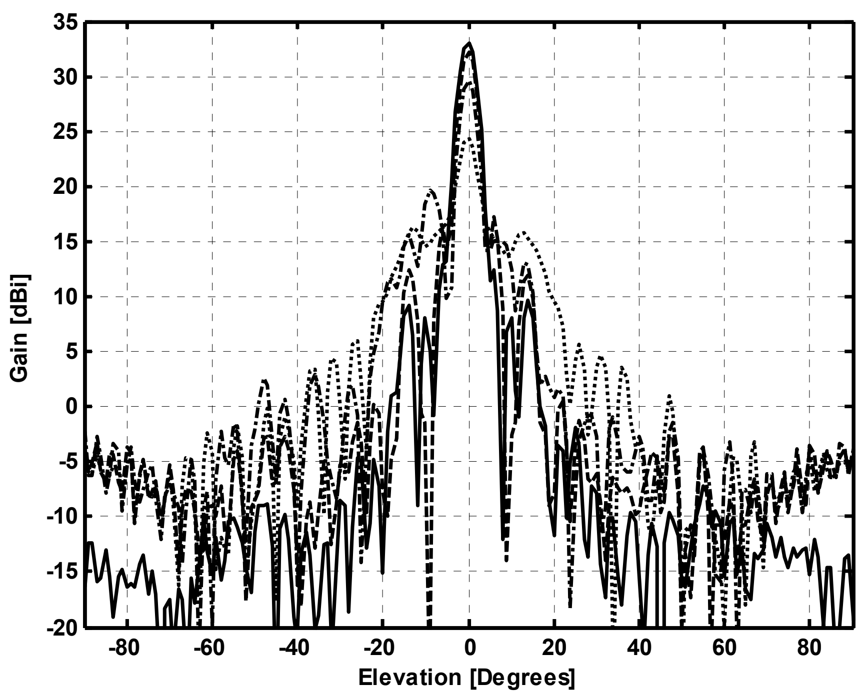

Figure 5.38 – Antenna gain pattern of four fragmented reflectarrays at 11.2 GHz (E-plane gain shown) with gain curves: (———) Design D, (– – – –) Design C, (• – • –) Design B, (• • • •) Design A

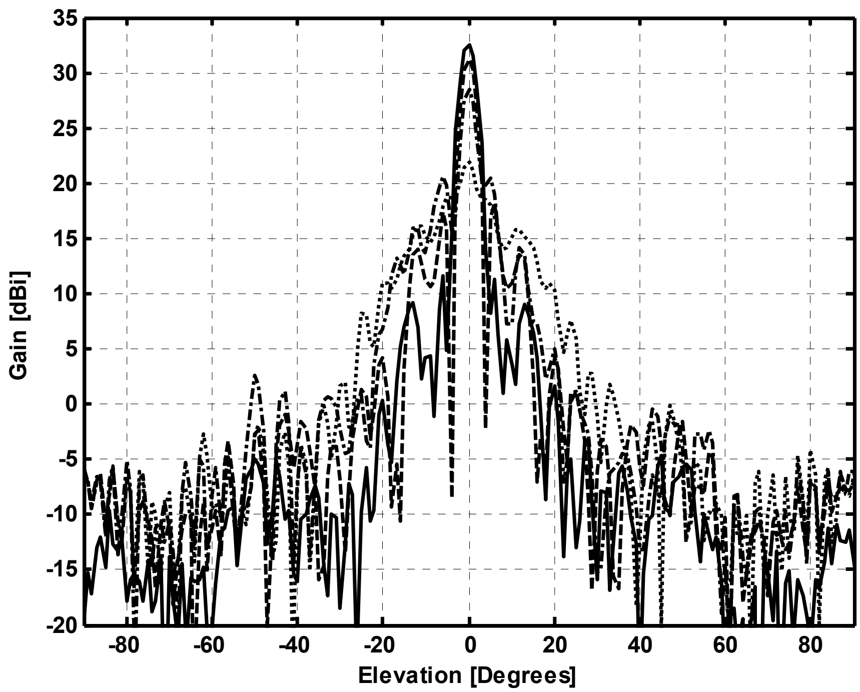

Figure 5.39 – Antenna gain pattern of four fragmented reflectarrays at 12 GHz (E-plane gain shown) with gain curves: (———) Design D, (– – – –) Design C, (• – • –) Design B, (• • • •) Design A

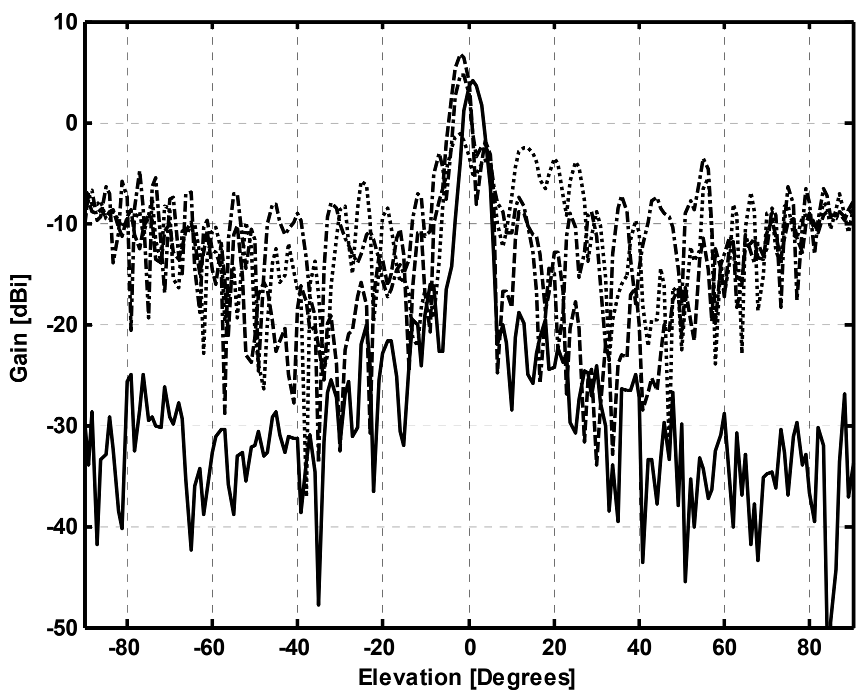

Figure 5.40 – Antenna E-plane cross-pol at 11.2 GHz of four fragmented reflectarrays over frequency with gain curves: (———) Design D, (– – – –) Design C, (• – • –) Design B, (• • • •) Design A

5.4.9 – Measurement Results Comparison of the Similarity and Dissimilarity Optimized Reflectarrays

The motivation for designing a “dissimilarity-optimized” reflectarray was to quantify what effect there is, if any, of having high and low degrees of similarity between elements on performance. After designing, fabricating and measuring the four reflectarrays from Section 5.4.8, using different substrates and layout techniques, we were confident that the higher-quality FR4 was a sound choice and that fixing the vertices mitigated the fabrication issues associated with the shared vertices of the moment method mesh. We proceeded with the fabrication of the “dissimilarity-optimized” reflectarray on the higher-quality FR4 and fixed the vertices appropriately. A comparison of the gain versus frequency of the two fragmented reflectarray designs is shown in Figure 5.41. The similarity-optimized design manages to obtain higher gain for all frequencies and on the average has at least 0.5dB higher gain (and over 1 dB at 11.6 GHz). That being said, it is clear that the dissimilarity-optimized reflectarray did not perform poorly. An additional plot of the far-field patterns of the two reflectarrays is shown in Figure 5.42, with higher side lobe levels apparent for the dissimilarity optimized reflectarray. Higher side lobes can often be attributed to phase error in reflectarray design (and array design in general).

The justifications for the reasonably good performance of the dissimilarity optimized reflectarray are found mainly in the central regions of the reflectarrays. If one refers back to Figures 5.23 and 5.24, we noted that the elements responsible for -120, -110 and -100 degrees reflection phase are nearly identical between the two design approaches. These elements predominantly populate the central regions of both reflectarrays. Coincidentally, this is also the region where the majority of power is incident from the feed and will therefore act to collimate the greatest amount of power. If the region of greatest incident power is nearly identical in both examples, then one would expect the performance of even the dissimilarity optimized reflectarray to be acceptable. Nevertheless, it is clear that the similarity optimized reflectarray yields the higher gain with no significant additional effort over a reflectarray that has not been similarity-optimized and is therefore an attractive design approach for high gain reflectarray design. A side-by-side comparison of the similarity and dissimilarity reflectarray is shown in Figure 5.43(a) and 5.43(b) while a closer look at the outlying and central regions of the dissimilarity optimized reflectarray is shown in Figure 5.44. A fairly strong similarity between elements is observed for the central region while outlying regions show dissimilarity, albeit with lower incident field amplitudes from the feed.

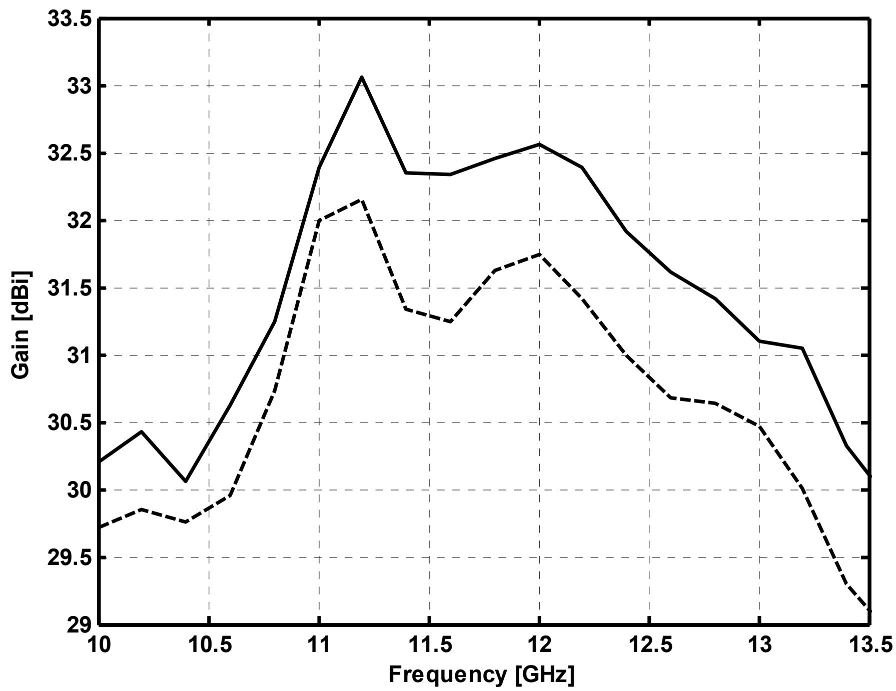

Figure 5.41 – Plot of Gain versus Frequency for the Similarity (———) and Dissimilarity-Optimized (– – – –) Reflectarrays

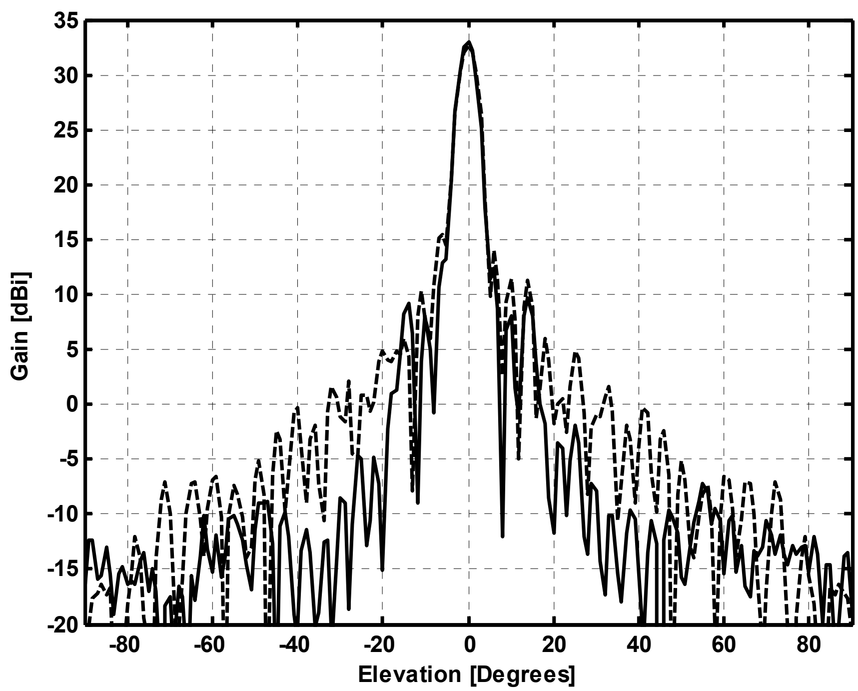

Figure 5.42 – Plot of the gain pattern at 11.2 GHz for similarity-optimized reflectarray (Design D) shown with (——) and the dissimilarity-optimized reflectarray shown as (– – – –)

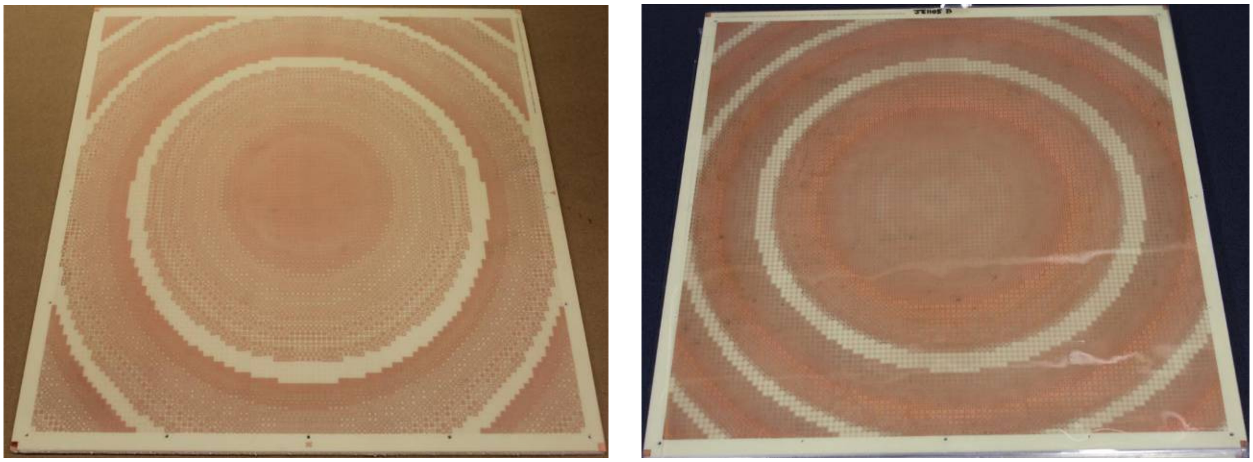

(a) (b)

Figure 5.43 – Photographs of the (a) dissimilarity and (b) similarity optimized Reflectarrays, side-by-side comparison

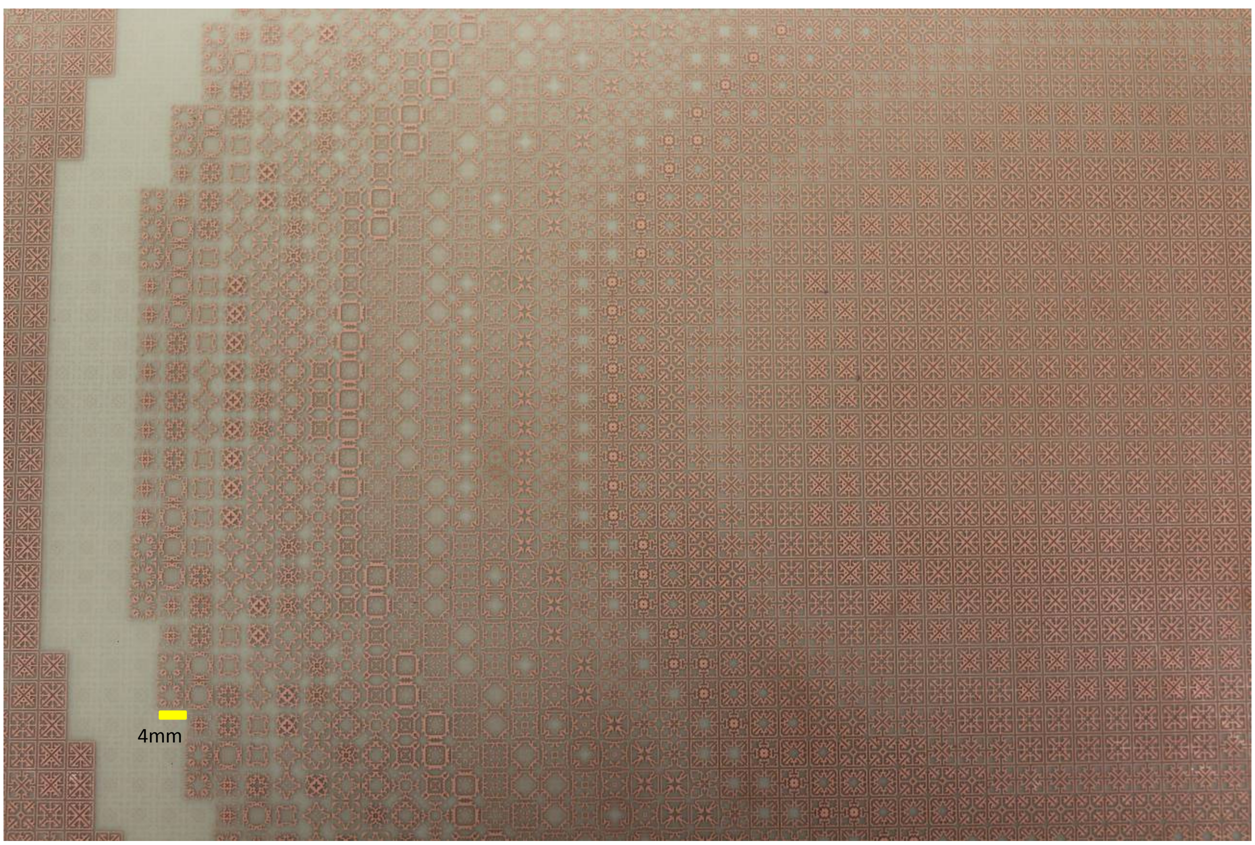

Figure 5.44 – Detailed photograph of dissimilarity optimized reflectarray shows fairly strong similarity within the central regions of the reflectarray, with regions having dissimilarity only appearing on the outer regions away from the centre of the reflectarray and for regions where the incident power density is much lower than the power density at the center of the reflectarray

A single central row of both the similarity and dissimilarity optimized reflectarrays (99 elements in total) was simulated using HFSS. The structure was simulated to be in an infinite periodic structure, with PMC boundary conditions placed along the edge of the row, effectively repeating the rows in the manner shown in Figure 5.45 and 5.46 with the periodicity along y. While this is not representative of the true reflectarray, it is as close as current high-end simulation software and computers can reliably simulate for the fragmented elements being used here. This is principally due to the very high degree of detail each fragmented element requires[14], thereby dramatically increasing memory requirements. This single row of the reflectarray was illuminated with a plane wave from the direction of the feed location (though the feed was not included) with the resulting phase of the reflected field shown in Figure 5.47 for both the similarity and dissimilarity reflectarrays. In the same figure the desired reflection phase (given the feed location and the desired beam direction) is shown as well. It is clear that the reflected phase from the fragmented element based similarity-optimized reflectarray yields the lowest phase error and matches closely with the desired reflection phase, which is further emphasized in Figure 5.48. It is also interesting to note that the phase error caused by the reduced phase range of the elements (300^o rather than the full 360^o) is effectively non-existent in the similarity-optimized reflectarray due to the smoothness of the geometric variation across the Fresnel zone boundary. This is not the case for the dissimilarity-optimized design since the phase error is double what would be expected from truncated phase range alone. The combination of both truncated phase range and abrupt geometric transitions leads to greater-than-expected reflection phase error.

In Figure 5.49, we emphasize the simulated row (using a blue bounding box) and the regions where phase error occurs (using red bounding boxes) and note two distinct regions on the dissimilarity optimized reflectarray with large phase errors: (1) between 40mm and 80mm from the center of the reflectarray and (2) between 110mm and 170mm from the centre – these locations can be observed in Figure 5.48. In Figure 5.49, we identify these problematic regions and note that there is a very strong correlation between the regions with large reflection phase error and the regions with the lowest similarity within the reflectarray, further justifying our claims as to why superior performance is observed in the reflectarray with a high degree of inter-element similarity. It should also be noted that

[14] In order to pre-emptively address potential questions regarding whether incident fields can even "see" the small, sub-wavelength features of the elements, we direct the reader to Figures 5.23 and 5.24, where these small features are capable of delivering a full 300^o of reflection phase variation.

the similarity-optimized reflectarray shows very low reflection phase error through the Fresnel zone boundaries.

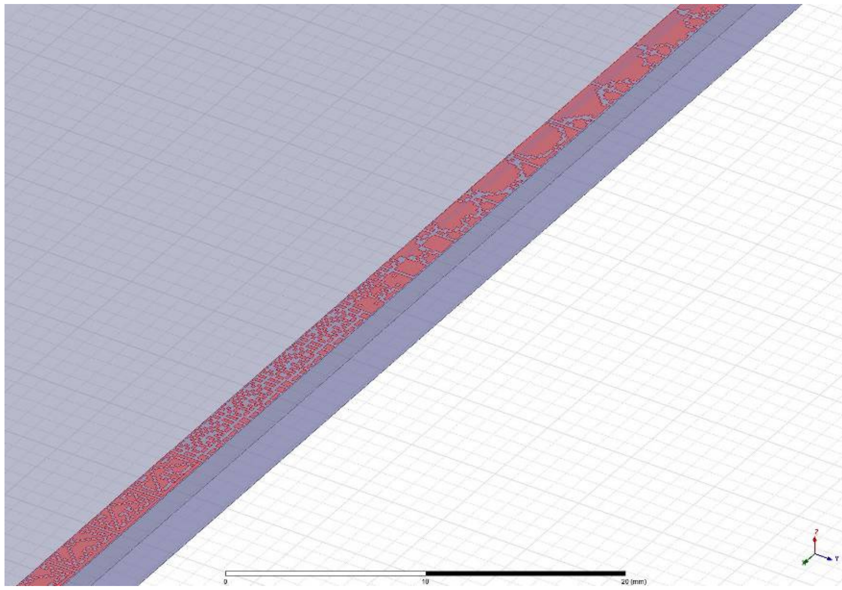

Figure 5.45 – Example single row of reflectarray (similarity-optimized) simulated in HFSS

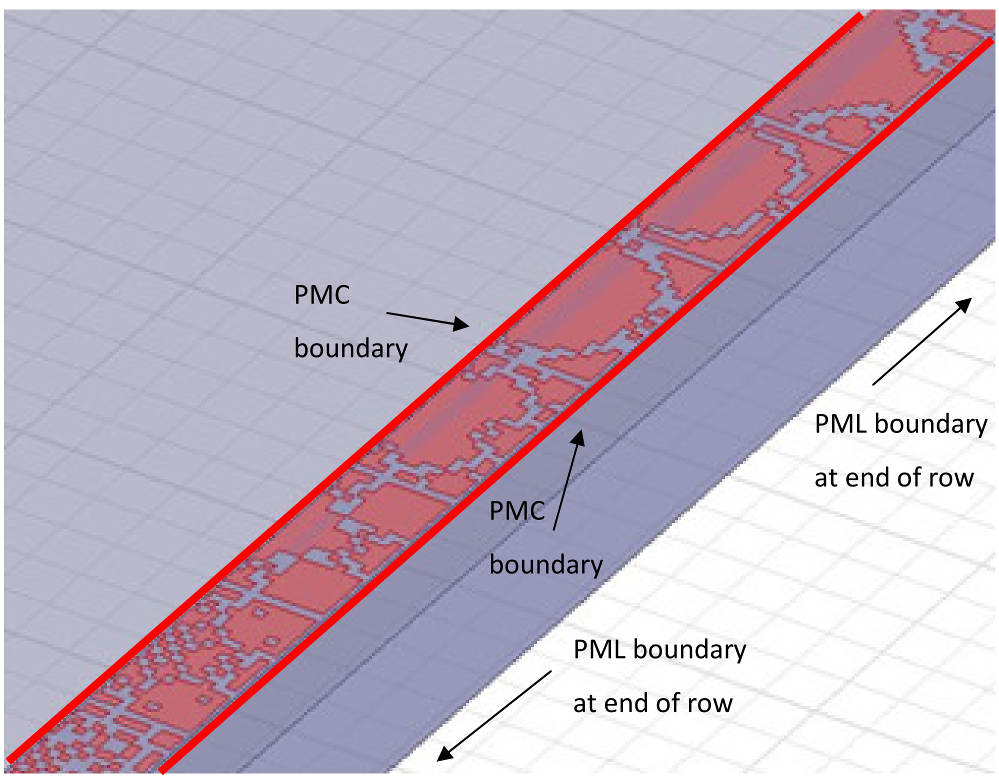

Figure 5.46 – Example single row of reflectarray (similarity-optimized) simulated in HFSS with the boundary conditions used to simulate an infinite collection of these reflectarray rows

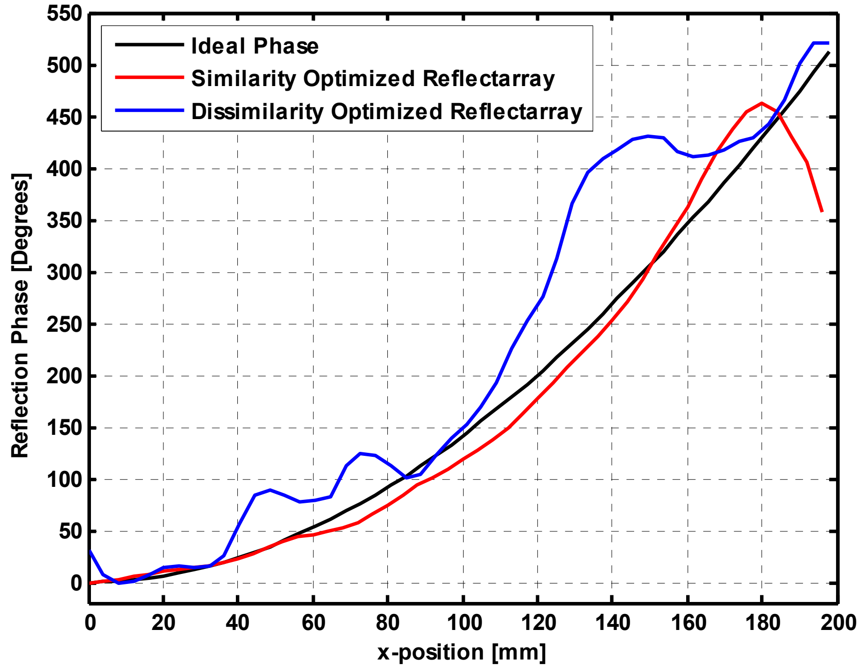

Figure 5.47 – Simulated reflection phase from a single-row of the reflectarray surface for both the similarity and dissimilarity optimized reflectarrays. Ideal (desired) reflection phase is shown for reference.

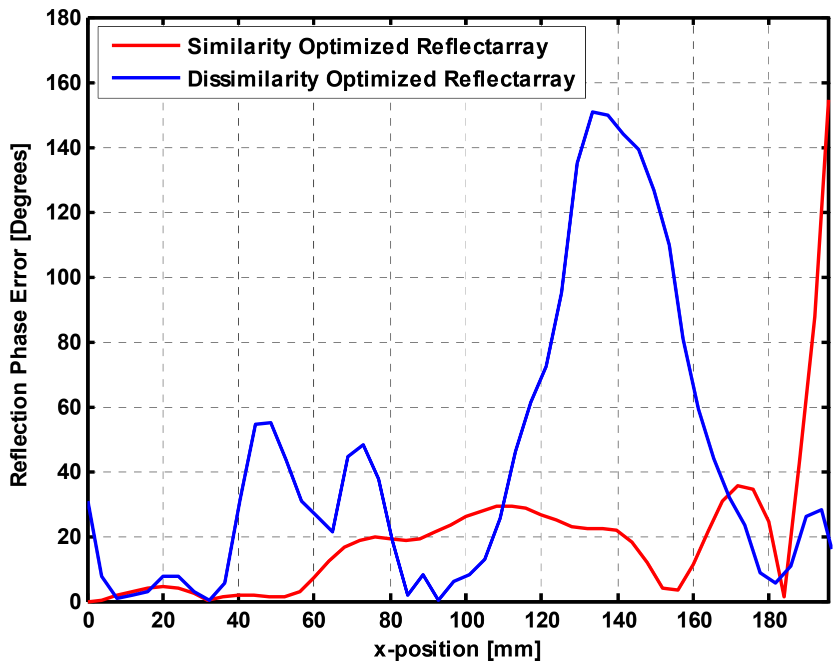

Figure 5.48 – Reflection phase error from a single-row of the reflectarray surface

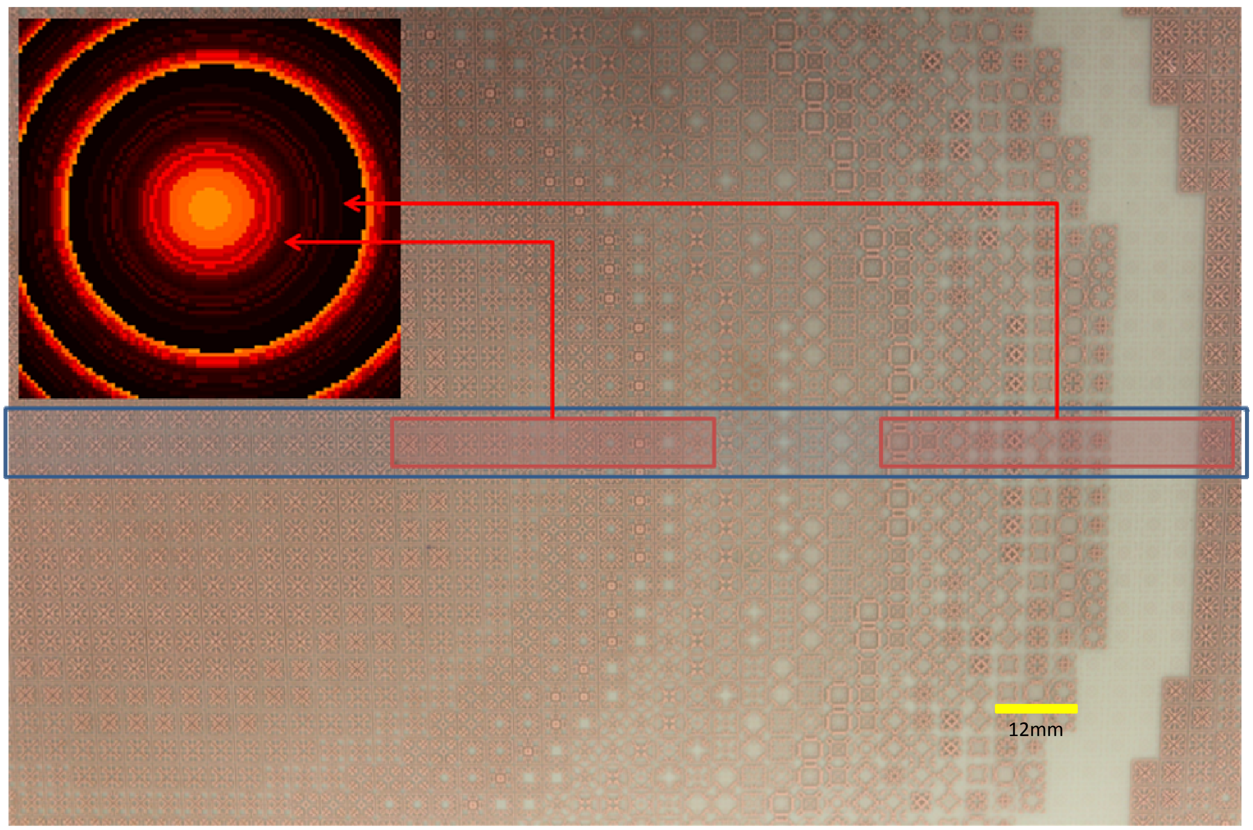

Figure 5.49 – Close-up photograph of dissimilarity optimized reflectarray with the simulated single row outlined in blue and the problematic regions outlined in red. These problematic regions correspond to the two distinct regions where the reflection phase error peaks (40mm to 80mm and 110mm to 170mm from Figure 5.48). The plot of the similarity amongst element is shown overlaid with the approximate problematic regions identified. There is a fairly strong correlation between regions (effectively rings) of low similarity and regions with the highest reflection phase errors.

5.4.10 – A Closer Look at the Performance of the Similarity-Optimized Reflectarray

It is worthwhile investigating to what degree we are maximizing the gain of the reflectarray. There exists an upper bound on the gain of every reflectarray that is mostly dependent on the pattern of the feed and the phase over the reflectarray aperture. Ideally, one would desire a feed that uniformly illuminates the aperture with all of the radiated power of the feed being captured and reflected by the aperture with precisely the required reflection phase [12], [18].

The illumination efficiency of a reflectarray can be computed using

$$\eta_i = \frac{1}{S}\frac{\left[\int_S \left|E(x,y)\right| dS\right]^2}{\int_S \left|E(x,y)\right|^2 dS} \tag{4.56}$$

where S is the area of the aperture, $\left|E(x,y)\right|$ is the co-polarized incident field from the feed and the integration is taken over the aperture of the reflectarray. The spillover efficiency of the reflectarray can be written

$$\eta_s = \frac{P_{rad,aperture}}{P_{rad,total}} \tag{4.57}$$

where $P_{rad,aperture}$ is the power radiated into the aperture by the feed and $P_{rad,total}$ is the total power radiated by the feed. Lastly, the phase efficiency of the reflectarray, a measure of how well the reflectarray synthesizes the required reflection phase, can be computed using

$$\eta_p = \frac{\left|\int_S E(x,y) dS\right|^2}{\int_S \left|E(x,y)\right|^2 dS} \tag{4.58}$$

Additionally, one would want the cross-polarization of the feed to be negligible as any power radiated into undesirable polarization will act to reduce the gain. The feed would also need to minimally block the reflected fields from the reflectarray. These concepts are discussed in further detail in [12] and [18]. Fortunately, these latter two sources of loss (reduction in gain) can be largely mitigated: (1) for most applications a low cross-pol feed horn is not difficult to procure, thereby making cross-polarization losses negligible [12] and (2) by designing an offset reflectarray, it is possible to largely negate the effects of feed blockage [18]. This leaves us with the issue of illumination and spillover efficiency. Typical feed horns have some form of smoothly varying antenna pattern, making it necessary to incur some form of loss due to the non-ideal taper and the lost power radiated into regions other than the aperture. The combination of these two efficiencies gives a good estimate for the upper bound on the achievable aperture efficiency, and thus gain, for any reflectarray with a given aperture size and feed configuration.

In other words, in the ideal scenario the upper bound on reflectarray gain is limited by

$$G_{\max,RA} = \eta_p \eta_s \eta_i G_{\max,ap} \tag{4.59}$$

where $G_{\max,ap}$ is the gain of an ideal aperture which follows the ubiquitous formula $G_{\max,ap} = 4\pi A / \lambda^2$. In practice, however, negligible loss due to phase error is rarely the case. Results from Section 5.4.9 show that the similarity-optimization approach using fragmented elements greatly improves η_p.

The horn antenna described in Section 5.4.6 is used as our test case for determining illumination and spillover efficiency. The horn was simulated in FEKO [7] with the resulting fields measured over an imaginary square aperture of the same size as the reflectarray in our design examples. The resulting meshed horn and example simulated aperture fields are shown in Figure 5.50(a) and (b) respectively. Note that the actual reflectarray is not present – the fields are measured in freespace and represent the incident field in the presence of the reflectarray antenna. The resulting illumination, spillover and combined efficiencies are shown in Figure 5.51. The maximum gain for a uniformly illuminated aperture is shown with the upper bounds on gain for the selected combination of feed horn, aperture and feed location shown as well. Note that these results additionally consider the directivity losses due to beam steering to 16° from broadside which amounts to an additional 0.17 dB of losses.

From Figure 5.51, the theoretical maximum gain for our reflectarray design at 11.2 GHz is 33.17 dBi with the ideal (but impossible) upper bound of 34.73 dBi for a uniformly illuminated aperture with no spillover. The inability to reach maximum gain of an aperture is due to the 0.96 dB of spillover and 0.60 dB of illumination losses and hence the true maximum gain of 33.17 dBi. Recall that Design D (the similarity optimized reflectarray) obtained a gain of 33.06 dBi. This implies that Design D has a measured gain that is within 0.11 dB (97.4%) of the theoretically maximum possible gain for the selected feed and aperture size combination. This further implies that the aperture phase efficiency is approximately 97.4%, assuming the feed blockage and cross-polarization efficiencies are close enough to 100%. It should be noted that the reflectarray is also assumed lossless, which is not truly the case due to the presence of glue layers to adhere the foam to the FR4, with the lossy FR4 and finite-conductivity copper elements also contributing to loss. In truth, our phase efficiency is potentially higher because of the fact that these losses are not accounted for, however small they might be. In any case, since we are using coupled resonant elements, we expect much lower losses than traditional resonant elements [22]. For the gains quoted, we have obtained an aperture efficiency of 65.5% compared to the theoretical maximum aperture efficiency of 67.2%. It would appear for all intents and purposes that the similarity optimization approach in reflectarray design is flirting with the ideal maximum gain performance.

Note that the aperture size used in the calculation was 420mm x 420mm and not the smaller 396mm x 396mm. The larger size accounts for the reflectarray's borders where no elements are present. It is expected that if these borders were filled with fragmented elements, the upper bound on gain would be approached even closer. Let us further consider that since we are not fully utilizing the aperture provided, our aperture efficiency arguably resides somewhere between the efficiencies computed for 396mm x 396mm and 420mm x 420mm. If the smaller aperture size were used in the calculations, a measured aperture efficiency of 73.7% would be obtained. We conclude that the aperture efficiency obtained if the borders were filled with elements would be greater than 65.5%. However, without experimental confirmation, this is simply conjecture and we will remain quoting the 65.5% aperture efficiency. Despite the non-ideal fabrication parameters, we still find excellent performance. It is expected that as these phenomena are accounted for or corrected in the design process, the closer the measured aperture efficiency will approach that of the fundamental limits.

For a comparison with other reflectarrays found in the literature, we consider examples in [19] – [22]. In [19], which is perhaps the most cited article on reflectarrays, the highest aperture efficiency obtained was 54%. While this paper is from some time ago (circa 1997), it does represent the pinnacle of microstrip patch-based reflectarray designs. In [20], a single-band (single-layer) example reflectarray design obtained 60.6% aperture efficiency. Additionally, in [21], 60% aperture efficiency is claimed. References [19] – [21] use resonant elements (λ/2-spaced). Lastly, we consider reference [22] which obtained a 55% aperture efficiency using similarly-sized sub-wavelength elements as our fragmented elements. In general, it would seem that aperture efficiencies between 40% and 50% are the norm in reflectarray designs, with 60% representing an approximate limit on the most efficient designs reported thus far. At the very least, we are fully confident that the similarity-shaped fragmented elements yield a reflectarray with aperture efficiency far surpassing previous sub-wavelength based reflectarray designs and certainly competes with if not exceeding the aperture efficiencies obtained in other resonant element based reflectarrays. We therefore suggest that the similarity-optimized sub-wavelength fragmented elements provides an improved design approach to further increase the aperture efficiencies of reflectarray antennas.

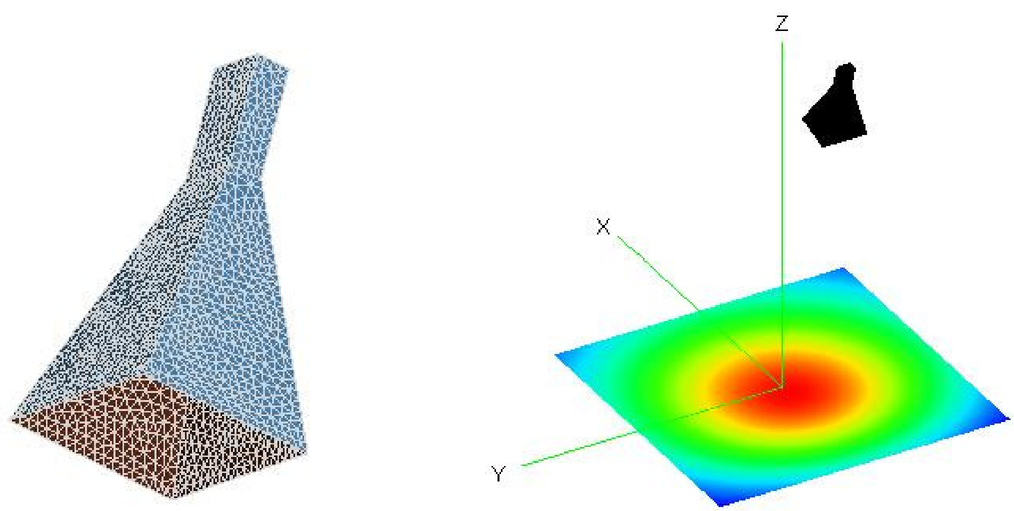

(a) (b)

Figure 5.50 – Example horn (a) meshed in FEKO and (b) illuminating a bare aperture with the same physical size as the reflectarray aperture in our design examples (aperture fields shown for illustrative purposes only)

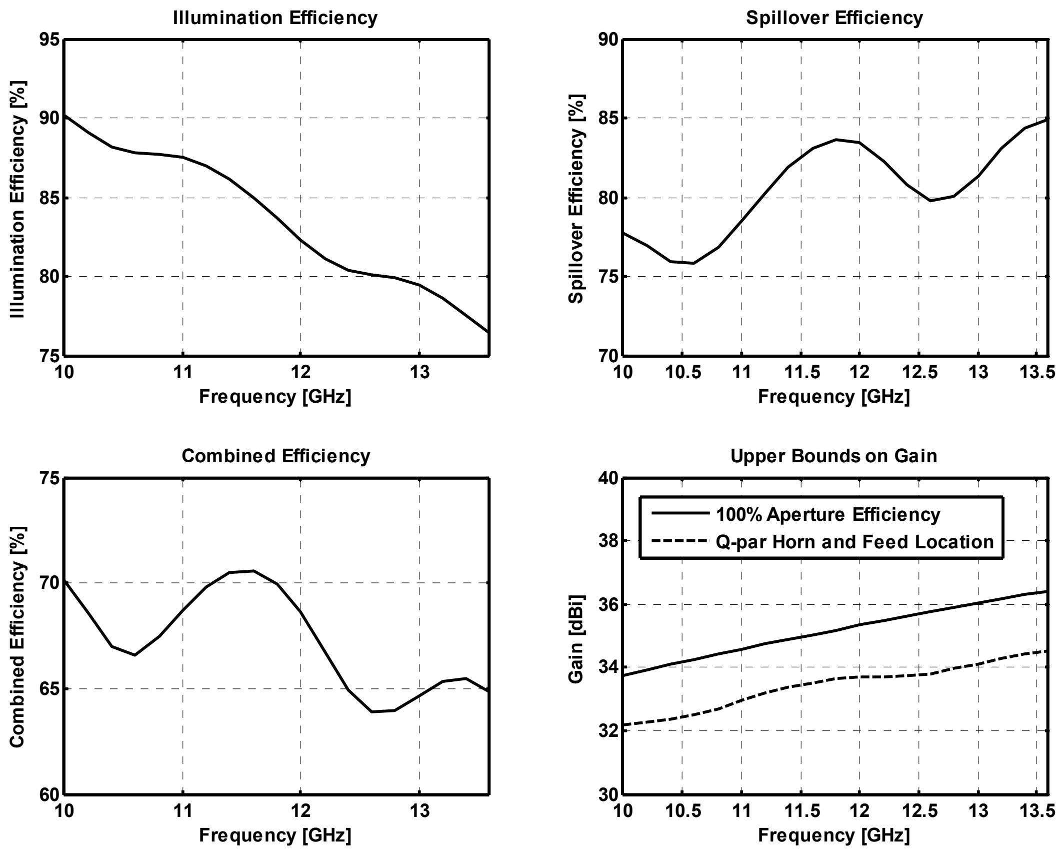

Figure 5.51 – Illumination, spillover and combined efficiencies and the upper bounds on antenna gain for an ideal aperture and the actual aperture illumination/spillover using the Q-par horn in our design examples

5.5 – The Mosaic Reflectarray

5.5.1 – Introductory Remarks

Oftentimes one is presented with an idea in engineering where the immediate response is "that can't possibly work" or "it might work, but it will perform so poorly that it will be worthless." This sort of response can be given to a request that in and of itself has no bearing on the measurable performance of a given design and in fact can be detrimental to the design as a whole. The motivation for such a decision can stem from a cost perspective, as was recently found to be the case for the antenna design in a popular mobile phone [23]. The motivation can be for purely marketing reasons – the design is made to look aesthetically pleasing without any particular regard to the impact on performance (or, in the least desirable scenario, despite a negative impact on performance). If the performance is not impacted greatly, but the design is such that it becomes a more desirable product, then the benefits are clearly apparent. To quote a great aeronautical engineer,

Scientists study the world as it is, engineers create the world that never has been

- Theodore von Karman

If the author could be so bold as to append to this quote, he would add the phrase

and marketers convince us we want to live in a world that engineers can create.

Engineers are very often driven to develop products and, whether they like it or not, are tasked to maintain non-technical features in the name of increased sales. In moments where an engineer can produce an excellent design from the technical perspective while simultaneously creating an aesthetically pleasing design as per marketing requirements, the engineer is in a good situation to please all the parties concerned; truly a cause for celebration. Having said all of that, the author must now stop digressing and come clean with the admission that such things are of no concern in this thesis. The pursuit of knowledge for the sake of knowledge is reward enough and there are no such aforementioned parties concerned in this work. Nevertheless, let us now consider a novel and *marketing-friendly* approach to the design of high-performance reflectarrays.

5.5.2 – Putting the Element Indexing Approach to Further Use

The indexing approach offers a great deal more than what was explicitly used thus far in the thesis. In particular, there is no limit to the number of elements that can occupy an index. The work performed previously united a single unique element with each index, thereby giving a single option for desired reflection phases in close proximity to the phase of said element. This was to our advantage as we wanted to maintain a high degree of similarity between elements. Alternatively, one can tie each index to a particular reflection phase and fill a 'bin' with a multitude of uniquely shaped elements, each having the same reflection phase. This offers the designer a choice: which element among many is best suited for a given location in the reflectarray, beyond meeting the reflection phase criterion? The answer is entirely dependent on the application.

One such application, for example, is the use of these fragmented elements in the design of a reflectarray that both meets the requirements of a particular set of reflection phases over the surface (e.g. the reflectarrays we have designed thus far) and simultaneously attempts to synthesize an optical image with its surface patterning. The latter image synthesis concept is used extensively in photography and is known as a photo mosaic [24]. The general idea is to use a collection of photos, shapes and/or patterns that is aggregated in a manner that resembles some other photo, shape or pattern. The novelty is that there is a great amount of detail contained deep within the image though simultaneously conveying an immediately noticeable single overall image.

Our proposal is therefore to utilize the fragmented reflectarray elements in a manner that both meets the requirements of reflection phase as well as using the metal density (which can be thought of as an optical property of the element) to simultaneously mimic an optical image, thus forming a mosaic. In a perhaps poetic sense we can think of such a structure as a dual-band device: a collimated, high gain antenna at microwave frequencies and an image at optical frequencies.

5.5.3 – Mosaic Based Reflectarray Design

A secondary metric is now used to classify a fragmented element: its metal density. This quantity will be defined in a basic fashion, giving no concern to the actual shape and positional dependence of the metal density. It will simply be defined as the ratio of the total number of triangles in a given element divided by the total number of triangles in the starting element shape (a solid patch in all of our examples).

The first step in our design process is generating a wide variety of elements with which to design our mosaic reflectarray. The ideal collection of elements would entail groups of elements with reflection phase in, for example, 10^o steps (as was done before) only now each reflection phase (effectively an index) has numerous elements associated with it, each with a different shape and optimistically with a variety of different metal densities. As a first optimization approach, we will simply optimize the elements to achieve the desired phase to within 2^o error in steps of 10^o, which is precisely the same approach used previously in Section 5.4.6. The only difference now is we demand 128 elements from the optimizer for each index, thereby synthesizing nearly 4,000 fragmented elements. While generating 4,000 elements appears, at first glance, to be an unreasonably large number of elements, it was nonetheless generated within one day of simulations using a high-end computer with fairly modest specifications. One minor change was made to the design which involved changing the vacuum substrate height from 4mm down to 3mm due to a change in the availability of the previously mentioned Rohacell^{TM}.

In order to emphasize the variability, let us plot the minimum, maximum and average metal densities of each index, as shown in Figure 5.52. Note that the average metal density falls neatly between the upper and lower bounds, indicating a good spread of choices in metal density. The indices between 2 and 25 have a very large range of metal densities. For the indices between 26 and 31, the reflection phase is negative (-70^o to -120^o). It is clear that for these indices, the variability in the element metal density is low. This is mainly due to the fact that it is not trivial to obtain an element with these phases for sub-wavelength designs [18]. Nevertheless, we find this will not hamper our ability to synthesize mosaics since the achievable variability appears sufficient. It should also be noted there is a lack of variability in metal density for the first index (index 1), or 180^o reflection phase. In fact, one observes a low metal density as well. This is due to the ideal 180^o element having no metallization (a blank unit cell, with a ground plane boundary of course) with the best approximation necessarily having a relatively low percentage of metal coverage.

As an illustrative example, consider Figure 5.53 where 128 elements are shown for index 19, or 0^o reflection phase. Note the unique shape of each element and the varying levels of metal density. Note also that there exists an additional 30 groups of 128 elements such us these, with each element having a unique shape. By selecting the correct element based on the metal density (assuming it meets the criteria of reflection phase) it is possible to generate a mosaic using the fragmented elements. As an additional sorting technique, the elements are ordered from least dense to most dense (in terms of metallization) with the least dense occurring at the top left-most of the image for the example in Figure 5.53, with increasing density shown across rows (the most dense element occurring at the bottom-right). The range of density varies from 45% to 70%, indicating a reasonable range of densities with which to form our reflectarray mosaics.

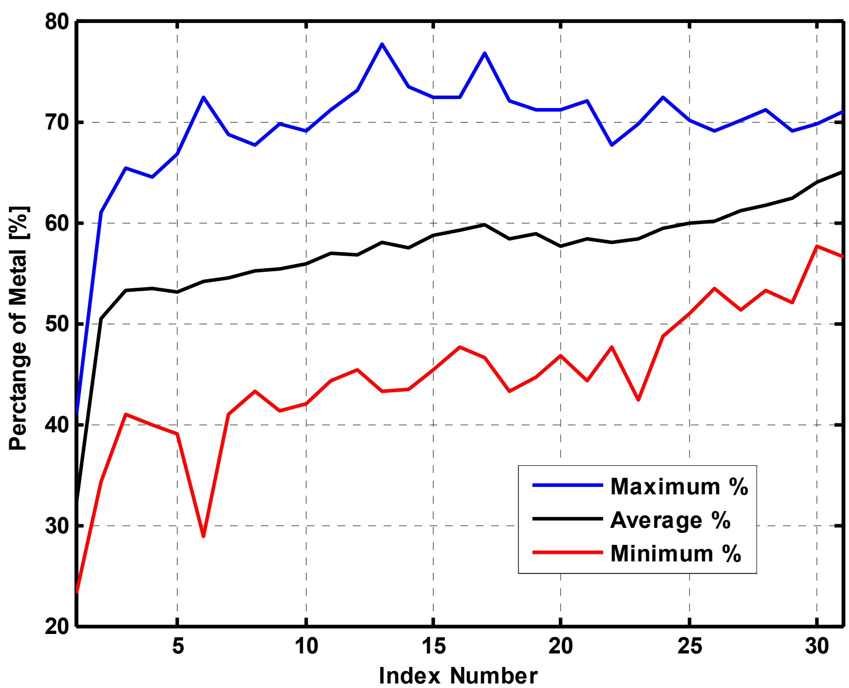

Figure 5.52 – Maximum, average and minimum percentage of metal for each reflection phase index in the generating database of fragmented reflectarray elements (average % is computed by taking the average metal density of 128 elements occupying each index)

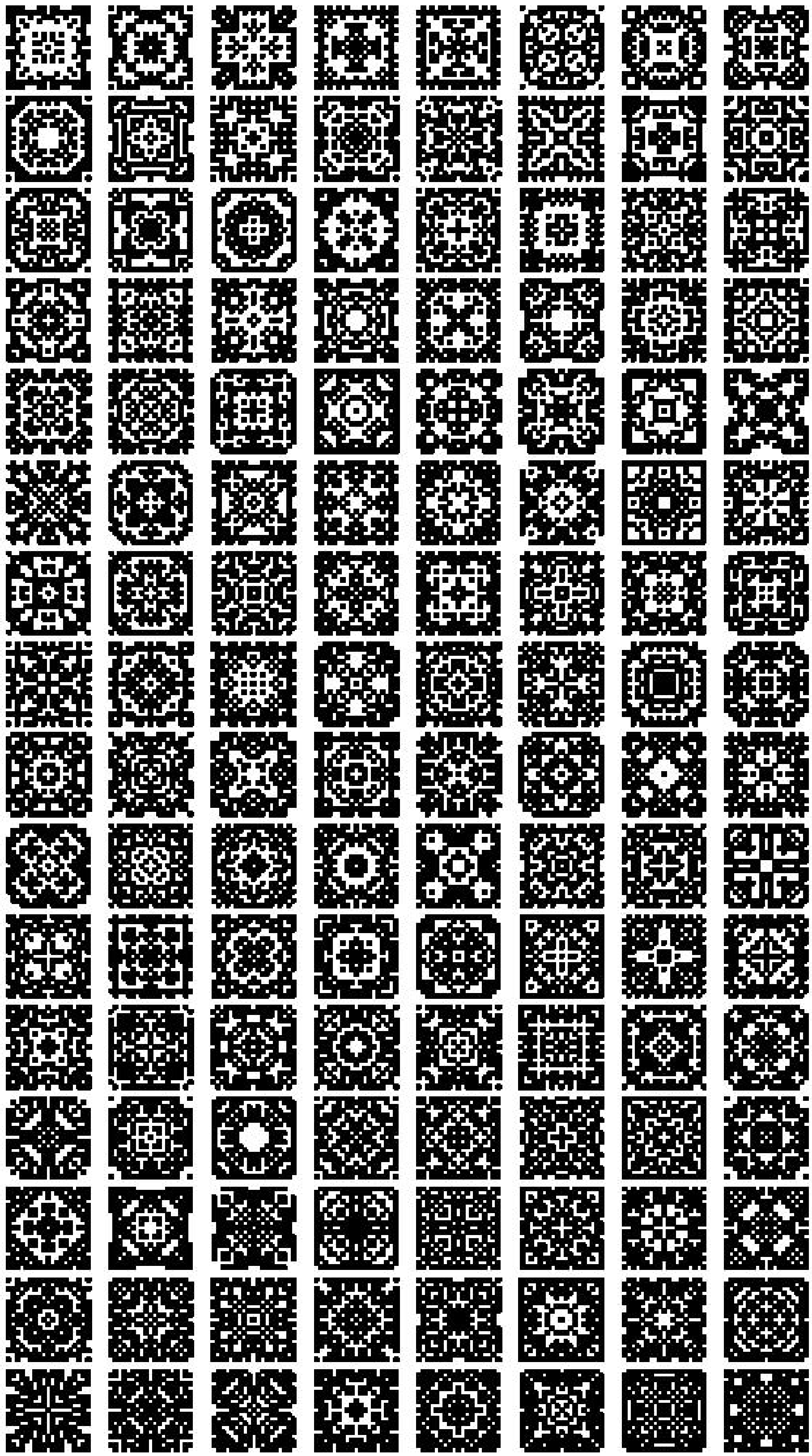

Figure 5.53 – Collection of 128 fragmented elements. Note that each element has a reflection phase that is within 2^o phase of 0^o and yet 128 uniquely shaped elements are shown (metal density varies from 40% to 70%)

Since our elements have a single optical colour due to the copper etching, all of our images must be viewable in grayscale. An upper and lower limit is computed from the range of metal densities available. In our case, the database has a reasonable selection of elements across all indices for the metal densities between 40% and 70%. We therefore re-normalize our densities from 40% - 70% to 0% to 100% in order to suitably generate a mosaic for any given image. Next, we must discretize the image from its possibly higher resolution to a resolution that matches the number of elements in our reflectarray. Since we wish to remain consistent with previous work, we shall design a 99 x 99 element reflectarray (9,801 elements total) identical in size and specifications to our previous work in Section 5.4. As a result, our image must be down-sampled to a 99 x 99 pixel image (for a total of 9,801 pixels).

The first example we will consider is a collage of maple leafs (an iconic Canadian symbol) with the CRC logo, recognizing the research centre that was gracious enough to fabricate and measure many of the reflectarrays. The original colour image and its down-sampled, grayscale equivalent 99x99 pixel image is shown in Figure 5.54(a) and (b) respectively. Using the same database as discussed in the previous example, the metal density of the synthesized mosaic reflectarray is shown in Figure 5.55, plotted element-by-element in terms of the elements' metal density. Note that the scaling is from 0 to 100 representing 0% to 100% optical density. From this figure we are confident that the mosaic is properly synthesized, and so we proceed with the reflectarray fabrication. While we are synthesizing a mosaic reflectarray, we are also simultaneously trying to obtain the desired reflection phase for a high gain reflectarray. Figure 5.56 shows the desired phase (which is the same reflection phase required for the reflectarrays from Section 5.4), the element phase (including the selection of elements for the purpose of generating a mosaic) and the phase error. Notice that the phase error is quite low except around the Fresnel zone boundaries. Notice that the large phase error is confined to the same regions as in the examples of Section 5.4 – the result of which had negligible impact on the gain of the reflectarray.

(a) (b)

Figure 5.54 – Example images for mosaic reflectarray, (a) original image in full colour and (b) grayscale image discretized down to 99 x 99 pixels to match reflectarray element density

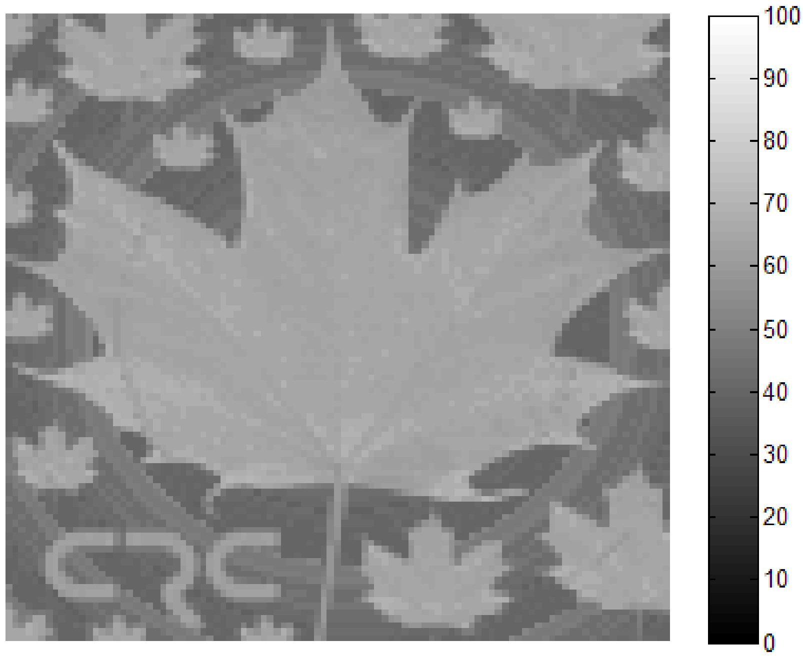

Figure 5.55 – Mosaic reflectarray plot of surface metal density (with densities between 40% and 70%)

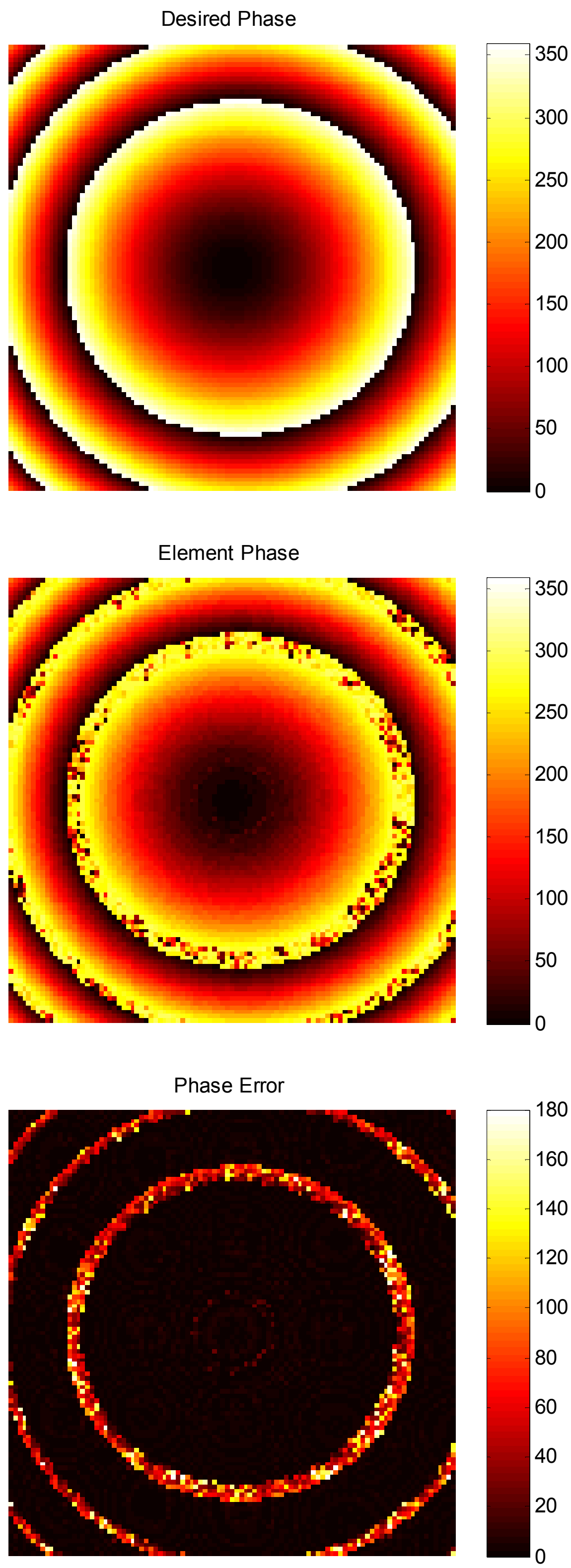

Figure 5.56 – Example maple leaf mosaic reflectarray design showing the desired phase, element phase and lastly the phase error. Note that the realized phase and phase error simultaneously generate the mosaic.

The next example mosaic we will consider involves the University of Ottawa (uOttawa) logo, shown in Figure 5.57. The obtained logo was already of low enough resolution that the transfer to the small 99x99 pixel image had little impact on the image quality. The resulting best-approximation mosaic using the database of elements is shown in Figure 5.58. Additionally, the desired phase, achieved phase and phase error is shown in Figure 5.59. Much the same as for the previous mosaic reflectarray, the phase error is quite low in all regions but the Fresnel zone boundaries, which regions we expect to have minimal impact on the reflectarray performance, as discussed in Section 5.4.

Figure 5.57 – uOttawa Logo to be Synthesized as a Mosaic Reflectarray

Figure 5.58 – Mosaic reflectarray plot of surface metal density (with densities between 40% and 70%)

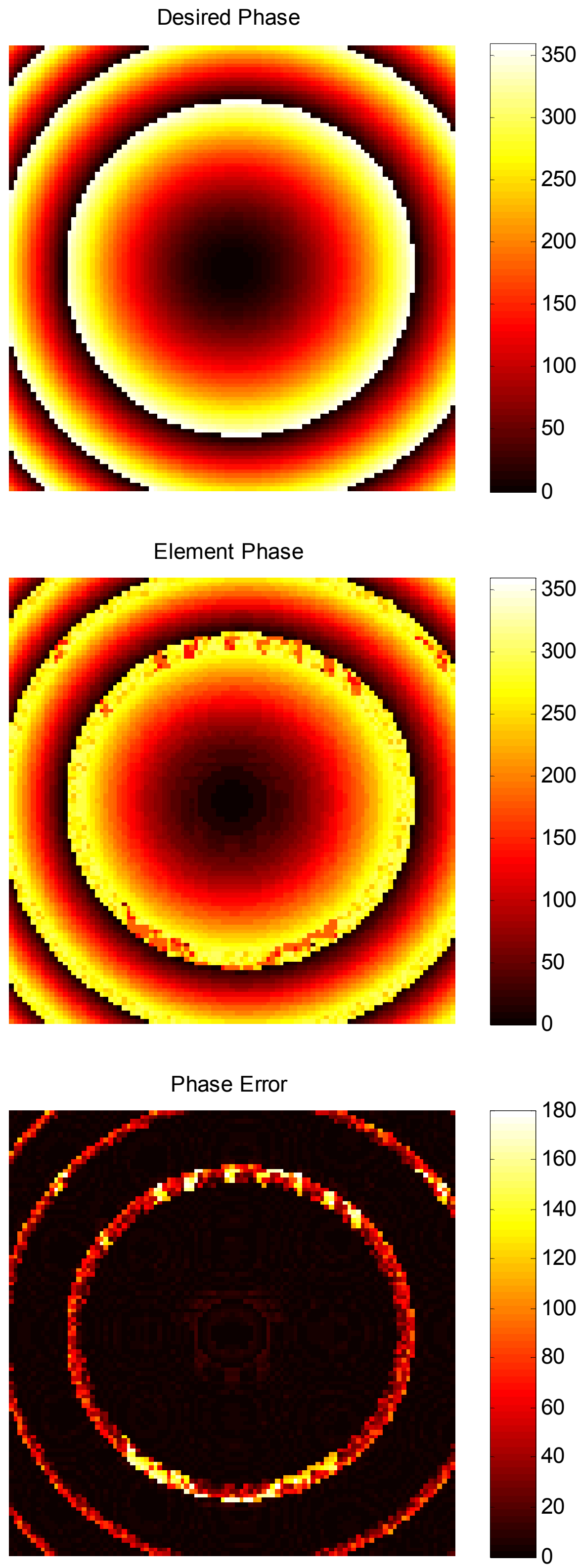

Figure 5.59 – Example uOttawa logo mosaic reflectarray showing the desired phase, element phase (realized) and lastly the Phase Error. Note that the realized phase and phase error simultaneously generate the mosaic

It should be noted that in these examples we are leveraging quite heavily on the sub-wavelength element concept. Namely, the element density in the reflectarray is such that we can well approximate an image using the mosaic technique since we are effectively provided with 99 x 99 pixels. If a reflectarray were designed using a half-wavelength lattice, the resolution would drop to 33 x 33 pixels. The uOttawa logo and maple leaf / CRC logo mosaic reflectarrays are shown in Figure 5.60(a) and 5.60(b) respectively for the case of λ/2 spacing. While some details are recognizable, it does not do justice to the original image. We believe that the mosaic reflectarray is only feasible using fragmented sub-wavelength elements, further adding to their novel and useful properties.

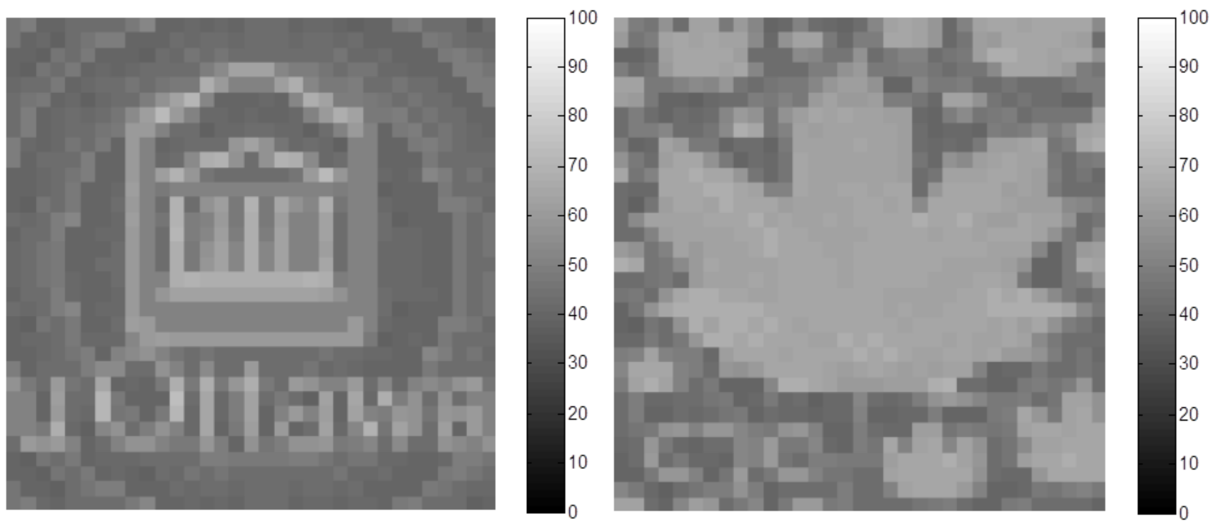

(a) (b)

Figure 5.60 – Example mosaic reflectarrays showing metal density surface plots, assuming the use of λ/2 spaced elements for the case of (a) uOttawa logo and (b) maple leaf and CRC logo

5.5.4 – Measured Results and Comparison of the Mosaic Reflectarray Designs

The two mosaic reflectarrays were fabricated using the same approach as the successful similarity (and dissimilarity) optimized reflectarrays from Section 5.4. By using a high quality very thin substrate as the supporting structure, and breaking the single vertices in the moment method mesh to prevent unwanted shorting of these non-physical connections, we expect that any performance degradation can be isolated and attributed to the non-ideal mosaic patterning. The fabricated uOttawa and Maple Leaf / CRC reflectarrays are shown in Figure 5.61 and 5.62 respectively. The resulting measured gain versus frequency of the two mosaic reflectarrays is shown in Figure 5.63, with the gains of the similarity and dissimilarity optimized reflectarrays shown for reference. Additionally, the measured far-field patterns of the two mosaic reflectarrays are shown in Figure 5.64 at 11.2 GHz. We see remarkably good gain for the mosaic designs, outperforming the dissimilarity optimized reflectarray for some frequencies and generally performing well despite the non-ideal patterning. The similarity optimized reflectarray clearly has the best performance, but at the cost of 0.7 – 1.0 dB of gain, one can successfully (and convincingly) pattern the surface of a reflectarray with a mosaic. It should also be noted that the gains achieved for the two mosaic reflectarrays at 11.2 GHz (and at 12 GHz) are quite high and one might argue they are within the range of, if not better than, the majority of similarly sized (electrically-speaking) reflectarrays found in the literature. These results are summarized in Table 5.3.

Design	*Maximum Gain (11.2 GHz)*	*1-dB Gain % bandwidth*	*1st Side-lobe Level*	*Cross-pol (11.2 GHz)*	*Maximum Gain (12.0 GHz)*
Similarity (Design D)	33.06 dBi	12.3%	12.44 dBi (-20.62 dB)	4.19 dBi (-28.87 dB)	32.56 dBi
Dissimilarity	32.15 dBi	12.6%	14.96 dBi (-17.19 dB)	4.06 dBi (-27.09 dB)	31.75 dBi
Mosaic uOttawa	32.36 dBi	3.8% (12.8%)[15]	12.21 dBi (-20.15 dB)	6.43 dBi (-25.93 dB)	31.79 dBi
Mosaic Leaf & CRC	32.05 dBi	3.6% (12.2%)[14]	10.89 dBi (-21.16 dB)	6.33 dBi (-25.72 dB)	31.52 dBi

Table 5.3 – Summary of electrical performance for the four successfully fabricated fragmented reflectarrays

[15] Note that if a 1.5 dBi gain bandwidth were specified, the bandwidth would increase in the 12% range for both mosaic reflectarrays. This is due to the sudden drop in gain (~ 1.5 dBi) from 11.2 to 11.4 GHz.

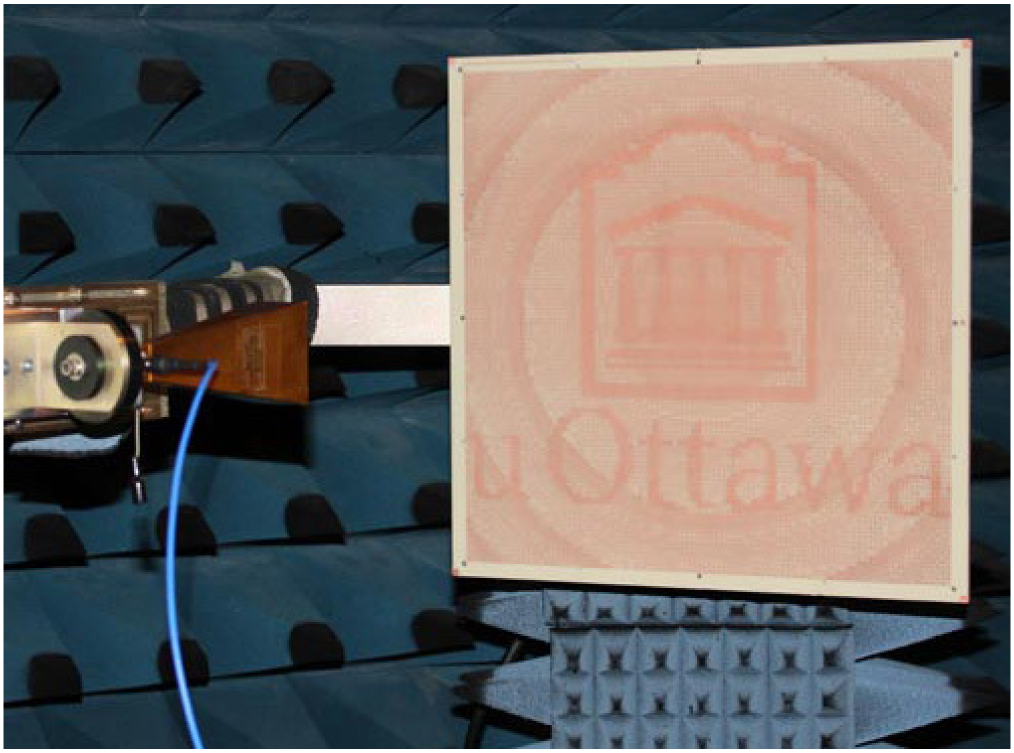

Figure 5.61 – Fabricated mosaic reflectarray in CRC's anechoic measurement chamber – uOttawa Logo

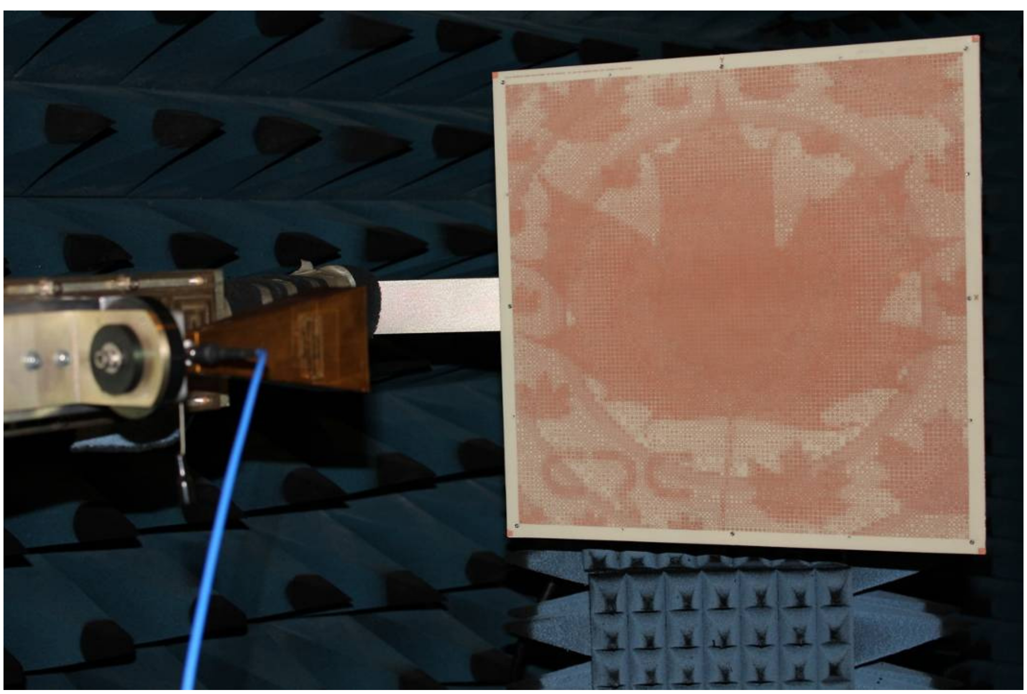

Figure 5.62 – Fabricated mosaic reflectarray in CRC's anechoic measurement chamber – maple leaf & CRC logo

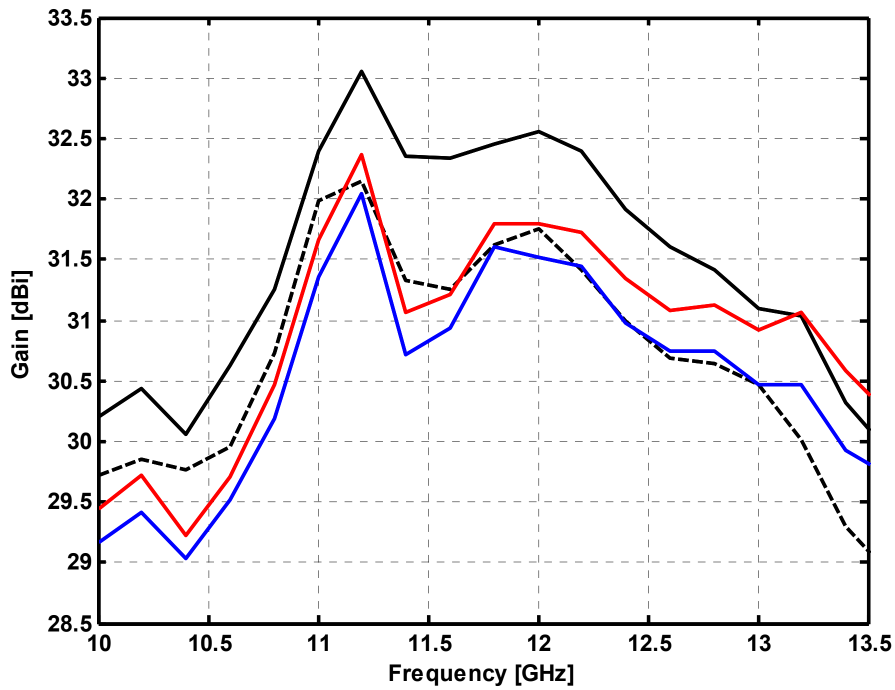

Figure 5.63 – Antenna E-plane gain of four fragmented reflectarrays over frequency with gain curves: (———) similarity optimized, (– – – –) dissimilarity optimized, (———) uOttawa mosaic, (———) CRC & leaf mosaic.

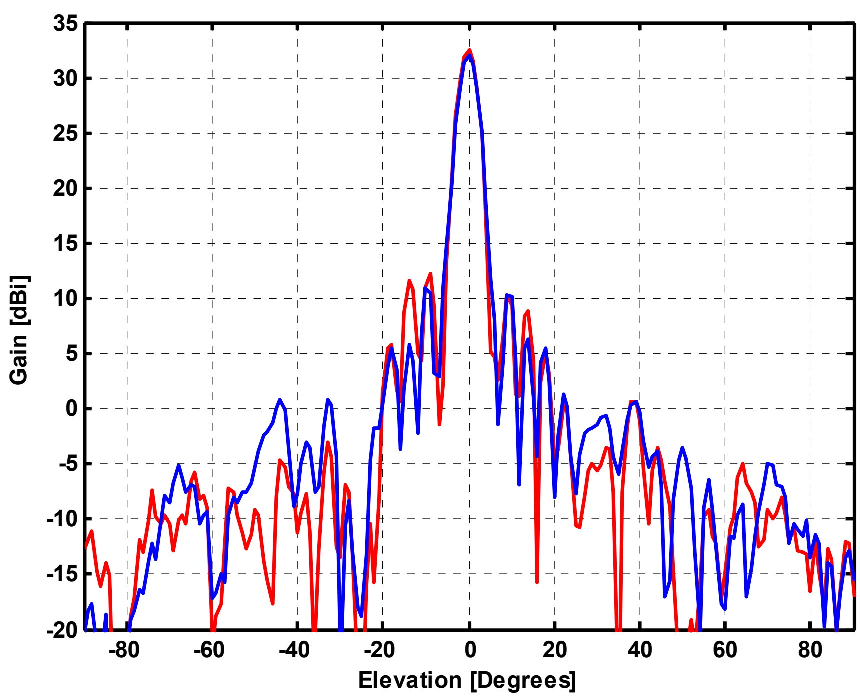

Figure 5.64 – Antenna E-plane gain pattern of mosaic fragmented reflectarrays: (———) uOttawa mosaic reflectarray, (———) CRC & leaf mosaic reflectarray at 11.2 GHz.

5.6 – Concluding Remarks

The characteristic modes of periodic structures were investigated in this chapter. This does not appear to have been done elsewhere in the literature. We began with a description of the issues that arise when dealing with a scatterer of infinite extent, which led to a slightly different interpretation of the CMs compared to the classical approach. Nevertheless, the CMs of periodic structures were shown to be of value for both analysis and synthesis problems. In Section 5.2 we developed a new moment method approach, which we named the infinite-from-finite (IFF) method that allowed us to analyze infinite periodic structures. This gave us access to the impedance matrix describing an infinite periodic structure and allowed us to obtain the characteristic modes of said periodic structure. The novelty of the newly derived formulation is the ability to take any existing finite structure freespace moment method formulation and use it to obtain the properties of an infinite periodic array of such structures.

In Section 5.3 we investigated the characteristic mode properties of infinite periodic structures. Critical performance metrics such as transmission and reflection coefficients were shown to be retrievable from the characteristic mode eigenvalues. Additionally, computationally efficient shortcuts were derived that made use of the impedance matrix trace operator, forgoing the need to perform actual eigenanalysis. The transmission and reflection coefficients of free-standing, and ground plane backed, periodic structures were shown to be obtainable without having to acquire excitation currents. These results form a set of objective functions useful in the synthesis of single-mode periodic structures.

In Section 5.4, we applied the characteristic mode based objective function in the synthesis of high-gain reflectarrays through fragmented element shape synthesis. A new and unconventional optimization technique was proposed whereby the adjacent elements in the reflectarray are optimized to be as physically similar as possible while still maintaining the necessary variation in the element reflection phase. This helps to maintain the periodic structure condition despite being placed in a quasi-periodic and finite array of elements. This leads to near negligible aperture phase error, and hence the very high aperture efficiencies that were experimentally measured. The concept was further extended in Section 5.5 where the novel design concept of mosaic reflectarrays was introduced. It was shown that a reflectarray surface can be simultaneously patterned with an optical (visual) image while still maintaining the desired reflection phase from its surface to yield a high-gain reflectarray.

Chapter 5 References

[1] R.C.Hansen, *Microwave Scanning Antennas* (Peninsula Publ. 1986).

[2] B.Munk, *Frequency Selective Surfaces* (Wiley, 2000).

[3] A.K.Bhattacharyya, *Phased Array Antennas* (Wiley, 2006)

[4] R.C.Hansen, *Phased Array Antennas* (Wiley, 2010).

[5] F.Capolino, D.R.Wilton and W.A.Johnson, "Efficient computation of the 2-D Green's function for 1-D periodic structures using the Ewald method", *IEEE Transactions on Antennas and Propagation*, Vol.53, No.9, Sept.2005, pp. 2977-2984.

[6] S. N. Makarov, *Antenna and EM Modeling with MATLAB®*. New York: John Wiley & Sons, 2002.

[7] EM Software & Systems (USA) Inc. Langley Research Park, 144 Research Drive, Hampton, VA 23666. (*FEKO Electromagnetics Simulator*)

[8] R.F. Harrington, J. Mautz, "Theory of Characteristic Modes for Conducting Bodies," *IEEE Transactions on Antennas and Propagation*, Vol. AP-19, No. 5, pp. 622 – 628, September 1971.

[9] H. Rajagopalan and Y. Rahmat-Samii, "Dielectric and Conductor Loss Quantification for Microstrip Reflectarray: Simulation and Measurements," *IEEE Transactions on Antennas and Propagation*, Vol. 56, No. 4, April 2008, pp. 1192 – 1196.

[10] S. Ramo, J.R. Whinnery, T. Van Duzer, *Fields and Waves in Communication Electronics,* 2nd Edition. New York: John Wiley & Sons, 1984.

[11] D. M. Pozar, *Microwave Engineering,* 3rd Edition. New Jersey: John Wiley & Sons, 2005.

[12] J. Huang, A. Encinar, *Reflectarray Antennas*, Institute of Electrical and Electronics Engineers, John Wiley & Sons, 2008.

[13] M.-A. Milon, D. Cadoret, R. Gillard and H. Legay, “Surrounded element approach for the simulation reflectarray radiating cells,” *IET Microwaves, Antennas & Propagation*, Vol. 1, Issue 2, 2007, pp. 289 – 293.

[14] M.-A. Milon, R. Gillard, D. Cadoret, and H. Legay, “Comparison between the infinite array approach and the surrounded-element approach for the simulation reflectarray antennas,” *Antennas and Propagation Society International Symposium*, 2006, pp. 4339 – 4342.

[15] R. El Hani, J. Laurin, “Phase analysis for off-specular reflectarray antennas,” *IEEE International Symposium on Antennas and Propagation* (APS/URSI 2011), July 2011.

[16] L. Moustafa, R. Gillard, F. Peris, R. Loison, H. Legay, E. Girard, “The Phoenix Cell: A New Reflectarray Cell with Large Bandwidth and Rebirth Capabilities”, *IEEE Antennas and Wireless Propagation Letters*, Vol. 10, 2011, pp. 71 – 74.

[17] E. Almajali, D. McNamara, J. Shaker, M.R. Chaharmir, “Derivation and Validation of the Basic Design Equations for Symmetric Sub-Reflectarrays,” to appear in *IEEE Transactions on Antennas and Propagation.*

[18] J. Shaker, M. R. Chaharmir, “Microstrip Reflectarray Antennas”, Chapter 5 in D. Guha, Y.M.M. Antar, *Microstrip and Printed Antennas: New Trends, Techniques and Applications*, (Wiley, 2010).

[19] D.M. Pozar, S.D. Targonski, H.D. Syrigos, “Design of millimeter wave microstrip reflectarrays,” *IEEE Transactions on Antennas and Propagation*, Vol. 45, Issue 2, February 1997, pp. 287 – 296.

[20] C. Han, J. Huang, K. Chang, “A high efficiency offset-fed X/Ka-dual-band reflectarray using thin membranes,” *IEEE Transactions on Antennas and Propagation*, Vol. 53, Issue 9, 2005, pp. 2792 – 2798.

[21] M.R. Chaharmir, J. Shaker, "Broadband reflectarray with combination of cross and rectangle loop elements," *Electronics Letters*, Vol. 44, Issue 11, 2008, pp. 658 – 659.

[22] J. Ethier, M. R. Chaharmir, J. Shaker, "Reflectarray design comprised of sub-wavelength coupled-resonant square loop elements," *Electronics Letters*, Vol. 47, No. 22, October 2011, pp. 1215 – 1217.

[23] P. Burrows, C. Guglielmo, *Apple Engineer Told Jobs IPhone Antenna Might Cut Calls*, [Online] Available http://www.bloomberg.com/news/2010-07-15/apple-engineer-said-to-have-told-jobs-last-year-about-iphone-antenna-flaw.html, Retrieved December 10, 2011.

[24] F. Van Der Weeën, "Algorithms for draping fabrics on doubly-curved surfaces," *International Journal for Numerical Methods in Engineering*, Vol. 31, Issue 7, May 1991, pp 1415 – 1426.

Chapter 6

Conclusions and Future Work

6.1 – Summary of the Contributions of the Thesis

The principal contributions of this thesis are as follows:

- An entirely new approach was devised for the shape synthesis of antennas which are subject to geometry restrictions (eg. must fit within a specified planar area). It is novel since it allows the shape optimization process to proceed unrestricted by a fixed feedpoint location (and was designated as being a "feedless" approach). The feedpoint selection is done after the optimum shape has been found, guided by the current distribution and impedance map of the resulting shaped structure. This is not possible with existing shape synthesis methods, and removes restrictions on the shaping process. The approach was made possible through connecting antenna performance parameters to characteristic mode concepts. The objective functions derived for this new shape synthesis approach were shown to be computationally efficient.

- The shape synthesis technique was successfully applied to numerous electrically small antenna shapes, obtaining bandwidths that closely approach the fundamental limits for the shaped geometries considered. These results were supported by experimental results. The synthesis technique was further applied to multi-band antenna synthesis. The feedless aspect allows the synthesis process to guide the selection of different feedpoints for different bands after the shaping has been done. This would not be forthcoming from existing shape synthesis methods, and knowing how to select such points *a priori* would be difficult.

- A new sub-structure characteristic mode concept for electromagnetic systems was devised. It extends the range of applicability of the feedless shape-synthesis technique to cases where external requirements might not allow certain parts of the structure to be shaped and/or contain feed points. The application of this procedure was successfully illustrated theoretically and experimentally.

- The concept of sub-wavelength fragmented elements and similarity optimized elements in reflectarray design are first proposed in this thesis. The combination of these concepts and, in particular, the optimization for maximum similarity between adjacent elements in a reflectarray, leads to near-optimal performance of reflectarrays in terms of aperture efficiency. It is believed that the similarity optimized fragmented reflectarray's aperture efficiency is the closest a reflectarray has come to achieving the maximum gain for a given feed configuration.

- The invention of a reflectarray design designated the mosaic reflectarray. This reflectarray design technique was shown to be capable of patterning an optical (visual) mosaic image on to the surface of the reflectarray while still maintaining the desired reflection phase from the surface of the reflectarray. The impact on reflectarray gain was marginal, with the performance remaining competitive with (if not better than) traditional half-wavelength-spaced reflectarray designs.

Some of the lesser contributions of the thesis, although still significant, are as follows:

- The development of a new numerical technique for obtaining static polarizability using a time-harmonic moment method formulation. It is possible, using this formulation, to obtain the bounds on antenna Q (a static derived quantity) via the same moment method formulation used to obtain the frequency-dependent parameters such as input impedance and matched bandwidth. This allows one to immediately determine whether a given shape synthesized antenna design is performing optimally, given the geometric shape, all from the same numerical method.

- The theoretical development of a convenient moment method formulation denoted the infinite-from-finite method, for the analysis of infinite periodic structures. This was accomplished using a technique that allows any traditional freespace-based moment method formulation to analyze periodic structure in a relatively simple manner. This approach was used throughout Chapter 5, with substantial experimental results confirming the accuracy and wide applicability of the formulation.

- The further development of a moment method code capable of analyzing PEC structures is now capable of analyzing finite conductivity scatterers ranging from electrically small, to intermediately sized and finally to infinitely large periodic structures. The computation of the characteristic modes for all such formulations is possible.

- The characteristic mode analysis of periodic structures was investigated for the first time. Fundamental limitations of single-mode periodic structures were derived (Appendix K), some of which can be found in the literature, while others are likely new contributions. The result of these derivations was used in Chapter 5 to rapidly determine the reflection coefficients of reflectarray elements. Suggestions for future work on this topic are presented in Section 6.2

6.2 – Future Work

The following future work might prove fruitful by exploiting more of what characteristic mode theory has to offer:

- A thorough theoretical investigation of the identities, properties, implications and application of the sub-structure characteristic modes is in order as it provides an entirely new view of characteristic mode concepts.

- Determining the fundamental bounds on antenna Q for a structure with “do not touch” regions would add to the knowledge base on the limits of antenna behaviour. This work would certainly involve the use of the sub-structure characteristic modes introduced in Chapter 4.

- The use of characteristic modes to shape-synthesize UWB antennas in a feedless manner was initially investigated in Appendix E. The results of Appendix E should provide a springboard for future work on this antenna synthesis problem.

- The new concept of the fragmented reflectarray was successfully used to maximize the aperture efficiency of reflectarray antennas. The flexibility of fragmented elements is apparent in that the number of possible shapes they can take is a colossal number compared to traditional geometrically varied elements. A consequence of this is there are numerous areas of reflectarray research that have not been explored that would benefit greatly from fragmented elements:

    - One in particular is the synthesis of wideband reflectarrays. Fragmented elements offer one the opportunity to synthesize elements that yield the precise reflection phase necessary for wideband reflectarray operation rather than using the traditional approach of database lookup and/or the use of wideband elements.

    - Another interesting application of fragmented elements involves the synthesis of elements for shaped-beam reflectarrays, since the latter are notorious for having very high geometric variation over their surface due to the large variations in reflection phase. Similarity-shaped fragmented elements would provide the means to reduce this geometric variation over the surface, which would certainly improve the performance of shaped-beam reflectarrays.

- Including dielectrics in a future iteration of the periodic structure moment method code would dramatically improve the applicability of the synthesis approach. It should be noted that including the effects of the dielectric substrate would further improve the already stellar performance of the similarity-optimized reflectarray discussed in Section 5.4. This would also open up the possibility of synthesizing, among other things, electromagnetic absorbers.

- A wide variety of alternative periodic structure based antenna design concepts should be explored using the fragmented element approach. These include the optimization of transmitarrays, thin-lenses, FSS structures, AMC structures, absorbers and low-RCS surfaces. There are very specific gaps in these research areas that fragmented elements can help to address, such as computational efficiency (e.g. for thin lenses) as well as improved angular sensitivity (e.g. for absorbers and low-RCS devices).

- The modal character of multi-mode periodic structures was briefly investigated in Appendix H. Initial investigations of the behaviour of periodic structures purported to exhibit metamaterial-like behaviour suggests that modal decomposition of these structures will prove to be illuminating.

Appendix A: Succinct Introduction to the Method of Moments

The method of moments is an invaluable numerical method used predominantly for antenna design and analysis. The moment method solves an integral equation by discretizing the domain in which the unknown is defined. The unknown quantity in the method of moments is surface and/or volume current density. These currents can be the result of some chosen method of excitation, be it with a source defined somewhere on the surface or an incident field scattered by the object. We can begin by defining a typical integral equation

$$\int_a^b f(x')G(x,x')dx' = g(x) \tag{A.1}$$

where $a \le x \le b$

- $f(x')$ is the unknown function we wish to determine, and typically takes the form of a surface and/or volume current (but in the 1D case, it is a line current)
- $G(x,x')$ is the kernel of the integral equation. In electromagnetics, this function is almost always a Green's function that has a hand in describing the domain in which $f(x')$ is defined.
- $g(x)$ is known as a source function or driving function. It is considered the driving force behind the unknown function $f(x')$

In order to solve for the unknown $f(x')$, we expand the function in terms of a set of linearly independent expansion functions.

$$f(x') = \sum_{n=1}^{\infty} a_n f_n(x') \tag{A.2}$$

Since we are using finite resources we must discretize the domain and therefore use a finite number of expansion functions N to model the unknown $f(x')$.

$$f(x') \approx \sum_{n=1}^{N} a_n f_n(x') \tag{A.3}$$

Our integral equation after substitution of the approximated unknown then becomes:

$$\int_a^b \left(\sum_{n=1}^{N} a_n f_n(x') \right) G(x, x') \, dx' \approx g(x) \tag{A.4}$$

Integral operators are linear, and hence we can write:

$$\sum_{n=1}^{N} a_n \int_a^b f_n(x') G(x, x') \, dx' \approx g(x) \tag{A.5}$$

We note that currently our only unknowns are the coefficients a_n, so we are clearly on the right track to developing a numerical method to solve the integral equation. Examining (A.5), we note that we have effectively discretized the kernel over x' by expanding the unknown using the expansion functions $f_n(x')$, but we still have the x-dependent portion of the kernel and the continuous function $g(x)$ that have yet to be discretized. We therefore define another set of weighting functions $g_m(x)$ in which to expand $g(x)$. We choose these weighting functions to be the same as the expansion functions, yielding what is known as a Galerkin method. This is a very important concept for characteristic mode analysis, as a Galerkin method will produce a symmetric impedance matrix [Z], as required by CM theory. We therefore set our weighting functions to be the same as the expansion functions, multiply and integrate both sides of the integral equation, noting the new set of indices:

$$\sum_{n=1}^{N} a_n \int_a^b \int_a^b f_n(x') G(x, x') f_m(x) \, dx' dx \approx \int_a^b g(x) f_m(x) \, dx \tag{A.6}$$

We now have all known functions discretized over the domain, with the coefficients a_n remaining unknown. We can now consider the above expression as a system of linear equations if we consider m = 1, 2, … N weighting functions (one at a time), and group terms in matrix form as shown below:

$$\sum_{n=1}^{N} a_n \underbrace{\int_a^b \int_a^b f_n(x') G(x, x') f_m(x) \, dx' dx}_{Z_{mn}} \approx \underbrace{\int_a^b g(x) f_m(x) \, dx}_{V_{\mathrm{m}}} \tag{A.7}$$

This allows us to write:

$$\sum_{n=1}^{N} a_n Z_{mn} \approx V_{\mathrm{m}} \qquad \text{with } m = 1, 2, \ldots, N \tag{A.8}$$

Expression (A.8) is of course equivalent to the matrix expression

$$\begin{bmatrix} Z_{11} & \cdots & Z_{1N} \\ \vdots & \ddots & \vdots \\ Z_{N1} & \cdots & Z_{NN} \end{bmatrix} \begin{bmatrix} a_1 \\ \vdots \\ a_N \end{bmatrix} = \begin{bmatrix} V_1 \\ \vdots \\ V_N \end{bmatrix} \tag{A.9}$$

where the column vector $\begin{bmatrix} a_1 & \cdots & a_N \end{bmatrix}^T$ is the collection of unknowns to be solved for. We have considered a 1D domain, but the same method can be extended to 2 and 3 dimensions, with newly defined integral equations with the currents as unknowns to be solved for.

The moment method is a general numerical method used to solve electromagnetics problems, and the details change depending on the formulation. The expansion functions can exist over discretized portions of the domain or possibly over the entire domain. The properties of the expansion functions change depending on the application. Three high level categories can be considered for moment method expansion functions, namely wire-type, surface-type and volumetric-type. As their names imply, the expansion functions are application specific. For our purposes, we shall employ surface-type or triangular patch expansion functions. Many commercial software tools are available that use a moment method formulation, but access to the details of the formulation, namely the impedance matrix [Z], is often restricted. For the purposes of eigenanalysis, we require access to [Z]. An ideal solution was found using the moment method engine designed by Makarov [Ch. 2, Ref. 71]. With the moment method formulation in hand, we were able to develop the additional software components required for eigenanalysis. The expansion functions used in Makarov's formulation are known as RWG edge elements. They were first proposed by Rao, Wilton and Glisson [Ch. 2, Ref. 72] from which the expansion functions' name is derived. The surface that defines our antenna is discretized into triangles, with every pair of triangles sharing a common edge forming an RWG edge element. One can think of each RWG expansion function as an equivalent elementary dipole of current, and the Z matrix as the description of the mutual and self interactions of these dipoles. From this perspective, we can approximate the current across each edge using these edge elements, and subsequently determine quantities such as input impedance, radiation efficiency and far-field patterns. More importantly, we can compute the characteristic modes of the meshed structure using the impedance operator [Z]. We restrict our designs to be infinitesimally thin conducting surfaces, thereby forgoing the need to design with volumetric RWG elements. That being said, we are not limited to two dimensions since we can construct 3D objects provided they can be described as a surface and not a penetrable volume.

Appendix B: Characteristic Mode Analysis of a Single-Mode Antenna

The reader should cover Section 3.2 – 3.4 before reading this appendix.

A great deal of the thesis is concerned with the analysis and synthesis of single-mode antennas. As such, we will perform characteristic mode analysis of a typical electrically small antenna in this appendix. The geometry of the example antenna is shown in Figure B.1, with the ideal[16] feed location shown with a red circle. The largest linear dimension of the antenna is 116.5mm (with a line width of 5mm), with the resonance frequency occurring at 300 MHz for the copper variety of the antenna. Combining the largest linear dimension of the antenna (2a, where 'a' is the radius of the smallest circumscribing sphere) with the resonance frequency indicates the antenna is resonant at an electrical size ka = 0.366, well into the small antenna regime. The antenna input impedance is shown in Figure B.2, and the input reflection coefficient using reference impedance value $Z_o = 5\Omega$ in Figure B.3. The selected reference impedance is rather low due to low input resistance which is a consequence of its electrically small size. The impedance matrix for this antenna is computed and the resulting CM matrix trace is computed, with the real and imaginary parts shown in Figure B.4 and a more detailed view in Figure B.5. The magnitude and phase of the CM matrix is also shown in Figure B.6. The resonance is clearly identified with zero phase of the trace, or zero imaginary part. Figure B.7 shows the radiation efficiency of this antenna, obtained both using the traditional means of direct excitation via a feed, and the newly proposed "feedless" or excitation-free approach of Section 3.3 that uses the CM matrix trace and its value at resonance. There is indeed very close agreement at resonance. Additionally, we consider the antenna Q, obtained using expression (2.57), and the alternative approach using the frequency derivative of the CM matrix trace and find very good agreement again, but as expected from the thesis valid only at the resonance of the antenna, as shown in Figure B.8. Note that this antenna has very large antenna Q and low radiation efficiency. Lastly, for the sake of completeness, the dominant characteristic mode current distribution on the antenna at 300 MHz is shown in Figure B.9.

[16] The feed location is ideal because of symmetry but also, as we will see, the dominant CM currents peak here.

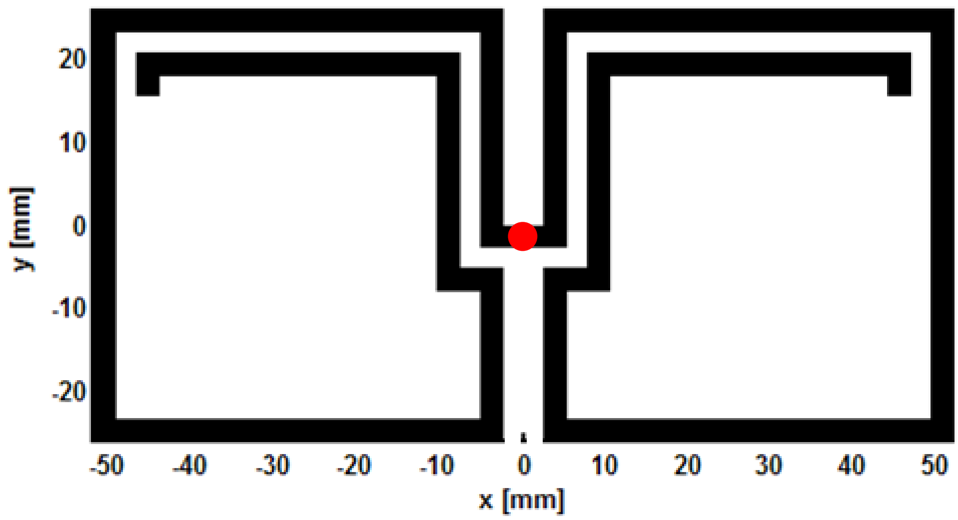

Figure B.1 – Example electrically small, single-mode antenna

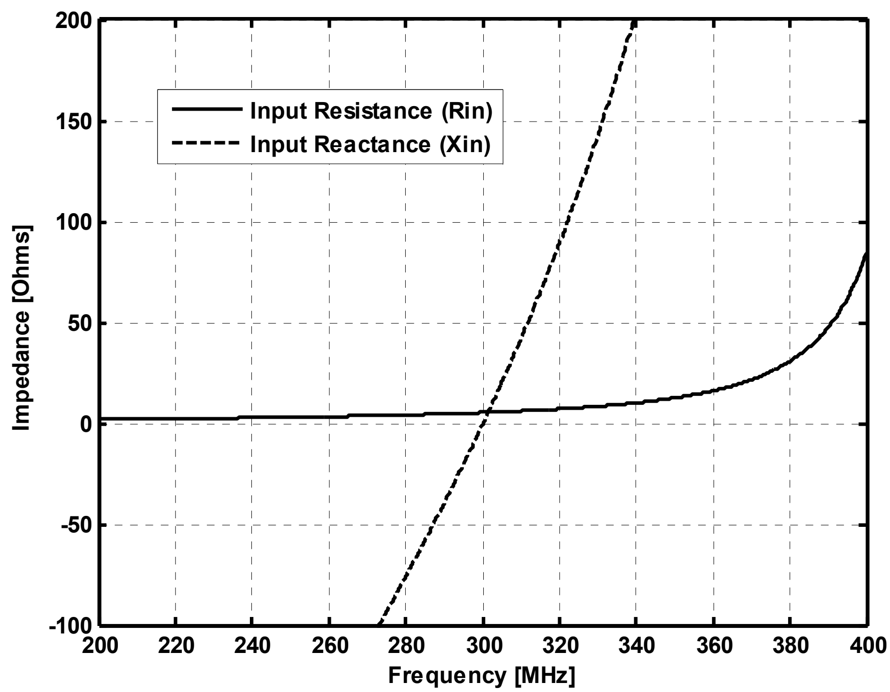

Figure B.2 – Input impedance of example electrically small, single-mode antenna

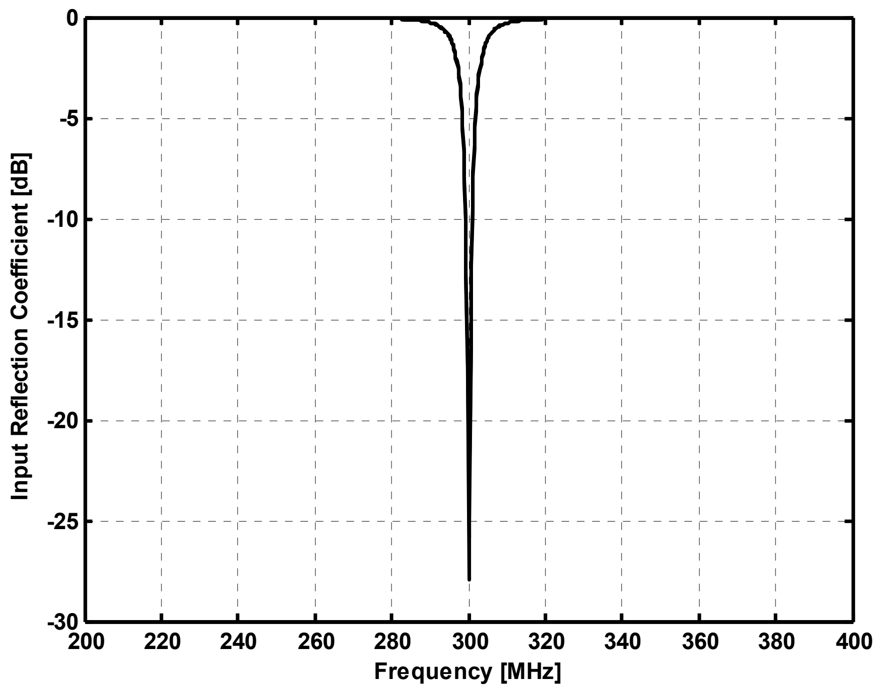

Figure B.3 – Input reflection coefficient (Z_o = 5Ω) of example electrically small, single-mode antenna

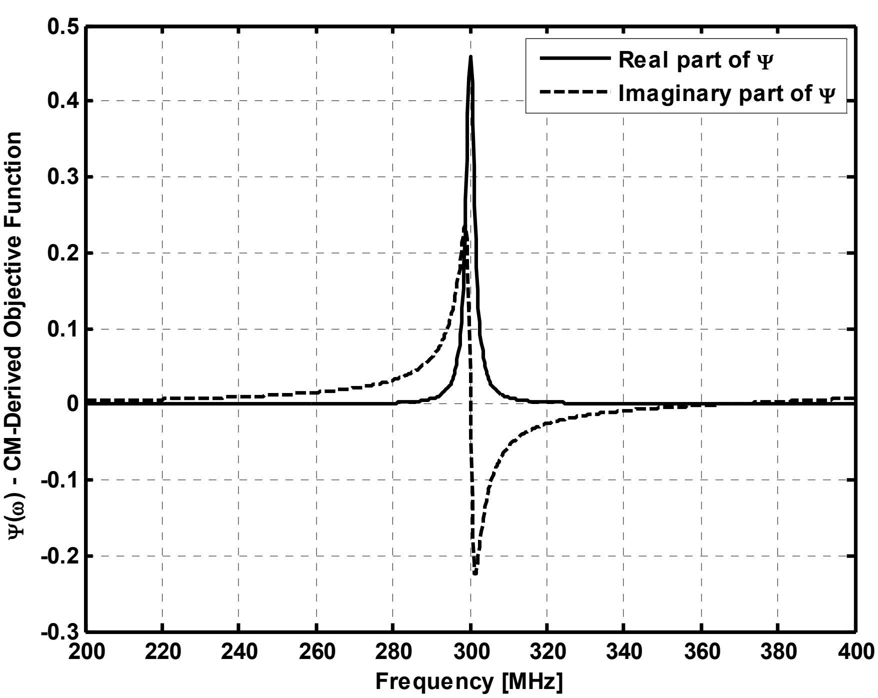

Figure B.4 – Real and imaginary parts of the CM matrix trace for single-mode antenna

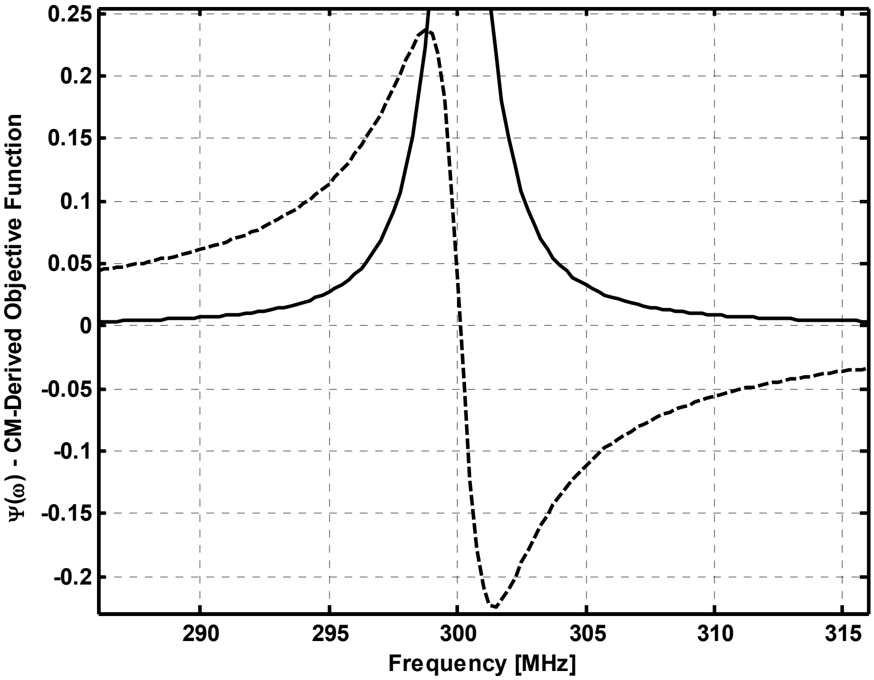

Figure B.5 – Expanded view of the real and imaginary parts of the CM matrix trace for single-mode antenna

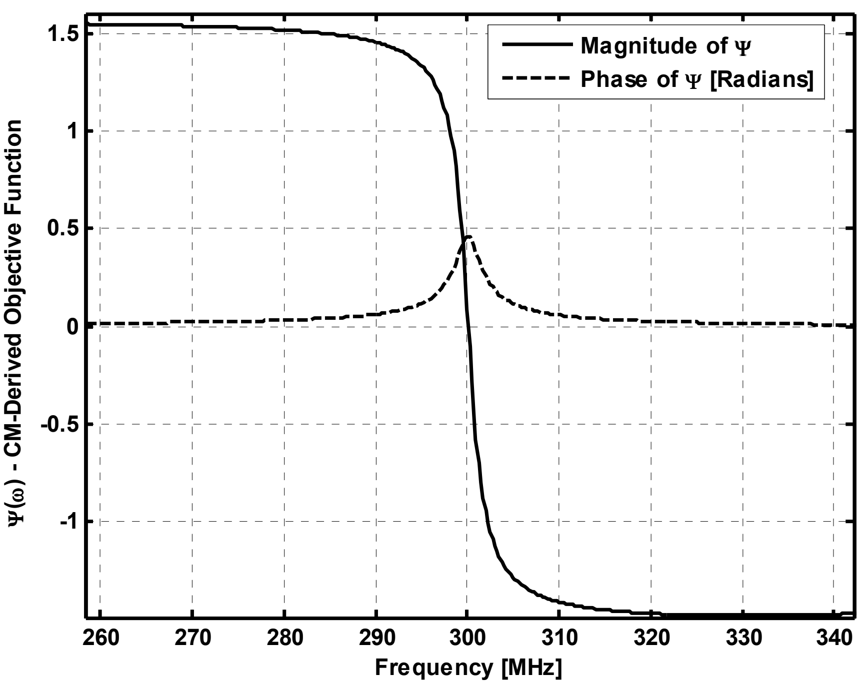

Figure B.6 – Magnitude and phase of the CM matrix trace for single-mode antenna

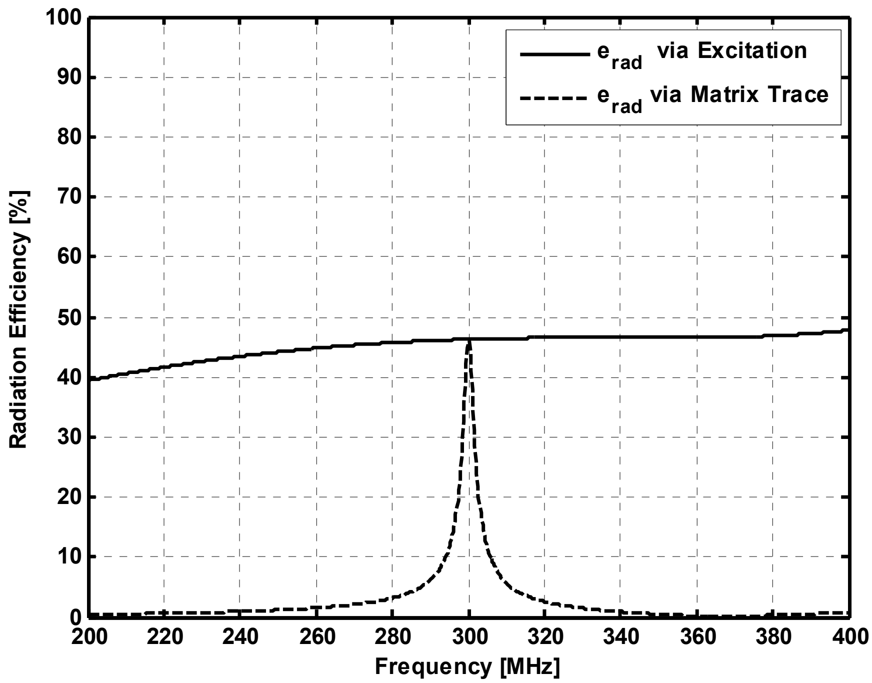

Figure B.7 – Radiation efficiency obtained from the traditional means of excitation and alternatively from the CM matrix trace for single-mode antenna

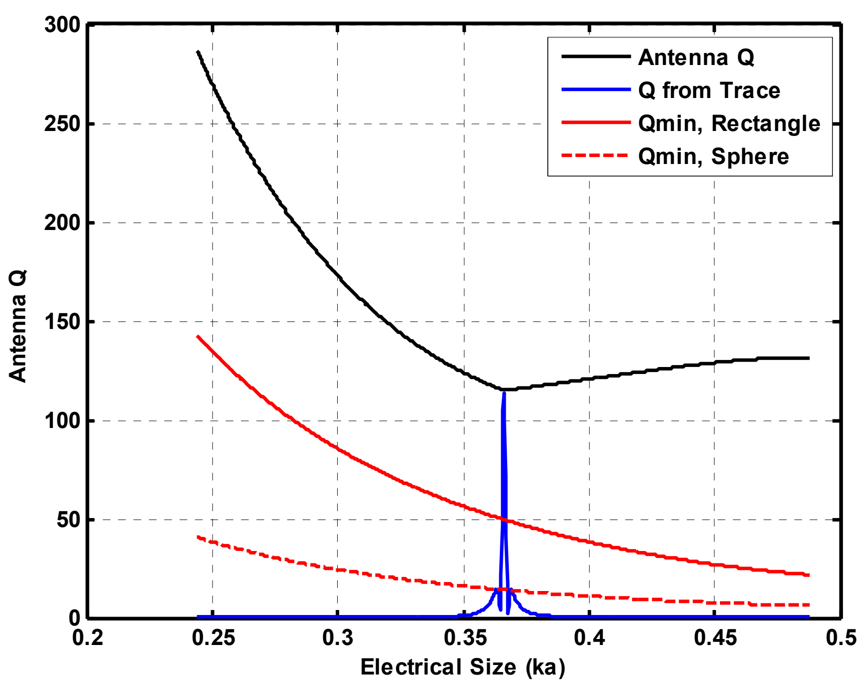

Figure B.8 – Antenna Q computed from input impedance (black curve), from the matrix trace (blue curve) and the minimum Q for rectangular plate (2:1 ratio) and sphere

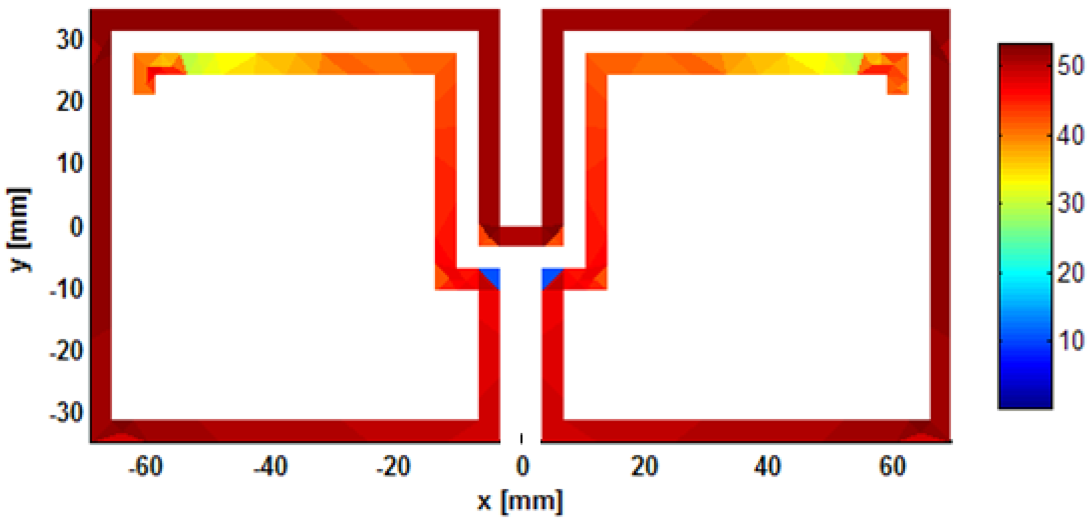

Figure B.9 – Dominant Characteristic Mode Current at 300 MHz (the antenna is resonant, input reactance is zero). CM eigenvalue magnitude is 0, signifying resonance as well. Current density is in dB and normalized to radiate 1 watt.

The ability to compute the resonance frequency, radiation efficiency and bandwidth of a single-mode antenna in a feedless manner was shown in Chapter 3 as well as in the examples shown thus far in Appendix B. We can further emphasize this concept by plotting maps of various quantities on the surface of the electrically small antenna shown in Figure B.1. These include maps of input resistance (Figure B.10), input reactance (Figure B.11), radiation efficiency (B.12), antenna Q (Figure B.13) and single-mode purity (Figure B.14). These five quantities are computed at the centre frequency of 300 MHz and are plotted as a function of position over the surface of the antenna shown in Figure B.1. This mapping concept effectively places a port at every possible location on the surface of the antenna and determines the five aforementioned antenna metrics as functions of the port location.

The impedance maps of input resistance (Figure B.10) and input reactance (Figure B.11) show that the majority of the antenna structure will present similar input impedances, regardless of the selected feed location. In a very similar manner, the radiation efficiency (Figure B.12) and antenna Q (Figure B.13) shows near uniform behaviour over the surface of the antenna structure. As a last (and most important) investigation, consider the single-mode excitation purity measure, shown in Figure B.14. The purity measurement is simply the percentage of power that enters the antenna port that couples to the dominant characteristic mode (n = 1) of the structure. We see for nearly every selected port location, the majority (nearly 100%) of the power is coupled to the dominant characteristic mode. These results are valid for any single-mode electrically small antenna.

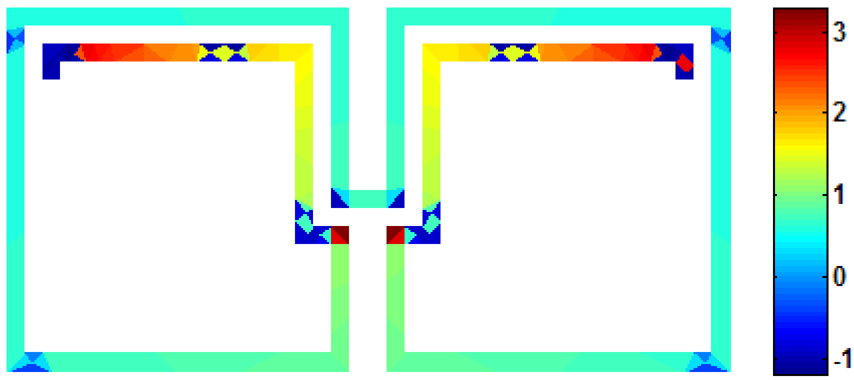

Figure B.10 – Map of input resistance (Rin) as a function of position on electrically small, single-mode antenna. Input resistance is plotted as $\log_{10}$(Rin)

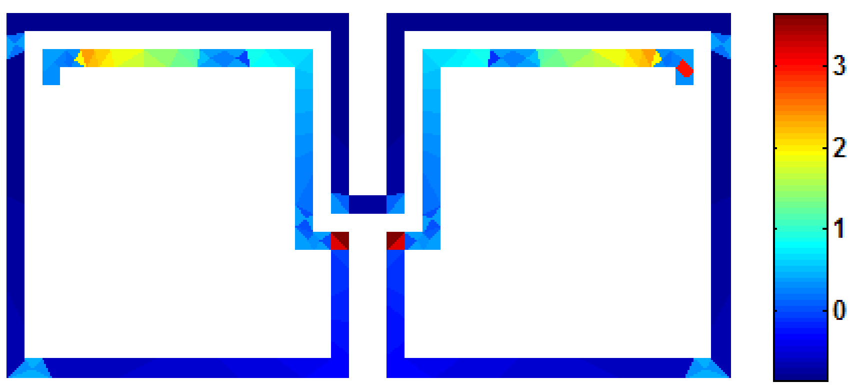

Figure B.11 – Map of input reactance (Xin) as a function of position on electrically small, single-mode antenna. Input reactance is plotted as $\log_{10}$(|Xin|)

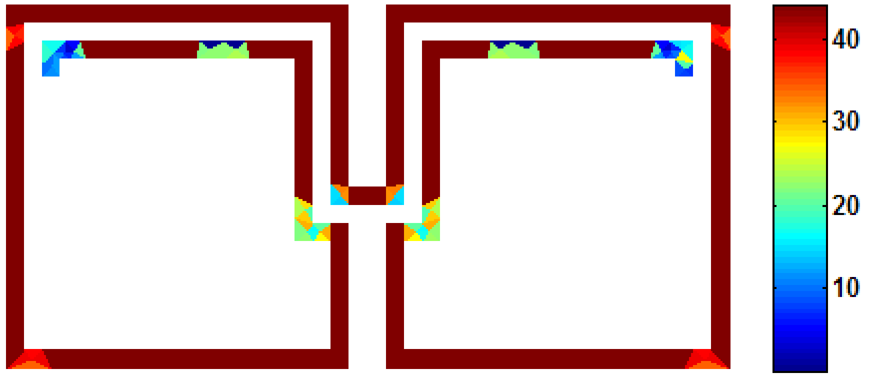

Figure B.12 – Map of radiation efficiency (e_{rad}) as a function of position on electrically small, single-mode antenna. Radiation efficiency is plotted in linear units as a percentage.

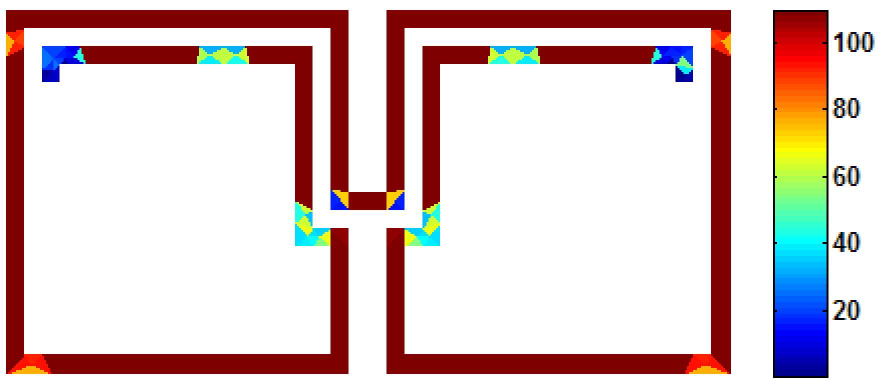

Figure B.13 – Map of antenna Q as a function of position on electrically small, single-mode antenna. Antenna Q is plotted in linear units.

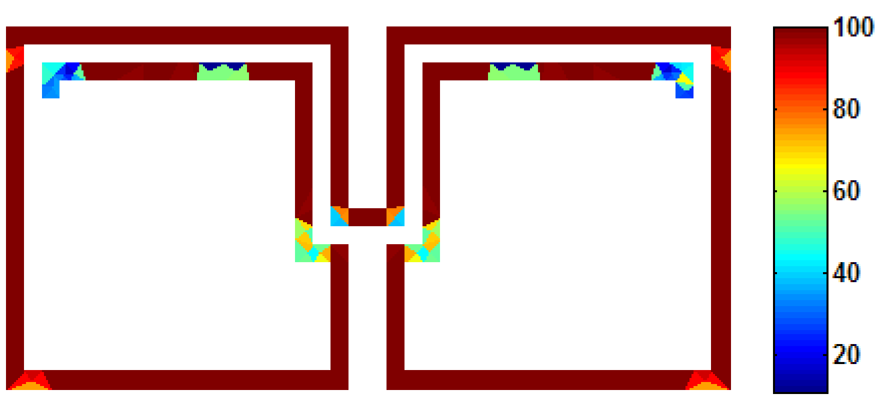

Figure B.14 – Map of single-mode purity as a function of position on electrically small, single-mode antenna. Units are plotted in percentage, where percentage is a measure of the amount of input power coupling to the dominant characteristic mode of the electrically small antenna.

Appendix C: Obtaining Static Polarizability from a Time-Harmonic Moment Method Formulation

In [1] the authors give a relationship for estimating the bounds on the directivity to quality-factor ratio (D/Q) of electrically small antennas in a "sharper" manner than existing methods, since it holds for arbitrary non-spherical antenna volumes (the widely used ones). It requires computation of certain components of the so-called high-contrast polarizability $\tilde{\gamma}_\infty$ (the tilde denoting that it is a dyadic) of the radiating structure, obtained via the solution of a related electrostatic problem [1]. We can identify an expression whereby the same integral equation based moment method formulation used to determine the input impedance and radiation patterns of an antenna can be used to accurately estimate the required components of its $\tilde{\gamma}_\infty$, and hence its D/Q bounds. Consider a conducting antenna structure with surface S, and let $\rho_{\text{static}}(\overline{r})$ be the surface charge density induced on the structure when it is placed in an impressed uniform unit-amplitude static electric field whose orientation is $\hat{e}$. This charge density can be shown to be the solution of the integral equation [1]

$$\iint_S \frac{\rho_{\text{static}}(\overline{r}\,')}{4\pi\varepsilon_0 \left|\overline{r}-\overline{r}\,'\right|} dS' = \hat{e}\cdot\overline{r} + C_o \tag{C.1}$$

where quantity C_o is determined subject to the condition that the total charge on S is zero, namely $\iint_S \rho_{\text{static}}(\overline{r})\, dS = 0$. We here use $\rho_{\text{static}}(\overline{r})$ to directly denote the surface charge density rather than the normalized charge density. The $\hat{e}$-component of the polarizability dyadic $\tilde{\gamma}_\infty$ for an $\hat{e}$-oriented impressed field (in fact the $\hat{e}$-component of the induced electric dipole moment $\overline{p}$ for the specified impressed field orientation $\hat{e}$) can then be obtained from $\rho_{\text{static}}(\overline{r})$ using [1]

$$\hat{e}\cdot\tilde{\gamma}_\infty\cdot\hat{e} = \hat{e}\cdot\overline{p}(\hat{e}) = \hat{e}\cdot\iint_S \overline{r}\,\rho_{\text{static}}(\overline{r})\, dS \tag{C.2}$$

This can be used [1] to determine an upper bound for D/Q. In order to avoid confusion with symbols used to denote various other polarizabilities we will refer to the scalar quantity in eq. C.2 as $\gamma_{\text{imp}} = \hat{e}\cdot\tilde{\gamma}_\infty\cdot\hat{e}$, the subscript "imp" pointing to the fact that it is the high-contrast polarizability component in the direction of the impressed field.

The question which arises is as follows. Suppose we are using an EFIE-based moment method model (e.g. ref. [2]) of the antenna of interest, where the unknown quantity is the surface current density $\overline{J}_s$. If we specify a uniform incident plane wave with polarization unit vector $\hat{e}$, could we not simply specify an extremely low value for the frequency (to approximate a static impressed electric field), find the surface charge density from the continuity relation $\rho_s = (-1/j\omega)\nabla_s\cdot\overline{J}_s$, assume that $\rho_{\text{static}}(\overline{r}) \approx \rho_s(\overline{r})$, and hence determine the polarizability of the antenna structure? This might be so if we had an exact solution for $\overline{J}_s$. But in the so-called "very low-frequency region" this approach cannot be used to accurately determine ρ_s from conventional moment method solutions for $\overline{J}_s$, for reasons clearly set out in reference [3] and elsewhere. However, it should be remembered that it is $\iint_S \overline{r}\,\rho_{\text{static}}(\overline{r})\,dS$ we actually wish to determine, and not $\rho_{\text{static}}(\overline{r})$. Papas [4, Chap.4] has shown that this quantity can be expressed directly in terms of the integral of the electric current density, namely

$$\overline{p} = \iint_S \rho_s(\overline{r})\,\overline{r}\,dS = \frac{j}{\omega}\iint_S \overline{J}(\overline{r})\,dS \tag{C.3}$$

Thus explicit knowledge of the charge density is not necessary to determine γ_{imp} from expression (C.2). We therefore conjecture that we can determine γ_{imp} using

$$\gamma_{\text{imp}} = \hat{e}\cdot\iint_S \overline{r}\,\rho_{\text{static}}(\overline{r})\,dS = \hat{e}\cdot\lim_{\omega\to\omega_\ell}\left\{\frac{j}{\omega}\iint_S \overline{J}_s(\overline{r})\,dS\right\} \tag{C.4}$$

where ω_ℓ is some selected very low frequency.

In a moment method formulation that uses RWG expansion functions the resultant current density over the *n*-th triangle is given by reference [5]

$$\overline{J}_n(\overline{r}) = I_1\overline{f}_1(\overline{r}) + I_2\overline{f}_2(\overline{r}) + I_3\overline{f}_3(\overline{r}) \tag{C.5}$$

where $\overline{f}_i(\overline{r})$ is the expansion function associated with *i*–th edge of that triangle and is a function of position $\overline{r}$ on the triangle, and I_i is the coefficient associated with that same edge (in fact an element of the moment method solution vector), integer *i* here being a local numbering index. We approximate the resultant current density $\bar{J}_n$ on the *n*-th triangle as being constant over the triangle and equal to its vector value at the triangle centroid $\bar{r}_c$. Thus (4) becomes

$$\gamma_{\text{imp}} = \frac{j}{\omega_\ell} \sum_{\forall n} \left\{ \hat{e} \cdot \bar{J}_n(\bar{r}_c) \right\} \Delta S_n \tag{C.6}$$

where ΔS_n is the area of the triangle, and the summation is over all individual triangles. A detailed integration of the complete RWG representation (C.5) of $\bar{J}_n(\bar{r})$ can be done over each triangle in evaluating (C.4), but (C.6) is sufficient. Note that since the polarizability is a real scalar quantity, the current must be imaginary in the time-harmonic solution as frequency approaches zero. This, and the validity of the approach represented by expression (C.4), is confirmed by simulation in Section III. With regards to which value of ω_ℓ to use, in what follows we have gone as low as 1/2π radians/second, but find little difference in the computed γ_{imp} when computed at that frequency and 10^6/2π radians/second for planar conducting objects of maximum dimension 1m or so.

In the results presented here we will follow the practice of [6] and show the quantity $\gamma_{\text{imp}} / a_{\text{sph}}^3$, referred to in [6] as the normalized polarizability, with a_{sph} the radius of the smallest sphere that can circumscribe the object. The first validation example is a sphere of radius a = 1m (for which shape clearly $a_{\text{sph}} = a$) selected for convenience. Fig. C.1 shows the computed value of $\gamma_{\text{imp}} / a_{\text{sph}}^3$ for the sphere versus electrical size $k_\ell a = \omega_\ell \sqrt{\mu_0 \varepsilon_0}\, a$. As the frequency decreases the normalized polarizability indeed approaches the analytical value from [1]; this represents the limiting operation in (C.4). Our interest lies principally with thin planar conducting antenna structures. We therefore next consider a thin circular plate of radius a = 1m (the plate has the same radius value as the sphere in the previous example), and so once again $a_{\text{sph}} = a$. The applied electric field has $\hat{e}$ parallel to the plane of the disc. We see from Fig. C.2 that once again the method proposed clearly predicts a value of $\gamma_{\text{imp}} / a_{\text{sph}}^3$ identical to that obtained from the closed-form expression in [6]. The γ_{imp} for the circular plate is much less than that for the sphere, even though they both have the same circumscribing sphere. This is what is meant by the statement in [1] that use of the polarizability in question provides a sharper way of establishing small antenna bounds than conventional methods. It can distinguish between thin and voluminous objects which have the same circumscribing spheres.

In order to examine the effect of mesh density on the accuracy of the $\gamma_{\rm imp}$ computation we selected the frequency to be $\omega_\ell = 1/2\pi$ Hz and modeled a circular plate of radius 1m, corresponding at this frequency to an electrical size $k_\ell a = 2.1\times10^{-8}$. The meshing used was purposefully not ideal for this application (it meshes everywhere equally) and is the reason for the relatively slow convergence evident in Fig. C.3. If one uses an adaptive mesh with denser meshing along edges (where charge density accumulates), the convergence with respect to mesh density is more rapid. Nevertheless, this result confirms that the proposed approach is an accurate tool for the prediction of polarizability. In order to test the accuracy of the approach for geometries other than rotationally symmetric ones we consider a thin rectangular plate of variable length ℓ_1 and width ℓ_2, and hence changing aspect ratio $\xi = \ell_1/\ell_2$. In this case $a_{\rm sph} = \sqrt{(\ell_1/2)^2 + (\ell_2/2)^2} = \frac{1}{\sqrt{2}}\sqrt{\ell_1^{\,2} + \ell_2^{\,2}}$, and Fig. C.4, shows that the results using the approach of Section II are identical to that obtained from the analytical estimates in [1].

As a final example we consider the highly irregular thin plate shown in Fig. C.5, with dimensions such that $a_{\rm sph} \approx 1\,\rm m$ as for the previous examples. This is simply meant to represent a complicated geometry for which analytical estimates of $\gamma_{\rm imp}$ are not at all easily determined. We are not implying that one will necessarily construct an antenna of such a shape, but not discounting this either. The applied electric field has $\hat{e}$ as illustrated in Fig. C.5, parallel to the plane of the disc (the xy-plane), whose precise orientation can be specified through the angle $\phi_{\rm pol}$. The resulting normalized polarizability as a function of $\phi_{\rm pol}$ is shown in Fig. C.6, and has distinct maxima and minima at $\phi_{\rm pol} = 125^{\rm o}$ and $\phi_{\rm pol} = 35^{\rm o}$, respectively. It would not have been possible to "guess" the maximum and minimum angles for this geometry. This is a useful feature of the polarizability viewpoint proposed in [1] since by knowing the orientation with the largest $\gamma_{\rm imp}$ we can select antenna orientations so that the widest bandwidth response for a geometry in question can be obtained with proper design. The structure in Fig. C.5 will have the widest bandwidth response to fields polarized as shown in Fig. C.7, and hence (invoking reciprocity) should be fed such that fields of this polarization are the predominant ones generated. The field orientation resulting in the lowest value of $\gamma_{\rm imp}$ is that in Fig. C.8. A simple method has been proposed for obtaining computational estimates of the polarizability $\gamma_{\rm imp}$ of conducting antenna structures of arbitrary shape, via the same moment method formulation being used for the analysis of the radiating performance of the antenna itself. This can be done with sufficient accuracy through use of expression (C.4), and so a separate static analysis is not necessary.

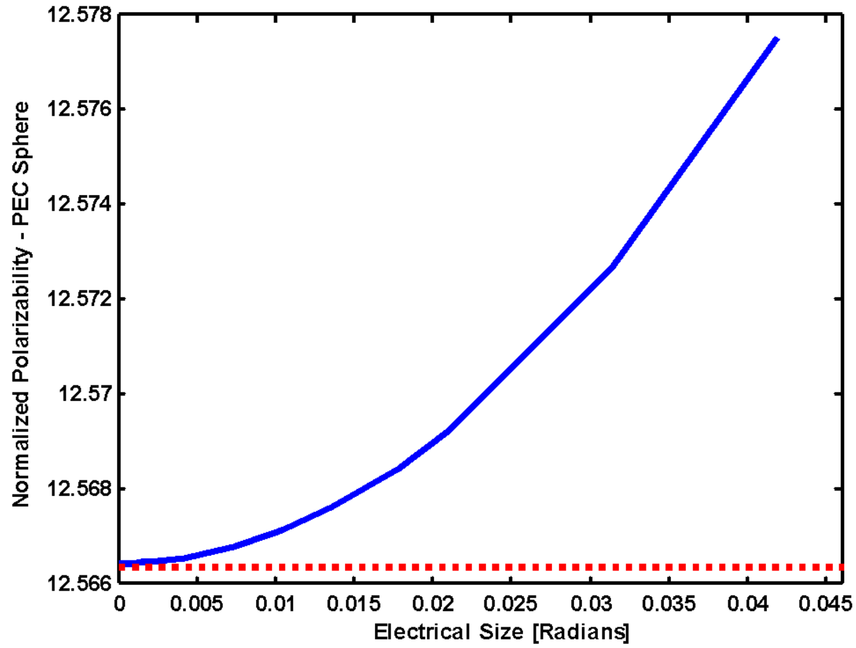

Fig. C.1. Convergence of computed values (▬▬) of normalized γ_{imp} for a sphere to the analytical value (▪▪▪▪▪▪) [1, 6] as the value of ω_ℓ decreases.

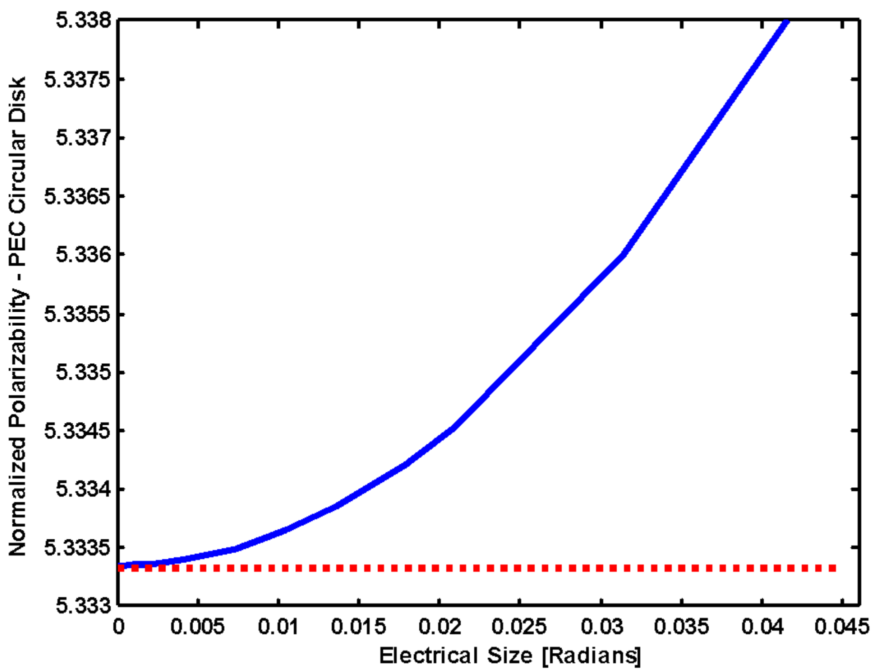

Fig. C.2. Convergence of computed values (▬▬) of normalized γ_{imp} for a thin circular plate to the analytical value (▪▪▪▪▪▪) [1, 6] as the value of ω_ℓ decreases.

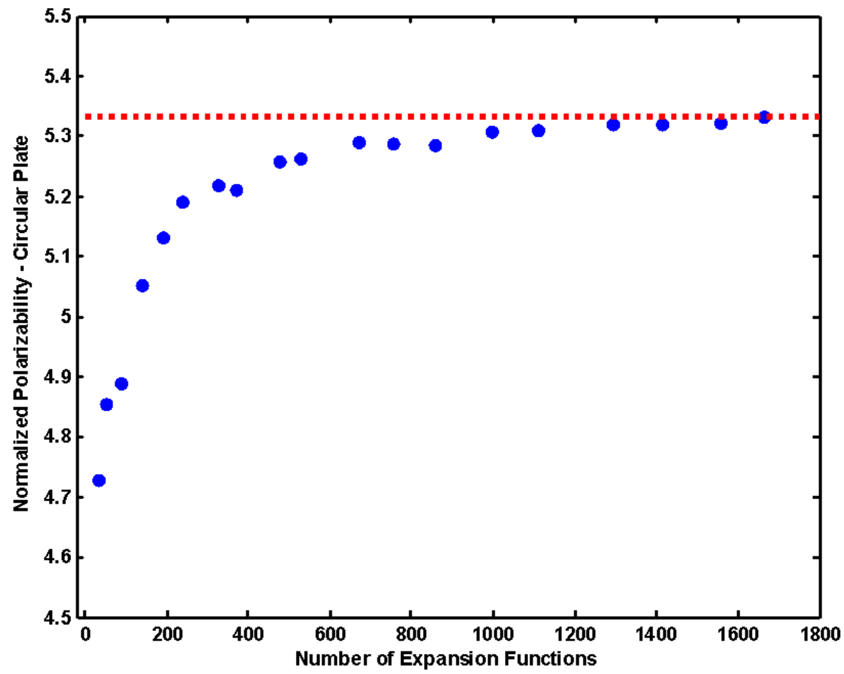

Fig. C.3. Convergence of the normalized γ_{imp} of a thin circular plate computed (●●●●●) using the approach outlined to the closed-form estimate (▪▪▪▪▪▪) from [1], as a function of mesh density.

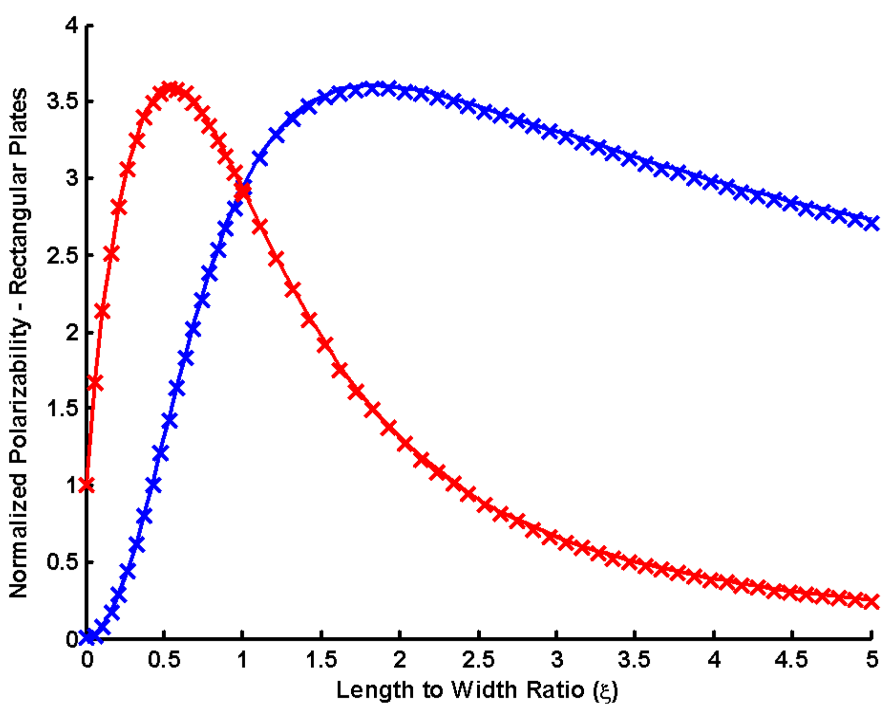

Fig. C.4. Normalized polarizability of a rectangular plate for the cases $\hat{e}=\hat{x}$ (blue) and $\hat{e}=\hat{y}$ (red). The crosses indicate the analytical estimates [1], the solid lines the values computed using eq. C.6

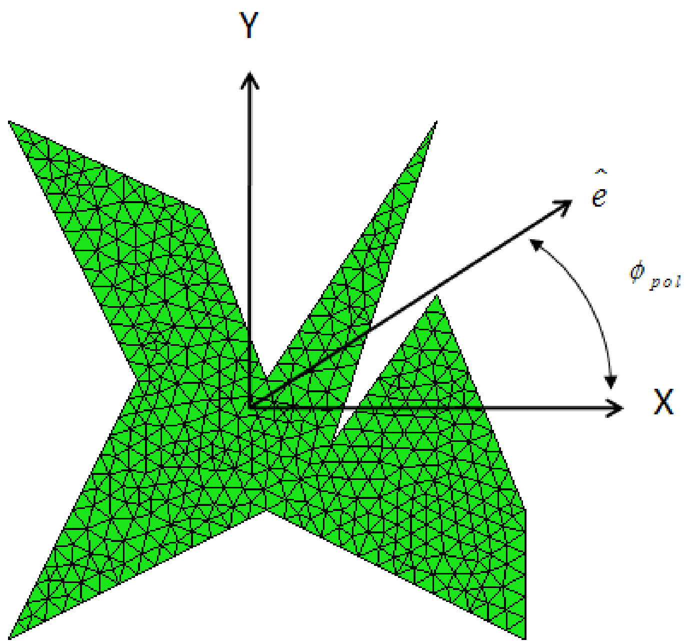

Fig. C.5. Highly irregular thin plate geometry representative of structures for which analytical estimates of the normalized polarizability are not available.

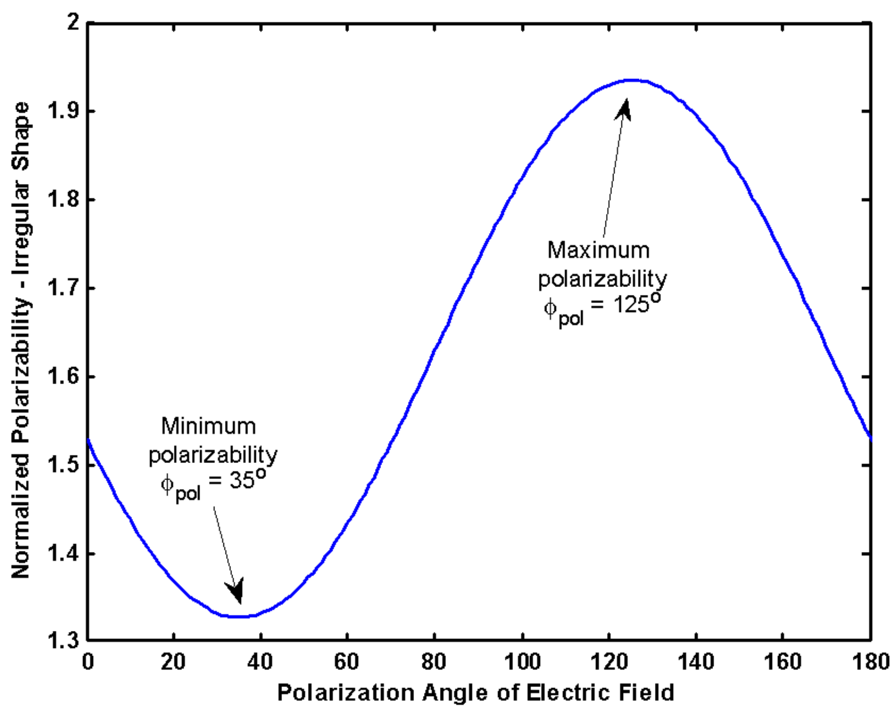

Fig. C.6 Normalized polarizability of the highly irregular thin plate shown in Fig. C.4 for applied field orientation $\hat{e} = \hat{x}\cos\phi_{\text{pol}} + \hat{y}\sin\phi_{\text{pol}} + 0\hat{z}$.

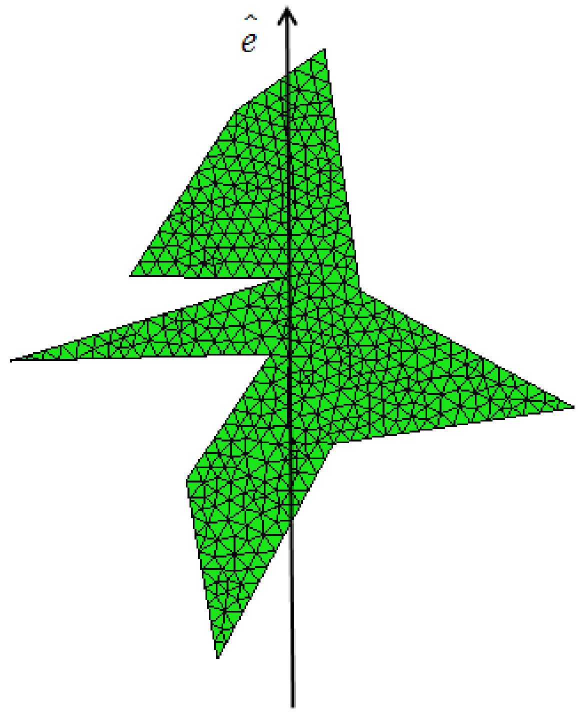

Fig. C.7 Impressed electric field orientation ($\phi_{\text{pol}} = 125^{\circ}$) for maximum γ_{imp} .

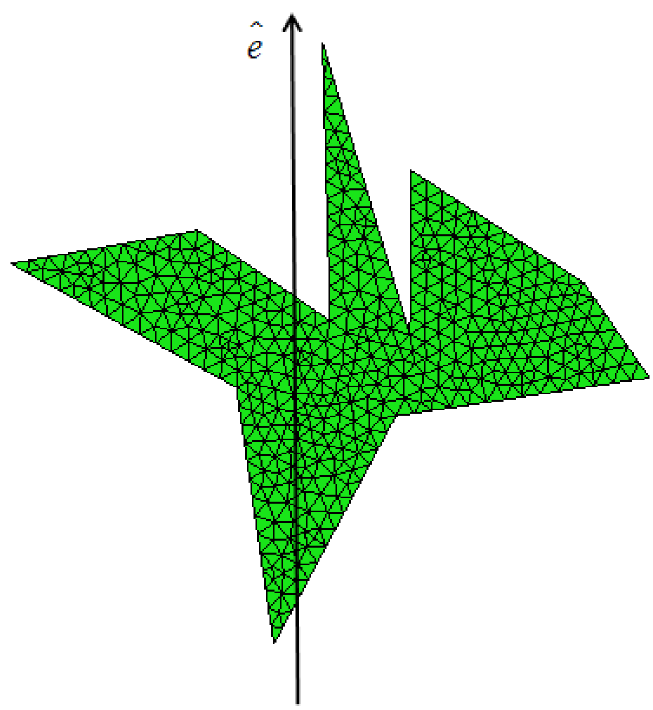

Fig. C.8 Impressed electric field orientation ($\phi_{\text{pol}} = 35^{\circ}$) for minimum γ_{imp} .

References for Appendix C

[1] M. Gustafsson, C. Sohl and G. Kristensson, "Illustrations of new physical bounds on linearly polarized antennas", IEEE Trans. Antennas Propagat., Vol.57, No.5, pp.1319-1327, May 2009.

[2] S.N. Makarov, *Antenna and EM Modeling with Matlab*, Wiley, 2002.

[3] J.R. Mautz and R.F. Harrington, "An E-field solution for a conducting surface small or comparable to the wavelength", *IEEE Transactions on Antennas and Propagation*, Vol.AP-32, No.4, pp.330-339, April 1984.

[4] C.H. Papas, *Theory of Electromagnetic Wave Propagation* (Dover Publications Inc., 1965).

[5] S.M.Rao, D.R.Wilton and A.W.Glisson, "Electromagnetic scattering by surfaces of arbitrary shape", *IEEE Trans. Antennas Propagat.*, Vol.30, pp.409-418, May 1982.

[6] M.Gustafsson, "Polarizability and physical bounds on antennas in cylindrical and rectangular boundaries", Rept. TEAT-7195, Dept. Electrical & Information Tech., Lund University, Sweden, May 2010.

Appendix D: Absorption Efficiency Computation Examples

From the derivations, statements and conclusions made by Gustafsson et. al. [1], one can be fairly confident that the single-mode antennas synthesized in Chapter 3 have absorption coefficients approximately equal to 50%. In particular, Gustafsson [1, Sec. 2] states that an absorption coefficient of 50% *"is observed for many small antennas that are matched at a dominant first resonance* k_o*. This is partly explained by the fact that the absorption efficiency* $\sigma_a(k)/\sigma_{ext}(k) = 1/2$ *for minimum scattering antennas, that is, small single mode antennas absorb and scatter the same amount of power at the resonance frequency."* Given that the antennas in Chapter 3 are, by definition, single-mode antennas, we expect the absorption efficiency to obey the approximate equality $\tilde{\eta} \approx 1/2$. Nevertheless, we shall confirm this fact through simulation for selected antennas from Chapter 3.

Two important quantities must be computed in order to estimate the absorption efficiency. The first is the absorption cross section, defined in [1, eq. 5]. It is a function of directivity and reflection coefficient only, is scaled by the square of the wave number and is defined as

$$\sigma_a(k) = \frac{D(k)\left(1 - \left|\Gamma(k)\right|^2\right)\pi}{k^2} \tag{D.1}$$

where $D(k)$ is the maximum antenna directivity, $\Gamma(k)$ is the antenna's reflection coefficient and k is the freespace wave number. The function $\sigma_a(k)$ is also called the effective antenna aperture. We next require the quantity known as the extinction cross-section, as defined in [2, eq. 10] and given as

$$\sigma_{ext}(k) = \frac{4\pi}{k^2} \operatorname{Im}\left(\frac{\hat{p}_o \cdot \underline{F}}{E_o}\right) \tag{D.2}$$

where $\underline{F}(\hat{k})$ is the far-field pattern (with spherical wave dependence removed) in the direction of the incident plane wave, E_o is the magnitude of the incident plane wave and $\hat{p}_o$ is the sense of polarization to be measured (the same as the polarization of the incident plane wave). The absorption coefficient is then defined as the weighted integral ratio of these two functions

$$\tilde{\eta} = \frac{\int_0^\infty k^{-2} \sigma_a(k) \, dk}{\int_0^\infty k^{-2} \sigma_{ext}(k) \, dk} \tag{D.3}$$

The term k^{-2} within the integrand will act to dramatically reduce the effects of higher frequency contributions and thus any low-frequencies where cross sections are large (around resonances) will dominate the behaviour of the ratio of integrals.

We first consider antenna Design A from Section 3.4.7. The absorption (D.1) and extinction (D.2) cross-sections, normalized to k^{-2}, are shown in Figure D.1 for antenna Design A. Note the very strong resonance and thus large cross-sections at 600 MHz. Higher frequency resonances occur as well, but their effects are substantially reduced by the scaling factor k^{-2}, and hence do not contribute greatly to the integrals in (D.3). Computation of these integrals leads to an absorption efficiency of 0.47 which is nearly equal to the value of 0.50 assumed in Chapter 3, and in the majority of works found in the literature. The fact that the absorption efficiency is not precisely equal to 0.50 is mainly due to the second unwanted resonance occurring around 1800 MHz. We next consider the same scaled cross-sections for antenna Design B in Figure D.2. We observe similar results to those for Design A, only now the second resonance has a lower extinction cross-section and thus we expect less contribution to the absorption efficiency. This is precisely the case with the computed absorption efficiency computed as 0.49, closer to the 0.50 that is characteristic of single mode antennas.

References for Appendix D

[1] M. Gustafsson, M. Cismasu, S. Nordebo, "Absorption Efficiency and Physical Bounds on Antennas," *International Journal of Antennas and Propagation*, Vol. 2010, Article 946746, 7 pages.

[2] J. Bach Anderson, A. Frandsen, "Absorption Efficiency of Receiving Antennas," *IEEE Transactions on Antennas and Propagation*, Vol. 53, No. 9, September 2005, pp 2843 – 2849.

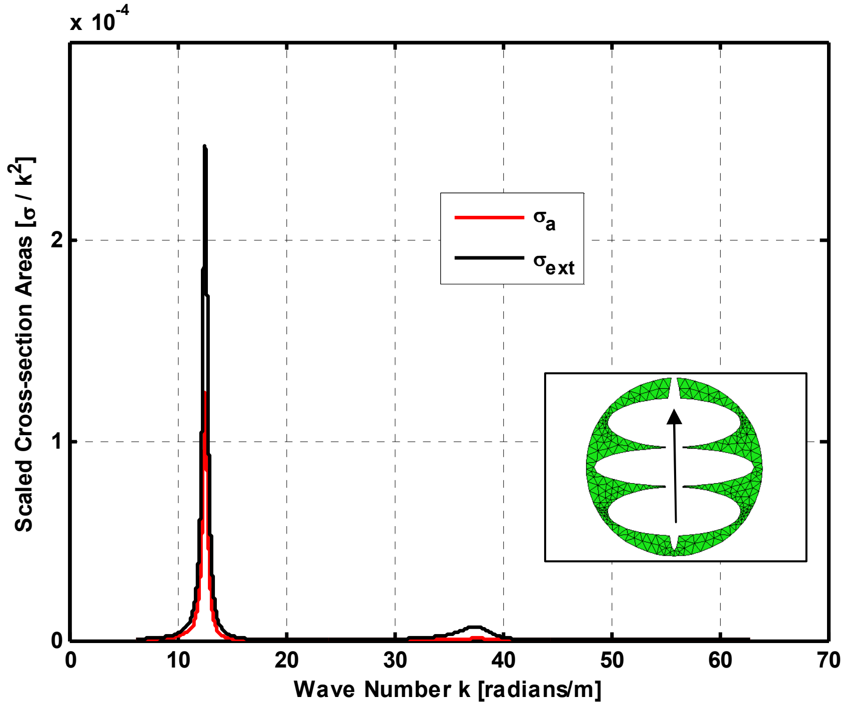

Figure D.1 – Scaled cross-sections for antenna Design A from Section 3.4.7. The antenna is shown overlaid with the dominant polarization used in determining the cross-sections.

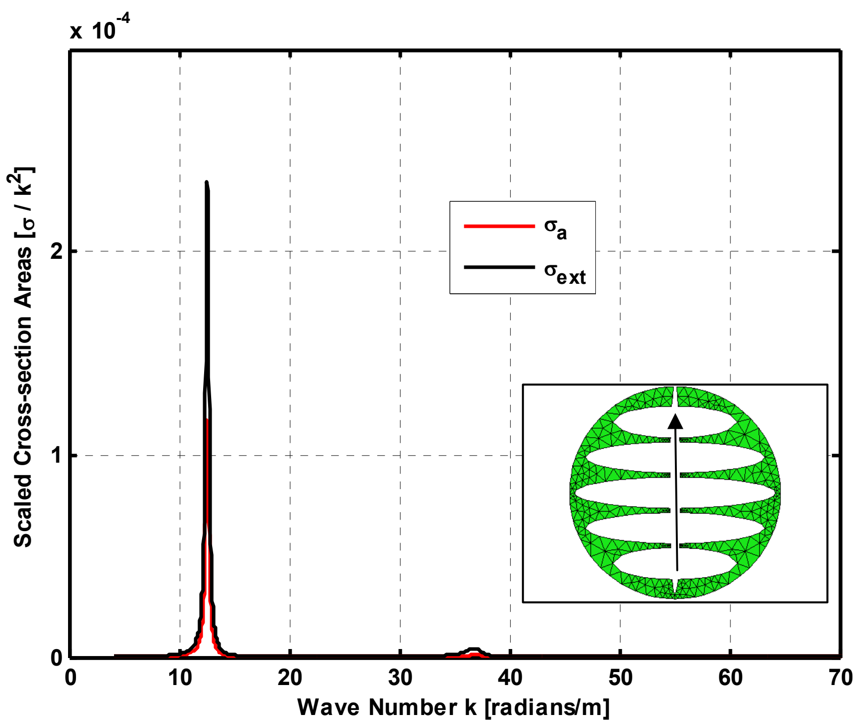

Figure D.2 – Scaled cross-sections for antenna Design B from Section 3.4.7. The antenna is shown overlaid with the dominant polarization used in determining the cross-sections.

Appendix E: UWB Multi-mode Antenna Synthesis using Feedless Optimization

Another aspect of antenna design that has not been discussed thus far is the design of UWB antennas. The term UWB refers to ultrawideband and has various definitions to classify antennas as UWB or not. According to the FCC [1], an ultra-wideband antenna is defined as any antenna with a bandwidth greater than 500 MHz or a bandwidth at least 20% relative to its center frequency. One example of an unlicensed spectrum is the frequency range 3.1 to 10.6 GHz (a bandwidth of 7.5 GHz or 109.5%). In our work we will simply attempt to obtain a bandwidth as large as possible for a given antenna area/volume in order to avoid restricting ourselves to any particular applications. For the readers' convenience, reference [2] is likely the most popular[17] UWB antenna design reference found in the literature.

The characteristic mode analysis of UWB antennas (and wideband antennas in general) has been investigated in [3] – [6]. The conclusion from these references is that an UWB antenna's behaviour is described by multiple modes, where portions of the antenna's well-matched bandwidth is due to particular resonant modes, with the dominant mode(s) exchanging roles in allowing the antenna to be resonant. Hence, the UWB antenna is wideband (in the cases discussed) due to multiple near-resonant modes existing over different frequency regimes.

Whether a single mode can result in wideband behaviour is a worthwhile question to pose, but it is expected that a single-mode antenna is restricted in bandwidth even in the electrically large regimes by the bounds imposed by Chu and Gustafsson. However, electrically intermediate and large antennas tend to be multi-mode and so the Chu limit is rarely imposed for these larger structures. In other words, single mode antennas are subject to traditional bandwidth restrictions imposed by Q-limits. Multi-mode antennas are not subject to this restriction which is likely the reason the UWB antennas analyzed in [3] – [6] are all multi-mode antennas. The concept of a wideband single mode antenna that is not electrically small (e.g. intermediately sized) will not be discussed in this thesis, but is proposed as a relevant research topic for future work.

[17] According to Google Scholar, http://scholar.google.ca/, retrieved November 2011

We will perform CM analysis on an example UWB slot antenna, with the antenna shown in Figure E.1. A plot of the eigenvalue magnitudes of the antenna for various frequencies is shown in Figure E.2. As the frequency increases, the number of low magnitude eigenvalue modes dramatically increases.

If the antenna is excited at the center of the slot, one obtains the input impedance shown in Figure E.3, simulated from 500 MHz to 10 GHz. The input reflection coefficient with reference impedance 100Ω is shown in Figure E.4. There is an excellent match starting at around 1.9 GHz and beyond. If one defines the bandwidth to be a reflection coefficient below -10dB, the operating band spans from 1.9 GHz to 5.3 GHz. This corresponds to a percentage bandwidth of 94.44%. If a reference impedance of 50 Ohms is used, the operating band begins at 1.5 GHz but is restricted to 2.7 GHz in the upper range. It should also be noted that if a 6 dB RL is defined for matching purposes, the bandwidth is quite large, beginning around 1.5 GHz and extending well beyond 10 GHz.

The angle of the matrix trace function, Ψ, is shown in Figure E.5. Note that over the bandwidth where the impedance matching is good (in particular from 1 GHz onwards) the matrix trace angle is small and is nearly equal to zero. Though a ripple in the trace angle occurs in between 1 and 3 GHz, we still consider the trace angle to be small in magnitude from 1 GHz and above. This has implications on how the matrix trace can be used in UWB antenna synthesis, as discussed next.

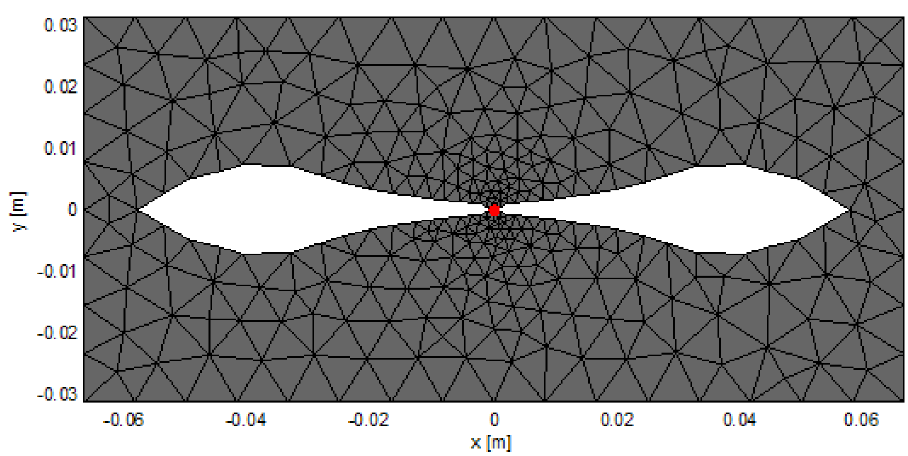

Figure E.1 – Example UWB Radiating Slot Structure

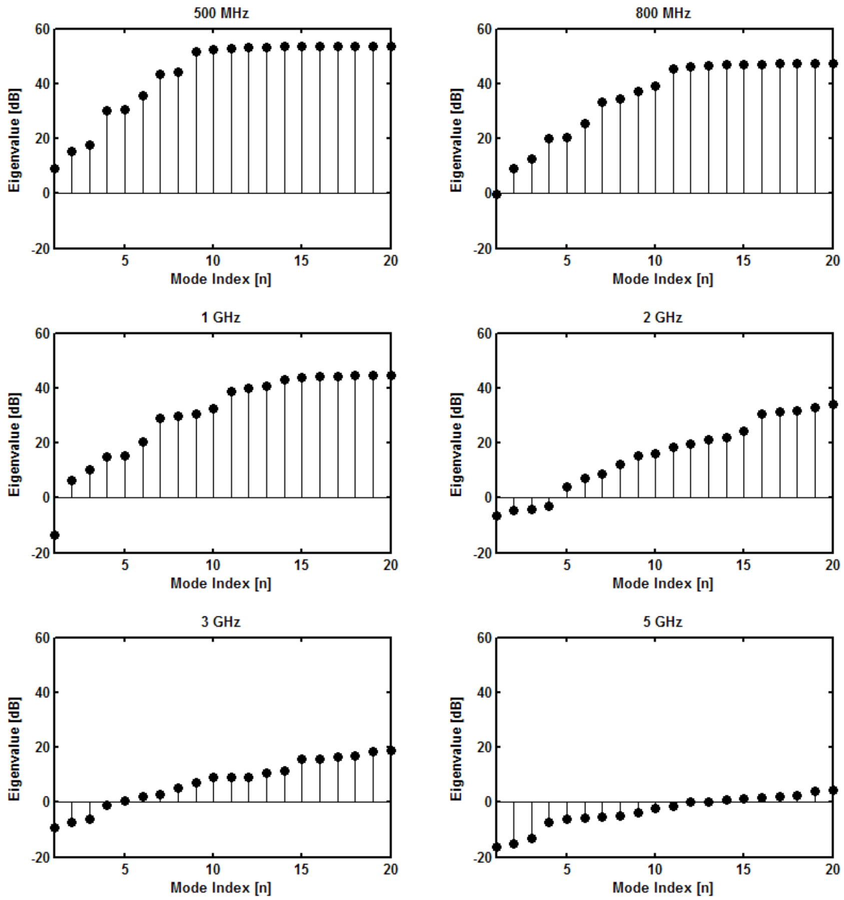

Figure E.2 – Mode Spectrum of the UWB Structure for Different Frequencies over its UWB Regime

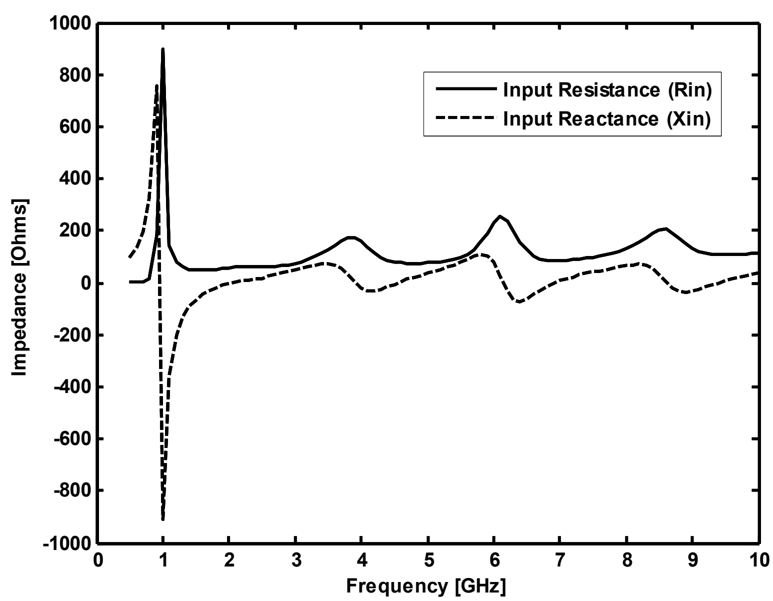

Figure E.3 – Input Impedance of the UWB Antenna clearly showing wideband performance through the relative flatness of the resistance and reactance

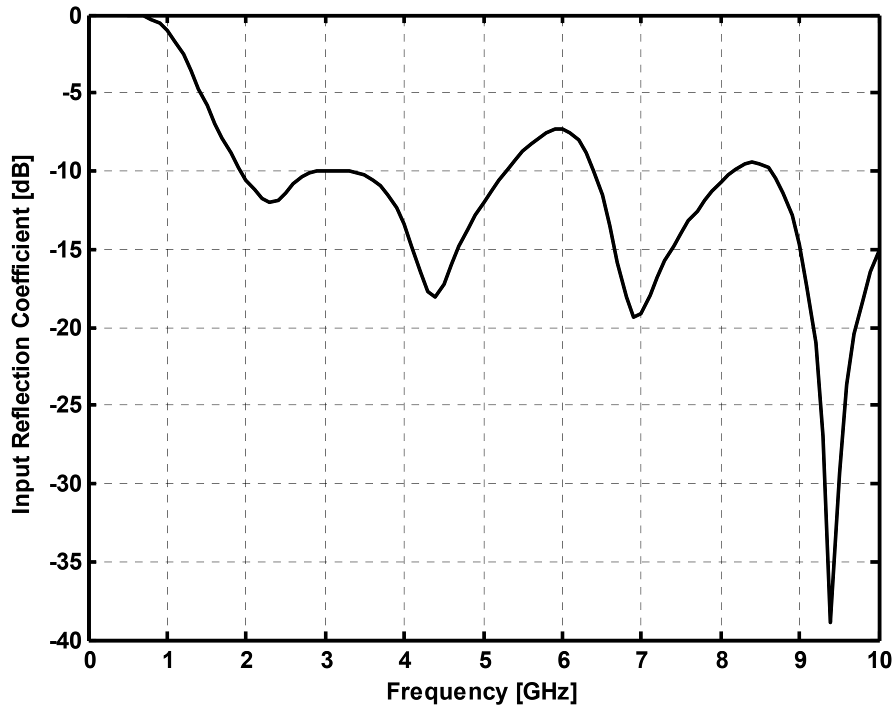

Figure E.4 – Input Reflection Coefficient of the UWB Radiating Slot for a Reference Impedance of 100-Ohms

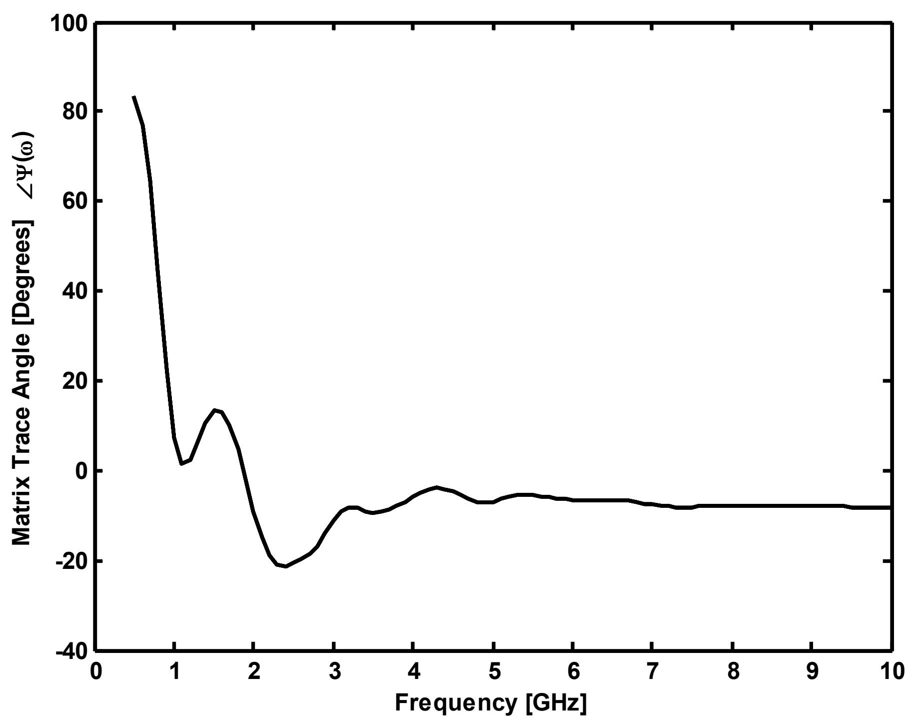

Figure E.5 – A plot of the angle of the CM matrix trace for the wideband radiating slot. The trace angle is clearly small in magnitude (nearly zero) over the antenna's wideband operating regime.

From our perspective, we are interested in whether the objective functions in expressions (3.77) to (3.79) can be used effectively in UWB antenna synthesis. As pointed out in [3] – [6], an UWB antenna consists of many significant characteristic modes. The presence of multiple simultaneously dominant modes as opposed to multiple dominant modes separated in frequency changes the applicability of the matrix trace. Consider, once again, the CM matrix trace of a PEC structure, defined as

$$Trace\left(\left[Z\right]^{-1}\left[R\right]\right)=\frac{1}{1+j\lambda_1}+\frac{1}{1+j\lambda_2}+\cdots+\frac{1}{1+j\lambda_M}+\cdots+\frac{1}{1+j\lambda_N} \tag{E.1}$$

Assume the first M modes of N total modes are significant contributors to the trace. As a first step, let us assume that these first M modes are not only dominant, but also near-resonant. As such, the trace can be approximated by

$$Trace\left(\left[Z\right]^{-1}\left[R\right]\right)\approx\frac{1}{\underbrace{1+j\lambda_1}_{\approx 1}}+\frac{1}{\underbrace{1+j\lambda_2}_{\approx 1}}+\cdots+\frac{1}{\underbrace{1+j\lambda_M}_{\approx 1}} \tag{E.2}$$

The matrix trace magnitude $\left|\Psi\right|$ and phase $\angle\Psi$ can be stated to be approximately equal to

$$\left|\Psi\right|\approx M \tag{E.3}$$

$$\angle\Psi\approx 0 \tag{E.4}$$

Such a scenario would connect well with our previous work where the presence of a single dominant resonant mode was shown to dominate the antennas electrical performance. We expect the same would be true in this scenario: an antenna with multiple (as opposed to single) dominant and resonant modes will be dominated by these modes' behaviour. The difference is that now multiple modes work in tandem to yield a resonant antenna over a wide range of frequencies.

Our objective function for the synthesis of UWB antennas will be the enforcement of expression (E.4) over the bandwidth of interest. Contrary to the previous work in Chapter 3 and Chapter 4, there is less determinism in the use of expression E.4 as an objective function. One can understand this if we consider the case where two modes are present and dominant (low magnitude eigenvalues) with the remaining modes deemed insignificant:

$$Trace\left(\left[Z\right]^{-1}\left[R\right]\right) \approx \frac{1}{1+j\lambda_1} + \frac{1}{1+j\lambda_2} \tag{E.5}$$

For arguments sake, assume that $\lambda_1 \approx |\lambda|$ and $\lambda_2 \approx -|\lambda|$. The magnitude $|\lambda|$ is such that it is orders of magnitude smaller than the magnitudes for modes n $\geq$ 3, but not always small enough to be negligible. Under these conditions, the matrix trace then becomes

$$Trace\left(\left[Z\right]^{-1}\left[R\right]\right) \approx \frac{1-j|\lambda|}{1+|\lambda|^2} + \frac{1+j|\lambda|}{1+|\lambda|^2} \approx \frac{2}{1+|\lambda|^2} \tag{E.6}$$

Expression (E.6) has zero phase (no imaginary part) for any given value of eigenvalue $|\lambda|$. However, one would surmise that there is no guarantee that the superposition of modes 1 and 2 would give rise to a resonant structure. In fact, it could very well be the case that excitation of the antenna will result in the individual excitation of either modes 1 or 2, but possibly not both. This would imply that the matrix trace can be misleading since the excitation of one of these modes alone would lead to non-resonant behaviour due to the non-zero and potentially moderately sized eigenvalue.

These results suggest that there is indeed the possibility of returning a false-positive in optimization. Namely, an optimizer could produce an antenna with very small trace angle over a wide bandwidth and yet it might very well contain non-resonant modes and thus be incapable of resonant behaviour. In this sense, the proposed algorithm for UWB synthesis is not as robust and consistent as the other synthesis techniques (Chapter 3's small antenna and Chapter 4's multi-band synthesis). In any case one must determine the suitability and practicality of an optimized antenna before making conclusions and if a false-positive does result, the optimization process must be re-started.

The optimization flow diagram is shown in Figure E.6(a). The optimization scheme was applied to a square metal region, 150mm by 150mm. The frequency band over which impedance matching was of interest began around 500 MHz and run upwards to 3 GHz. Any results obtained can be applied to alternative frequency bands through the properties of antenna scaling. What is important from any results obtained is the percentage bandwidth and the electrical dimensions of the antenna considered.

Various multi-objective functions schemes were attempted but it was ultimately settled on a min-max routine. That is to say, the objective function became the largest angle of the trace over all frequencies with the goal of minimizing this function. This specific algorithm is shown in Figure E.6(b). Four optimizations runs were selected for further analysis and are discussed next.

A mother structure consisting of a square plate sized 150mm x 150mm was used in the UWB synthesis. The angle of the CM matrix trace was minimized (in a min-max scenario) over the bandwidth 1 GHz to 6 GHz. This optimization scheme was applied in numerous runs, where four antennas were selected with their matrix trace angle shown in Figure E.7. The fabricated antennas are shown E.8(a) – (d) with the feed location of design C shown in greater in Figure E.8(e). The four antennas have trace angles less than +/- 20 degrees between 1 and 6 GHz. The resulting simulated and measured reflection coefficients for the four designs are shown in Figures E.9 through E.12. We see a distinct lack of UWB behaviour, though experiment and simulation agree quite well.

In order to discern why the optimization technique seems to have failed we consider the experimentally measured input resistance and reactance of the four antennas, shown in Figures E.13 and E.14 respectively. Firstly, we recognize that the input resistance has a very large dynamic range over the band from 1 to 6 GHz, peaking in the hundreds of Ohms and dropping to as low as 5 Ohms. This makes the antennas incapable of a wideband match, even through the use of alternative reference impedances. Additionally, the reactance appears to experience a very large dynamic range as well, which is tied to the resistance since the peaks in both cases are due to anti-resonances. It would appear that rather than synthesizing a collection of UWB antennas we have obtained a collection of multi-resonant antennas. While not a success, we have (unintentionally) shown a technique to obtain a multi-resonant structure, albeit not in a deterministic fashion.

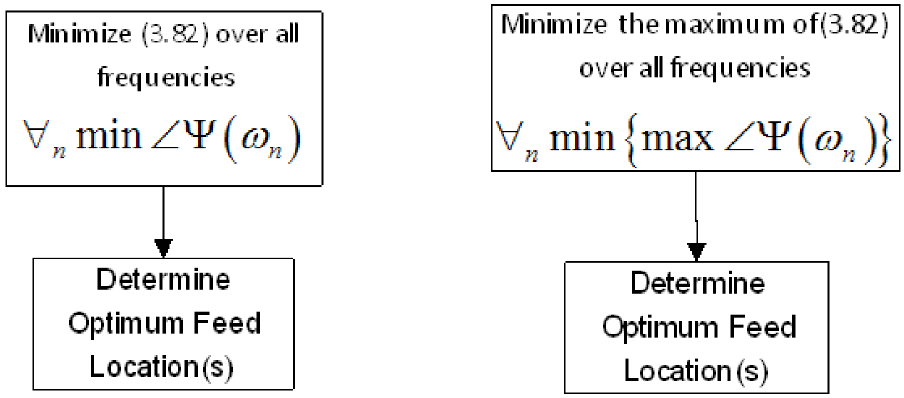

(a) (b)

Figure E.6 – Example optimization schemes whereby one (a) minimizes the trace angle at each frequency or better yet, (b) minimizes the maximum trace angle at each frequency of interest

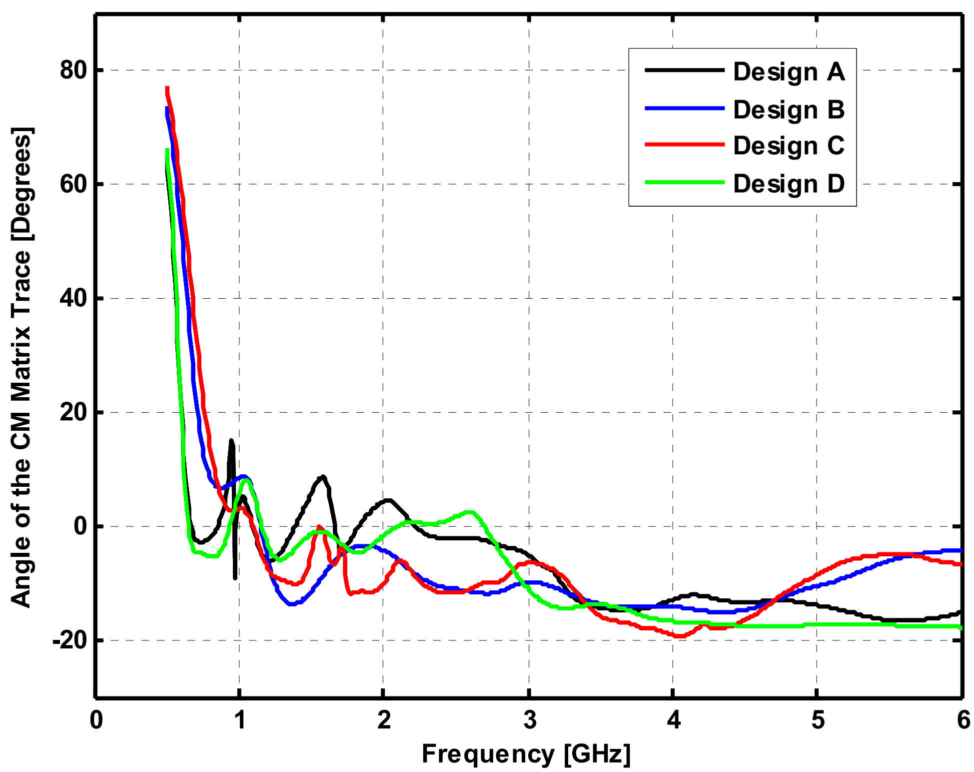

Figure E.7 – Angle of the CM Matrix Trace for the UWB Designs A through D

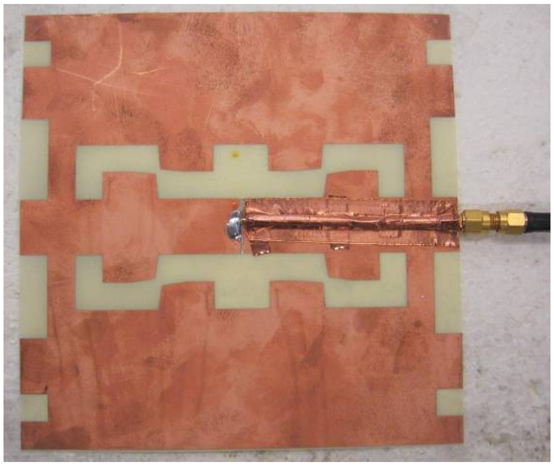

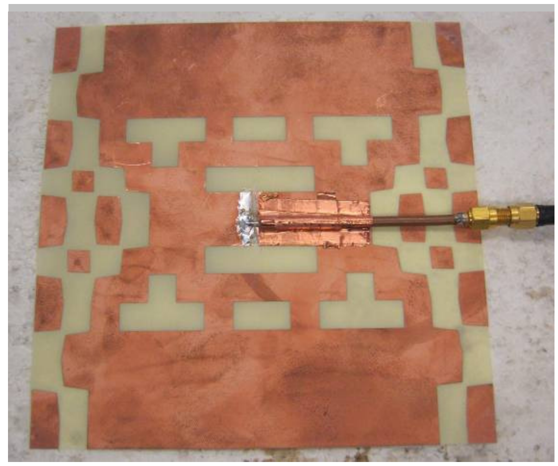

(a) (b)

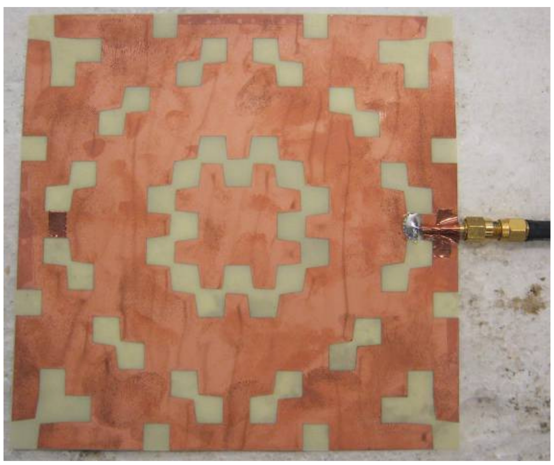

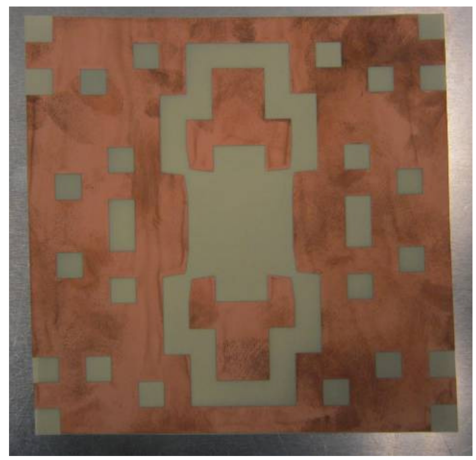

(c) (d)

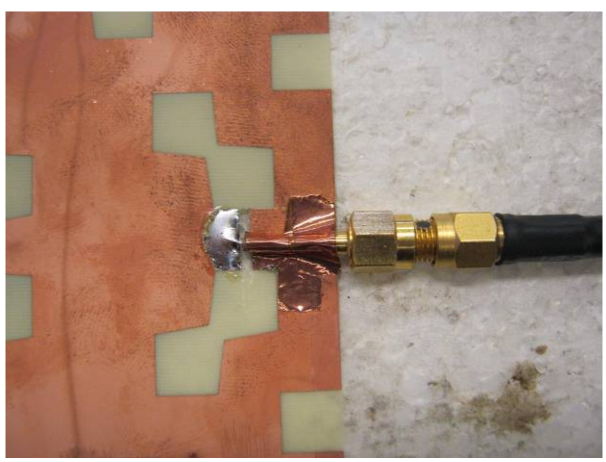

(e)

Figure E.8 – Example Antenna designs A through D denoted as such. The details of the feeding mechanism of Design C is shown with greater detail in (e)

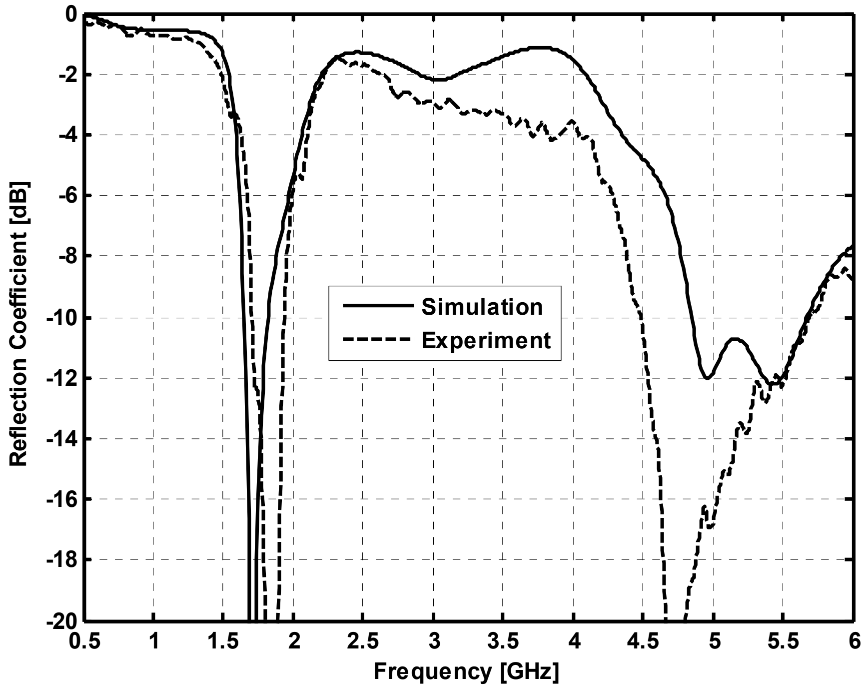

Figure E.9 – Reflection Coefficient for Design A (Z_o = 50Ω, Simulation and Experiment)

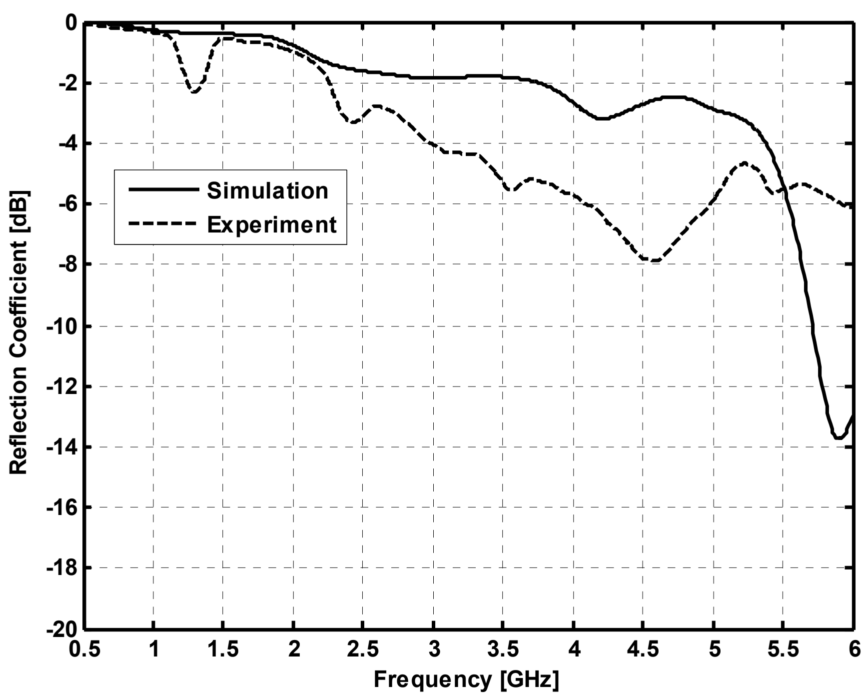

Figure E.10 – Reflection Coefficient for Design B (Z_o = 50Ω, Simulation and Experiment)

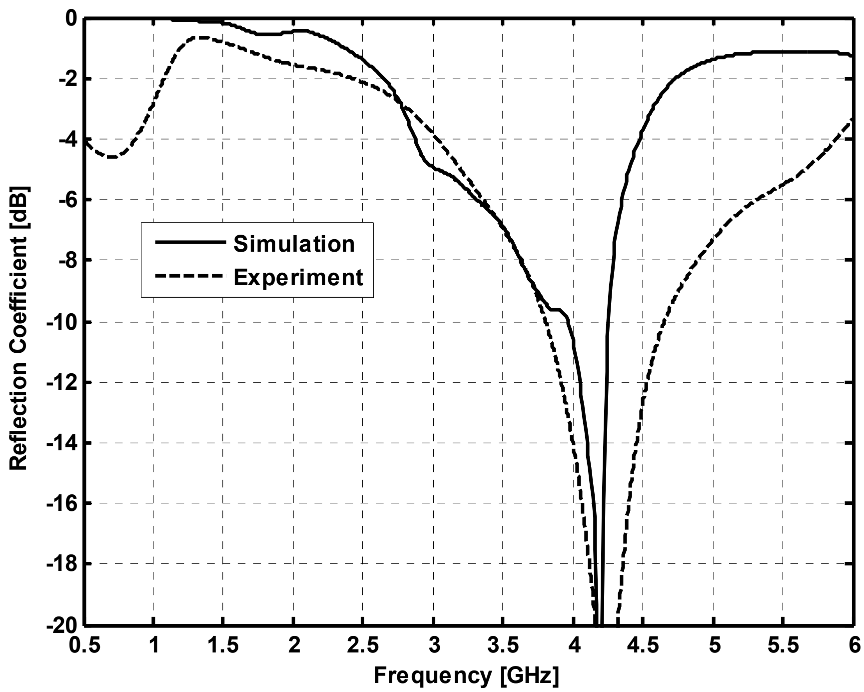

Figure E.11 – Reflection Coefficient for Design C (Z_o = 50Ω, Simulation and Experiment)

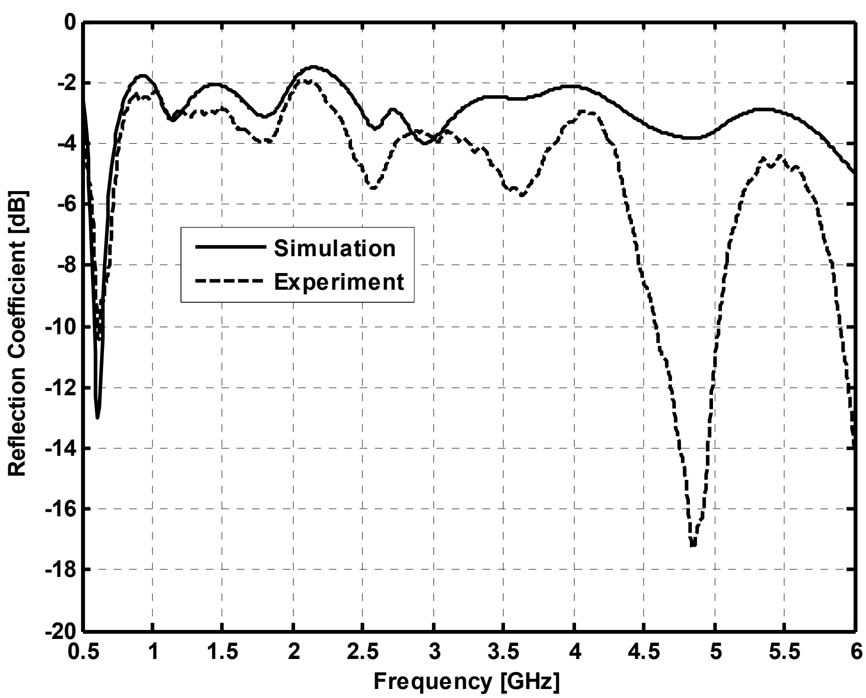

Figure E.12 – Reflection Coefficient for Design D (Z_o = 50Ω, Simulation and Experiment)

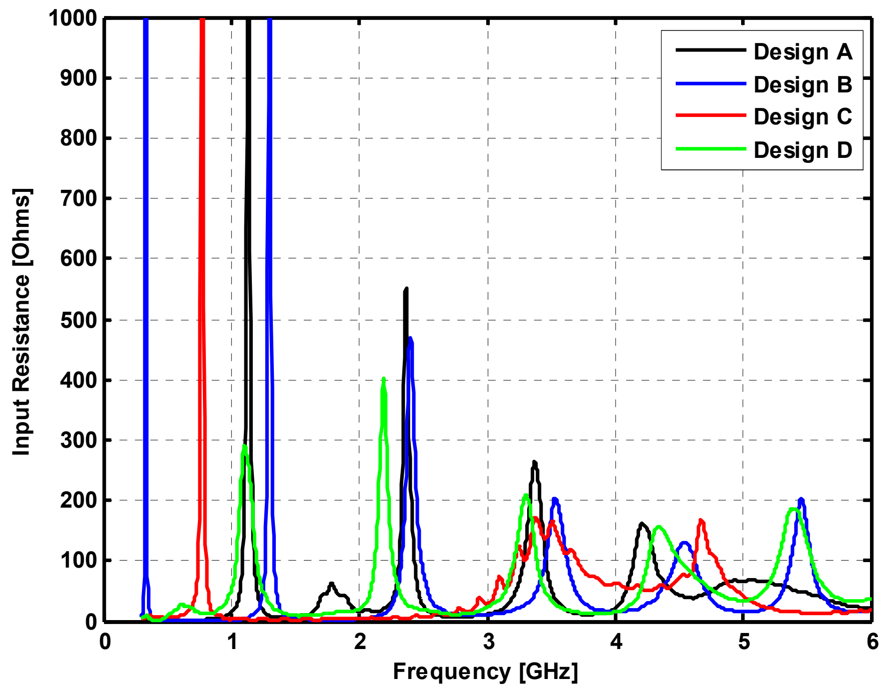

Figure E.13 – Experimentally Measured Input Resistance of UWB Designs A through D

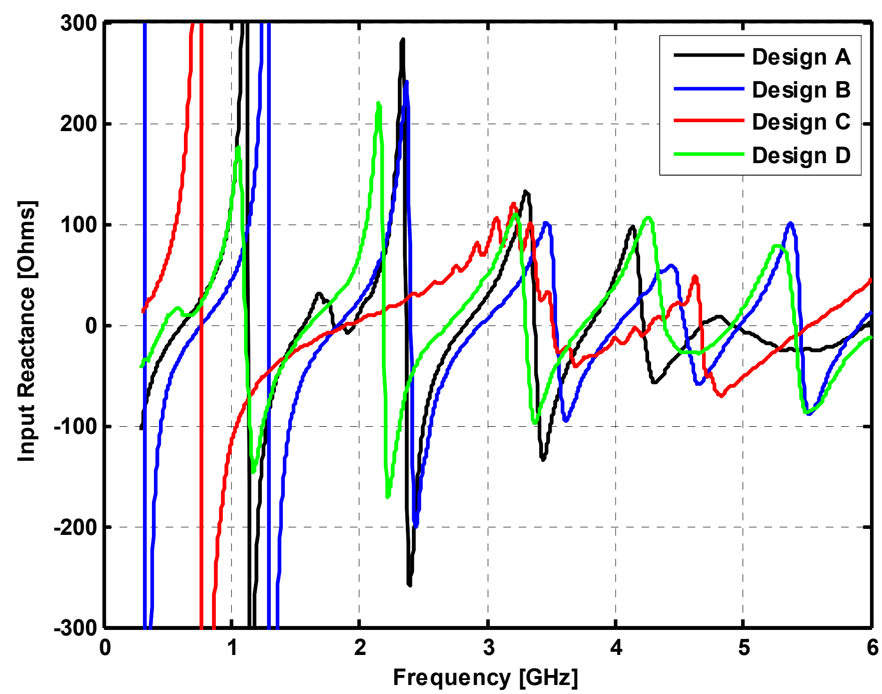

Figure E.14 – Experimentally Measured Input Reactance of UWB Designs A through D

So as to not waste an experimental result, it was considered whether there are applications of the resulting attempts at UWB antenna designs. One possible application is found through noting that the input resistance varies quite widely, leading to a very large range of ideal reference impedances. The reactance also varies significantly as well which implies that matching will be very sensitive to the reference impedance selected. As such, we consider sweeping reference impedances from 1-Ohm to 500-Ohm and track the frequencies where a good match occurs for the antenna designs in question. We consider -10dB to be a well matched reflection coefficient. In Figure E.15 we show a scatter plot of the well matched frequencies as a function of varying reference impedance for Design A. We see that a good match is possible between 4.8 GHz and 6 GHz as well as 1.65 GHz to 2.25 GHz. Should reconfigurable matching networks exist that can vary their matched impedance from 1 to 500 Ohm, the antenna considered would be capable of reconfiguring its matched frequency as shown.

If we consider antenna Design C, the tuning range is considerably wider, as shown in Figure E.16. The operating range begins at 2.80 GHz and moves upwards in frequency to 5.35 GHz, representing a tuning range of 2.55 GHz or 62.5%. The required range of reference impedances is narrower than 1 to 500 Ohms and is in fact limited between 125 to 350 Ohms. Other reference impedances are possible, but this is the sufficient range to cover the entire band of matched frequencies. While these designs may not be practical as of yet, they do show that the selected reference impedance plays a great role in determining where in frequency the antenna is well matched, with the frequencies varying substantially for a single antenna design.

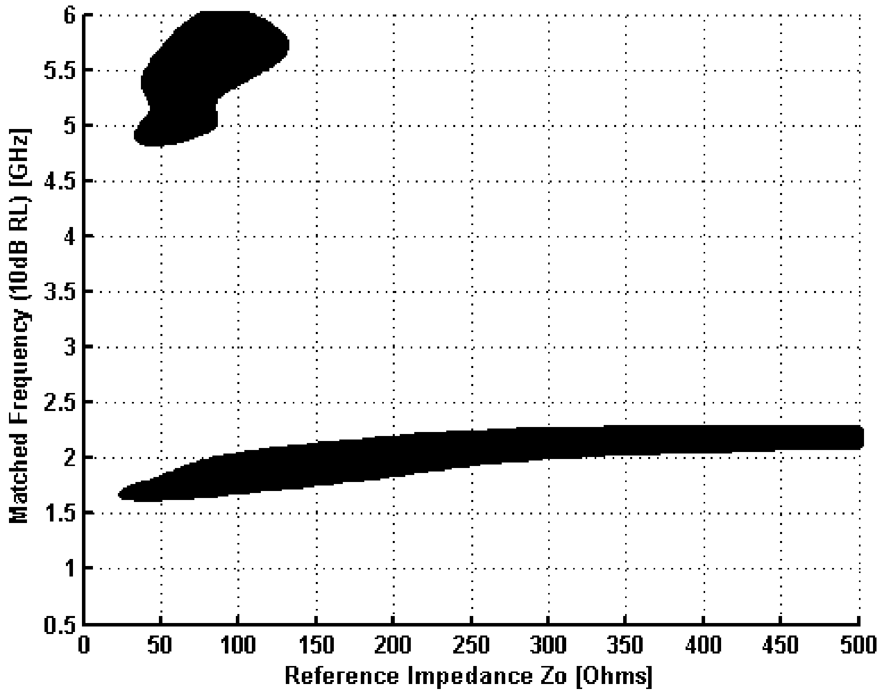

Figure E.15 – Plot of Matched Frequency (10dB RL) versus Reference Impedance for Design A

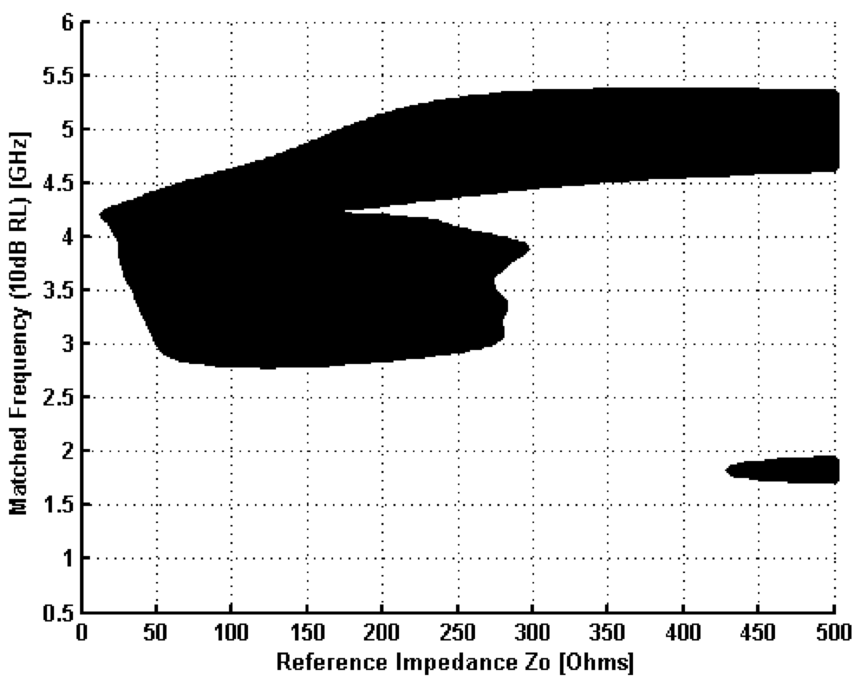

Figure E.16 – Plot of Matched Frequency (10dB RL) versus Reference Impedance for Design C

References for Appendix E

[1] Federal Communications Commission, *Code of Federal Regulations: Chapter 15*, National Archives and Records Administration, [Online http://www.access.gpo.gov/nara/cfr/waisidx_05/47cfr15_05.html] Retrieved November 2011.

[2] Y. Kim, D.-H. Kwon, "CPW-fed Planar Ultra Wideband Antenna having a Frequency band notch function," *Electronics Letters*, Vol. 40, Issue 7, April 2004, pp. 403 – 405.

[3] M. Ferrando-Bataller, Antonino-Daviu, M. Cabedo-Fabres, A. Valero-Nogueira, "UWB antenna design based on modal analysis," *Proceedings of the 3rd European Conference on Antennas and Propagation 2009 (EuCAP 2009)*, 23 – 27 March 2009, pp. 3530 – 3534.

[4] E. Antonino-Daviu, M. Cabedo-Fabres, M. Ferrando-Bataller, V.M.R. Penarrocha, "Modal Analysis and Design of Band-Notched UWB Planar Monopole Antennas," *IEEE Transactions on Antennas and Propagation*, vol. 58, Issue 5, May 2010, pp 1457 – 1467.

[5] W. Weixia, Y.P. Zhang, "Analysis of Ultra-Wideband Printed Planar Quasi-Monopole Antennas using the Theory of Characteristic Modes," *IEEE Antennas and Propagation Magazine*, Vol. 52, Issue 6, Dec. 2010, pp. 67 – 77.

[6] B.T. Strojny, R.G. Rojas, "Characteristic mode analysis of electrically large conformal bifilar helical antenna," *Proceedings of the 4th European Conference on Antennas and Propagation 2010 (EuCAP 2010)*, 12 – 16 April 2010, pp. 1 – 5.

Appendix F: Convergence and Validation for the Infinite-from-Finite (IFF) Method

Additional convergence data is shown in this Appendix (Figures F.1 through F.4) for the purpose of validating the IFF method. In order to validate the periodic structures we use the matrix trace $\Psi = Tr\left\{Z^{-1}R\right\}$ as the convergence indicator as it is representative of all of the characteristic modes of the periodic structure (for the selected angle of incidence) and hence simultaneously validates all polarizations as well as transmission and reflection coefficients in a single inclusive test. All four Figures F.1 through F.3 consider 3.8mm patches in a 4mm lattice over a very wide range of frequencies. Figure F.4 considers 6mm patches in a 7mm lattice in freespace. Note that in all cases convergence is obtained. However, the convergence appears to be slower for freespace periodic structures, thereby requiring additional elements (resulting in additional coupling matrices) to be added to the periodic structure for accurate modeling. The reason for the slow convergence, or rather the faster convergence of the periodic structures with ground planes, is the canceling effect of the ground plane image currents. As shown in Appendix G, the image currents result in the addition of the negative of the coupling matrices. This acts to partially cancel the contribution of the periodic structure's coupling matrices, thereby leading to faster overall convergence.

In an attempt to visualize the convergence of the periodic structure, we consider plots of the coupling between the central scatterer (element 1) and the adjacent circling elements (scatterers 2 through M). The methodology for visualizing these results involves plotting the magnitudes of the entries in the coupling matrices in the IFF method, namely the $\left[Z_{1m}\right]$ matrices for m > 1. Plots of these magnitudes are shown in Figures F.5 and F.6 for the cases of ground plane (4mm height) and freespace respectively. Both cases involve 3.8mm patches in a 4mm lattice.

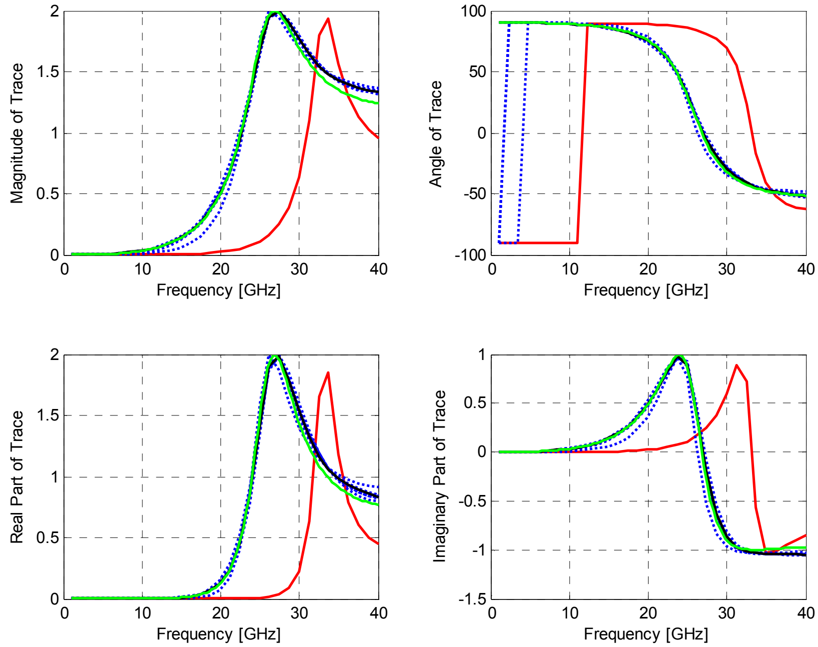

Figure F.1 – Convergence and validation for array of patches, 0.5mm separation from ground plane, RED – 1 element, BLUE – intermediate, BLACK – 64 elements (8x8), GREEN – commercial code FEKO

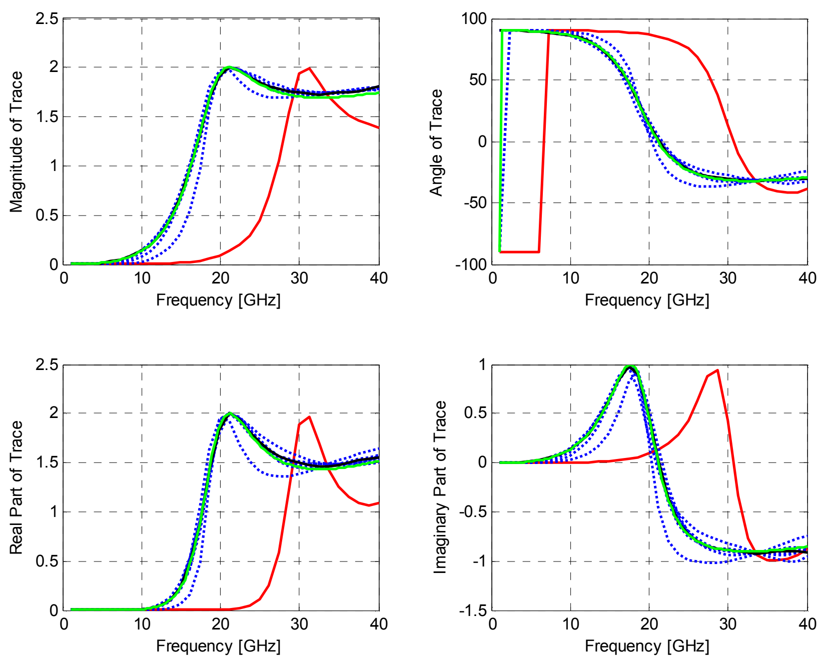

Figure F.2 – Convergence and validation for array of patches, 1mm separation from ground plane RED – 1 element, BLUE – intermediate, BLACK – 64 elements (8x8), GREEN – FEKO (commercial code)

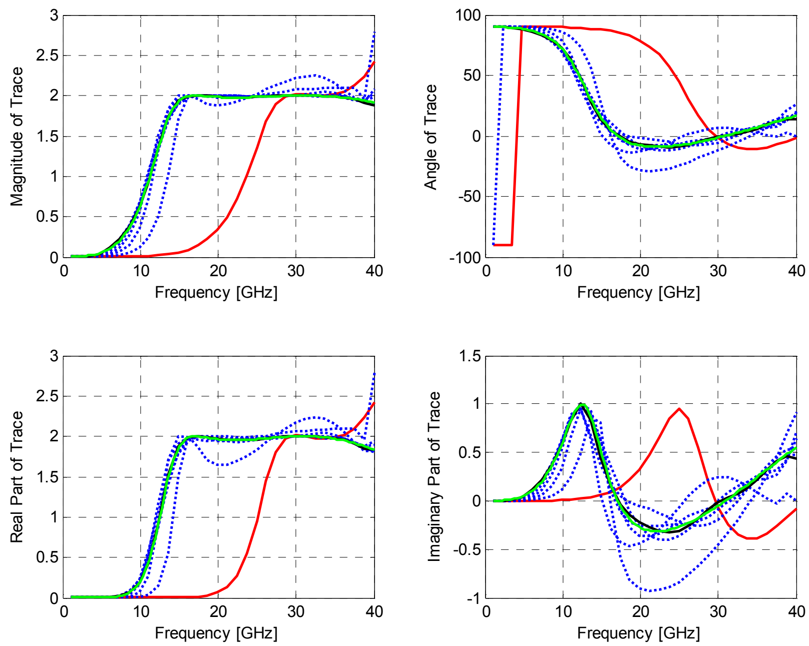

Figure F.3 – Convergence and validation for array of patches, 2mm separation from ground plane, RED – 1 element, BLUE – intermediate, BLACK – 64 elements (8x8), GREEN – FEKO (commercial code)

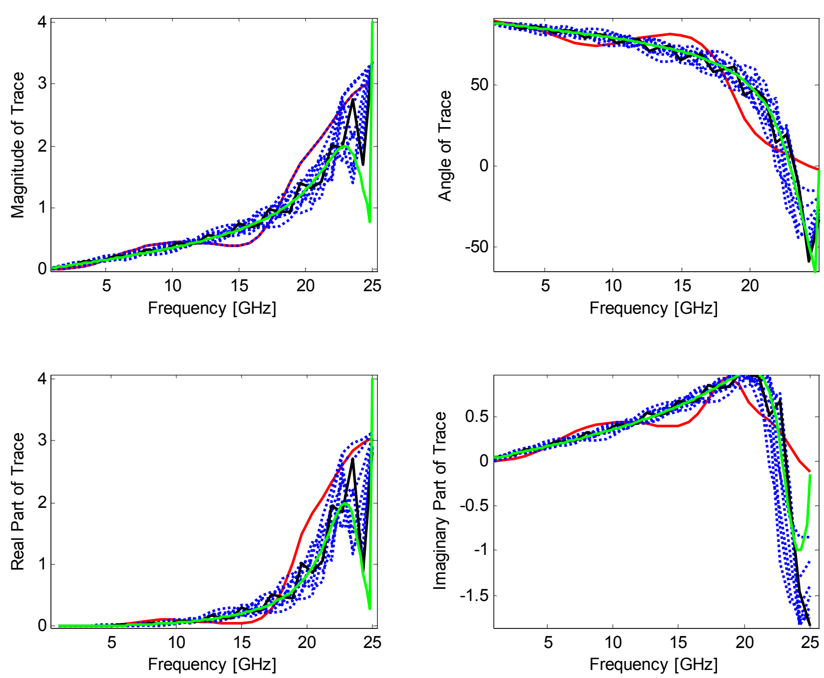

Figure F.4 – Convergence and validation for array of 6mm patches in freespace, RED – 1 element, BLUE – intermediate configurations, BLACK – 400 elements (20x20), GREEN – FEKO

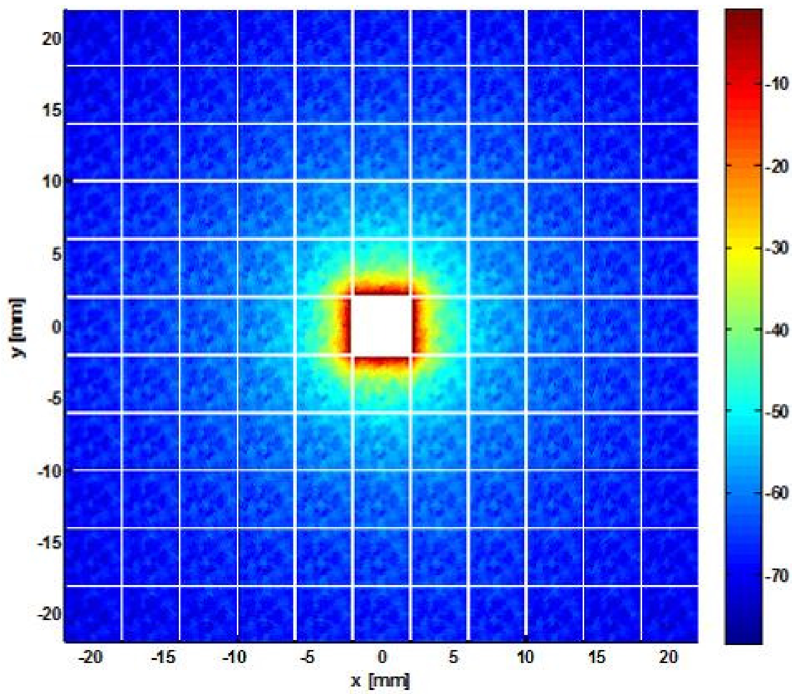

Figure F.5 – Magnitude of coupling between central element and outer elements [ground plane]

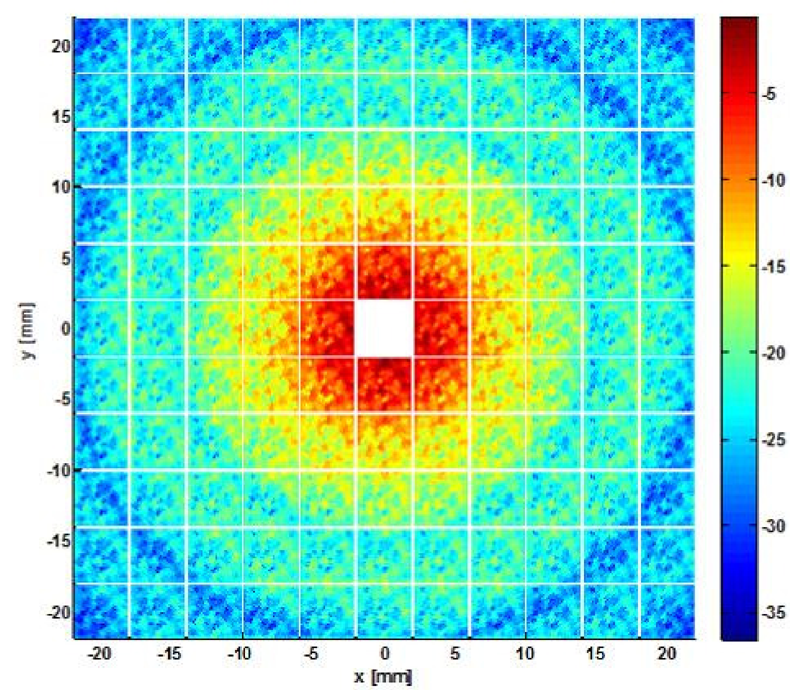

Figure F.6 – Magnitude of coupling between central element and outer elements [freespace]

Appendix G: Including the Effects of an Infinite Ground Plane in the Method of Moments

In order to incorporate the effects of an infinite ground plane on a scatterer, one can incorporate its effects into the Green's function. This can either be accomplished with a *modified Green's function* or with a *numerical Green's function* approach. In order to reduce the overhead in developing software to incorporate the actual Green's function, we instead consider a numerical technique that uses existing computational electromagnetics code. Moreover, in order to simplify things as much as possible, we only consider planar structures that are oriented such that they are parallel to the infinite ground plane. In such a scenario the currents on the planar structure are entirely parallel to the infinite ground plane, which dramatically simplifies the numerical techniques we can use to analyze their behaviour. By image theory, currents above and parallel to the infinite ground plane will be imaged in the opposite direction below the ground plane, with fields produced by the current and its image being valid in regions above the ground plane.

If we place an identical scatterer a distance 2h below the original scatterer (where h is the distance from the scatterer to the infinite ground plane) i.e. at the image plane, we can proceed with a technique to numerically include the effects of the infinite ground plane. Such a scenario is shown in Figure G.1. In the same figure, the currents are shown to be representative of the enforcement of image theory. In this scenario of two scatterers we can fully describe the electromagnetics via their impedance matrix, broken up into block matrices for the scatterers A and B, as shown in expression G.1.

$$\begin{bmatrix} [Z_{AA}] & [Z_{AB}] \\ [Z_{BA}] & [Z_{BB}] \end{bmatrix} \begin{bmatrix} [J_A] \\ [J_B] \end{bmatrix} = \begin{bmatrix} [V_A] \\ [V_B] \end{bmatrix} \tag{G.1}$$

If the currents $[J_B]$ were indeed image currents, they would have the condition $[J_B] = -[J_A]$. Under such a condition, the matrix equation (G.1) can be written as

$$\begin{bmatrix} [Z_{AA}] & [Z_{AB}] \\ [Z_{BA}] & [Z_{BB}] \end{bmatrix} \begin{bmatrix} [J_A] \\ -[J_A] \end{bmatrix} = \begin{bmatrix} [V_A] \\ [V_B] \end{bmatrix} \tag{G.2}$$

which gives us an expression relating the current to the field on the scatterer A as follows

$$\{[Z_{AA}]-[Z_{AB}]\}[J_A]=[V_A] \tag{G.3}$$

Let us denote the impedance matrix for planar structures over an infinite ground plane as

$$\left[Z_{A,gp}\right]=[Z_{AA}]-[Z_{AB}] \tag{G.4}$$

The matrix $\left[Z_{A,gp}\right]$ therefore relates the current and field on a scatterer (as any impedance matrix must) and can be obtained numerically from any freespace Green's function formulation by computing the impedance matrix of the scatterer and the coupling matrix between the scatterer and its image. The only restriction imposed is that the scatterer must be planar such that its currents are entirely parallel to the infinite ground plane.

This approach can be re-derived for scatterers with purely normal currents in which case the impedance matrix takes the form $\left[Z_{A,gp}\right]=[Z_{AA}]+[Z_{AB}]$. For scatterers that support both parallel and normal currents a mixed approach is required. However, such a scenario is no longer trivial to implement in a numerical code, nor is it of interest in the present thesis.

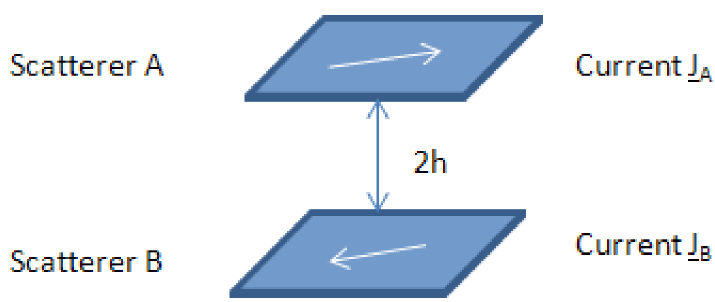

Figure G.1 – Example pair of planar scatterers A and B separated by a distance '2h' with currents representative of a single scatterer A over an infinite ground plane at a distance 'h'.

Appendix H: Multi-mode Periodic Structure Analysis

While we will not explicitly use it in this thesis, the concept of multi-mode periodic structures is a concept worth exploring. First and foremost, it is expected that at the very least some of the restrictions imposed by a single-mode periodic structure from Section 5.3.6 are no longer valid. Some of these concepts are indeed restrictive, i.e. being incapable of synthesizing an AMC without a ground plane as well as the limiting range of transmission and reflection phase and magnitude obtainable from a single-mode structure.

An example of a multi-mode periodic structure is the stacked square patch element shown in Figure H.1. The unit cell size is 5mm by 5mm with the square PEC plates measuring 4mm by 4mm. The characteristic mode spectrum of this structure from DC to 60 GHz reveals two dominant modes (four in total, but a mode degeneracy of two). Both modes have eigencurrents similar to the distribution in Figure 5.14, with one mode showing parallel currents on the top and bottom plates while the other shows anti-parallel currents. The eigenvalue behaviour over frequency is shown in Figure H.2. The actual reflection coefficient for a normally incident plane wave (polarized either along x or y) is shown with a solid black curve in Figure H.3. In the same figure, the modal reflection coefficients of the two modes are shown with dashed and dotted curves. Note that neither of the modal reflection coefficients match well with the actual reflection coefficient and hence, the structure is not a single mode periodic structure.

From the theory introduced in Section 5.3.1, the reflection coefficient can be written as a linear superposition of the individual modal reflection coefficients as follows

$$\Gamma = \sum_n a_n \Gamma_n \tag{H.1}$$

where the coefficients a_n are yet to be determined and the Γ_n are the modal reflection coefficients in expression (5.34). In our example, since we have a two mode structure, the reflection coefficient can be written as

$$\Gamma = a_1 \Gamma_1 + a_2 \Gamma_2 \tag{H.2}$$

It was found that the magnitudes of the coefficients are unity over the entire band from DC to 60 GHz. The phases of the coefficients on the other hand are frequency dependent. This dependency can be expressed as follows

$$\Gamma = e^{j\psi(\omega)}\Gamma_1 - e^{j\psi(\omega)}\Gamma_2 = e^{j\psi(\omega)}\left(\Gamma_1 - \Gamma_2\right) \qquad \text{(H.3)}$$

where the phase function $\psi(\omega)$ is shown in Figure H.4 (this is not to be confused with the trace of the CM matrix, which uses an uppercase psi). Using these coefficients, one finds that expression (H.3) does indeed match identically with the actual reflection coefficient of the periodic structure. The reflection coefficient phase matches in the same way.

As a last point of interest, consider the fact that the periodic structure itself is completely reflective around 38.8 GHz and yet neither of the modes is resonant. This implies that a multi-mode periodic structure need not have resonant eigenvalues in order to be resonant itself – the mutual interaction between the modes yields a structure that overall exhibits a resonance. At 38.8 GHz, the eigenvalues, modal reflection coefficients, and coefficients a_n are as follows:

$$\boxed{\begin{gathered} \lambda_{1/2} = +1.1720\,, \\ \Gamma_{1/2} = 0.761\angle -139.6^o \\ a_{1/2} = 1\angle 99.1^o \\ \lambda_{3/4} = -0.8524 \\ \Gamma_{3/4} = 0.649\angle 130.5^o \\ a_{3/4} = 1\angle -80.9^o \end{gathered}}$$

A great deal more investigation is needed to fully understand the modal character of multi-mode periodic structures. In particular, an investigation as to the theoretical limitations of multi-mode structures would likely prove a worthwhile endeavour.

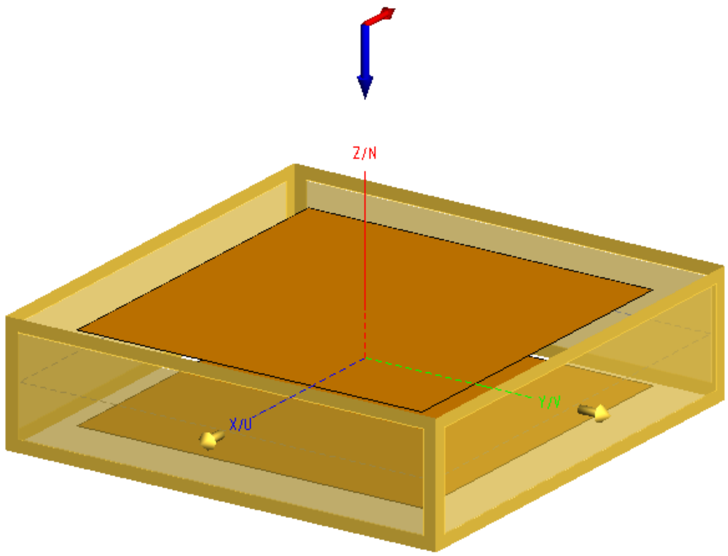

Figure H.1 – Example multi-modal periodic structure consisting of two layers of patches

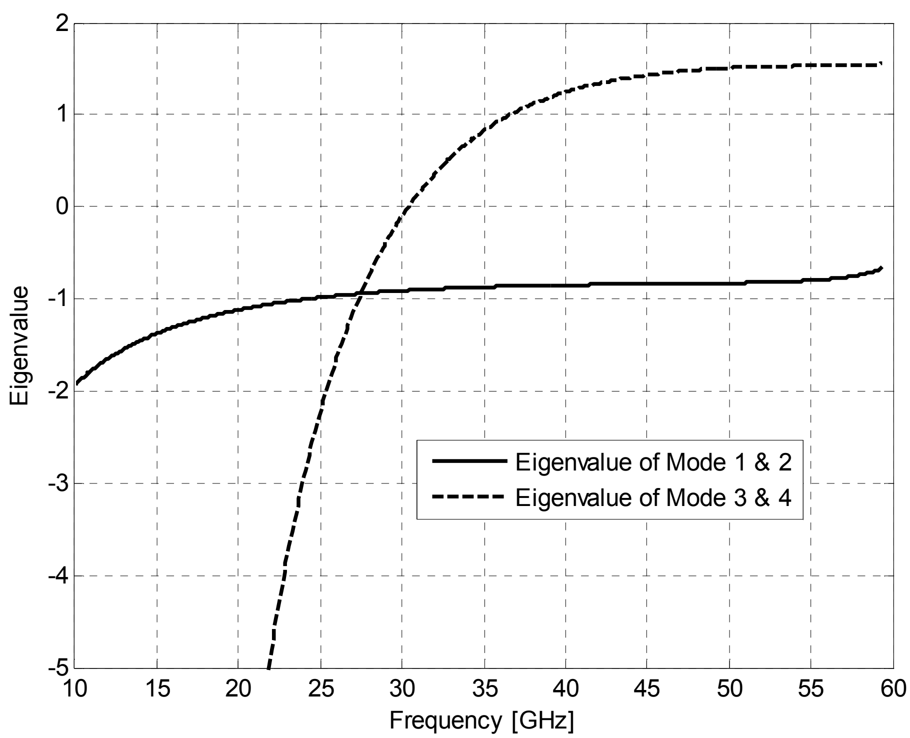

Figure H.2 – Eigenvalues of example multi-modal periodic structure (two layer freespace patch periodic structure)

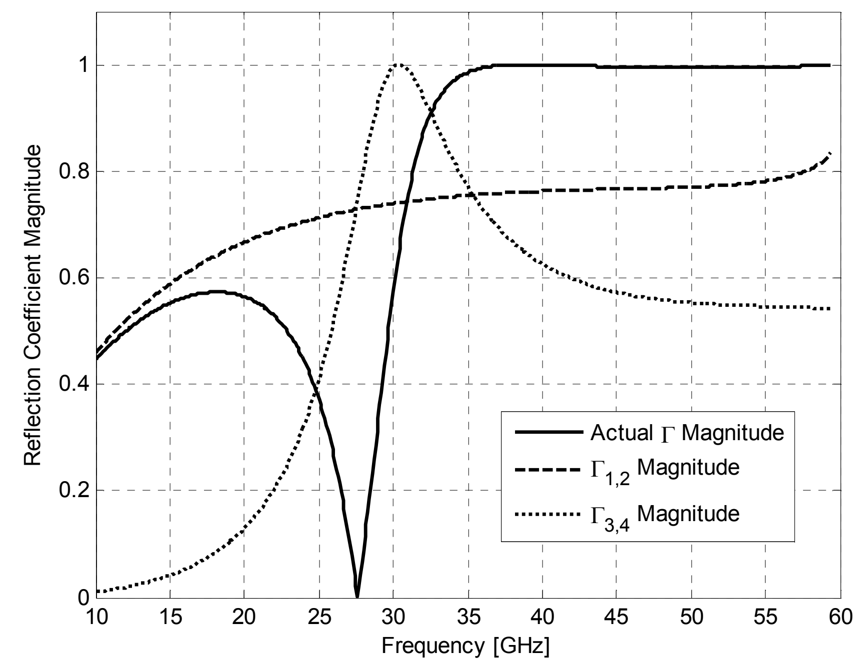

Figure H.3 – Actual reflection coefficient compared to modal reflection coefficients

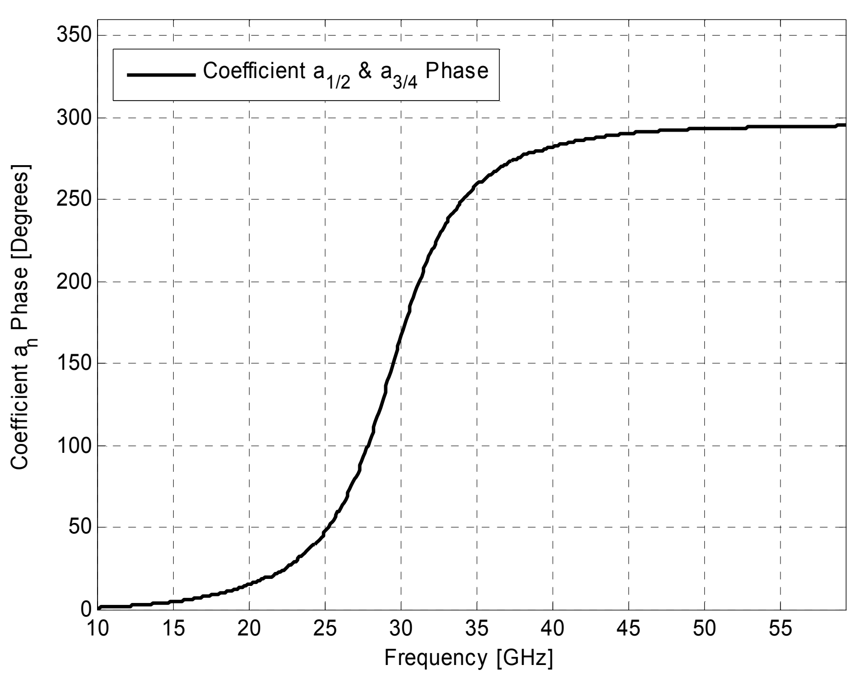

Figure H.4 – Phase of modal expansion coefficients (the excitation phase difference between the modes for a given plane wave excitation)

Appendix I: Additional Photographs of Fragmented Reflectarrays

This appendix contains additional photographs of the reflectarrays synthesized in Chapter 5.

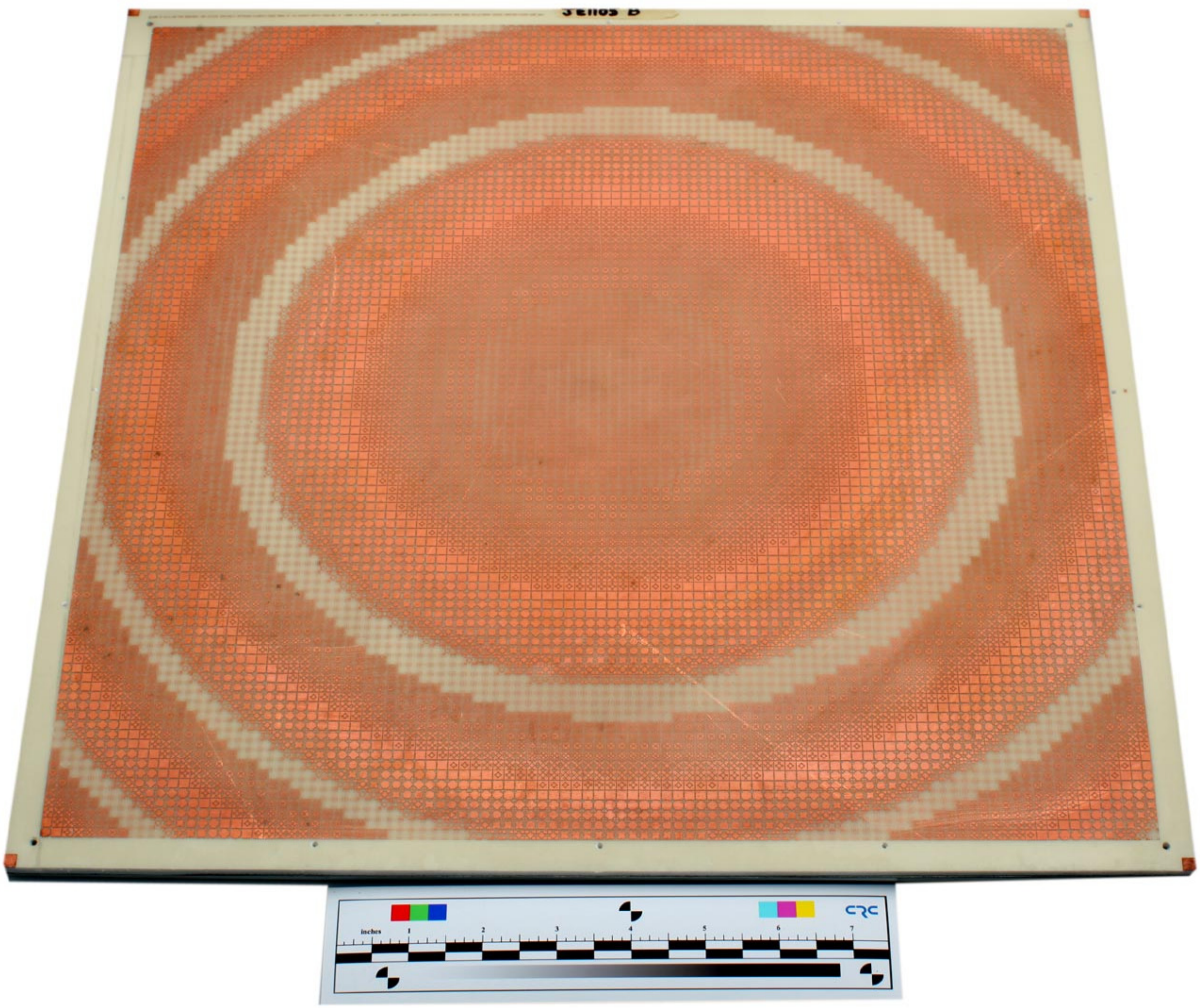

Figure I.1 – Similarity-optimized fragmented reflectarray (Design D from Chapter 5)

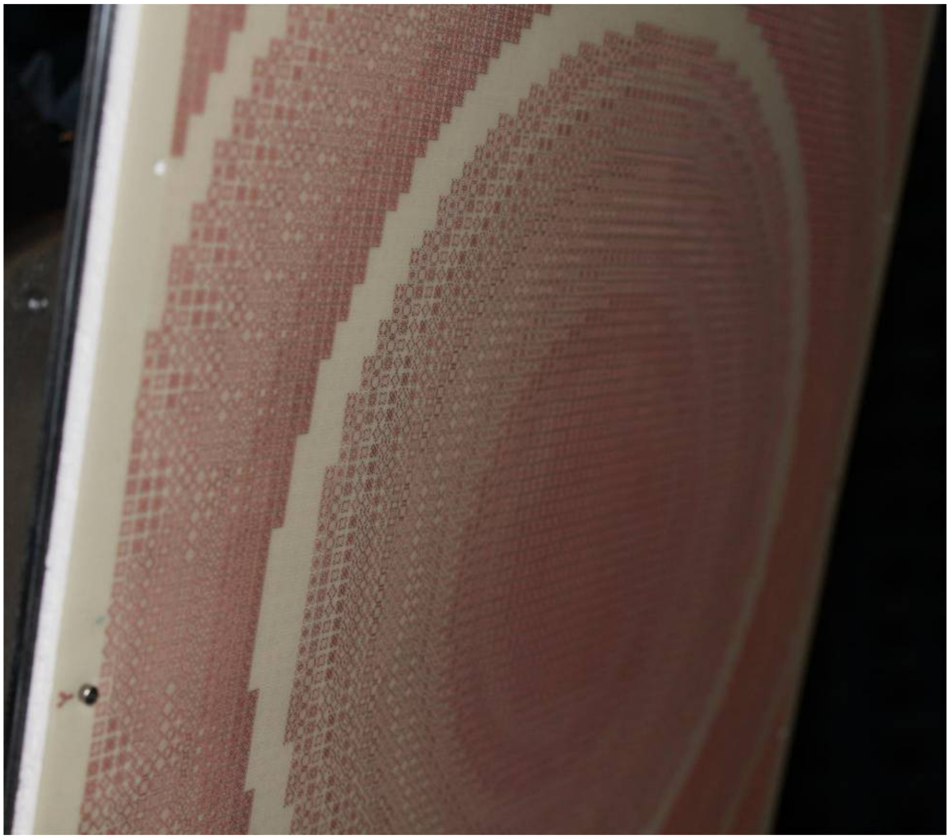

Figure I.2 – Dissimilarity-optimized fragmented reflectarray

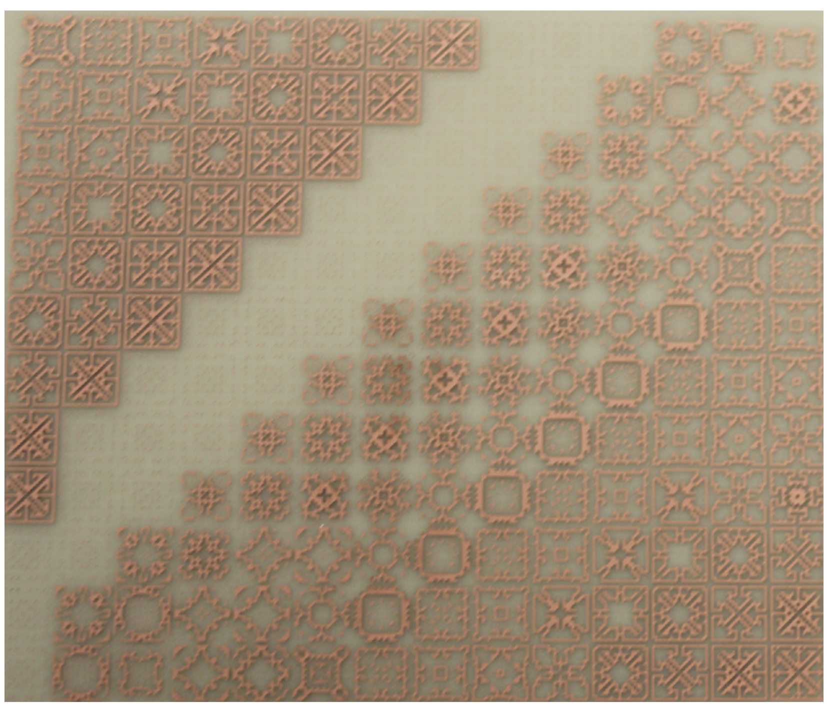

Figure I.3 – Dissimilarity-optimized fragmented reflectarray, close-up view of elements

Figure I.4 – CRC & maple leaf Ku-band mosaic reflectarray

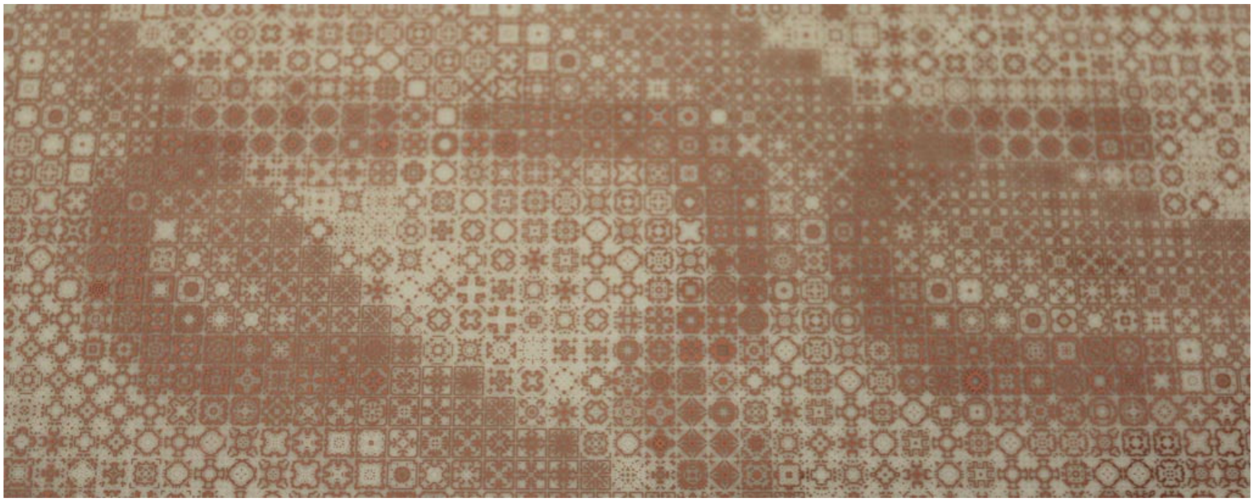

Figure I.5 – CRC & maple leaf Ku-band mosaic reflectarray, close-up of CRC logo

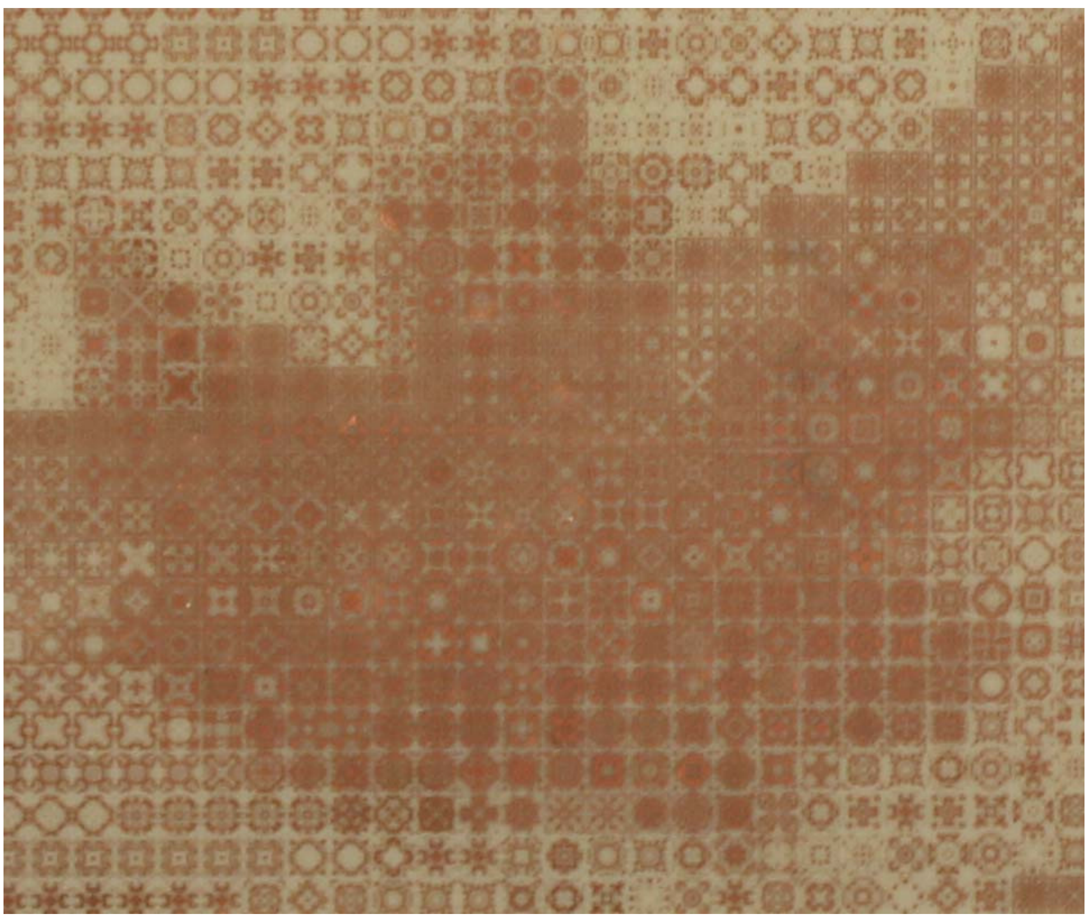

Figure I.6 – CRC & maple leaf Ku-band mosaic reflectarray, close-up of one of the smaller maple leafs

Figure I.7 – University of Ottawa (uOttawa) logo Ku-band mosaic reflectarray

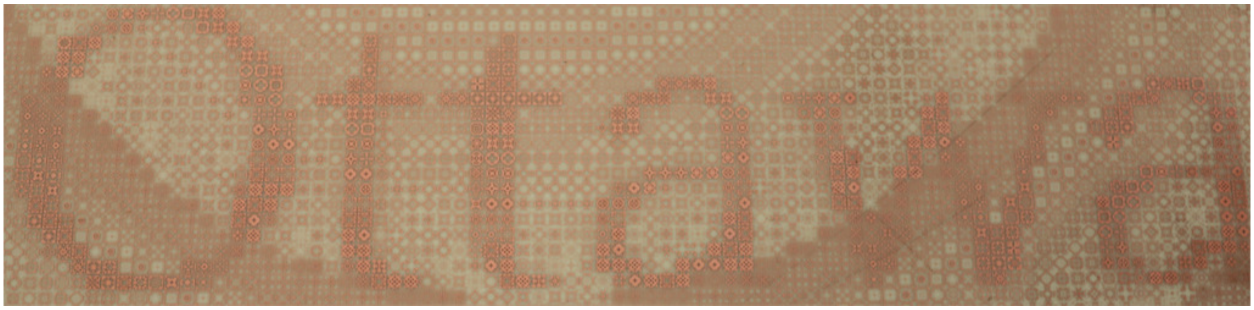

Figure I.8 – University of Ottawa logo Ku-band mosaic reflectarray, close up of uOttawa lettering

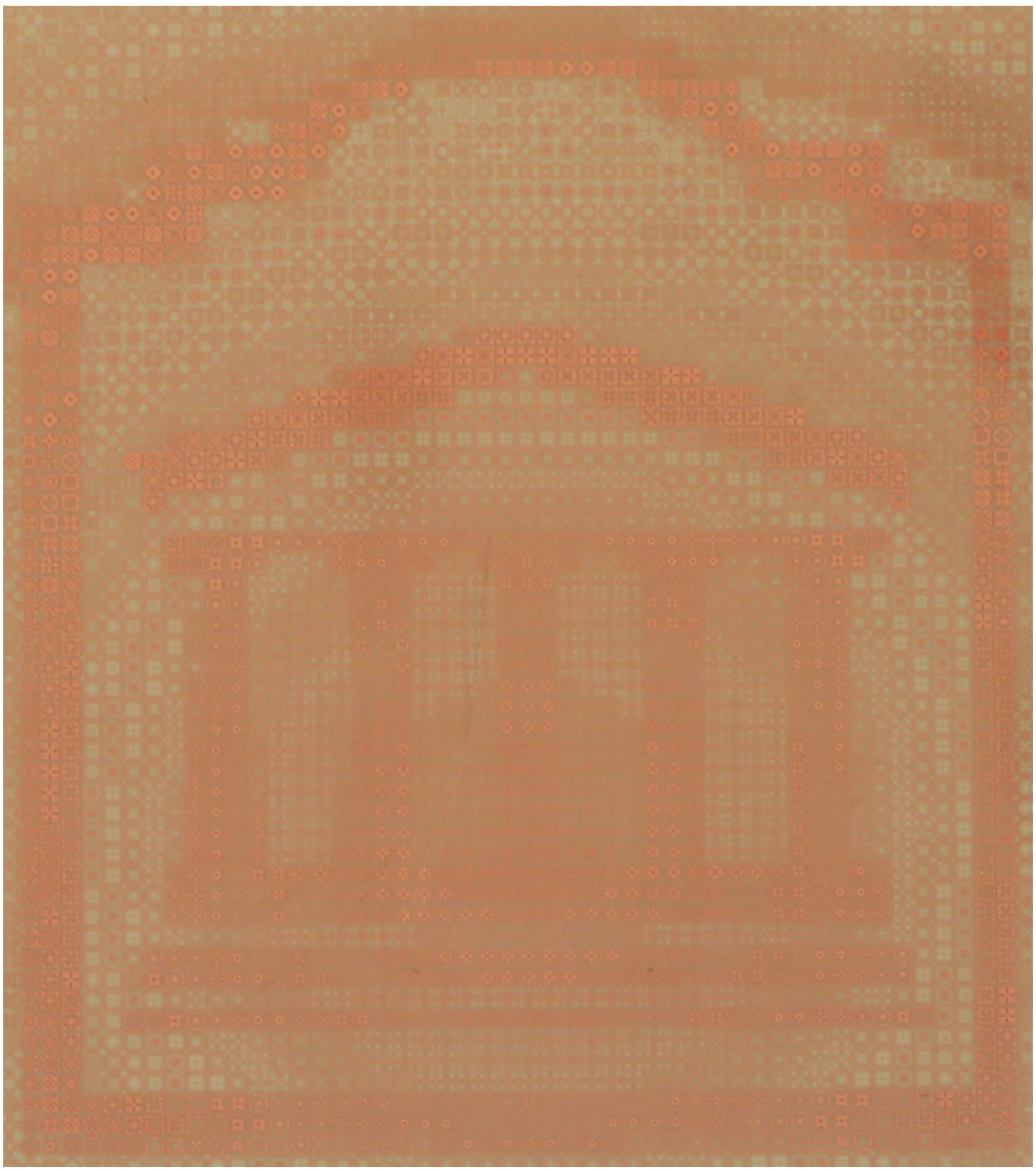

Figure I.9 – University of Ottawa logo Ku-band mosaic reflectarray, close up of parthenon

Appendix J: Angle of Incidence and Finite Conductivity in the Infinite-from-Finite (IFF) Method

If losses are present in the periodic structure, they can be included via the loading operator $\left[Z_L\right]$ as in Chapter 3. The operator equation in this instance becomes

$$\left\{\begin{bmatrix} [Z_{11}] & [Z_{12}] & \cdots & [Z_{1M}] \\ [Z_{21}] & [Z_{22}] & \cdots & [Z_{2M}] \\ \vdots & \vdots & \ddots & \vdots \\ [Z_{M1}] & [Z_{M2}] & \cdots & [Z_{MM}] \end{bmatrix} + \begin{bmatrix} [Z_{L,11}] & [Z_{L,12}] & \cdots & [Z_{L,1M}] \\ [Z_{L,21}] & [Z_{L,22}] & \cdots & [Z_{L,2M}] \\ \vdots & \vdots & \ddots & \vdots \\ [Z_{L,M1}] & [Z_{L,M2}] & \cdots & [Z_{L,MM}] \end{bmatrix}\right\} \begin{bmatrix} [I] \\ [I] \\ \vdots \\ [I] \end{bmatrix} = \begin{bmatrix} [V] \\ [V] \\ \vdots \\ [V] \end{bmatrix} \tag{J.1}$$

which simply places an addendum on the original expression for the periodic structure

$$\left[Z^{(M)}\right]_{ps} = \left\{[Z_{11}] + \left[Z_{L,11}\right]\right\} + \sum_{n=2}^{M} \left\{[Z_{1n}] + \left[Z_{L,1n}\right]\right\} \tag{J.2}$$

Since we are interested in computing the characteristic modes of periodic structures, we would ideally prefer to keep matrices in the appropriate forms in order to solve eigenvalue problems. Therefore, we denote the periodic structure loading operator as

$$\left[Z_L^{(M)}\right]_{ps} = \left[Z_{L,11}\right] + \sum_{n=2}^{M} \left[Z_{L,1n}\right] \tag{J.3}$$

It should also be noted that the largest source of losses in periodic structures or quasi-periodic structures is usually due to dielectric losses and not metal losses [Ref. 9, Ch. 5]. We do not include dielectrics in the CM analyses in this thesis. Thus, the above-mentioned losses will not play a large role in our investigations. This was experimentally confirmed in Sections 5.4 and 5.5.

If we wish to consider cases where a plane wave is incident from an arbitrary angle, we need to consider the effect such a scenario has on the current and voltage vectors. If a periodic structure is indeed infinite, the magnitude of the current and excitation is the same for all elements, even for the case of arbitrary angle of incidence. However, the relative phase of the current and voltage will change depending on the element being considered, but this phase is a predictable quantity [Ref. 2, Ch. 5]. Additionally, the current and voltage will vary over the element itself since we have non-normal plane wave incidence. This variation is identical for every element, save for a predictable phase difference. The phase offset at each element will simply be equal to [Ref. 2, Ch. 5]:

$$\psi\left(k_x,k_y\right)=e^{j\left(k_x x+k_y y\right)} \tag{J.4}$$

which can be expressed in terms of angle theta/phi as

$$\psi\left(\theta,\phi\right)=e^{jk\left(\sin\theta\cos\phi x+\sin\theta\sin\phi y\right)} \tag{J.5}$$

This phase factor is then included in the expression connecting the current and excitation. Note that this expression is a function of (x, y) coordinates, which would be the coordinate of the center of the lattice of the element being considered. Let us simply denote this function ψ_m where m refers to the m[th] element. Hence, we can write the impedance matrix simply as

$$\begin{bmatrix}[Z_{11}] & [Z_{12}] & \cdots & [Z_{1M}]\\ [Z_{21}] & [Z_{22}] & \cdots & [Z_{2M}]\\ \vdots & \vdots & \ddots & \vdots\\ [Z_{M1}] & [Z_{M2}] & \cdots & [Z_{MM}]\end{bmatrix}\begin{bmatrix}[I]\psi_1\\ [I]\psi_2\\ \vdots\\ [I]\psi_M\end{bmatrix}=\begin{bmatrix}[V]\psi_1\\ [V]\psi_2\\ \vdots\\ [V]\psi_M\end{bmatrix} \tag{J.6}$$

If we take the first row of the Z-matrix, we find

$$\psi_1[Z_{11}][I]+\psi_2[Z_{12}][I]+\cdots+\psi_M[Z_{1M}][I]=\psi_1[V] \tag{J.7}$$

Factoring out the current vector, we obtain

$$\left\{\psi_1[Z_{11}]+\psi_2[Z_{12}]+\cdots+\psi_M[Z_{1M}]\right\}[I]=\psi_1[V] \tag{J.8}$$

Dividing through by ψ_1, we obtain

$$\left\{\frac{\psi_1}{\psi_1}[Z_{11}]+\frac{\psi_2}{\psi_1}[Z_{12}]+\cdots+\frac{\psi_M}{\psi_1}[Z_{1M}]\right\}[I]=[V] \tag{J.9}$$

Therefore, we have obtained an impedance operator that describes the relationship between the current vector [I] and voltage vector [V]:

$$\left[T^{(M)}\right]=\frac{\psi_1}{\psi_1}\left[Z_{11}\right]+\frac{\psi_2}{\psi_1}\left[Z_{12}\right]+\cdots+\frac{\psi_M}{\psi_1}\left[Z_{1M}\right] \tag{J.10}$$

Notice that each coupling matrix includes a multiplicative factor ψ_m/ψ_n where m is the mth element, and n is the nth element, here taken to be n = 1 because we consider only the first row. For the sake of simplicity, we will set the central element to be at the origin and centered. This will allow us to simply set $\psi_1 = 1$, and to denote the coupling terms simply as

$$\left[Z_{1m}\right]' = \psi_m \left[Z_{1m}\right] \tag{J.11}$$

Our operator then becomes

$$\left[T^{(M)}\right]=\left[Z_{11}\right]+\left[Q\right]' \tag{J.12}$$

where the expression for [Q]' is

$$\left[Q\right]' = \sum_{n=2}^{M}\left[Z_{1m}\right]' = \sum_{n=2}^{M}\psi_m\left[Z_{1m}\right] \tag{J.13}$$

The only fundamental difference between normal incidence and arbitrary angle of incidence is a simple phase factor that augments each of the coupling matrices. In fact, we can think of the case of normal incidence occurring when all of the phase factors are unity, i.e. $\psi_m = 1 \;\; \forall m$.

Appendix K: The Theoretical Limitations of Single-Mode Periodic Structures

An interesting consequence of the characteristic mode analysis of single mode periodic structures is the ability to determine the performance limits of such structures. In particular, consider the expression for the modal transmission and reflection coefficients for a freespace periodic structure as magnitude and phase:

$$\left|\Gamma_n\right| = \frac{1}{\sqrt{1+\lambda_n^2}} \tag{K.1}$$

$$\angle\Gamma_n = \arctan\left(\frac{\lambda_n}{-1}\right) \tag{K.2}$$

$$\left|\mathrm{T}_n\right| = \frac{\left|\lambda_n\right|}{\sqrt{1+\lambda_n^2}} \tag{K.3}$$

$$\angle\mathrm{T}_n = \arctan\left(\frac{1}{\lambda_n}\right) \tag{K.4}$$

Since the reflection coefficient is determined by a single parameter, the eigenvalue λ_n, the magnitude and phase are linked for every single mode periodic structure. In other words, by selecting the reflection magnitude, the phase is immediately specified and vice versa. Some interesting consequences of this interdependency are (for freespace periodic structures):

(1) A single mode periodic structure is 100% reflective if the dominant mode's eigenvalue is zero.

(2) If a single mode periodic structure is 100% reflective, it must have 180 degrees reflection phase.

(3) The reflection phase must be less than -90 degrees or greater than 90 degrees. A reflection phase between -90 and 90 degrees is forbidden. In other words, the reflection coefficient must reside in the left-hand side of the complex plane.

(4) A reflection coefficient of $\Gamma = +1$ (artificial magnetic conductor or AMC) cannot be synthesized from a single-mode periodic structure

(5) A single-mode periodic structure is 100% transparent if the dominant eigenvalue has infinite magnitude

(6) If a single mode periodic structure is 100% transparent, it must have 0 degree transmission phase of zero degrees. This is a fairly restrictive limit as it immediately implies a transparent single mode periodic structure cannot impart any phase delay or advance to the transmitted wave.

(7) The transmission phase is bound between 90 and -90 degrees. Transmission phase is strictly forbidden outside of this region. In other words, the transmission coefficient vector must reside in the right-hand side of the complex plane.

(8) The ratio of the transmission magnitude to the reflection magnitude is equal to the magnitude of the eigenvalue since $\mathrm{T}_n / \Gamma_n = -j\lambda_n$ and thus $|\mathrm{T}_n| / |\Gamma_n| = |\lambda_n|$

We next consider the dispersive properties of periodic structures. The frequency derivatives of the transmission and reflection phase

$$\frac{d}{d\omega}(\angle \mathrm{T}_n) = \frac{d}{d\omega}\left\{\arctan\left(\frac{1}{\lambda_n}\right)\right\} = \frac{d}{d\omega}\left\{\frac{\pi}{2} - \arctan(\lambda_n)\right\} = \frac{-1}{1+\lambda_n^2}\frac{d\lambda_n}{d\omega} \qquad \text{(K.5)}$$

and

$$\frac{d}{d\omega}(\angle \Gamma_n) = \frac{d}{d\omega}\left\{\arctan(-\lambda_n)\right\} = -\frac{d}{d\omega}\left\{\arctan(\lambda_n)\right\} = \frac{-1}{1+\lambda_n^2}\frac{d\lambda_n}{d\omega} \qquad \text{(K.6)}$$

Three main observations are made for the frequency dispersion of the transmission and reflection coefficients' phase

(1) The frequency dispersion of the phase is identical for both reflection and transmission. This is an interesting result as it suggests the inability to separate their frequency behaviour.

(2) The phase dispersion is equal to the negative of the slope of the eigenvalue for $\lambda_n = 0$. This is very similar to the expression for antenna Q in Chapter 3, reinforcing the fact that the dispersion of reflection/transmission phase is related to the bandwidth of the structure at resonance.

(3) Consider the fact that (a) the structure is lossless, (b) the eigenvalue λ_n represents the net stored energy of the system and (c) lossless 1-port systems must have positive frequency derivatives (Foster's reactance theorem [Ch. 5, Ref. 10]) and hence $d\lambda_n/d\omega$ would appear to be restricted to positive only quantities. However, a freespace periodic structure is not a 1-port device – it is a 2-port device since freespace straddles both sides of the periodic structure. It would therefore be premature to apply Foster's reactance theorem in this scenario.

Lastly, let us consider the same investigation, but for the case of the reflection coefficient of a single mode periodic structure in the presence of an infinite ground plane. The reflection coefficient can be written in terms of its real and imaginary parts as

$$\Gamma_n = \frac{1-\lambda_n^2}{1+\lambda_n^2} - j\frac{2\lambda_n}{1+\lambda_n^2} \tag{K.7}$$

Since both the real and imaginary parts can be both positive and negative, this implies that the reflection phase can take any value and is no longer restricted, unlike the previous freespace periodic structure analysis. Using the double angle trigonometric identity for the tan function, the reflection phase can be expressed simply as

$$\angle\Gamma_n = -2\arctan(\lambda_n) \tag{K.8}$$

We can make the following observations:

(1) If the eigenvalue approaches zero, the reflection coefficient becomes $\Gamma_n = +1$ and thus has a reflection phase of 0 degrees. The periodic structure behaves like a perfect magnetic conductor, and so would be called an artificial magnetic conductor (AMC).

(2) If the eigenvalue approaches positive or negative infinity, the reflection coefficient becomes $\Gamma_n = -1$ for a reflection phase of +/- 180 degrees. The periodic structure behaves like a ground

plane in this scattering scenario. As mentioned previously, this occurs because the infinite net stored energy in the system causes the periodic structure itself (sans ground plane) to be transparent and thus only the ground plane is observed by the incident wave (hence $\Gamma_n = -1$).

(3) A reflection phase spanning +180 to -180 degrees (the full 360 degree span) is possible from a single mode periodic structure with an adjacent ground plane by spanning the range of eigenvalues from $+\infty$ to $-\infty$.

(4) If the eigenvalue is positive (inductive mode) the reflection phase becomes negative. Conversely, if the eigenvalue is negative (capacitive mode) the reflection phase becomes positive.

As for the frequency dispersion of the reflection phase, we take the frequency derivative of expression (K.8) and obtain

$$\frac{d}{d\omega}\left(\angle\Gamma_n\right) = \frac{-2}{1+\lambda_n^2}\frac{d\lambda_n}{d\omega} \tag{K.9}$$

Due to Foster's reactance theorem (which is applicable now that we are considering a periodic structure with an infinite ground plane, i.e. a 1-port device), one expects the frequency derivative of the eigenvalue to always remain positive and hence the dispersion of the reflection phase must remain negative at all times. Notice also that when the mode is resonant (eigenvalue equal to zero) the dispersion of the reflection phase is twice the negative of the frequency derivative of the eigenvalue. Interestingly, this result is twice that of the freespace case, perhaps owing to the fact that this solution space only exists in a half-space as opposed to all of freespace, but this has not be explored rigorously.

Appendix L

Multi-Band Antenna Designs and Baluns

Near-field measurements were taken of the three prototype multi-band handheld antennas discussed in Chapter 4, Section 4.3.2. Figures L.1 – L.4 of this addendum show that the antennas in question do indeed require a balun, as pointed out by Examiner A, due to the balanced feed assumed in simulation and the use of an unbalanced excitation using a coax cable in experiments. This is shown to be the case through undesired radiation from the cable regions of the antennas.

It is shown that beginning with Design #1 towards Design #3, the cable radiation decreases, with Design #3 showing minimal cable radiation. These results are further supported with the measured S-parameters (Fig. 4.27 – 4.29 from the thesis) given that Design #3 experimental measurements and simulated data show a more favourable comparison in contrast to Designs #1 and #2.

A possible solution for all three design examples would be to drill a hole in the partial ground plane, have the outer conductor shorted to said ground plane and thus have the centre conductor pass through the drilled hole and shorted to the other side of the destined gap where excitation must occur (as would be the case for any antenna making use of a large ground plane). Other possibilities include using a surface mount discrete balun (transformer), an RF choke (using ferrites) and possibly designing a coax transition region where the outer conductor is tapered to facilitate the unbalanced-to-balanced transformation

A. Design #1: 700 MHz Single-band Design

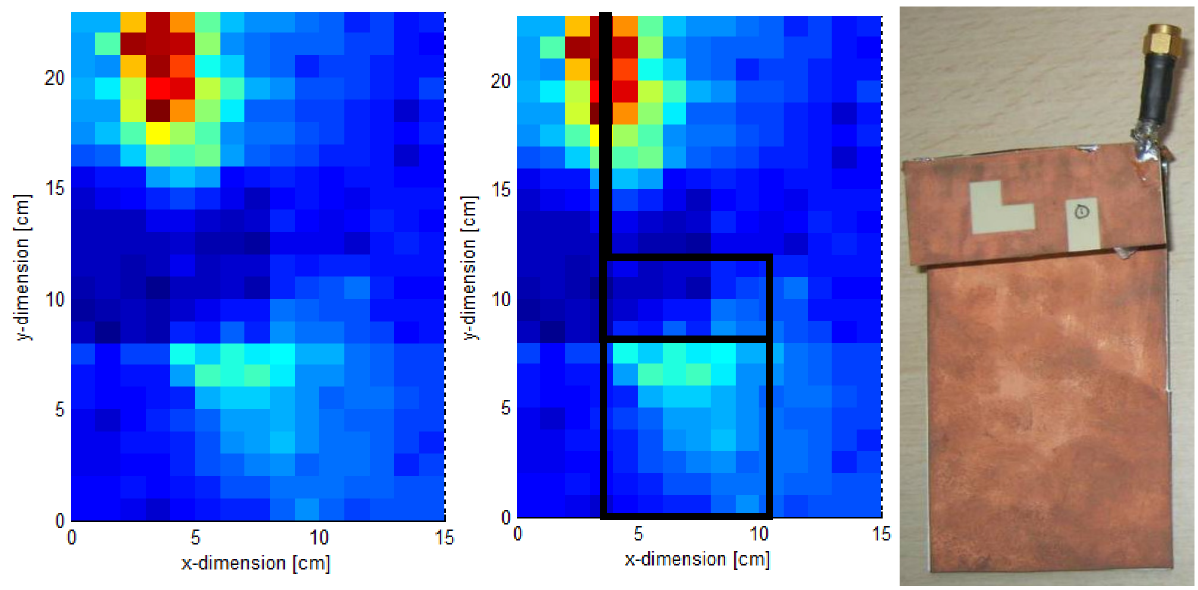

(a) (b) (c)

Figure L.1 – Near-field measurement of design 1 at 700 MHz (single band, 700 MHz) with near-field measurement field intensity shown in (a) and again with the antenna and feeding cable shown overlaid and (c) photograph of the actual antenna. There is significant radiation from the cable regions. This design is in dire need of a balun!

B. Design #2: 700 / 1900 MHz Dual-Band Design

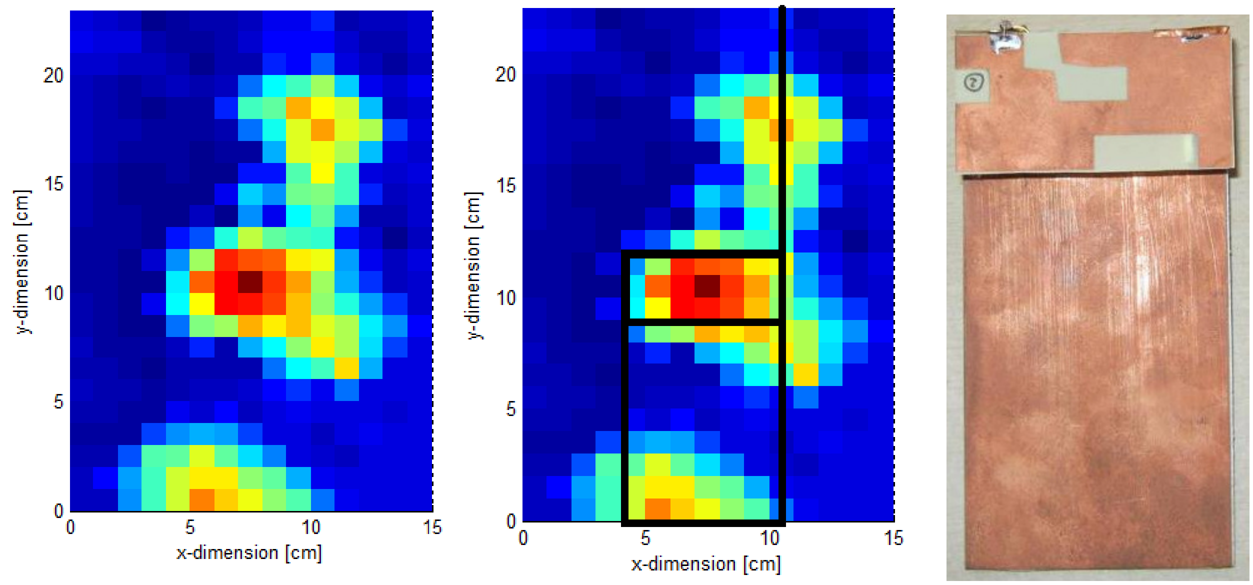

(a) (b) (c)

Figure L.2 – Near-field measurement of design 2 at 1900 MHz (dual band, 700 and 1900 MHz) with near-field measurement field intensity shown in (a) and again with the handheld and feeding cable shown overlaid and (c) photograph of the actual antenna. There is radiation from the cable, "antenna" and ground plane regions. This design is in need of a balun, but the situation is not as dire as the previous example!

C. Design #3: 700 / 1525 / 2500 MHz Tri-Band Design

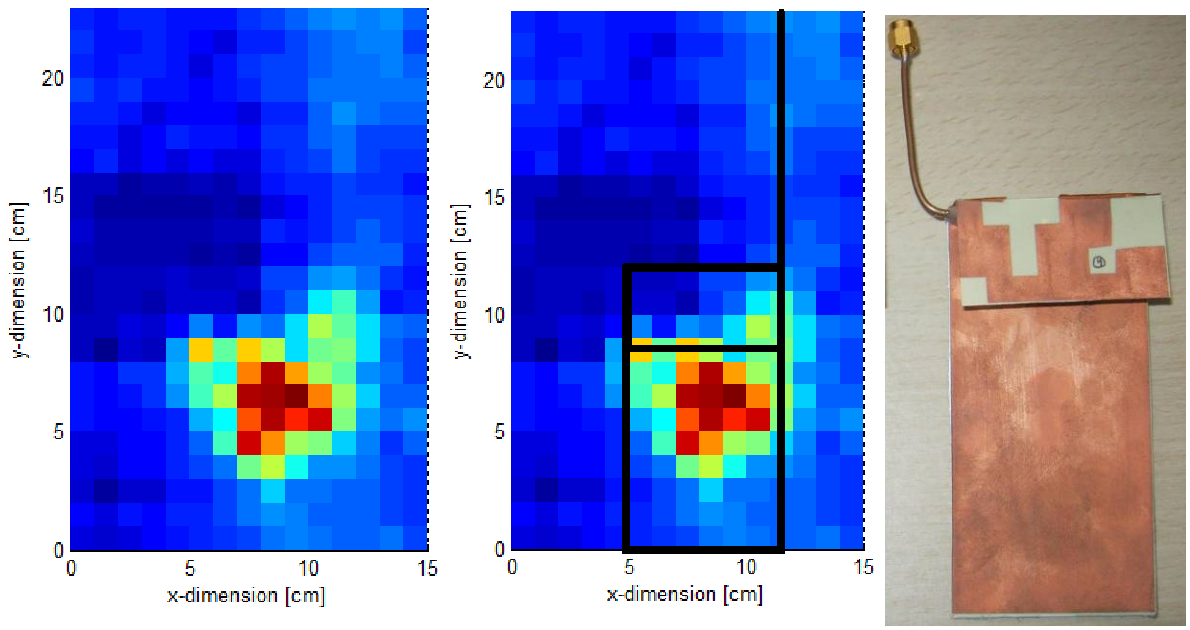

(a) (b) (c)

Figure L.3 – Near-field measurement of design 3 at 700 MHz (tri band, 700, 1525, 2500 MHz) with near-field measurement field intensity shown in (a) and again with the antenna and feeding cable shown overlaid and (c) photograph of the actual antenna. There is very little radiation from the cable, with the majority coming from the "antenna" and ground plane regions.

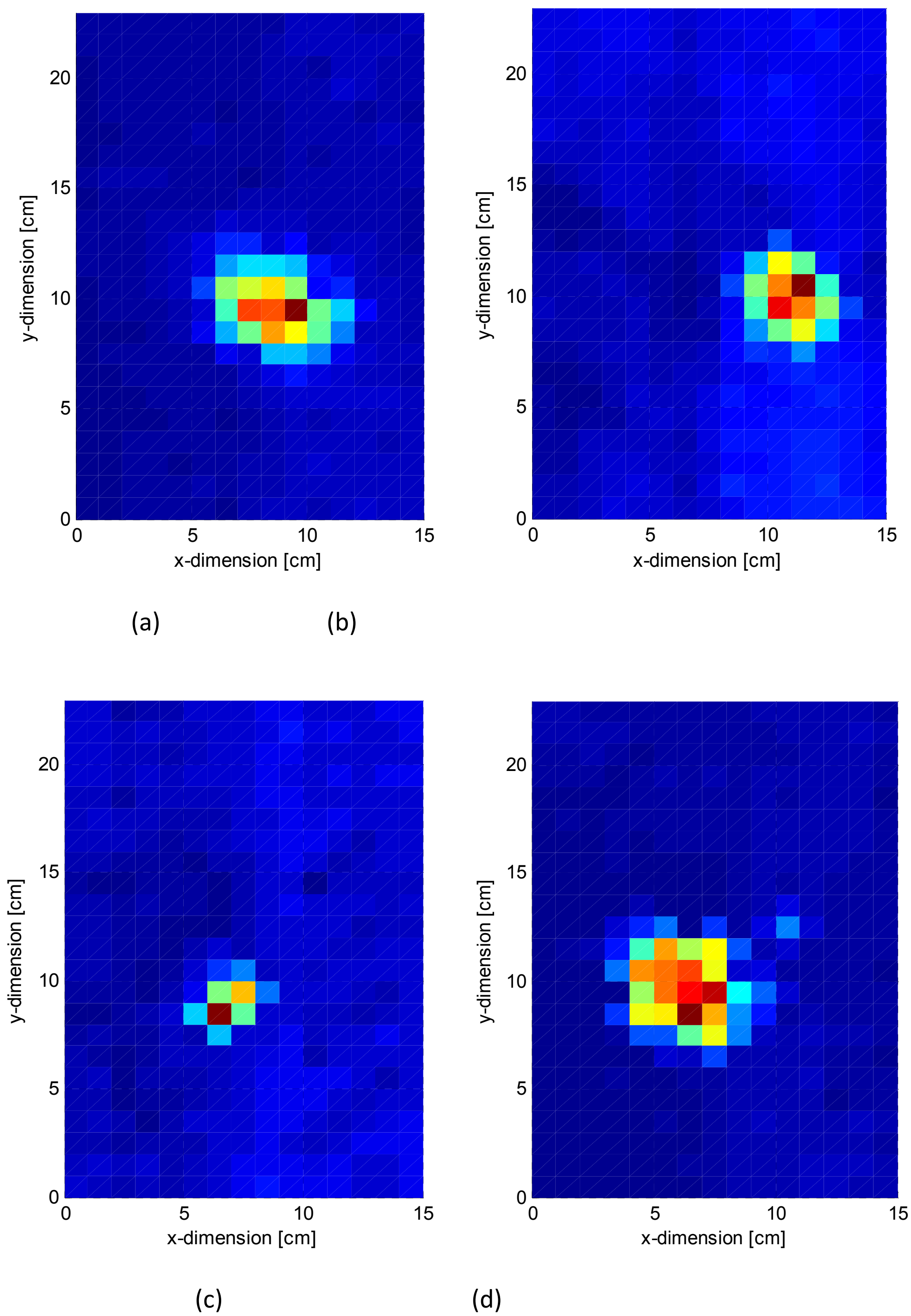

Figure L.4 – Near-field measurement of design 3 at (a) 1200, (b) 1525, (c) 2000 and (d) 2500 MHz. There is very little (if any) radiation from the cable at these four additional frequency points, with the majority coming from the "antenna" regions for these higher frequencies.

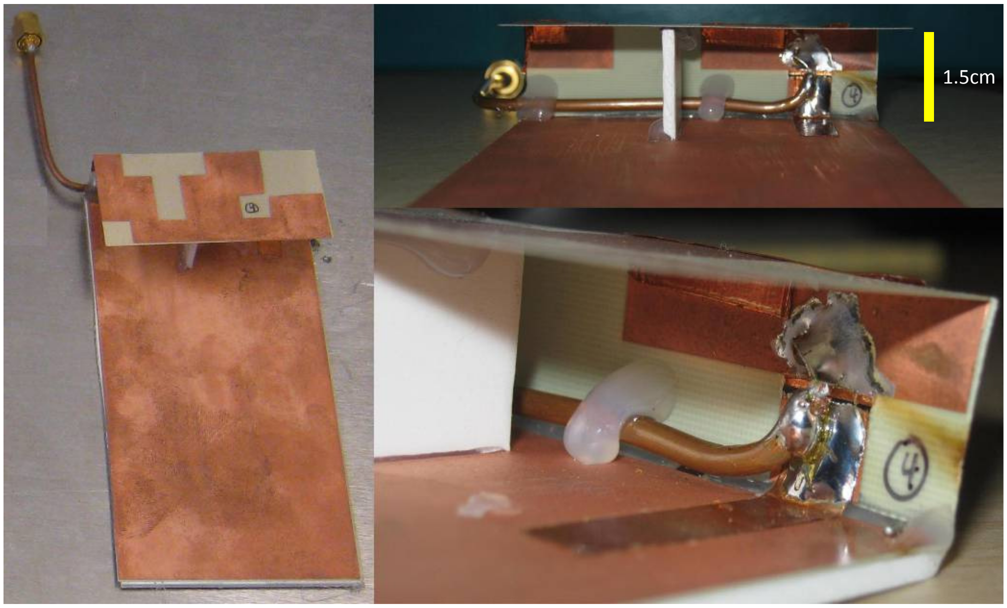

Figure L.5 – Design 3 appears to perform better than Design 1 & 2 because the design makes use of the finite (partial) ground plane and acts to “self-balun” the design. This unbalanced-to-balanced connection does not have the greatest finesse, but certainly improves over the other designs.

In order to emphasize these results further, consider Design A and C from the thesis, Appendix E. Design A is shown in Figure L.6c, where the coaxial connector and its outer conductor connects to half of the antenna, while the center conductor connects to the remaining half of the antenna. The near-field measurement in Figure L.6a and L.6b (antenna overlaid) emphasize that the entire antenna radiates, with very little field intensity surrounding the cable region. This antenna would appear to be fairly well fed in an unbalanced-to-balanced manner[18]. On the other hand, Figure L.7c shows antenna Design C, which shows very strong field intensity surrounding the cable connection to the antenna. The cable in this example uses very little of the radiating structure to connect to the outer grounded conducting sheath of the coaxial cable and hence does not perform the unbalanced-to-balanced transition properly.

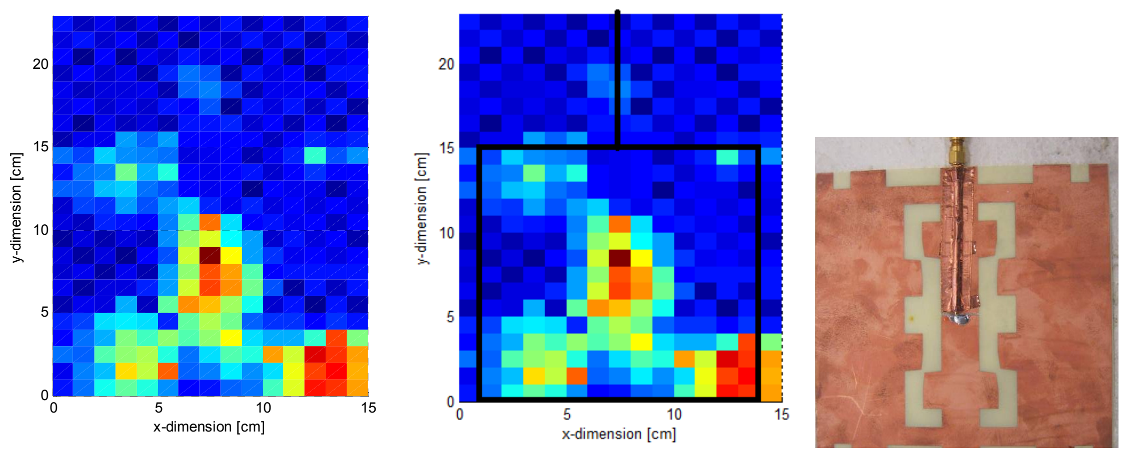

(a) (b) (c)

Figure L.6 – Near-field measurement of Design A shown in (a) with the antenna overlaid in (b) and a photo in (c).

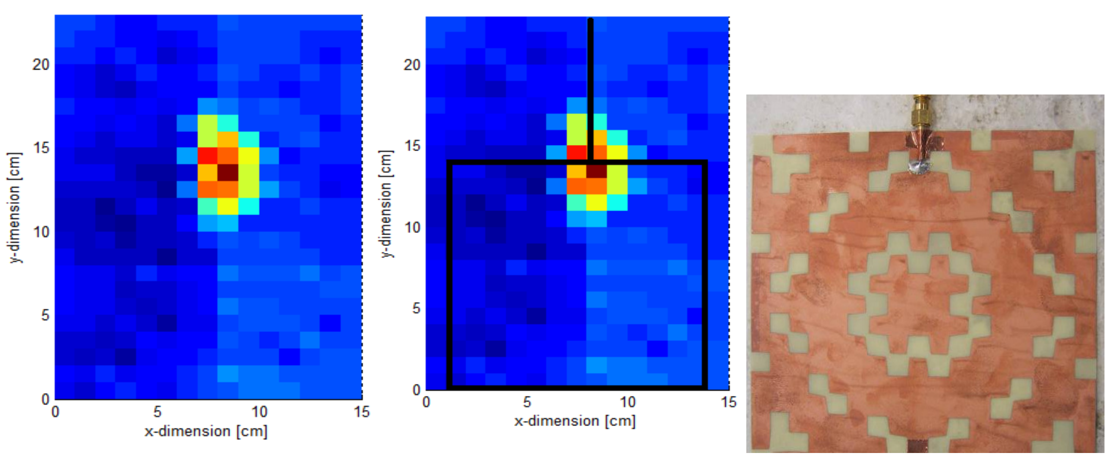

(a) (b) (c)

Figure L.7 – Near-field measurements shown in (a), antenna footprint overlaid in (b) and photo in (c).

[18] Examiner A noted that Design A (Fig. 6c) exploits a balun design approach known as a "Dyson Balun"